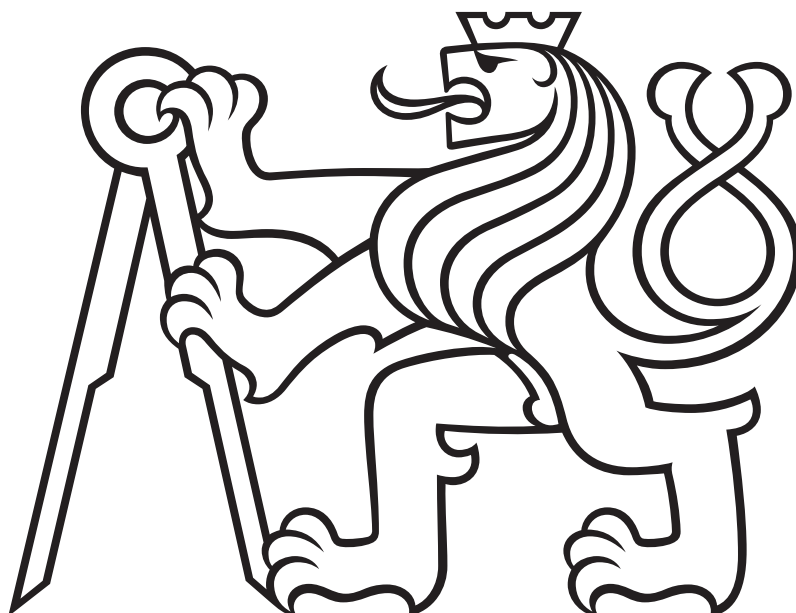


Czech Technical University in Prague
Faculty of Transportation Sciences
Department of Mechanics and Materials



**Advanced numerical methods
for modelling of elastic wave propagation
in solids and contact-impact problems**

Habilitation Thesis

Ing. Radek Kolman, Ph.D.

Prague
June 10, 2022

Copyright

The works presented in the habilitation thesis are protected by the copyright of *International Journal for Numerical Methods in Engineering*, *Wave Motion*, *Applied Mathematical Modelling*, *Mathematics and Computers in Simulation*, *Composite Structures* and *Applied Acoustics*, *Journal of Materials Research and Technology*. They are presented and reprinted in accordance with the copyright agreements with the respective publishers. Further copying or reprinting can be done exclusively with the permission of the respective publishers.

Acknowledgments

At the first, I would like to thank my friends and close collaborators for a long-time cooperation on the topics related to the habilitation thesis, manely to Prof. José González, Dr. Ján Kopačka, Dr. Arkadi Berezovski, Dr. Jiří Plešek, Dr. Dušan Gabriel, Dr. Alena. Kruisová, Ing. Michal Mračko, Prof. Ondřej Jiroušek, Dr. Tomáš. Fíla, Ing. Radim Dvořák, Dr. Robert Cimrman, Dr. Vítězslav Adámek, Dr. Jan Kober, Assoc. Prof. Jan Červ, Dr. Jan Trnka, Dr. Zdeněk Převorovský, Assoc. Prof. Ivan Němec, and Assoc. Prof. Anton Tkachuk.

Warm acknowledgments for long-time discussions on the issues of habilitation thesis and mentoring belong to Prof. K.C. Park and Prof. Miloslav Okrouhlík.

Memories devoted to the discussion on topics of related to the presented works also belong to Prof. Cyril Höschl.

Thanks is also given to my wife, children and parents for a long-time support of activities related to the habilitation thesis.

Abstract

This habilitation thesis summarizes relevant advancements in numerical modelling of elastic wave propagation in solids and contact-impact problems. The advanced numerical methods for accurate numerical wave modelling in solids and contact-impact modelling are presented to improve cardinal phenomena which pollute the numerical results as spurious oscillations of the stress field in the wave propagation, improve convergence rate for free vibration tasks, analysis of dispersion errors in the finite element modelling in explicit time schemes and avoid the stability trouble in the penalty-based dynamic contact-impact modelling with stabilization of contact force oscillations. On that topics, the author of the thesis worked for twelve years to improving standard numerical technologies in FEM which can be implemented into commercial software for dynamics, wave propagation and contact-impact problems.

The first Section presents the analysis of the **dispersive properties of the finite element method in elastic wave propagation**. The dispersive properties of plane square bilinear and biquadratic FEs are analyzed for the full spatial/grid discretization and also for the temporal-spatial semidiscretization with the explicit and implicit time integration. The higher-order FEM discretization via the spline-based shape functions is studied with intention to describe dispersion and effects of order and smoothness of the spline shape function are discussed with respect to the the dispersion behaviour.

The second Section summaries the activities in the area of the **advanced time stepping** for the finite element discretized equations of motions, the analysis of its accuracy and stability. The main attention is paid to diminishing the dispersion errors and spurious stress oscillations of the numerical results. **The partitioned longitudinal and shear wave algorithm** was found, implemented and tested. The spline based FEM together with several time explicit and implicit schemes are studied with respect to the spurious oscillations. Finally, the **heterogenous time stepping algorithm** for elastic wave propagation is presented. It is based on the localized Lagrange multipliers and solving of the interface problems without dissipation of the energy on the interfaces.

The third Section focuses on applications of the **finite element method in elastic wave propagation in layered and heterogeneous media**. The verification of the numerical results by the experimental and analytical approaches are presented. The applications of the FEM for time reversal tasks and in nondestructive testing of materials and structures are mentioned. The review of elastic wave propagation in 3D printed structures and identification of the residual stresses in bodies is introduced.

In the fourth Section, the advanced numerical methods based on higher-order FEM are presented. Mainly, the **isogeometric analysis applied into the free vibration problems** is shown with the discussion on convergence rate in eigen-value computations. The **direct inversion mass matrix - called reciprocal mass matrix - in free vibration problems** is mentioned and discussed.

The fifth Section focuses on the advanced numerical methods for modelling of the **contact-impact problems based on the bipenalty method** as an extension of the classical penalty method. On the numerical tests, the accuracy and stability of the nominated methods for contact-impact are summarized and commented for one-dimensional and two-dimensional problems.

The thesis finishes with the summary and comments of possible future works and today challenging directions for the studies in the areas of the thesis.

Contents

1	Introduction	11
2	Background	13
3	Dispersive properties of Finite element method	15
3.1	Dispersion errors of numerical methods	15
3.2	Grid dispersion of FEM	15
3.3	Temporal-spatial dispersion of FEM	17
3.4	Dispersion of spline-based FEM	19
3.5	Author's papers related to the section	20
4	Advanced time schemes in wave propagation	21
4.1	Time stepping for IGA	21
4.2	A time stepping for migimiting of spurious stress oscillations	21
4.3	Author's papers related to the section	23
5	Finite element method in elastic wave propagation tasks	25
5.1	Applications of FEM in elastic wave propagation	25
5.2	Author's papers related to the section	26
6	Finite element method in free-vibration problems	29
6.1	IGA in free vibration problems	29
6.2	Inverse mass matrix in free vibration and transient problems	29
6.3	Author's papers related to the section	30
7	Advanced methods for contact-impact problems	31
7.1	Bipenalty method in contact-impact problems	31
7.2	Author's papers related to the section	33
8	Conclusions and Future works	35
9	List of attached papers	44
10	Attached papers	46

1 Introduction

The finite element method has a long-time tradition in numerical modelling of physical and engineering tasks based on the ordinal and partial differential equations. Nowadays, the displacement based finite element method (FEM) is an accepted numerical method/approach for problems of solid mechanics including dynamics and nonlinear behaviour materials and their fracture. It is a standard issue that constructors and designers use the commercial software based on FEM and predict and estimate the mechanical behaviour and responses including lifetime of complex technical units as air-crafts, cars, satellites or others.

On the other side, we know that standard-usual FE approach in elastic wave propagation in solids and their impact problems are not fully developed with respect to numerical errors of the FEM, optimal accuracy and stability in elastic wave propagation and impact problems. For that reason, during the past 12 years, the author of the thesis paid attention to the improving the FEM approaches as a powerful, accurate and robust numerical tool for modelling of elasto-dynamic problems of solids and their contact-impact problems. It should be emphasised that contact-impact problems are highly non-linear and besides the elastic waves, the plastic waves also play a considerable role. Still, the elastic approach is the best first approximation to what happens later.

Solved scientific problems in the thesis are summarized as follows:

- analysis of dispersive properties of classical linear and quadratic FEM
- analysis of dispersive properties of higher-order/smooth FEM including spline-based approximation
- analysis of temporal-spatial dispersive properties of FEM in implicit and explicit time stepping
- suggestion of advanced time stepping for suppressing of dispersion errors in FEM with explicit direct time integration
- suggestion of explicit heterogeneous time stepping for suppressing the spurious stress oscillations in FEM for wave propagation in heterogeneous media
- applications of FEM for modelling of elastic wave propagation in solids, as in non-destructive areas, wave propagation in heterogeneous and 3D printed media
- improving FEM in free-vibration problems via the higher-order and smooth FE discretization and direct inversion of mass matrix called reciprocal mass matrix
- improving the penalty method in contact-impact problems via the bipenalty method due to the stability and accuracy of the time history of contact forces and their spurious oscillations.

The defined scientific questions and their solutions were published in several papers overviewed in this thesis. All mentioned items are presented and commented in the following Sections.

2 Background

The accurate, fast and robust numerical modelling of wave propagation and wave processes in solid bodies is a still important issue for real problems including non-destructive testing in civil and mechanical engineering, seismic problems, bio-mechanical or space applications together with impact problems. In this thesis we summarize the improving the finite element method in elastic wave propagation, transient and free-vibration problems and contact-impact problems of solids.

One important issue in usage of the finite element method in elastic wave propagation is its dispersive properties of this numerical method. It is known that the finite element method as a tool for the spatial and temporal discretization produces dispersive behaviors of the numerical model – the wave speed through a FE mesh depends on the frequency/wavelength of the propagating wave and the FE model behaves as a frequency filter. However, the continuum model of elastic wave propagation on an unbounded domain is non-dispersive. The dispersive properties of FEM are needed to analyze not only for the spatial discretization but also with the effect of the time discretization via the time stepping schemes. In the thesis, the temporal-spatial dispersive properties in explicit and implicit time methods are mentioned.

Generally, the dispersion of acoustic branches can be controlled by the higher-order discretization and smoothness of shape functions. For that reason, the spline-based shape functions were tested due to the dispersion errors. A modern approach in computational continuum mechanics is represented by the Isogeometric Analysis. This modification of FEM employs shape functions of different spline types as B-splines and NURBS, T-splines, etc. In addition, the IGA approach provides higher-order of continuity of the field of unknown quantities than that offered by FEM based on Lagrangian polynomials. This higher-order approximation really produces the better dispersion errors of the acoustic branches but they produce the optical branches as a by-side-effect of this approximation. The issue is also commented and summarized in the thesis.

In FEM modelling of wave propagation, the method of semidiscretization with direct time integration is generally applied. Often, the implicit and explicit direct time scheme are used. In this research, the attention has been paid to the improving of explicit time integration with respect to numerical dispersion and accuracy, mainly measured by the level of spurious oscillations of the stress field. Also the task of efficient inversion of mass matrix of consistent type has been studied, where the reciprocal mass matrix has been suggested in connection with the mass scaling for lower and higher-order FEM and IGA.

3 Dispersive properties of Finite element method

3.1 Dispersion errors of numerical methods

Dynamic non-stationary stress states and wave propagation occur in a variety of engineering problems such as non-destructive testing of materials, impact and shock loading of bodies, acoustic scattering, earthquake and seismic problems. Analytical modelling of stress wave propagation in bodies of complex geometries and with complicated material properties is practically impossible – that is why various numerical approaches in wave propagation tasks are used. Today, in the engineering applications, the finite element method is a dominant numerical approach but not alone, as the finite volume method, boundary element method and others can be used. The finite element method is often employed for the numerical solution of wave propagation in complex heterogeneous media. Spatial discretization by FEM ([1, 2, 3]) can easily approximate the boundaries of domain of interest and boundary conditions, accounting for complex material behaviour.

Generally, a suitable numerical method must be able to minimize numerical errors as attenuation or amplification, polarization errors, numerical anisotropy, error in phase and group velocities (dispersion), extraneous parasitic (spurious) modes, and numerical diffraction. It is possible to reduce these numerical errors by tuning the discretization of space and time and by a proper choice of numerical techniques. It is known that spatial discretization by FEM introduces so-called dispersion errors, which may be viewed as mere solution artefacts that do not actually exist in the continuum. The dispersion behaviour of FEM encompasses change of direction and wave speeds and, in general, affects the way of the wave propagating. Furthermore, the FEM mesh behaves as a frequency filter – not all the frequencies can be transmitted (Reference [4, 5]). The dispersive behaviour of media is characterized as a relationship between the wave speed of wave propagation and its frequency. Sometimes, the dispersion relationship is given as the function of wavelength. During wave motion in the dispersive media the wave with different frequencies/wavelengths propagates with different wave speed. It means the the pulse consists of several pulses with different frequencies is distorted due to the dispersion of each wave component.

3.2 Grid dispersion of FEM

The theoretical basis of the dispersion analysis related to FEM for the solution of hyperbolic partial differential equation was perhaps initiated in [6], where the Gibb's effect in the FEM solution was observed in the form of stress jump oscillations that did not vanish upon mesh refinement. Later on, the Fourier method (sometimes called the von Neumann method) was recognized as the dispersion analysis tool for hyperbolic partial differential systems (References [7]). A very simple and efficient approach to the complex wave numbers Fourier analysis of FEM is presented in Reference [8]. In 1973, Krieg and Key (Reference [9]) studied one-dimensional constant strain elements employed in the numerical solution of the one-dimensional Helmholtz equation. They discovered a hidden interrelation between the mass matrix approximation and temporal discretization. Belytschko and Mullen (Reference [10]) extended this dispersion analysis to higher order (quadratic) one-dimensional elements. It was shown that an optical branch in the spectrum existed. This notion refers to Brillouin's original text, in which the lowest characteristics were called the *acoustic* branches and the higher ones *optical* branches. The existence of optical modes accounts for the noise associated with the propagation of discontinuities. In that well-known study, the dispersion analysis revealed the 'stopping' bands in the frequency spectrum of biquadratic elements, whose corresponding solutions in the frequency range decayed exponentially.

Holmes and Belytschko (Reference [11]) showed numerically that an abrupt change of mesh size produced interior reflections, contributing to the propagation of spurious waves. Their magnitude was analytically estimated by Bažant and Celep in References [12]. The same authors subsequently proved

in Reference [13] that mesh grading (insertion of transition domain) did not provide much assistance, i.e. it could not absorb the spurious modes. One-dimensional Lagrangian and Hermitian elements were studied, along the same lines, by Okrouhlik and Höschl in Reference [14]. The response of the one-dimensional constant strain element mesh to the Heaviside loading was solved in Reference [15] and stress oscillations as well as the appearance of spurious waves were reported again. It was proved that the spurious oscillations could not be entirely removed but only partially eliminated. The intensity of such oscillations depends solely on the number of finite elements through which the elastic wave has passed. Generally, it depends on the frequency spectrum of the loading pulse.

Mullen and Belyschko (Reference [5]) extended the dispersion analysis to two-dimensional wave equation using bilinear elements, where the effects of mesh layout, mass approximation and underintegration were examined. In this work, the passing bands in dispersion spectrum have been detected for a plane mesh consisting of 3-node linear triangle finite elements. The mesh layout of different structured FE meshes from 3-node linear elements exert considerable influence on dispersion behaviour. Passing bands exist for two-dimensional or three-dimensional multi-mass-spring systems, for details see Reference [16]. The dispersion properties of triangular, rectangular and square finite elements, respectively, for two-dimensional domains have been determined and analyzed in References [17, 18]. Dispersion analysis of the three-dimensional second-order scalar wave equation (the three-dimensional Helmholtz equation) was carried out by Abboud and Pinsky in Reference [19]. The analysis was performed for trilinear rectangular 8-node elements, for triquadratic rectangular 27-node elements and for serendipity rectangular 20-node elements with the investigation of mass approximation to follow.

In the paper [20], the dispersive properties of square plane bilinear and biquadratic finite element have been studied. The dispersion relationships of a plane square biquadratic serendipity finite element are examined and compared with a bilinear one. Dispersion analysis is carried out for the consistent and lumped mass matrices. A dispersive 'improved' lumped mass matrix for biquadratic serendipity elements is proposed. The numerical dispersive solver for higher-order method has been suggested and implemented. This solver can be apply to arbitrary FE mesh and order of approximation.

The dispersion analysis of higher-order FEM provide also the higher order dispersion curves which are the product of higher order discretization. These higher curves correspond to the optical wave modes where the neighboring nodes vibrate in the opposite directions. Also for several wave propagation directions, the negative numerical group speeds have been observed. This effect is non-physical due to the spatial discretization via higher order FEM.

The paper [20] closes with the recommendation of a choice of permissible dimensionless wavelengths for bilinear and biquadratic serendipity finite element meshes. The mesh size is only one way how to control the dispersive behaviour of FEM solution obtained by the commercial softwares.

On the basis of this dispersion analysis, the mesh size (prescribed by the length of element edge H) with respect to the given wavelength of a propagating wave λ has been recommended for plane square bilinear and biquadratic serendipity finite elements. It was suggested to use uniform finite element meshes satisfying the following conditions for the transient elastodynamic analysis:

- $H \leq 20\lambda$ for bilinear square finite elements with the lumped mass matrix,
- $H \leq 10\lambda$ for biquadratic square finite elements with the lumped mass matrix,
- $H \leq 10\lambda$ for bilinear square finite elements with the consistent mass matrix,
- $H \leq 4\lambda$ for biquadratic square finite elements with the consistent mass matrix.

The appropriate mesh sizes for the given wavelength guarantee permissible dispersion errors and the accuracy of the numerical solution of elastodynamics transient problems. The suitable estimation of

λ_{min} could be set as $\lambda_{min} = c_2/f_{max}$, where f_{max} is the maximal loading frequency in [Hz] given by the character of external loading and c_2 is the speed of transverse wave in elastic media.

In the following Section, the effect of temporal discretization is mentioned.

3.3 Temporal-spatial dispersion of FEM

The time stepping produces the numerical damping and elongation/shortening of the time period of the response depended on the direct time integration method. For that reason it is needed that the temporal and spatial dispersive properties of the semidiscretized numerical method have to be taken into account together and the temporal-spatial dispersion relationships are obtained from the dispersion analysis including the spatial and temporal discretizations.

In principle, dispersion errors in FE computations are influenced by a choice of mass matrix, type of the time integration, its numerical parameters and, in addition by the time step size. It is known that some methods of direct time integration cause period elongation of pulse in time (Reference [1]). For certain choices of mass matrices and time integration methods, the dispersion and period elongation errors can suppress each other. It was shown for linear finite elements in one-dimensional problems that an optimal choice is based on the combination of the central difference method with the diagonal mass matrix and the Newmark method with the consistent mass matrix (Reference [5]). Also, the results of full (both temporal and spatial together) dispersion analysis of the Newmark method and the central difference method with the consistent as well as lumped mass matrices became known (Reference [10]). It was shown that the consistent mass matrix overestimates numerical wave speed, on the other hand, the diagonal mass matrix underestimates numerical wave speed. Based on these considerations, the Newmark method was recommended to be used with the consistent mass matrix, whereas the central difference method was identified as a suitable counterpart to mass lumping procedures.

In most FE commercial software, the central difference method (Reference [21]) as an explicit time integrator and the Newmark method (Reference [22]) as an implicit time integrator are often implemented. In general, the central difference method in time is combined with the diagonal mass matrix due to the efficient solution of equations of motion (Reference [23]). With respect to the efficient solution of the nonlinear dynamic problems, the linear shape functions in spatial discretization are employed in explicit time integration with one-point Gauss integration connected with the Hourglass stabilization (Reference [24, 23]). This combination of linear FEM, diagonal mass matrix and explicit time integration via the central difference method produces a suitable temporal-spatial dispersion effect on the numerical errors, (Reference [20]). The explicit time schemes in FEA are preferred for modelling of fast and shock responses of bodies and structures. Explicit methods with a diagonal mass matrix require a vector solver only, but mostly they are merely conditionally stable. Thus, the time step size must satisfy the stability limit, see References [24, 25].

Conversely, the Newmark method in the implicit form is recommended to be used with the consistent mass matrix (Reference [23]). Implicit computation needs a much larger computational effort per time step due to the solving a large system of linear algebraic equations, where the corresponding matrix of the linear problem is given by the linear combination of the mass matrix, damping matrix and linearized stiffness matrix (Reference [1]). In wave-like problems, the implicit time schemes are used with the consistent mass matrix due to suitable dispersion errors. However, implicit methods were derived and occur the unconditional stability for linear cases and then the time step size could be chosen rather freely based only on the characteristics of the physical problem to be solved. The implicit time schemes are employed in the numerical solution of lower and middle frequency response and mainly together with the higher-order finite element spatial discretization. Several variants of the Newmark family method have been studied in Reference [26] as the average acceleration method, the linear acceleration method, the Fox-Goodwin method as well as the central difference method. Overview

of the properties of these time schemes are mentioned in Reference [1]. Today, the generalized- α time scheme in the implicit time stepping (Reference [27]) is very popular due numerical damping and filtering effect of higher frequency spectra via the time stepping without extra post-processing techniques.

The full (both temporal and spatial together) dispersion analysis of the Newmark method and the central difference method with the consistent as well as diagonal mass matrices has been presented for 1D FEM in [10]. It was shown that the consistent mass matrix overestimates numerical wave speed, on the other hand, the diagonal mass matrix underestimates numerical wave speed. It was shown for linear finite elements in one-dimensional problems, that an optimal choice is based on the combination of the central difference method with the diagonal mass matrix and the Newmark method with the consistent mass matrix [5]. Dispersion analysis of FEM associated full temporal-spatial discretization was studied in [28].

The results of full (both temporal and spatial together) dispersion analysis of the Newmark method [22] and the central difference method [21] with both consistent and lumped mass matrix became known. It was shown that the dispersion relations for time integration numerical schemes were influenced by the magnitude of the time step. Based on these considerations, the Newmark method was recommended to be used with the consistent mass matrix, whereas the central difference method was identified as a suitable counterpart to mass lumping procedures making the diagonal mass matrix.

The work [29] presents the temporal-spatial (full) dispersion and stability analysis of plane square linear and biquadratic serendipity finite elements in explicit numerical solution of transient elastodynamic problems. In this paper, the grid dispersion analysis of plane square biquadratic serendipity finite elements from Reference [20] is extended to study of influence of time integration by the central difference method in connection with the diagonal mass matrix. The evaluation of the critical time step size with respect to stability (for whole class of permissible lumped mass matrices) was also studied. All obtained results are compared with those of square bilinear finite elements. The dispersion computation strategy is adopted from the paper [20]), where a lumping strategy for the quadratic serendipity FE has been proposed. We report on a computational strategy for temporal-spatial dispersion relationships, where eigenfrequencies from grid/spatial dispersion analysis are adjusted to comply with the time integration method. Moreover, the suggestion of an ‘optimal’ lumped mass matrix with respect to stability and good dispersion behaviour is reported. It should be noted that the continuous Galerkin formulation with Lagrangian shape functions (Reference [1]) is utilized in the paper [20].

In the paper [30], the temporal-spatial dispersive properties of plane square bilinear and biquadratic serendipity finite elements in implicit direct time integration of elastic wave propagation problems in solids are studied. In the time integration, the implicit methods of the Newmark type (the average acceleration method, the linear acceleration method, the Fox-Goodwin method) are employed and the close form for the dispersion temporal-spatial dependencies are found. Based on the temporal-spatial dispersion analysis, the mesh size and time step size are recommended for accurate modelling of elastic wave propagation in the implicit time simulations via the finite element method. The results of implicit temporal-spatial dispersion analysis as well as suitability of the ‘proper’ choice of the mesh size and time step size were illustrated on the two numerical problems.

Based on the temporal-spatial dispersion in implicit and explicit time integration and its stability analysis, respectively, presented in the papers [30] and [29], relationships suggesting the ‘proper’ choice of mesh size and time step size from knowledge of the loading spectrum are presented.

With respect to the temporal-spatial dispersion analysis of plane bilinear and biquadratic serendipity FEs in the explicit time integration used for transient elastodynamics and wave propagation analysis, we suggest using *uniform* finite element meshes (H) and time step sizes (Δt) satisfying the following conditions [29]:

- for the time step size given by $\Delta t = H/c_1$ - for linear FEM
- for the time step size given by $\Delta t = 0.2H/c_1$ - for biquadratic FEM

where c_1 marks the wave speed of longitudinal wave.

Following, the time step size is recommended to use with respect to the temporal-spatial errors for the Newmark method and consistent mass matrix [30]:

- $\Delta t = H/c_1$ - for bilinear FEM
- $\Delta t = 0.5H/c_1$ - for biquadratic FEM

In this case, we set the numerical parameters of the FE model so that the temporal-spatial errors are smaller than 1%.

3.4 Dispersion of spline-based FEM

Another approach for improving FEM dispersion properties is based on a choice of completely different shape functions than the Lagrangian interpolation polynomials. Shape functions in the form of Legendre polynomials (hp-version of FEM) and hierarchic Fourier functions (Reference [8]), Chebyshev polynomials (References [31, 32]), B-splines (Reference [7]) or NURBS (non-uniform rational B-splines) (References [33, 34]) are considered.

A modern approach to computational continuum mechanics is the Isogeometric Analysis (IGA) [35], taking its inspiration from Computer Aided Design (CAD). This modification of FEM employs shape functions of splines (for examples, B-splines, NURBS–Non-Uniform Rational B-spline, T-splines and others). The advantage of spline-oriented FEM is that geometry and approximation of the field of unknown quantities are prescribed by the same technique. Another benefit is that the approximation is smooth with a higher order of continuity and also some 2D and 3D geometries could be precisely described [36]. IGA aims at integrating FEM ideas in CAD systems without the necessity of generating new computational meshes as required by the conventional FEM.

It has been shown that IGA produces optimal convergence rate and dispersion properties in elastodynamics problems [33, 34]. B-spline based FEM exhibits small dispersion errors in wave propagation in an one-dimensional unbounded elastic medium [7, 34]. It has also been shown that the higher *optical* modes did not exist and, subsequently, dispersion errors were reported to decrease with the increasing order of B-spline shape functions [33, 34]. IGA improves the dispersion errors and frequency spectrum in the comparison to higher-order Lagrangian finite elements. This can be ascertained from the fact that B-spline basis functions are uniform (homogeneous) for a uniform knot vector. This means that constituent basis functions are the same, but they are moved in the parametric space with an identical distance [36]. For this reason, equations of motion are repeated and the discretized medium subsequently produces a low level of dispersion errors with no stopping bands [34]. On the other hand, the high order of continuity of B-spline basis functions generates not only propagating waves, but also evanescent waves with a pure imaginary wavenumber. With respect to the high level of attenuation of evanescent waves, the IGA numerical solutions are not being polluted by these waves [34]. Generally, the B-spline or NURBS basis functions for bounded domains are not uniform [36]. For this reason, the non-homogeneity of basis functions close to the boundary of the domain produces the dispersion and attenuation behaviour.

Based on an extensive study of the literature, it has been opted to contribute to the subject with a complex wavenumber Fourier analysis of the B-spline based FEM in elastic wave propagation through a 1D infinite domain divided into segments with the C^0 connection, see [37]. The main attention

of the dispersion analysis is devoted to the study of influence of the C^0 continuity between spline segments and also of parameterization inside the B-spline segments. It was shown for the higher-order B-spline based FEM, that the optical modes did not occur in the case of infinite domains, unlike the higher-order Lagrangian and Hermitian finite elements, and also the dispersion errors are smaller. The paper's main focus [37] is the wave propagation through B-spline multi-patch/segment discretization with the C^0 connection of B-spline segments and, chiefly, to the determining of dispersion and attenuation dependencies. The numerical optimization process employed leads to substantial minimization of dispersion errors by the choice of parameterization. Furthermore, the errors decrease with the increasing order of the B-spline elements/segments, with the local refinement, and also by the particular choice of the positions of control points through the optimizing procedure.

3.5 Author's papers related to the section

- [20] **R. Kolman**, J. Plešek, M. Okrouhlík, D. Gabriel. Grid dispersion analysis of plane square bi-quadratic serendipity finite elements in transient elastodynamics, *International Journal for Numerical Methods in Engineering*, Vol. 96(1), pp. 1–28, 2013. (IF=2.056). <https://doi.org/10.1002/nme.4539>
- [29] **R. Kolman**, J. Plešek, J. Červ, M. Okrouhlík, P. Pařík. Temporal-spatial dispersion and stability analysis of finite element method in explicit elastodynamics, *International Journal for Numerical Methods in Engineering*, Vol. 106(2), pp. 113–128, 2016. (IF=2.055). <https://doi.org/10.1002/nme.5010>
- [37] **R. Kolman**, J. Plešek, M. Okrouhlík. Complex wavenumber Fourier analysis of the B-spline based finite element method, *Wave Motion*, Vol. 51(2), pp. 348–359, 2014. (IF=1.467). <https://doi.org/10.1016/j.wavemoti.2013.09.003>

4 Advanced time schemes in wave propagation

4.1 Time stepping for IGA

In the previous section, the dispersion analysis of IGA has been mentioned and actually, the numerical solution of wave propagation based on FEM is realized together with direct time integration. The basic using of the direct time integration methods in FEM, as the central difference method and Newmark's family method have been commented in the previous section, as well as the standard setting of mass matrix connected to explicit and implicit time method and limits on the time step size.

Now, we will mention the properties of higher-order FEM connected to direct time integration and dissipative time stepping methods, mainly in the explicit time computations. In principle, non-physical higher vibration modes occur in frequency spectrum of higher-order FEM [10, 20, 37, 38] and of IGA on multipatches with C^0 continuity [37]. Therefore time integration methods should be derived in such a way that the dissipation of higher frequencies is optimal and minimized for the low frequency spectra. Attempts to do so are presented by the Hilber-Hughes-Taylor (HHT- α) method [39, 40] or the generalized- α method [41, 27]. Implicit time integration schemes are preferred in higher-order FEM and in IGA [35]. In the case of explicit time integration, the presence of high frequency modes in the spectrum causes fragility of higher-order elements and spline based FEM regarding numerical stability condition for the setting of time step size. The two-time step method for application for higher-order FEM and IGA has been presented in [42].

In order to take advantage of IGA approach in explicit dynamics, one uses a lumped mass matrix formulation. Due to positive values of spline shape functions, all the terms of the consistent mass matrix in the Galerkin approximation method are also positive. Thus, the 'row-sum' technique [1] for the lumped mass matrix in IGA can be employed. The lumped mass matrix losses the second-order accuracy of IGA in higher modes [35]. One way how to overcome the lumping issue in IGA is to provide explicit predictor/multi-corrector algorithms as described in [43, 1, 44]. Here, the lumped or consistent mass matrix is used for the 'left-hand-side' matrix and the consistent mass is used in calculation of the 'right-hand-side' residual vector.

In the paper [45], several time scheme have been tested in connection with the B-spline higher order discretizations. Here, the accuracy of stress distributions and spurious oscillations of the B-spline based FEM are studied in numerical modelling of one-dimensional propagation of stress discontinuities in a bar, where the analytical solution is known. For time integration, the Newmark method, implicit form of the generalized- α method, the central difference method and the predictor/multi-corrector method are tested and compared. The use of lumped and consistent mass matrices in explicit time integration was discussed. Accuracy considerations lead to the conclusion that, the consistent mass matrix is preferred in explicit time integration in IGA.

4.2 A time stepping for migimiting of spurious stress oscillations

In the FEM modelling of wave propagation, fast response problems and shock problems, the explicit direct time schemes are preferred. The most used explicit methods in FEM are summarized here: the central difference method [21, 9], the Trujillo method [46], the Park variable-step central difference method [47], the Chung and Lee method [48], the explicit form of the generalized- α method [41], the Zhai method [49], the Tchamwa-Wielgosz method [50], the explicit predictor-multicorrector method [1], the Krenk method [51], the Tamma *et al.* method [52, 53], the Idesman method [54], the Chang pseudo-dynamic method [55], the multi-time step (KCP) Park method [56, 57], the two-time step Bathe method [58] and other second- or higher-order accuracy explicit methods could be mentioned [59]. The comparative study of numerical explicit time integration algorithms for impact problems has been presented in [60, 61].

Dissipative explicit methods, for examples the Tchamwa-Wielgosz method, the generalized- α method in the explicit form or the Chang method, are often used due to reduction of spurious oscillations induced by dispersion behavior of spatial and time discretization. Unfortunately, in this case, a part of total energy is lost due to numerical dissipation. The effect of numerical damping and dissipation of spurious oscillations in explicit computations has been studied in [62]. One way, how to partially reduce spurious oscillations without additional numerical dissipation, is application of multi-time step methods, time sub-cycling methods [59, 63, 64]. Presently, heterogeneous and asynchronous time integrators [65, 66, 67] and variational time integrators [68, 69] are very popular in structural dynamics and these approaches have got a big potential for application in wave propagation problems involving different time step sizes and different time integrators on different domain.

For the reason mentioned in the previous section, the local time stepping method connected to push-forward method has been developed, see [70]. The standard explicit time scheme in finite element analysis is not able to keep accuracy of stress distribution through meshes with different local Courant numbers for each finite element. The used two-time step scheme with the diagonal mass matrix is based on the modification of the central difference method with pullback interpolation. Using this approach, the dispersion behaviour of linear FEM is suppressed with minimal level of dissipation of energy [70]. A numerical example of one-dimensional wave propagation in a bimaterial elastic bar has shown the quality of time stepping process. Based on numerical tests, the employed time scheme with pullback interpolation and local stepping technique is able to eliminate spurious oscillations in stress distribution in numerical modelling of shock wave propagation in heterogeneous materials [70]. The method has been extended for explicit asynchronous time stepping with different time step for each domain [71].

In nature, many types of waves propagating in solids are observed as longitudinal and shear waves, surface Rayleigh's waves, Lamb's waves, Love's waves, von Schmidt's waves and others. We know from the theoretical prediction of multi-dimensional wave propagation in unbounded continuum that longitudinal and shear waves propagate with different speeds [72]. Therefore, the mismatch in the wave speeds of these two types of wave components produces spurious oscillations in numerical solution by FEM with direct time integration. Further, in computations using the central difference method as in one-time step scheme, the stability limit is given by the fastest propagating wave – longitudinal wave. This explains why the shear waves cannot be integrated as accurately as the longitudinal waves by an one-time step scheme. This is the main disadvantage of the central difference method employing in multi-dimensional wave propagation problems in solids. Moreover, we have also to take into account anisotropy of grid dispersive behavior of FEM in unbounded domains [20, 73] and in a Rayleigh's wave propagating along stress-free boundaries [74].

Suppression and diminishing of spurious oscillations in finite element simulations of discontinuous wave propagation in solids for multidimensional tasks is still an current open problem to be studied. A suggestion of time integration scheme based on partitioned shear and longitudinal wave equations, where these partitioned equations of motion are integrated separately with individual CFL stability limits [75], were presented in [57] and extended with effective implementation in [76]. It is possible to mitigate temporal-spatial dispersion errors and spurious oscillations resulting dispersion behavior of finite element method. The equations of motion are decomposed on the element-by-element level as application of decomposed operators on elemental forces. Then, we use the pullback interpolation formula for evaluation of longitudinal and shear displacement fields at the same time level. After that, the sum of the partitioned longitudinal and shear displacement fields is employed as a predictor for the central difference computation by the stable time step size. The partitioned wave time scheme is presented in depth in a predictor-corrector form as a modification of the originally published four-time step version in [57]. In [76], the three-time step version in the predictor-corrector form is presented with a detailed step-by-step flowchart. By this modification of the presented time scheme, the computational time is reduced by 25% with holding the same order and accuracy of computations as the original

version of the partitioned wave time scheme [57].

The present three-time step integration method [76] has been completely explicit with a diagonal mass matrix requirement, of second-order accurate, conditionally stable and has a minimal sensitivity behavior on the time step size satisfying the stability limit [76]. Moreover, the new presented three-time step scheme gives the same results as previous version [57]. Linear 4-noded quadrilateral and 8-noded hexahedral one-point integrated finite elements are then preferred option to model solid components, avoiding detrimental volumetric locking under nearly incompressible dynamic behavior. This paper describes how to apply the shock-capturing algorithm to the partitioned equations of motion and how to implement it in a predictor-corrector form into standard finite element codes. The algorithm was implemented into an open research code *Tahoe*. The partitioned wave method has been extended into heterogeneous explicit multi-step time integration for discontinuous elastic stress wave propagation in heterogeneous solids [77].

4.3 Author's papers related to the section

[45] **R. Kolman**, M. Okrouhlík, A. Berezovski, D. Gabriel, J. Kopačka, J. Plešek. B-spline based finite element method in one-dimensional discontinuous elastic wave propagation, *Applied Mathematical Modelling*, Vol. 46, pp. 382–395, 2017. (IF=2.291). <https://doi.org/10.1016/j.apm.2017.01.077>

[76] **R. Kolman**, S.S. Cho, K.C. Park. Efficient implementation of an explicit partitioned shear and longitudinal wave propagation algorithm, *International Journal for Numerical Methods in Engineering*, Vol. 107(7), pp. 543–579, 2016. (IF=2.100). <https://doi.org/10.1002/nme.5174>

[77] S.S. Cho, **R. Kolman**, J. González, K.C. Park. Explicit multistep time integration for discontinuous elastic stress wave propagation in heterogeneous solids, *International Journal for Numerical Methods in Engineering*, Vol. 118, pp. 276–302, 2019. (IF=2.746). <https://doi.org/10.1002/nme.6027>

[70] **R. Kolman**, J. Kopačka, A. González, S.S. Cho, K.C. Park. Bi-penalty stabilized technique with predictor-corrector time scheme for contact-impact problems of elastic bars. *Mathematics and Computers in Simulation*, Vol. 189, pp. 305–324, 2021. (IF=2.463). <https://doi.org/10.1016/j.matcom.2021.03.023>

[71] R. Dvořák, **R. Kolman**, T. Fíla, J. Faltá, K.C. Park. Explicit asynchronous time scheme with local push-forward stepping for discontinuous elastic wave propagation: One-dimensional heterogeneous cases and Hopkinson bar experiment, *Wave Motion*, submitted, 2022. (IF=2.02).

5 Finite element method in elastic wave propagation tasks

5.1 Applications of FEM in elastic wave propagation

The elastic wave propagation in solids has potential applications in several branches in engineering as nondestructive testing in civil and mechanical engineering, biomechanics, aircraft, and space applications. One task in that area is to understand wave processes in solids under dynamic, shock, and impact loading of bodies and predict the critical value of loading reaching the material limit. In this case, understanding the stress concentration around geometrical discontinuities and cracks including the wave interactions is an important part of studies in wave propagation. The second one lies in the interaction of waves inside the bodies producing the internal stress intensity for potential internal plastic or fracture zones as hidden defects in the bodies. The third application pays attention to non-destructive testing, acoustic emission, time-reversal technique, and ultrasound method for detection of cracks and defects via wave propagation phenomenon. The fourth one of applications is controlling of wave processes, wave interaction, and scattering in the meaning of acoustic lens or space-time materials for modulation of wave processes in solids. With today high-technologies for manufacturing including multi-material 3D printing of metals and meta-materials, it is possible to manufacture a body with arbitrary multi-material distribution inside the body. By this material distribution, one can control/attenuate/amplify the stress intensity and/or kinetic energy passing through the area of interest. For all that applications, robust, accurate, and stable numerical solvers are needed to use and/or develop for analysis and predicting of wave processes inside the elastic bodies with strong material heterogeneities for possible applications. Residual stresses after production is a important issue which affect the lifetime of bodies and non-controllable deformation. Residual stresses are prone to appear in any production technique, which remain a challenge to be measured. Among nondestructive testing techniques, acoustic and ultrasonic waves remain widely used to determine stresses, voids and defects in a wide array of parts. In [78], ultrasonic testing is highlighted as an alternative for measuring residual stress both during and after fabrication.

The promising application of computational wave propagation in a digital twin in identification and localization cracks via the acoustic emission and refocusing of waves. The time reversal uses the reversibility property of wave propagation to focus the energy to the original source location in space and time. If the original source is very local, then this procedure is called refocusing. In [79], there is a study of the accuracy and robustness of the computational time reversal approach based on the explicit finite element method for application in nondestructive testing in solids. In practice, the process of localization is accomplished in two steps. The first step, based on forward propagation, is measuring on a real structure. In the second step, the measured signals are reversed in time and transmitted to the computational model, where based on back propagation, energy is focused into the location of the original source. Generally, one works only with partial information (incomplete data from sensors), since it is not possible to record response signals in the whole structure. There are two approaches of performing effective refocusing using TR method. The first one is using a substantial number of transducers in combination with short record (and computational) time, the second one is the exact opposite – using only one or several transducers combined with long record times. The second approach exploits reflections from structure boundaries which are compensating a lack of the direct information, altogether creating a virtual time-reversal mirror. For numerical modeling of frontal (forward) and reverse (backward) problems of elastic wave propagation, we use the finite element method and explicit time integration with the lumped mass matrix. A special attention is paid to prescription of boundary conditions/loading for the reverse problem for accurate reconstruction of time history of the original source. Based on several numerical tests, effects of prescription of boundary conditions/loading in time reversal, effect of mesh size and time step size, a shape of domain of interest, a number of sources, and noise on the correctness of reconstruction of the original source have been shown.

Using the FEM in elastic wave propagation in heterogeneous media, as layered structures with different layering, has been commented with the analysis of numerical dispersion of pulse in [80]. Here, the finite element method and the finite volume method have been applied in parallel for the simulation of a pulse propagation in periodically layered composites beyond the validity of homogenization methods. The direct numerical integration of a pulse propagation demonstrates dispersion effects and dynamic stress redistribution in physical space on example of a one-dimensional layered bar. Analytical solution as well as numerical computations showed the strong influence of the composition of constituents on the dispersion of a pulse in a heterogeneous bar and the equivalence of results obtained by two numerical methods – finite element method and the finite volume method. In [81], wave propagation in a two-layer composite strip is investigated analytically and numerically. The strip is loaded by a very short transverse stress pulse. Three cases of the strip problem are assumed: (i) isotropic aluminum *Al* strip and two-layer strips made of (ii) *Al* and the ceramics Al_2O_3 and (iii) the ceramics Al_2O_3 and *Al*. The analytical method is based on Laplace and Fourier transform. The in-house finite element algorithm and thermodynamic consistent finite volume scheme are employed for computations, while the explicit time stepping procedure is used in both cases. The comparison of analytical and numerical results determines the degree of the accuracy of calculations, which is important for simulation of complex wave propagation problems in general heterogeneous media. In [82], two-dimensional wave propagation in an aluminium strip has been examined experimentally, analytically, and numerically. The main question is the suitability of numerical procedures to represent the transient wavefield observed in the experiment. It was demonstrated that standard finite volume and finite element algorithms conform analytical results and the numerical results are in a good agreement with experiment for time observation including several wave reflections from upper and bottom boundaries. The experimental, analytical, and numerical results presented in this study can be used as a benchmark data for the investigation of transient waves in a two-dimensional elastic medium to validate other numerical or semi-analytical methods.

5.2 Author's papers related to the section

[79] M. Mračko, J. Kober, **R. Kolman**, Z. Převorovský, A. Tkachuk, J., Plešek. Finite element method based computational time reversal in elastodynamics: Refocusing, reconstruction and its numerical sensitivity, *Mathematics and Computers in Simulation*, Vol. 189, pp. 163–190, 2021. (IF=2.463). <https://doi.org/10.1016/j.matcom.2020.11.004>

[80] A. Berezovski, **R. Kolman**, M. Berezovski, D. Gabriel, V. Adámek. Full field computing for elastic pulse dispersion in inhomogeneous bars, *Composite Structures*, Vol. 204, pp. 388–394, 2018. (IF=4.101). <https://doi.org/10.1016/j.compstruct.2018.07.055>

[81] V. Adámek, A. Berezovski, M. Mračko, **R. Kolman**. A two-layer elastic strip under transverse impact loading: Analytical solution, finite element, and finite volume simulations. *Mathematics and Computers in Simulation*, Vol. 189, pp. 126–140, 2021. (IF=2.463). <https://doi.org/10.1016/j.matcom.2020.10.007>

[82] M. Mračko, V. Admek, A. Berezovski, J. Kober, **R. Kolman**. Experimental, analytical, and numerical study of transient elastic waves from a localized source in an aluminium strip. *Applied Acoustics*, Vol. 178, pp. 107983, 2021. (IF=2.440). <https://doi.org/10.1016/j.apacoust.2021.107983>

[78] R. Acevedo, P. Sedlák, **R. Kolman**, M. Fredel, Residual stress analysis of additive manufacturing of metallic parts using ultrasonic waves: State of the art review, *Journal of Materials Research and*

Technology, Vol. 9(4), pp. 9457–9477, 2020. (IF=5.289). <https://doi.org/10.1016/j.jmrt.2020.05.092>

6 Finite element method in free-vibration problems

6.1 IGA in free vibration problems

It is well known in FEM modelling of eigen-vibration problems, that the higher-order FEM produces better accuracy and larger convergence rate than the linear FEM. There is a relation between order of shape functions and rate of convergence of eigen-values (eigen-frequencies) of dynamic problems [1]. Also we know that the values of eigen-frequencies for the consistent mass matrix converge from above [1].

The paper [38] is devoted to numerical solution of free vibration problems for elastic bodies of canonical shapes by means of a spline based finite element method – Isogeometric Analysis. It has an advantage that the geometry is described exactly and the approximation of unknown quantities is smooth due to higher-order continuous shape functions. IGA exhibits very convenient convergence rates and small frequency errors for higher frequency spectrum. In this paper, the IGA strategy is used in computation of eigen-frequencies of a block and cylinder as benchmark tests. Results are compared with the standard FEM, the Rayleigh-Ritz method and available experimental data. The main attention is paid to the comparison of convergence rate, accuracy, and time-consuming of IGA against FEM and also to show a spline order and parameterization effects. In addition, the potential of Isogeometric Analysis in resonant ultrasound spectroscopy measurements of elastic properties of general anisotropy solids is discussed.

6.2 Inverse mass matrix in free vibration and transient problems

In several applications, the having the inversion of mass matrix is a helpful tool. For example, the explicit time integration needs the evaluation of accelerations from the equation of motion [1]. We can evaluate them as

$$\ddot{\mathbf{u}} = \mathbf{M}^{-1} (\mathbf{r} - \mathbf{B}\boldsymbol{\lambda}) \quad (1)$$

where \mathbf{r} is the residual force vector and the term $\mathbf{B}\boldsymbol{\lambda}$ corresponds to the reaction force due to the constraints. When we use the diagonal mass matrix, the inversion of the mass matrix is trivial, but not in the case of consistent mass matrix or employing mass scaling. Note, the inversion of band type mass matrix with off-diagonal terms is fully filled. The inversion of sparse and off-diagonal mass matrix gives the full matrix and for that reason the simple inversion is not possible to use. In the paper [83], the reciprocal mass matrix as the approximation of the inversion mass matrix has been suggested in the form

$$\mathbf{M}^{-1} = \mathbf{A}^{-\top} \mathbf{C} \mathbf{A}^{-1} \quad (2)$$

where \mathbf{A} is the dual-base projection matrix, \mathbf{C} the global reciprocal mass matrix. This reciprocal mass matrix has the structure as the original mass matrix, it preserves the total mass and produces suitable eigen-frequencies of lower part of full spectra.

An efficient method for generating the mass matrix inverse of structural dynamic problems is presented, which can be tailored to improve the accuracy of target frequency ranges and/or wave contents. The present method bypasses the use of biorthogonal construction of a kernel inverse mass matrix that requires special procedures for boundary conditions and free edges or surfaces, and constructs the free-free inverse mass matrix employing the standard FEM procedure. The various boundary conditions are realized by the method of localized Lagrange multipliers. In particular, the present paper constructs the kernel inverse matrix by employing the standard FEM elemental mass matrices. It is shown that the accuracy of the present inverse mass matrix is almost identical to that of a conventional consistent mass matrix or a combination of lumped and consistent mass matrices. Numerical

experiments with the proposed inverse mass matrix are carried out to validate its effectiveness when applied to vibration analysis of bars, beams and plain stress problems.

In the paper [84], the reciprocal mass matrix has been extended for IGA. A variational framework is employed to generate inverse mass matrices for isogeometric analysis. As different dual bases impact not only accuracy but also computational overhead, several dual bases are extensively investigated. Specifically, locally discontinuous biorthogonal basis functions are evaluated in detail for B-splines of high continuity and Bzier elements with a standard C^0 continuous finite element structure. The boundary conditions are enforced by the method of localized Lagrangian multipliers after generating the inverse mass matrix for completely free body. Thus, unlike inverse mass matrix methods without employing the method of Lagrange multipliers, no modifications in the reciprocal basis functions are needed to account for the boundary conditions. Hence, the present method does not require internal modifications of existing IGA software structures. Numerical examples show that globally continuous dual basis functions yield better accuracy than locally discontinuous biorthogonal functions, but with much higher computational overhead. Locally discontinuous dual basis functions are found to be an economical alternative to lumped mass matrices when combined with mass parameterization. The resulting inverse mass matrices are tested in several vibration problems and applied to explicit transient analysis of structures.

6.3 Author's papers related to the section

[38] **R. Kolman**, S.V. Sorokin, S.V. Bastl, J. Kopačka, J. Plešek. Isogeometric analysis of free vibration of simple shaped elastic samples, *Journal of the Acoustical Society of America*, Vol. 137(4), pp. 2089–2100, 2015. (IF=1.646). <https://doi.org/10.1121/1.4916199>

[83] J. González, **R. Kolman**, S.S. Cho, C. Felippa, K.C. Park. Inverse mass matrix via the method of localized Lagrange multipliers, *International Journal for Numerical Methods in Engineering*, Vol. 113(2), pp. 277–295, 2018. (IF=2.162). <https://doi.org/10.1002/nme.5613>

[84] J. González, J. Kopačka, **R. Kolman**, S.S. Cho, K.C. Park. Inverse mass matrix for isogeometric explicit transient analysis via the method of localized Lagrange multipliers, *International Journal for Numerical Methods in Engineering*, Vol. 117(9), pp. 939–966, 2019. (IF=2.591). <https://doi.org/10.1002/nme.5986>

7 Advanced methods for contact-impact problems

Contact-impact problem is still an important task in engineering areas as in mechanical, civil, biomechanical and in space applications. The accurate and robust numerical solution of the contact-impact problem is a challenging task in computational mechanics, where the non-linearities due to the non-penetration condition on contact areas, friction laws, satisfying the equations of motion and behaviour of materials should be taken into account. Generally, analytical solutions of impact-contact problems can be found only for limited number of simple cases. For that reason, the numerical solution is needed to be employed in real and technical realizations. Also in dynamics, we have to add the persistency condition together with non-penetration condition into the system of governing equations. For that task, several numerical approaches have been developed and used in FEM modelling.

The task of simulating dynamic impact problems with penalty methods in a robust and efficient way, remains as one of the most elusive problems in computational contact mechanics. Among the different solution techniques available for the explicit solution of dynamic contact problems, the stiffness based-penalty method is very popular mainly due to its efficiency and implementation simplicity. The principle of the penalty method implies that the contact impenetrability condition is satisfied only approximately, achieving a more precise fulfillment using stiffer penalty parameters. This makes penalty methods generally not consistent within the variational formulation of the problem and the final matrix form is ill-conditioned. Moreover, it is well known that the results of contact problems obtained via penalty-like methods are very sensitive to the magnitude of the penalty parameter. A direct consequence of an inexact fulfillment of the contact constraints is non-zero penetration, which causes the contact stresses to produce non-physical energy associated to the contact interfaces. Different rules of thumb, strongly based on experience, are then used in penalty methods to decide stable values for the stiffness penalty accompanied, at the same time, with acceptable violation of the contact constraints and affordable time integration steps. But these rules are problem-dependent and it does not exist a general and theoretically sound solution to avoid all these effects, clearly limiting the applicability of penalty methods in contact-impact applications.

7.1 Bipenalty method in contact-impact problems

Most frequently, penalty methods, Lagrange multipliers method, its localized variant and augmented Lagrangian methods are applied for modelling dynamic contact problems in the context of the finite element analysis, e.g. see [85, 86, 87, 88]. In explicit finite element analysis, the penalty method is preferred due to its implementation simplicity and fast evaluation of contact forces [85] which, in comparison to Lagrange Multipliers method, does not increase the number of unknowns. It is also needed to mention the works related to efficient active set approaches in contact problems as [89]. In principle, the penalty method can be simply implemented into existing dynamic explicit finite element codes. On the other hand, the main disadvantage of the penalty method in elastodynamics is the fact that the stability limit of the explicit time integration scheme is destroyed by a large value of the numerical stiffness penalty parameter used for contact constraints enforcement [85]. The stable time step size rapidly decreases with increasing value of the penalty stiffness parameter as is depicted in Fig. 1. For that reason, the bipenalty method for avoiding this issue has been studied.

The bipenalty method [90] adds the term to the strain energy to enforce the zero-gap on the contact boundary and at the same time, an extra term to the kinetic energy to enforce the zero-velocity-gap on the contact boundary. By this way, we define a penalization term associated to the contact interface as

$$\mathcal{W}_c(u, \dot{u}) = \int_{\Gamma_c} \left(-\frac{1}{2} \epsilon_s \langle g \rangle^2 + \frac{1}{2} \epsilon_m \langle \dot{g} \rangle^2 \right) d\Gamma, \quad (3)$$

where the operator $\langle \bullet \rangle$ are the so-called Macaulay's brackets defined as $\langle \bullet \rangle = \frac{|\bullet| + \bullet}{2}$. The parameters

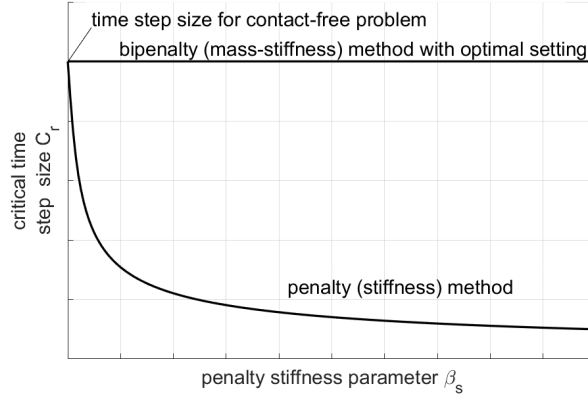


Figure 1: Characteristic dependence of the stable time step size for the penalty and bipenalty methods with optimal setting. In the penalty method, the stable time step size is strongly affected by the penalty stiffness parameter β_s while bipenalty with optimal setting remains unaffected.

ϵ_s [$\text{kg m}^{-2} \text{s}^{-2}$] and ϵ_m [kg m^{-2}] are the stiffness and mass penalty parameters, respectively, g defines the gap function and \dot{g} marks the gap-rate, Γ_c has a meaning of contact area.

In the paper [90], the stability and reflection-transmission properties of the bipenalty method have been studied in applications to explicit finite element analysis of one-dimensional contact-impact problems. In this paper, the influence of the penalty ratio (ratio of stiffness and mass penalty parameters) on stability and reflection-transmission properties in one-dimensional contact-impact problems using the same material and mesh size for both domains is studied. The paper closes with numerical examples demonstrating the stability and reflection-transmission behaviour of the bipenalty method in one-dimensional contact-impact and wave propagation problems of homogeneous materials.

The paper [70] presents a stabilization technique for the finite element modeling of contact-impact problems of elastic bars via a *bipenalty method* for enforcing contact constraints while employing an explicit predictor-corrector time integration algorithms. The present proposed method combines three salient features in carrying out explicit transient analysis of contact-impact problems: the addition of a penalty term associated with a kinetic energy expression of gap constraints, in addition to the conventional internal energy penalty term of the gap constraints; an explicit integration method that alleviates spurious oscillations; and, a judicious selection of two penalty parameters such that the stable time steps of the resulting explicit method is least compromised. Numerical experiments have been carried out with three explicit methods: the standard central difference method, the stabilized predictor-predictor method [91] and a method for mitigating spurious oscillations [56] as applied to simulate one-dimensional contact-impact problems of the Signorini problem and the impact of two elastic bars. Results indicates that the proposed method can maintain the contact-free stability limit of the central difference and yield improved accuracy compared with existing bipenalty methods.

The work [92] presents an efficient and accuracy-improved time explicit solution methodology for the simulation of contact-impact problems with finite elements. The proposed solution process combines four different existent techniques. First, the contact constraints are modeled by a bipenalty contact-impact formulation [90] that incorporates stiffness and mass penalties preserving the stability limit of contact-free problems for efficient explicit time integration. Second, a method of localized Lagrange multipliers [93] is employed, which facilitates the partitioned governing equations for each substructure along with the completely localized contact penalty forces pertaining to each *free* substructure. Third, a method for the direct construction of sparse inverse mass matrices of the free bodies in contact [83] that is combined with the localized Lagrange multipliers approach. Finally, an element-by-element

mass matrix scaling technique [84] that allows the extension of the time integration step is adopted to improve the overall performance of the algorithm. A judicious synthesis of the four numerical techniques has resulted in an increased stable explicit step-size that boosts the performance of the bipenalty method for contact problems. Classical contact-impact numerical examples have been used to demonstrate the effectiveness of the proposed methodology.

7.2 Author's papers related to the section

[90] J. Kopačka, A. Tkachuk, D. Gabriel, **R. Kolman**, M. Bischoff, J. Plešek. On stability and reflection-transmission analysis of the bipenalty method in contact-impact problems: a one-dimensional, homogeneous case study, *International Journal for Numerical Methods in Engineering*, Vol. 113(10), pp. 1607–1629, 2018. (IF=2.162). <https://doi.org/10.1002/nme.5712>

[70] **R. Kolman**, J. Kopačka, A. González, S.S. Cho, K.C. Park. Bi-penalty stabilized technique with predictor-corrector time scheme for contact-impact problems of elastic bars. *Mathematics and Computers in Simulation*, Vol. 189, pp. 305–324, 2021. (IF=2.463). <https://doi.org/10.1016/j.matcom.2021.03.023>

[92] J. González, J. Kopačka, **R. Kolman**, K.C. Park. Partitioned formulation of contact-impact problems with stabilized contact constraints and reciprocal mass matrices, *International Journal for Numerical Methods in Engineering*, Vol. 122(17), pp. 4609–4636, 2021. (IF=3.477). <https://doi.org/10.1002/nme.6739>

8 Conclusions and Future works

The systematic work on advanced numerical methodologies based on the finite element method for modelling of elastic wave propagation and contact-impact problems is summarized and presented in this habilitation thesis. The special focus has been paid to the improving of accuracy and robustness and also to avoiding the troubles with spurious stress oscillations, temporal-spatial dispersion of FE semidiscretization connected with direct time integration and contact force oscillations. All suggested methodologies can be implemented into existing FE codes, because the methodologies have been developed with respect to these requirements. At the moment, the author of the thesis is in touch with the company developing the software COMSOL about the implementation of the bipenalty method into this software.

For future works, it is in mind the following open and challenging problems in computational mechanics and multi-physics problems, that have a potential for novelties in the numerical mechanics and multi-physics problems and publishing in prestige impacted journals:

- asynchronous heterogeneous time stepping for cloud computations for strong heterogeneous solid problems
- three-field decomposition of wave equations based on the Helmholtz-Hodge decomposition
- localized bipenalty method and its stability connection with asynchronous heterogeneous time stepping
- reciprocal mass matrix for higher-order FEM, shells and plates
- elasto-plastic wave propagation and high-velocity impact with application of plasma shock peening
- Taylor test modelling and material parameter identification based on artificial intelligence
- multi-physics of electro-active materials and dynamics of soft robots
- dynamics of grippers for robotics and soft robotics
- bipenalty stabilization for differential-algebraic equations (DEAs) for multibody dynamics of rigid and deformable bodies.

References

- [1] T.J.R. Hughes. *The Finite Element Method, Linear Static and Dynamic Finite Element Analysis*. Dover Publication, 2000.
- [2] K. J. Bathe. *Finite Element Procedures*. Prentice-Hall, Englewood Cliffs, New Jersey, 1996.
- [3] O. C. Zienkiewicz, R.L. Taylor, and J.Z. Zhu. *The Finite Element Method: Its Basis and Fundamentals*. Butterworth-Heinemann, 2000.
- [4] T. Belytschko and T. J. R. Hughes. *Computational Methods for Transient Analysis. Vol. 1*. North-Holland Pub. Co., Amsterdam, London, 1983.
- [5] R. Mullen and T. Belytschko. Dispersion analysis of finite element semidiscretizations of the two-dimensional wave equation. *International Journal for Numerical Methods in Engineering*, 18(1):11–29, 1982.
- [6] R.C.Y. Chin. Dispersion and Gibbs phenomenon associated with difference approximations to initial boundary-value problems for hyperbolic equations. *Journal of Computational Physics*, 18(3):233–247, 1975.
- [7] R. Vichnevetsky and J.B. Bowles. *Fourier Analysis of Numerical Approximations of Hyperbolic Equations*. Philadelphia, Pa. : Society for Industrial and Applied Mathematics, 1982.
- [8] L. L. Thompson and P. M. Pinsky. Complex wave-number fourier-analysis of the p-version finite element method. *Computational Mechanics*, 13:255–275, 1995.
- [9] R.D. Krieg and S.W. Key. Transient shell response by numerical time integration. *International Journal for Numerical Methods in Engineering*, 7(3):273–286, 1973.
- [10] T. Belytschko and R. Mullen. On dispersive properties of finite element solutions. In J. Miklowitz and J. Achenbach, editors, *Modern Problems in Elastic Wave Propagation*, pages 67–82. John Wiley and Sons, 1978.
- [11] N. Holmes and T. Belytschko. Postprocessing of finite element transient response calculations by digital filters. *Computers & Structures*, 6(3):211–216, 1976.
- [12] Z.P. Bažant and Z. Celep. Spurious reflection of elastic waves in nonuniform meshes of constant and linear strain unite elements. *Computers & Structures*, 15(4):451–459, 1982.
- [13] Z. Celep and Z.P. Bažant. Spurious reflection of elastic waves due to gradually changing finite element size. *International Journal for Numerical Methods in Engineering*, 19(5):631–646, 1983.
- [14] M. Okrouhlík and C. Höschl. A contribution to the study of dispersive properties of one-dimensional Lagrangian and Hermitian elements. *Computers & Structures*, 49(5):779–795, 1993.
- [15] L. Jiang and R.J. Rogers. Effects of spatial discretization on dispersion and spurious oscillations in elastic wave propagation. *International Journal for Numerical Methods in Engineering*, 29(6):1205–1218, 1990.
- [16] L. Brillouin. *Wave Propagation in Periodic Structures*. Dover Publication, 1953.
- [17] R. Brepta and M. Okrouhlík. Dispersion properties of a plane continuum model consisted of rectangular triangular finite elements. Research Report Z-966/84, Institute of Thermomechanics, Prague, Czech Republic, 1984.

- [18] R. Brepta and M. Okrouhlík. Dispersive properties of rectangular and square element in 2D regions. Research Report Z-998/86, Institute of Thermomechanics, Prague, Czech Republic, 1986.
- [19] N. N. Abboud and P. M. Pinsky. Finite element dispersion analysis for the three-dimensional second-order scalar wave equation. *International Journal for Numerical Methods in Engineering*, 35(6):1183–1218, 1992.
- [20] **Kolman, R.**, J. Plešek, M. Okrouhlík, and D. Gabriel. Grid dispersion analysis of plane square biquadratic serendipity finite elements in transient elastodynamics. *International Journal for Numerical Methods in Engineering*, 96(1):1–28, 2013.
- [21] M.A. Dokainish and K. Subbaraj. A survey of direct time-integration methods in computational structural dynamics. explicit methods. *Computers & Structures*, 32(6):1371–1386, 1989.
- [22] N. M. Newmark. Method of computation for structural dynamics. *Journal of the Engineering Mechanics Division*, 85(3):67–94, 1959.
- [23] T. Belytschko, W. K. Liu, and B. Moran. *Nonlinear Finite Elements for Continua and Structures*. John Wiley and Sons, Chichester, 2000.
- [24] T. Belytschko and W.E. Bachrach. Efficient implementation of quadrilaterals with high coarse-mesh accuracy. *Computer Methods in Applied Mechanics and Engineering*, 54(3):279–301, 1986.
- [25] K. C. Park. Practical aspects of numerical time integration. *Computers & Structures*, 7(3):343–353, 1977.
- [26] G. L. Goudreau and R. L. Taylor. Evaluation of numerical integration methods in elastodynamics. *Computer Methods in Applied Mechanics and Engineering*, 2(1):69–97, 1973.
- [27] J. Chung and G. M. Hulbert. A time integration algorithm for structural dynamics with improved numerical dissipation: The generalized- α method. *Journal of Applied Mechanics*, 60(2):371–375, 1993.
- [28] H.L. Schreyer. Dispersion of semidiscretized and fully discretized systems. In T. Belytschko and T.J.R. Hughes, editors, *Computational Methods for Transient Analysis*, pages 267–299. North-Holland, 1983.
- [29] **Kolman, R.**, J. Plešek, J. Červ, M. Okrouhlík, and P. Pařík. Temporal-spatial dispersion and stability analysis of finite element method in explicit elastodynamics. *International Journal for Numerical Methods in Engineering*, 106(2):113–128, 2016.
- [30] A. Kruisová, M. Mračko, **R. Kolman**, and M. Okrouhlík. Temporal-spatial dispersion analysis of finite element method and implicit time integration by newmark family methods in elastodynamics. *International Journal for Numerical Methods in Engineering*, page submitted, 2022.
- [31] W. Dauksher and A.F. Emery. The solution of elastostatic and elastodynamic problems with chebyshev spectral finite elements. *Computer Methods in Applied Mechanics and Engineering*, 188(1):217–233, 2000.
- [32] G. Seriani. Double-grid chebyshev spectral elements for acoustic wave modeling. *Wave Motion*, 39(4):351–360, 2004. New computational methods for wave propagation.
- [33] J.A. Cottrell, A. Reali, Y. Bazilevs, and T.J.R. Hughes. Isogeometric analysis of structural vibrations. *Computer Methods in Applied Mechanics and Engineering*, 195(41):5257–5296, 2006. John H. Argyris Memorial Issue. Part II.

- [34] T. J. R. Hughes, A. Reali, and G. Sangalli. Duality and unified analysis of discrete approximations in structural dynamics and wave propagation: Comparison of p-method finite elements with k-method NURBS. *Computer Methods in Applied Mechanics and Engineering*, 197(49):4104–4124, 2008.
- [35] J.A. Cottrell, T.J.R. Hughes, and Y. Bazilevs. *Isogeometric Analysis: Toward Integration of CAD and FEA*. John Wiley & Sons, Ltd, 2009.
- [36] L. Piegl and W. Tiller. *The NURBS Book*. Springer, Berlin, Heidelberg, 1995.
- [37] **R. Kolman**, J. Plešek, and M. Okrouhlík. Complex wavenumber fourier analysis of the b-spline based finite element method. *Wave Motion*, 51(2):348–359, 2014.
- [38] **R. Kolman**, S.V. Sorokin, B. Bastl, J. Kopačka, and J. Plešek. Isogeometric analysis of free vibration of simple shaped elastic samples. *The Journal of the Acoustical Society of America*, 137(4):2089–2100, 2015.
- [39] H.M. Hilber and T.J. R. Hughes. Collocation, dissipation and overshoot for time integration schemes in structural dynamics. *Earthquake Engineering & Structural Dynamics*, 6(1):99–117, 1978.
- [40] H.M. Hilber, T.J.R. Hughes, and R.L. Taylor. Improved numerical dissipation for time integration algorithms in structural dynamics. *Earthquake Engineering & Structural Dynamics*, 5(3):283–292, 1977.
- [41] G.M. Hulbert and J. Chung. Explicit time integration algorithms for structural dynamics with optimal numerical dissipation. *Computer Methods in Applied Mechanics and Engineering*, 137(2):175–188, 1996.
- [42] Y. Mirbagheri, H. Nahvi, J. Parvizian, and A. Düster. Reducing spurious oscillations in discontinuous wave propagation simulation using high-order finite elements. *Comput. Math. Appl.*, 70(7):16401658, oct 2015.
- [43] T.J.R. Hughes, K.S. Pister, and R.L. Taylor. Implicit-explicit finite elements in nonlinear transient analysis. *Computer Methods in Applied Mechanics and Engineering*, 17-18:159–182, 1979.
- [44] F. Auricchio, L. Beiro da Veiga, T.J.R. Hughes, A. Reali, and G. Sangalli. Isogeometric collocation for elastostatics and explicit dynamics. *Computer Methods in Applied Mechanics and Engineering*, 249-252:2–14, 2012. Higher Order Finite Element and Isogeometric Methods.
- [45] **R. Kolman**, M. Okrouhlík, A. Berezovski, D. Gabriel, J. Kopačka, and J. Plešek. B-spline based finite element method in one-dimensional discontinuous elastic wave propagation. *Applied Mathematical Modelling*, 46:382–395, 2017.
- [46] D.M. Trujillo. An unconditionally stable explicit algorithm for structural dynamics. *International Journal for Numerical Methods in Engineering*, 11:1579–1592, 1977.
- [47] P. G. Underwood and K. C. Park. A variable-step central difference method for structural dynamics analysis- part 2. implementation and performance evaluation. *Computer Methods in Applied Mechanics and Engineering*, 23:259–279, 1980.
- [48] J. Chung and J.M. Lee. A new family of explicit time integration methods for linear and non-linear structural dynamics. *International Journal for Numerical Methods in Engineering*, 37(23):3961–3976, 1994.

- [49] W. Zhai. Two simple fast integration methods for largescale dynamic problems in engineering. *International Journal for Numerical Methods in Engineering*, 39:4199–4214, 1996.
- [50] B. Tchamwa, T. Conway, and C. Wielgosz. An accurate explicit direct time integration method for computational structural dynamics. In Kwon Y.W. and Chung H.H., editors, *Recent advances in solids and structures 398*, pages 77–84. ASME PUBLICATIONS-PVP, 1999.
- [51] S. Krenk. Dispersion-corrected explicit integration of the wave equation. *Computer Methods in Applied Mechanics and Engineering*, 191(8):975–987, 2001.
- [52] K.K. Tamma, D. Sha, and X. Zhou. Time discretized operators. part 1: towards the theoretical design of a new generation of a generalized family of unconditionally stable implicit and explicit representations of arbitrary order for computational dynamics. *Computer Methods in Applied Mechanics and Engineering*, 192(3):257–290, 2003.
- [53] D. Sha, X. Zhou, and K.K. Tamma. Time discretized operators. part 2: towards the theoretical design of a new generation of a generalized family of unconditionally stable implicit and explicit representations of arbitrary order for computational dynamics. *Computer Methods in Applied Mechanics and Engineering*, 192(3):291–329, 2003.
- [54] A.V. Idesman, M. Schmidt, and R.L. Sierakowski. A new explicit predictormulticorrector high-order accurate method for linear elastodynamics. *Journal of Sound and Vibration*, 310(1-2):217–229, 2008.
- [55] S.-Y. Chang. An explicit method with improved stability property. *International Journal for Numerical Methods in Engineering*, 77(8):1100–1120, 2009.
- [56] K.C. Park, S.J. Lim, and H. Huh. A method for computation of discontinuous wave propagation in heterogeneous solids: basic algorithm description and application to one-dimensional problems. *International Journal for Numerical Methods in Engineering*, 91:622 – 643, 2012.
- [57] S. S. Cho, K. C. Park, and Hoon Huh. A method for multidimensional wave propagation analysis via componentwise partition of longitudinal and shear waves. *International Journal for Numerical Methods in Engineering*, 95, 2013.
- [58] G. Noh and K.-J. Bathe. An explicit time integration scheme for the analysis of wave propagations. *Computers & Structures*, 129:178–193, 2013.
- [59] T C Fung. Numerical dissipation in time-step integration algorithms for structural dynamic analysis. *Progress in Structural Engineering and Materials*, 5(3):167–180, 2003.
- [60] G. Rio, A. Soive, and V. Grolleau. Comparative study of numerical explicit time integration algorithms. *Advances in Engineering Software*, 36(4):252–265, 2005.
- [61] N. Nsiampa, J.-P. Ponthot, and L. Noels. Comparative study of numerical explicit schemes for impact problems. *International Journal of Impact Engineering*, 35(12):1688–1694, 2008. Hyper-velocity Impact Proceedings of the 2007 Symposium.
- [62] L. Maheo, V. Grolleau, and G. Rio. Numerical damping of spurious oscillations: a comparison between the bulk viscosity method and the explicit dissipative tchamwa–wielgosz scheme. *Computational Mechanics*, 51(1):109–128, Jan 2013.
- [63] P. Smolinski, T. Belytschko, and M. Neal. Multi-time-step integration using nodal partitioning. *International Journal for Numerical Methods in Engineering*, 26(2):349–359, 1988.

- [64] W.J.T. Daniel. A partial velocity approach to subcycling structural dynamics. *Computer Methods in Applied Mechanics and Engineering*, 192(3):375–394, 2003.
- [65] N. Mahjoubi, A. Gravouil, and A. Combescure. Coupling subdomains with heterogeneous time integrators and incompatible time steps. *Computational Mechanics*, 44(6):825–843, Nov 2009.
- [66] N. Mahjoubi, A. Gravouil, A. Combescure, and N. Greffet. A monolithic energy conserving method to couple heterogeneous time integrators with incompatible time steps in structural dynamics. *Computer Methods in Applied Mechanics and Engineering*, 200(janvier):1069–1086, 2011.
- [67] A. Gravouil, A. Combescure, and M. Brun. Heterogeneous asynchronous time integrators for computational structural dynamics. *International Journal for Numerical Methods in Engineering*, 102(3-4):202–232, 2015.
- [68] A. Lew, J. E. Marsden, M. Ortiz, and M. West. Variational time integrators. *International Journal for Numerical Methods in Engineering*, 60(1):153–212, 2004.
- [69] S.S. Cho, H. Huh, and K.C. Park. A time-discontinuous implicit variational integrator for stress wave propagation analysis in solids. *Computer Methods in Applied Mechanics and Engineering*, 200(5):649–664, 2011.
- [70] **R. Kolman**, J. Kopačka, J. A. González, S.S. Cho, and K.C. Park. Bi-penalty stabilized technique with predictorcorrector time scheme for contact-impact problems of elastic bars. *Mathematics and Computers in Simulation*, 189:305–324, 2021.
- [71] R. Dvořák, **R. Kolman**, T. Fíla, J. Falta, and K.C. Park. Explicit asynchronous time scheme with local push-forward stepping for discontinuous elastic wave propagation: One-dimensional heterogeneous cases and hopkinson bar experiment. *Wave Motion*, page submitted, 2022.
- [72] J. D. Achenbach. *Wave Propagation in Elastic Solids*. North-Holland, Amsterdam, 1973.
- [73] I. Harari. Reducing spurious dispersion, anisotropy and reflection in finite element analysis of time-harmonic acoustics. *Computer Methods in Applied Mechanics and Engineering*, 140(1-2):39–58, January 1997.
- [74] R. Brepta, F. Valeš, J. Červ, and B. Tikal. Rayleigh wave dispersion due to spatial (fem) discretization of a thin elastic solid having non-curved boundary. *Computers & Structures*, 58(6):1233–1244, 1996.
- [75] R. Courant, K. Friedrichs, and H. Lewy. On the partial difference equations of mathematical physics. *IBM Journal of Research and Development*, 11(2):215–234, 1967.
- [76] **R. Kolman**, S.S. Cho, and K.C. Park. Efficient implementation of an explicit partitioned shear and longitudinal wave propagation algorithm. *International Journal for Numerical Methods in Engineering*, 107(7):543–579, 2016.
- [77] S. S. Cho, **Kolman, R.**, J.A. González, and K.C. Park. Explicit multistep time integration for discontinuous elastic stress wave propagation in heterogeneous solids. *International Journal for Numerical Methods in Engineering*, 118(5):276–302, 2019.
- [78] R. Acevedo, P. Sedlák, **R. Kolman**, and M. Fredel. Residual stress analysis of additive manufacturing of metallic parts using ultrasonic waves: State of the art review. *Journal of Materials Research and Technology*, 9(4):9457–9477, 2020.

- [79] M. Mračko, J. Kober, **R. Kolman**, Z. Převorovský, A. Tkachuk, and J. Plešek. Finite element method based computational time reversal in elastodynamics: Refocusing, reconstruction and its numerical sensitivity. *Mathematics and Computers in Simulation*, 189:163–190, 2021.
- [80] A. Berezovski, **R. Kolman**, M. Berezovski, D. Gabriel, and V. Adámek. Full field computing for elastic pulse dispersion in inhomogeneous bars. *Composite Structures*, 204:388–394, 2018.
- [81] V. Adámek, A. Berezovski, M. Mračko, and **R. Kolman**. A two-layer elastic strip under transverse impact loading: Analytical solution, finite element, and finite volume simulations. *Mathematics and Computers in Simulation*, 189:126–140, 2021.
- [82] M. Mračko, V. Adámek, A. Berezovski, J. Kober, and **R. Kolman**. Experimental, analytical, and numerical study of transient elastic waves from a localized source in an aluminium strip. *Applied Acoustics*, 178:107983, 2021.
- [83] J.A. González, **Kolman, R.**, S. S. Cho, C. A. Felippa, and K. C. Park. Inverse mass matrix via the method of localized lagrange multipliers. *International Journal for Numerical Methods in Engineering*, 113(2):277–295, 2018.
- [84] J.A. González, J. Kopačka, **Kolman, R.**, S. S. Cho, and K. C. Park. Inverse mass matrix for isogeometric explicit transient analysis via the method of localized lagrange multipliers. *International Journal for Numerical Methods in Engineering*, 117(9):939–966, 2019.
- [85] T. Belytschko and M.O. Neal. Contact-impact by the pinball algorithm with penalty and lagrangian methods. *International Journal for Numerical Methods in Engineering*, 31(3):547–572, 1991.
- [86] N.J. Carpenter, R.L. Taylor, and M.G. Katona. Lagrange constraints for transient finite element surface contact. *International Journal for Numerical Methods in Engineering*, 32(1):103–128, 1991.
- [87] J.A. Gonzalez, K.C. Park, and C.A. Felippa. Partitioned formulation of frictional contact problems using localized lagrange multipliers. *Communications in Numerical Methods in Engineering*, 22(4):319–333, 2006.
- [88] T.A. Laursen and V. Chawla. Design of energy conserving algorithms for frictionless dynamic contact problems. *International Journal for Numerical Methods in Engineering*, 40(5):863–886, 1997.
- [89] Barbara Wohlmuth. Variationally consistent discretization schemes and numerical algorithms for contact problems. *Acta Numerica*, 20:569734, 2011.
- [90] J. Kopačka, A. Tkachuk, D. Gabriel, **Kolman, R.**, M. Bischoff, and J. Plešek. On stability and reflection-transmission analysis of the bipenalty method in contact-impact problems: A one-dimensional, homogeneous case study. *International Journal for Numerical Methods in Engineering*, 113(10):1607–1629, 2018.
- [91] Shen R. Wu. A priori error estimates for explicit finite element for linear elasto-dynamics by galerkin method and central difference method. *Computer Methods in Applied Mechanics and Engineering*, 192(51):5329–5353, 2003.
- [92] J.A. González, J. Kopačka, **Kolman, R.**, and K.C. Park. Partitioned formulation of contact-impact problems with stabilized contact constraints and reciprocal mass matrices. *International Journal for Numerical Methods in Engineering*, 122(17):4609–4636, 2021.

- [93] K. C. Park and Carlos A. Felippa. A variational principle for the formulation of partitioned structural systems. *International Journal for Numerical Methods in Engineering*, 47(1-3):395–418, 2000.

9 List of attached papers

R. Kolman, M. Okrouhlík, A. Berezovski, D. Gabriel, J. Kopačka, J. Plešek. B-spline based finite element method in one-dimensional discontinuous elastic wave propagation, *Applied Mathematical Modelling*, Vol. 46, pp. 382–395, 2017. (IF=2.291). <https://doi.org/10.1016/j.apm.2017.01.077>

S.S. Cho, **R. Kolman**, J. González, K.C. Park. Explicit multistep time integration for discontinuous elastic stress wave propagation in heterogeneous solids, *International Journal for Numerical Methods in Engineering*, Vol. 118, pp. 276–302, 2019. (IF=2.746). <https://doi.org/10.1002/nme.6027>

R. Kolman, J. Kopačka, A. González, S.S. Cho, K.C. Park. Bi-penalty stabilized technique with predictor-corrector time scheme for contact-impact problems of elastic bars. *Mathematics and Computers in Simulation*, Vol. 189, pp. 305–324, 2021. (IF=2.463). <https://doi.org/10.1016/j.matcom.2021.03.023>

M. Mračko, J. Kober, **R. Kolman**, Z. Převorovský, A. Tkachuk, J., Plešek. Finite element method based computational time reversal in elastodynamics: Refocusing, reconstruction and its numerical sensitivity, *Mathematics and Computers in Simulation*, Vol. 189, pp. 163–190, 2021. (IF=2.463). <https://doi.org/10.1016/j.matcom.2020.11.004>

A. Berezovski, **R. Kolman**, M. Berezovski, D. Gabriel, V. Adánek. Full field computing for elastic pulse dispersion in inhomogeneous bars, *Composite Structures*, Vol. 204, pp. 388–394, 2018. (IF=4.101). <https://doi.org/10.1016/j.compstruct.2018.07.055>

V. Adánek, A. Berezovski, M. Mračko, **R. Kolman**. A two-layer elastic strip under transverse impact loading: Analytical solution, finite element, and finite volume simulations. *Mathematics and Computers in Simulation*, Vol. 189, pp. 126–140, 2021. (IF=2.463). <https://doi.org/10.1016/j.matcom.2020.10.007>

M. Mračko, V. Adánek, A. Berezovski, J. Kober, **R. Kolman**. Experimental, analytical, and numerical study of transient elastic waves from a localized source in an aluminium strip. *Applied Acoustics*, Vol. 178, pp. 107983, 2021. (IF=2.440). <https://doi.org/10.1016/j.apacoust.2021.107983>

R. Acevedo, P. Sedlák, **R. Kolman**, M. Fredel, Residual stress analysis of additive manufacturing of metallic parts using ultrasonic waves: State of the art review, *Journal of Materials Research and Technology*, Vol. 9(4), pp. 9457–9477, 2020. (IF=5.289). <https://doi.org/10.1016/j.jmrt.2020.05.092>

J. González, **R. Kolman**, S.S. Cho, C. Felippa, K.C. Park. Inverse mass matrix via the method of localized Lagrange multipliers, *International Journal for Numerical Methods in Engineering*, Vol. 113(2), pp. 277–295, 2018. (IF=2.162). <https://doi.org/10.1002/nme.5613>

J. González, J. Kopačka, **R. Kolman**, S.S. Cho, K.C. Park. Inverse mass matrix for isogeometric explicit transient analysis via the method of localized Lagrange multipliers, *International Journal for Numerical Methods in Engineering*, Vol. 117(9), pp. 939–966, 2019. (IF=2.591). <https://doi.org/10.1002/nme.5986>

J. Kopačka, A. Tkachuk, D. Gabriel, **R. Kolman**, M. Bischoff, J. Plešek. On stability and reflection-transmission analysis of the bipenalty method in impact-contact problems: a one-dimensional, homogeneous case study, *International Journal for Numerical Methods in Engineering*, Vol. 113(10), pp. 1607–1629, 2018. (IF=2.162). <https://doi.org/10.1002/nme.5712>

J. González, J. Kopačka, **R. Kolman**, K.C. Park. Partitioned formulation of contact-impact problems with stabilized contact constraints and reciprocal mass matrices, *International Journal for Numerical Methods in Engineering*, Vol. 122(17), pp. 4609–4636, 2021. (IF=3.477). <https://doi.org/10.1002/nme.6739>

10 Attached papers



B-spline based finite element method in one-dimensional discontinuous elastic wave propagation



R. Kolman^{a,*}, M. Okrouhlík^{a,b}, A. Berezovski^c, D. Gabriel^a, J. Kopačka^a, J. Plešek^a

^a Institute of Thermomechanics, The Czech Academy of Sciences, Dolejškova 5, 182 00, Prague Czech Republic

^b Faculty of Production Technology and Management, J. E. Purkyně University in Ústí nad Labem, Na Okraji 1001, 400 01, Ústí nad Labem Czech Republic

^c Centre for Nonlinear Studies, Institute of Cybernetics at Tallinn University of Technology, Akadeemia tee 21, 12618, Tallinn Estonia

ARTICLE INFO

Article history:

Received 25 July 2015

Revised 7 January 2017

Accepted 24 January 2017

Available online 2 February 2017

Keywords:

Discontinuous elastic wave propagation

B-spline finite element method

Isogeometric analysis

Implicit and explicit time integration

Dispersion

Spurious oscillations

ABSTRACT

The B-spline variant of the finite element method (FEM) is tested in one-dimensional discontinuous elastic wave propagation. The B-spline based FEM (called Isogeometric analysis IGA) uses spline functions as testing and shape functions in the Galerkin continuous content. Here, the accuracy of stress distribution and spurious oscillations of the B-spline based FEM are studied in numerical modeling of one-dimensional propagation of stress discontinuities in a bar, where the analytical solution is known. For time integration, the Newmark method, implicit form of the generalized- α method, the central difference method and the predictor/multi-corrector method are tested and compared. The use of lumped and consistent mass matrices in explicit time integration is discussed. Due to accuracy, the consistent mass matrix is preferred in explicit time integration in IGA.

© 2017 Elsevier Inc. All rights reserved.

1. Introduction

Many methods for numerical modeling of wave propagation problems in elastic solids have been developed and tested (see. e.g., [1]). Unfortunately, the majority of these numerical methods produce spurious oscillations occurring in stress distributions in cases of shock loading. As a rule, discrete numerical methods are able to describe successfully a response of body on harmonic or generally smooth loadings, but they have got a trouble with modeling of problems corresponding to shocks. Other approaches for the description of displacement/strain/stress discontinuous fields in continuum mechanics should be mentioned as the Discontinuous Galerkin methods [2] or eXtended Finite Element methods (XFEM) [3–5].

In this paper, the semidiscretization method [6] is tested in the case of one-dimensional elastic wave propagation. For the spatial discretization, the continuous Galerkin approximation method is employed [7], where the Finite element method (FEM) with spline shape functions, called the Isogeometric Analysis (IGA) [8], is used.

Standard results of numerical simulations of fast transient elastodynamic problems by FEM [7] are influenced by dispersion errors caused by both spatial and temporal discretizations [9]. A monochromatic harmonic stress wave propagates in unbounded elastic continuum uniformly regardless of its frequency and correspondingly a wave packet propagates

* Corresponding author.

E-mail addresses: kolman@it.cas.cz (R. Kolman), ok@it.cas.cz (M. Okrouhlík), Arkadi.Berezovski@cs.ioc.ee (A. Berezovski), gabriel@it.cas.cz (D. Gabriel), kopacka@it.cas.cz (J. Kopačka), plesek@it.cas.cz (J. Plešek).

URL: <http://www.it.cas.cz/en/kolman> (R. Kolman), <http://www.it.cas.cz/en/ok> (M. Okrouhlík), <http://www.cs.ioc.ee/~berez/> (A. Berezovski), <http://www.it.cas.cz/en/gabriel> (D. Gabriel), <http://www.it.cas.cz/en/jankopacka> (J. Kopačka), <http://www.it.cas.cz/en/plesek> (J. Plešek)

<http://dx.doi.org/10.1016/j.apm.2017.01.077>

0307-904X/© 2017 Elsevier Inc. All rights reserved.

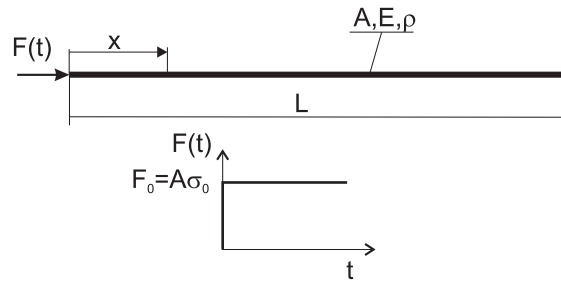


Fig. 1. Scheme of an elastic free-fixed bar under a shock loading.

without distortion. However, when these propagating phenomena are modeled by FEM, the speed of a single harmonic wave depends on its frequency and thus a wave packet is distorted. Furthermore, the high frequency errors of the high vibration mode increase with increasing order of higher-order Lagrangian finite elements [9,10].

The Isogeometric analysis [8,11–13] represents a modern approach in computational mechanics. In this modification of FEM, the shape and testing functions are based on various types of splines. This approach has an advantage that the geometry and approximation of unknown field quantities are prescribed by the same technique. Another benefit is that the approximation is smooth. We should mention that the B-spline representation is sufficient for approximation of an one-dimensional domain.

It was shown for Isogeometric analysis with homogeneous spline shape functions, that the optical modes do not exist, which is not the case for higher-order Lagrangian finite elements [12,13]. Further, dispersion and frequency errors for Isogeometric analysis were reported to decrease with increasing order of splines [12,13]. The dispersion analysis of B-spline Galerkin based FEM has been studied in [12,14] for one-dimensional case and in [15] for two-dimensional case. The effect of inhomogeneity of spline shape functions and of parameterization of the B-spline representation on the dispersion and attenuation behavior was studied in [14]. Furthermore, IGA is a very efficient tool for vibration analysis of elastic objects [13,16,17] and for solving tasks of quantum mechanics [18]. IGA solution with the consistent mass matrix not only accurately predicts eigenvalues in the full frequency spectrum but also provides an excellent approximation for eigenmodes [19].

In principle, non-physical higher vibration modes occur in frequency spectrum of higher-order FEM [9,14,20,21] and of IGA on multipatches with C^0 continuity [14]. Therefore time integration methods should be derived in such a way that the dissipation of higher frequencies is optimal and minimized for the low frequency range. Attempts to do so are presented by the Hilber–Hughes–Taylor (HHT- α) method [22,23] or the generalized- α method [24,25]. Implicit time integration schemes are preferred in higher-order FEM and in IGA [8]. In the case of explicit time integration, the presence of high frequency modes in the spectrum causes fragility of higher-order elements and spline based FEM regarding numerical stability condition for the setting of time step size. The two-time step method for application for higher-order FEM and IGA has been presented in [26].

In order to take advantage of IGA approach in explicit dynamics, one uses a lumped mass matrix formulation. Due to positive values of spline shape functions, all the terms of the consistent mass matrix in the Galerkin approximation method are also positive. Thus, the ‘row-sum’ technique [7] for the lumped mass matrix in IGA can be employed. The lumped mass matrix loses the second-order accuracy of IGA in higher modes [8]. One way how to overcome the lumping issue in IGA is to provide explicit predictor/multi-corrector algorithms as described in [7,27,28]. Here, the lumped or consistent mass matrix is used for the ‘left-hand-side’ matrix and the consistent mass is used in calculation of the ‘right-hand-side’ residual vector.

Due to the variety of methods, it is not clear which one should be chosen for the efficient and accurate solution of wave propagation problems. Therefore, in this paper, we study the ability of time integration methods with the B-spline based finite element method to treat spurious oscillations using one-dimensional discontinuous wave propagation as a suitable benchmark. The paper is organized as follows. In Section 2, the problem description of discontinuous wave propagation in an elastic bar is presented as well as the analytical solution is mentioned. The fundamentals of the B-spline based FEM (Galerkin based IGA) in the one-dimensional case are shown in Section 3. The direct time integration schemes suitable for IGA are reported in Section 4 as well as results of numerical solutions of wave propagation in an elastic bar. The paper closes with conclusions in Section 5.

2. Problem description

For the purposes of this paper, we use a benchmark problem - wave propagation in an elastic bar under shock loading (see Fig. 1), where shock loading generates a discontinuous sharp stress and velocity wavefront.

The governing equation of one-dimensional elastic wave propagation in a bar (as an one-dimensional continuum) has the form (see, e.g. [29]),

$$A\rho \frac{\partial^2 u}{\partial t^2} - AE \frac{\partial^2 u}{\partial x^2} = 0, \quad (1)$$

where $u(x, t)$ is the axial displacement, $x \in [0, L]$ is the axial coordinate, L is the length of the bar, $t \geq 0$ denotes the time, ρ is the mass density, A is the area of a cross-section and E denotes the Young modulus. Wave speed in an elastic bar is given by $c_0 = \sqrt{E/\rho}$ [29]. The right-hand side of the bar is fixed, therefore the boundary condition of the bar takes

$$u(x = L, t) = 0, \quad t \geq 0. \tag{2}$$

The loading by a force applied on the left free-end of the bar leads to

$$F(t) = -A\sigma(x = 0, t), \tag{3}$$

where the time dependence of stress σ is given by the Heaviside step function $H(t)$ in the form $\sigma(x = 0, t) = \sigma_0 H(t)$, where $\sigma_0 = F_0/A$. The bar in the time $t = 0$ is at the rest.

For this benchmark, the analytical solution of this wave propagation problem can be found in [29], where the displacement field $u(x, t)$ without a wave reflection in the time range $t \in [0, L/c_0]$ is described as

$$u(x, t) = v_0 (t - x/c_0) H(t - x/c_0). \tag{4}$$

The impact velocity v_0 is computed from the relationship $\sigma_0 = \rho c_0 v_0$ [29]. The stress field is then given following Eq. (4)

$$\sigma(x, t) = -\sigma_0 H(t - x/c_0). \tag{5}$$

In what follows, the stress dependence given by Eq. (5) is used for comparison of solutions obtained by IGA.

3. B-spline based FEM – Galerkin based IGA

In this section, the basics of B-spline based finite element method are shortly introduced. In Computer-Aided Design (CAD), coordinates of a point of the B-spline curve $\mathbf{C} \in \mathbb{R}^d$ with order p is given by the linear combination of B-spline basis functions $N_{i,p}$ [30]

$$\mathbf{C}(\xi) = \sum_{i=1}^n N_{i,p}(\xi) \mathbf{B}_i, \tag{6}$$

where $\mathbf{B}_i \in \mathbb{R}^d, i = 1, 2, \dots, n$ are corresponding coordinates of control points and d marks the dimension of the Euclidean space of a curve, $d = 1, 2, 3$, respectively. B-spline basis functions $N_{i,p}(\xi)$ of order p are defined in the standard IGA sense (see [30]), n is the number of basis functions and ξ is a parameter.

In the B-spline based FEM [8] applied to one-dimensional problems, the approximations of domain of interest $\Omega = [0, L]$ and displacement field u^h on Ω are given by

$$x(\xi) = \sum_{i=1}^n N_{i,p}(\xi) x_i^B \quad \text{and} \quad u^h(\xi) = \sum_{i=1}^n N_{i,p}(\xi) u_i^B, \tag{7}$$

where x_i^B is the x -coordinate of the control points and u_i^B is the component of the vector of control variables – displacements corresponding to the control points. It should be noted that the linear B-spline based FEM is identical to the standard linear FEM, i.e. with the hat shape functions. In what follows, the continuous Galerkin approximation method [7] for the numerical solution of partial differential equations is employed. Spatial discretization of elastodynamics problems by the continuous Galerkin approximation method [7] yields to

$$\mathbf{M}\mathbf{a} + \mathbf{K}\mathbf{u} = \mathbf{R}. \tag{8}$$

Here, \mathbf{M} is the mass matrix, \mathbf{K} the stiffness matrix, \mathbf{R} is the time-dependent load vector, \mathbf{u} and $\dot{\mathbf{u}} = \mathbf{a}$ contain control point variables – displacements and accelerations. The mass matrix, stiffness matrix and load vector are defined by the same relationships as in the standard FEM [7]. The element stiffness and mass matrices are given by

$$\mathbf{K}_e = \int_{V_e} E \mathbf{B}^T \mathbf{B} \, dV, \quad \mathbf{M}_e = \int_{V_e} \rho \mathbf{N}^T \mathbf{N} \, dV, \tag{9}$$

where \mathbf{B} is the strain-displacement matrix, \mathbf{N} stores the displacement shape functions and integration is carried over the non-deformed element domain V_e . The mass matrix defined by the relationship Eq. (9)₂ is called the consistent mass matrix. For lumping of the mass matrix of IGA in explicit time integration, we use the ‘row sum’ lumping approach [7]. In this paper, the mass and stiffness are evaluated by the Gauss-Legendre (full Gauss) quadrature formula of $p + 1$ order [7].

4. Results of direct time integration in IGA

In this section, results of wave propagation in a bar under shock loading are presented as well as the frequency spectrum of the discretized bar by linear, quadratic and cubic spline representations with the consistent and lumped mass matrices. For direct time integration in this paper, the Newmark method [31,32] and the generalized- α method [25] are used as implicit time integrators and the central difference method [33] and the predictor/multi-corrector [7,28] as explicit time integrators. The displacement, velocity and acceleration vectors at the time $t_n, t_n = n\Delta t$, are marked as follows: $\mathbf{u}_n, \mathbf{v}_n$, and \mathbf{a}_n , respectively. Δt denotes the constant time step size through the computations and n is a time step counter.

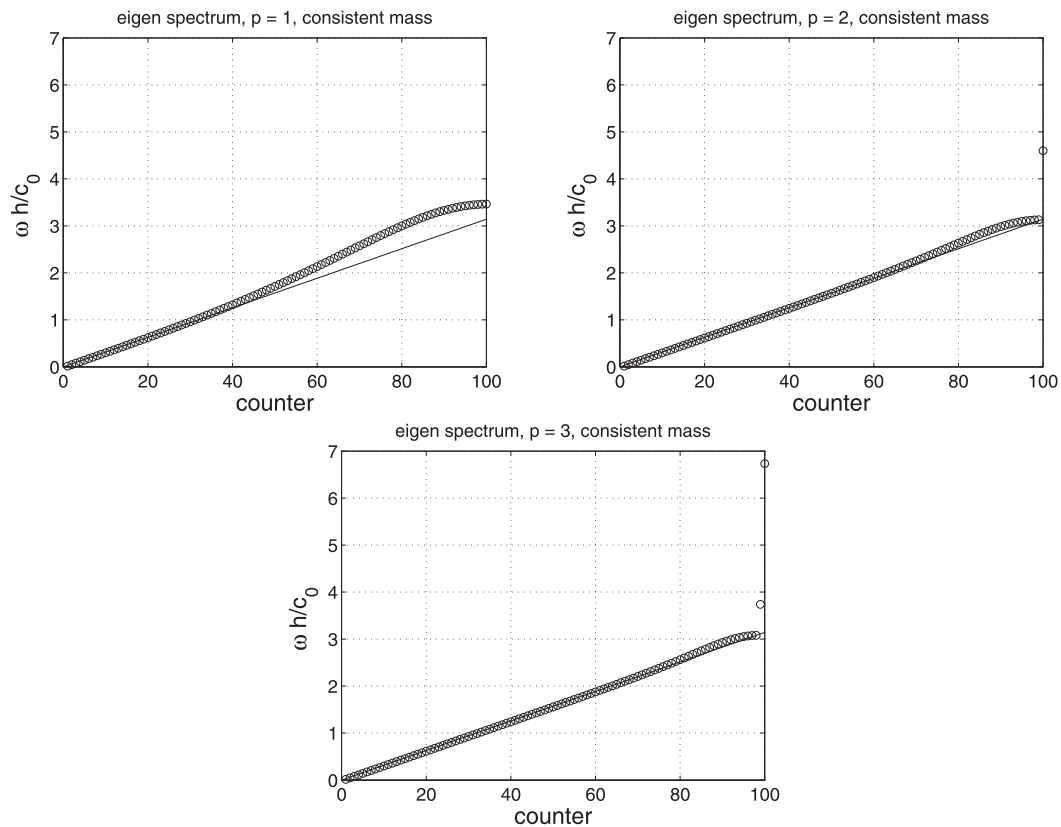


Fig. 2. Dimensionless eigenfrequencies of an elastic free-fixed bar discretized by linear ($p = 1$), quadratic ($p = 2$) and cubic ($p = 3$) B-spline with the consistent mass matrix. $h = L/(N - 1)$ denotes the averaged distance of control points.

4.1. Physical and numerical data of the bar test

Geometrical and material parameters of the task are set as follows (for simplicity): the bar length $L = 1$ m, the cross-section $A = 1$ m², the Young modulus $E = 1$ Pa, the mass density $\rho = 1$ kg/m³ and the amplitude of impact pressure $\sigma_0 = 1$ Pa. The time history of the loading is given by the Heaviside step function.

The bar is discretized either by linear ($p = 1$) or quadratic ($p = 2$) or cubic ($p = 3$) B-splines with $N = 101$ control points. In the B-spline discretization, the knot vector is employed as uniform one [30]. The position of control points along the bar is given by the Greville abscissa [34]. This parameterization is called linear one. It means that the mapping for the parametric space to the geometrical one is linear and Jacobians of this transformation are of a constant value. It is used since the linear parametrization produces smaller dispersion and frequency errors that characterized by uniformly-spaced control points [14].

4.2. Eigenfrequency analysis and selection of time step sizes

The discrete frequency spectrum of a bar discretized by the linear, quadratic and cubic B-spline approximations are presented in Fig. 2 for the consistent mass matrix and in Fig. 3 for the lumped mass matrix given by the ‘row sum’ approach [7]. The straight lines in Figs. 2 and 3 correspond to frequency distribution of dispersionless continuum. For the consistent mass matrix, one can see an improved progress of frequency spectrum with increasing spline order. On the other side, we lose accuracy of discrete frequency spectra for the lumped mass matrix and this effect is amplified for higher spline orders. Moreover, the ‘outlier frequencies’, which dictate maximum value of eigenfrequency, are observed for the higher-order spline discretizations for the both mass matrix types (see [12]). However, the ‘outlier frequencies’ are not observed for linear (FEM) IGA. The ‘outlier frequencies’ correspond to vibration of boundary part of a bar.

As it is known, the B-spline based FEM with the consistent mass matrix overestimates the real eigenfrequencies of an elastic free-fixed bar and errors of spectra decrease with increasing spline order. The B-spline based FEM with the lumped mass matrix underestimates the real eigenfrequencies of an elastic bar. For higher spline orders with the lumped mass matrix, the B-spline based FEM loses its accuracy in comparison with the consistent mass matrix [12,13,16].

In general, the maximum eigenfrequency of the discretized system defines the time step size and then accuracy of time stepping process and also stability of the computations for explicit methods. The maximum values of angular velocities ω_{max} of the tested bar discretized by the B-spline based IGA of different spline orders and for the consistent and lumped mass matrices are reported in Table 1. In the explicit computations by the central difference method, we chose the time step

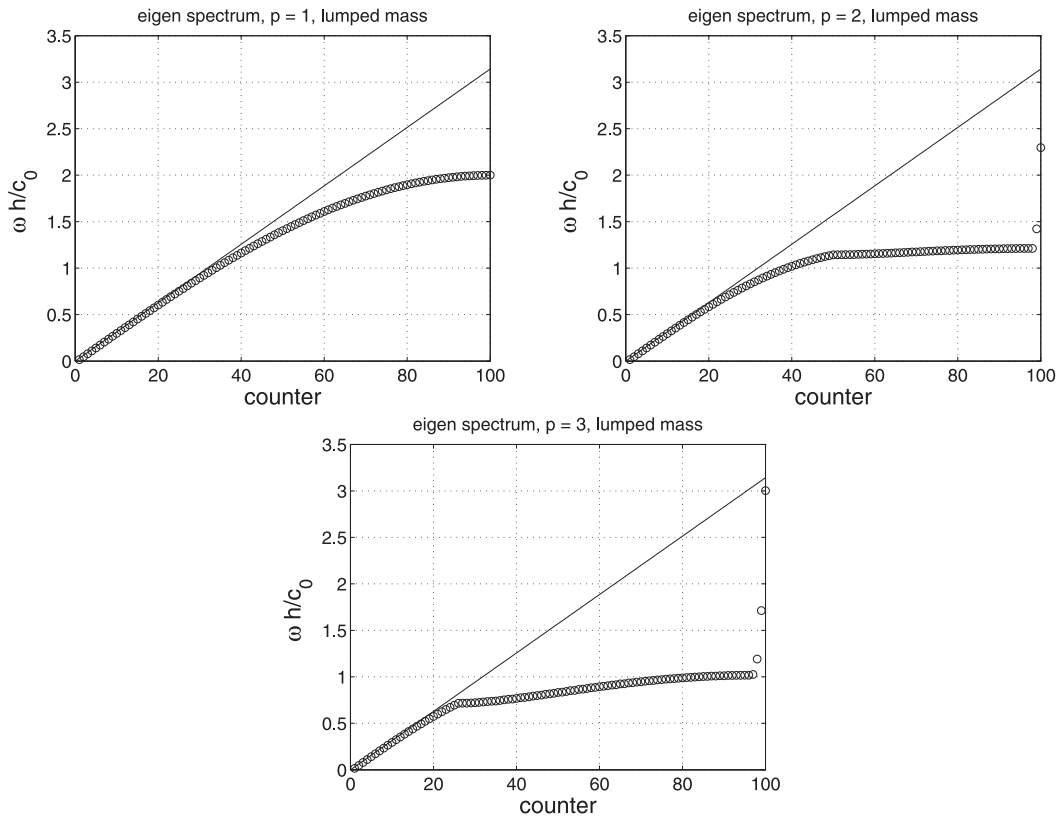


Fig. 3. Dimensionless eigenfrequencies of an elastic free-fixed bar discretized by linear ($p = 1$), quadratic ($p = 2$) and cubic ($p = 3$) B-spline with the lumped mass matrix by the ‘row sum’ approach. $h = L/(N - 1)$ denotes the averaged distance of control points.

Table 1
Dimensionless maximum eigenvalues $\bar{\omega}_{max} = \omega_{max}h/c_0$ for different bar discretizations and mass matrices.

Dimensionless maximum eigenvalues	Consistent mass $p = 1$	Consistent mass $p = 2$	Consistent mass $p = 3$	Lumped mass $p = 1$	Lumped mass $p = 2$	Lumped mass $p = 3$
$\bar{\omega}_{max} = \omega_{max}h/c_0$	3.464	4.599	6.733	2.000	2.297	3.003

Table 2
Time step sizes for implicit and explicit time schemes.

Time step sizes Δt [s] (Courant number $Co = \Delta t c_0/h$ [-])	Order $p = 1$	Order $p = 2$	Order $p = 3$
Implicit time schemes	0.00227 (0.227)	0.00171 (0.171)	0.00117 (0.117)
Explicit time schemes with lumped mass m.	0.01000 (1.000)	0.00871 (0.871)	0.00666 (0.666)
Explicit time schemes with consistent mass m.	0.00577 (0.577)	0.00435 (0.435)	0.00297 (0.297)

size with respect to the stability limit of the central difference method as $\Delta t^{exp} = \alpha \Delta t_{cr}$, $\alpha = 0.99999$, with $\Delta t_{cr} = 2/\omega_{max}$, see [35]. For the predictor/multi-corrector, the $\alpha = 0.9$ was selected. The both lumped and consistent mass matrices are exploited. In the implicit computations, we select the time step size so that $\Delta t^{imp} = 1/8 T_{min}$, where $T_{min} = 2\pi/\omega_{max}$. The values of the time step size for the implicit and explicit time integrations (for the lumped and consistent mass matrices) used in the paper are reported in Table 2. The values in brackets in Table 2 correspond to dimensionless values of the time step size $Co = \Delta t c_0/h$, where $h = L/(N - 1)$ denotes the averaged distance between control points. One can see the effect of decreasing of time step size with increasing spline order. Further, as we know, the critical time step for the consistent mass matrix is cardinally smaller than for the lumped mass matrix (see Table 2). This is due to the higher-order approximation of the B-spline representation and, mainly, due to the non-physical ‘outlier frequencies’ of IGA.

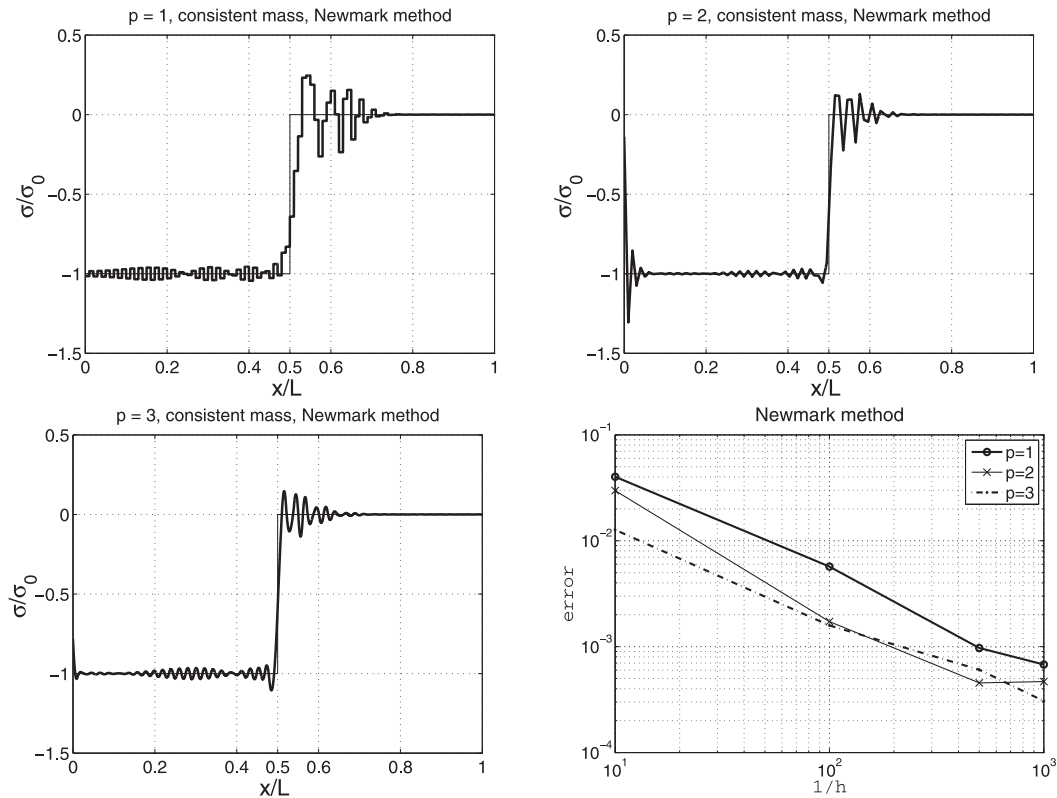


Fig. 4. Dimensionless stress in an elastic bar under the shock loading at time $t = 0.5L/c_0$ computed by the Newmark method with the consistent mass matrix for linear, quadratic and cubic B-spline spatial approximations. The thin line corresponds to the analytical solution of the wave propagation problem.

4.3. The Newmark method

The Newmark method [31] suggests of the following relations [32]

$$\mathbf{u}_{n+1} = \mathbf{u}_n + \Delta t \mathbf{v}_n + \frac{\Delta t^2}{2} ((1 - 2\beta)\mathbf{a}_n + 2\beta\mathbf{a}_{n+1}), \tag{10}$$

$$\mathbf{v}_{n+1} = \dot{\mathbf{u}}_t + \Delta t((1 - \gamma)\mathbf{a}_n + \gamma\mathbf{a}_{n+1}), \tag{11}$$

for solving the discretized equations of motion

$$\mathbf{M}\mathbf{a}_{n+1} + \mathbf{K}\mathbf{u}_{n+1} = \mathbf{R}_{n+1}, \tag{12}$$

where β and γ are the Newmark parameters. The parameters β and γ determine the stability and accuracy of the algorithm and were initially proposed by Newmark as $\beta = 1/4$ and $\gamma = 1/2$ thus securing the unconditional stability of the method. This method conserves total energy and this variant is often called the Newmark averaged acceleration method (for details see [31,32]). Further, the combination of the Newmark method (the averaged acceleration method with a suitable chosen time step size) and the consistent mass matrix produces spatial and temporal dispersion effect which could be mutually suppressed [9].

The space distribution of dimensionless stress σ/σ_0 along the bar at the time $t = 0.5L/c_0$ computed by the Newmark method ($\beta = 1/4$ and $\gamma = 1/2$) with the consistent mass matrix for linear, quadratic and cubic B-spline discretizations are shown in Fig. 4. Here, main spurious oscillations in the stress distribution along the bar obtained by the Newmark method take place in the front of the theoretical wavefront [29]. We call them front-shock oscillations. This phenomenon can be explained by dispersion behavior of spatial discretization. It is known, that values of wave speed of IGA system with the consistent mass matrix are overestimated [7,14], therefore the pulse is distorted in the front of the theoretical wavefront. The effect is more considerable for the linear discretization due to higher dispersion errors. The quadratic and cubic B-spline approximations produce smaller spurious oscillations due to better dispersion behavior. Moreover, dominant spurious oscillations can be observed at the free-end of the bar. This is due to existence of higher polluted 'outlier frequencies', which correspond to vibration of free-end (see Fig. 2). Also the convergence properties for different spline orders are presented in Fig. 4. The error of the numerical displacement field $u^h(t)$ is measured in the form $error = \frac{\|u^h(t) - u(t)\|_{L_2}}{\|u(t)\|_{L_2}}$, where $u(t)$ corresponds to the analytical solution Eq. 4.

4.4. Generalized- α method

The governing equations for the generalized- α method [25] are following:

$$\mathbf{M}\mathbf{a}_{n+1-\alpha_m} + \mathbf{K}\mathbf{u}_{n+1-\alpha_f} = \mathbf{R}_{n+1-\alpha_f}, \quad (13)$$

$$\mathbf{u}_{n+1} = \mathbf{u}_n + \Delta t \mathbf{v}_n + \Delta t^2 ((1/2 - \beta) \mathbf{a}_n + \beta \mathbf{a}_{n+1}), \quad (14)$$

$$\mathbf{v}_{n+1} = \mathbf{v}_n + \Delta t ((1 - \gamma) \mathbf{a}_n + \gamma \mathbf{a}_{n+1}), \quad (15)$$

$$\mathbf{u}_{n+1-\alpha_f} = (1 - \alpha_f) \mathbf{u}_{n+1} + \alpha_f \mathbf{u}_n, \quad (16)$$

$$\mathbf{v}_{n+1-\alpha_f} = (1 - \alpha_f) \mathbf{v}_{n+1} + \alpha_f \mathbf{v}_n, \quad (17)$$

$$\mathbf{a}_{n+1-\alpha_m} = (1 - \alpha_m) \mathbf{a}_{n+1} + \alpha_m \mathbf{a}_n, \quad (18)$$

$$\mathbf{R}_{n+1-\alpha_f} = (1 - \alpha_f) \mathbf{R}_{n+1} + \alpha_f \mathbf{R}_n \quad \text{or} \quad \mathbf{R}_{n+1-\alpha_f} = \mathbf{R}(t_{n+1-\alpha_f}), \quad (19)$$

$$t_{n+1-\alpha_f} = (1 - \alpha_f) t_{n+1} + \alpha_f t_n = t_{n+1} - \alpha_f \Delta t, \quad (20)$$

where α_f , α_m , γ , β are selected to ensure second-order accuracy, unconditional stability and optimal dissipation effects [25]. The generalized- α method with the following parameters

$$\begin{aligned} \alpha_m &= \frac{2\rho_\infty - 1}{\rho_\infty + 1}, & \alpha_f &= \frac{\rho_\infty}{1 + \rho_\infty}, \\ \beta &= \frac{1}{4}(1 - \alpha_m + \alpha_f)^2, & \gamma &= \frac{1}{2} - \alpha_m + \alpha_f, \end{aligned} \quad (21)$$

is an unconditionally stable, second-order accurate algorithm possessing an optimal combination of high-frequency and low-frequency dissipation [25]. The spectral radius ρ_∞ specifies the dissipation of the high-frequency modal components and minimal low-frequency dissipative properties. In this paper, we select the spectral radius value as $\rho_\infty = 0.5$. The effective computation with the generalized- α method based on the predictor-corrector procedure in the implicit form has been published, e.g., in [36]. The implicit form of the generalized- α method is unconditionally stable [24], therefore the time step size Δt can be chosen arbitrary. We select the time step size equal to that for the Newmark method.

The stress response of the bar obtained by the generalized- α method with the spectral radius $\rho_\infty = 0.5$ for IGA discretizations is shown in Fig. 5. One can see similar graphs of stress distribution as those in the Newmark method. The results obtained by the generalized- α method are accompanied by the lower level of spurious oscillations. This effect is due to the dissipative properties of this time integration scheme, where higher frequencies are suppressed. At the same time, front-shock spurious oscillations still appear near the theoretical wavefront. On the other side, the oscillations near the free-end of the bar are suppressed by this time integration method and, in general, the level of pollution of the results by spurious oscillations is smaller than that obtained by the Newmark method. Therefore, the generalized- α method is a suitable tool for direct time integration in implicit IGA computations of elastic wave propagation problems with discontinuities and shock loadings.

4.5. Central difference method

The central difference method [33] is based on the approximate relationships between the kinematical quantities

$$\mathbf{v}_n = \frac{1}{2\Delta t} (\mathbf{u}_{n+1} - \mathbf{u}_{n-1}), \quad \mathbf{a}_n = \frac{1}{\Delta t^2} (\mathbf{u}_{n+1} - 2\mathbf{u}_n + \mathbf{u}_{n-1}). \quad (22)$$

The latter relationships are then substituted into the equations of motion written at the time t^n . Consequently, we get a system of algebraic equations for the resolution displacements at the time $t^n + \Delta t$

$$\mathbf{M}^{\text{eff}} \mathbf{u}_{n+1} = \mathbf{R}^{\text{eff}}, \quad (23)$$

with the effective quantities

$$\mathbf{M}^{\text{eff}} = \mathbf{M}/\Delta t^2, \quad \mathbf{R}^{\text{eff}} = \mathbf{R}_n - (\mathbf{K} - 2\mathbf{M}/\Delta t^2) \mathbf{u}_n - (\mathbf{M}/\Delta t^2) \mathbf{u}_{n-1}. \quad (24)$$

The process is effective only if the mass matrix is made diagonal by a suitable lumping method. In this paper, the lumping process by the ‘row sum’ method is employed [7]. Presently, there are attempts to use the direct inversion of the consistent mass matrix in explicit integration [37]. In linear cases, the consistent mass matrix does not change and can be inverted only once before the integration process. This algorithm is time efficient, since only a matrix-vector multiplication

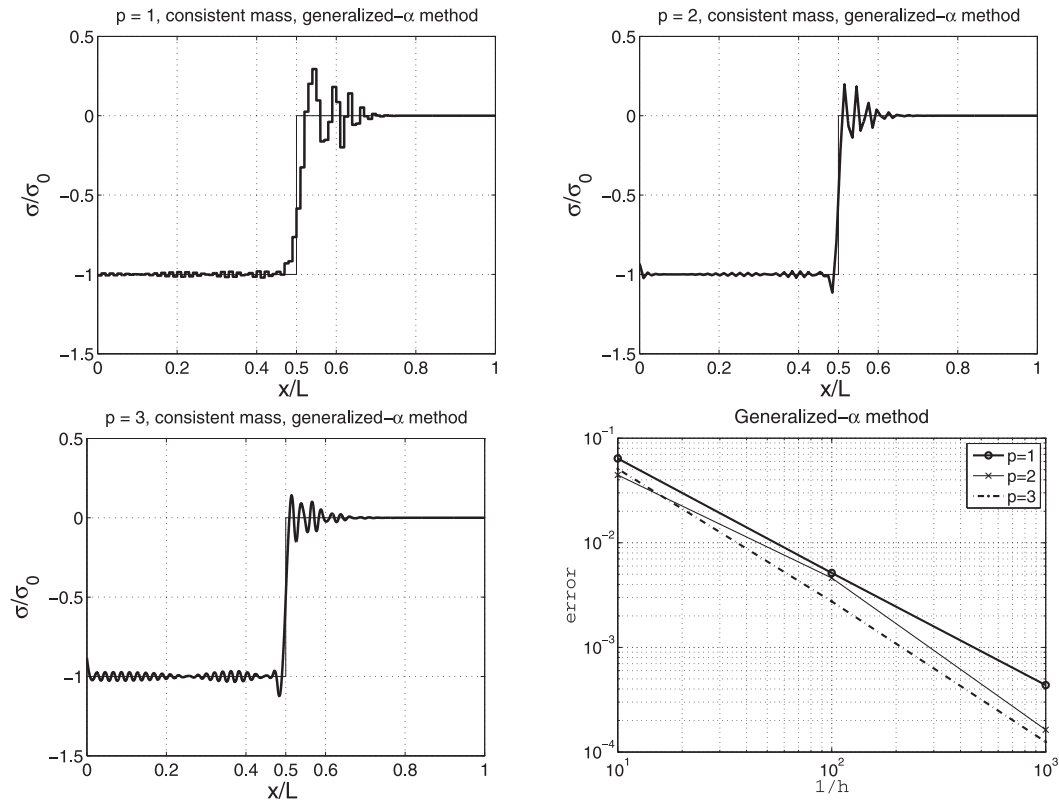


Fig. 5. Stress in an elastic bar under the shock loading at time $t = 0.5L/c_0$ computed by the implicit generalized- α method with the spectral radius $\rho_\infty = 0.5$ with the consistent mass matrix for linear, quadratic and cubic B-spline spatial approximations.

is needed in every time step. On the other hand, the critical time step size for the consistent mass matrix is cardinally smaller than for the lumped once. In this paper, we test the lumped mass matrix as well as the consistent mass matrix in explicit integration.

4.5.1. Central difference method with the lumped mass matrix

The space distribution of dimensionless stress σ/σ_0 along the bar at the time $t = 0.5L/c_0$ computed by the central difference method with the lumped mass matrix for linear, quadratic and cubic B-spline discretizations is shown in Fig. 6. For linear IGA (i.e. linear FEM) with the lumped mass matrix and the central difference method with the time step size near to the stability limit, the discretized system does not produce the temporal-spatial dispersion errors [21,38] and the numerical wave speed is equal to the theoretical value of elastic wave speed in a bar c_0 . For the linear FEM, the stress distribution in the form of Heaviside step function is excellently approximated. These results could only be achieved for one-dimensional finite element meshes with the same critical time step size for each element. On the other hand, the ‘outlier frequencies’ do not exist for linear FEM/IGA unlike higher order B-spline approximations. In mutli-dimensional problems, the spurious oscillations can not be fully suppressed by the optimal choice of the time step size due to existence of longitudinal and shear waves propagating with different wave speeds, (for suggestion for eliminating of spurious oscillations in explicit integration see [38]).

For higher order spline approximations, the spurious oscillations are observed in the stress distributions along the bar. The post-shock oscillations (oscillations occurring behind the theoretical wavefront) are typical for the central difference method with a lumped mass matrix. It is known, that eigenfrequencies and wave speed for the lumped mass matrix are underestimated with respect to values of theoretical eigenfrequencies and wave speed in an elastic bar considered as continuum [7,9]. The ‘row sum’ diagonal mass matrix is only of second order of accuracy [8], thus high frequencies provide considerable errors. Moreover, quadratic and cubic B-splines produce outlier frequencies in the frequency spectrum (see Fig. 3), thus the global critical time step size is given by the highest non-physical eigenfrequency. For that reason, spurious oscillations for the higher order B-spline discretization substantially influence the accuracy of the central difference computations. So, the central difference method with lumped mass matrix for higher order B-spline based FEM is not a good candidate for explicit time computations and the choice of a suitable accurate lumped mass matrix is still an open question.

4.5.2. Central difference method with the consistent mass matrix

The space distribution of dimensionless stress σ/σ_0 along the bar at the time $t = 0.5L/c_0$ computed by the central difference method with the consistent mass matrix for linear, quadratic and cubic B-spline discretizations is shown in Fig. 7. One

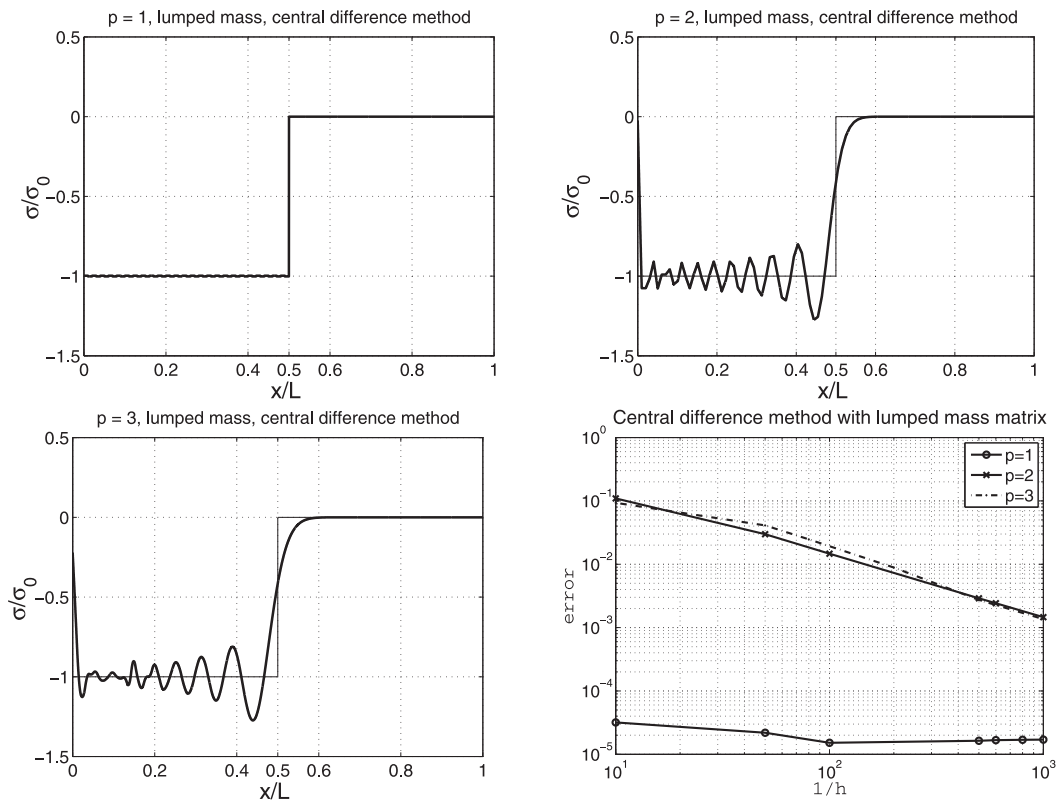


Fig. 6. Dimensionless stress in an elastic bar under the shock loading at time $t = 0.5L/c_0$ computed by the central difference method with the lumped mass matrix for linear, quadratic and cubic B-spline spatial approximations.

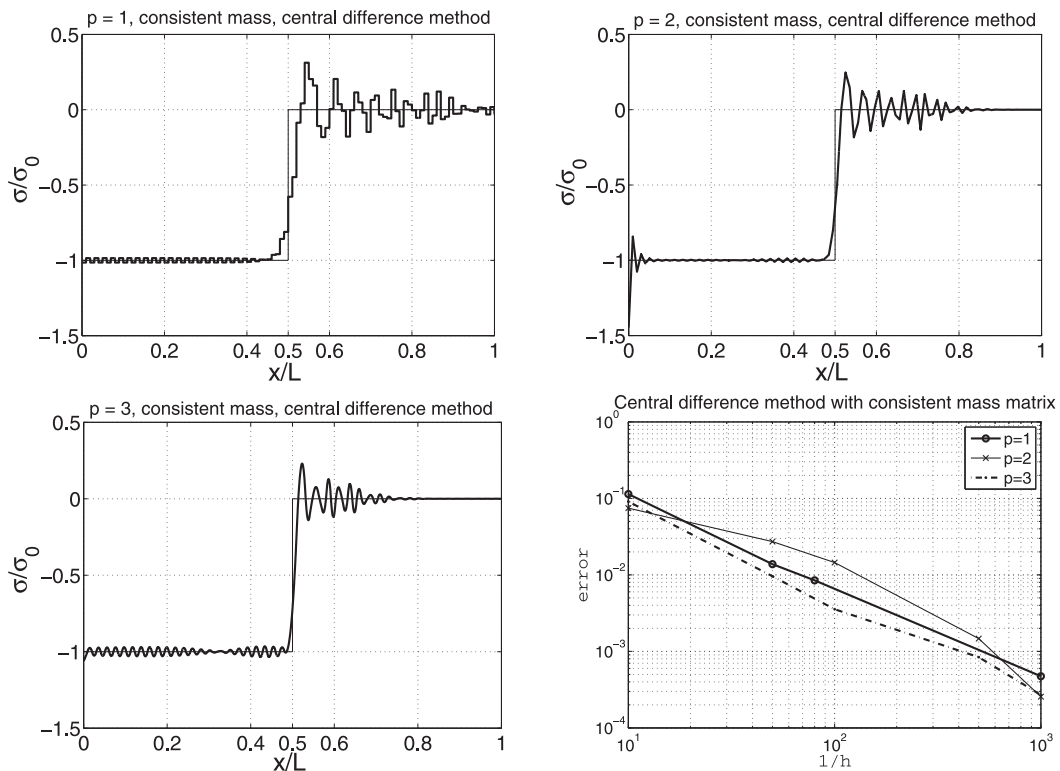


Fig. 7. Dimensionless stress in an elastic bar under the shock loading at time $t = 0.5L/c_0$ computed by the central difference method with the consistent mass matrix for linear, quadratic and cubic B-spline spatial approximations.

can see for the linear IGA (i.e. linear FEM) that the stress distribution is polluted by front-shock oscillations of larger level like for the results obtained by the Newmark method. It is a product of overestimation of numerical wave speed in linear IGA with the consistent mass matrix. On the other hand, the stress distributions for higher IGA contain smaller front-shock spurious oscillations than for linear IGA and the theoretical wavefront of sharp shape is very well approximated. For that reason, the consistent mass matrix is a good choice of a mass matrix in IGA explicit time integration due to the accuracy of approximation of stress fields with discontinuous shape.

4.6. Predictor/multi-corrector form of the generalized- α method

We shortly introduce the predictor/multi-corrector method (for details see [7,28,39]). The stability and accuracy of the predictor/multi-corrector (multi-pass) method has been studied in [39]. In this paper, we adopt the predictor/multi-corrector method based on the implicit form of the generalized- α method introduced in the previous section.

The modification of the predictor/multi-corrector method is mentioned below. In the following text, r marks an iteration counter. In the time stepping process, we compute for $r \geq 1$

$$\left. \begin{aligned} \mathbf{a}_{n+1}^{(0)} &= \mathbf{0} \\ \mathbf{v}_{n+1}^{(0)} &= \mathbf{v}_n + \Delta t(1 - \gamma)\mathbf{a}_n \\ \mathbf{u}_{n+1}^{(0)} &= \mathbf{u}_n + \Delta t\mathbf{v}_n + \frac{\Delta t^2}{2}(1 - 2\beta)\mathbf{a}_n \end{aligned} \right\} \text{predictor phase,} \tag{25}$$

$$\left. \begin{aligned} \text{for } i &= 0, 1, \dots, r - 1 \\ \mathbf{a}_{n+1-\alpha_m}^{(i)} &= (1 - \alpha_m)\mathbf{a}_{n+1}^{(i)} + \alpha_m\mathbf{a}_n \\ \mathbf{v}_{n+1-\alpha_f}^{(i)} &= (1 - \alpha_f)\mathbf{v}_{n+1}^{(i)} + \alpha_f\mathbf{v}_n \\ \mathbf{d}_{n+1-\alpha_f}^{(i)} &= (1 - \alpha_f)\mathbf{d}_{n+1}^{(i)} + \alpha_f\mathbf{d}_n \\ \mathbf{R}_{n+1-\alpha_f}^{(i)} &= (1 - \alpha_f)\mathbf{R}_{n+1} + \alpha_f\mathbf{R}_n \\ \mathbf{M}^L\Delta\mathbf{a}^{(i)} &= \mathbf{R}_{n+1-\alpha_f} - \mathbf{M}^R\mathbf{a}_{n+1-\alpha_m}^{(i)} - \mathbf{K}\mathbf{d}_{n+1-\alpha_f}^{(i)} \\ \mathbf{a}_{n+1}^{(i+1)} &= \mathbf{a}_{n+1}^{(i)} + \Delta\mathbf{a}^{(i)} \\ \mathbf{v}_{n+1}^{(i+1)} &= \mathbf{v}_{n+1}^{(i)} + \gamma\Delta t\Delta\mathbf{a}^{(i)} \\ \mathbf{u}_{n+1}^{(i+1)} &= \mathbf{u}_{n+1}^{(i)} + \beta\Delta t^2\Delta\mathbf{a}^{(i)} \\ \text{end} \end{aligned} \right\} \text{corrector phase,} \tag{26}$$

where r is the iteration counter.

In this paper, we select numerical parameters α_m , α_f , β and γ with respect to values for the implicit form of the generalized- α method (see (21)), for the value $\rho_\infty = 0.5$. We use the number of iteration loops as $r = 3$ satisfying the fourth order of accuracy [28]. In the algorithm presented above, \mathbf{M}^L and \mathbf{M}^R mark the left-hand-side and right-hand-side mass matrices, respectively. The right-hand-side mass matrix is chosen of the consistent type and the left-hand-side mass matrix is used in the diagonal form and also as the consistent mass matrix. In this paper, the diagonal left-hand-side mass matrix \mathbf{M}^L is computed by the ‘row sum’ lumped process [7].

4.6.1. Predictor/multi-corrector form of the generalized- α method with lumped \mathbf{M}^L

The stress response of the bar obtained by the predictor/multi-corrector form of the generalized- α method with the spectral radius $\rho_\infty = 0.5$ for linear, quadratic and cubic IGA discretizations is shown in Fig. 8. Here, the lumped left-hand-side mass matrix and the consistent right-hand-side mass matrix were used and only three-pass iteration loops were sufficient to satisfy the equation of motion for the generalized- α method with sufficient precision. For linear IGA/FEM, one can see small post- and front-shock spurious oscillations near the theoretical wavefront and the central difference method produces better results than the predictor/multi-corrector method. On the other hand, the predictor/multi-corrector gives better results than the central difference method for higher order spline approximations. Post-shock spurious oscillations still exist in the stress distribution along the bar. We can say that the partial suppressing of spurious oscillations is due to the dissipative effect of the predictor/multi-corrector method based on the generalized- α method and the spurious oscillations have lower level of pollution than that for the central difference method. For that reason, the predictor/multi-corrector form of the generalized- α method as an explicit time integration in higher-order IGA is a suitable candidate for explicit time computations of elastic wave propagation problems with discontinuities. Another advantage of the predictor/multi-corrector form of the generalized- α method is that it does not need the right-hand-side mass matrix of a lumped type.

4.6.2. Predictor/multi-corrector form of the generalized- α method with consistent \mathbf{M}^L

The stress response of the bar obtained by the predictor/multi-corrector form of the generalized- α method with the spectral radius $\rho_\infty = 0.5$ for linear, quadratic and cubic IGA discretizations is shown in Fig. 9. Here, the consistent left-hand-side mass matrix and the consistent right-hand-side mass matrix with three-pass iteration loops are used. This choice of

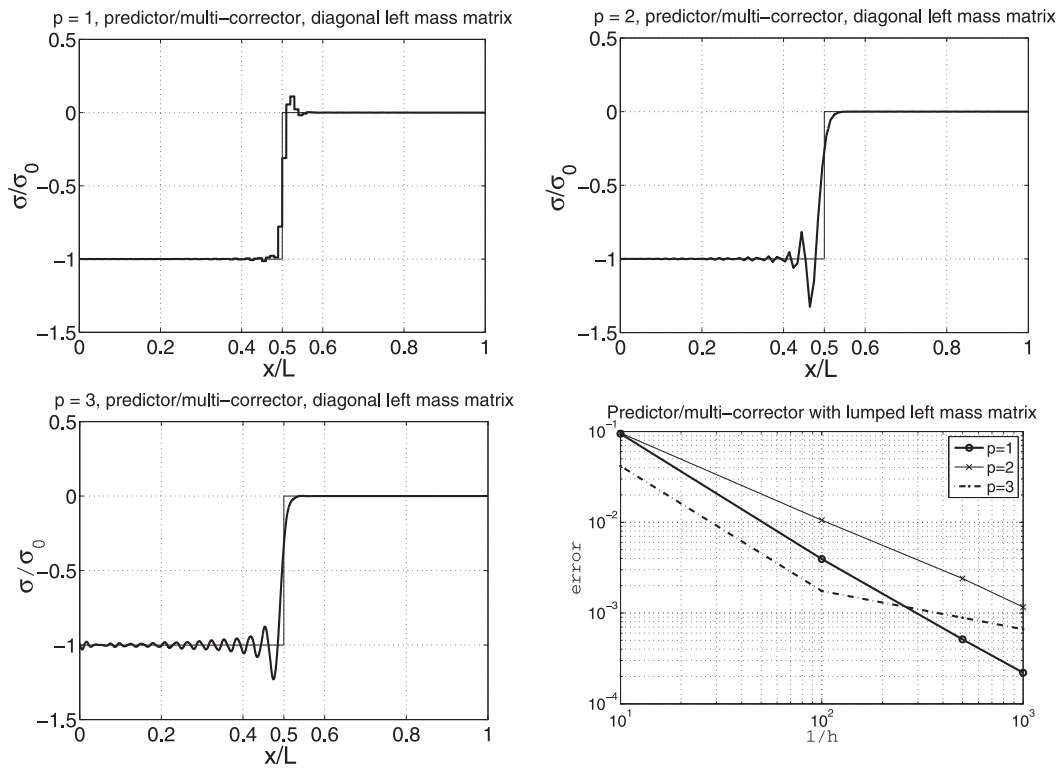


Fig. 8. Dimensionless stress in an elastic bar under the shock loading at time $t = 0.5L/c_0$ computed by the predictor/multi-corrector form of the generalized- α method with the spectral radius $\rho_\infty = 0.5$ and with the left-side lumped mass matrix and the right-side consistent mass matrix for linear, quadratic and cubic B-spline spatial approximations.

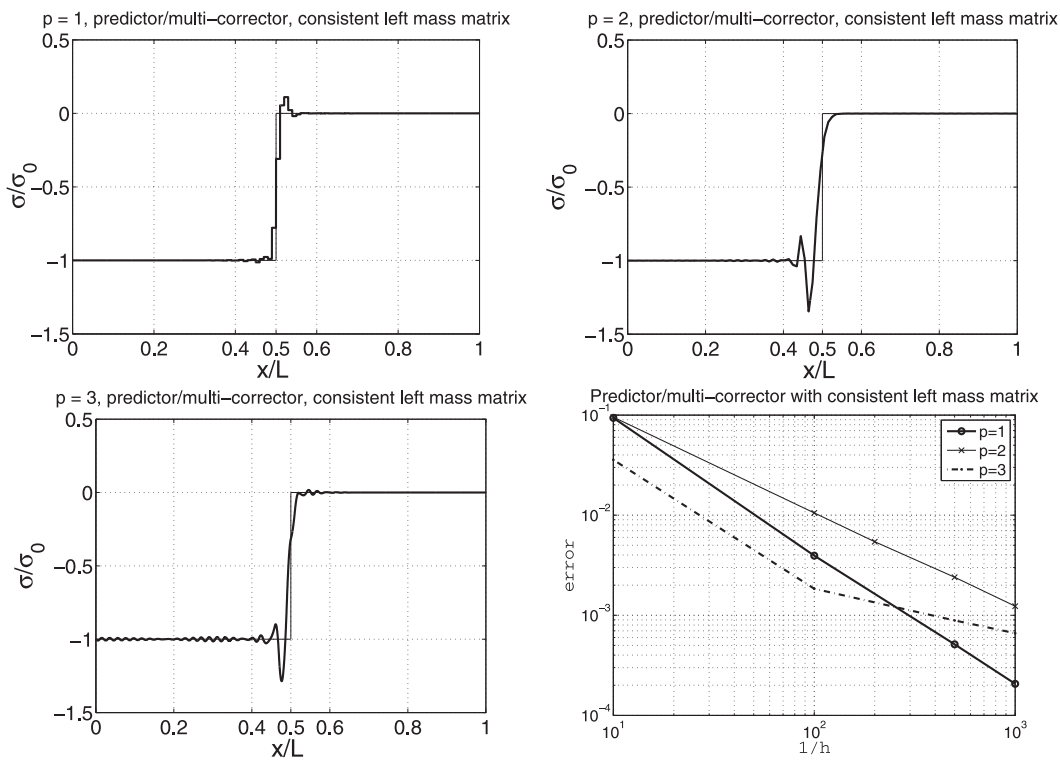


Fig. 9. Dimensionless stress in an elastic bar under the shock loading at time $t = 0.5L/c_0$ computed by the predictor/multi-corrector form of the generalized- α method with the spectral radius $\rho_\infty = 0.5$ and with the left-side consistent mass matrix and the right-side consistent mass matrix for linear, quadratic and cubic B-spline spatial approximations.

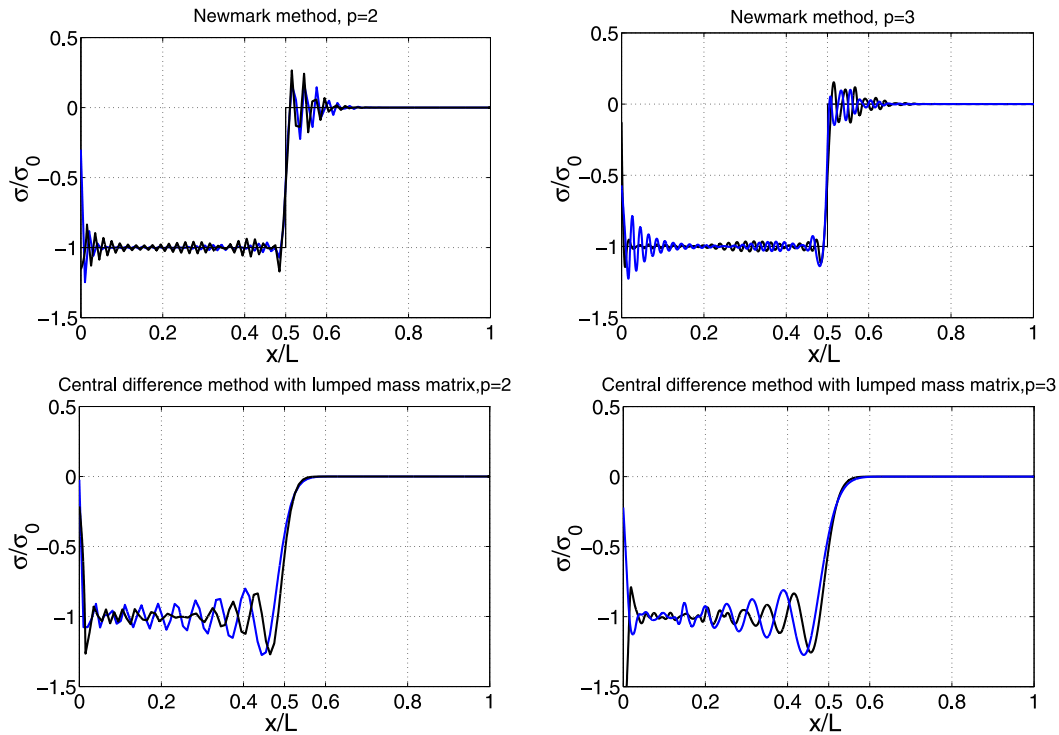


Fig. 10. An effect of linear (blue line) and nonlinear (black line) parameterization: Dimensionless stress in an elastic bar under the shock loading at time $t = 0.5L/c_0$ computed by the Newmark method and the central difference method with the lumped mass matrix for quadratic and cubic B-spline spatial approximations. (For interpretation of the references to color in this figure legend, the reader is referred to the web version of this article.)

mass matrices of consistent type for the predictor/multi-corrector scheme produces good results for higher/order IGA with acceptable level of post- and front-shock spurious oscillations and with good approximation of the theoretical wavefront. Therefore, the right-hand-side and left-hand-side mass matrices of consistent type are preferred for higher-order IGA. In this case, a special lumping process and mass matrix development is not needed for higher-order IGA.

4.7. Effect of parameterization

The effect of parameterization in the B-spline based FEM on dispersion behavior has been studied in [14], where the linear parameterization given by the Greville abscissa (called the linear one) and the nonlinear one given by uniformly-spaced control points have been compared with a special setting of control points with optimal dispersive behavior of the B-spline based FEM.

In the paper, we compare the stress distribution for the linear and nonlinear B-spline parameterizations on an one-dimensional domain of interest. The results obtained by the Newmark method and the central difference method are presented in Fig. 10. One can see that the linear parameterization produces better stress distribution near the theoretical wavefront than the nonlinear one, but spurious oscillations near a free boundary crop up. On the other hand, these higher frequency spurious oscillations are partially eliminated by integration with the implicit or predictor/multi-corrector form of the generalized- α method.

Generally, a multi-patch discretization with C^0 continuity or free boundaries in IGA produce spurious oscillations, higher non-physical frequency behavior with optical modes and outlier frequencies [14] as well as reflection-transmission errors in wave propagation problems. Each non-homogeneity in IGA discretization produces reflection-transmission errors. Therefore, IGA discretization with full continuity of spatial discretization is preferred in wave propagation problems. For detailed reflection-transmission analysis of FEM with different mesh sizes and unstructural meshes see [40] or the Cohen's book [41].

4.8. Notes to implementation of explicit scheme with consistent mass matrix

In the central difference method, the cardinal issue is effectively to solve the equation of motion in the form $\mathbf{M}_{n+1}\mathbf{a}_{n+1} = \mathbf{f}_{n+1}^{ext} - \mathbf{f}_{n+1}^{int}$ for fully nonlinear tasks in each time step for corresponding mass matrix. Here \mathbf{f}_{n+1}^{ext} and \mathbf{f}_{n+1}^{int} mark the external and internal nodal forces, respectively. As we said above, the inversion of the lumped mass matrix represents a trivial numerical task. On the other side, based on presented numerical tests for IGA in this paper, the consistent mass matrix is recommended against the lumped mass matrix due to accuracy of stress distribution. In principle, the inversion of consistent mass matrix is an extremely expensive task for computing it in each time step for time-dependent or large deformation

problems. One can use an approach for direct inversion of the consistent mass matrix presented in [37] with modification to IGA.

Practically, the stepping process with the consistent mass matrix can be implemented in the following form

$$\mathbf{I}\mathbf{a}^{n+1} = \mathbf{M}_{n+1}^{-1}(\mathbf{f}_{ext}^{n+1} - \mathbf{f}_{int}^{n+1}), \quad (27)$$

where \mathbf{I} is the unit matrix. In that case, the standard explicit computational process is retained and only the multiplying residual forces by the inverted mass matrix is needed.

5. Conclusions

In this paper, the B-spline based FEM (IGA) of the Galerkin type has been tested on the example of one-dimensional discontinuous stress wave propagation in elastic medium. The special attention has been paid to comparison of spurious oscillations emerging for different orders of B-spline discretizations and for various direct time integration methods. Also the convergence rates have been computed and compared. In addition, discrete frequency spectra of a free-fixed elastic bar discretized by the B-spline based FEM has been analyzed for various spline orders and for the consistent and lumped mass matrices. Further, The influence of spline orders and mass matrix type on the critical time step size in explicit integration are also reported.

In the case of implicit time integration, we have tested the Newmark method and the generalized- α method. Based on the comparison of the stress distributions along the bar loading by a shock, the generalized- α method gives better results of stress than the Newmark method in the sense of stress accuracy. The reason is that the generalized- α method can efficiently suppress higher non-physical modes of the discretized bar and the stress distributions exhibit lower level of spurious oscillations. In general, results of the B-spline based FEM in implicit time computations are polluted by front-shock spurious oscillations, i.e., oscillations of stresses in front of theoretical wavefront. Nevertheless, this time integration scheme is preferred in implicit time integration in IGA computations of time-depend problems in solids.

Using explicit time integration, we have tested the central difference method and the predictor/multi-corrector form of the generalized- α method. The both methods have been tested for consistent and lumped left-hand side mass matrix. For linear FEM/IGA, the lumped mass matrix is preferred in connection with the both tested explicit time schemes. On the other hand, the consistent left- and right-hand side mass matrices are recommended to use for higher-order IGA computations. Based on the numerical testing, explicit computations by the central difference method with the consistent mass matrix is a good choice for accurate elastic wave modeling. Even better results can be obtained by the time scheme in the predictor/multi-corrector form of the generalized- α method with left- and right-hand side mass matrices of consistent type.

In the future, our attention will be focused to an optimal choice of the time step size for implicit and explicit direct integration methods in IGA, to a choice of optimal numerical quadrature rules and the development of higher-order accurate mass matrix with the direct inversion for IGA.

Acknowledgments





The work of D. Gabriel was supported by the Centre of Excellence nonlinear dynamic behavior of advanced materials in engineering CZ.02.1.01/0.0/0.0/15_003/0000493 (Excellent Research Teams) in the framework of Operational Programme Research, Development and Education. The work of R. Kolman was supported by the grant project of the Czech Science Foundation, GAP101/12/2315. The work of J. Kopačka was supported by the grant project of the Czech Science Foundation, GA 16-03823S, within institutional support RVO:61388998. Further, the joint work has been supported by the bilateral project between the Estonian Academy of Sciences and the Czech Academy of Sciences (project No. ETA-15-03 entitled 'Advanced numerical modeling of dynamic processes in solids'). Results have been discussed with Anne Schäuble of the University of Stuttgart under the bilateral mobility project No. DAAD-16-12.

References

- [1] N.A. Kampanis, V.A. Dougalis, J.A. Ekaterinaris, *Effective computational methods for wave propagation*, Chapman & Hall/CRC, Boca Raton, 2008.
- [2] M.J. Grote, A. Schneebeli, D. Schöotzau, Discontinuous Galerkin finite element method for the wave equation, *SIAM J. Numer. Anal.* 44 (2006) 2408–2431.
- [3] J. Réthoré, A. Gravouil, A. Combescure, A combined space-time extended finite element method, *Int. J. Numer. Meth. Eng.* 64 (2005a) 260–284.
- [4] J. Réthoré, A. Gravouil, A. Combescure, An energy-conserving scheme for dynamic crack growth using the eXtended finite element method, *Int. J. Numer. Meth. Eng.* 63 (2005b) 631–659.
- [5] T. Menouillard, J. Réthoré, A. Combescure, H. Bung, Efficient explicit time stepping for the extended finite element method (X-FEM), *Int. J. Numer. Meth. Eng.* 68 (2006) 911–939.
- [6] T. Belytschko, T.R.J. Hughes, *Computational method for transient analysis*, first ed., North Holland, Amsterdam, 1986.
- [7] T.J.R. Hughes, *The Finite element method: Linear and dynamic finite element analysis*, first ed., Prentice-Hall, Englewood Cliffs, New York, 1983.
- [8] J.A. Cottrell, T.J.R. Hughes, Y. Bazilevs, *Isogeometric Analysis: Toward Integration of CAD and FEA*, first ed., John Wiley & Sons, New York, 2009.
- [9] T. Belytschko, R. Mullen, On dispersive properties of finite element solutions, in: J. Miklowitz, J. Achenbach, et al. (Eds.), *Modern Problems in Elastic Wave Propagation*, John Wiley & Sons Inc., New York, 1978, pp. 67–82.
- [10] M. Okrouhlik, C. Höschl, A contribution to the study of dispersive properties of one-dimensional lagrangian and hermitian elements, *Comp. Struct.* 49 (1993) 779–795.
- [11] J.A. Cottrell, T.J.R. Hughes, A. Reali, Studies of refinement and continuity in Isogeometric structural analysis, *Comput. Methods Appl. Mech. Eng.* 196 (2007) 4160–4183.

- [12] T.J.R. Hughes, A. Reali, G. Sangalli, Duality and unified analysis of discrete approximations in structural dynamics and wave propagation: Comparison of p-method finite elements with k-method NURBS, *Comput. Methods Appl. Mech. Eng.* 197 (2008) 4104–4124.
- [13] J.A. Cottrell, A. Reali, Y. Bazilevs, T.J.R. Hughes, Isogeometric analysis of structural vibrations, *Comput. Methods Appl. Mech. Eng.* 195 (2006) 5257–5296.
- [14] R. Kolman, J. Plešek, M. Okrouhlík, Complex wavenumber Fourier analysis of the B-spline based finite element method, *Wave Motion* 51 (2014) 348–359.
- [15] L. Dedè, C. Jäggli, A. Quarteroni, Isogeometric numerical dispersion analysis for two-dimensional elastic wave propagation, *Comput. Methods Appl. Mech. Eng.* 284 (2015) 320–348.
- [16] A. Reali, An Isogeometric analysis approach for the study of structural vibrations, *J. Earthq. Eng.* 10 (2006) 1–30.
- [17] R. Kolman, S.V. Sorokin, B. Bastl, J. Kopačka, J. Plešek, Isogeometric analysis of free vibration of simple shaped elastic samples, *J. Acoust. Soc. Am.* 137 (2015) 2089–2100.
- [18] R. Cimrman, M. Novák, R. Kolman, M. Tůma, J. Vackář, Isogeometric analysis in electronic structure calculations, *Mathematics and Computers in Simulation* (2016), in press, <http://dx.doi.org/10.1016/j.matcom.2016.05.011>
- [19] T.J.R. Hughes, J.A. Evans, A. Reali, Finite element and NURBS approximations of eigenvalue, boundary-value, and initial-value problems, *Comput. Methods Appl. Mech. Eng.* 272 (2014) 290–320.
- [20] R. Kolman, J. Plešek, M. Okrouhlík, D. Gabriel, Grid dispersion analysis of plane square biquadratic serendipity finite elements in transient elastodynamics, *Int. J. Numer. Meth. Eng.* 96 (2013) 1–28.
- [21] R. Kolman, J. Plešek, J. Červ, M. Okrouhlík, P. Pařík, Temporal-spatial dispersion and stability analysis of finite element method in explicit elastodynamics, *Int. J. Numer. Meth. Eng.* 106 (2016) 113–128.
- [22] H.M. Hilber, T.J.R. Hughes, Collocation, dissipation and overshoot for time integration schemes in structural dynamics, *Earthq. Eng. Struct.* 5 (1977) 99–117.
- [23] H. Hilber, T.J.R. Hughes, R.L. Taylor, Improved numerical dissipation for time integration algorithms in structural dynamics, *Earthquake Eng. Struct.* 5 (1977) 283–292.
- [24] G.M. Hulbert, J. Chung, Explicit time integration algorithms for structural dynamics with optimal numerical dissipation, *Comput. Methods Appl. Mech. Eng.* 137 (1996) 175–188.
- [25] J. Chung, G.M. Hulbert, A time integration algorithm for structural dynamics with improved numerical dissipation: The generalized- α method, *J. Appl. Mech.-T ASME* 60 (1993) 371–375.
- [26] Y. Mirbagheri, H. Nahvi, J. Parvizian, A. Düster, Reducing spurious oscillations in discontinuous wave propagation simulation using high-order finite elements, *Comput. Math. Appl.* 70 (2015) 1640–1658.
- [27] T.J.R. Hughes, K.S. Pister, R.L. Taylor, Implicit-explicit finite elements in nonlinear transient analysis, *Comput. Methods Appl. Mech. Eng.* 17/18 (1979) 159–182.
- [28] F. Auricchio, L.B.a.d. Veiga, T.J.R. Hughes, A. Reali, G. Sangalli, Isogeometric collocation for elastostatics and explicit dynamics, *Comput. Methods Appl. Mech. Eng.* 249–252 (2012) 2–14.
- [29] K.F. Graff, *Wave motion in elastic solids*, first ed., Oxford University Press, 1975.
- [30] L. Piegl, W. Tiller, *The NURBS book*, first ed., Springer-Verlag, 1997.
- [31] N.M. Newmark, A method of computation for structural dynamic, *J. Eng. Mech. Div.-ASCE* 85 (1959) 67–94.
- [32] K. Subbaraj, M.A. Dokainish, A survey of direct time-integration methods in computational structural dynamics - II, *Implicit Methods*, *Comp. Struct.* 32 (1989) 1387–1401.
- [33] M.A. Dokainish, K. Subbaraj, A survey of direct time-integration methods in computational structural dynamics - I, *Explicit Methods*, *Comp. Struct.* 32 (1989) 1371–1386.
- [34] T.N.E. Greville, On spline function, in: O. Shiska (Ed.), *Inequalities*, Academic Press, New York, 1967, pp. 255–291.
- [35] K.C. Park, Practical aspect of numerical time integration, *Comp. Struct.* 7 (1977) 343–353.
- [36] E. Grosu, I. Harari, Stability of semidiscrete formulations for elastodynamics at small time steps, *Finite Elem. Anal. Des.* 43 (2007) 533–542.
- [37] A. Tkachuk, M. Bischoff, Direct and sparse construction of consistent inverse mass matrices: general variational formulation and application to selective mass scaling, *Int. J. Numer. Meth. Eng.* 101 (2015) 435–469.
- [38] R. Kolman, S.S. Cho, K.C. Park, Efficient implementation of an explicit partitioned shear and longitudinal wave propagation algorithm, *Int. J. Numer. Meth. Eng.* 107 (2016) 543–579.
- [39] T.J.R. Hughes, T.E. Tezduyar, Stability and accuracy analysis of some fully-discrete algorithms for the one-dimensional second-order wave equation, *Comp. Struct.* 19 (1984) 665–668.
- [40] Z.P. Bažant, Spurious reflection of elastic waves in nonuniform finite elements grids, *Comput. Methods Appl. Mech. Eng.* 16 (1978) 91–100.
- [41] G.C. Cohen, *Higher-Order Numerical Methods for Transient Wave Equation*, Springer-Verlag, Berlin Heidelberg, 2002.

Explicit multistep time integration for discontinuous elastic stress wave propagation in heterogeneous solids

S. S. Cho¹  | R. Kolman²  | J. A. González³  | K. C. Park⁴ 

¹RAM Transportation and Storage Technology Division, Korea Atomic Energy Research Institute, Daejeon, Korea

²Institute of Thermomechanics, The Czech Academy of Sciences, Prague, Czech Republic

³Escuela Técnica Superior de Ingeniería, Universidad de Sevilla, Seville, Spain

⁴Department of Aerospace Engineering Sciences, University of Colorado, Boulder, Colorado

Correspondence

K. C. Park, Department of Aerospace Engineering Sciences, University of Colorado, Boulder, CO 80309-429.
Email: kcpark@colorado.edu

Funding information

Nuclear Safety Research Program; Korea Foundation of Nuclear Safety (KOFONS), Nuclear Safety and Security Commission (NSSC), Republic of Korea, Grant/Award Number: 1403013 and 1803015; Centre of Excellence; Operational Program Research, Development and Education, and Czech Science Foundation, Grant/Award Number: 17-22615S and RVO:61388998

Summary

A multistep explicit time integration algorithm is presented for tracking the propagation of discontinuous stress waves in heterogeneous solids whose subdomain-to-subdomain critical time step ratios range from tens to thousands. The present multistep algorithm offers efficient and accurate computations for tracking discontinuous waves propagating through such heterogeneous solids. The present algorithm, first, employs the partitioned formulation for representing each subdomain, whose interface compatibility is enforced via the method of the localized Lagrange multipliers. Second, for each subdomain, the governing equations of motion are decomposed into the extensional and shear components so that tracking of waves of different propagation speeds is treated with different critical step sizes to significantly reduce the computational dispersion errors. Stability and accuracy analysis of the present multistep time integration is performed with one-dimensional heterogeneous bar. Analyses of the present algorithm are also demonstrated as applied to the stress wave propagation in one-dimensional heterogeneous bar and in heterogeneous plain strain problems.

KEYWORDS

component-wise partitioned equations of motion, explicit multistep time integration, heterogeneous solids, localized Lagrange multipliers

1 | INTRODUCTION

Recently, as the performance of the mechanical technology has been improved, various kinds of materials have been used in the machine, and as the operation speed has increased, it has become a necessary requirement to design the machine so as to perform its functions while being subjected to an impact load. Therefore, the study on the impact problem of a machine made of different materials is recognized as an important issue not only in the safety design of the machine but also in the overall machine industry. Since the deformation behavior of the dissimilar materials subjected to the impact load is determined by the transmission and reflection of the stress wave at their own interfaces, it is necessary to study the propagation of the stress wave at the interface of the heterogeneous materials. Currently, the propagation of the stress wave on a single material and the dispersion and dissipation error due to numerical analysis have been studied extensively.

However, there are very few research works on the propagation of stress wave on heterogeneous materials. The study of stress waves began in the mid-nineteenth century, and Kolsky¹ conducted a limited study on simple one-dimensional or two-dimensional problems, although the theory of propagation of stress waves in elastodynamics was first systematized. Since the governing equation of this wave propagation is represented by the hyperbolic equation, the definition of the stress wave has discontinuity or singularity at the wave front. Therefore, theoretical approaches to the propagation of stress waves by the computation of the stress fields in complex solids have been limited, and many researchers have been actively studying the methods of solving the hyperbolic equations using the finite element method.² Reed and Hill³ drastically reduced the numerical dispersion error by introducing a discontinuous Galerkin method for the calculation of the neutron transport equation consisting of hyperbolic equations. Hughes and Hulbert^{4,5} and Huang and Costanzo⁶ proposed a finite element method using a space-time discontinuous Galerkin method to analyze the propagation of stress wave in a solid body and conducted a study on convergence and stability. Wendlandt and Marsden⁷ and Kane et al⁸ numerically integrated the equations governing the mechanical system by taking the variational principle in the action integral of the discrete Hamiltonian rather than the equations of motion. Casadei and Halleux⁹ proposed the binary spatial partitioning of the central-difference time integration scheme for explicit fast transient dynamics using a time step variable not only in time but also in space, and Chang¹⁰ presented a new family of explicit time integration, which had the same characteristic equation as the Newmark family method for linear structural dynamics. However, their time integrators seem to be less effective in capturing the discontinuous stress waves. Cho et al¹¹ proposed a method to reduce dispersion error and dissipation error of stress wave by introducing a discontinuity operator in the variational integrator. Ye et al¹² proposed an selective mass scaling (SMS) method for computing the shear wave propagation in nearly incompressible materials in which shear deformation is dominant. The SMS was derived based on volumetric and shear mode decomposition and increased the stable time step size in explicit analysis. González et al¹³ proposed the efficient method for generating the inverse mass matrix of structural dynamics problem to improve the accuracy of target frequency ranges and/or wave contents.

Numerical analysis of transmission and reflection of stress waves in heterogeneous solids was done by a few researchers. Prager¹⁴ described mathematically the continuous conditions of displacement and stress at the discontinuous interface in the linear elastic problem as a classical principle of variational method and described how to apply to the finite element method. Virieux^{15,16} proposed the velocity-stress finite difference method to numerically calculate the P-SV and SH wave propagation problems in heterogeneous media in the viewpoint of seismologists. Park et al¹⁷ proposed the new integration formula that is obtained by push-forward pullback operators in time element-by-element designed to filter postshock oscillation, and the central difference method (CDM) that intrinsically filters front-shock oscillations. A judicious combination of these two characteristics has been shown to substantially reduce both spurious front-shock and postshock oscillations in one-dimensional heterogeneous solids. For multidimensional solids, the component-wise partitioned equations of motions of extensional and shear stress components were developed, each of the decomposed equations of motion are integrated by the push-forward pullback operators.¹⁸ As a result, the front-shock and postshock spurious oscillations are shown to be significantly reduced and the wave fronts of different speeds were tailored to track by way of stiffness decomposition of the total stiffness into extension and shear components. Kolman et al¹⁹ proposed an improving method for efficiently performing the work of Cho et al¹⁸ and extended this method to impact problems with contact conditions. Gravouil and Combescure^{20,21} proposed the multiple time step with different time discretization in each subdomain, which allows to couple explicit and implicit numerical methods. They also presented heterogeneous asynchronous time integrators for computational structural dynamics, which used an alternative dual approach based on the velocity continuity at the interface between heterogeneous time integrators.²²

This paper presents a multistep time integration algorithm for computing the discontinuous stress wave propagation in heterogeneous solids. Different time step advancing can be adopted for each partition domains by using their own critical time step sizes. In this paper, integration process employing different step sizes for different partitions is labeled *multiple integration*. This study adopts the component-wise partitioned equations of motion for each partition and the push-forward pullback time integration¹⁸ to reduce the computational dispersion errors in heterogeneous materials with significantly large time step ratios. The continuity of the interface between heterogeneous time integrators considers traction and acceleration, all of which are enforced via the method of localized Lagrange multipliers.²³ It is emphasized that the main focus of the present work is to minimize spurious oscillations (due largely to the Gibbs phenomena) of discontinuous wave (eg, stress waves) and at the same track the wave fronts of solid wave components (such as axial, shear, and surface waves) as accurately as possible. For continuous wave propagation the reader may consult standard time integration literature (see, eg, the work of Newmark²⁴).

2 | GOVERNING EQUATIONS

This section briefly reviews the fundamental equation of motion for the dynamic problem and the corresponding component-wise partitioned equations of the longitudinal and shear stress waves in solids and the push-forward and pullback explicit time integration algorithm.^{18,19,25,26}

2.1 | Strong form of dynamic problem in solids

Let $(\Omega \subset \mathbb{R}^3)$ be an open and bounded domain with piecewise smooth boundary $\Gamma = \partial\Omega$. The strong formulation of dynamic problem in solid is written as follows:

$$\begin{aligned}
 \rho \ddot{u}_i &= \sigma_{ij,j} + b_i \text{ in } \Omega \times [t^0, T] \\
 \sigma_{ij} &= C_{ijkl} u_{k,l} \\
 u_i &= g_i \text{ on } \Gamma_{D_i} \times [t^0, T] \\
 \sigma_{ij} n_j &= h_i \text{ on } \Gamma_{N_i} \times [t^0, T] \\
 u_i(\mathbf{x}, t^0) &= u_i^0 \text{ for } \mathbf{x} \in \Omega \\
 \dot{u}_i(\mathbf{x}, t^0) &= \dot{u}_i^0 \text{ for } \mathbf{x} \in \Omega,
 \end{aligned} \tag{1}$$

where $b_i : \Omega \times [t^0, T] \rightarrow \mathbb{R}$, $g_i : \Gamma_{D_i} \times [t^0, T] \rightarrow \mathbb{R}$, $h_i : \Gamma_{N_i} \times [t^0, T] \rightarrow \mathbb{R}$. In the aforementioned relationships, the superimposed dots denote the derivatives with respect to time. Equation (1) has a meaning of the equation of motion and σ_{ij} is the Cauchy stress tensor and C_{ijkl} is the fourth-order tensor for the material constants. g_i and h_i prescribe the kinematic (Dirichlet type) boundary conditions and the traction (Neumann type) boundary conditions, respectively. u_i^0 and \dot{u}_i^0 are the initial displacement and velocity. Furthermore, the piecewise smooth boundary is denoted as $\Gamma = \overline{\Gamma_{D_i} \cup \Gamma_{N_i}}$ and $\Gamma_{D_i} \cap \Gamma_{N_i} = \emptyset$.

2.2 | Component-wise partitioned equations of motion in homogeneous solids

On the basis of the previous study,¹⁸ the total discrete displacement (\mathbf{u}) in element-by-element level can be decomposed into the discrete longitudinal and shear displacements ($\mathbf{u}_\sigma, \mathbf{u}_\tau$) by the following formula:

$$\begin{aligned}
 \mathbf{u} &= \mathbf{u}_\sigma + \mathbf{u}_\tau \\
 \mathbf{u}_\sigma &= \mathbf{D}_\sigma \mathbf{u} \\
 \mathbf{u}_\tau &= \mathbf{D}_\tau \mathbf{u},
 \end{aligned} \tag{2}$$

where $(\mathbf{D}_\sigma, \mathbf{D}_\tau)$ are the component-wise partitioning operators for deriving the component-wise partitioned equations of motion. Moreover, the subscripts σ and τ mean the longitudinal and shear components, respectively. It can be shown that the component-wise partitioning matrices $(\mathbf{D}_\sigma, \mathbf{D}_\tau)$ possess the following properties:

$$\begin{aligned}
 \text{Partition of unity: } & \mathbf{D}_\sigma + \mathbf{D}_\tau = \mathbf{I}, \\
 \text{Projector property: } & \mathbf{D}_\tau^T \mathbf{D}_\tau = \mathbf{D}_\tau, \quad \mathbf{D}_\sigma^T \mathbf{D}_\sigma = \mathbf{D}_\sigma \\
 \text{Symmetry: } & \mathbf{D}_\sigma^T = \mathbf{D}_\sigma, \quad \mathbf{D}_\tau^T = \mathbf{D}_\tau \\
 \text{Orthogonality: } & \mathbf{D}_\sigma \mathbf{D}_\tau = \mathbf{D}_\tau \mathbf{D}_\sigma = \mathbf{0} \\
 \text{Element mass commutability: } & \mathbf{D}_\sigma^T \mathbf{M} = \mathbf{M} \mathbf{D}_\sigma, \quad \mathbf{D}_\tau^T \mathbf{M} = \mathbf{M} \mathbf{D}_\tau \\
 \text{Element mass orthogonality: } & \mathbf{D}_\sigma^T \mathbf{M} \mathbf{D}_\tau = \mathbf{M} \mathbf{D}_\sigma \mathbf{D}_\tau = \mathbf{0} \\
 \text{Element stiffness orthogonality: } & \mathbf{D}_\sigma^T \mathbf{K} \mathbf{D}_\tau = \mathbf{D}_\tau^T \mathbf{K} \mathbf{D}_\sigma = \mathbf{0} \\
 \text{Element stiffness decomposition: } & \mathbf{K} = \mathbf{K}_\sigma + \mathbf{K}_\tau, \\
 & \mathbf{K}_\sigma = \mathbf{D}_\sigma^T \mathbf{K} \mathbf{D}_\sigma, \quad \mathbf{K}_\tau = \mathbf{D}_\tau^T \mathbf{K} \mathbf{D}_\tau.
 \end{aligned} \tag{3}$$

The properties had been rigorously validated by symbolic computations and the performance had been proven by several examples as long as the element is rectangular.^{18,19}

The virtual work for a generic element may be written as follows:

$$\delta\Pi(\mathbf{u}) = \delta\mathbf{u}^T(\mathbf{f} - \mathbf{K}\mathbf{u} - \mathbf{M}\ddot{\mathbf{u}}). \quad (4)$$

The first step to affect component-wise partitioning of the aforementioned elemental virtual work is to insert the partition of unity relation to obtain

$$\begin{aligned} \delta\Pi(\mathbf{u}) &= \delta\mathbf{u}^T (\mathbf{D}_\sigma^T + \mathbf{D}_\tau^T)^2 (\mathbf{f} - \mathbf{K}(\mathbf{D}_\sigma + \mathbf{D}_\tau)\mathbf{u} - \mathbf{M}(\mathbf{D}_\sigma + \mathbf{D}_\tau)\ddot{\mathbf{u}}) \\ &\quad \text{Employ the partition of unity relation(3)} \\ &\Downarrow \\ &= \underbrace{(\delta\mathbf{u}_\sigma^T + \delta\mathbf{u}_\tau^T) (\mathbf{D}_\sigma^T + \mathbf{D}_\tau^T) [\mathbf{f} - \mathbf{K}(\mathbf{D}_\sigma + \mathbf{D}_\tau)(\mathbf{u}_\sigma + \mathbf{u}_\tau)}_{\text{Employ the component-wise decomposition(??)}} \\ &\quad - \mathbf{M}(\mathbf{D}_\sigma + \mathbf{D}_\tau)(\ddot{\mathbf{u}}_\sigma + \ddot{\mathbf{u}}_\tau) \end{aligned} \quad (5)$$

Employing the element mass commutability, the element mass, and the stiffness orthogonality relations and substituting Equations (3) into Equation (5), the virtual work can be decomposed into the longitudinal and shear virtual work (see, eg, the works of Cho et al¹⁸ and Kolman et al¹⁹), ie,

$$\delta\Pi(\mathbf{u}_\sigma, \mathbf{u}_\tau) = \delta\mathbf{u}_\sigma^T(\mathbf{f}_\sigma - \mathbf{K}_\sigma\mathbf{u}_\sigma - \mathbf{M}\ddot{\mathbf{u}}_\sigma) + \delta\mathbf{u}_\tau^T(\mathbf{f}_\tau - \mathbf{K}_\tau\mathbf{u}_\tau - \mathbf{M}\ddot{\mathbf{u}}_\tau), \quad (6)$$

where

$$\mathbf{f} = \mathbf{f}_\sigma + \mathbf{f}_\tau, \quad \mathbf{f}_\sigma = \mathbf{D}_\sigma^T\mathbf{f}, \quad \mathbf{f}_\tau = \mathbf{D}_\tau^T\mathbf{f}. \quad (7)$$

From which one obtains the following equation set:

$$\begin{aligned} \text{Longitudinal component equation : } &\mathbf{M}\ddot{\mathbf{u}}_\sigma + \mathbf{K}_\sigma\mathbf{u}_\sigma = \mathbf{f}_\sigma \\ \text{Shear component equation : } &\mathbf{M}\ddot{\mathbf{u}}_\tau + \mathbf{K}_\tau\mathbf{u}_\tau = \mathbf{f}_\tau. \end{aligned} \quad (8)$$

In addition, the element total displacement (\mathbf{u}) needs to be related to the assembled global displacement (\mathbf{w}) via the following assembly operator:

$$\begin{aligned} \mathbf{u} &= \mathbf{L}\mathbf{w} \\ \mathbf{w} &= (\mathbf{L}^T\mathbf{L})^{-1}\mathbf{L}^T\mathbf{u}, \end{aligned} \quad (9)$$

where \mathbf{L} is the assembly Boolean matrix that is readily available in most finite element analysis codes.

2.3 | Push-forward pullback time integration for component-wise partitioned equations of motion

The explicit time integration algorithm for component-wise partitioned equations of motion has been proposed in the works of Cho et al¹⁸ and Kolman et al.¹⁹ In this section, we briefly describe the algorithm for a general nonlinear dynamic problem in homogeneous solid, and Figure 1 shows the relations between the three time steps for the proposed algorithm in multidimensional problem.

Step 1: Assuming we have $(\mathbf{w}^n, \dot{\mathbf{w}}^n, \ddot{\mathbf{w}}^n)$ at time $t = t^n$, obtain the component-wise displacements at two critical time steps ($t^{n+C_\sigma} = t^n + \Delta t_{C_\sigma}$, $t^{n+C_\tau} = t^n + \Delta t_{C_\tau}$), ie,

$$\begin{aligned} \mathbf{w}^{n+C_\sigma} &= \mathbf{w}^n + \Delta t_{C_\sigma} \dot{\mathbf{w}}^n + \frac{\Delta t_{C_\sigma}^2}{2} \ddot{\mathbf{w}}^n \\ \mathbf{w}^{n+C_\tau} &= \mathbf{w}^n + \Delta t_{C_\tau} \dot{\mathbf{w}}^n + \frac{\Delta t_{C_\tau}^2}{2} \ddot{\mathbf{w}}^n. \end{aligned} \quad (10)$$

Step 2: Compute the accelerations at two critical time steps (longitudinal and shear components), ie,

$$\begin{aligned} \ddot{\mathbf{u}}_\sigma^{n+C_\sigma} &= \mathbf{M}^{-1} \left(\mathbf{f}_\sigma^{n+C_\sigma} - \mathbf{K}_\sigma\mathbf{u}_\sigma^{n+C_\sigma} \right) \\ \ddot{\mathbf{u}}_\tau^{n+C_\tau} &= \mathbf{M}^{-1} \left(\mathbf{f}_\tau^{n+C_\tau} - \mathbf{K}_\tau\mathbf{u}_\tau^{n+C_\tau} \right). \end{aligned} \quad (11)$$

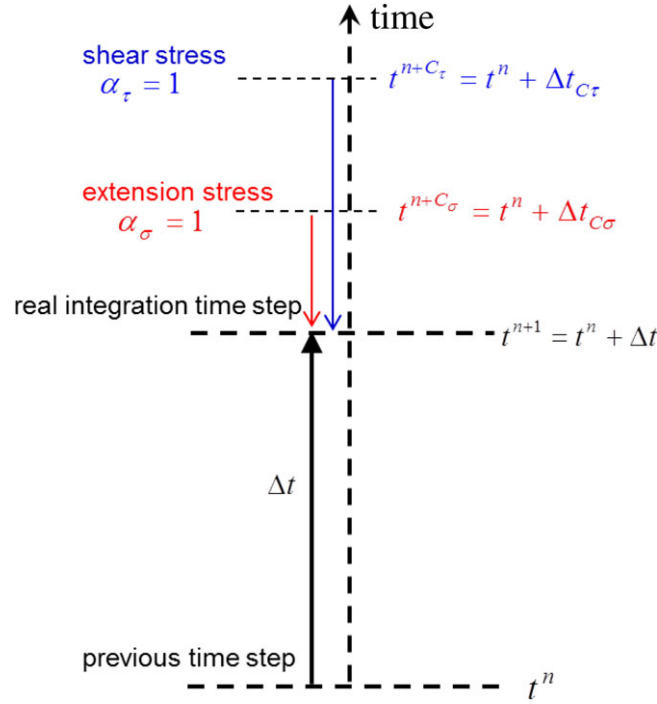


FIGURE 1 The relations between the three time steps in push-forward pullback time integration for component-wise partitioned equations of motion [Colour figure can be viewed at wileyonlinelibrary.com]

Step 3: Perform the push-forward pullback time integration with a parameter $\theta \in [0, 1]$ ($\theta = 1/2$ for the averaged displacement of the push-forward and pullback time integrations, $\theta = 0$ for the conventional CDM), ie,

$$\begin{aligned} \mathbf{u}^{n+1} &= \mathbf{u}^n + \Delta t \dot{\mathbf{u}}^n + \beta_{1\sigma} (\Delta t_{C_\sigma})^2 \ddot{\mathbf{u}}_\sigma^n + \beta_{2\sigma} (\Delta t_{C_\sigma})^2 \ddot{\mathbf{u}}_\sigma^{n+C_\sigma} \\ &\quad + \beta_{1\tau} (\Delta t_{C_\tau})^2 \ddot{\mathbf{u}}_\tau^n + \beta_{2\tau} (\Delta t_{C_\tau})^2 \ddot{\mathbf{u}}_\tau^{n+C_\tau} \\ \ddot{\mathbf{u}}^{n+1} &= \mathbf{M}^{-1} (\mathbf{f} - \mathbf{K} \mathbf{u}^{n+1}) \\ \dot{\mathbf{u}}^{n+1} &= \dot{\mathbf{u}}^n + \Delta t \{ (1 - \gamma) \ddot{\mathbf{u}}^n + \gamma \ddot{\mathbf{u}}^{n+1} \}, \end{aligned} \quad (12)$$

where

$$\begin{aligned} \alpha_\sigma &= \Delta t / \Delta t_{C_\sigma}, \quad \alpha_\tau = \Delta t / \Delta t_{C_\tau} \\ \beta_{1\sigma} &= \frac{\alpha_\sigma}{6} (3\alpha_\sigma + \theta - \theta \alpha_\sigma^2), \quad \beta_{2\sigma} = \frac{\theta \alpha_\sigma}{6} (\alpha_\sigma^2 - 1) \\ \beta_{1\tau} &= \frac{\alpha_\tau}{6} (3\alpha_\tau + \theta - \theta \alpha_\tau^2), \quad \beta_{2\tau} = \frac{\theta \alpha_\tau}{6} (\alpha_\tau^2 - 1) \end{aligned} \quad (13)$$

Stability condition : $\Delta t \leq \Delta t_{C_\sigma}$.

Step 4: Decompose the acceleration $\ddot{\mathbf{u}}^{n+1}$ to longitudinal and shear components $\ddot{\mathbf{u}}_\sigma^{n+1}$ and $\ddot{\mathbf{u}}_\tau^{n+1}$, ie,

$$\ddot{\mathbf{u}}^{n+1} = \ddot{\mathbf{u}}_\sigma^{n+1} + \ddot{\mathbf{u}}_\tau^{n+1}. \quad (14)$$

Step 5: Obtain the assembled displacement, velocity, and acceleration, ie,

$$\begin{aligned} \mathbf{w}^{n+1} &= (\mathbf{L}^T \mathbf{L})^{-1} \mathbf{L}^T \mathbf{u}^{n+1} \\ \dot{\mathbf{w}}^{n+1} &= (\mathbf{L}^T \mathbf{L})^{-1} \mathbf{L}^T \dot{\mathbf{u}}^{n+1} \\ \ddot{\mathbf{w}}^{n+1} &= (\mathbf{L}^T \mathbf{L})^{-1} \mathbf{L}^T \ddot{\mathbf{u}}^{n+1}. \end{aligned} \quad (15)$$

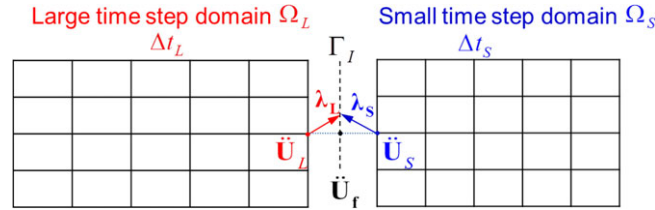


FIGURE 2 Two dimensional heterogeneous solids including L-domain and S-domain [Colour figure can be viewed at wileyonlinelibrary.com]

3 | PARTITIONED EXPLICIT-EXPLICIT INTEGRATION FOR TWO-DIMENSIONAL PROBLEM

Figure 2 shows two domains for two-dimensional heterogeneous problem. L-domain means a region with a larger time step, and S-domain is a region with a smaller time step. Γ_I is the interface boundary between the heterogeneous domains, and \mathbf{u}_f denote the global displacement corresponding to the frame nodes in Γ_I . Two localized Lagrange multipliers, λ_L and λ_S , are the interface loads at the corresponding frame nodes between two domains.²³

The equations of motion in two heterogeneous domains can be written as follows.

Component - wise partitioned equations of motion

(1) Extensional components

$$\begin{aligned} \mathbf{M}_L \ddot{\mathbf{u}}_{L\sigma} + \mathbf{K}_{L\sigma} \mathbf{u}_L &= \mathbf{D}_\sigma^T (\mathbf{f}_L - \mathbf{B}_L \lambda_L) \text{ in } \Omega_L \\ \mathbf{M}_S \ddot{\mathbf{u}}_{S\sigma} + \mathbf{K}_{S\sigma} \mathbf{u}_S &= \mathbf{D}_\sigma^T (\mathbf{f}_S - \mathbf{B}_S \lambda_S) \text{ in } \Omega_S. \end{aligned} \quad (16)$$

(2) Shear components

$$\begin{aligned} \mathbf{M}_L \ddot{\mathbf{u}}_{L\tau} + \mathbf{K}_{L\tau} \mathbf{u}_L &= \mathbf{D}_\tau^T (\mathbf{f}_L - \mathbf{B}_L \lambda_L) \text{ in } \Omega_L \\ \mathbf{M}_S \ddot{\mathbf{u}}_{S\tau} + \mathbf{K}_{S\tau} \mathbf{u}_S &= \mathbf{D}_\tau^T (\mathbf{f}_S - \mathbf{B}_S \lambda_S) \text{ in } \Omega_S. \end{aligned} \quad (17)$$

The subscripts (L and S) designate the larger time step domain and the smaller time step domain, respectively. Moreover, \mathbf{B}_L and \mathbf{B}_S are the Boolean matrices that extracts the interface DOFs for each domains. The accelerations and the interface loads at the interface DOFs should be continuous kinematically and kinetically as follows.

Kinematic interface continuities

$$\begin{aligned} \mathbf{B}_L^T \ddot{\mathbf{u}}_L - \mathbf{L}_L \ddot{\mathbf{u}}_f &= 0 \text{ on } \Gamma_I \\ \mathbf{B}_S^T \ddot{\mathbf{u}}_S - \mathbf{L}_S \ddot{\mathbf{u}}_f &= 0 \text{ on } \Gamma_I; \end{aligned} \quad (18)$$

Traction continuities

$$\mathbf{L}_L^T \lambda_L + \mathbf{L}_S^T \lambda_S = 0 \text{ on } \Gamma_I, \quad (19)$$

where $\ddot{\mathbf{u}}_f$ and \mathbf{u}_f denote the global acceleration and displacement corresponding to the frame nodes. Γ_I is the interface boundary between two domains. \mathbf{L}_L and \mathbf{L}_S are the Boolean matrices that relates the interface DOFs to the global acceleration and displacement, and these are obtained by removing columns with all zero elements from $\mathbf{B}_L^T \mathbf{L}$ and $\mathbf{B}_S^T \mathbf{L}$, respectively.

The aforementioned three equations are the continuity conditions for obtaining the Lagrange multipliers (λ_L , λ_S and \mathbf{u}_f) of the corresponding interface nodes at the current integration time step. However, when two solids are perfectly bonded in highly heterogeneous materials, there is a possibility of “drifting” that the displacement and velocity at the corresponding interface nodes of each material can differ during the actual time integration. Therefore, the following continuity conditions are simply applied to each integration step (t^{n+1}) of L-domain to prevent such the drifting phenomenon.

Kinematic continuities to prevent the drifting

$$\begin{aligned} \mathbf{B}_L^T \dot{\mathbf{u}}_L - \mathbf{L}_L \dot{\mathbf{u}}_f &= \mathbf{B}_L^T \mathbf{u}_L - \mathbf{L}_L \mathbf{u}_f = 0 \text{ on } \Gamma_I \\ \mathbf{B}_S^T \dot{\mathbf{u}}_S - \mathbf{L}_L \dot{\mathbf{u}}_f &= \mathbf{B}_S^T \mathbf{u}_S - \mathbf{L}_S \mathbf{u}_f = 0 \text{ on } \Gamma_I. \end{aligned} \quad (20)$$

Let us suppose that time step of large time step domain (L-domain) is two times larger than that of the small time step domain (S-domain), as shown in Figure 3. In this case, during one time integration in the large time step domain,

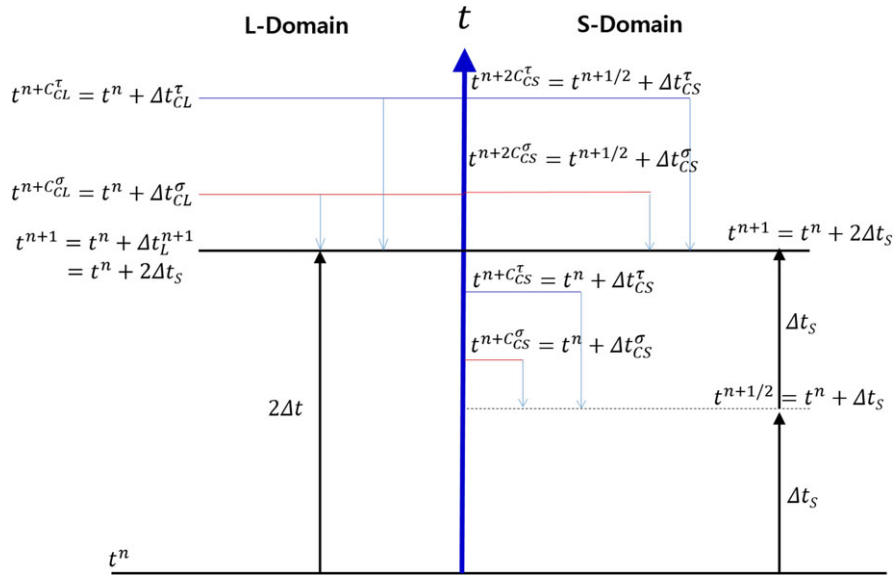


FIGURE 3 Procedures of multistep time integration for multidimensional heterogeneous solids [Colour figure can be viewed at wileyonlinelibrary.com]

two time integration procedures should be separately done in small time step domain. Since we can skip one time integration procedures at L-domain in Figure 3, we can reduce the total computing time.

The time step and the critical time step for L-domain are defined as follows:

$$\begin{aligned}
 &\text{Time at } L - \text{domain} : t^{n+1} = t^n + \Delta t_L^{n+1} \\
 &\Delta t_{CL}^\sigma = L_{\min}^e / C_L^\sigma = \text{Critical time step size for longitudinal component} \\
 &\Delta t_{CL}^\tau = L_{\min}^e / C_L^\tau = \text{Critical time step size for shear component} \\
 &\text{Integration time step size in } L - \text{domain} : \Delta t_L^{n+1} = \Delta t_L \quad (21) \\
 &\text{Ratio of two time step sizes} \\
 &\alpha_L^\sigma = \Delta t_L / \Delta t_{CL}^\sigma \\
 &\alpha_L^\tau = \Delta t_L / \Delta t_{CL}^\tau,
 \end{aligned}$$

where L_{\min}^e means the minimum characteristic length of an element, and C_L^σ and C_L^τ are the propagation speed of longitudinal and shear stress in L-domain, respectively.

The time step in S-domain can be defined, as shown in Equation (22), ie,

$$\begin{aligned}
 &\text{Time at } S - \text{domain} : t^{n+j} = t^n + k\Delta t^{n+j} \\
 &\Delta t_{CS}^\sigma = L_{\min}^e / C_S^\sigma = \text{Critical time step size for longitudinal component} \\
 &\Delta t_{CS}^\tau = L_{\min}^e / C_S^\tau = \text{Critical time step size for shear component} \\
 &\text{Integration time step size in } sub - \text{step} : \Delta t^{n+j} = \Delta t_S \quad (22) \\
 &\text{Ratio of two time step sizes} \\
 &\alpha_S^\sigma = \Delta t_S / \Delta t_{CS}^\sigma \\
 &\alpha_S^\tau = \Delta t_S / \Delta t_{CS}^\tau,
 \end{aligned}$$

where C_S^σ and C_S^τ are the propagation speed of longitudinal and shear stress in S-domain, respectively.

In addition, “j” means the kth integration substep in S-domain, and it is defined as follows:

$$\begin{aligned}
 &j = \frac{k}{m} \text{ for } k = 1, 2, \dots, m \\
 &m = \Delta t_L / \Delta t_S,
 \end{aligned} \quad (23)$$

where “m” is the ratio of two time step sizes and is the integer, and “k” is the order of substep in S-domain during a time step in L-domain. Therefore, we can describe the displacement and acceleration at kth substep of S-domain before computing the (n+1)th step of L-domain, which are shown as follows.

All element on S-domain at $t^{n+j} = t^n + k\Delta t_S$

$$\begin{aligned}
\mathbf{u}_S^{n+j} &= \mathbf{u}_S^{n+j_0} + \Delta t_S \dot{\mathbf{u}}_S^{n+j_0} + \beta_{1S}^\sigma (\Delta t_{CS}^\sigma)^2 \ddot{\mathbf{u}}_{S\sigma}^{n+j_0} + \beta_{2S}^\sigma (\Delta t_{CS}^\sigma)^2 \ddot{\mathbf{u}}_{S\sigma}^{n+j_0 C_S^\sigma} \\
&\quad + \beta_{1S}^\tau (\Delta t_{CS}^\tau)^2 \ddot{\mathbf{u}}_{S\tau}^{n+j_0} + \beta_{2S}^\tau (\Delta t_{CS}^\tau)^2 \ddot{\mathbf{u}}_{S\tau}^{n+j_0 C_S^\tau} \\
\ddot{\mathbf{u}}_S^{n+j} &= \mathbf{M}_S^{-1} (\mathbf{f}_S - \mathbf{K}_S \mathbf{u}_S^{n+j}) - \mathbf{M}_S^{-1} \mathbf{B}_S \boldsymbol{\lambda}_S^{n+j} = \tilde{\mathbf{u}}_S^{n+j} - \mathbf{M}_S^{-1} \mathbf{B}_S \boldsymbol{\lambda}_S^{n+j} \\
\ddot{\mathbf{u}}_{S\sigma}^{n+j C_S^\sigma} &= \tilde{\mathbf{u}}_S^{n+j C_S^\sigma} - \mathbf{M}_S^{-1} \mathbf{D}_\sigma^T \mathbf{B}_S \boldsymbol{\lambda}_S^{n+j C_S^\sigma} \\
\ddot{\mathbf{u}}_{S\tau}^{n+j C_S^\tau} &= \tilde{\mathbf{u}}_S^{n+j C_S^\tau} - \mathbf{M}_S^{-1} \mathbf{D}_\tau^T \mathbf{B}_S \boldsymbol{\lambda}_S^{n+j C_S^\tau} \\
\mathbf{u}_S^{n+j C_S^\sigma} &= \mathbf{u}_S^{n+j_0} + \Delta t_{CS}^\sigma \dot{\mathbf{u}}_S^{n+j_0} + \frac{1}{2} (\Delta t_{CS}^\sigma)^2 \ddot{\mathbf{u}}_S^{n+j_0} \\
\mathbf{u}_S^{n+j C_S^\tau} &= \mathbf{u}_S^{n+j_0} + \Delta t_{CS}^\tau \dot{\mathbf{u}}_S^{n+j_0} + \frac{1}{2} (\Delta t_{CS}^\tau)^2 \ddot{\mathbf{u}}_S^{n+j_0} \\
\tilde{\mathbf{u}}_S^{n+j} &= \mathbf{M}_S^{-1} (\mathbf{f}_S^{n+j} - \mathbf{K}_S \mathbf{u}_S^{n+j}) \\
\tilde{\mathbf{u}}_S^{n+j C_S^\sigma} &= \mathbf{M}_S^{-1} (\mathbf{f}_S^{n+j C_S^\sigma} - \mathbf{K}_S \mathbf{u}_S^{n+j C_S^\sigma}) \\
\tilde{\mathbf{u}}_S^{n+j C_S^\tau} &= \mathbf{M}_S^{-1} (\mathbf{f}_S^{n+j C_S^\tau} - \mathbf{K}_S \mathbf{u}_S^{n+j C_S^\tau}) \\
j_0 &= \frac{k-1}{m} \quad \text{for } k = 1, 2, \dots, m \\
\alpha_S^\sigma &= \Delta t_S / \Delta t_{CS}^\sigma \\
\alpha_S^\tau &= \Delta t_S / \Delta t_{CS}^\tau \\
\beta_{1S}^\sigma &= \frac{\alpha_S^\sigma}{6} (3\alpha_S^\sigma + \theta (\alpha_S^\sigma)^2), \beta_{2S}^\sigma = \frac{\theta \alpha_S^\sigma}{6} ((\alpha_S^\sigma)^2 - 1) \\
\beta_{1S}^\tau &= \frac{\alpha_S^\tau}{6} (3\alpha_S^\tau + \theta (\alpha_S^\tau)^2), \beta_{2S}^\tau = \frac{\theta \alpha_S^\tau}{6} ((\alpha_S^\tau)^2 - 1).
\end{aligned} \tag{24}$$

Since the k th integration substep in L-domain is not needed, we need only $(n+1)$ th integration step, as shown in the following.

All element on L-domain at $t^{n+1} = t^n + \Delta t_L = t^n + m\Delta t_S$

$$\begin{aligned}
\mathbf{u}_L^{n+1} &= \mathbf{u}_L^n + \Delta t_L \dot{\mathbf{u}}_L^n + \beta_{1L}^\sigma (\Delta t_{CL}^\sigma)^2 \ddot{\mathbf{u}}_{L\sigma}^n + \beta_{2L}^\sigma (\Delta t_{CL}^\sigma)^2 \ddot{\mathbf{u}}_{L\sigma}^{n+C_L^\sigma} \\
&\quad + \beta_{1L}^\tau (\Delta t_{CL}^\tau)^2 \ddot{\mathbf{u}}_{L\tau}^n + \beta_{2L}^\tau (\Delta t_{CL}^\tau)^2 \ddot{\mathbf{u}}_{L\tau}^{n+C_L^\tau} \\
\ddot{\mathbf{u}}_L^{n+1} &= \mathbf{M}_L^{-1} (\mathbf{f}_L - \mathbf{K}_L \mathbf{u}_L^{n+1}) - \mathbf{M}_L^{-1} \mathbf{B}_L \boldsymbol{\lambda}_L^{n+1} = \tilde{\mathbf{u}}_L^{n+1} - \mathbf{M}_L^{-1} \mathbf{B}_L \boldsymbol{\lambda}_L^{n+1} \\
\ddot{\mathbf{u}}_{L\sigma}^{n+C_L^\sigma} &= \tilde{\mathbf{u}}_L^{n+C_L^\sigma} - \mathbf{M}_L^{-1} \mathbf{D}_\sigma^T \mathbf{B}_L \boldsymbol{\lambda}_L^{n+C_L^\sigma} \\
\ddot{\mathbf{u}}_{L\tau}^{n+C_L^\tau} &= \tilde{\mathbf{u}}_L^{n+C_L^\tau} - \mathbf{M}_L^{-1} \mathbf{D}_\tau^T \mathbf{B}_L \boldsymbol{\lambda}_L^{n+C_L^\tau} \\
\mathbf{u}_L^{n+C_L^\sigma} &= \mathbf{u}_L^n + \Delta t_{CL}^\sigma \dot{\mathbf{u}}_L^n + \frac{1}{2} (\Delta t_{CL}^\sigma)^2 \ddot{\mathbf{u}}_L^n \\
\mathbf{u}_L^{n+C_L^\tau} &= \mathbf{u}_L^n + \Delta t_{CL}^\tau \dot{\mathbf{u}}_L^n + \frac{1}{2} (\Delta t_{CL}^\tau)^2 \ddot{\mathbf{u}}_L^n \\
\tilde{\mathbf{u}}_L^{n+1} &= \mathbf{M}_L^{-1} (\mathbf{f}_L^{n+1} - \mathbf{K}_L \mathbf{u}_L^{n+1}) \\
\tilde{\mathbf{u}}_L^{n+C_L^\sigma} &= \mathbf{M}_L^{-1} (\mathbf{f}_L^{n+C_L^\sigma} - \mathbf{K}_L \mathbf{u}_L^{n+C_L^\sigma}) \\
\tilde{\mathbf{u}}_L^{n+C_L^\tau} &= \mathbf{M}_L^{-1} (\mathbf{f}_L^{n+C_L^\tau} - \mathbf{K}_L \mathbf{u}_L^{n+C_L^\tau}) \\
\alpha_L^\sigma &= m\Delta t_S / \Delta t_{CL}^\sigma = \Delta t_L / \Delta t_{CL}^\sigma \\
\alpha_L^\tau &= m\Delta t_S / \Delta t_{CL}^\tau = \Delta t_L / \Delta t_{CL}^\tau \\
\beta_{1L}^\sigma &= \frac{\alpha_L^\sigma}{6} (3\alpha_L^\sigma + \theta - \theta (\alpha_L^\sigma)^2), \beta_{2L}^\sigma = \frac{\theta \alpha_L^\sigma}{6} ((\alpha_L^\sigma)^2 - 1) \\
\beta_{1L}^\tau &= \frac{\alpha_L^\tau}{6} (3\alpha_L^\tau + \theta - \theta (\alpha_L^\tau)^2), \beta_{2L}^\tau = \frac{\theta \alpha_L^\tau}{6} ((\alpha_L^\tau)^2 - 1).
\end{aligned} \tag{25}$$

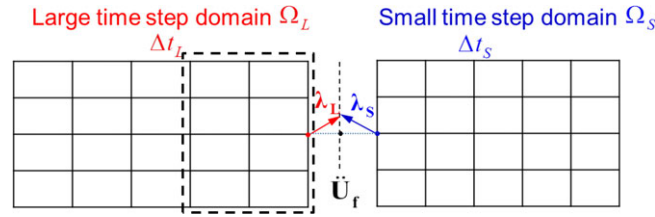


FIGURE 4 Two layers affecting on the interface loads λ_L and λ_S [Colour figure can be viewed at wileyonlinelibrary.com]

However, the conditions that the displacement and the reaction force are continuous between L-domain and S-domain should be considered.¹⁴ For this purpose, it is not necessary to consider all of the entire L-domain to satisfy the continuity conditions of Equations (18) and (19) during the k th integration substep of S-domain. Only two layers of L-domain next to the interface boundary have only to satisfy the continuous conditions with S-domain for each substep, as shown in Figure 4. The following Equation (26) is the k th substep of two layers of L-domain next to the interface boundary.

Two layer elements of L-domain adjacent to interface at $t^{n+j} = t^n + k\Delta t_S$

$$\begin{aligned}
 \mathbf{u}_L^{n+j} &= \mathbf{u}_L^n + k\Delta t_S \dot{\mathbf{u}}_L^n + \beta_{1L}^\sigma (\Delta t_{CL}^\sigma)^2 \ddot{\mathbf{u}}_{L\sigma}^n + \beta_{2L}^\sigma (\Delta t_{CL}^\sigma)^2 \ddot{\mathbf{u}}_{L\sigma}^{n+C_L^c} \\
 &\quad + \beta_{1L}^\tau (\Delta t_{CL}^\tau)^2 \ddot{\mathbf{u}}_{L\tau}^n + \beta_{2L}^\tau (\Delta t_{CL}^\tau)^2 \ddot{\mathbf{u}}_{L\tau}^{n+C_L^c} \\
 \ddot{\mathbf{u}}_L^{n+j} &= \mathbf{M}_L^{-1} (\mathbf{f}_L - \mathbf{K}_L \mathbf{u}_L^{n+j}) - \mathbf{M}_L^{-1} \mathbf{B}_L \lambda_L^{n+j} = \tilde{\mathbf{u}}_L^{n+j} - \mathbf{M}_L^{-1} \mathbf{B}_L \lambda_L^{n+j} \\
 \ddot{\mathbf{u}}_{L\sigma}^{n+C_L^c} &= \tilde{\mathbf{u}}_L^{n+C_L^c} - \mathbf{M}_L^{-1} \mathbf{D}_\sigma^T \mathbf{B}_S \lambda_L^{n+C_L^c} \\
 \ddot{\mathbf{u}}_{L\tau}^{n+C_L^c} &= \tilde{\mathbf{u}}_L^{n+C_L^c} - \mathbf{M}_L^{-1} \mathbf{D}_\tau^T \mathbf{B}_L \lambda_L^{n+C_L^c} \\
 \mathbf{u}_L^{n+C_L^c} &= \mathbf{u}_L^n + \Delta t_{CL}^\sigma \dot{\mathbf{u}}_L^n + \frac{1}{2} (\Delta t_{CL}^\sigma)^2 \ddot{\mathbf{u}}_L^n \\
 \mathbf{u}_L^{n+C_L^c} &= \mathbf{u}_L^n + \Delta t_{CL}^\tau \dot{\mathbf{u}}_L^n + \frac{1}{2} (\Delta t_{CL}^\tau)^2 \ddot{\mathbf{u}}_L^n \\
 \alpha_L^\sigma &= k\Delta t_S / \Delta t_{CL}^\sigma \\
 \alpha_L^\tau &= k\Delta t_S / \Delta t_{CL}^\tau.
 \end{aligned} \tag{26}$$

Two layers in L-domain are integrated at time ($t^{n+j} = t^n + k\Delta t_S$) on the basis of time (t^n), ($t^n + \Delta t_{CL}^\sigma$) and ($t^n + \Delta t_{CL}^\tau$). Therefore, the total calculation time can be reduced by integrating only two layers of L-domain at each substep. The accelerations with “tilde” in Equation (26) can be obtained as same with Equation (25).

The next step is to find the variables (λ_S^{n+j} , λ_L^{n+j} , $\ddot{\mathbf{u}}_f^{n+j}$) of the interface, Γ_I . To do this, we first have to find the interface reaction forces at the critical time to obtain those variables. The sequence of calculation of the respective variables on interface, Γ_I , is as follows:

$$\begin{aligned}
 (\lambda_S^{n+jC_S^c}, \lambda_S^{n+jC_S^c}) &\rightarrow \ddot{\mathbf{u}}_S^{n+jC_S^c} \rightarrow \lambda_S^{n+j} \\
 (\lambda_L^{n+C_L^c}, \lambda_L^{n+C_L^c}) &\rightarrow \ddot{\mathbf{u}}_L^{n+C_L^c} \rightarrow \lambda_L^{n+j}.
 \end{aligned} \tag{27}$$

First, we obtain ($\lambda_S^{n+jC_S^c}$, $\lambda_S^{n+jC_S^c}$) at the interface of S-domain as follows.

Computation of $\lambda_S^{n+jC_S^c}$ at the interface Γ_I of S-domain for $k = 1 : m$

$$\begin{aligned}
 \Delta t &\triangleq \Delta t_{CS}^\tau \\
 \begin{bmatrix} \mathbf{B}_L^T \mathbf{M}_L^{-1} \mathbf{B}_L & 0 & \mathbf{L}_L \\ 0 & \mathbf{B}_S^T \mathbf{M}_S^{-1} \mathbf{B}_S & \mathbf{L}_S \\ \mathbf{L}_L^T & \mathbf{L}_S^T & 0 \end{bmatrix} \begin{bmatrix} \lambda_L \\ \lambda_S \\ \ddot{\mathbf{u}}_f \end{bmatrix}^{n+jC_S^c} &= \begin{bmatrix} \mathbf{B}_L^T \tilde{\mathbf{u}}_L \\ \mathbf{B}_S^T \tilde{\mathbf{u}}_S \\ 0 \end{bmatrix}^{n+jC_S^c} \quad \text{on } \Gamma_I \\
 \ddot{\mathbf{u}}_f^{n+jC_S^c} &= \left[\mathbf{L}_L^T (\mathbf{B}_L^T \mathbf{M}_L^{-1} \mathbf{B}_L)^{-1} \mathbf{L}_L + \mathbf{L}_S^T (\mathbf{B}_S^T \mathbf{M}_S^{-1} \mathbf{B}_S)^{-1} \mathbf{L}_S \right]^{-1} \\
 &\quad \left[\mathbf{L}_L^T (\mathbf{B}_L^T \mathbf{M}_L^{-1} \mathbf{B}_L)^{-1} \mathbf{B}_L^T \tilde{\mathbf{u}}_L^{n+jC_S^c} + \mathbf{L}_S^T (\mathbf{B}_S^T \mathbf{M}_S^{-1} \mathbf{B}_S)^{-1} \mathbf{B}_S^T \tilde{\mathbf{u}}_S^{n+jC_S^c} \right] \\
 \lambda_S^{n+jC_S^c} &= (\mathbf{B}_S^T \mathbf{M}_S^{-1} \mathbf{B}_S)^{-1} \left(\mathbf{B}_S^T \tilde{\mathbf{u}}_S^{n+jC_S^c} - \mathbf{L}_S \ddot{\mathbf{u}}_f^{n+jC_S^c} \right).
 \end{aligned} \tag{28}$$

Computation of $\lambda_S^{n+jC_S^\sigma}$ at the interface Γ_I of S-domain for $k = 1 : m$

$$\begin{aligned} \Delta t &\triangleq \Delta t_{CS}^\sigma \\ \begin{bmatrix} \mathbf{B}_L^T \mathbf{M}_L^{-1} \mathbf{B}_L & 0 & \mathbf{L}_L \\ 0 & \mathbf{B}_S^T \mathbf{M}_S^{-1} \mathbf{B}_S & \mathbf{L}_S \\ \mathbf{L}_L^T & \mathbf{L}_S^T & 0 \end{bmatrix} \begin{bmatrix} \lambda_L \\ \lambda_S \\ \ddot{\mathbf{u}}_f \end{bmatrix}^{n+jC_S^\sigma} &= \begin{bmatrix} \mathbf{B}_L^T \tilde{\mathbf{u}}_L \\ \mathbf{B}_S^T \tilde{\mathbf{u}}_S \\ 0 \end{bmatrix}^{n+jC_S^\sigma} \quad \text{on } \Gamma_I \\ \ddot{\mathbf{u}}_f^{n+jC_S^\sigma} &= \left[\mathbf{L}_L^T (\mathbf{B}_L^T \mathbf{M}_L^{-1} \mathbf{B}_L)^{-1} \mathbf{L}_L + \mathbf{L}_S^T (\mathbf{B}_S^T \mathbf{M}_S^{-1} \mathbf{B}_S)^{-1} \mathbf{L}_S \right]^{-1} \\ &\quad \left[\mathbf{L}_L^T (\mathbf{B}_L^T \mathbf{M}_L^{-1} \mathbf{B}_L)^{-1} \mathbf{B}_L^T \tilde{\mathbf{u}}_L^{n+jC_S^\sigma} + \mathbf{L}_S^T (\mathbf{B}_S^T \mathbf{M}_S^{-1} \mathbf{B}_S)^{-1} \mathbf{B}_S^T \tilde{\mathbf{u}}_S^{n+jC_S^\sigma} \right] \\ \lambda_S^{n+jC_S^\sigma} &= (\mathbf{B}_S^T \mathbf{M}_S^{-1} \mathbf{B}_S)^{-1} \left(\mathbf{B}_S^T \tilde{\mathbf{u}}_S^{n+jC_S^\sigma} - \mathbf{L}_S \ddot{\mathbf{u}}_f^{n+jC_S^\sigma} \right). \end{aligned} \quad (29)$$

We can also get $(\lambda_L^{n+C_L^c}, \lambda_L^{n+C_L^c})$ at the interface of L-domain in the similar way as in S-domain. Different thing is that we adopted the time level of S-domain as $(t_s = t^{n+j_0})$ for getting the stable solution of $(\lambda_L^{n+C_L^c}, \lambda_L^{n+C_L^c})$.

Computation of $(\lambda_L^{n+C_L^c})$ at the interface Γ_I of L-domain for $k = 1 : m$

$$\begin{aligned} \Delta t &\triangleq \Delta t_{CL}^c \\ \tilde{\mathbf{u}}_S^{n+C_L^c} &\rightarrow \tilde{\mathbf{u}}_S^{n+j_0} \\ \begin{bmatrix} \mathbf{B}_L^T \mathbf{M}_L^{-1} \mathbf{B}_L & 0 & \mathbf{L}_L \\ 0 & \mathbf{B}_S^T \mathbf{M}_S^{-1} \mathbf{B}_S & \mathbf{L}_S \\ \mathbf{L}_L^T & \mathbf{L}_S^T & 0 \end{bmatrix} \begin{bmatrix} \lambda_L \\ \lambda_S \\ \ddot{\mathbf{u}}_f \end{bmatrix}^{n+C_L^c} &= \begin{bmatrix} \mathbf{B}_L^T \tilde{\mathbf{u}}_L \\ \mathbf{B}_S^T \tilde{\mathbf{u}}_S \\ 0 \end{bmatrix}^{n+C_L^c} \triangleq \begin{bmatrix} \mathbf{B}_L^T \tilde{\mathbf{u}}_L^{n+C_L^c} \\ \mathbf{B}_S^T \tilde{\mathbf{u}}_S^{n+j_0} \\ 0 \end{bmatrix} \quad \text{on } \Gamma_I \\ \ddot{\mathbf{u}}_f^{n+C_L^c} &= \left[\mathbf{L}_L^T (\mathbf{B}_L^T \mathbf{M}_L^{-1} \mathbf{B}_L)^{-1} \mathbf{L}_L + \mathbf{L}_S^T (\mathbf{B}_S^T \mathbf{M}_S^{-1} \mathbf{B}_S)^{-1} \mathbf{L}_S \right]^{-1} \\ &\quad \left[\mathbf{L}_L^T (\mathbf{B}_L^T \mathbf{M}_L^{-1} \mathbf{B}_L)^{-1} \mathbf{B}_L^T \tilde{\mathbf{u}}_L^{n+C_L^c} + \mathbf{L}_S^T (\mathbf{B}_S^T \mathbf{M}_S^{-1} \mathbf{B}_S)^{-1} \mathbf{B}_S^T \tilde{\mathbf{u}}_S^{n+j_0} \right] \\ \lambda_L^{n+C_L^c} &= (\mathbf{B}_L^T \mathbf{M}_L^{-1} \mathbf{B}_L)^{-1} \left(\mathbf{B}_L^T \tilde{\mathbf{u}}_L^{n+C_L^c} - \mathbf{L}_L \ddot{\mathbf{u}}_f^{n+C_L^c} \right). \end{aligned} \quad (30)$$

Computation of $(\lambda_L^{n+C_L^c})$ at the interface Γ_I of L-domain for $k = 1 : m$

$$\begin{aligned} \Delta t &\triangleq \Delta t_{CL}^\sigma \\ \tilde{\mathbf{u}}_S^{n+C_L^c} &\rightarrow \tilde{\mathbf{u}}_S^{n+j_0} \\ \begin{bmatrix} \mathbf{B}_L^T \mathbf{M}_L^{-1} \mathbf{B}_L & 0 & \mathbf{L}_L \\ 0 & \mathbf{B}_S^T \mathbf{M}_S^{-1} \mathbf{B}_S & \mathbf{L}_S \\ \mathbf{L}_L^T & \mathbf{L}_S^T & 0 \end{bmatrix} \begin{bmatrix} \lambda_L \\ \lambda_S \\ \ddot{\mathbf{u}}_f \end{bmatrix}^{n+C_L^c} &= \begin{bmatrix} \mathbf{B}_L^T \tilde{\mathbf{u}}_L \\ \mathbf{B}_S^T \tilde{\mathbf{u}}_S \\ 0 \end{bmatrix}^{n+C_L^c} \triangleq \begin{bmatrix} \mathbf{B}_L^T \tilde{\mathbf{u}}_L^{n+C_L^c} \\ \mathbf{B}_S^T \tilde{\mathbf{u}}_S^{n+j_0} \\ 0 \end{bmatrix} \quad \text{on } \Gamma_I \\ \ddot{\mathbf{u}}_f^{n+C_L^c} &= \left[\mathbf{L}_L^T (\mathbf{B}_L^T \mathbf{M}_L^{-1} \mathbf{B}_L)^{-1} \mathbf{L}_L + \mathbf{L}_S^T (\mathbf{B}_S^T \mathbf{M}_S^{-1} \mathbf{B}_S)^{-1} \mathbf{L}_S \right]^{-1} \\ &\quad \left[\mathbf{L}_L^T (\mathbf{B}_L^T \mathbf{M}_L^{-1} \mathbf{B}_L)^{-1} \mathbf{B}_L^T \tilde{\mathbf{u}}_L^{n+C_L^c} + \mathbf{L}_S^T (\mathbf{B}_S^T \mathbf{M}_S^{-1} \mathbf{B}_S)^{-1} \mathbf{B}_S^T \tilde{\mathbf{u}}_S^{n+j_0} \right] \\ \lambda_L^{n+C_L^c} &= (\mathbf{B}_L^T \mathbf{M}_L^{-1} \mathbf{B}_L)^{-1} \left(\mathbf{B}_L^T \tilde{\mathbf{u}}_L^{n+C_L^c} - \mathbf{L}_L \ddot{\mathbf{u}}_f^{n+C_L^c} \right). \end{aligned} \quad (31)$$

$(\lambda_S^{n+jC_S^\sigma}, \lambda_S^{n+jC_S^\sigma})$ are calculated explicitly in every substep, as shown in Equations (28)-(29). Furthermore, $(\lambda_L^{n+C_L^c}, \lambda_L^{n+C_L^c})$ of interface Γ_I should be also updated in every substep, as shown in Equations (30)-(31), because $(\lambda_S^{n+jC_S^\sigma}, \lambda_S^{n+jC_S^\sigma})$ are recalculated in each substep. Then, $(\lambda_L^{n+j}, \lambda_S^{n+j}, \mathbf{u}_f^{n+j})$ are calculated at each interface nodes, as shown in Equation (32), ie,

$$\begin{bmatrix} \mathbf{B}_L^T \mathbf{M}_L^{-1} \mathbf{B}_L & 0 & \mathbf{L}_L \\ 0 & \mathbf{B}_S^T \mathbf{M}_S^{-1} \mathbf{B}_S & \mathbf{L}_S \\ \mathbf{L}_L^T & \mathbf{L}_S^T & 0 \end{bmatrix} \begin{bmatrix} \lambda_L \\ \lambda_S \\ \mathbf{u}_f \end{bmatrix}^{n+j} = \begin{bmatrix} \mathbf{B}_L^T \tilde{\mathbf{u}}_L^{n+j} \\ \mathbf{B}_S^T \tilde{\mathbf{u}}_S^{n+j} \\ 0 \end{bmatrix} \quad \text{for } k = 1 : m \quad \text{on } \Gamma_I. \quad (32)$$

Equation (32) can be summarized as follows:

$$\begin{bmatrix} \lambda_L \\ \ddot{\mathbf{u}}_f \end{bmatrix}^{n+j} = \begin{bmatrix} \mathbf{B}_L^T \mathbf{M}_L^{-1} \mathbf{B}_L & \mathbf{L}_L \\ \mathbf{L}_L^T & -\mathbf{L}_S^T (\mathbf{B}_S^T \mathbf{M}_S^{-1} \mathbf{B}_S)^{-1} \mathbf{L}_S \end{bmatrix}^{-1} \begin{bmatrix} \mathbf{B}_L^T \tilde{\mathbf{u}}_L^{n+j} \\ -\mathbf{L}_S^T (\mathbf{B}_S^T \mathbf{M}_S^{-1} \mathbf{B}_S)^{-1} \mathbf{B}_S^T \tilde{\mathbf{u}}_S^{n+j} \end{bmatrix} \quad (33)$$

$$\lambda_S^{n+j} = (\mathbf{B}_S^T \mathbf{M}_S^{-1} \mathbf{B}_S)^{-1} \left[\mathbf{B}_S^T \tilde{\mathbf{u}}_S^{n+j} - \mathbf{L}_S \mathbf{u}_f^{n+j} \right].$$

There is also an alternative method for obtaining $(\lambda_S^{n+jC_S^\sigma}, \lambda_S^{n+jC_S^\tau})$ and $(\lambda_L^{n+C_L^\sigma}, \lambda_L^{n+C_L^\tau})$, which is to use an extrapolation by linear convex combination as following Equations (34)-(35) as a similar way with the work of Gravouil et al.²²

Alternative method of computing $(\lambda_S^{n+jC_S^\sigma}, \lambda_S^{n+jC_S^\tau})$ on S - domain

$$\begin{aligned} \alpha_\sigma &= \Delta t_S / \Delta t_{CS}^\sigma \\ \alpha_\tau &= \Delta t_S / \Delta t_{CS}^\tau \\ \lambda_S^{n+j} &= (1 - \alpha_\sigma) \lambda_S^{n+(j-1)} + \alpha_\sigma \lambda_S^{n+jC_S^\sigma} \\ \lambda_S^{n+j} &= (1 - \alpha_\tau) \lambda_S^{n+(j-1)} + \alpha_\tau \lambda_S^{n+jC_S^\tau}. \end{aligned} \quad (34)$$

Alternative method of computing $(\lambda_L^{n+C_L^\sigma}, \lambda_L^{n+C_L^\tau})$ on L - domain

$$\begin{aligned} \alpha_\sigma &= k \Delta t_S / \Delta t_{CL}^\sigma \\ \alpha_\tau &= k \Delta t_S / \Delta t_{CL}^\tau \\ \lambda_L^{n+j} &= (1 - \alpha_\sigma) \lambda_L^n + \alpha_\sigma \lambda_L^{n+C_L^\sigma} \\ \lambda_L^{n+j} &= (1 - \alpha_\tau) \lambda_L^n + \alpha_\tau \lambda_L^{n+C_L^\tau}. \end{aligned} \quad (35)$$

However, our numerical experiment using the alternative method showed that $\lambda_S^{n+j} \neq \lambda_L^{n+j}$ in case of $\Delta t_{CL}^\sigma \gg \Delta t_{CS}^\sigma$. Therefore, we did not adopt the alternative method for obtaining more accurate solution in the present algorithm. Despite our present algorithm is shown as more or less complicated, the present algorithm has the advantage that the calculation time is drastically reduced because L-domain is computed only in two elements next to the internal interface at each substep, and that the solution is more accurate especially even in case of $\Delta t_{CL}^\sigma \gg \Delta t_{CS}^\sigma$. Finally, we describe the flowchart of the multistep time integration for multidimensional problem.

Flowchart of multistep time integration for two-dimensional heterogeneous solids:

Start of main step $n = 1 : N$ on L-domain;

Step 1: Prepare $(\mathbf{u}_L^n, \dot{\mathbf{u}}_L^n, \ddot{\mathbf{u}}_L^n)$;

Start of substep $k = 1 : m$ on S-Domain);

Step 2: Prepare $(\mathbf{u}_S^{n+j_0}, \dot{\mathbf{u}}_S^{n+j_0}, \ddot{\mathbf{u}}_S^{n+j_0})$ and $(\mathbf{u}_f^{n+j_0}, \dot{\mathbf{u}}_f^{n+j_0}, \ddot{\mathbf{u}}_f^{n+j_0})$;

Step 2.1: Compute $(\lambda_S^{n+jC_S^\sigma}, \lambda_S^{n+jC_S^\tau}, \lambda_L^{n+C_L^\sigma}, \lambda_L^{n+C_L^\tau})$ at the interface, Γ_I ;

Step 2.1.1: Compute $(\lambda_S^{n+jC_S^\sigma}, \lambda_S^{n+jC_S^\tau})$;

Step 2.1.2: Compute $(\lambda_L^{n+C_L^\sigma}, \lambda_L^{n+C_L^\tau})$;

Step 2.2: Compute $(\lambda_S^{n+j}, \lambda_L^{n+j})$ and $\ddot{\mathbf{u}}_f^{n+j}$;

Step 2.3: Compute $(\dot{\mathbf{u}}_S^{n+j}, \ddot{\mathbf{u}}_S^{n+j})$

$$\begin{aligned} \ddot{\mathbf{u}}_S^{n+j} &= \tilde{\mathbf{u}}_S^{n+j} - \mathbf{M}_S^{-1} \mathbf{B}_S \lambda_S^{n+j} \\ \dot{\mathbf{u}}_S^{n+j} &= \dot{\mathbf{u}}_S^{n+(j-1)} + \Delta t_S \left\{ (1 - \gamma) \ddot{\mathbf{u}}_S^{n+(j-1)} + \gamma \ddot{\mathbf{u}}_S^{n+j} \right\}; \end{aligned} \quad (36)$$

Step 2.4: Update $(\mathbf{u}_f^{n+j}, \dot{\mathbf{u}}_f^{n+j})$ and $(\dot{\mathbf{u}}_S^{n+j}, \ddot{\mathbf{u}}_S^{n+j})$ at the interface, Γ_I ,

$$\begin{aligned} \dot{\mathbf{u}}_f^{n+j} &= \dot{\mathbf{u}}_f^{n+(j-1)} + \Delta t_S \left\{ (1 - \gamma) \ddot{\mathbf{u}}_f^{n+(j-1)} + \gamma \ddot{\mathbf{u}}_f^{n+j} \right\} \\ \mathbf{u}_f^{n+j} &= \mathbf{u}_f^{n+(j-1)} + \Delta t_S \dot{\mathbf{u}}_f^{n+j}; \end{aligned} \quad (37)$$

END of substep on S-domain.

Step 3: Compute $(\dot{\mathbf{u}}_L^{n+1}, \ddot{\mathbf{u}}_L^{n+1})$ on entire L-domain**Step 3.1: Compute $(\dot{\mathbf{u}}_L^{n+1}, \ddot{\mathbf{u}}_L^{n+1})$**

$$\begin{aligned}\ddot{\mathbf{u}}_L^{n+1} &= \tilde{\mathbf{u}}_L^{n+1} - \mathbf{M}_L^{-1} \mathbf{B}_L \lambda_L^{n+1} \\ \dot{\mathbf{u}}_L^{n+1} &= \dot{\mathbf{u}}_L^n + \Delta t_L \left\{ (1 - \gamma) \ddot{\mathbf{u}}_L^n + \gamma \ddot{\mathbf{u}}_L^{n+1} \right\};\end{aligned}\quad (38)$$

Step 3.2: Update $(\mathbf{u}_L^{n+1}, \dot{\mathbf{u}}_L^{n+1})$ only at the interface, Γ_I , to prevent the drifting of the interface

$$\begin{aligned}\mathbf{L}_L \mathbf{u}_L^{n+1} &= \mathbf{B}_L^T \mathbf{u}_f^{n+1} \\ \mathbf{L}_L \dot{\mathbf{u}}_L^{n+1} &= \mathbf{B}_L^T \dot{\mathbf{u}}_f^{n+1};\end{aligned}\quad (39)$$

END of main step on L-domain.

4 | STABILITY AND ACCURACY ANALYSIS OF THE PRESENT ALGORITHM

Two important algorithmic properties of the present multiple integration algorithm are numerical stability limit and wave-front tracking ability with minimal spurious oscillations. Computational efficiency of multiple explicit integration is dictated by its stability limit with respect to the stiff partition. Although algorithmic accuracy (often measured in terms of numerical damping and frequency distortion) is important for tracing continuous responses, the ability of wave-front tracking is of primary importance in discontinuous wave propagation problems. Nevertheless, we will also assess the damping and frequency errors. In order to elucidate the stability limit of the present multiple integration algorithm, we will specialize the present multiple integration algorithm to one-dimensional wave propagation consisting of two partitions whose maximum frequency ratio is two.

A rationale for assessing the stability limit of the proposed multiple integration algorithm as applied to one-dimensional problem is as follows. For two- and three-dimensional problems, the fastest wave speeds are due to extensional waves as the speeds of shear and surface waves are slower than that of the extensional waves. Thus, computational stability is dictated by the stability limit of extensional wave propagation. As one-dimensional bar problem consists of only extensional waves, it is deemed that one-dimensional stability analysis would offer essentially the stability limit for two- or three-dimensional stability limits as well.

4.1 | Partitioned equations of motion in one-dimensional heterogeneous solids

Figure 5 shows two domains for one-dimensional heterogeneous problem. L-domain means a region with a larger time step, and S-domain is a region with a smaller time step. Γ_I is the internal interface between two domains, and \mathbf{u}_f denotes the global displacement corresponding to the frame nodes in Γ_I . Two localized Lagrange multipliers, λ_L and λ_S , are the internal interface loads at the corresponding frame nodes between two domains.²³

Therefore, the equations of motion in two heterogeneous domains can be written as follows:

Equations of motion

$$\begin{aligned}\mathbf{M}_L \ddot{\mathbf{u}}_L + \mathbf{K}_L \mathbf{u}_L &= \mathbf{f}_L - \mathbf{B}_L \lambda_L \quad \text{in } \Omega_L \\ \mathbf{M}_S \ddot{\mathbf{u}}_S + \mathbf{K}_S \mathbf{u}_S &= \mathbf{f}_S - \mathbf{B}_S \lambda_S \quad \text{in } \Omega_S.\end{aligned}\quad (40)$$

The subscripts L and S designate the larger time step domain and the smaller time step domain, respectively. \mathbf{B}_L and \mathbf{B}_S are the Boolean matrices that extracts the interface DOFs for each domains.

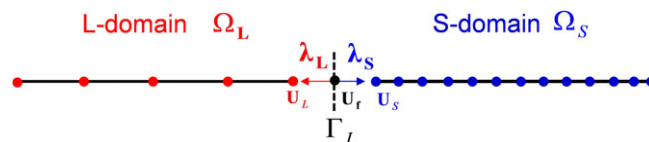


FIGURE 5 One dimensional heterogeneous solids including L-domain and S-domain [Colour figure can be viewed at wileyonlinelibrary.com]

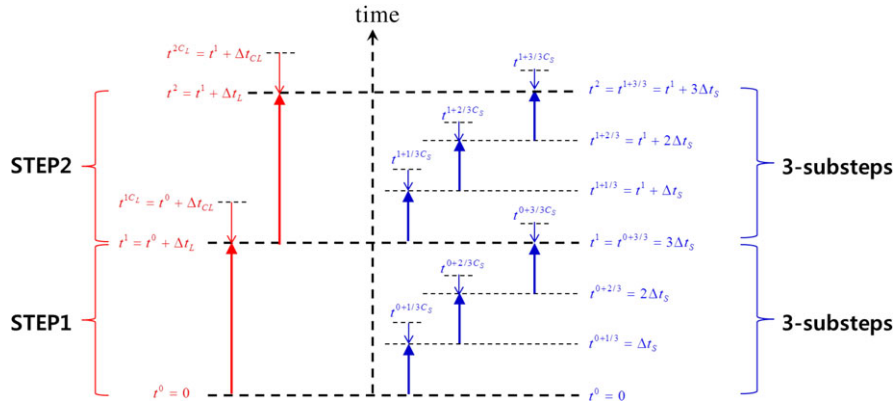


FIGURE 6 Procedures of multistep time integration for one dimensional heterogeneous solids [Colour figure can be viewed at wileyonlinelibrary.com]

The accelerations and the interface loads at the interface DOFs should be continuous kinematically and kinetically as follows:

Kinematic interface continuities

$$\begin{aligned} \mathbf{B}_L^T \ddot{\mathbf{u}}_L - \mathbf{L}_L \ddot{\mathbf{u}}_f &= 0 \quad \text{on } \Gamma_I \\ \mathbf{B}_S^T \ddot{\mathbf{u}}_S - \mathbf{L}_S \ddot{\mathbf{u}}_f &= 0 \quad \text{on } \Gamma_I, \end{aligned} \tag{41}$$

Traction continuities

$$\mathbf{L}_L^T \lambda_L + \mathbf{L}_S^T \lambda_S = 0 \quad \text{on } \Gamma_I, \tag{42}$$

where \mathbf{L}_L and \mathbf{L}_S are the Boolean matrices that relate the interface DOFs to the global acceleration and displacement, and these are obtained by removing columns with all zero elements from $\mathbf{B}_L^T \mathbf{L}$ and $\mathbf{B}_S^T \mathbf{L}$, respectively. Equation (41) and Equation (42) satisfy all discontinuity conditions of displacement, strains, and stresses at the interface between the heterogeneous domains.¹⁴ The three continuity conditions is to obtain the Lagrange multipliers (λ_L , λ_S and \mathbf{u}_f) at the current integration time step. However, when two solids are perfectly bonded in highly heterogeneous materials, there is a possibility of “the drifting” that the displacement and velocity at the corresponding interface can differ during the actual time integration. Therefore, the kinematic continuity conditions to prevent the drifting are applied to each integration step (t^{n+1}) of L-domain.

Kinematic continuities to prevent the drifting

$$\begin{aligned} \mathbf{B}_L^T \dot{\mathbf{u}}_L - \mathbf{L}_L \dot{\mathbf{u}}_f &= \mathbf{B}_L^T \mathbf{u}_L - \mathbf{L}_L \mathbf{u}_f = 0 \quad \text{on } \Gamma_I \\ \mathbf{B}_S^T \dot{\mathbf{u}}_S - \mathbf{L}_L \dot{\mathbf{u}}_f &= \mathbf{B}_S^T \mathbf{u}_S - \mathbf{L}_S \mathbf{u}_f = 0 \quad \text{on } \Gamma_I. \end{aligned} \tag{43}$$

Let us suppose that time step of large time step domain (L-domain) is three times larger than that of the small time step domain (S-domain), as shown in Figure 6. In this case, during one time integration in the large time step domain, three time integration procedures should be separately done in small time step domain. Since we can skip two time integration procedures at L-domain in Figure 6, we can reduce the total computing time.

The time step and the critical time step for L-domain are defined as follows:

$$\begin{aligned} \text{Time at } L - \text{domain} : t^{n+1} &= t^n + \Delta t^{n+1} \\ \text{Critical time step size} : \Delta t_{CL} &= L_{\min}/C_L, \quad C_L = \sqrt{E_L/\rho_L} \\ \text{Integration time step size} : \Delta t^{n+1} &= \Delta t_L \\ \text{Ratio of two time step sizes} : \alpha_L &= \Delta t_L/\Delta t_{CL}. \end{aligned} \tag{44}$$

As in L-domain, the information of time step in S-domain can be written as follows:

$$\begin{aligned} \text{Time at } S - \text{domain} : t^{n+j} &= t^n + k\Delta t^{n+j} \\ \text{Critical time step size} : \Delta t_{CS} &= L_{\min}/C_S, \quad C_S = \sqrt{E_S/\rho_S} \\ \text{Integration time step size} : \Delta t^{n+j} &= \Delta t_S \\ \text{Ratio of two time step sizes} : \alpha_S &= \Delta t_S/\Delta t_{CS}, \end{aligned} \tag{45}$$

where “j” means the k th integration substep in S-domain, and it is defined as follows:

$$j = \frac{k}{m} \leq 1 \text{ for } k = 1, 2, \dots, m \quad (46)$$

$$m = \Delta t_L / \Delta t_S,$$

where “m” is the ratio of two time step sizes and is the integer, and “k” is the order of substep in S-domain during a time step in L-domain. Therefore, we can compute the displacement and acceleration of k th substep of S-domain during $(n+1)$ th step of L-domain as same way as multidimensional problem.

4.2 | Stability and accuracy analysis of one-dimensional multistep time integration.

We assess the stability and accuracy of the proposed multistep time integration for one-dimensional heterogeneous case by assuming that the bar consists of soft (L-domain) and stiff (S-domain), as shown in Figure 7. The mass and stiffness matrices of two materials are assumed for easy implementation of the interested analysis as Equation (47), ie,

$$\mathbf{M}_L = \mathbf{M}_S = \begin{bmatrix} 1 & 0 \\ 0 & 1 \end{bmatrix}$$

$$\mathbf{K}_L = \frac{1}{2} \begin{bmatrix} 1 & -1 \\ -1 & 1 \end{bmatrix} \quad (47)$$

$$\mathbf{K}_S = \frac{1}{2} \left(\frac{\Delta t_{CL}}{\Delta t_{CS}} \right)^2 \mathbf{K}_L.$$

From Equation (47), one can calculate the respective critical time steps of L-domain and S-domain, as Equation (48), ie,

$$\omega_{\max,S} = 2 \rightarrow \Delta t_{CS} = \frac{2}{\omega_{\max,S}} = 1 \quad (48)$$

$$\omega_{\max,L} = 1 \rightarrow \Delta t_{CL} = \frac{2}{\omega_{\max,L}} = 2.$$

When the present algorithm (Equations (24)-(33)) is specialized to one-dimensional case (Equations (40)-(42)), the following difference equation results

$$\mathbf{Y}^{n+1} = \mathbf{A}\mathbf{Y}^n, \quad \mathbf{Y}^T = \begin{bmatrix} \mathbf{Y}_S^T & \mathbf{Y}_L^T & \mathbf{Y}_f^T \end{bmatrix}$$

$$\mathbf{Y}_S = [\mathbf{u}_S \ \dot{\mathbf{u}}_S \ \ddot{\mathbf{u}}_S]^T = [u_S^1 \ u_S^2 \ \dot{u}_S^1 \ \dot{u}_S^2 \ \ddot{u}_S^1 \ \ddot{u}_S^2]^T \quad (49)$$

$$\mathbf{Y}_L = [\mathbf{u}_L \ \dot{\mathbf{u}}_L \ \ddot{\mathbf{u}}_L]^T = [u_L^1 \ u_L^2 \ \dot{u}_L^1 \ \dot{u}_L^2 \ \ddot{u}_L^1 \ \ddot{u}_L^2]^T$$

$$\mathbf{Y}_f = [u_f \ \dot{u}_f \ \ddot{u}_f]^T.$$

Stability of the difference Equation (49) can be assessed by seeking the solution in the form of

$$\mathbf{Y}^{n+1} = \lambda \mathbf{Y}^n$$

$$\Downarrow$$

$$[\mathbf{A} - \lambda \mathbf{I}] \mathbf{Y}^n = 0 \rightarrow \det(\mathbf{A} - \lambda \mathbf{I}) = 0 \quad (50)$$

where $|\lambda| \leq 1$ for stability.

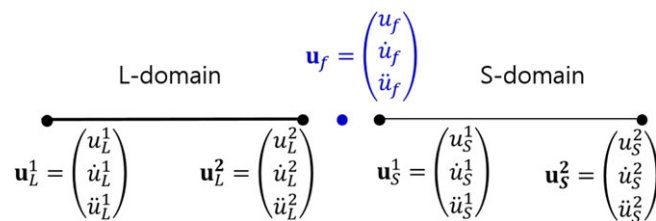


FIGURE 7 Partitioned system (L-domain and S-domain) for the stability and accuracy analysis for one-dimensional multistep time integration when $\Delta t_{CL} / \Delta t_{CS} = 2$ [Colour figure can be viewed at wileyonlinelibrary.com]

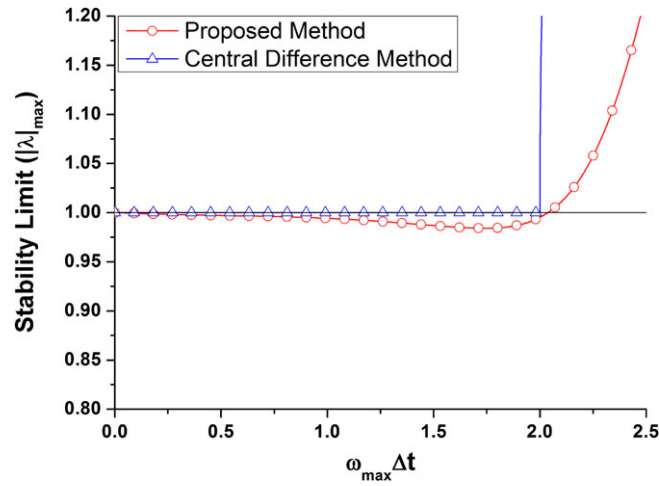


FIGURE 8 Stability limits for the present one-dimensional multistep time integration when $\Delta t_{CL}/\Delta t_{CS} = 2$ [Colour figure can be viewed at wileyonlinelibrary.com]

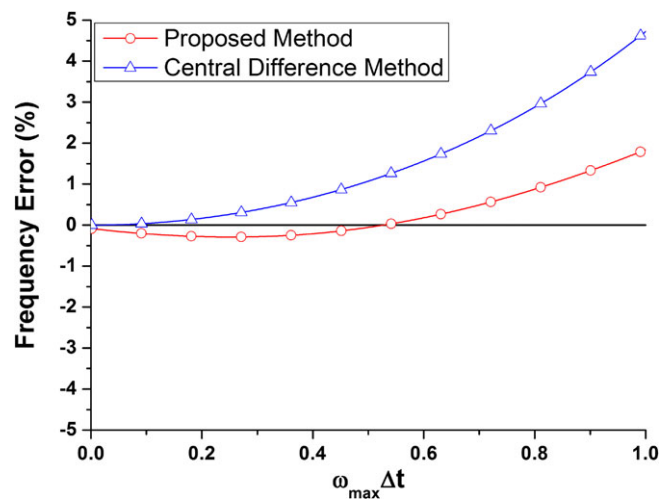


FIGURE 9 Frequency errors for the present one-dimensional multistep time integration when $\Delta t_{CL}/\Delta t_{CS} = 2$ [Colour figure can be viewed at wileyonlinelibrary.com]

For assessing accuracy, the numerical damping and frequency per time step are given by

$$\begin{aligned} \text{Frequency Error} &= \tan^{-1} \left(\frac{\text{Im}(\lambda)}{\text{Re}(\lambda)} \right)_{|\lambda|_{\max}} / (\omega_{\max} T) \\ \text{Damping Error} &= -\frac{\log(|\lambda|_{\max})}{\omega_{\max} T}. \end{aligned} \tag{51}$$

Figure 8 shows the stability limits of the present method and the conventional CDM versus the step size ($\omega_{\max,S} \Delta t$). The stability limit of the CDM is given by

$$\Delta t_C \leq \frac{2}{\omega_{\max}}. \tag{52}$$

It is observed from Figure 8 that the stability limit of the present multiple integration algorithm essentially maintains that of the CDM. Figure 9 shows the frequency error results. The frequency error of the present algorithm is lower than that of the CDM. It means the present multistep time integration can remove the spurious oscillation more than the CDM when the discontinuous stress wave is propagated. Figure 10 shows the damping analysis results. While the CDM introduces no damping, the present method does introduce the numerical damping error. Although the numerical damping error (which is not insignificant) can contribute to artificial viscosity-like dissipation, for the purpose of front-wave tracking simulations, we have not noticed significant compromise of the overall wave tracking ability of the present algorithm. For continuous waves and long-time response computations, however, we do not recommend the proposed algorithm.

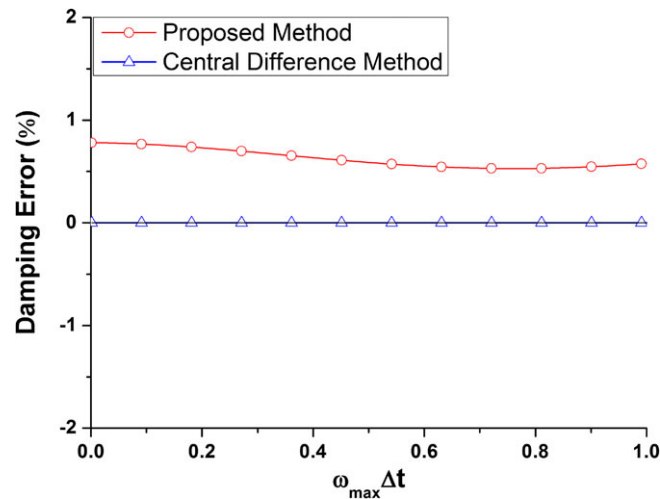


FIGURE 10 Damping errors for the present one-dimensional multistep time integration when $\Delta t_{CL}/\Delta t_{CS} = 2$ [Colour figure can be viewed at wileyonlinelibrary.com]

5 | NUMERICAL EXPERIMENTS

We choose two problems of discontinuous elastic wave propagation in heterogeneous solids to demonstrate the salient features of the present algorithm: one-dimensional heterogeneous rods and a crack tip problems subjected to mode-II loadings in a heterogeneous solid with plane strain condition. The simulation of the crack tip problems is chosen because various types of discontinuous waves, including Rayleigh and Schmidt waves, will emanate from the crack tip and these waves have high singularities at the crack tip.

5.1 | Stress wave propagated from L-domain (soft) to S-domain (hard) in one-dimensional heterogeneous rod

As a first example, we have chosen the stress wave propagation problem in a rod consisting of two materials. As shown in Figure 11, the one-dimensional rod consists of a soft material on the left side (length=50 mm, density=8000 kg/m³, the number of element=300) and a hard material on the right side (length=50 mm, density=8000 kg/m³, the number of element=300). Since the elastic modulus of each material is 0.02 GPa and 200 GPa, the propagation speed of the stress wave is 50 m/s and 5000 m/s, respectively. Thus, if the element sizes are equal in all elements of the two materials, the ratio of their critical time steps is 100. The boundary condition is fixed at the right end, as shown in Figure 11. The initial velocity of 10 m/s was imposed at the left end to allow the stress wave to propagate from the soft material (L-domain) to the hard material (S-domain).

Figure 12 shows the reference solutions at time=2600 μ s and 3800 μ s, respectively, in terms of the velocity distribution along the two materials. When the incident stress wave propagated from the left end reaches the interface ($x=50$ mm) and continues to propagate into the right-half hard bar, due to the large difference of the wave speeds of the two bars, the partially reflected wave propagates to the left end. Since the impedance difference between two materials is high, the amplitude of the transmitted wave propagating in the right half of the bar becomes very small. When the transmitted wave reflects reaches the fixed right boundary and reflects back toward the left bar, the amplitude of the reflected wave from the right end becomes small, and this transmission and reflection phenomena continues with each reflection repeating smaller and smaller waves. This is illustrated in Figure 12.

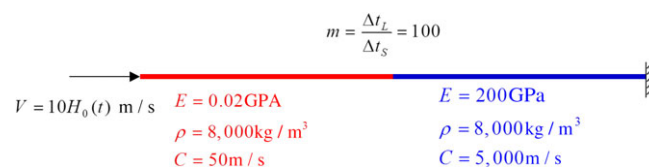


FIGURE 11 One-dimensional problem for the stress wave propagated from L-domain to S-domain [Colour figure can be viewed at wileyonlinelibrary.com]

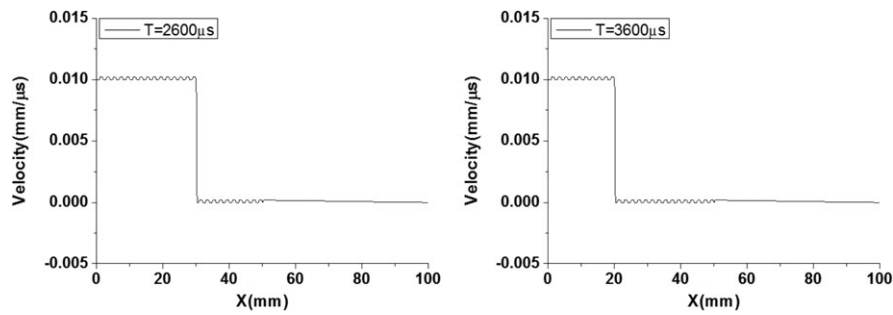


FIGURE 12 One-dimensional problem for the stress wave problem propagated from L-domain to S-domain at $t = 2600 \mu\text{s}$ and $3800 \mu\text{s}$: Reference Solutions obtained from x-t diagram

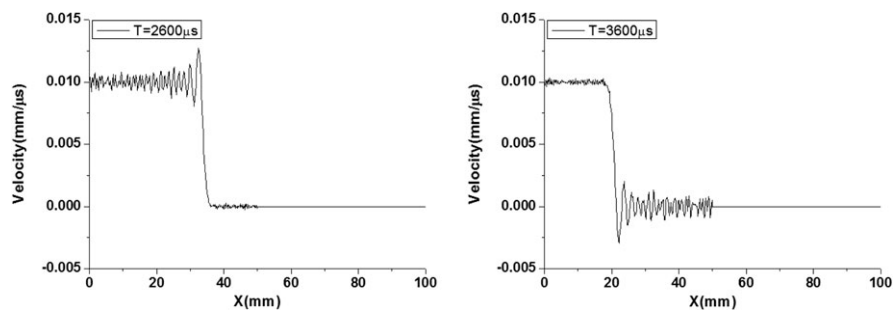


FIGURE 13 One-dimensional problem for the stress wave problem propagated from L-domain to S-domain at $t = 2600 \mu\text{s}$ and $3800 \mu\text{s}$: Central difference method (single step) in nonpartitioned system

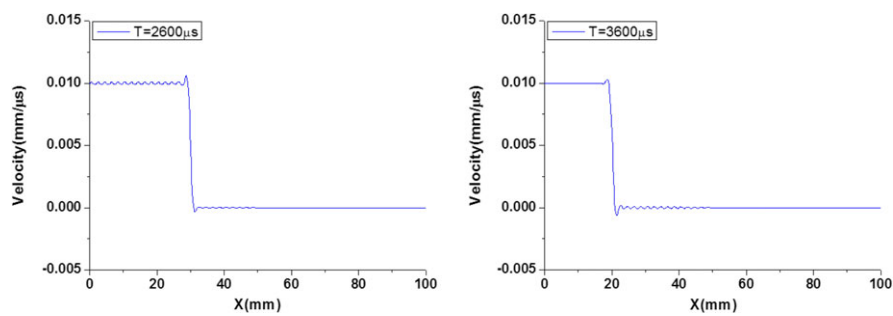


FIGURE 14 One-dimensional problem for the stress wave problem propagated from L-domain to S-domain at $t = 2600 \mu\text{s}$ and $3800 \mu\text{s}$: Push-forward pullback time integration (single step) in nonpartitioned system [Colour figure can be viewed at wileyonlinelibrary.com]

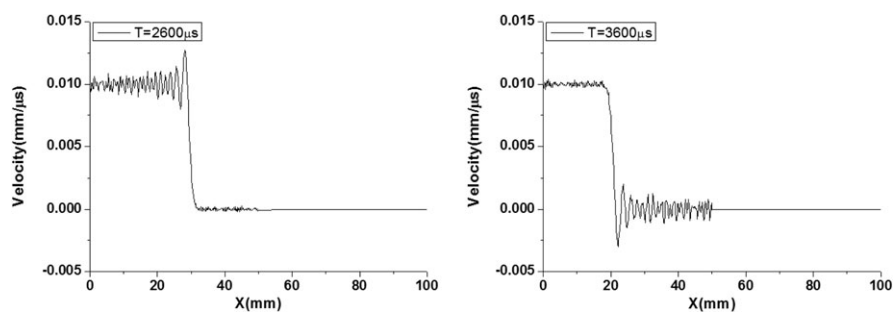


FIGURE 15 One-dimensional problem for the stress wave problem propagated from L-domain to S-domain at $t = 2600 \mu\text{s}$ and $3800 \mu\text{s}$: Central difference method (single step) in partitioned system

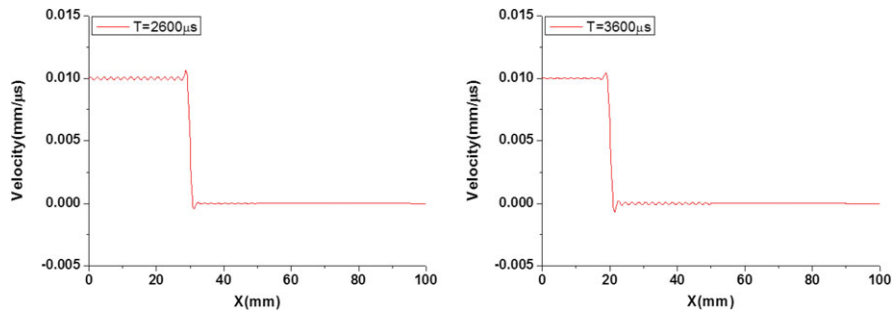


FIGURE 16 One-dimensional problem for the stress wave problem propagated from L-domain to S-domain at $t = 2600 \mu s$ and $3800 \mu s$: Push-forward pullback time integration (single step) in partitioned system [Colour figure can be viewed at wileyonlinelibrary.com]

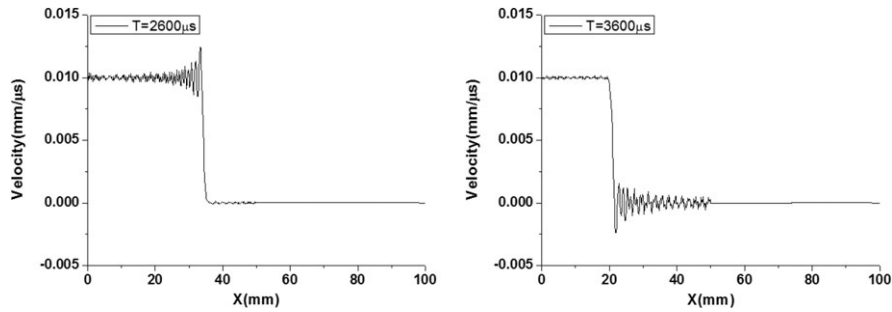


FIGURE 17 One-dimensional problem for the stress wave problem propagated from L-domain to S-domain at $t = 2600 \mu s$ and $3800 \mu s$: Central difference method (multistep) in partitioned system

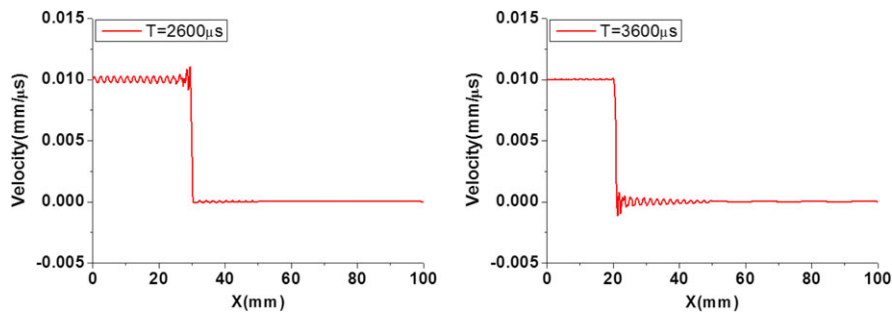


FIGURE 18 One-dimensional problem for the stress wave problem propagated from L-domain to S-domain at $t = 2600 \mu s$ and $3800 \mu s$: Push-forward pullback time integration (multistep) in partitioned system (the present algorithm) [Colour figure can be viewed at wileyonlinelibrary.com]

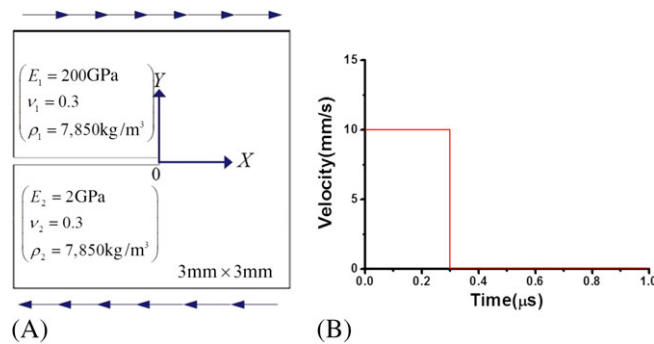


FIGURE 19 Plane strain rectangular model(mode-II) with initial crack tip subjected to a Heaviside initial velocity input: A, Geometry and boundary conditions; B, Imposed velocity [Colour figure can be viewed at wileyonlinelibrary.com]

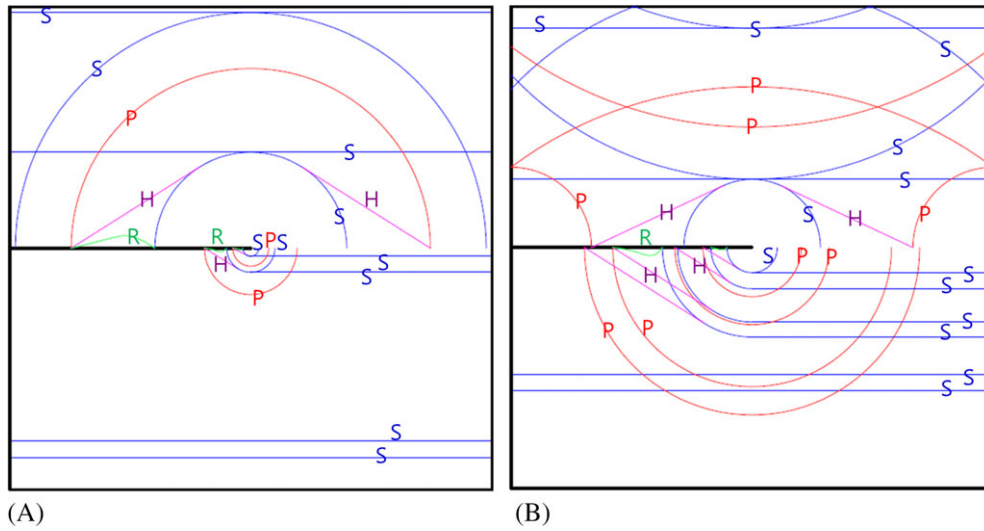


FIGURE 20 Reference solution: A, $t = 0.97 \mu\text{s}$; B, $t = 2.26 \mu\text{s}$. (P: primary stress wave, S: shear stress wave, R: Rayleigh stress wave, H: von-Schmidt (head) stress wave)

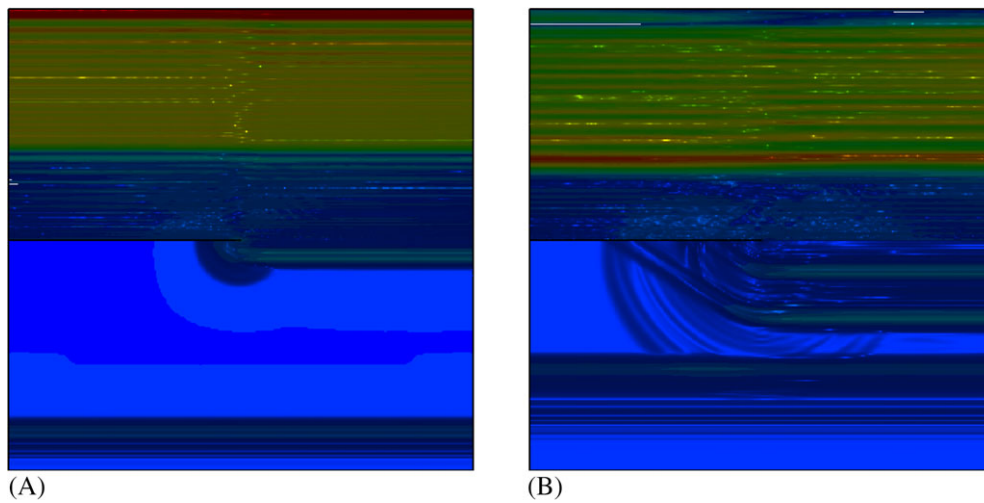


FIGURE 21 Maximum shear stress contour plots of central difference method (single step) in nonpartitioned system: A, $t = 0.97 \mu\text{s}$; B, $t = 2.26 \mu\text{s}$ [Colour figure can be viewed at wileyonlinelibrary.com]

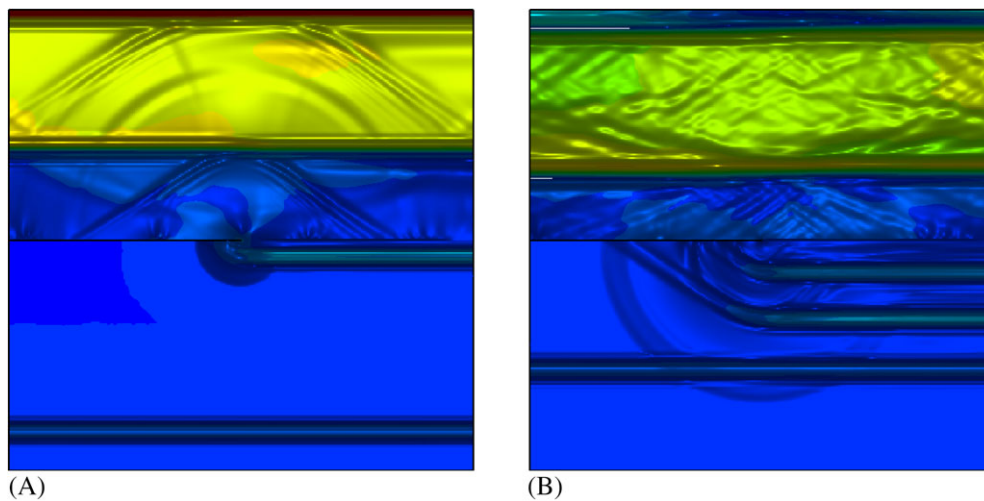


FIGURE 22 Maximum shear stress contour plots of push-forward pullback time integration (single step) in nonpartitioned system: A, $t = 0.97 \mu\text{s}$; B, $t = 2.26 \mu\text{s}$ [Colour figure can be viewed at wileyonlinelibrary.com]

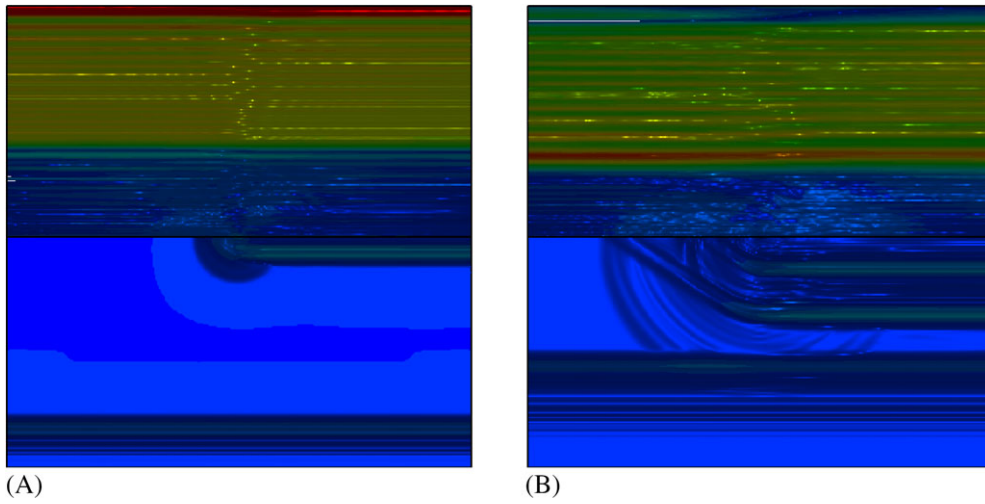


FIGURE 23 Maximum shear stress contour plots of central difference method (single step) in partitioned system: A, $t = 0.97 \mu\text{s}$; B, $t = 2.26 \mu\text{s}$ [Colour figure can be viewed at wileyonlinelibrary.com]

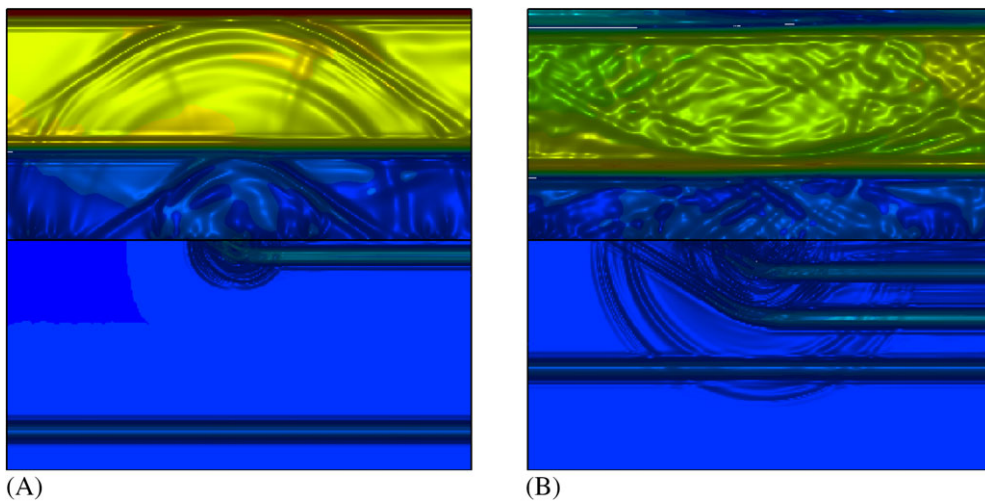


FIGURE 24 Maximum shear stress contour plots of push-forward pullback time integration (single step) in partitioned system: A, $t = 0.97 \mu\text{s}$; B, $t = 2.26 \mu\text{s}$ [Colour figure can be viewed at wileyonlinelibrary.com]

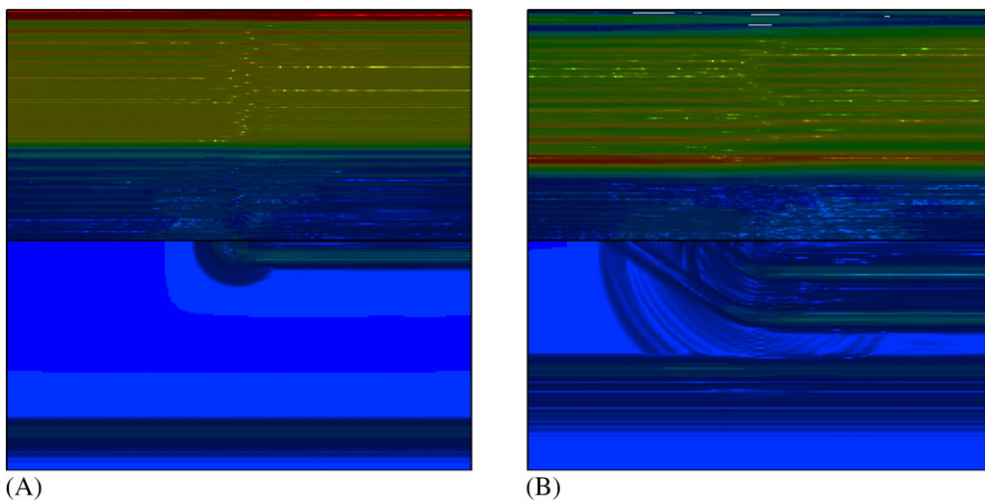


FIGURE 25 Maximum shear stress contour plots of central difference method (multistep) in partitioned system: A, $t = 0.97 \mu\text{s}$; B, $t = 2.26 \mu\text{s}$ [Colour figure can be viewed at wileyonlinelibrary.com]

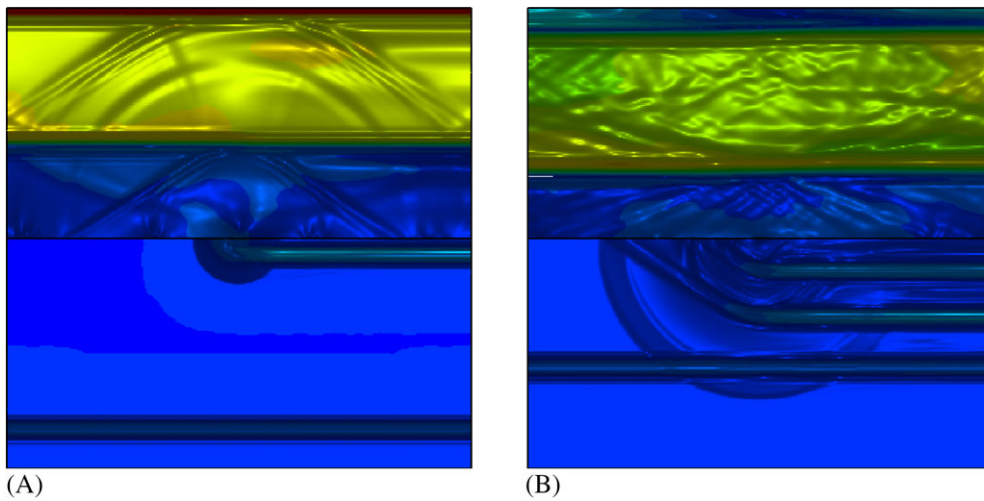


FIGURE 26 Maximum shear stress contour plots of push-forward pullback time integration (multistep) in partitioned system (the present algorithm): A, $t = 0.97 \mu\text{s}$; B, $t = 2.26 \mu\text{s}$ [Colour figure can be viewed at wileyonlinelibrary.com]

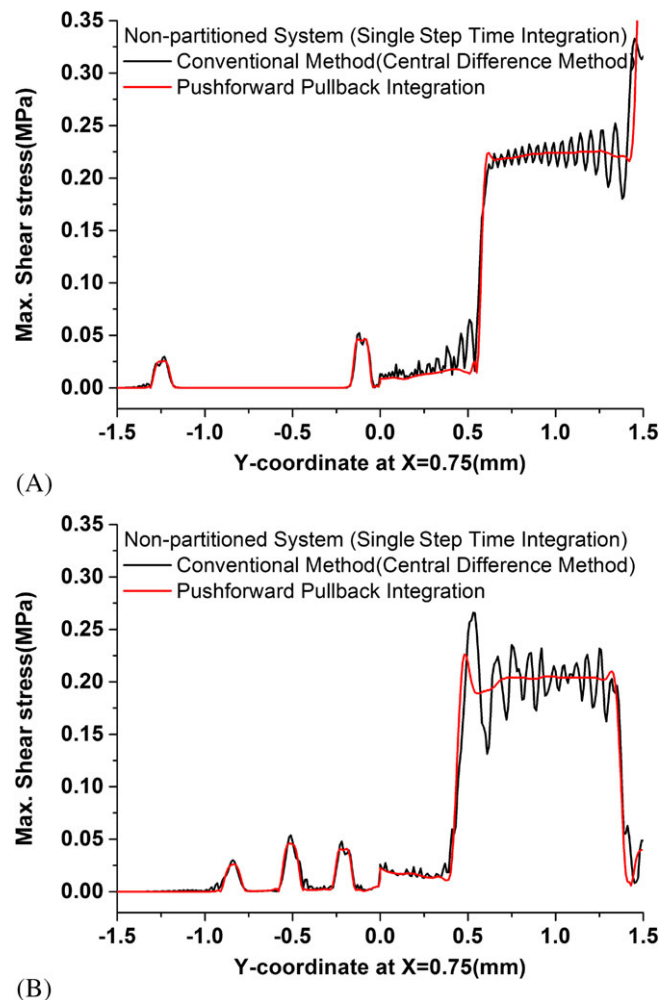


FIGURE 27 Comparison results of the maximum shear stress distribution of single step time integration along Y-axis at $X=0.75$ (mode-II problem) in nonpartitioned system: A, $t = 0.97 \mu\text{s}$; B, $t = 2.26 \mu\text{s}$

First, Figure 13 shows the results of the conventional CDM as applied with a single step integration in nonpartitioned system, which exhibit the deleterious pre-shock dispersion errors. It should be noted that, at time $t = 2600 \mu\text{s}$ (shown at the left), the incoming wave is propagating from the left to the right, and, at time $t = 3600 \mu\text{s}$, the wave is reflecting back from the right fixed end. The same problem analyzed by the push-forward pullback time integration method¹⁷ employing the nonpartitioned system is shown in Figure 14, which shows a significant reduction in spurious oscillations for both the incoming and reflecting waves. Second, the same problem is simulated by single step time integration in the partitioned system via the method of Lagrange multipliers, employing the CDM and the push-forward pullback time integration method, respectively. Figure 15 shows a similar level of dispersion errors to the CDM in nonpartitioned system. In addition, Figure 16 shows that the push-forward pullback time integration method also shows an improved performance in terms of the spurious oscillations comparing with that of the CDM, as shown in Figure 15. The problem is finally analyzed by multistep time integration, employing the CDM and the push-forward pullback time integration method in the partitioned system. Although the dispersion error in the CDM is reduced a little comparing with those of the single step time integration of nonpartitioned system, the level of the dispersion error is still noticeable, as shown in Figure 17. Figure 18 shows that the push-forward pullback time integration method also shows a more improved performance in terms of the spurious oscillations comparing with those of the other methods. Especially, it is seen that a small oscillating reflection wave generated from the hard material side appears conspicuously.

We have analyzed wave propagation from the left end to the right end of a heterogeneous bar whose left half is now made of hard material and the right half is made of soft materials. The improved performance of the proposed multistep inte-

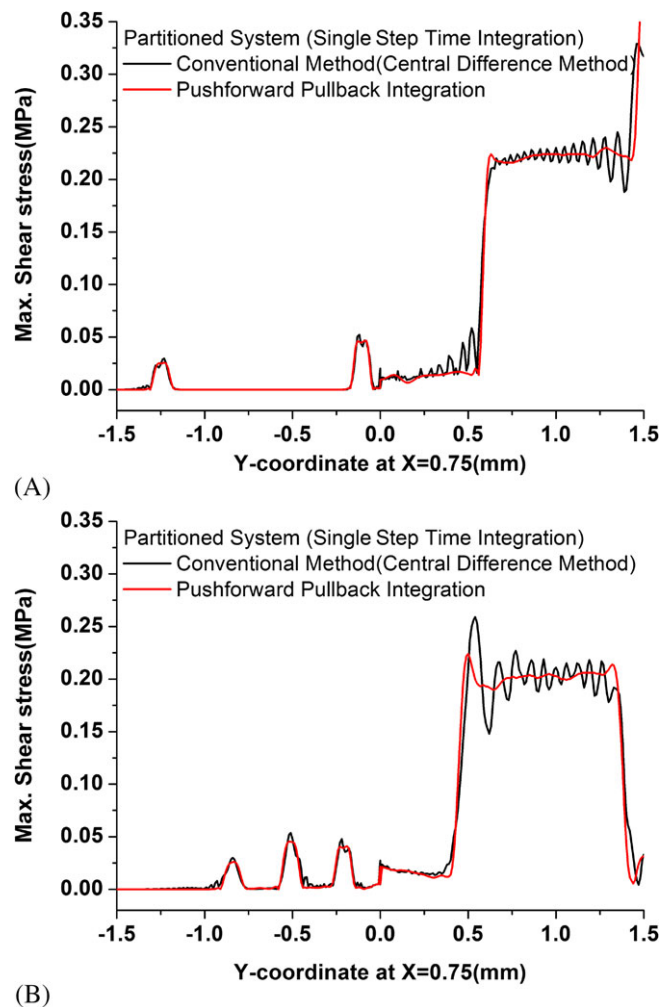


FIGURE 28 Comparison results of the maximum shear stress distribution of single step time integration along Y-axis at $X = 0.75$ (mode-II problem) in partitioned system: A, $t = 0.97 \mu\text{s}$; B, $t = 2.26 \mu\text{s}$

gration algorithm is similarly observed. Encouraged by the improved performance of the proposed multistep integration algorithm as applied to one-dimensional problems, we now move on to two-dimensional problem discussed later.

5.2 | Crack tip at the center of heterogeneous plate subjected to mode-II type incident wave

The preceding one-dimensional wave propagation through heterogeneous materials analyzed by the present multistep integration algorithm indicates that the proposed partitioned multistep explicit integration algorithm is accurate and efficient compared to the conventional CDM-based multistep results. We now proceed to an analysis of discontinuous wave propagation through two-dimensional heterogeneous materials.

A plane strain problem with crack tip between the heterogeneous solids is subjected to a mode-II type incident wave, as shown in Figure 19. The upper part of the plate is a hard material and the lower part is a soft material. Since the elastic modulus and density of each material are 200 GPa, 8000 kg/m³, and 2 GPa, 8000 kg/m³, the ratio of the critical time step sizes is equal to 10 if the two materials have the same element size (the number of element=300x300).

Figure 20 shows the reference solution when the stress wave is propagated and reflected at the respective domains, based on the respective wave speeds of the longitudinal stress and the shear stress waves. Figure 21 shows the results of the maximum shear stress contour plots of the conventional CDM with a single step integration in nonpartitioned system for both the stiff and soft (upper half and lower half in Figure 19) portions of the structure. Notice that the CDM fails to exhibit the surface wave (viz, Rayleigh wave and von-Schmidt waves) in the stiff portion of the structure, as shown in Figure 21A. Even for the lower soft part of the structure, significant computational dispersion is detected, as illustrated in Figure 21B. This is clearly manifested when compared with the results obtained by the push-forward pullback time integration with a single step integration in nonpartitioned system, as shown in Figures 22A and 22B, which clearly demonstrate the surface

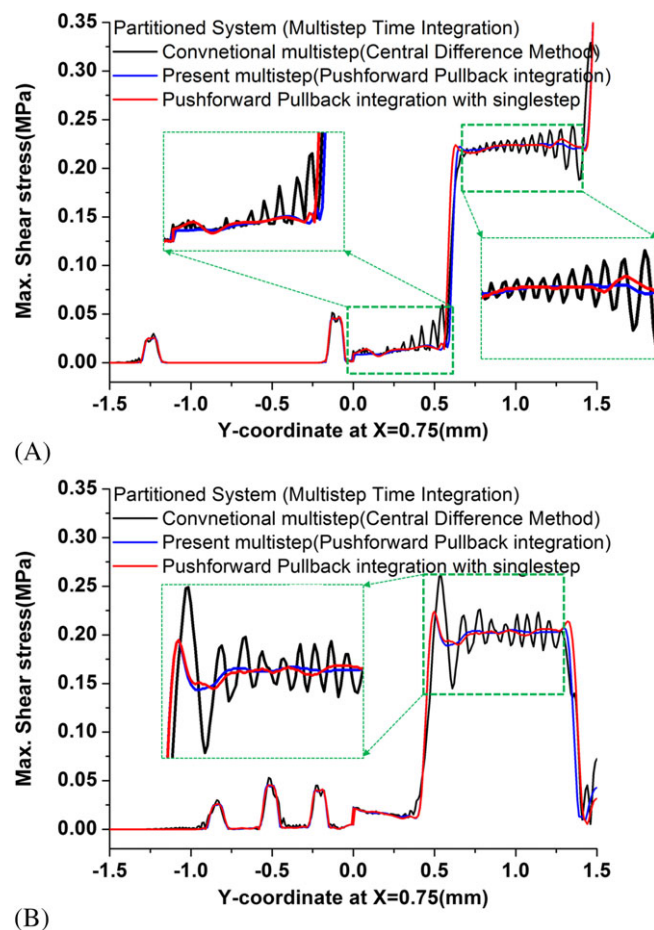


FIGURE 29 Comparison results of the maximum shear stress distribution of Multistep Time Integration along Y-axis at X = 0.75 (mode-II problem) in Partitioned System: A, $t = 0.97 \mu\text{s}$; B, $t = 2.26 \mu\text{s}$

waves propagating in the upper stiff portion and relatively minor dispersion in the lower soft portion. Results for a single step integration with the partitioned system are shown in Figures 23 and 24. Their results are similar to those reported in Figures 21 and 22 with the same single time integration obtained in nonpartitioned system. Multistep integration with the partitioned system via the method of Lagrange multipliers has been carried out, employing both the CDM and the push-forward and pullback integration method. Figures 25 and 26 illustrate that the results are similar to those of the single step integration in partitioned system as shown in Figures 23 and 24. There is a fraction of dissipation of the energy being carried away by the surface waves, but not significant enough to affect the principal portion of the energy associated with shear stress waves.

Second, the maximum shear stress distributions across the cross section at $X = 0.75$ mm are plotted in Figures 27, 28, and 29 at two different times, $t = 0.97 \mu\text{s}$ and $t = 2.26 \mu\text{s}$. The dispersion error in the CDM with the single step time integration of partitioned system is reduced a little comparing with those of the single step time integration of nonpartitioned system a partitioned system, but the level of the dispersion error is still noticeable, as shown in Figures 27 and 28. In an earlier work,¹⁸ it was demonstrated that the push-forward and pull-back integration method outperforms several explicit methods in terms of capturing the predominant shear stress wave magnitudes. In this paper, the same superior performance is also demonstrated especially in the multistep push-forward and pullback integration in the partitioned system, as shown in 29.

Finally, we want to analyze how the time step size affects the analysis of discontinuous stress wave propagation when the standard CDM and the present method are applied. Figure 30 shows the respective results versus various time step size for the single step CDM in the nonpartitioned system. Even if the time step size is reduced to $Cr=0.1$ from $Cr=0.9$ in

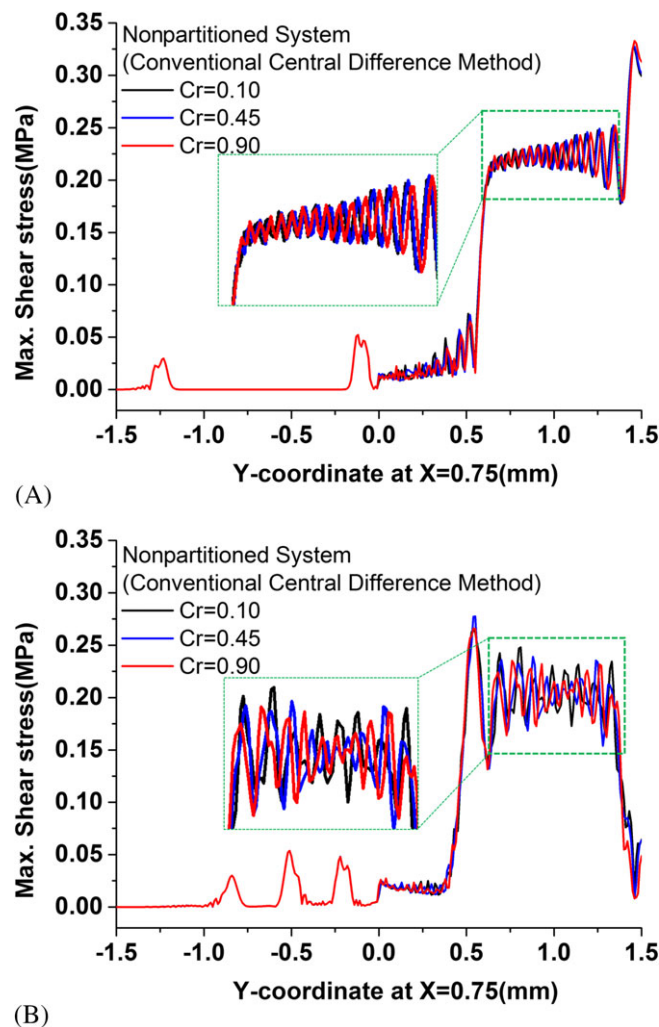


FIGURE 30 Comparison results of the maximum shear stress distribution of Multistep Time Integration along Y-axis at $X = 0.75$ (mode-II problem) in Partitioned System: A, $t = 0.97 \mu\text{s}$; B, $t = 2.26 \mu\text{s}$

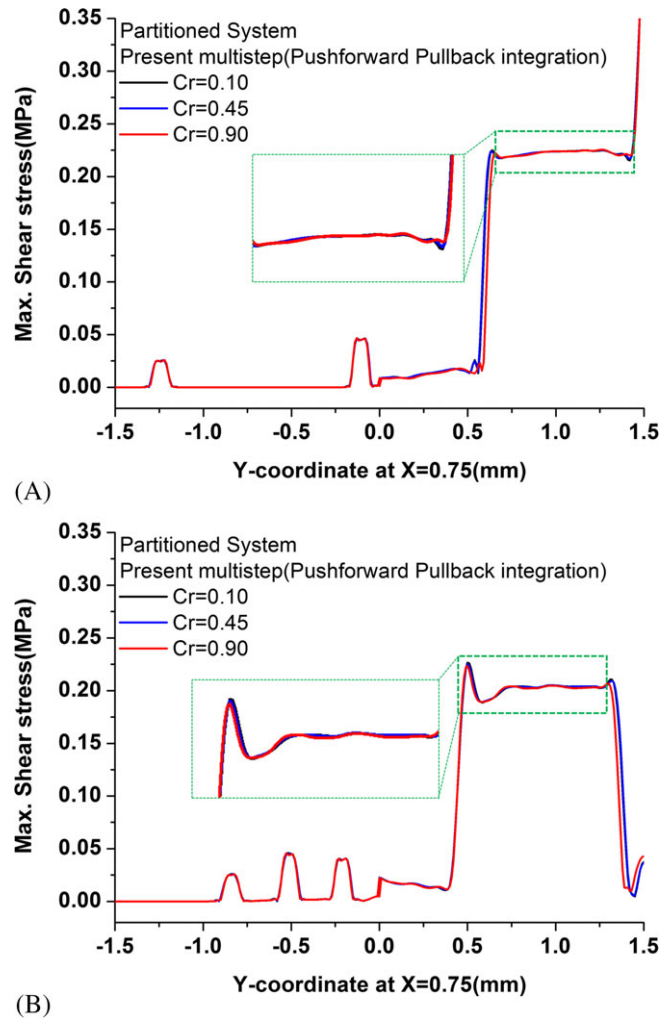


FIGURE 31 Comparison results of the maximum shear stress distribution of multistep time integration along Y-axis at X = 0.75 (mode-II problem) in partitioned system (the present algorithm): A, $t = 0.97 \mu\text{s}$; B, $t = 2.26 \mu\text{s}$

terms of Courant number ($Cr = \Delta t / \Delta t_{Cr}$), the magnitude of the dispersion errors remains almost unchanged with only a slight change in phase. Figure 31 also shows the results for the present multistep integration method in the partitioned system. It shows very good results with little dispersion errors for all time step sizes. However, even if the time step size is reduced to $Cr=0.1$ from $Cr=0.9$, the spurious oscillation errors do not decrease.

These results lead to the following conclusions that it does not apply in case of the discontinuous wave propagation problem: the smaller the time step size, the more accurate the solution becomes.

6 | CONCLUSIONS

An explicit-explicit multistep time integration algorithm for computing the discontinuous stress wave propagation for heterogeneous solids is presented. The proposed algorithm reduces the front-shock and post-shock vibrations of discontinuous stress waves and accurately traces the wave fronts propagated at various speeds in heterogeneous solids. The present algorithm maintains its robustness up to 100 critical times step ratio and the results are comparable with those integrated with a single critical step of the stiff materials, thus leading to significant computational savings. While numerical experiments are carried out employing two-domain problems, the proposed algorithm can be extended to problems consisting of several partitions, thus yielding significant computational savings for heterogeneous systems subjected to discontinuous loading conditions.

ACKNOWLEDGEMENTS

This work was partially supported by the Nuclear Safety Research Program through the Korea Foundation of Nuclear Safety (KOFONS), granted financial resource from the Nuclear Safety and Security Commission (NSSS), Republic of Korea (No. 1403013 and No. 1803015). The work of R. Kolman was supported by the Centre of Excellence for nonlinear dynamic behavior of advanced materials in engineering CZ.02.1.01/0.0/0.0/15 003(0000493) (Excellent Research Teams) in the framework of Operational Program Research, Development and Education, and the grant project of the Czech Science Foundation, 17-22615S, within institutional support RVO:61388998.

ORCID

S. S. Cho  <https://orcid.org/0000-0003-0306-4694>

R. Kolman  <https://orcid.org/0000-0002-8167-3535>

J. A. González  <https://orcid.org/0000-0003-3282-0049>

K. C. Park  <https://orcid.org/0000-0002-6303-1010>

REFERENCES

1. Kolsky H. *Stress Waves in Solids*. Mineola, NY: Dover Publications; 1963.
2. Harari I. Special issue on new computational methods for wave propagation. *Wave Motion*. 2004;39(4):279-280.
3. Reed WH, Hill TR. *Triangular Mesh Methods for the Neutron Transport Equation*. Technical Report LA-UR-73-479. Los Alamos, NM: Los Alamos Scientific Laboratory; 1973.
4. Hughes TJR, Hulbert GM. Space-time finite element methods for elastodynamics: formulations and error estimates. *Comput Methods Appl Mech Eng*. 1988;66:339-363.
5. Hulbert GM, Hughes TJR. Space-time finite element methods for second order hyperbolic equations. *Comput Methods Appl Mech Eng*. 1990;84:327-347.
6. Huang H, Costanzo F. On the use of space-time finite elements in the solution of elasto-dynamic problems with strain discontinuities. *Comput Methods Appl Mech Eng*. 2002;191:5315-5343.
7. Wendlandt JM, Marsden JE. Mechanical integrators derived from a discrete variational principle. *Physica D*. 1997;106:223-246.
8. Kane C, Marsden JE, Ortiz M, West M. Variational integrators and the Newmark algorithm for conservative and dissipative mechanical systems. *Int J Numer Methods Eng*. 2000;49:1295-1325.
9. Casadei T, Halleux J. Binary spatial partitioning of the central-difference time integration scheme for explicit fast transient dynamics. *Int J Numer Methods Eng*. 2009;78:1436-1473.
10. Chang SY. A new family of explicit methods for linear structural dynamics. *Comput Struct*. 2010;88:755-772.
11. Cho SS, Huh H, Park KC. A time-discontinuous implicit variational integrator for stress wave propagation analysis in solids. *Comput Methods Appl Mech Eng*. 2011;200:649-664.
12. Ye W, Bel-brunon A, Catheline S, Rochette M, Combescure A. A selective mass scaling method for shear wave propagation analyses in nearly incompressible materials. *Int J Numer Methods Eng*. 2017;107:155-173.
13. González JA, Kolman R, Cho SS, Felippa CA, Park KC. Inverse mass matrix via the method of localized Lagrange multipliers. *Int J Numer Methods Eng*. 2018;113:277-295.
14. Prager W. Variational principles of linear elastostatics for discontinuous displacements, strains, and stresses. *Recent Prog Appl Mech*. 1967:463-474.
15. Virieux J. SH-wave propagation in heterogeneous media: velocity-stress finite-difference method. *Geophysics*. 1984;49:1933-1942.
16. Virieux J. Wave propagation in heterogeneous media: velocity-stress finite-difference method. *Geophysics*. 1986;51:889-901.
17. Park KC, Lim SJ, Huh H. A method for computation of discontinuous wave propagation in heterogeneous solids: basic algorithm description and application to one-dimensional problems. *Int J Numer Methods Eng*. 2012;91:622-643.
18. Cho SS, Park KC, Huh H. A method for multidimensional wave propagation analysis via component-wise partition of longitudinal and shear waves. *Int J Numer Methods Eng*. 2013;95:212-237.
19. Kolman R, Cho SS, Park KC. Efficient implementation of an explicit partitioned shear and longitudinal wave propagation algorithm. *Int J Numer Methods Eng*. 2016;107:543-579.
20. Gravouil A, Combescure A. Multi-time-step explicit-implicit method for non-linear structural dynamics. *Int J Numer Methods Eng*. 2001;50:199-225.
21. Gravouil A, Combescure A. Multi-time-step and two-scale domain decomposition method for non-linear structural dynamics. *Int J Numer Methods Eng*. 2003;58:1545-1569.
22. Gravouil A, Combescure A, Brun M. Heterogeneous asynchronous time integrators for computational structural dynamics. *Int J Numer Methods Eng*. 2015;102(3-4):202-232.
23. Park KC, Felippa CA, Gumaste UA. A localized version of the method of Lagrange multipliers and its applications. *Computational Mechanics*. 2000;24(6):476-490.

24. Newmark NM. A method of computation for structural dynamics. *J Eng Mech.* 1959;85(3):67-94.
25. Park KC, Felippa CA. A variational framework for solution method developments in structural mechanics. *J Appl Mech.* 1998;65(1):242-249.
26. Park KC, Felippa CA. A variational principle for the formulation of partitioned structural systems. *Int J Numer Methods Eng.* 2000;47:395-418.

How to cite this article: Cho SS, Kolman R, González JA, Park KC. Explicit multistep time integration for discontinuous elastic stress wave propagation in heterogeneous solids. *Int J Numer Methods Eng.* 2019;118:276–302. <https://doi.org/10.1002/nme.6027>



ELSEVIER



Available online at www.sciencedirect.com

ScienceDirect

Mathematics and Computers in Simulation 189 (2021) 305–324



MATHEMATICS
AND
COMPUTERS
IN SIMULATION

www.elsevier.com/locate/matcom

Original articles

Bi-penalty stabilized technique with predictor–corrector time scheme for contact-impact problems of elastic bars

Radek Kolman^{a,*}, Ján Kopačka^a, José A. González^b, S.S. Cho^c, K.C. Park^d

^a Institute of Thermomechanics of the CAS, v. v. i., Dolejškova 1402/5, 182 00 Praha 8, Czech Republic

^b Escuela Técnica Superior de Ingeniería, Universidad de Sevilla, Camino de los Descubrimientos s/n, Seville E-41092, Spain

^c Reactor Mechanical Engineering Division, Korea Atomic Energy Research Institute, 999-111 Daedeok-Daero, Yuseong-gu, Daejeon 305-353, Republic of Korea

^d Ann and H. J. Smead Aerospace Engineering Sciences, University of Colorado at Boulder, CO 80309-429, USA

Received 8 February 2020; received in revised form 17 November 2020; accepted 17 March 2021

Available online 8 April 2021

Abstract

This paper presents a stabilization technique for the finite element modelling of contact-impact problems of elastic bars via a *bi-penalty method* for enforcing contact constraints while employing an explicit predictor–corrector time integration algorithms. The present proposed method combines three salient features in carrying out explicit transient analysis of contact-impact problems: the addition of a penalty term associated with a kinetic energy expression of gap constraints, in addition to the conventional internal energy penalty term of the gap constraints; an explicit integration method that alleviates spurious oscillations; and, a judicious selection of two penalty parameters such that the stable time steps of the resulting explicit method is least compromised. Numerical experiments have been carried out with three explicit methods: the standard central difference method, the stabilized predictor–corrector method (Wu, 2003 [50]) and a method for mitigating spurious oscillations (Park et al., 2012 [44]) as applied to simulate one-dimensional contact-impact problems of the Signorini problem and the impact of two elastic bars. Results indicate that the proposed method can maintain the contact-free stability limit of the central difference and yield improved accuracy compared with existing bi-penalty methods.

© 2021 International Association for Mathematics and Computers in Simulation (IMACS). Published by Elsevier B.V. All rights reserved.

Keywords: Finite element method; Explicit integration; Contact-impact problems; Bi-penalty method; Stability analysis

1. Introduction

Obtaining fast, stable and accurate solutions of contact-impact problems remain at the forefront of computational mechanics research. Applications in this field appear in real-world problems from mechanical and civil engineering, bio-mechanics, ballistics, or aviation and aerospace engineering. In this paper, we focus on the finite element modelling of contact-impact problems of elastic bars under the linear deformation theory without damping. In the space discretization, linear finite elements and the consistent, lumped, and averaged mass matrices are employed.

* Corresponding author.

E-mail addresses: kolman@it.cas.cz (R. Kolman), kopacka@it.cas.cz (J. Kopačka), japerez@us.es (J.A. González), sscho96@kaist.ac.kr (S.S. Cho), kcpark@colorado.edu (K.C. Park).

<https://doi.org/10.1016/j.matcom.2021.03.023>

0378-4754/© 2021 International Association for Mathematics and Computers in Simulation (IMACS). Published by Elsevier B.V. All rights reserved.

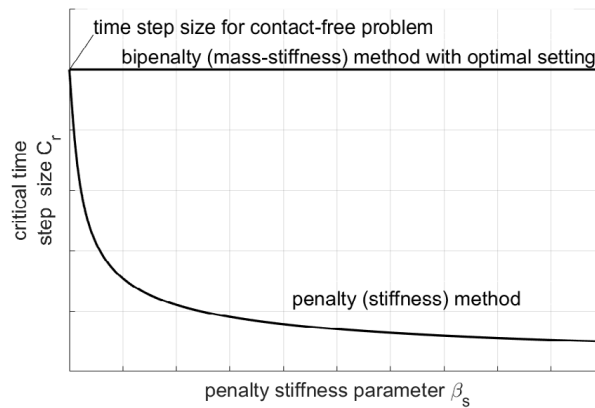


Fig. 1. Characteristic dependence of the stable time step size for the penalty and bi-penalty methods with optimal setting. In the penalty method, the stable time step size is strongly affected by the penalty stiffness parameter β_s while bi-penalty with optimal setting remains unaffected.

Attention is paid only to the explicit time integration with a constant time step and its stability. For contact constraints enforcement, the classical stiffness penalty method and the bi-penalty modification are considered.

Most frequently, penalty methods, Lagrange multipliers method, its localized variant and augmented Lagrangian methods are applied for modelling dynamic contact problems in the context of the finite element analysis, e.g. see [6,9,21,37]. In explicit finite element analysis, the penalty method is preferred due to its implementation simplicity and fast evaluation of contact forces [6] which, in comparison to Lagrange Multipliers method, does not increase the number of unknowns. It is also needed to mention the works related to efficient active set approaches in contact problems as [15,48]. On the other hand, the main disadvantage of the penalty method in elastodynamics is the fact that the stability limit of the explicit time integration scheme is destroyed by a large value of the numerical stiffness penalty parameter used for contact constraints enforcement [6]. The stable time step size rapidly decreases with increasing value of the penalty stiffness parameter as is depicted in Fig. 1.

A complete review of time integration strategies for contact-impact/dynamic contact problems in finite element modelling can be found in [49]. In general, one can use implicit or explicit time integration schemes. In this paper, we focus only on explicit time integration. For examples, the implicit time schemes have been applied in impact-contact problems in [1,2,29,37,38,46]. On the other hands, the explicit time schemes for the contact-impact problems have been employed in [6–9,23,24]. The explicit–implicit time scheme in contact-impact problems has been adopted in [31]. The explicit predictor–corrector algorithm has been designed for dynamic contact with smooth and non-smooth surface geometries in [12].

Moreover, it is well known that the results of contact problems modelled via the penalty-like methods depend on the used value of the penalty parameter. The principle of the penalty method implies that impenetrability conditions are always met only approximately. With a higher value of the penalty parameter, more precise fulfilment of the impenetrability conditions occurs. We know that penalty methods are generally not consistent [49] within the variational formulation of the problem and the final matrix form is ill-conditioned. Often, the solution of the contact problem depends on the penalty parameters and the convergence to the correct solution is not guaranteed [49]. A direct consequence of only approximate fulfilment of the contact constraints is a non-zero penetration, which causes the contact term to produce non-physical energy corresponding to the contact interfaces. A good solution to the oscillations on contact forces is the application of time schemes based on predictor and corrector phases for evaluating kinematical quantities. The regularization of the penalty approach in the finite element method of the impact of elastic bars is presented in Otto's work [39] and extension to the spectral 3D finite element method with NURBS contact tying for contact surfaces is published in [40]. In these works, the nonlinear penalty stiffness parameter is employed with explicit Runge–Kutta time integration of order 4. In this field, it is also important to mention the works of C. Felippa [13,17,18].

Also, during the convergence process, final penetration is not exactly zero as corresponds to contact non-penetration condition. As a consequence, there is lost energy included in the penalty contact term, which is not a physical one and it is a product of numerical behaviour of the method. One way to eliminate this undesired

numerical effect is to use the bi-penalty method [27]. In Fig. 1, the effect on the stability limit of the penalty method is shown, as well as the optimal setting for the bi-penalty method, for details see [27,36].

In the bi-penalty method, an extra mass term is added into the mass distribution corresponding to a contact domain of interest with a stiffness term at the same time as in the classical penalty method. This modification of the penalty method is known from Asano [3] and later from Armero [2]. Excellent progress and different applications to several problems have been made by Hetherington [25–27]. The penalty based method in multibody dynamics is also a well-known technique for stabilization of constraints, for example, see the Park's method [43] and Baumgarte's method [4]. In this area, the bi-penalty or tri-penalty modification is a common technique used for stabilization of oscillations in the constraints connecting the bodies. In numerical analysis, the bi-penalty method is known as the *consistent penalty method*, see [41].

Another important problem in the numerical modelling of contact-impact problems comes from spurious oscillations of contact forces, often caused by activation and deactivation (zig-zag effect) of contact constraints during the solution process. A lot of numerical techniques and strategies have been proposed in the literature for elimination and stabilization of spurious oscillations in the contact forces. One can mention the work of Doyen [16], the stabilized implicit Newmark method for non-smooth dynamics and contacts [14,31], mass redistribution techniques [32], singular mass techniques [45,47] or the stabilized explicit scheme with the penalty method [51]. The last mentioned technique can be also applied in connection with the bi-penalty method for stabilization of spurious oscillations of contact forces.

In this paper, we present an explicit time integration scheme for finite element solution of contact-impact problems based on the central difference method [5], in particular, its stabilized version using the predictor–corrector approach [49,51] and Park explicit time scheme with predictor–corrector stabilization of contact forces [44] in combination with the bi-penalty formulation [36]. Superior behaviour of the presented method for modelling contact-impact problems is demonstrated using the impact problem of elastic bars and the Signorini problem. The obtained results are compared with the standard time integration scheme used in explicit finite element procedures for impact-contact problems, the central difference method [5]. It is observed, the standard explicit central difference method is not able to integrate accurately in time the wave propagation problem with a time step size smaller than the stability limit. It is known that only the combination in explicit time integration via the central difference method on the uniform linear finite element mesh, with lumped mass matrix and time step corresponding to the critical time step size in a uniform gives exact results of wave propagation. Otherwise, the results are polluted by spurious stress oscillations, provided that the time step size is smaller than the stability limit. Park explicit time scheme [44] is able to track a wavefront eliminating the effect of time step size on accuracy so it is a suitable tool for modelling contact-impact problems.

The paper is organized as follows. In Section 2, the governing equations for impact of elastic bars with the definition of the gap function for contact interfaces are presented and introduced with strong and weak forms. In Section 3, the finite element discretized equations for the motion of elastic bars with the bi-penalty method are derived. The explicit time integration of contact-impact problems in the finite element method is presented in Section 4 together with the stability limit. Also, the optimal setting for the penalty mass matrix is derived. Results for numerical tests in one-dimensional case – the Signorini and Huněk tests – are presented in Section 5 with comments on the behaviour and superior properties of the proposed methodology. The paper closes with the conclusions in Section 6.

2. Formulation of the contact problem and governing equations

In this section, we define the strong and weak formulations of the impact-contact problem for elastic bars, including the definition of a gap function to enforce the contact constraints with the bi-penalty method. In the following, we assume that the elastic bars in contact are homogeneous with the same constant cross-section A , Young modulus E and mass density ρ . The lengths are different for each bar as well as their initial velocities of v_{i0} .

2.1. Strong formulation of contact initial–boundary value problem in 1D

The correct mathematical formulation of the dynamic contact problems including the impenetrability condition as well as the persistency condition is presented in [29]. The one-dimensional contact-impact problem for linear

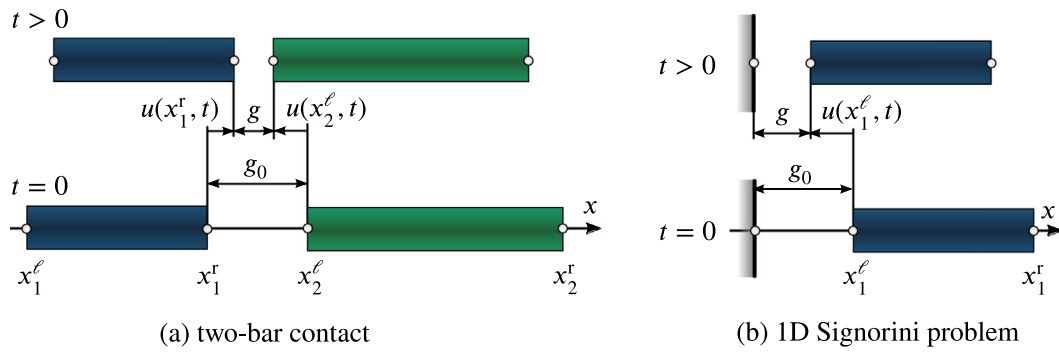


Fig. 2. Definition of domains of interest, their boundaries and the gap function.

isotropic homogeneous bars is governed by the following constrained initial–boundary value problem (IBVP) [49]:

$$\begin{cases} Eu'' = \rho \ddot{u} & \text{in } \mathbf{I} \times \mathbf{T} \\ u(x, 0) = u_0(x) & \text{in } \bar{\mathbf{I}} \\ \dot{u}(x, 0) = v_0(x) & \text{in } \bar{\mathbf{I}} \\ u(x, t) = \bar{u}(x) & \text{on } \Gamma_u \\ Eu'(x, t) = \bar{\sigma}(x) & \text{on } \Gamma_\sigma \\ g(t) \leq 0 & \text{on } \Gamma_c \times \mathbf{T} \\ p_c \geq 0 & \text{on } \Gamma_c \times \mathbf{T} \\ g(t)p_c = 0 & \text{on } \Gamma_c \times \mathbf{T} \\ \dot{g}(t)p_c = 0 & \text{on } \Gamma_c \times \mathbf{T} \end{cases} \quad (1)$$

where $\mathbf{I} = \bigcup_i \mathbf{I}_i = (x_i^l, x_i^r)$; $i = 1, 2$ is the union of intervals of spatial points $x_i \in \mathbf{I}_i \subset \mathbf{R}$ defining the contacting bodies (see Fig. 2), and $\mathbf{T} = (0, t_{\text{end}})$; $t_{\text{end}} \in \mathbf{R}$ is the time interval. For one-bar contact problem with a rigid obstacle only one body is considered and $\mathbf{I} = \mathbf{I}_1$. In the first Eq. (1), which governs the balance of the linear momentum, $u(x, t) : \mathbf{I} \times \mathbf{T} \mapsto \mathbf{R}$ is the unknown displacement function, $E \in \mathbf{R}^+$ is Young’s elasticity modulus, and $\rho \in \mathbf{R}^+$ is the mass density. The penultimate condition in Eq. (1) is the classical KKT complementarity condition between gap $g(t)$ and pressure p_c , requiring that surface forces exist only during actual contact ($g = 0$). The last condition in Eq. (1) is termed the persistency condition, see [38]. Note that for the sake of simplicity, the second partial derivative with respect to x is denoted by double prime, $(\bullet)''$, whereas the second partial derivative with respect to t by superimposed dots, $(\bullet)''$.

The governing equation (1)₁ is complement with the initial conditions (1)_{2,3}, Dirichlet and Neumann boundary conditions (1)_{4,5}, contact conditions (1)_{6–8} and persistency condition (1)₉, where $g(t)$ and $\dot{g}(t)$ is the gap function and its rate defined in the following section and $p_c(t)$ is the contact pressure. In the initial conditions, $u_0(x) : \bar{\mathbf{I}} \mapsto \mathbf{R}$ is the initial displacement function and $v_0(x) : \bar{\mathbf{I}} \mapsto \mathbf{R}$ is the initial velocity function; both prescribed at time $t = 0$. Similarly for the boundary conditions, $\bar{u}(x) : \Gamma_u \mapsto \mathbf{R}$ is the displacement function and $\bar{\sigma}(x) : \Gamma_\sigma \mapsto \mathbf{R}$ is the traction function; both constant in time. Γ_u and Γ_σ are sets of boundary points where displacements and stresses are prescribed.

2.2. Definition of the gap function

Finally the contact constraints are prescribed by the Signorini–Hertz–Moreau conditions (1)_{6–8}, with the aid of the gap function, g , and contact pressure, p_c , on the set $\Gamma_c = \{x_2^r, x_1^l\}$. The contact pressure $p_c(x, t) : \bar{\mathbf{T}} \mapsto \mathbf{R}$ is equal to $-Eu'$, assuming Hooke’s law, and the gap function $g(t) : \bar{\mathbf{T}} \mapsto \mathbf{R}$ for the two-bar contact is defined as

$$g(t) = -[u(x_1^l, t) - u(x_2^r, t) + g_0] \quad (2)$$

where g_0 denotes the initial gap, cf. Fig. 2. For the one-bar contact the gap function can be considered as the special case of (2), assuming $x_2^r = 0$ and $u(x_2^r, t) = 0$

$$g(t) = -[u(x_1^l, t) + g_0] \tag{3}$$

According to this definition, the gap function has a positive sign in the case of penetration. Therefore, the inequality (1)₆ is called the impenetrability condition.

In the contact-impact problems, constraints on the normal components of the velocities of points in the contact are needed to include in the formulation. This condition is called the persistency condition. For 1D cases, the persistency condition can be prescribed via the gap rate as

$$\dot{g}(t) = -[\dot{u}(x_1^l, t) - \dot{u}(x_2^r, t)] \tag{4}$$

which should fulfil the condition (1)₉.

Note, that it was assumed that the first body is on the right and therefore its contact interface forms the left boundary point, x_1^l . Analogously for the second body. For the one-bar contact Γ_c reduces to single-element set $\Gamma_c = \{x_1^l\}$. All three sets Γ_u, Γ_σ , and Γ_c disjointly cover the boundaries of intervals I_i .

2.3. Weak form of contact-impact problem via bi-penalty method

In this section, we introduce the weak form of the contact-impact problems via the bi-penalty method, for details see [36]. The Lagrangian functional, $\mathcal{L}(u, \dot{u})$ of the problem of interest corresponding to Eq. (1) is given as

$$\mathcal{L}(u, \dot{u}) = \mathcal{T}(\dot{u}) - (\mathcal{U}(u) - \mathcal{W}(u)) + \mathcal{W}_c(u, \dot{u}), \tag{5}$$

where

$$\mathcal{T}(\dot{u}) = \int_I \frac{1}{2} \rho A \dot{u}^2 dx \tag{6}$$

$$\mathcal{U}(u) = \int_I \frac{1}{2} E A u^2 dx \tag{7}$$

$$\mathcal{W}(u) = \int_I u b A dx + \sum_{x \in \Gamma_\sigma} u A \bar{\sigma} \tag{8}$$

are the kinetic energy, the strain energy, and the work of external forces, respectively. Note, that the cross-section area is marked by A .

Bi-penalty method adds the penalization term to the strain energy (7) to enforce the zero-gap on the contact boundary [49] and at the same time, an extra term to the kinetic energy (6) to enforce the zero-velocity-gap on the contact boundary. This way, we define a penalization term associated to the contact interface as

$$\mathcal{W}_c(u, \dot{u}) = -\frac{1}{2} \epsilon_s A \langle g \rangle^2 + \frac{1}{2} \epsilon_m A \langle \dot{g} \rangle^2, \tag{9}$$

where the operator $\langle \bullet \rangle$ are the so-called Macaulay’s brackets defined as $\langle \bullet \rangle = \frac{|\bullet| + \bullet}{2}$. The parameters ϵ_s [kg m⁻² s⁻²] and ϵ_m [kg m⁻²] are the stiffness and mass penalty parameters, respectively.

The standard procedure for the stationary solution of (5), defined as $\delta \int_T \mathcal{L}_p(u, \dot{u}) dt = 0$, gives us

$$\int_I \delta u \rho \ddot{u} dx + \int_I \delta u' E A u' dx + H(g) A [\delta g (\epsilon_s g + \epsilon_m \ddot{g})] = \int_I \delta u A b dx + \sum_{x \in \Gamma_\sigma} \delta u A \bar{\sigma} \tag{10}$$

which is the framework for the finite element discretized equation of motion including the contact constraints by the bi-penalty method. Note the identity $\langle g \rangle = g H(g)$, where $H(g)$ is the Heaviside step function which ensures that the penalization term is active only in the case of penetration.

It is known that the standard/classical (stiffness) penalty method is not consistent [49], because it allows non-zero penetration at the contact interface. On the other hand, the zero-gap velocity condition represents a geometric condition of velocities equality at the contact interface. This geometric condition is required by the true solution. It is often enforced using the so-called persistence condition [38], where the product of the normal traction component and the gap velocity is required to be equal to zero. Although the bi-penalty method in the derivation penalizes

the gap velocity through the term which can be interpreted as kinetic energy in (9), however, after the application of Hamilton’s variational principle, one gets a residual term that contains the second time derivative of the gap functions. Geometric condition of velocity equality at the contact interface thus is imposed indirectly by penalizing the second time derivative, which ultimately leads to smaller oscillations of the gap function and its velocity — stabilization of contact problem.

3. Bi-penalty method in finite element method for contact-impact problems

In the finite element procedures [5] for elastodynamic problems with contact constraints, the equations of motion yield the following system of nonlinear ordinary differential equations

$$\mathbf{M}\ddot{\mathbf{u}} + \mathbf{K}\mathbf{u} = \mathbf{r}(t) - \mathbf{r}_c(\mathbf{u}, \ddot{\mathbf{u}}) \tag{11}$$

where \mathbf{M} is the mass matrix, \mathbf{K} is the stiffness matrix, \mathbf{u} and $\ddot{\mathbf{u}}$ are nodal displacements and accelerations, \mathbf{r} is the vector of external loading with time dependency, \mathbf{r}_c is the vector of contact forces. For a detailed derivation of the discretized equation of motion Eq. (11) for the finite element method with the bi-penalty method see the work [36].

The linear FEM is applied in the rest of the paper for one-dimensional problems. The fully integrated elemental stiffness is assumed as

$$\hat{\mathbf{K}} = \frac{EA}{h_e} \begin{bmatrix} 1 & -1 \\ -1 & 1 \end{bmatrix} \tag{12}$$

The averaged mass matrix $\hat{\mathbf{M}}$ as a linear combination of the consistent $\hat{\mathbf{M}}$ mass matrix

$$\hat{\mathbf{M}}_C = \frac{\rho h_e A}{6} \begin{bmatrix} 2 & 1 \\ 1 & 2 \end{bmatrix} \tag{13}$$

and the lumped mass matrix

$$\hat{\mathbf{M}}_L = \frac{\rho h_e A}{2} \begin{bmatrix} 1 & 0 \\ 0 & 1 \end{bmatrix} \tag{14}$$

is given as

$$\hat{\mathbf{M}} = (1 - \gamma)\hat{\mathbf{M}}_C + \gamma\hat{\mathbf{M}}_L = \frac{\rho h_e A}{6} \begin{bmatrix} 2 + \gamma & 1 - \gamma \\ 1 - \gamma & 2 + \gamma \end{bmatrix}. \tag{15}$$

In the previous text, it was assumed that cross-section area A , Young’s modulus E , and density ρ are constant. h_e is the length of the finite element. As it is known the lumped mass matrices are preferred in explicit finite element analysis, but in this paper, we study the effect of contact oscillations due to the choice of the mass matrix.

In the bi-penalty formulation [36], the global contact residual vector, \mathbf{r}_c , is assembled from the local counterparts $\hat{\mathbf{r}}_c$ as the contribution of stiffness and mass terms to the contact residual vector which can be written as

$$\hat{\mathbf{r}}_c(\hat{\mathbf{u}}, \ddot{\hat{\mathbf{u}}}) = \hat{\mathbf{M}}_p \ddot{\hat{\mathbf{u}}} + \hat{\mathbf{K}}_p \hat{\mathbf{u}} + \hat{\mathbf{f}}_p \tag{16}$$

where

$$\hat{\mathbf{M}}_p = \int_{\Gamma_c} \epsilon_m H(g) \mathbf{Z} \mathbf{Z}^T dS \quad \hat{\mathbf{K}}_p = \int_{\Gamma_c} \epsilon_s H(g) \mathbf{Z} \mathbf{Z}^T dS \quad \hat{\mathbf{f}}_p = \int_{\Gamma_c} \epsilon_s H(g) \mathbf{Z} g_0 dS \tag{17}$$

Here, $\hat{\mathbf{M}}_p$ is the additional (penalized) elemental mass matrix due to inertia penalty, $\hat{\mathbf{K}}_p$ is the additional (penalized) elemental stiffness matrix due to stiffness penalty, and $\hat{\mathbf{f}}_p$ is the part of the elemental contact force due to the initial gap g_0 ; g is the gap function; $H(g)$ is the Heaviside step function for prescribing active or inactive contact constraints; ϵ_m and ϵ_s are mass and stiffness penalty parameters; Γ_c is one of the contact surfaces, usually called slave, on which the contact terms are evaluated; the matrix \mathbf{Z} represents an operator from the displacement field \mathbf{u} to the gap function g in the contact

$$g = \mathbf{Z}^T \mathbf{u} + g_0 \tag{18}$$

Remark. Note that the gap function g is positive in separation and the Heaviside function $H(g)$ is one for $g > 0$. This means that the penalty matrices are acting only during separation. This is solved by defining $g \geq 0$ as the penetration.

The particular form of matrix \mathbf{Z} follows from the considered contact discretization. A comprehensive overview can be found e.g., in the textbook [49]. For the 1D case, see the definition of the gap function in (2), the corresponding representation of the gap function g takes the form

$$g = \mathbf{Z}^T \mathbf{u} + g_0 = \begin{bmatrix} 1 & -1 \end{bmatrix} \begin{bmatrix} u_l \\ u_r \end{bmatrix} + g_0 \tag{19}$$

as well as for the Signorini problem (3)

$$g = \mathbf{Z}^T \mathbf{u} + g_0 = [1] [u_l] + g_0 \tag{20}$$

where u_l and u_r are the displacements of the contacted nodes in the contact pair.

For the particular case of two bodies in contact, integration of (17) results in the following additional stiffness and mass matrices

$$\hat{\mathbf{K}}_p = H(g) \frac{\beta_s EA}{h_e} \begin{bmatrix} 1 & -1 \\ -1 & 1 \end{bmatrix}, \quad \hat{\mathbf{M}}_p = H(g) \frac{\beta_m \rho h_e A}{2} \begin{bmatrix} 1 & -1 \\ -1 & 1 \end{bmatrix} \tag{21}$$

and for the Signorini problem

$$\hat{\mathbf{K}}_p = H(g) \frac{\beta_s EA}{h_e} [1], \quad \hat{\mathbf{M}}_p = H(g) \beta_m \rho h_e A [1]. \tag{22}$$

Here we have defined dimensionless stiffness and mass penalty parameters for the one-dimensional case as β_m and β_s , as follows

$$\beta_s = \frac{h_e}{EA} \epsilon_s, \quad \beta_m = \frac{2}{\rho h_e A} \epsilon_m \tag{23}$$

and their dimensionless penalty ratio

$$r = \frac{1 + 2\gamma}{6} \frac{\beta_s}{\beta_m}. \tag{24}$$

In the following, the necessary condition for the parameter r will be shown so that the stability limit for several types of mass matrix is not affected.

Remark. The penalized mass matrix $\hat{\mathbf{M}}_p$ is singular and the corresponding total mass included in this mass matrix is zero. This is very a good physical behaviour of $\hat{\mathbf{M}}_p$.

4. Explicit time integration schemes for contact-impact problems

We now consider the time integration of the semi-discretized system (11) respecting the bi-penalty terms (16) in the framework of the central difference method in time [5] as

$$(\mathbf{M}^t + \mathbf{M}_p^t) \frac{\mathbf{u}^{t+\Delta t} - 2\mathbf{u}^t + \mathbf{u}^{t-\Delta t}}{\Delta t^2} + (\mathbf{K}^t + \mathbf{K}_p^t) \mathbf{u}^t + \mathbf{f}_p^t - \mathbf{r}^t = \mathbf{0}. \tag{25}$$

Assuming that displacements are known at times $t - \Delta t$ and t , one can resolve unknown displacements at time $t + \Delta t$, where Δt denotes the time step size. Note, that the matrices \mathbf{M}_p^t and \mathbf{K}_p^t are time-dependent because they are associated with active contact constraints. In the following text, we mention the stability behaviour of the bi-penalized system and explicit time integration of Eq. (25).

4.1. Stability limit of the bi-penalty method

It is known that the standard penalty method [6], where an additional stiffness term corresponding to contact boundary conditions is applied, significantly attacks the stability limit (the critical time step size Δt_{cr}) of the finite element model. Note, the stability limit for explicit time integration by the central difference method [42] is given as $\Delta t_{cr} = 2/\omega_{max}$, where ω_{max} is the maximum eigenfrequency of the discretized model.

For the averaged mass matrix with arbitrary γ , the maximum eigen-frequency of the separated finite element is given as

$$\omega_{max} = \sqrt{\frac{12}{1 + 2\gamma} \frac{c_0}{h_e}}, \tag{26}$$

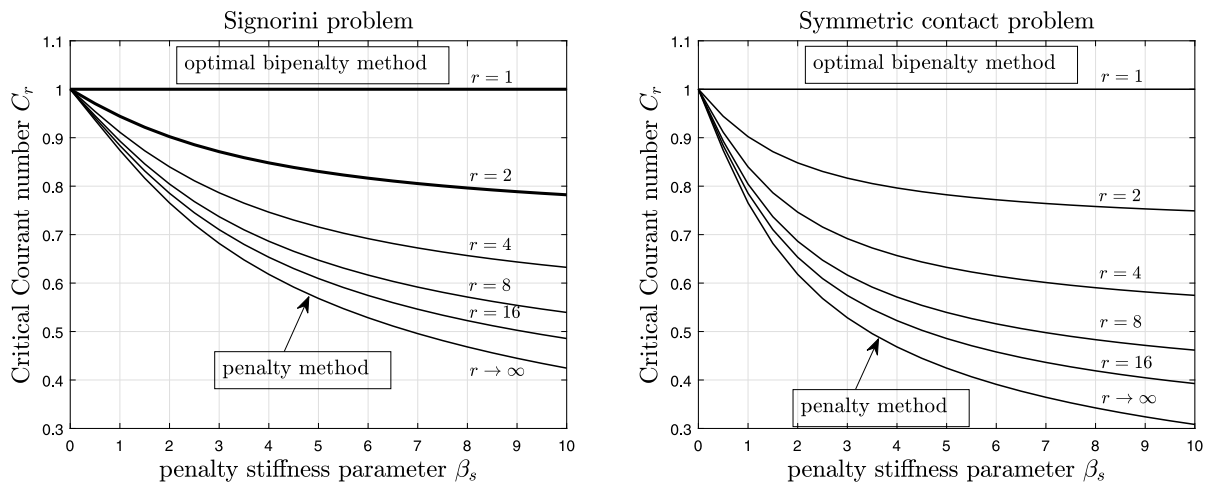


Fig. 3. Stability limits for the bi-penalty method for the bi-penalized Signorini problem (on the left) and the symmetric contact problem (on the right): Dependence of the critical Courant number C_r on the dimensionless stiffness penalty β_s for selected dimensionless penalty ratios r with the lumped mass matrix. For details see work [36].

therefore the stability limit is computed as

$$\Delta t_{cr} = 2/\omega_{max} = \sqrt{\frac{1 + 2\gamma}{3}} \frac{h_e}{c_0}. \tag{27}$$

where $c_0 = \sqrt{E/\rho}$ is the wave speed in a bar and h_e is the length of finite element.

The Courant number, let us define as

$$C = \frac{\Delta t}{\Delta t_{cr}} \tag{28}$$

where Δt is the time step size using in wave propagation simulations and thus $\Delta t = C \Delta t_{cr}$.

Generally, the critical time step size Δt_{cr} rapidly decreases with increasing penalty stiffness [6]. On the other hand, this numerical effect can be eliminated by a particular choice of additional mass penalty term [27]. The stability limit for the bi-penalty method has been studied in work of Kopačka [36], where the optimal ratio of stiffness and mass penalty parameters as $r = 1$ were found for one-dimensional problems with the lumped mass matrix. The general problem with respect to the stability of bi-penalized terms has been studied in the work of Hetherington [26]. The critical time step size Δt_{cr} associated with contact-free bodies are preserved for this optimal setting of mass penalty parameter with respect to the stiffness penalty parameter. Thus stability limit for the contact problem is not attacked by the stiffness penalty term. In principle, one can integrate contact-impact problems by an arbitrary stable time step size $\Delta t < \Delta t_{cr}$. In Fig. 3, one can see the stability graphs for the Signorini and two element contact symmetric problems, where the dimensionless critical Courant number C_r is computed as $C_r = c_0 \Delta t_{cr} / h_e$ for the lumped mass matrix. For details of the stability analysis see work [36], where numerical tests have verified this stability analysis for the central difference method for direct time integration.

4.2. Optimal setting of the penalized mass matrix

From a general point of view, mass and stiffness penalty matrices present the same structure, see Eq. (17), where only the constants ε_m and ε_s are different. This means that there exists a linear relationship between $\hat{\mathbf{M}}_p$ and $\hat{\mathbf{K}}_p$. Let us then analyse the frequency content of the mass penalty matrix expressed in the form

$$\hat{\mathbf{M}}_p = \alpha \hat{\mathbf{K}}_p \tag{29}$$

where α is a free parameter [$1/s^2$]. Now, Let us find an “optimal” value of the parameter α , see [26] so that the maximum eigen-frequency of the penalized dynamic system ω_{max} defined as

$$[-\omega_{max}^2 (\mathbf{M} + \mathbf{M}_p) + (\mathbf{K} + \mathbf{K}_p)] \Phi_{max} = \mathbf{0} \tag{30}$$

has the same maximum eigen-frequency ω_{max} and corresponding mode shape Φ_{max} as the contact-free dynamic system expressed as

$$[-\omega_{max}^2 \mathbf{M} + \mathbf{K}] \Phi_{max} = \mathbf{0}. \tag{31}$$

We assume that ω_{max} is nonzero and the previous relationships need to satisfy the following relationship

$$\hat{\mathbf{M}}_p = \frac{1}{\omega_{max}^2} \hat{\mathbf{K}}_p \tag{32}$$

thus $\alpha = 1/\omega_{max}^2$, which is in an agreement with [26]. This is a very simple formula that can be used for the evaluation of the mass penalized matrix with arbitrary stiffness penalty parameters. Based on comparison of (21), (24), (26) and (32), the optimal setting of dimensionless penalty ratio is found to be $r = 1$.

It is needed to mention that ω_{max} is the maximum eigen-frequency of the finite element mesh in contact and it will be computed from

$$(-\omega^2 \hat{\mathbf{M}} + \hat{\mathbf{K}}) \hat{\Phi} = \mathbf{0} \tag{33}$$

and ω_{max} for the 1D case studied in this paper is given by (26). It means that there is a strong coupling of the dynamic behaviour of finite elements in contact constraints and dynamic behaviour of the bi-penalty terms corresponding to contact constraints. The coupling of dynamics of contacted bodies and bi-penalty contact terms is through the maximum eigen-frequency ω_{max} of the finite elements in the contact constraints. The condition shown in (32) is a sufficient condition for the keeping of the same stability limit of a contact-free problem and bi-penalized contact problem. For that reason, one can estimate the stable time step size of contact-impact problems without a knowledge of contact constraints of bodies where the condition for penalized matrices (32) is valid. This evaluation of penalized stiffness and mass matrices for the bi-penalty method is given on elemental level, and the global matrices are assembled in a standard finite element process. In real computations, one can use the setting of the mass penalty matrix $\hat{\mathbf{M}}_p = \Delta t^2 \hat{\mathbf{K}}_p$, where Δt is the time step size during the explicit time stepping.

4.3. Central difference scheme for contact-impact problems

In this paper, we use the following form of the central difference (CD) scheme for explicit direct time integration of elastodynamic problems with contact constraints based on the bi-penalty method with the flowchart [5] as:

- Given $\mathbf{u}^t, \dot{\mathbf{u}}^{t-\Delta t/2}$ satisfying Dirichlet boundary conditions, and computed external force \mathbf{r}^t
- Contact search for given \mathbf{u}^t , compute gap vector \mathbf{g} and contact forces $\mathbf{f}_p^t = -\mathbf{K}_p^t \mathbf{u}^t - \mathbf{f}_p^0$
- Compute accelerations $\ddot{\mathbf{u}}^t = (\mathbf{M}^t + \mathbf{M}_p^t)^{-1}(\mathbf{r}^t - \mathbf{K}^t \mathbf{u}^t + \mathbf{f}_p^t)$
- Mid-point velocities $\dot{\mathbf{u}}^{t+\Delta t/2} = \dot{\mathbf{u}}^{t-\Delta t/2} + \Delta t \ddot{\mathbf{u}}^t$
- New displacements $\mathbf{u}^{t+\Delta t} = \mathbf{u}^t + \Delta t \dot{\mathbf{u}}^{t+\Delta t/2}$
- $t \rightarrow t + \Delta t$

Here, we used the lumped version of the mass matrix \mathbf{M} by the row-summing. In general, the bi-penalized mass matrix \mathbf{M}_p^t is a symmetrical block diagonal matrix with terms corresponding to nodes in contacts, thus the inversion of total mass $(\mathbf{M}^t + \mathbf{M}_p^t)^{-1}$ is a trivial numerical issue. For an efficient implementation of this approach, the partitioned analysis of the contact-impact problems via the localized Lagrangian multipliers [21] can be adopted.

4.4. Stabilized explicit predictor–corrector scheme for contact-impact problems

In the works [50,51], characteristics of the fully explicit time integration scheme with a stabilized technique for contact-impact problems were analysed. For the predictor–corrector time scheme [28], it is needed to split the accelerations corresponding to the external/internal forces and accelerations corresponding to the contact forces as mentioned in [49]. After that, the time integration of each acceleration field is integrated in time separately. In essence, it is a predictor–corrector form for accelerations of corresponding external/internal forces and contact forces as, see [49],

$$\ddot{\mathbf{u}} = \ddot{\mathbf{u}}_{pred (bulk)} + \ddot{\mathbf{u}}_{corr (contact)} \tag{34}$$

where the predictor acceleration vector $\ddot{\mathbf{u}}_{pred}$ corresponds to external/internal forces $(\mathbf{r}^t - \mathbf{K}\mathbf{u}^t)$ and the corrector acceleration vector $\ddot{\mathbf{u}}_{corr}$ corresponds to the contact forces \mathbf{r}_c^t .

The mentioned time integration scheme takes the following flowchart with splitting of bulk (contact-free problem) $\ddot{\mathbf{u}}_{pred}$ and contact accelerations $\ddot{\mathbf{u}}_{corr}^t$:

- Given $\mathbf{u}^t, \dot{\mathbf{u}}^{t-\Delta t/2}, \mathbf{r}^t$
- Compute accelerations of predictor phase $\ddot{\mathbf{u}}_{pred}^t = \mathbf{M}^{-1}(\mathbf{r}^t - \mathbf{K}\mathbf{u}^t)$
- Mid-point velocities of predictor phase $\dot{\mathbf{u}}_{pred}^{t+\Delta t/2} = \dot{\mathbf{u}}^{t-\Delta t/2} + \Delta t \ddot{\mathbf{u}}_{pred}^t$
- Displacements of predictor phase $\mathbf{u}_{pred}^{t+\Delta t} = \mathbf{u}^t + \Delta t \dot{\mathbf{u}}_{pred}^{t+\Delta t/2}$
- Contact search for given $\mathbf{u}_{pred}^{t+\Delta t}$, compute gap vector \mathbf{g} and contact forces $\mathbf{f}_{p\ pred} = -\mathbf{K}_p \mathbf{u}_{pred}^{t+\Delta t} - \mathbf{f}_p^0$
- Compute accelerations of corrector phase $\ddot{\mathbf{u}}_{corr}^t = (\mathbf{M} + \mathbf{M}_p)^{-1}(\mathbf{f}_{p\ pred})$
- Compute total accelerations $\ddot{\mathbf{u}}^t = \ddot{\mathbf{u}}_{pred}^t + \ddot{\mathbf{u}}_{corr}^t$
- Mid-point velocities of corrector phase $\dot{\mathbf{u}}_{pred}^{t+\Delta t/2} = \dot{\mathbf{u}}_{pred}^{t+\Delta t/2} + \Delta t \ddot{\mathbf{u}}_{corr}^t$
- New displacements of corrector phase $\mathbf{u}^{t+\Delta t} = \mathbf{u}^t + \Delta t \dot{\mathbf{u}}_{pred}^{t+\Delta t/2}$
- Contact search for given $\mathbf{u}^{t+\Delta t}$, compute gap vector \mathbf{g} and contact forces $\mathbf{f}_p^{t+\Delta t} = -\mathbf{K}_p \mathbf{u}^{t+\Delta t} - \mathbf{M}_p \ddot{\mathbf{u}}^{t+\Delta t} - \mathbf{f}_p^0$
- $t \rightarrow t + \Delta t$

In this two-time step scheme, bulk accelerations in the predictor phase $\ddot{\mathbf{u}}_{pred}^t$ are computed due to internal and external forces as a contact-free problem. It is calculated with the standard mass matrix \mathbf{M} . After updating of velocities and displacements, contact constraints are analysed and contact forces $\mathbf{f}_{p\ pred}$ are evaluated. For these contact forces, contact accelerations in the corrector phase $\ddot{\mathbf{u}}_{corr}^t$ are computed with the additional penalized mass matrix together with the mass matrix $(\mathbf{M} + \mathbf{M}_p)$ which needs inversion of this total mass matrix. After, the velocities and displacements are updated concerning these corrected accelerations taking into account contact constraints. Finally, the contact forces are evaluated in the consistent way, see the Asano’s paper [3].

Remark. In the corrector phase, the contact nodal forces $\mathbf{f}_{p\ pred}$ correspond to the nodes in the contact; thus, the force vector is sparse. For that reason, the mass matrix $\mathbf{M} + \mathbf{M}_p$ can be evaluated only for nodes in the contact and inverse of the total mass matrix $(\mathbf{M} + \mathbf{M}_p)^{-1}$ can be computed easily, because the matrix is blocked diagonal and the dimension of this matrix is small.

Remark. It can also be used a diagonalized version of the penalized mass matrix \mathbf{M}_p composed as a row-summing of absolute values and the inversion of $(\mathbf{M} + \mathbf{M}_p)^{-1}$ becomes a trivial operation. In this case, the extra penalty masses are added only into the contact interfaces and the total mass is not preserved like in the consistent definition of the penalty mass matrix given by the definition (17).

It is well known that the central difference method in time and linear finite element in space with the lumped mass matrix is a good choice of temporal–spatial discretization due to dispersion behaviour [33]. If one uses the time step size as a stability limit for regular mesh, the dispersion errors are eliminated and we are able to obtain an exact solution of elastic wave propagation in the bar. On the other hand, when we integrate using a time step size smaller than the stability limit, we obtain the stress distribution with stress spurious oscillations which are an outcome of the temporal–spatial discretizations.

4.5. Stabilized Park time integration scheme for contact-impact problems

For the correct solution of the impact contact problem, it is also needed to eliminate the stress spurious oscillations. An example of the time scheme, which is to be able to mitigate these numerical errors, is the Park time scheme [44]. This scheme is based on front-shock and pullback integration, where the wave speed is preserved and the numerical dispersion errors can be eliminated [35]. The time scheme has been presented in the work of Park [44] for the 1D case, and for multi-dimensional cases for separate integration of longitudinal and shear waves see [10,11,33]. Next, we plan to extend the Park time integration scheme to contact-impact problems in predictor–corrector explicit time sense for elimination stress wave propagation inside the elastic bars and contact forces at the same time.

The algorithm adopted for linear wave propagation problems uses the following steps:

- Given $\mathbf{u}^t, \dot{\mathbf{u}}^t, \ddot{\mathbf{u}}^t, \mathbf{r}^t$
- Front-shock displacement $\mathbf{u}_{fs}^{t+\Delta t_c} = \mathbf{u}^t + \Delta t_c \dot{\mathbf{u}}^t + \frac{\Delta t_c^2}{2} \ddot{\mathbf{u}}^t$ for given Δt_c
- Front-shock acceleration $\ddot{\mathbf{u}}_{fs}^{t+\Delta t_c} = \mathbf{M}^{-1}[\mathbf{r}^{t+\Delta t_c} - \mathbf{K}\mathbf{u}_{fs}^{t+\Delta t_c}]$
- Pullback interpolation $\mathbf{u}_{fs}^{t+\Delta t} = \mathbf{u}^t + \Delta t \dot{\mathbf{u}}^t + \Delta t_c^2 \beta_1(\alpha) \ddot{\mathbf{u}}^t + \Delta t_c^2 \beta_2(\alpha) \ddot{\mathbf{u}}_{fs}^{t+\Delta t_c}$ with $\alpha = \frac{\Delta t}{\Delta t_c}$, $\beta_1(\alpha) = \frac{1}{6}\alpha(1 + 3\alpha - \alpha^2)$, $\beta_2(\alpha) = \frac{1}{6}\alpha(\alpha^2 - 1)$
- Pushforward displacement $\mathbf{u}_{cd}^{t+\Delta t} = \mathbf{u}^t + \Delta t \dot{\mathbf{u}}^t + \frac{\Delta t^2}{2} \ddot{\mathbf{u}}^t$
- Averaged displacement as predictor phase $\mathbf{u}_{pred}^{t+\Delta t} = \theta \mathbf{u}_{fs}^{t+\Delta t} + (1 - \theta) \mathbf{u}_{cd}^{t+\Delta t}$ for given θ
- Acceleration for predictor phase $\ddot{\mathbf{u}}_{pred}^{t+\Delta t} = \mathbf{M}^{-1}[\mathbf{r}^{t+\Delta t} - \mathbf{K}\mathbf{u}_{pred}^{t+\Delta t}]$
- Velocity for predictor phase $\dot{\mathbf{u}}_{pred}^{t+\Delta t} = \dot{\mathbf{u}}^t + \frac{\Delta t}{2} (\ddot{\mathbf{u}}^t + \ddot{\mathbf{u}}_{pred}^{t+\Delta t})$
- Contact search for given $\mathbf{u}_{pred}^{t+\Delta t}$, compute gap vector \mathbf{g} and contact forces $\mathbf{f}_{p\ pred} = -\mathbf{K}_p \mathbf{u}_{pred}^{t+\Delta t} - \mathbf{f}_p^0$
- Compute accelerations of corrector phase $\ddot{\mathbf{u}}_{corr}^{t+\Delta t} = (\mathbf{M} + \mathbf{M}_p)^{-1}(\mathbf{f}_{p\ pred})$
- Compute total accelerations $\ddot{\mathbf{u}}^{t+\Delta t} = \ddot{\mathbf{u}}_{pred}^{t+\Delta t} + \ddot{\mathbf{u}}_{corr}^{t+\Delta t}$
- Compute total velocities $\dot{\mathbf{u}}^{t+\Delta t} = \dot{\mathbf{u}}_{pred}^{t+\Delta t} + \frac{\Delta t}{2} \ddot{\mathbf{u}}_{corr}^{t+\Delta t}$
- Total displacement $\mathbf{u}^{t+\Delta t} = \mathbf{u}_{pred}^{t+\Delta t}$
- Search contact for given $\mathbf{u}^{t+\Delta t}$, compute gap vector \mathbf{g} and contact forces $\mathbf{f}_p^{t+\Delta t} = -\mathbf{K}_p \mathbf{u}^{t+\Delta t} - \mathbf{M}_p \ddot{\mathbf{u}}^{t+\Delta t} - \mathbf{f}_p^0$
- $t \rightarrow t + \Delta t$

The stabilized *Park* time integration scheme can be characterized as the three-time step scheme with two steps for the wave propagation problem without including contact constraints, for details see [44]. The first step uses the critical time step size Δt_{cr} and the second one the complete time step size Δt which is smaller than Δt_{cr} . The last step includes the contact constraints into the response without producing spurious oscillations in the stress distribution along the bars. The scheme produces excellent results with the lumped mass matrix due to temporal-spatial dispersion errors in the numerical model. We choice the time step size as $\Delta t = 0.5\Delta t_{cr}$ and averaged parameter as $\theta = 0.5$ which is based on numerical tests in [44].

5. Numerical tests — impact of elastic bars

In this section, we present two tests for analysis of the behaviour of the suggested approach for finite element modelling of contact-impact problems — the Signorini (impact of a bar on a rigid wall) and Huněk problems (impact of two elastic bars).

5.1. Numerical test I — Signorini problem

In the first example, we study an one-dimensional impact problem of an elastic bar against a rigid wall. This one-dimensional test is well known as the Signorini problem.

5.1.1. Problem definition

A scheme of this test is depicted in Fig. 4. The bar is moving to the right side with the constant velocity $v_{01} = 0.1$ [m/s]. The geometrical, material and numerical parameters were set up as: the length $L = 10$ [m], the Young’s modulus $E = 100$ [Pa], the mass density $\rho = 0.01$ [kg m⁻³], the cross-sectional area $A = 1$ [m²]. The initial contact gap is $g_0 = 0$ [m] and the duration time is $T = 0.3$ [s]. The value of the contact force from the analytical prediction is $F_0 = A\rho c_0 v_0 = -0.1$ [N] for $t = 0 \dots 0.2$ [s] and zero otherwise, see [22], where wave speed in a bar $c_0 = \sqrt{E/\rho} = 100$ [m/s].

5.1.2. Numerical parameters

For numerical verification of the methodology for this test, we set β_s as follows $\beta_s = \{1e0; 1e4; 1e8; 1.e12\}$ and β_m is set with respect to optimal value given by Eq. (24) with $r = 1$ or equivalently via (32). The number of finite linear elements for the bar, $n = 100$, thus the uniform finite element lengths are set up as $h_e = 0.1$ [m].

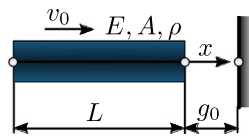


Fig. 4. A scheme of one-dimensional impact problem of an elastic bar against a rigid wall — the Signorini problem.

The time step size is chosen as $\Delta t = C \Delta t_{cr}$, where Courant dimensionless number is used $C = 0.5$. The critical time step size is set with respect to (27) for given γ . This time step size is stable for all value of β_s with optimal setting of β_m . We present results of the contact-impact problem in the form of the time history of kinetic and strain energies and work of contact forces, the time history of dimensionless gap function g/h_e and the time history of contact force. Results for the consistent ($\gamma = 0$), averaged ($\gamma = 0.5$) and lumped ($\gamma = 1$) mass matrices are presented.

5.1.3. Results for CD method

In Fig. 5, one can see the results of the test obtained by the central difference method for the penalty stiffness parameter $\beta_s = 1e0$ and corresponding optimal β_m . All three type of mass matrices were taken into account. The histories of the contact forces show spurious oscillations. The consistent mass matrix produces a higher level of spurious oscillation which is given by spurious oscillations of stress during wave processes in the bar. This effect is not so evident for the lumped mass and averaged mass matrix due to better dispersion behaviour of FEM in wave propagation. The relative gap is $g/h_e = -1e-3$. For $\beta_s = 1e0$ the results are physically correct, where the penalty stiffness has the same of order as the stiffness of finite elements in the contact. One can also see that the contact energy comes to zero for $\beta_s = 1e0$.

In Fig. 6, the results for the CD scheme, $\beta_s = 1e4$ and the lumped mass matrix are presented. The results show a stable solution but the spurious oscillations of gap function and contact forces are observed. Based on numerical observation, there is a *zig-zag* effect in contact constraint where contact is switched-on and switched-off. It is a product of a large value of penalty stiffness parameter. Naturally, one can see this behaviour for a large value of β_s independently of mass matrix type. The stress distributions in the bar for all three types of the mass matrix are depicted in Fig. 7. In contact, the oscillations of stress occur. This behaviour relating to spurious oscillations of contact forces was explained in [9] and it is an outcome of a one-time step scheme. Therefore, we employ in the next text the stabilized predictor–corrector scheme and *Park* schemes, where the integration of bulk and contact accelerations are split.

5.1.4. Results for the stabilized predictor–corrector scheme

In Fig. 8, we present the results obtained by the stabilized predictor–corrector scheme for $\beta_s = 1e4$. One can see the results of time histories of contact forces, gap functions and energy balance. The results are shown for all three mass matrix types. One can see superior results for the lumped mass matrix. Based on several tests for different values of $\beta_s = \{1e0, 1e4, 1e8, 1e12\}$, the results are not influenced of the choice of the stiffness penalty parameter β_s with condition of the optimal setting of β_m . The same results can be detected for the averaged mass matrix. On the other hand, the consistent mass matrix produces the spurious oscillations at the end of the time history of active contact force which is an outcome of spurious oscillations of stresses along the bar as a product of dispersion behaviour of FEM. This effect is depicted in Fig. 9 as stress distribution along the bar for all three types of the mass matrix. It is needed to mention that the stress oscillations on the contacted side were eliminated by using the stabilized predictor–corrector time scheme. We can speak about the stabilization effect of this time scheme on the stress and contact force results. The corresponding of the dimensionless gap values with respect to the β_s are $g/h_e = \{-1e-4, 1e-7, 1e-10, 1e-15\}$ for all three mass matrix types. The convergence properties of this predictor–corrector time scheme with the bi-penalty method are observed.

5.1.5. Results for Park method

The *Park* non-spurious time scheme with connection with the linear finite element and lumped mass matrix has been analysed as a suitable approach for eliminating of stress spurious oscillations [44]. Therefore, we adopted this scheme in the predictor–corrector form for contact-impact problems. We have to mention that this scheme

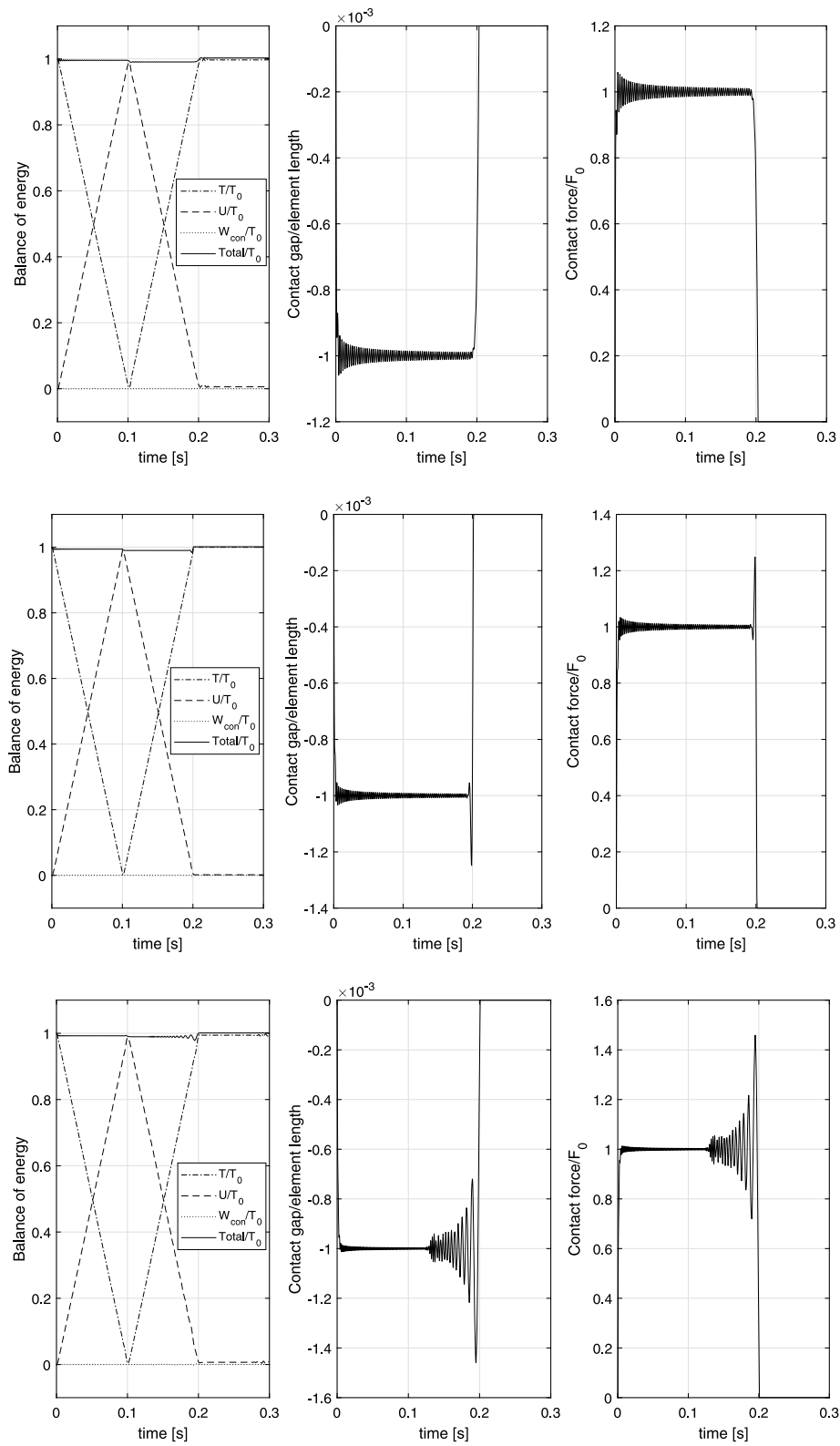


Fig. 5. Results of the Signorini problem obtained by the central difference method with $C = 0.5$, $\beta_s = 1e0$, optimal setting of β_m , for lumped (above), averaged (middle) and consistent (below) mass matrix: Balance of energy in time (on the left), the time history of gap function (in the middle), the time history of contact force (on the right).

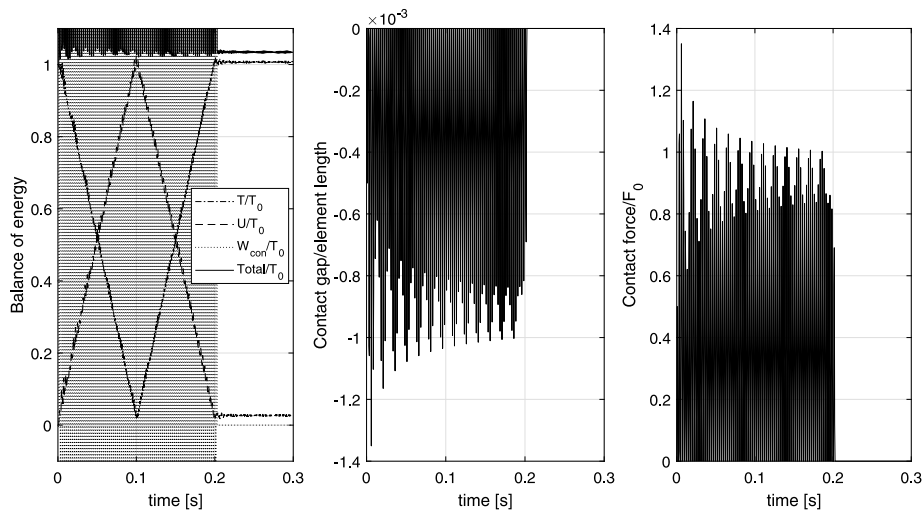


Fig. 6. Results of the Signorini problem obtained by the central difference method with $C = 0.5$, $\beta_s = 1e4$, optimal setting of β_m , for lumped mass matrix: Balance of energy in time (on the left), the time history of gap function (in the middle), the time history of contact force (on the right).

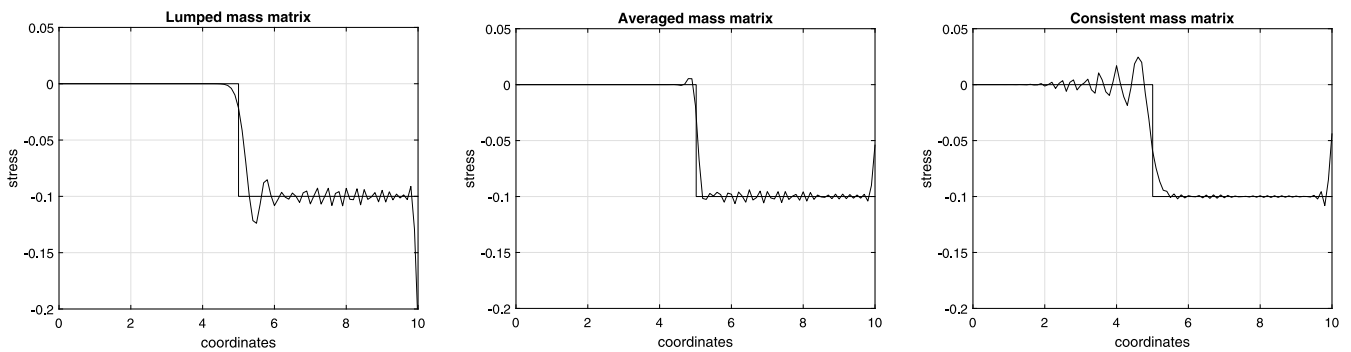


Fig. 7. Stress distributions at the time $t = 0.5$ [s] as results of the Signorini problem obtained by the central difference method with $C = 0.5$, $\beta_s = 1e4$, optimal setting of β_m , lumped (left), averaged (middle) and consistent (right) mass matrices. The analytical solution of wave propagation is attached.

produces superior results of stress distributions for the lumped mass matrix and we apply only this mass matrix for the computations in this part.

In Fig. 10, the results of the Park scheme with stabilization for contact-impact problems are presented for $\beta_s = 1e4$ with the optimal setting of β_m . The computation gives excellent results for a time history of contact forces. But only the oscillations can be seen at the initial time of contact activation. The same results are found for the different values of β_s and we could say that the results do not depend on β_s . In Fig. 11, the stress distribution along the bar is shown. One can see the distribution without dominant spurious oscillations inside the bar and also no spurious oscillations at the contact area. Based on that results, the Park scheme with predictor–corrector explicit time scheme can eliminate spurious oscillation effects of both, stress waves propagating along the bar, and contact forces.

5.2. Numerical test II — Impact of two bars with different lengths (Huněk problem)

In the second example, we study an one-dimensional contact-impact problem of two elastic bars with different lengths prescribed in the work of Huněk [30].

5.2.1. Problem definition

A scheme of this test is depicted in Fig. 12. The left bar is moving to the right with the constant velocity $v_{01} = 0.1$ [m/s]. The right bar with fixed right-hand side is at the rest. The geometrical, material and numerical

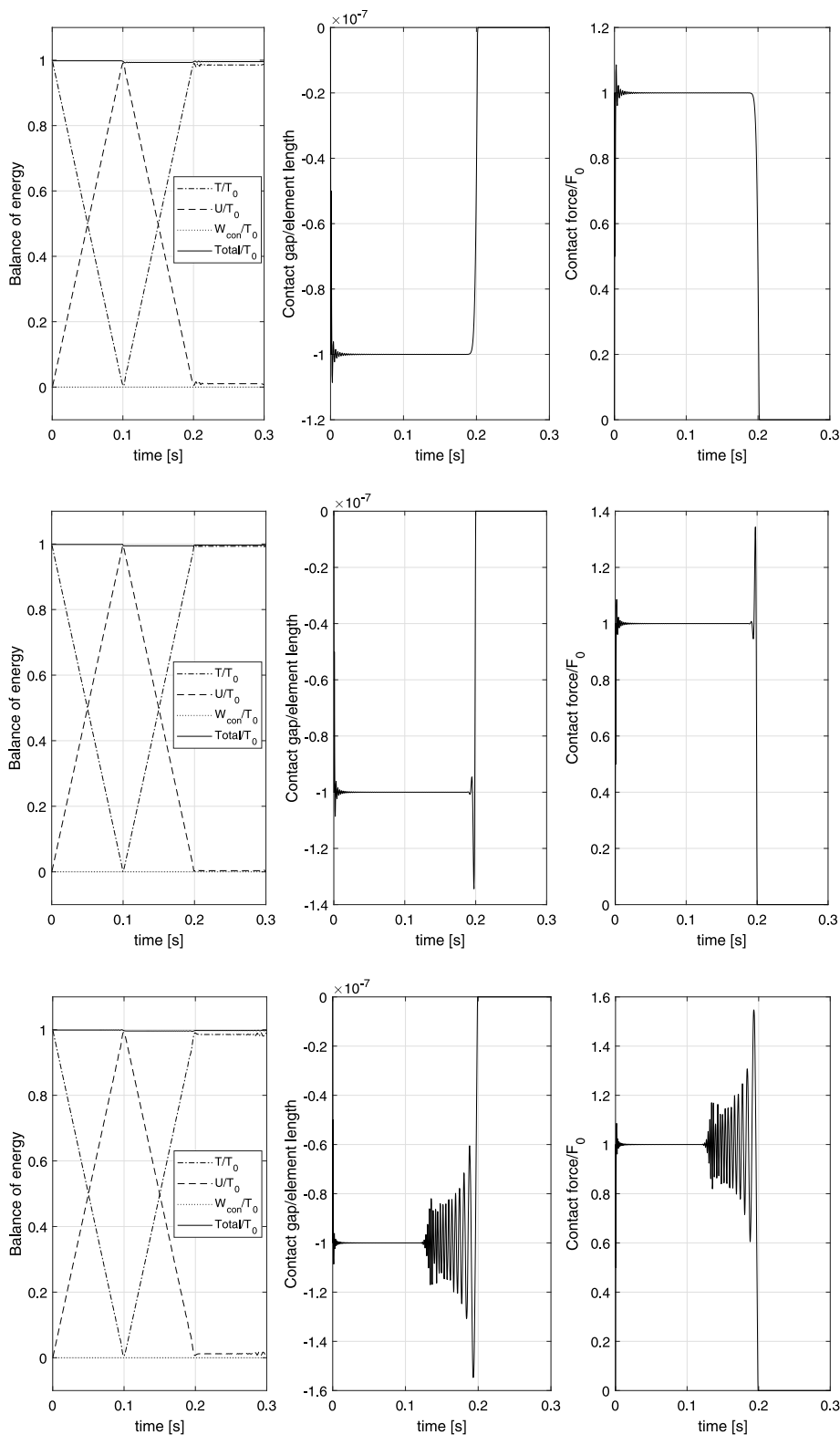


Fig. 8. Results of the Signorini problem obtained by the stabilized predictor–corrector method with $C = 0.5$, $\beta_s = 1e4$, optimal setting of β_m , for lumped (above), averaged (middle) and consistent (below) mass matrix: Balance of energy in time (on the left), the time history of gap function (in the middle), the time history of contact force (on the right).

parameters were set up: the lengths $L_1 = 10$ [m] and $L_2 = 20$ [m], the Young’s modulus $E_1 = E_2 = 100$ [Pa], the mass density $\rho_1 = \rho_2 = 0.01$ [kg m⁻³], the cross-sectional area $A_1 = A_2 = 1$ [m²], the number of finite linear

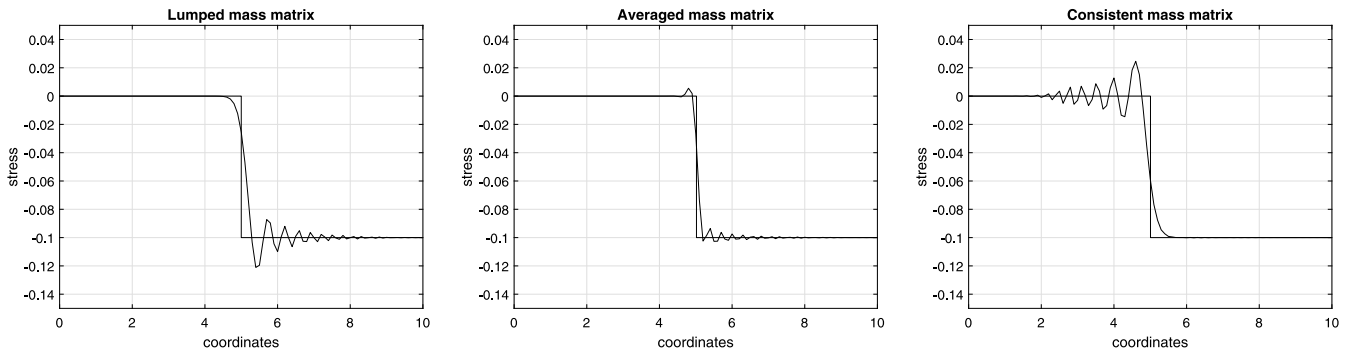


Fig. 9. Stress distributions at the time $t = 0.5$ [s] as results of the Signorini problem obtained by the stabilized predictor–corrector scheme with $C = 0.5$, $\beta_s = 1e4$, optimal setting of β_m , lumped (left), averaged (middle) and consistent (right) mass matrices. The analytical solution of wave propagation is attached.

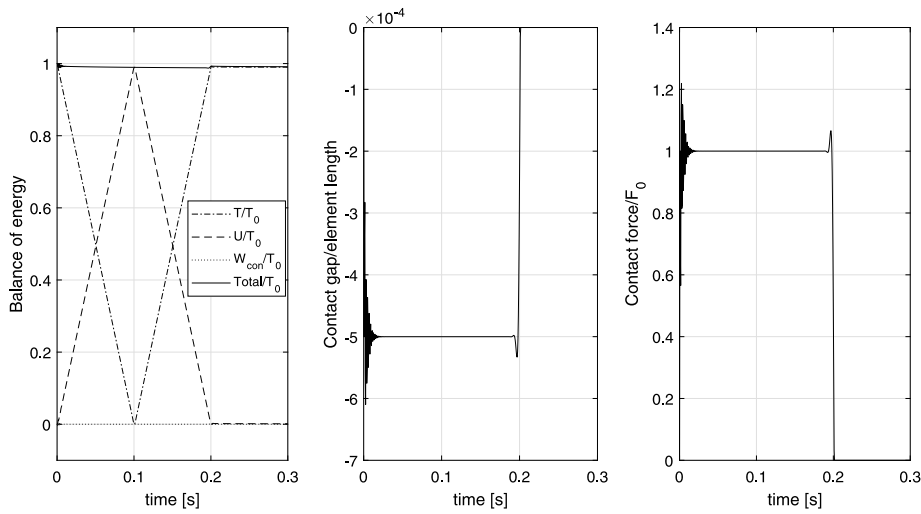


Fig. 10. Results of the Signorini problem obtained by the stabilized Park method with $C = 0.5$, $\beta_s = 1e4$, optimal setting of β_m , for lumped mass matrix.

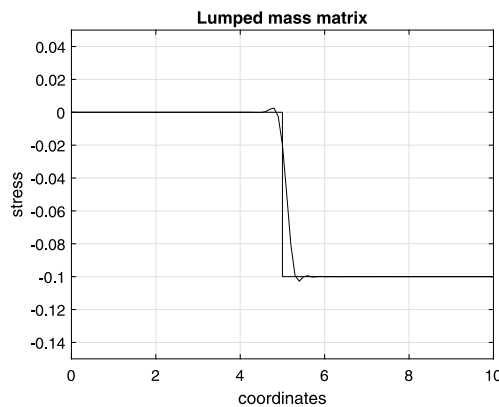


Fig. 11. Stress distribution at the time $t = 0.5$ [s] as results of the Signorini problem obtained by the stabilized Park method with $C = 0.5$, $\beta_s = 1e4$, optimal setting of β_m , lumped mass matrix.

elements for each bar $n_1 = 50$, $n_2 = 100$, thus the finite element lengths are set up as $h_1 = h_2 = 0.2$ [m], the initial contact gap $g_0 = 0$ [m], the duration time $T = 0.7$ [s]. The value of the contact force from the analytical prediction is $F_0 = 0.05$ [N] for $t = 0 \dots 0.2$ [s] and $t = 0.4 \dots 0.6$ [s] and zero otherwise, see [22].

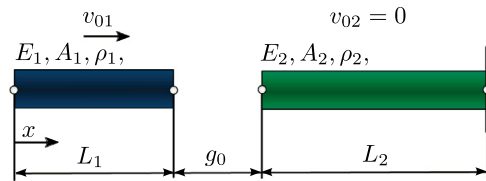


Fig. 12. A scheme of an one-dimensional impact of two bars with different lengths.

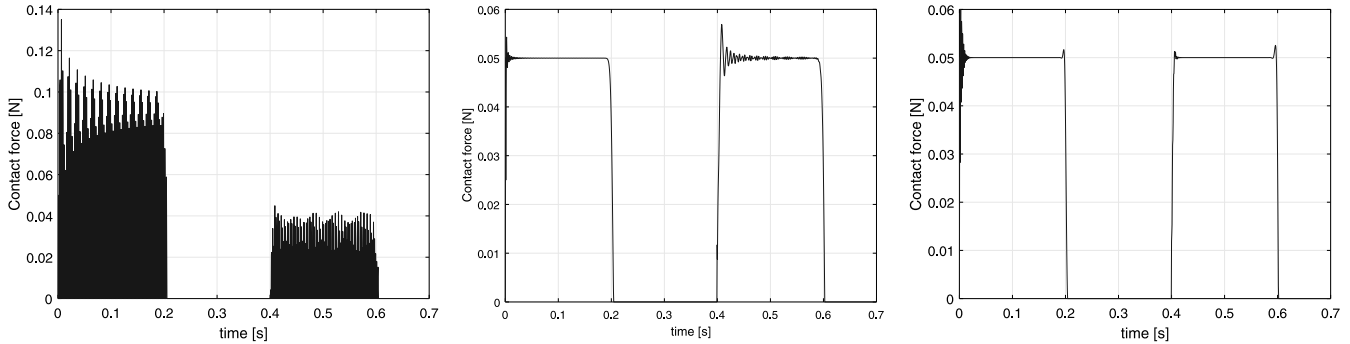


Fig. 13. Time history of contact force for impact of two bars with different lengths — CD (left), the stabilized predictor–corrector scheme (middle) and Park (right) method with Courant number $C = 0.5$, $\beta_s = 1e4$, optimal β_m , lumped mass matrix.

5.2.2. Numerical parameters

In this test, we use the same definition of dimensionless stiffness and mass penalty parameters for the bi-penalty method as in the previous case with $r = 1$. The mass matrix is of the lumped type. The dimensionless stiffness penalty parameter was as follows: $\beta_s = \{1e0; 1e4; 1e8; 1e12\}$. The time step size was also the same as in the previous test.

5.2.3. Results

In Fig. 13, one can see the time histories of contact forces between two elastic bars from Fig. 12 computed by the central difference method, the stabilized explicit predictor–corrector scheme and the Park scheme with stabilization of contact forces. The value of $\beta_s = 1e4$ was chosen, β_m was set with respect to the optimal stability limit as $r = 1$. For the CD method, the spurious oscillations occur as in the Signorini problems. Against, the solutions for the stabilized explicit predictor–corrector scheme and Park schemes. The stabilized predictor–corrector scheme gives the history of contact forces with the low level of spurious oscillations, which is an outcome of the stress spurious oscillation inside the bar. The Park scheme gives the more correct history of contact forces due to the elimination of stress spurious oscillations. One can observe the same character of the time history of contact forces for all three time-schemes for different values of β_s .

6. Conclusions

A numerical approach for one-dimensional contact-impact problems modelled by the finite element method has been presented. The approach is based on the combination of the bi-penalty stabilization method with time integration in a predictor–corrector form. Thanks to the bi-penalty method, we can retain the stability limit of contact-free problems. We also have found evidence of the optimal setting of the ratio of mass and stiffness penalty parameters for the bi-penalty term, that it depends on the maximum eigen-frequency of the finite element meshes in contact. In time-stepping, a modification of the explicit method with the splitting of bulk and contact accelerations has been used. In this case, we compare the results of the central difference method, its stabilized predictor–corrector version and the Park scheme with predictor–corrector parts. Based on the results on numerical tests, one can see that the bi-penalty stabilization works, and the predictor–corrector form of the time stepping is needed for elimination of contact force oscillations.

Furthermore, we have proposed a method to eliminate spurious oscillations of contact forces in the impact of elastic bars. The Park scheme gives us more accurate solutions concerning stress spurious oscillations and contact

forces, and it is preferred in the numerical modelling of contact-impact problems concerning contact forces and stress propagation.

Based on the numerical tests, we can conclude that a motivated approach is an efficient tool for accurate modelling of contact-impact problems with minimum pollution of contact force by spurious oscillations. The results obtained by the stabilized explicit schemes in the connection with the bi-penalty method are *less sensitive* to the choice of the penalty parameter in contrast to the standard penalty approach. The gap function during the contact state converges correctly to zero for higher values of the penalty stiffness parameter. This issue needs a mathematical proof as in future work.

As the future work, we will focus on applications of the presented approach to multidimensional problems, analysing its performance, stability and accuracy with more complicated geometries and higher-order spatial discretization [34]. Also, the partitioned formulation of the presented approach connected with the direct inversion of mass matrix with the mass scaling [19,20] is a promising tool for numerical modelling of contact-impact problems in solids mechanics. An important remaining challenge is the solution of contact-impact problems of heterogeneous bodies with different compliances and different mesh sizes, where the stability limits for each contacted bodies are different.

Acknowledgements

The work of Radek Kolman and Ján Kopačka were supported by the grant projects with No. GA19-02288J of the Czech Science Foundation (CSF) within institutional support RVO:61388998 and the Centre of Excellence for Nonlinear Dynamic Behaviour of Advanced Materials in Engineering, Czech Republic CZ.02.1.01/0.0/0.0/15_003/0000493 (Excellent Research Teams) in the framework of Operational Programme Research, Development and Education. K.C. Park was partially supported by the contract (#G06200018) from the Korean Atomic Energy Research Institute to KAIST, Republic of Korea.

References

- [1] F. Armero, E. Petőcz, A new dissipative time-stepping algorithm for frictional contact problems: formulation and analysis, *Comput. Methods Appl. Mech. Engrg.* 179 (1) (1999) 151–178, [http://dx.doi.org/10.1016/S0045-7825\(99\)00036-5](http://dx.doi.org/10.1016/S0045-7825(99)00036-5), URL <http://www.sciencedirect.com/science/article/pii/S0045782599000365>.
- [2] F. Armero, E. Petocz, Formulation and analysis of conserving algorithms for frictionless dynamic contact/impact problems, *Comput. Methods Appl. Mech. Engrg.* 158 (3–4) (1998) 269–300, [http://dx.doi.org/10.1016/S0045-7825\(97\)00256-9](http://dx.doi.org/10.1016/S0045-7825(97)00256-9), URL <http://www.sciencedirect.com/science/article/pii/S0045782597002569>.
- [3] N. Asano, A virtual work principle using penalty function method for impact contact problems of two bodies, *Bull. JSME* 29 (249) (1986) 731–736, <http://dx.doi.org/10.1299/jsme1958.29.731>.
- [4] J. Baumgarte, Stabilization of constraints and integrals of motion in dynamical systems, *Comput. Methods Appl. Mech. Engrg.* 1 (1) (1972) 1–16.
- [5] T. Belytschko, W.K. Liu, B. Moran, *Nonlinear Finite Elements for Continua and Structures*, Wiley, Chichester, 2008.
- [6] T. Belytschko, M.O. Neal, Contact-impact by the pinball algorithm with penalty and lagrangian methods, *Internat. J. Numer. Methods Engrg.* 31 (3) (1991) 547–572, <http://dx.doi.org/10.1002/nme.1620310309>.
- [7] D.J. Benson, Computational methods in lagrangian and eulerian hydrocodes, *Comput. Methods Appl. Mech. Engrg.* 99 (2) (1992) 235–394, [http://dx.doi.org/10.1016/0045-7825\(92\)90042-I](http://dx.doi.org/10.1016/0045-7825(92)90042-I), URL <http://www.sciencedirect.com/science/article/pii/004578259290042I>.
- [8] D.J. Benson, J.O. Hallquist, A single surface contact algorithm for the post-buckling analysis of shell structures, *Comput. Methods Appl. Mech. Engrg.* 78 (2) (1990) 141–163, [http://dx.doi.org/10.1016/0045-7825\(90\)90098-7](http://dx.doi.org/10.1016/0045-7825(90)90098-7), URL <http://www.sciencedirect.com/science/article/pii/0045782590900987>.
- [9] N.J. Carpenter, R.L. Taylor, M.G. Katona, Lagrange constraints for transient finite element surface contact, *Internat. J. Numer. Methods Engrg.* 32 (1) (1991) 103–128, <http://dx.doi.org/10.1002/nme.1620320107>.
- [10] S.S. Cho, R. Kolman, J.A. González, K.C. Park, Explicit multistep time integration for discontinuous elastic stress wave propagation in heterogeneous solids, *Internat. J. Numer. Methods Engrg.* 118 (5) (2019) 276–302, <http://dx.doi.org/10.1002/nme.6027>, arXiv:<https://onlinelibrary.wiley.com/doi/pdf/10.1002/nme.6027>, URL <https://onlinelibrary.wiley.com/doi/abs/10.1002/nme.6027>.
- [11] S.S. Cho, K.C. Park, H. Huh, A method for multidimensional wave propagation analysis via component-wise partition of longitudinal and shear waves, *Internat. J. Numer. Methods Engrg.* 95 (3) (2013) 212–237, <http://dx.doi.org/10.1002/nme.4495>, arXiv:<https://onlinelibrary.wiley.com/doi/pdf/10.1002/nme.4495>, URL <https://onlinelibrary.wiley.com/doi/abs/10.1002/nme.4495>.
- [12] F. Cirak, M. West, Decomposition contact response (dcr) for explicit finite element dynamics, *Internat. J. Numer. Methods Engrg.* 64 (8) (2005) 1078–1110, <http://dx.doi.org/10.1002/nme.1400>, arXiv:<https://onlinelibrary.wiley.com/doi/pdf/10.1002/nme.1400>, URL <https://onlinelibrary.wiley.com/doi/abs/10.1002/nme.1400>.
- [13] H.M. de la Fuente, C.A. Felippa, Ephemeral penalty functions for contact-impact dynamics, *Finite Elem. Anal. Des.* 9 (3) (1991) 177–191, [http://dx.doi.org/10.1016/0168-874X\(91\)90031-S](http://dx.doi.org/10.1016/0168-874X(91)90031-S), URL <http://www.sciencedirect.com/science/article/pii/0168874X9190031S>.

- [14] P. Deuffhard, R. Krause, S. Ertel, A contact-stabilized newmark method for dynamical contact problems, *Internat. J. Numer. Methods Engrg.* 73 (9) (2008) 1274–1290, <http://dx.doi.org/10.1002/nme.2119>.
- [15] Z. Dostál, T. Kozubek, M. Sadowska, V. Vondrák, *Scalable Algorithms for Contact Problems*, first ed., Springer, 2017.
- [16] D. Doyen, A. Ern, S. Piperno, Time-integration schemes for the finite element dynamic signorini problem, *SIAM J. Sci. Comput.* 33 (1) (2011) 223–249, <http://dx.doi.org/10.1137/100791440>, URL <http://epubs.siam.org/doi/abs/10.1137/100791440>.
- [17] C.A. Felippa, Error analysis of penalty function techniques for constraint definition in linear algebraic systems, *Internat. J. Numer. Methods Engrg.* 11 (4) (1977) 709–728, <http://dx.doi.org/10.1002/nme.1620110408>, arXiv:<https://onlinelibrary.wiley.com/doi/pdf/10.1002/nme.1620110408>, URL <https://onlinelibrary.wiley.com/doi/abs/10.1002/nme.1620110408>.
- [18] C.A. Felippa, Iterative procedures for improving penalty function solutions of algebraic systems, *Internat. J. Numer. Methods Engrg.* 12 (5) (1978) 821–836, <http://dx.doi.org/10.1002/nme.1620120508>, arXiv:<https://onlinelibrary.wiley.com/doi/pdf/10.1002/nme.1620120508>, URL <https://onlinelibrary.wiley.com/doi/abs/10.1002/nme.1620120508>.
- [19] J.A. González, R. Kolman, S.S. Cho, C.A. Felippa, K.C. Park, Inverse mass matrix via the method of localized lagrange multipliers, *Internat. J. Numer. Methods Engrg.* 113 (2) (2018) 277–295, <http://dx.doi.org/10.1002/nme.5613>, arXiv:<https://onlinelibrary.wiley.com/doi/pdf/10.1002/nme.5613>, URL <https://onlinelibrary.wiley.com/doi/abs/10.1002/nme.5613>.
- [20] J.A. González, J. Kopačka, R. Kolman, S.S. Cho, K.C. Park, Inverse mass matrix for isogeometric explicit transient analysis via the method of localized lagrange multipliers, *Internat. J. Numer. Methods Engrg.* 117 (9) (2019) 939–966, <http://dx.doi.org/10.1002/nme.5986>, arXiv:<https://onlinelibrary.wiley.com/doi/pdf/10.1002/nme.5986>, URL <https://onlinelibrary.wiley.com/doi/abs/10.1002/nme.5986>.
- [21] J.A. González, K.C. Park, C.A. Felippa, Partitioned formulation of frictional contact problems using localized lagrange multipliers, *Commun. Numer. Methods. Eng.* 22 (4) (2006) 319–333, <http://dx.doi.org/10.1002/cnm.821>, arXiv:<https://onlinelibrary.wiley.com/doi/pdf/10.1002/cnm.821>, URL <https://onlinelibrary.wiley.com/doi/abs/10.1002/cnm.821>.
- [22] K.F. Graff, *Wave Motion in Elastic Solids*, Clarendon Press, 1975.
- [23] J. Hallquist, G. Goudreau, D. Benson, Sliding interfaces with contact-impact in large-scale lagrangian computations, *Comput. Methods Appl. Mech. Engrg.* 51 (1) (1985) 107–137, [http://dx.doi.org/10.1016/0045-7825\(85\)90030-1](http://dx.doi.org/10.1016/0045-7825(85)90030-1), URL <http://www.sciencedirect.com/science/article/pii/0045782585900301>.
- [24] M.W. Heinstein, F.J. Mello, S.W. Attaway, T.A. Laursen, Contact—impact modeling in explicit transient dynamics, *Comput. Methods Appl. Mech. Engrg.* 187 (3) (2000) 621–640, [http://dx.doi.org/10.1016/S0045-7825\(99\)00342-4](http://dx.doi.org/10.1016/S0045-7825(99)00342-4), URL <http://www.sciencedirect.com/science/article/pii/S0045782599003424>.
- [25] J. Hetherington, H. Askes, Penalty methods for time domain computational dynamics based on positive and negative inertia, *Comput. Struct.* 87 (23–24) (2009) 1474–1482, <http://dx.doi.org/10.1016/j.compstruc.2009.05.011>, URL <http://www.sciencedirect.com/science/article/pii/S0045794909001692>.
- [26] J. Hetherington, A. Rodríguez-Ferran, H. Askes, A new bipenalty formulation for ensuring time step stability in time domain computational dynamics, *Internat. J. Numer. Methods Engrg.* 90 (3) (2012) 269–286, <http://dx.doi.org/10.1002/nme.3314>.
- [27] J. Hetherington, A. Rodríguez-Ferran, H. Askes, The bipenalty method for arbitrary multipoint constraints, *Internat. J. Numer. Methods Engrg.* 93 (5) (2013) 465–482, <http://dx.doi.org/10.1002/nme.4389>.
- [28] T.J.R. Hughes, *The Finite Element Method: Linear Static and Dynamic Finite Element Analysis*, Dover Publications, Mineola, NY, 2000.
- [29] T.J. Hughes, R.L. Taylor, J.L. Sackman, A. Curnier, W. Kanoknukulchai, A finite element method for a class of contact-impact problems, *Comput. Methods Appl. Mech. Engrg.* 8 (3) (1976) 249–276, [http://dx.doi.org/10.1016/0045-7825\(76\)90018-9](http://dx.doi.org/10.1016/0045-7825(76)90018-9), URL <http://www.sciencedirect.com/science/article/pii/0045782576900189>.
- [30] I. Huněk, On a penalty formulation for contact-impact problems, *Comput. Struct.* 48 (2) (1993) 193–203, [http://dx.doi.org/10.1016/0045-7949\(93\)90412-7](http://dx.doi.org/10.1016/0045-7949(93)90412-7), URL <http://www.sciencedirect.com/science/article/pii/0045794993904127>.
- [31] C. Kane, E. Repetto, M. Ortiz, J. Marsden, Finite element analysis of nonsmooth contact, *Comput. Methods Appl. Mech. Engrg.* 180 (1) (1999) 1–26, [http://dx.doi.org/10.1016/S0045-7825\(99\)00034-1](http://dx.doi.org/10.1016/S0045-7825(99)00034-1), URL <http://www.sciencedirect.com/science/article/pii/S0045782599000341>.
- [32] H.B. Khenous, P. Laborde, Y. Renard, Mass redistribution method for finite element contact problems in elastodynamics, *Eur. J. Mech. A Solids* 27 (5) (2008) 918–932, <http://dx.doi.org/10.1016/j.euromechsol.2008.01.001>.
- [33] R. Kolman, S.S. Cho, K.C. Park, Efficient implementation of an explicit partitioned shear and longitudinal wave propagation algorithm, *Internat. J. Numer. Methods Engrg.* 107 (7) (2016) 543–579, <http://dx.doi.org/10.1002/nme.5174>, arXiv:<https://onlinelibrary.wiley.com/doi/pdf/10.1002/nme.5174>, URL <https://onlinelibrary.wiley.com/doi/abs/10.1002/nme.5174>.
- [34] R. Kolman, M. Okrouhlík, A. Berezovski, D. Gabriel, J. Kopačka, J. Plešek, B-spline based finite element method in one-dimensional discontinuous elastic wave propagation, *Appl. Math. Model.* 46 (2017) 382–395, <http://dx.doi.org/10.1016/j.apm.2017.01.077>, URL <http://www.sciencedirect.com/science/article/pii/S0307904X17300835>.
- [35] R. Kolman, J. Plešek, J. Červ, M. Okrouhlík, P. Pařík, Temporal-spatial dispersion and stability analysis of finite element method in explicit elastodynamics, *Internat. J. Numer. Methods Engrg.* 106 (2) (2016) 113–128, <http://dx.doi.org/10.1002/nme.5010>, arXiv:<https://onlinelibrary.wiley.com/doi/pdf/10.1002/nme.5010>, URL <https://onlinelibrary.wiley.com/doi/abs/10.1002/nme.5010>.
- [36] J. Kopačka, A. Tkachuk, D. Gabriel, R. Kolman, M. Bischoff, J. Plešek, On stability and reflection-transmission analysis of the bipenalty method in contact-impact problems: A one-dimensional, homogeneous case study, *Int. J. Numer. Methods Eng.* 113 (10) (2018) 1607–1629, <http://dx.doi.org/10.1002/nme.5712>, arXiv:<https://onlinelibrary.wiley.com/doi/pdf/10.1002/nme.5712>, URL <https://onlinelibrary.wiley.com/doi/abs/10.1002/nme.5712>.
- [37] T.A. Laursen, V. Chawla, Design of energy conserving algorithms for frictionless dynamic contact problems, *Internat. J. Numer. Methods Engrg.* 40 (5) (1997) 863–886, [http://dx.doi.org/10.1002/\(SICI\)1097-0207\(19970315\)40:5<863::AID-NME92>3.0.CO;2-V](http://dx.doi.org/10.1002/(SICI)1097-0207(19970315)40:5<863::AID-NME92>3.0.CO;2-V).

- [38] T.A. Laursen, G.R. Love, Improved implicit integrators for transient impact problems—geometric admissibility within the conserving framework, *Internat. J. Numer. Methods Engrg.* 53 (2) (2002) 245–274, <http://dx.doi.org/10.1002/nme.264>, arXiv:<https://onlinelibrary.wiley.com/doi/pdf/10.1002/nme.264>, URL <https://onlinelibrary.wiley.com/doi/abs/10.1002/nme.264>.
- [39] P. Otto, L. De Lorenzis, J.F. Unger, A regularized model for impact in explicit dynamics applied to the split hopkinson pressure bar, *Comput. Mech.* 58 (4) (2016) 681–695, <http://dx.doi.org/10.1007/s00466-016-1311-1>.
- [40] P. Otto, L. Lorenzis, J.F. Unger, Explicit dynamics in impact simulation using a nurbs contact interface, *Int. J. Numer. Methods Eng.* n/a (n/a). arXiv:<https://onlinelibrary.wiley.com/doi/pdf/10.1002/nme.6264>, <http://dx.doi.org/10.1002/nme.6264>. URL <https://onlinelibrary.wiley.com/doi/abs/10.1002/nme.6264>.
- [41] E.A. Paraskevopoulos, C.G. Panagiotopoulos, G.D. Manolis, Imposition of time-dependent boundary conditions in fem formulations for elastodynamics: critical assessment of penalty-type methods, *Comput. Mech.* 45 (2) (2009) 157, <http://dx.doi.org/10.1007/s00466-009-0428-x>.
- [42] K.C. Park, Practical aspects of numerical time integration, *Comput. Struct.* 7 (3) (1977) 343–353, [http://dx.doi.org/10.1016/0045-7949\(77\)90072-4](http://dx.doi.org/10.1016/0045-7949(77)90072-4), URL <http://www.sciencedirect.com/science/article/pii/0045794977900724>.
- [43] K.C. Park, J.C. Chiou, Stabilization of computational procedures for constrained dynamical systems, *J. Guid. Control Dyn.* 11 (4) (1988) 365–370, <http://dx.doi.org/10.2514/3.20320>.
- [44] K.C. Park, S.J. Lim, H. Huh, A method for computation of discontinuous wave propagation in heterogeneous solids: basic algorithm description and application to one-dimensional problems, *Internat. J. Numer. Methods Engrg.* 91 (6) (2012) 622–643, <http://dx.doi.org/10.1002/nme.4285>, arXiv:<https://onlinelibrary.wiley.com/doi/pdf/10.1002/nme.4285>, URL <https://onlinelibrary.wiley.com/doi/abs/10.1002/nme.4285>.
- [45] Y. Renard, The singular dynamic method for constrained second order hyperbolic equations: Application to dynamic contact problems, *J. Comput. Appl. Math.* 234 (3) (2010) 906–923, <http://dx.doi.org/10.1016/j.cam.2010.01.058>, URL <http://www.sciencedirect.com/science/article/pii/S0377042710000713>.
- [46] R.L. Taylor, P. Papadopoulos, On a finite element method for dynamic contact/impact problems, *Internat. J. Numer. Methods Engrg.* 36 (12) (1993) 2123–2140, <http://dx.doi.org/10.1002/nme.1620361211>, arXiv:<https://onlinelibrary.wiley.com/doi/pdf/10.1002/nme.1620361211>, URL <https://onlinelibrary.wiley.com/doi/abs/10.1002/nme.1620361211>.
- [47] A. Tkachuk, Variational Methods for Consistent Singular and Scaled Mass Matrices (Ph.D. thesis), Institut für Baustatik und Baudynamik der Universität Stuttgart, Stuttgart, 2013.
- [48] B. Wohlmuth, Variationally consistent discretization schemes and numerical algorithms for contact problems, *Acta Numer.* 20 (2011) 569–734, <http://dx.doi.org/10.1017/S0962492911000079>.
- [49] P. Wriggers, *Computational Contact Mechanics*, second ed., Springer, Berlin; New York, 2006, URL <http://www.scribd.com/doc/9326570/Computational-Contact-Mechanics>.
- [50] S.R. Wu, A priori error estimates for explicit finite element for linear elasto-dynamics by galerkin method and central difference method, *Comput. Methods Appl. Mech. Engrg.* 192 (51) (2003) 5329–5353, <http://dx.doi.org/10.1016/j.cma.2003.08.002>, URL <http://www.sciencedirect.com/science/article/pii/S0045782503005152>.
- [51] S.R. Wu, A variational principle for dynamic contact with large deformation, *Comput. Methods Appl. Mech. Engrg.* 198 (21) (2009) 2009–2015, <http://dx.doi.org/10.1016/j.cma.2008.12.013>, advances in Simulation-Based Engineering Sciences – Honoring J. Tinsley Oden. URL <http://www.sciencedirect.com/science/article/pii/S0045782509000139>.



ELSEVIER



Available online at www.sciencedirect.com

ScienceDirect

Mathematics and Computers in Simulation 189 (2021) 163–190



MATHEMATICS
AND
COMPUTERS
IN SIMULATION

www.elsevier.com/locate/matcom

Original articles

Finite element method based computational time reversal in elastodynamics: Refocusing, reconstruction and its numerical sensitivity

M. Mračko^{a,*}, J. Kober^a, R. Kolman^a, Z. Převorovský^a, A. Tkachuk^b, J. Plešek^a

^a Institute of Thermomechanics of the CAS, v. v. i., Dolejškova 1402/5, 182 00 Praha 8, Czech Republic

^b Institute for Structural Mechanics, University of Stuttgart, Pfaffenwaldring 7, 70550 Stuttgart, Germany

Received 26 December 2019; received in revised form 27 August 2020; accepted 1 November 2020

Available online 19 November 2020

Abstract

In this paper, we study the accuracy and robustness of the computational time reversal approach based on the explicit finite element method for application in nondestructive testing in solids. The main goal of this paper is to find a methodology for correct and accurate reconstruction of the original source time history. For numerical modeling of frontal (forward) and reverse (backward) problems of elastic wave propagation, we use the finite element method and explicit time integration with the lumped mass matrix. The suggested methodology is applicable in each finite element open source or commercial software. A special attention is paid to prescription of boundary conditions/loading for the reverse problem for accurate reconstruction of time history of the original source. For evaluation of the reconstruction quality, we suggest certain cost functions. Based on several numerical tests, we show effects of prescription of boundary conditions/loading in time reversal, effect of mesh size and time step size, an unknown obstacle, a number of sources, and environmental disturbance (noise) on the correctness of reconstruction of the original source.

© 2020 International Association for Mathematics and Computers in Simulation (IMACS). Published by Elsevier B.V. All rights reserved.

Keywords: Time reversal; Nondestructive testing; Elastic wave propagation; Localization; Refocusing; Reconstruction; Explicit finite element method

1. Introduction

Correct and robust localization of cracks and defects in bodies and structures in energetics, civil or aerospace engineering is still an up to date topic despite the long history of this research. Moreover, this knowledge and information about cracks are needed for practical applications for safe operation in several branches, as for power plants, aircrafts, vehicles, satellites and many others. In this paper, we study the well-established time reversal (TR) method for localization of cracks and defects in elastic bodies. The TR uses the reversibility property of wave propagation to focus the energy to the original source location in space and time. If the original source is very local, then this procedure is called refocusing.

* Corresponding author.

E-mail addresses: mracko@it.cas.cz (M. Mračko), kober@it.cas.cz (J. Kober), kolman@it.cas.cz (R. Kolman), zp@it.cas.cz (Z. Převorovský), tkachuk@ibb.uni-stuttgart.de (A. Tkachuk), plesek@it.cas.cz (J. Plešek).

<https://doi.org/10.1016/j.matcom.2020.11.004>

0378-4754/© 2020 International Association for Mathematics and Computers in Simulation (IMACS). Published by Elsevier B.V. All rights reserved.

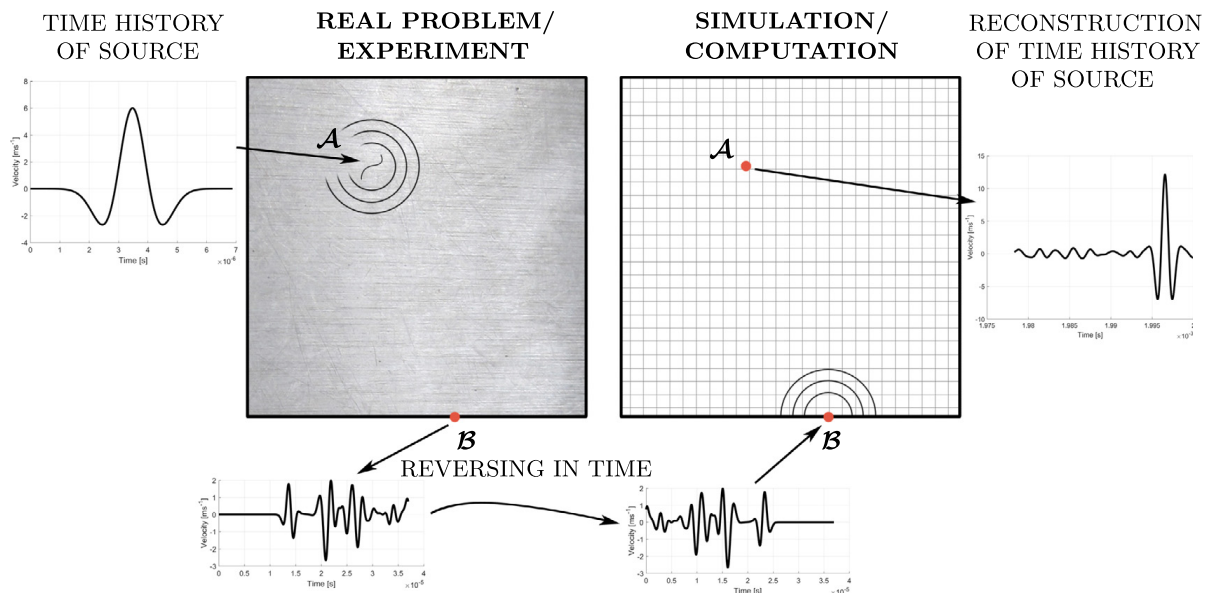


Fig. 1. Application of TR method in NDT.

The TR method is one of the members of the family of inverse methods in physics, based on properties of the Hamiltonian system. TR was first formulated in 1960s with the name “matched signal processing” for underwater acoustic communication of submarines, Parvulescu and Clay [36]. In 1990s, Fink and his collaborators, Fink [15], have done a huge amount of work in their research in application in acoustics and renamed the method to “time reversal (or time reversed acoustics)”. The TR method is a powerful tool applicable in various physical fields involving wave propagation. Nowadays, the most important applications are in nondestructive testing (NDT), underwater acoustics [23,41], biomedical ultrasound imaging [12], surgery and lithotripsy [17,18], or, last but not least, seismology [29].

In ultrasonic NDT, the TR method can be employed for detection of defects in materials and cracks in bodies. Depending on the approach, one can talk about passive and active detection. Generally, with passive detection, the emerging defects are detected (forming/propagating cracks, impacts, leakage in pipe), using for example acoustic emission, see e.g. [38]. With active detection, some “third” exciting signal is used for localization of the present flaw behaving as a scatterer for propagating elastic wave (present crack, cavity). A crack, when exposed to a wave passing through, acts as an additional source of waves and therefore can be localized, Mu et al. [33].

The computational TR method was widely employed, e.g. for localization of acoustic impact with temperature effect [37], localization of scatterers [2,20,30], for damage identification in beam structure [34], shape reconstruction of traction-free scatterers [25], or noise source localization in a road vehicle [28]. Noticeable progress has been made in using experimental data for damage identification [31]. Several works are devoted to study or improvement of the quality of reconstruction of the original source [3,4,35], but a methodology for performing TR in standard and widely used numerical method such as finite element method (FEM) was still not fully established. This work aims to improve the reconstruction of the exciting signal in time domain, meaning some present or forming flaw in material, and to determine the correct procedure for deployment of TR in practice, i.e. in commercial finite element (FE) software.

In practice, the process of localization is accomplished in two steps. The first step, based on forward propagation, is measuring on a real structure. In the second step, the measured signals are reversed in time and transmitted to the computational model, where based on backpropagation, energy is focused into the location of the original source. The mentioned process is schematically shown in Fig. 1. Generally, one works only with partial information (incomplete data from sensors), since it is not possible to record response signals in the whole structure. There are two approaches of performing effective refocusing using TR method. The first one is using a substantial number of transducers in combination with short record (and computational) time, the second one is the exact opposite — using only one or several transducers combined with long record times. The second approach exploits reflections from structure boundaries which are compensating a lack of the direct information, altogether creating a virtual

time-reversal mirror, see [16]. In this paper, we also perform the frontal problem computationally, simulating the experimental data.

The finite element method, e.g. like presented in [24], is used for spatial modeling of elastodynamic problems. Several time schemes could be employed for direct time integration of frontal and reverse problems, but a suitable time scheme must be reversible in time for correct modeling of time reversal in NDT. We know from the paper of Givoli [19] that the central difference method in time is of the second order of accuracy and, primarily, reversible in time. For that reason we apply this explicit time scheme for integration in time; it is needed to satisfy the stability limit for time step size, see [7].

With this paper, we study the accuracy and robustness of the computational TR based on explicit time integration of equation of motion discretized by the linear FEM with lumped mass matrix. In principle, we expand work of Givoli and Turkel, namely [20]. We focus on a practical use of the TR method and emerging obstacles during the whole process, and we pay a special attention to appropriate prescription of boundary conditions/loading.

The paper is organized as follows. In Section 2, governing equations of elastodynamics for frontal and reverse problem are mentioned with definition of necessary initial and boundary conditions. The introduction into explicit time integration for wave propagation problems in FEM is presented in Section 3. In Section 4, the cost functions for evaluation of quality of source signal reconstruction are defined. Numerical experiments with results are presented in Section 5. The paper closes with the conclusions in Section 6.

2. Problem definitions and governing equations

In this paper, we employ the classical theory of small deformations of elastic isotropic media for mathematical description of elastic wave propagation in solids, which is applied for frontal and reverse problem for TR in this section. For the problems definition, we follow the paper of Givoli [19].

2.1. Definition of the frontal problem

In the first step, we define the frontal problem with suitable boundary and initial conditions. We consider an open, bounded domain $\Omega \in \mathbb{R}^3$ with the smooth boundary $\partial\Omega$. Also we consider the linear equations of elastodynamics in the domain Ω and in the time $t \in [0, T]$. The governing equations of elastodynamics, see [32], are given by the kinematic relationship, the Hooke’s law, and the Cauchy equation without volume force, respectively, as

$$\nabla \cdot \boldsymbol{\sigma} = \rho \ddot{\mathbf{u}}, \quad \boldsymbol{\sigma} = \mathbf{C} : \boldsymbol{\varepsilon}, \quad \boldsymbol{\varepsilon} = \frac{1}{2}(\nabla \mathbf{u} + (\nabla \mathbf{u})^\top), \quad 0 \leq t \leq T, \quad \mathbf{x} \in \Omega, \tag{1a}$$

with boundary conditions

$$\mathbb{B} \mathbf{u} = \mathbf{0} \text{ on } \partial\Omega, \tag{1b}$$

and with initial conditions

$$\mathbf{u}(\mathbf{x}, t = 0) = \mathbf{u}^0(\mathbf{x}), \quad \dot{\mathbf{u}}(\mathbf{x}, t = 0) = \mathbf{v}^0(\mathbf{x}) \quad \mathbf{x} \in \Omega. \tag{1c}$$

In the aforesaid relationships, the superimposed dots, $\dot{\square}$, $\ddot{\square}$, denote the derivatives with respect to time t and operator $\nabla = \{\frac{\partial}{\partial x_1}, \frac{\partial}{\partial x_2}, \frac{\partial}{\partial x_3}\}$, $\boldsymbol{\sigma}$ is the Cauchy stress tensor, $\boldsymbol{\varepsilon}$ is the infinitesimal strain tensor, \mathbf{C} is the elastic tensor, and ρ is the mass density. Further, $\mathbf{u}(\mathbf{x}, t)$ is the displacement, $\dot{\mathbf{u}}(\mathbf{x}, t)$ is the velocity, and $\ddot{\mathbf{u}}(\mathbf{x}, t)$ is the acceleration. For isotropic elastic medium, we consider the Hooke’s law as $\boldsymbol{\sigma} = \lambda \text{tr}(\boldsymbol{\varepsilon})\mathbf{I} + 2G\boldsymbol{\varepsilon}$, where λ and G are Lamé’s constants related to engineering constants $\lambda = \nu E / [(1 + \nu)(1 - 2\nu)]$ and $G = E / [2(1 + \nu)]$, where E and ν are Young’s modulus and Poisson’s ratio, respectively.

Furthermore in (1b), \mathbb{B} is some boundary operator on the displacement field $\mathbf{u}(\mathbf{x}, t)$ as the operator prescribing boundary conditions on $\Gamma = \partial\Omega$. Neumann boundary conditions as stress-free boundary conditions are prescribed on Γ_N and Dirichlet boundary conditions are prescribed on Γ_D , where $\Gamma_D \cup \Gamma_N = \Gamma$ and $\Gamma_D \cap \Gamma_N = \emptyset$. The initial conditions are given by displacement field $\mathbf{u}^0(\mathbf{x})$ and velocity field $\mathbf{v}^0(\mathbf{x})$ at the initial time $t = 0$ as in (1c). In future text, notations like $\mathbf{u}(\mathbf{x}, t)$, $\mathbf{u}^t(\mathbf{x})$, and \mathbf{u}^t are equivalent.

Relationships (1c) represent an initial condition and we assume that \mathbf{u}^0 and \mathbf{v}^0 have a support in $\Omega_S \subset \Omega$, which is only local, i.e., the region Ω_S is much smaller than the whole domain Ω . Generally, we obtain the displacement field $\mathbf{u}(\mathbf{x}, t)$ as a solution of the problem defined in (1).

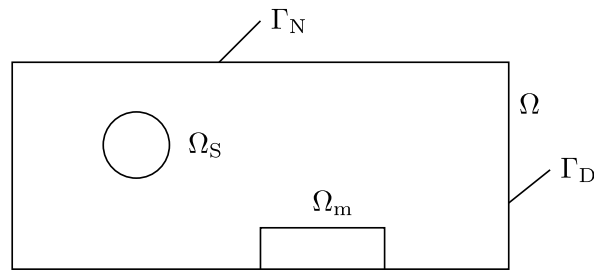


Fig. 2. Scheme of TR problem. Ω is the domain of interest, Ω_S is the support of the original source, and Ω_m is the area of measurement.

In this paper, the frontal problem simulates numerically the real measurement on a real structure, normally the time history of some displacement or velocity components. Here, we substitute the experimental data by recording the response of FE model. During the frontal problem, we record time history of velocity $\dot{\mathbf{u}}_m(\mathbf{x}, t)$ as a response in domain Ω_m , in time $t \in [0, T]$. From now, we will call this response from frontal problem as ‘experimental data’. The scheme of domain of interest for frontal and reverse problem is depicted in Fig. 2.

2.2. Definition of the reverse problem as a source identification problem

We consider the problem of TR as a passive detection of source in Ω_S from the frontal problem in the domain Ω with some information about the response in Ω_m . We assume that the region Ω_S is not known and we know the ‘experimental data’ $\mathbf{u}_m(\mathbf{x}, t)$ or $\dot{\mathbf{u}}_m(\mathbf{x}, t)$ in Ω_m .

Firstly, we have to define the “reverse time” τ for the reverse problem. The reverse time τ is defined by transformation in time as $\tau = T - t$. It means that the time τ is going backwards with respect to the time t from the frontal problem. We also define the “reversal field variable” – the displacement of the reverse problem $\mathbf{w}(\mathbf{x}, \tau)$, $\mathbf{x} \in \Omega$, $\tau \in [0, T]$. For the reverse problem, we keep the same geometry and material characteristics as for the frontal problem. Also the boundary conditions defined by the operator \mathbb{B} should be the same. Under these conditions, we are able to satisfy the same wave speeds and boundary conditions for reflection and transmitted wave propagation as in the frontal problem. It is a necessary condition for the correct application of the TR method in elastic wave propagation problems. The boundary and initial conditions for the reversal displacement field $\mathbf{w}(\mathbf{x}, \tau)$ are given from the measurement data \mathbf{u}_m and $\dot{\mathbf{u}}_m$. And we have to take into account the time history of the measurement data \mathbf{u}_m and $\dot{\mathbf{u}}_m$ in the domain Ω_m as an extra boundary condition in the domain Ω_m , i.e. $\mathbf{w}(\mathbf{x}, \tau) = \mathbf{u}_m(\mathbf{x}, t)$ and $\dot{\mathbf{w}}(\mathbf{x}, \tau) = -\dot{\mathbf{u}}_m(\mathbf{x}, t)$, $\mathbf{x} \in \Omega_m$. In Section 4, we discuss two techniques how to apply these boundary conditions in Dirichlet or Neumann sense for correct reversing in elastic wave propagation. In [19], there is mentioned that the measured velocity \bar{v} should be take with the opposite sign due to time derivative with respect to time τ . The proof can be found in the definition of time derivative $\partial/\partial\tau = -\partial/\partial t$, which comes from the definition of the reversal time $\tau = T - t$. For the following text, we use the bar, $\bar{\square}$, for marking of the reverse problem quantities.

The reverse problem then takes form

$$\nabla \cdot \bar{\boldsymbol{\sigma}} = \rho \bar{\ddot{\mathbf{w}}}, \quad \bar{\boldsymbol{\sigma}} = \mathbf{C} : \bar{\boldsymbol{\varepsilon}}, \quad \bar{\boldsymbol{\varepsilon}} = \frac{1}{2}(\nabla \mathbf{w} + (\nabla \mathbf{w})^T), \quad 0 \leq \tau \leq T, \quad \mathbf{x} \in \Omega, \tag{2a}$$

with boundary conditions

$$\mathbb{B} \mathbf{w} = \mathbf{0} \text{ on } \partial\Omega, \tag{2b}$$

with initial conditions

$$\mathbf{w}(\mathbf{x}, 0) = \mathbf{0}, \quad \dot{\mathbf{w}}(\mathbf{x}, 0) = \mathbf{0} \quad \mathbf{x} \in \Omega, \tag{2c}$$

and with kinematic conditions on Ω_m for TR identification as follows

$$\mathbf{w}(\mathbf{x}, \tau) = \mathbf{u}_m(\mathbf{x}, t), \quad \dot{\mathbf{w}}(\mathbf{x}, \tau) = -\dot{\mathbf{u}}_m(\mathbf{x}, t) \quad \mathbf{x} \in \Omega_m. \tag{2d}$$

For details on the TR problem formulation, see the work of Givoli and Turkel [20]. Prescribing these kinematic conditions $\mathbf{w}(\mathbf{x}, \tau)$ and $\dot{\mathbf{w}}(\mathbf{x}, \tau)$ on Ω_m into the governing equations (2) provides the time reversal of the original problem defined in Section 2.1.

2.3. Application of kinematic conditions on Ω_m in TR task

In simulations presented in this paper, we assume that we record only normal component of velocities on boundary $\partial\Omega_m - \dot{\mathbf{u}}_m(\mathbf{x}, t)$ – as a response from the frontal problem. That simulates recording of response in the form of normal velocities on $\partial\Omega_m$ by piezo-sensor or other measurement techniques. Then, $\dot{\mathbf{w}}_m(\mathbf{x}, \tau)$ is computed via (2d). This process is called the *time reversal of the signal*. In this way, we generate the ‘*experimental data*’ for the TR task defined in (2d) by the numerical model. After that, we have to apply these boundary conditions in a suitable form into the reverse problem. For application of the boundary conditions in Ω_m in the FE simulation we think about their application only on $\partial\Omega_m$ in two forms as

Type I: loading by normal velocity components in the Dirichlet sense

$$\dot{\mathbf{w}}_m^n(\mathbf{x}, \tau) \quad \mathbf{x} \in \partial\Omega_m, \quad 0 \leq \tau \leq T, \tag{3a}$$

Type II: loading by normal stress components in the Neumann sense

$$\sigma_m^n(\mathbf{x}, \tau) = \sigma_m^n(\mathbf{x}, \tau)\mathbf{n} = A\dot{\mathbf{w}}_m^n(\mathbf{x}, \tau) \quad \mathbf{x} \in \partial\Omega_m, \quad 0 \leq \tau \leq T. \tag{3b}$$

Here, \mathbf{n} is the outward normal direction to the boundary $\partial\Omega_m$. A is a constant with a suitable value depending on material parameters. For this normal traction loading σ_n we generate the external nodal force vector as \mathbf{f}_{ext} . In this case, we could say that we transfer the Dirichlet boundary conditions of velocity $\dot{\mathbf{w}}_m^n$ meaning to Neumann boundary condition as normal stress σ_m^n in $\partial\Omega_m$.

Remark 1. If $\Omega_m = \Omega$, an exact reconstruction of the initial wave field $\mathbf{u}(\mathbf{x}, t = 0)$ can be found. In our case, where we have only partial information of the wave field, $\dot{\mathbf{u}}_m(\mathbf{x}, t)$, the reconstructed wave field is only an approximation of the initial state $\mathbf{u}(\mathbf{x}, t = 0)$.

3. Numerical methods for modeling of TR problems

In this section, we introduce numerical methods and techniques for modeling of forward and backward wave propagation problems for needs of TR application in NDT. We focus only on elastic wave propagation in the context of theory of small deformations and its finite element modeling.

3.1. Explicit finite element analysis

For the finite element simulation, we use the standard FEM based on displacement formulation with linear shape functions, see [24]. As we know from [20], the central difference method as a time stepping technique, see [24], is reversible in time. Therefore, we use the classical explicit time integration in the finite element modeling with the lumped mass matrix. Also we include the one-point Gauss integration with hourglass control, which is a standard approach in explicit time integration in FEM for reduction of computational cost. Due to reduced integration we use hourglass control (Optimal Bending type) as described by Belytschko and Bachrach [7]. The procedure is such that to the element stiffness matrix $\mathbf{K}_{\text{el}}^{\text{1gp}}$ obtained by one-point Gauss integration is added a stabilization stiffness matrix \mathbf{K}_{stab} suppressing hourglass modes as $\mathbf{K}_{\text{el}} = \mathbf{K}_{\text{el}}^{\text{1gp}} + \mathbf{K}_{\text{stab}}$.

In FEM, we solve the system of equations of motion for elasto-dynamic problem, see e.g. [6],

$$\mathbf{M}\ddot{\mathbf{q}}(t) + \mathbf{K}\mathbf{q}(t) = \mathbf{f}_{\text{ext}}(t) \tag{4}$$

+ prescribing kinematic (Dirichlet) boundary conditions and initial conditions

where \mathbf{M} is the lumped mass matrix, \mathbf{K} is the stiffness matrix, $\mathbf{q}(t)$ is the nodal displacement vector, $\ddot{\mathbf{q}}(t)$ is the nodal acceleration vector, and $\mathbf{f}_{\text{ext}}(t)$ is the vector of external nodal forces at the time t . The mass matrix is lumped using row-summing procedure, Hughes [24]. The matrices \mathbf{K} and \mathbf{M} are constant for the elastodynamic problems under small deformation theory. For solving the system (4), we should include suitable Dirichlet and Neumann boundary and initial conditions for frontal and reverse problems. In the finite element method, we could prescribe the kinematic boundary conditions via given nodal displacement, velocity or acceleration controlling, for details see [24] or [10].

In this paper, for explicit integration in time we use the central difference (CD) scheme as described in a book of Belytschko et al. [8] where the update of nodal velocities in each time step is split into two half-steps, and

the desired value of velocities can be prescribed directly. This approach is also called the *leapfrog* integration. To summarize, in this paper we use the numerical approach for the modeling of elastic linear wave propagation problem based on the finite element method with linear shape functions — the first-order convergence in space, and explicit time integration via the central difference method — the second-order convergence in time.

We assume that we know quantities at the time t , $\mathbf{q}(t)$, $\dot{\mathbf{q}}(t)$, $\ddot{\mathbf{q}}(t)$, and the task is to find the quantities at the time $t + \Delta t$, where Δt is the time step. The CD scheme as the *leapfrog* integration takes the form presented in Alg. 1: Initialize $t^0 = 0$, \mathbf{q}^0 , $\dot{\mathbf{q}}^0$, assemble \mathbf{M} , \mathbf{K} , and compute $\ddot{\mathbf{q}}^0 = \mathbf{M}^{-1} (\mathbf{f}_{\text{ext}}^0 - \mathbf{K}\mathbf{q}^0)$

```

while  $t < T$  do
    Setting of the time step size  $\Delta t$ 
     $\dot{\mathbf{q}}(t + \frac{\Delta t}{2}) = \dot{\mathbf{q}}(t) + \ddot{\mathbf{q}}(t) \frac{\Delta t}{2}$ ;
     $\mathbf{q}(t + \Delta t) = \mathbf{q}(t) + \dot{\mathbf{q}}(t + \frac{\Delta t}{2}) \Delta t$ ;
    prescription of kinematic boundary conditions;
     $\mathbf{r}(t + \Delta t) = \mathbf{f}_{\text{ext}}(t + \Delta t) - \mathbf{K}\mathbf{q}(t + \Delta t)$ ;
     $\ddot{\mathbf{q}}(t + \Delta t) = \mathbf{M}^{-1}\mathbf{r}(t + \Delta t)$ ;
     $\dot{\mathbf{q}}(t + \Delta t) = \dot{\mathbf{q}}(t + \frac{\Delta t}{2}) + \ddot{\mathbf{q}}(t + \Delta t) \frac{\Delta t}{2}$ ;
    prescription of kinematic boundary conditions;
     $t = t + \Delta t$ ;
end
    
```

Algorithm 1: The central difference scheme in the *leapfrog* form for direct time integration of elastodynamic problems.

It is needed to mention, that the presented scheme is conditionally stable, see [24]. It means that the value of Δt has to satisfy the stability limit $\Delta t < \Delta t_{\text{cr}}$, where Δt_{cr} is the critical limit given as $\Delta t_{\text{cr}} = 2/\omega_{\text{max}}$, with ω_{max} being the maximum angular frequency of the discretized homogeneous system defined in (4). In following section we present two ways of prescription of boundary conditions, marked as Type I and Type II defined in Section 2.2, both called ‘loading’ for simplicity.

3.2. Explicit time integration in TR

In both following subsections, the prescribed quantities in CD schemes are meant to be prescribed only at some nodes. This effect is not additionally emphasized in the used symbols for better readability. Further, the asterisk in lower index, \square_* , denotes the prescribed value in corresponding time, and symbol $:=$ means assignment of the prescribed value.

3.2.1. Application of ‘loading’ Type I

We modify the CD scheme in order to include the measurement data in the form of normal velocities $\dot{\mathbf{w}}_{\text{normal}}$ as Type I. The following algorithm (5a)–(5e) shows use of CD scheme with marked spots where the desired values of velocity are prescribed at the boundary $\partial\Omega_m$ as $\dot{\mathbf{q}}_*$.

Application of ‘loading’ of **TYPE I**:

$$\dot{\mathbf{q}}(t + \frac{\Delta t}{2}) = \dot{\mathbf{q}}(t) + \ddot{\mathbf{q}}(t) \frac{\Delta t}{2} \tag{5a}$$

apply prescribed nodal velocity as $\dot{\mathbf{q}}(t + \frac{\Delta t}{2}) := \dot{\mathbf{q}}_*(t + \frac{\Delta t}{2})$ at $\partial\Omega_m$

$$\mathbf{q}(t + \Delta t) = \mathbf{q}(t) + \dot{\mathbf{q}}(t + \frac{\Delta t}{2}) \Delta t \tag{5b}$$

$$\mathbf{r}(t + \Delta t) = \mathbf{f}_{\text{ext}}(t + \Delta t) - \mathbf{K}\mathbf{q}(t + \Delta t) \tag{5c}$$

$$\ddot{\mathbf{q}}(t + \Delta t) = \mathbf{M}^{-1}\mathbf{r}(t + \Delta t) \tag{5d}$$

$$\dot{\mathbf{q}}(t + \Delta t) = \dot{\mathbf{q}}(t + \frac{\Delta t}{2}) + \ddot{\mathbf{q}}(t + \Delta t) \frac{\Delta t}{2} \tag{5e}$$

apply prescribed nodal velocity as $\dot{\mathbf{q}}(t + \Delta t) := \dot{\mathbf{q}}_*(t + \Delta t)$ at $\partial\Omega_m$

3.2.2. Application of ‘loading’ Type II

In Type II we assume loading in the form of prescribed external nodal force $\mathbf{f}_{\text{ext},*}$ on $\partial\Omega_m$ due to normal traction loading with the given time history. In the same principle as in the previous text, the following five equations (6a)–(6e) show the same algorithm with spot where the desired values of nodal force are prescribed.

Application of ‘loading’ of **TYPE II**:

$$\dot{\mathbf{q}}\left(t + \frac{\Delta t}{2}\right) = \dot{\mathbf{q}}(t) + \ddot{\mathbf{q}}(t) \frac{\Delta t}{2} \tag{6a}$$

$$\mathbf{q}(t + \Delta t) = \mathbf{q}(t) + \dot{\mathbf{q}}\left(t + \frac{\Delta t}{2}\right) \Delta t \tag{6b}$$

apply prescribed nodal force as $\mathbf{f}_{\text{ext}}(t + \Delta t) := \mathbf{f}_{\text{ext}}(t + \Delta t) + \mathbf{f}_{\text{ext},*}(t + \Delta t)$ at $\partial\Omega_m$

$$\mathbf{r}(t + \Delta t) = \mathbf{f}_{\text{ext}}(t + \Delta t) - \mathbf{K}\mathbf{q}(t + \Delta t) \tag{6c}$$

$$\ddot{\mathbf{q}}(t + \Delta t) = \mathbf{M}^{-1}\mathbf{r}(t + \Delta t) \tag{6d}$$

$$\dot{\mathbf{q}}(t + \Delta t) = \dot{\mathbf{q}}\left(t + \frac{\Delta t}{2}\right) + \ddot{\mathbf{q}}(t + \Delta t) \frac{\Delta t}{2} \tag{6e}$$

In the following text, we test the both approaches for application of reversal boundary conditions in TR.

Remark 2. If we update prescribed velocity as Givoli and Turkel [20], i.e. $\dot{\mathbf{q}}^t := \dot{\mathbf{q}}^t + \dot{\mathbf{q}}_*^t$, with a scaling parameter \mathcal{C} , while the choice of \mathcal{C} is subjected to preservation of the linear momentum balance, for one node as mass point with the mass m with prescribed value we get the relationship

$$\dot{\mathbf{q}}^{t+\frac{\Delta t}{2}} := \dot{\mathbf{q}}^t + \mathcal{C} \cdot \dot{\mathbf{q}}_*^{t+\frac{\Delta t}{2}}. \tag{7}$$

From impulse–linear momentum theorem

$$\mathbf{I} = \int_t^{t+\Delta t} \mathbf{f}_*(t) dt = \mathbf{p}(t + \Delta t) - \mathbf{p}(t) = \Delta\mathbf{p} = m\Delta\dot{\mathbf{q}} \tag{8}$$

where \mathbf{I} is the impulse of the force and \mathbf{p} is the linear momentum defined as $\mathbf{p} = m\dot{\mathbf{q}}$. Respecting using half-steps for prescription of the velocity, we derive the relationship as

$$\frac{\Delta t}{2} \mathbf{f}_* \equiv m \cdot \Delta\dot{\mathbf{q}}_* \frac{\Delta t}{2}, \tag{9}$$

where m is nodal mass, $\Delta\dot{\mathbf{q}}_* \frac{\Delta t}{2}$ is the change of the nodal velocity between times t and $t + \frac{\Delta t}{2}$ from Eq. (7), and \mathbf{f}_* is the acting equivalent nodal force. Hence, coefficient $\mathcal{C} = \frac{2m}{\Delta t}$. It is apparent that with this way of prescription of the nodal velocity with updating $\dot{\mathbf{q}}^t := \dot{\mathbf{q}}^t + \mathcal{C}\dot{\mathbf{q}}_*^t$ we obtain the same result, with numerical accuracy, as with loading by corresponding nodal force \mathbf{f}_* and no further scaling of recorded signals is necessary. Using \mathcal{C} with different value leads to the same signal with different magnitude, thanks to the linearity of the problem. This approach is illustrated in Section 5.

3.3. Elimination of rigid body motion in TR

Whereas in a physical experiment the observed model is somehow “softly fixed in space” and the recorded signals from transducers are relative to the model, in a numerical experiment the model floats in space and the recorded signals are relative to the default coordinate system. Therefore we need to handle the fact that the model is also undergoing rigid motion. For elimination of rigid motions or rigid body modes (RBMs) we use a method proposed by Felippa and Park [14]. This elimination is well known for FETI method, Farhat and Roux [13], for domain decomposition in structural mechanics or modeling of floating systems in aerospace applications. The RBMs are eliminated from the resulting state after computation or for each computational step.

Based on Felippa and Park [14], the final nodal displacement vector \mathbf{u} can be decomposed to rigid motion component $\mathbf{u}_R = \mathbf{R}\mathbf{R}^T\mathbf{u}$ and own deformation component \mathbf{d} as $\mathbf{u} = \mathbf{u}_R + \mathbf{d}$. Thus, the deformation component is computed as

$$\mathbf{d} = \mathbf{u} - \mathbf{R}\mathbf{R}^T\mathbf{u} = (\mathbf{I} - \mathbf{R}\mathbf{R}^T) \mathbf{u}, \tag{10}$$

where matrix \mathbf{R} consists of rigid body modes \mathbf{R}_i of number corresponding to total number of degrees of freedom of the body. The decomposition is performed using the matrix \mathbf{R} formed by eigen-vectors corresponding to RBM frequencies or direct building from the nodal positions for each rigid body mode for translational and rotational motion, see [14]. Vectors are ortho-normalized so that $\mathbf{R}^T\mathbf{R} = \mathbf{I}_{NR}$, with \mathbf{I}_{NR} being the identity matrix of order NR, where NR is a number of RBMs. Besides the artificial assembling of the vectors, they can be computed numerically. On the contrary, computed vectors are generally linear combinations of all zero-frequency modes and are not separated like from direct assembling. These linearly combined vectors can be ortho-normalized, e.g. by Gram–Schmidt orthogonalization process, Arfken [5].

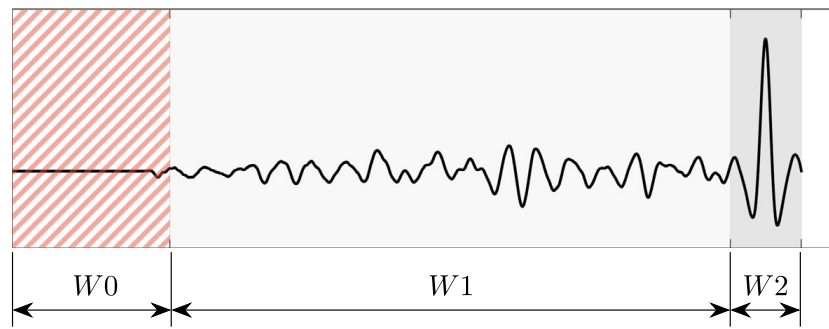


Fig. 3. Time windows for cost functions C_i .

4. Definition of cost functions

In this section, we define three local cost functions C_i and one global cost function C_G as a norm for measurement of distance/nearness of two functions of interest – lower value of the cost function means more accurate reconstruction in TR. In all costs we work with y-component of the reconstructed nodal velocity. We use these costs in Section 5.3.3 for decision of what type of loading, i.e. Type I or Type II, gives more accurate reconstruction of the loading pulse. We have found the inspiration for definition of cost functions in [20], but here we observe distribution of some quantities of interest in time. We expect the reconstructed signal to appear at the right position at the right time and measure the quality of reconstruction under these conditions. This assumption is confirmed at the beginning of Section 5.

For definition of cost functions, we split the reconstructed signal into three sections and call them time windows — W_0 , W_1 and W_2 , see Fig. 3 with an example. Time window W_0 (hatched) is cut off, since only the developed signal gives as a relevant information, W_1 (light gray) we can call a window of the delivering signal, and W_2 (dark gray) is the time window with the expected reconstructed pulse. The time window W_2 has the same length as the loading signal L in the frontal problem. These costs operate with known source and cannot be used in real TR problem with experimental data since the source signal, and therefore division into time windows, is not known in advance. In the following text, we describe the used local cost functions C_i and global cost function C_G .

The cost function C_1 represents a ratio of *kinetic energies* of the observed FE nodes in time windows W_1 and W_2 . This so-called kinetic energy is computed as a root mean square (RMS) of velocity in the corresponding time window. This procedure is known as *signal to noise ratio* in signal processing, Gonzalez [21]. The cost C_1 simply says whether the reconstructed pulse is distinguishable from surrounding signal as

$$C_1 = \frac{\text{RMS}_{W_1}}{\text{RMS}_{W_2}}. \tag{11}$$

Cost C_2 measures the perpendicularity of the original pulse and the reconstructed pulse, or more precisely, their parallelism. The vector of the original pulse L and the vector of the reconstructed pulse W_2 make an angle ϕ , while calculation of $\cos \phi$ is according to a well known formula from linear algebra described in (12), see e.g. [39], so

$$C_2 = 1 - \cos \phi = 1 - \frac{W_2 \cdot L}{|W_2| \cdot |L|}. \tag{12}$$

Cost C_3 measures how the reconstructed pulse is shifted in time by comparing time-positions of the maximum peaks of the original pulse and the reconstructed one. For computation of this cost, the time window W_2 is considered to start in time $t = 0$ s. Here $t_{\max L}$ and $t_{\max W_2}$ are time-positions of the maximum peak of the loading pulse and the reconstructed pulse, $lenL$ is the length of the loading pulse (and also of the time window W_2). Since the maximum peak of the loading pulse is right in the middle of the signal, only the half of the total length is taken as a possible shift in time. This produces the cost C_3 as

$$C_3 = \frac{|t_{\max L} - t_{\max W_2}|}{lenL/2}. \tag{13}$$

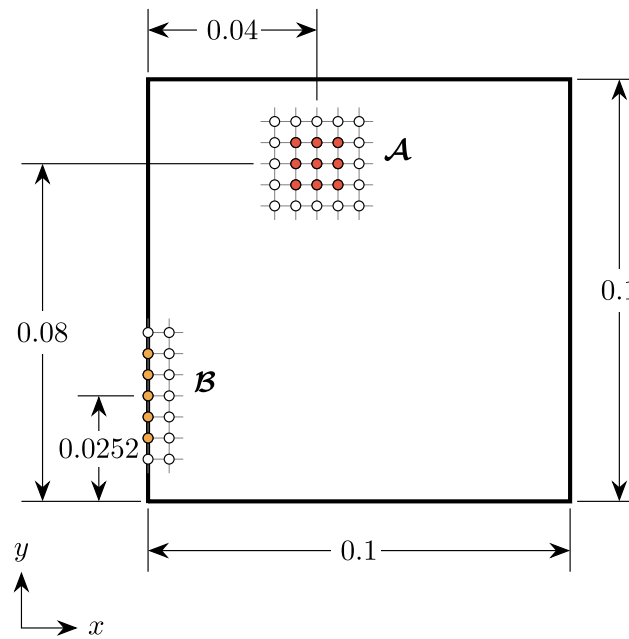


Fig. 4. Scheme of the domain of interest, [m].

Remark 3. Using the cost functions C_1 , C_2 and C_3 , where we need to know the time window W_2 , has limitation for real applications. In this paper, we use them for measuring of quality of reconstruction of known original sources and we can define the time windows of the signals.

For the numerical tests in TR, we use the global cost function C_G which is defined by the following equation

$$C_G = \frac{1}{\sum w_i} (w_1 C_1 + w_2 C_2 + w_3 C_3), \tag{14}$$

where w_i are weights of the local costs. Since we focus on the quality of reconstruction, the cost C_2 is given more importance. Hence, we choose weights as $w_1 = 1$, $w_2 = 2$, and $w_3 = 1$. In the following numerical test (Section 5.3), we have shown the sensitivity of each cost function C_1 , C_2 and C_3 on the global cost function C_G .

5. Numerical experiments in TR

In this section, we study the accuracy of the suggested TR technology based on the FEM. We present a set of numerical experiments to test the behavior of the proposed way of loading in TR. The specific details for each experiment are described in corresponding subsections.

The computations take approximately 30 min for computation of the explicit dynamic problem with 126 000 degrees of freedom and 20 000 time steps on a laptop (Windows 10; in-house dynamic solver in Matlab R2019a; Intel Core i7-7700HQ CPU @ 2.80 GHz, 16 GB RAM, NVIDIA GeForce GTX 1050).

5.1. Problem definition

For all numerical experiments we consider a two-dimensional square domain under plane stress condition with stress-free boundary, see its dimensions in Fig. 4. In this Figure, the areas \mathcal{A} and \mathcal{B} mark the position of application of the original source and position where the response is recorded, respectively. The locations of these areas were chosen arbitrarily, but \mathcal{B} should belong to the boundary. In \mathcal{A} , 3×3 nodes are prescribed the loading, while in \mathcal{B} , the number of nodes varies and is mentioned in each task description. The length of the element edge is 0.4 mm, thus the FE mesh consists of 62,500 bilinear four-noded square elements. The mesh was defined with respect to the maximum frequency contained in the loading signal and the dispersion behavior of the finite element method, see [26,27].

We assume a linear homogeneous isotropic material with Young’s modulus $E = 2 \cdot 10^{11}$ Pa, Poisson’s ratio $\nu = 0.3$, and mass density $\rho = 7850 \text{ kg m}^{-3}$, with neither material nor numerical damping. The longitudinal wave

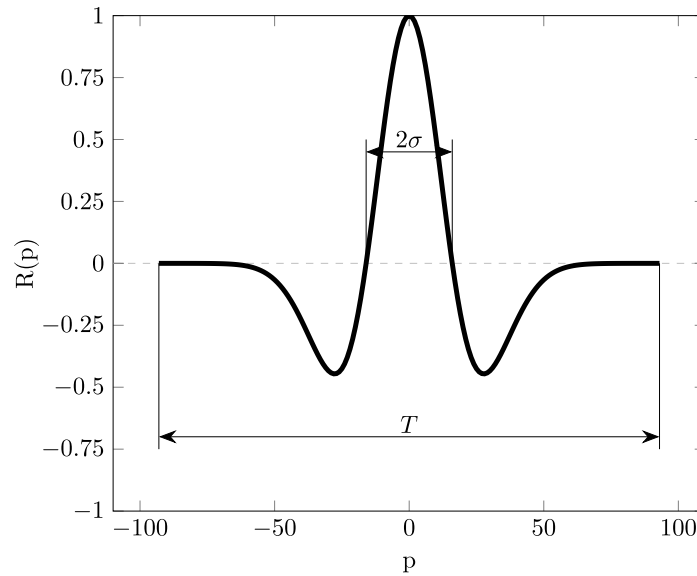


Fig. 5. Loading Ricker pulse with its parameters.

speed for plane stress problem is given as $c_L = \sqrt{\frac{E}{(1-\nu^2)\rho}} \doteq 5291.3 \text{ m s}^{-1}$. Time step size Δt is set to $4.009 \cdot 10^{-8} \text{ s}$ resulting in the Courant number $C \doteq 0.75$, where the Courant number is defined as $C = \Delta t c_L / H$, see [11]; H is the characteristic dimension of the finite element given as $H = A/D$, where A is the area of the element and D is the length of its longest diagonal, see [22]. The critical time step size Δt_{crit} is $5.345 \cdot 10^{-8} \text{ s}$; for $C = 1$ according to previously stated formula.

For loading function $f_{\text{ext}}(t) = A_0 R(t)$ in the area \mathcal{A} , with A_0 being the amplitude of loading, we use the Ricker pulse (Ricker wavelet), Wang [40], which is given by parametric formula with parameter p as

$$R(p) = -\frac{\sqrt{2\pi} \cdot \sigma \cdot \left(\left(\frac{p}{\sigma}\right)^2 - 1\right) \cdot e^{-0.5 \cdot \left(\frac{p}{\sigma}\right)^2}}{\sqrt{2\pi} \cdot \sigma}, \tag{15}$$

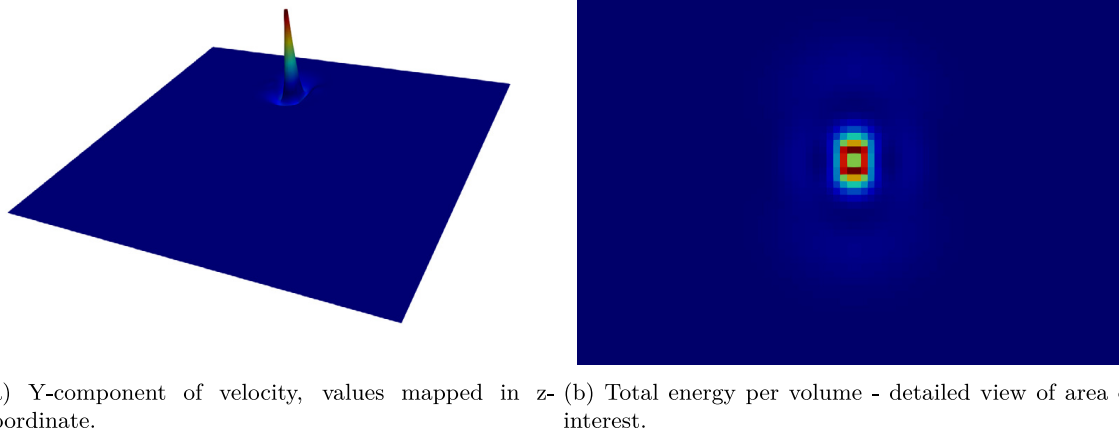
where $\sigma = 16 \cdot \Delta t$ and $p = \langle -93, 93 \rangle \cdot \Delta t$, the transformation between parameter p and time t is $t = p + 93 \cdot \Delta t$, and T is then $7.49683 \cdot 10^{-6} \text{ s}$, see Fig. 5. Amplitude $A_0 = 1$ in all numerical experiments.

We choose the Ricker pulse for the reason that this pulse is symmetrical and also the surfaces above and below the horizontal zero line are the same. It means that the total impulse of the pulse is zero. This implies that loading with Ricker pulse does not accelerate a free body and all kinematic quantities have a meaningful value. On the contrary, a general loading signal accelerates a free body in space. In order to analyze the results, one must deal with this rigid body motion, e.g., as described in Section 3.3.

5.2. Refocusing test

The first test of the paper is aiming on the analysis of refocusing of the original pulse. Several papers have been focused on that topic in numerical sense, see [20], and [19]. In those papers, the quality of refocusing has been studied.

For our test, we employ the geometry and material data mentioned in the previous section. In the frontal problem, we apply the loading as TYPE I or TYPE II, where the y-component of velocities or y-component of nodal forces are prescribed at the nodes of area corresponding to the point \mathcal{A} , see Fig. 4, with the time function in the form of the Ricker pulse. The loading applied at the point \mathcal{A} generates wave processes and the normal velocities at the point \mathcal{B} are recorded. Then, the loading via TYPE I (applied normal velocity) and TYPE II (applied traction normal force) generates the reverse wave processes and we could see the refocusing at the point of the original source, \mathcal{A} . The amplitudes of loading via TYPE I and TYPE II have been set so that they are not affected by rounding errors, with the use of linearity of our problem. The aim of this study is to show that the maximum peak is reconstructed at the location of the original source, \mathcal{A} , and at the correct time.



(a) Y-component of velocity, values mapped in z-coordinate. (b) Total energy per volume - detailed view of area of interest.

Fig. 6. A snapshot of y-component of velocity and total energy per volume distribution from the frontal problem for time $94 \Delta t$ corresponding to the maximum peak of loading pulse.

In Fig. 6 we show a snapshot of the y-component of velocity and the total energy per volume for the frontal problem with the loading of TYPE I at the time $94 \Delta t$, which corresponds to the highest peak of the loading function — Ricker pulse. In Fig. 7, snapshots of the reconstructed quantities as the y-component of velocity and total energy per volume are presented for several times, where T_M means the time of the highest peak of the reconstructed wave field. The loading is by TYPE I — loading by the prescribed normal velocity. One can see that the backpropagation leads to refocusing of the original source in the correct location. The same results, see Fig. 8, we obtain for the task with loading by TYPE II given as the loading by prescribed normal stresses in the form of nodal forces in the direction of outward normal to the surface $\partial\Omega_m$ related to the point \mathcal{B} . In Figs. 7 and 8 we also show how the reconstructed maximum peak forms its shape from times “ $t = T_M - 40 \Delta t$ ” to “ $t = T_M$ ”, and how it vanishes in times “ $t = T_M + 10 \Delta t$ ” and “ $t = T_M + 20 \Delta t$ ”. In all sub-figures on the left, only y-component of velocity is shown and is mapped into the z-direction for illustration.

Based on these results for the both loading types, one can see that the localization of the original source by FEM based TR works very well and we can proceed to reconstruction of the source in time domain, and we can observe the reconstructed signal directly at the point \mathcal{B} .

5.3. Reconstruction test

In this test, we plan to analyze the effect of the prescription of the TR boundary conditions on accuracy of reconstruction of the original source. The quality of reconstruction is measured by the cost functions defined in Section 4. Based on this knowledge, we suggest a flowchart for implementation of the suitable scheme with application of TR boundary conditions for accurate reconstruction in TR tasks.

5.3.1. Kinematic quantities at the loading point by TYPE II

Based on algorithm for application of reversal loading in the TR model defined in Section 3.2.1 and Section 3.2.2, we prefer the loading via TYPE II as nodal forces, because it is simple to apply into the TR model and this application of Neumann boundary conditions is implemented in each FE software. It means that the approach could be applied without any modification of the FE code.

In this section, we study the effect of response to loading nodal forces for visualization of time history of nodal displacement, velocity and acceleration for better understanding of an optimal application of reversed boundary conditions in TR problem. In order to test how the proposed way of loading by TYPE II as normal stress via nodal force behaves, algorithm presented in (6a)–(6e), we applied nodal force loading at the nodes of area \mathcal{A} in the y-direction with the time function of the Ricker pulse. Kinematic quantities as y-component of displacement, velocity and acceleration of the central node of \mathcal{A} are recorded, see Fig. 9. From numerical observation in Fig. 9, we can conclude that the time history of the displacement at \mathcal{A} corresponds to the time function of the loading nodal force. Based on this knowledge for correct reconstruction, we suggest to add the time integration of the reversed

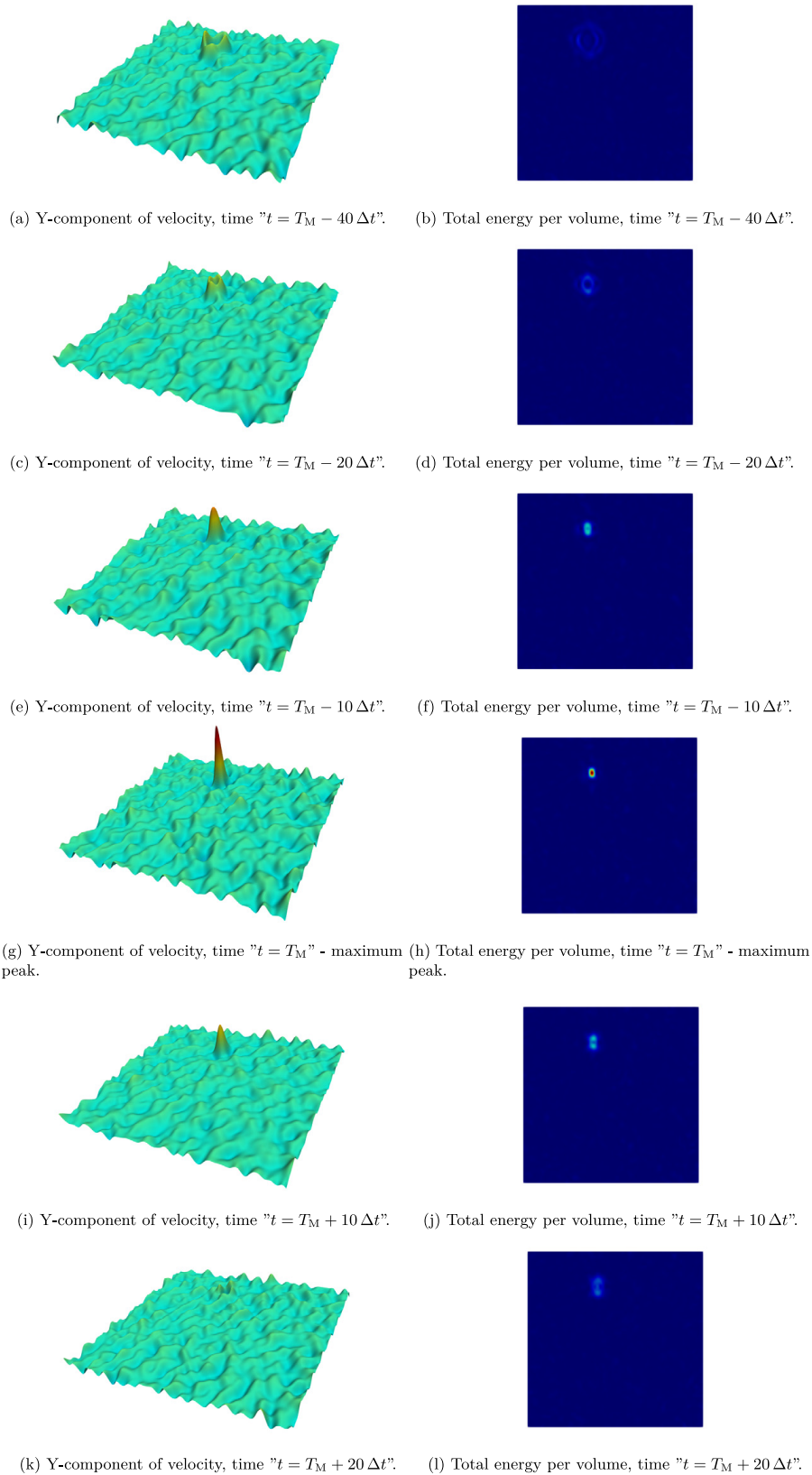


Fig. 7. A snapshot of reconstruction of y-component of velocity and total energy per volume distribution from the reverse problem for time of maximum peak T_M and several other times; loading by TYPE I — “velocity loading”, computational time $T = 100,000 \Delta t$.

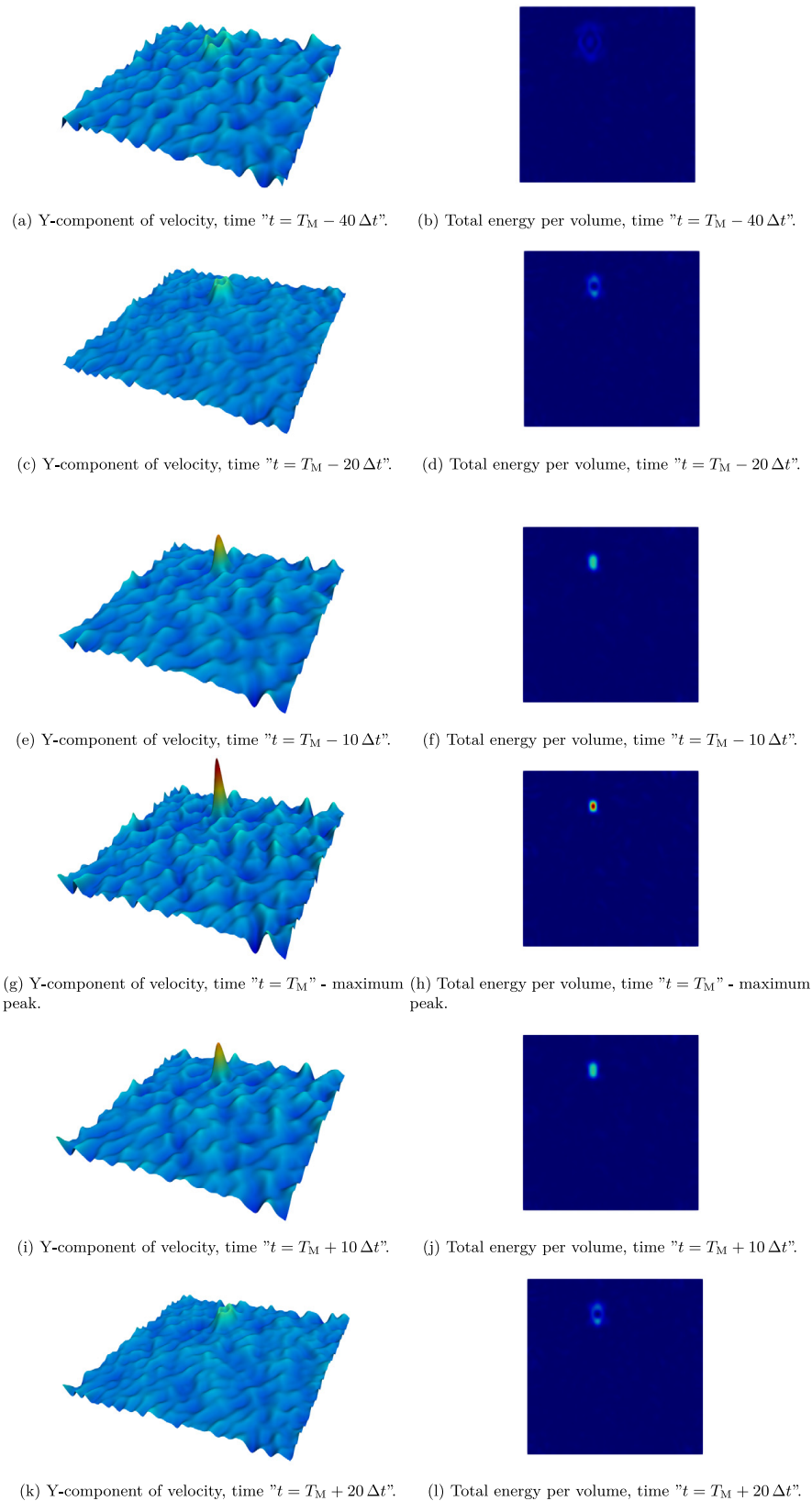


Fig. 8. A snapshot of reconstruction of y-component of velocity and total energy per volume distribution from the reverse problem for time of maximum peak T_M and several other times. Loading by TYPE II — “force nodal loading”, computational time $T = 100,000 \Delta t$.

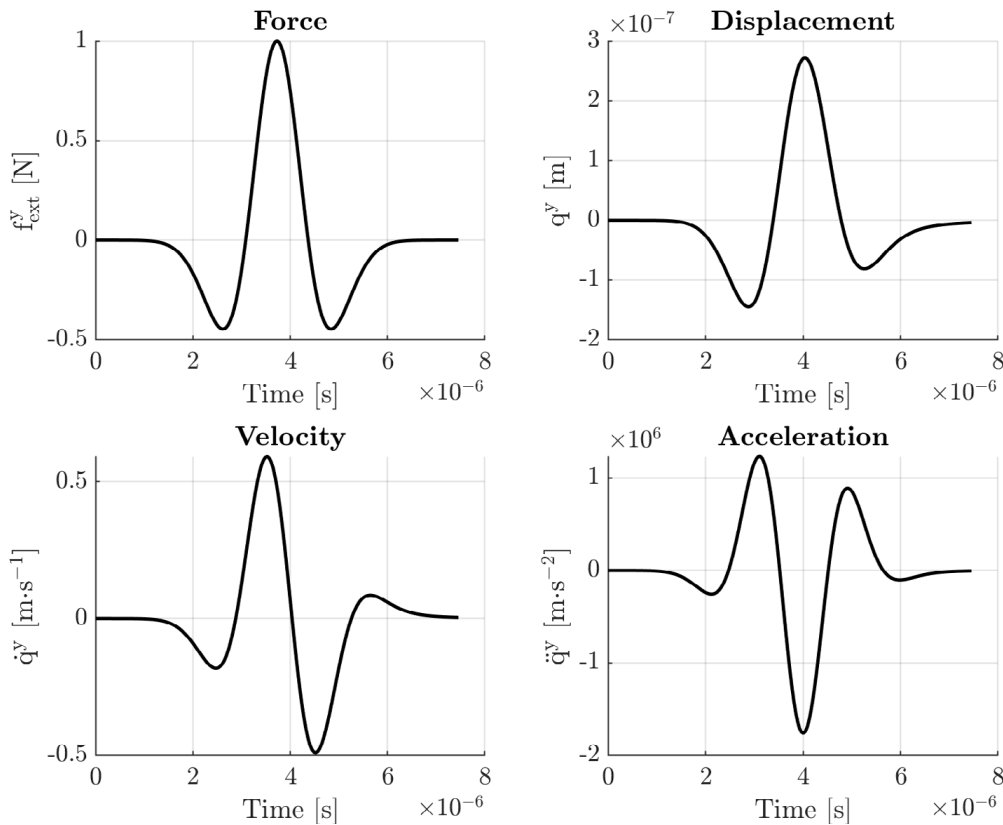


Fig. 9. Output quantities at the y -direction at the middle point of loading by nodal force. The time function of nodal force (top-left) was applied as a load, other graphs represent the response of FE model. Only the quantities in the middle node out of nine nodes in total at point \mathcal{A} were recorded.

pulse of velocity in Ω_m , and after that apply this integrated pulse as loading by nodal force in Ω_m into the TR task. The following numerical test shows the verification of this idea for a correct time reversal.

5.3.2. Numerical verification of the boundary conditions via TYPE II

In this section, we analyze the effect of application of boundary condition in TR computations. Let us imagine the same geometry as in Section 5.1. The nodes related to the point \mathcal{A} are loaded via nodal forces with the time history of the Ricker pulse defined in Section 5.1. Then, the normal velocity at the point \mathcal{B} is recorded from the forward task. The obtained signal is reversed in time and applied as the force loading via normal stress at the point \mathcal{B} . Finally the velocity response is recorded at the point \mathcal{A} . In Fig. 10 (left), one can see the time response in the form of velocity at the y -direction. In Fig. 10 (right), we show the original pulse needed to be reconstructed. Also, the first and second time derivatives of the original pulse are included here. Based on the comparison, we can say that the time history of the recorded velocity (left) corresponds to the second time derivative of the original loading pulse (right). It means that during the numerical TR computations (forward and reverse tasks together) we lost two time derivatives on the original pulse — each computation changes the time derivative of the output signal with respect to the input signal. This phenomenon could be explained via the relationship (8) where there is the relationship between the time history of applied force and velocity. For the correct reconstruction of the original pulse, one need to precede time integration of the loading pulse before both frontal and reverse task of the TR process. In the following text, we study this phenomenon in TR computations and the final form of the TR process in FEM is suggested.

Now, we can analyze a sequence of time integration of the original pulse of loading (in our case the Ricker pulse) and time integration of a velocity signal recorded at point \mathcal{A} . The integrated Ricker pulse is depicted in Fig. 11. Physically, it is a time history of the impulse of the external force with time history given by (15). Based on this analysis we could find a suitable combination of modification of the pulses for a correct time reversal at the

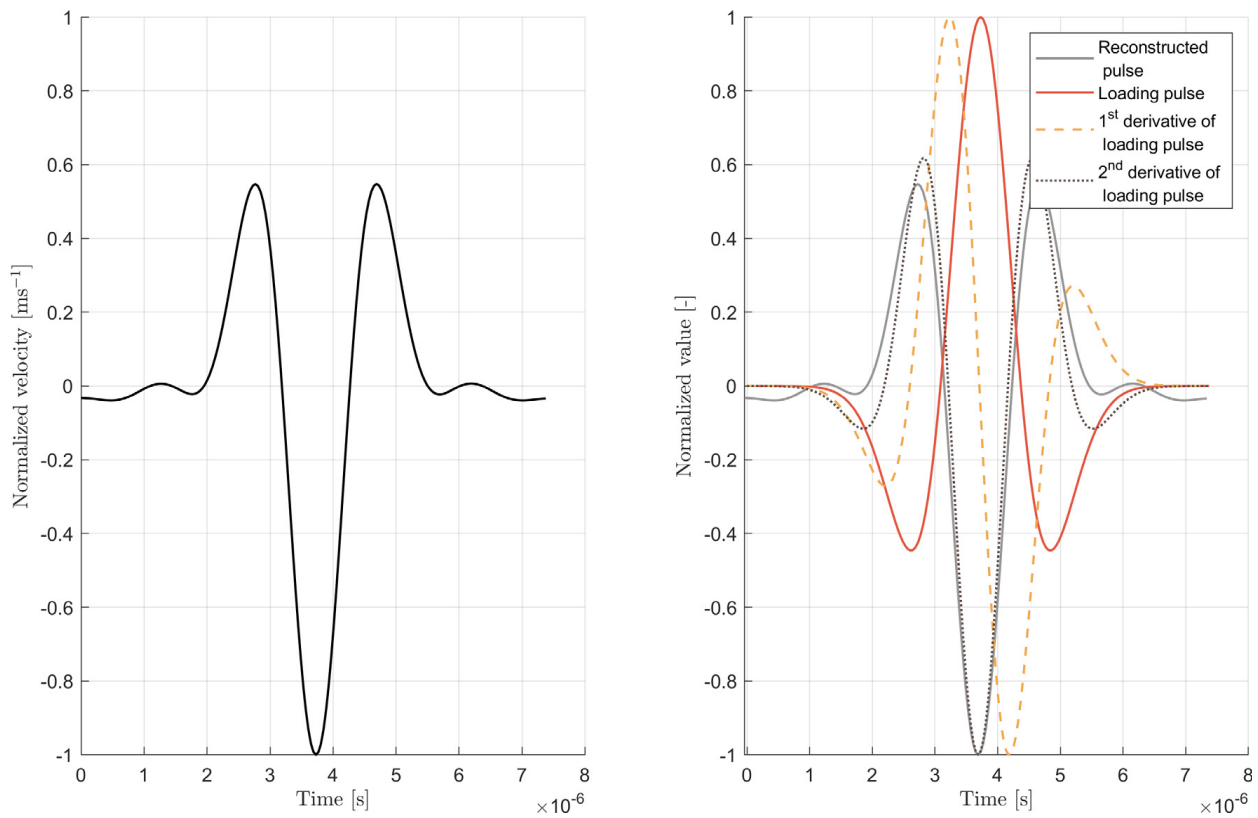


Fig. 10. Reconstruction of the original source (left); original loading pulse with its time derivatives (right), original pulse (red solid line), its 1st time derivative (orange dashed line), and its 2nd time derivative (brown dotted line); reconstructed pulse (gray solid line) is also added here for clarity. (For interpretation of the references to color in this figure legend, the reader is referred to the web version of this article.)

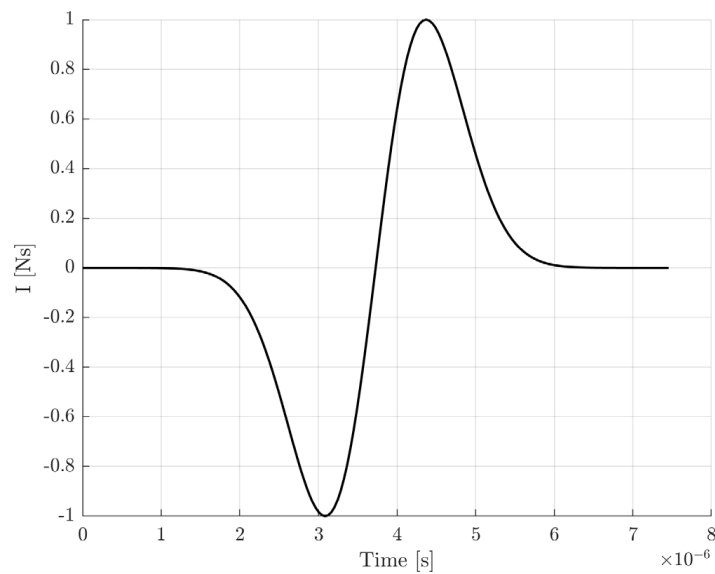


Fig. 11. An integrated Ricker pulse as a time integral $\int_0^T R(t)dt$.

point \mathcal{A} with respect to the reversal signal at point \mathcal{B} . This pulse is after the time reversing applied as nodal force in normal direction in the reverse task. The amplitudes of loading at points \mathcal{A} and \mathcal{B} are chosen with respect to the accuracy of computation and scale of the problems and material properties of the domain of interest.

We mark the computations in this section as **Int – Int**, **Int – Orig**, **Orig – Int**, **Orig – Orig**, where the first key means the loading time function at point \mathcal{A} for the forward problem, and the second key means the loading

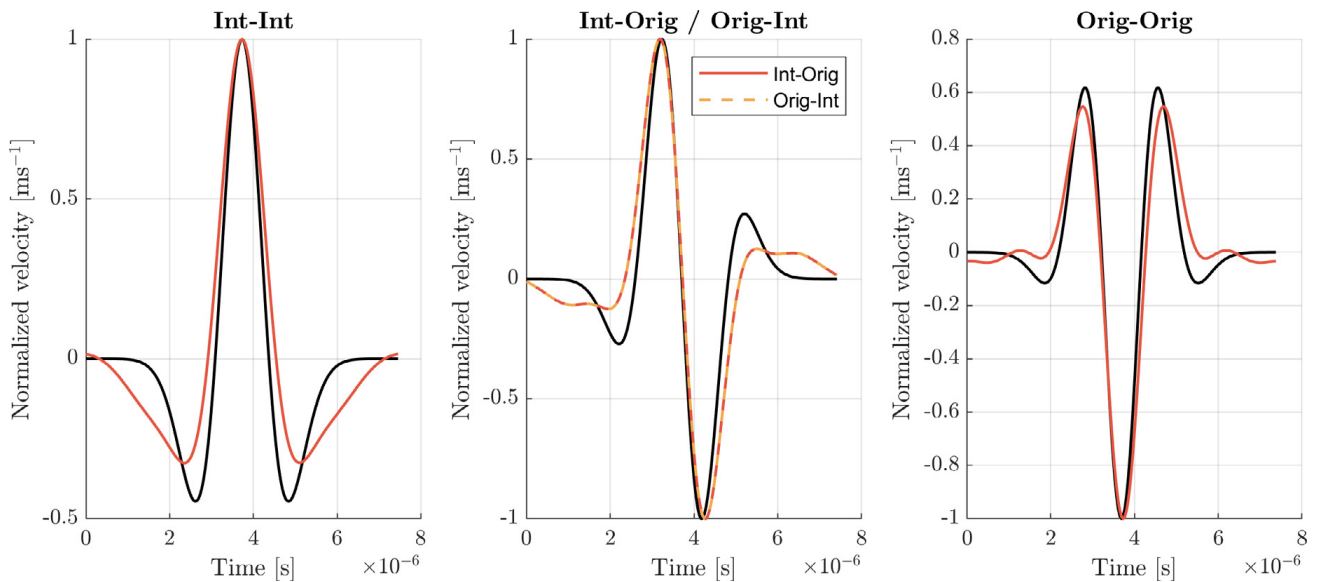


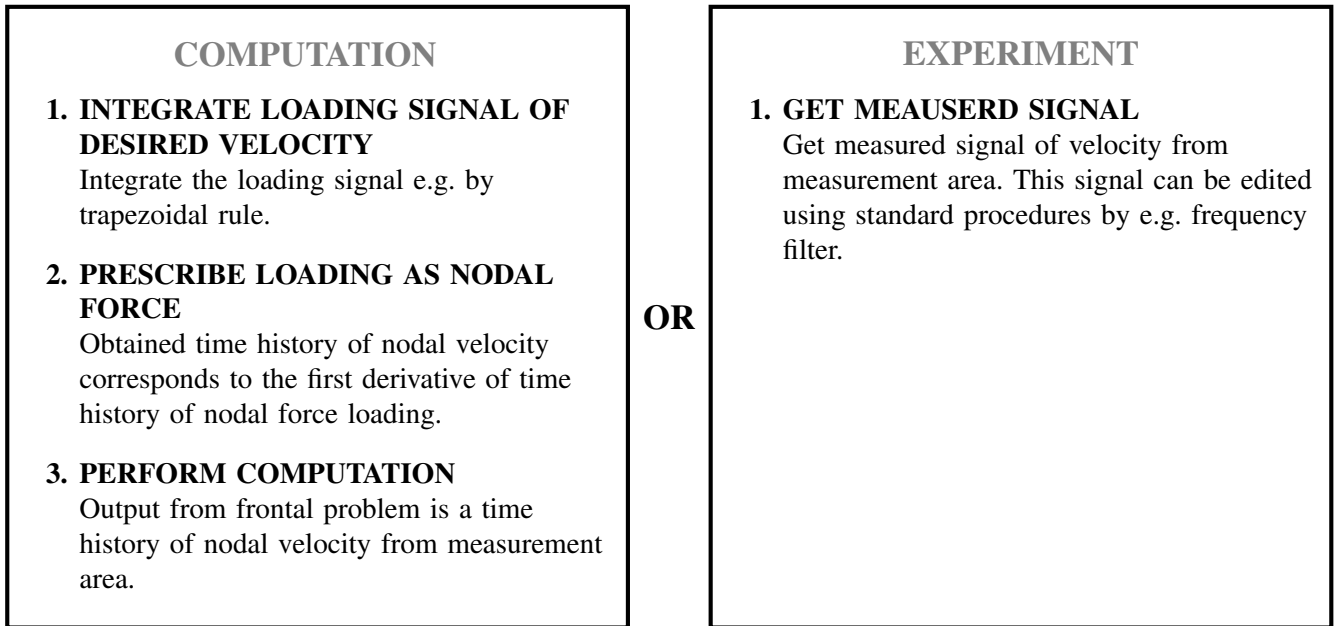
Fig. 12. Reconstructions of the original source for four different combinations of modification of loading signals in frontal and reverse problems, denoted as **Int** and **Orig**. The first indication refers to frontal problem, the second one refers to reverse problem. The key **Int** marks the time integration of the pulse and **Orig** marks the pulse without modification, i.e. without time integration. (For interpretation of the references to color in this figure legend, the reader is referred to the web version of this article.)

time function at the point **B** for reverse problem after reversing of the signal in time. The keys **Int** marks the time integration of the pulse and **Orig** marks the pulse without modification, i.e. without time integration. For example, the combination **Int – Orig** means, that the time function at point **A** is integrated in time and the time function recorded at point **B** is not integrated with respect to time and only reversed in time. Then it is applied into the reverse problem. For the numerical time integration of the signal, the trapezoidal rule is employed with the time step size as in the FE computation. Four combinations of keys occur (**Int – Int**, **Int – Orig**, **Orig – Int**, **Orig – Orig**) and this leads to four reconstructed signals. In the following text, we will see the effect of the time integration of the pulses on time reversal of the original pulse.

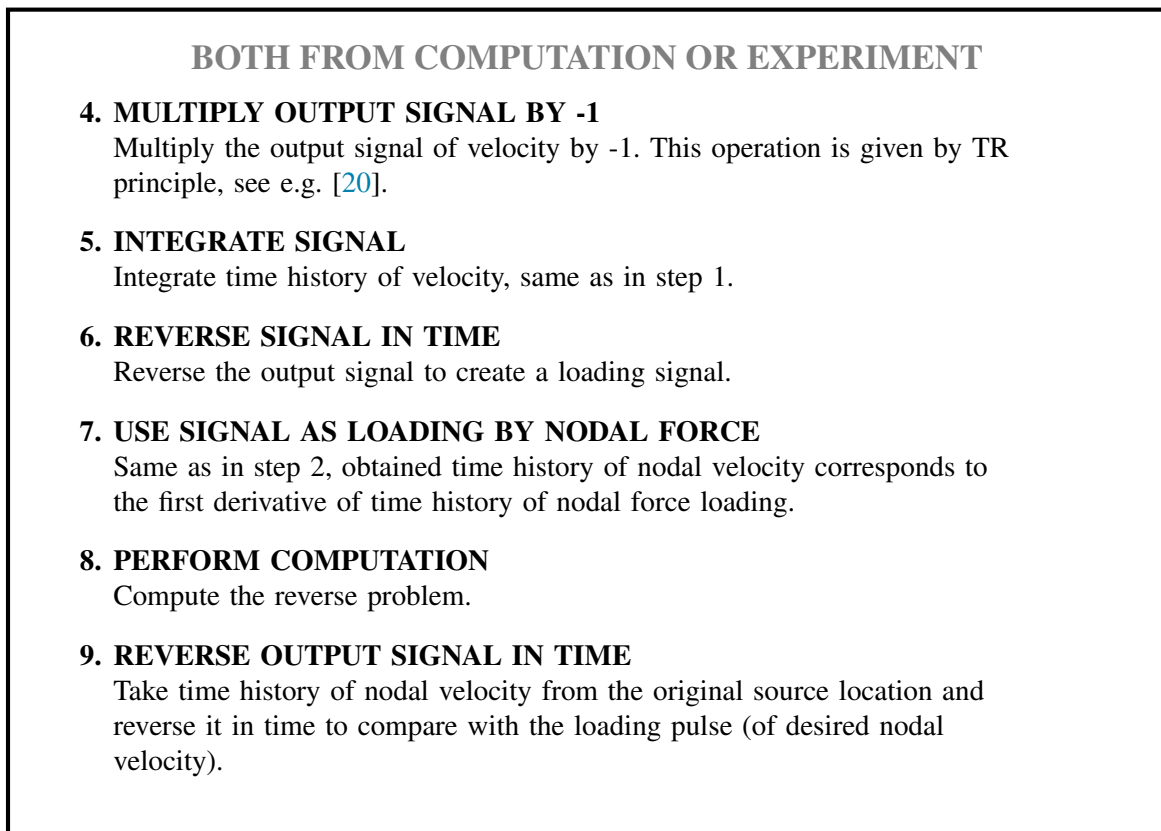
The results normalized with respect to the maximum value are presented in Fig. 12 (red/orange lines). In these graphs, the time histories of velocity are summarized for all four combinations of both integrated and not integrated loading signals. In Fig. 12, we show the time history of the y-components of the reconstructed velocity at the point **A** after the TR simulations for all four combinations of keys. It is needed to say that combinations **Int – Orig**, **Orig – Int** produce the same results due to the linearity of the problem. In all figures in Fig. 12, the corresponding pulse for analytical time history is added as black lines. These lines correspond to time derivatives of the original time function of loading by the nodal force. In Fig. 12(left), the black line corresponds to the Ricker pulse as an original loading pulse, in Fig. 12(middle) corresponds to the first time derivative, and finally in Fig. 12(right) corresponds to the second time derivative. We can say that the combination **Int – Int** produces the correct time history of the original pulse of nodal velocity. The combination **Int – Orig/ Orig – Int** gives the first time derivative of the original pulse, and combination **Orig – Orig** gives the second time derivative of the original pulse. The differences between theoretical pulses and their time derivatives, and numerical results are given by spreading of wave fronts in the reverse task where we use only partial information from the boundary of the domain of interest.

Based on the previous results, the variant **Int – Int** for reconstruction of the original time function is preferred and this TR approach gives to us the correct information for reconstruction of the original source. Based on that knowledge of behavior of time change (time integration) of pulse during the TR numerical experiments, we propose an algorithm for computational TR, Alg. 2. This algorithm, if all steps are kept, leads to a correct reconstruction of the original source. On the left side, one can see the flowchart for full computational approach for TR computations with generating of the ‘experimental data’ on domain Ω_m numerically. On the right side, one can see the flowchart for application of TR using real experimental data in the sense of measured velocity.

FRONTAL PROBLEM



REVERSE PROBLEM



Algorithm 2. Proposed algorithm for practical use of time reversal method. On the left, computational/computational approach, and on the right, experimental/computational approach is presented.

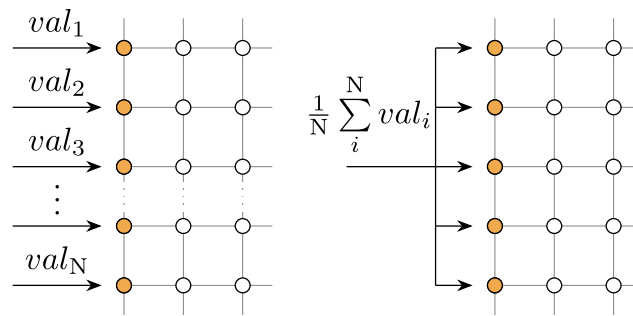


Fig. 13. Scheme of different ways of prescribing the loading values val . N nodes loaded (left), N nodes loaded — averaged (right).

Table 1

Table of computational times T_i .

Indication of task	Number of time steps	Computational time [s]	Number of reflections
T_1	1,000	0.00004009	2.12
T_2	2,000	0.00008018	4.24
T_3	5,000	0.00020045	10.61
T_4	10,000	0.00040090	21.21
T_5	20,000	0.00080180	42.43
T_6	30,000	0.00120270	63.64
T_7	40,000	0.00160360	84.85
T_8	50,000	0.00200450	106.06
T_9	75,000	0.00300675	159.10
T_{10}	100,000	0.00400900	212.13

5.3.3. Comparison of reconstruction accuracy for TYPE I and TYPE II and effect of size of domain Ω_m

In this set of numerical experiments we compare two types of loading — TYPE I (nodal velocity) and TYPE II (nodal force) for application in TR tasks. Also we compare an effect of number of active nodes for prescription of nodal information into the reverse task, where five different numbers of loaded nodes are assumed — one node, five nodes and eleven nodes with separate signals, and the same numbers with averaged signals, see Fig. 13.

Ten different computational times defined by the number of time steps, indicated as T_1, \dots, T_{10} are assumed — see Table 1 for the details. T_i means the time of computation both for frontal and reverse task. The time T_i can be reported as a number of reflections of the longitudinal wave in the domain of interest, for example, the time T_3 corresponds to approximately 10 reflections of longitudinal wave with wave speed c_L between the opposite edges.

Figs. 14 and 15 show values of global cost C_G from Section 4 for all tasks with different times of computation T_i and different numbers of active nodes with/without averaging in reverse task. Fig. 14 presents results for loading of TYPE I and Fig. 15 shows results for loading of TYPE II. Different numbers of active nodes and different lengths of computational times show how the quality of reconstruction changes. Two different types of loading, by nodal velocity and by nodal force, compare two approaches how to solve the problem with standard methods in commercial FE software. Fig. 16 shows contributions of local costs C_1, C_2 and C_3 into global cost for 11 loaded nodes with individual loading signals. One can see that C_1 and C_2 have similar values of the cost functions in this task. C_3 is not dominant for this task. For the evaluation of the global function C_G we prefer the main contribution of C_2 into C_G defined in (14).

For loading of TYPE I, Fig. 14, one can see that the averaging of information causes loss of the accuracy of reconstruction. There is also an effect of number of active nodes on quality of reconstruction. In the physical point view, when we apply prescribed signal as nodal velocity, the boundary is moved with rigidly and this boundary reflects the propagating waves as rigid boundary, which has opposite effect on reflection of stress than the stress-free boundary conditions, see e.g. the Achenbach’s book on wave propagation in solids, Achenbach [1]. Therefore, the TYPE II produces more stable results of reconstruction, see Fig. 15. For bigger amount of active nodes for application of boundary conditions this effect even increases. The time related to T_3 is enough for reconstruction. Based on this numerical study, the TYPE II is preferred in TR technology and as benefit, there is no need to modify the finite element code and only a suitable time integration of the reversed data is needed as a part of the flowchart.

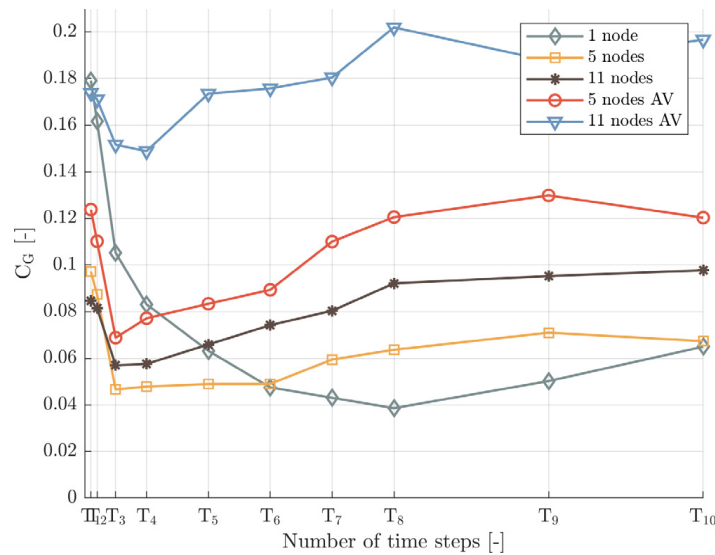


Fig. 14. Global cost C_G , TYPE I - loading by nodal velocities.

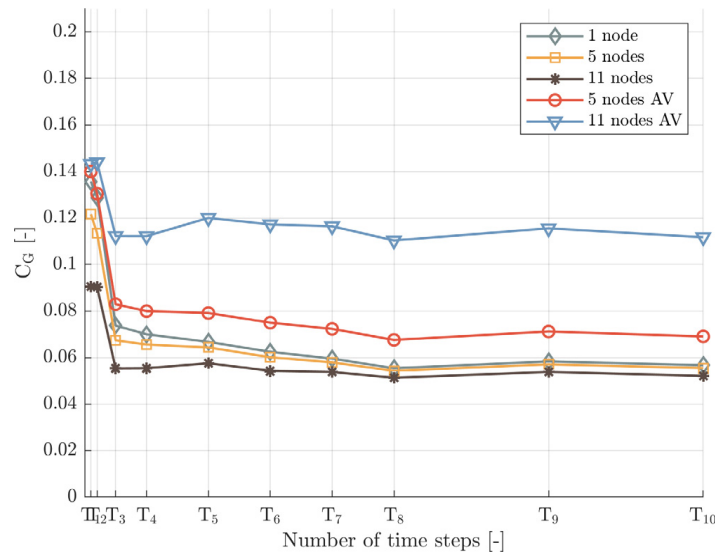


Fig. 15. Global cost C_G , TYPE II - loading by nodal forces.

For the local point of view at the localized point \mathcal{A} , the time histories of the normalized velocity after TR computation of the both types of loading are presented in Fig. 17 (loading by nodal velocity) and Fig. 18 (loading by nodal force). The computations were realized for the time T_{10} and for all numbers of active nodes as mentioned in the previous text. Each reconstructed signal is normalized such that the maximum value is equal to 1, again assuming a linear system which can be scaled arbitrarily. Then the signals are reversed in time, although not necessary thanks to the symmetry of the loading signal. This normalizing of signals enables at least some qualitative comparison of the reconstruction.

For the loading by TYPE I, one can see a different arrival time of the maximum peak depending on number of active nodes in reverse task and averaging of the reversed quantities. On the contrary, the results for the type of loading by TYPE II show stable character and deviation of the signal is relatively small. It means that the TYPE II is preferred for correct reconstruction of the original signal.

5.4. Numerical sensitivity study

We have performed five additional studies of numerical sensitivity, using presented algorithm, Alg. 2, (with loading of Type II). We study the effects of the time step size, mesh size, number of transmitters, domain shape

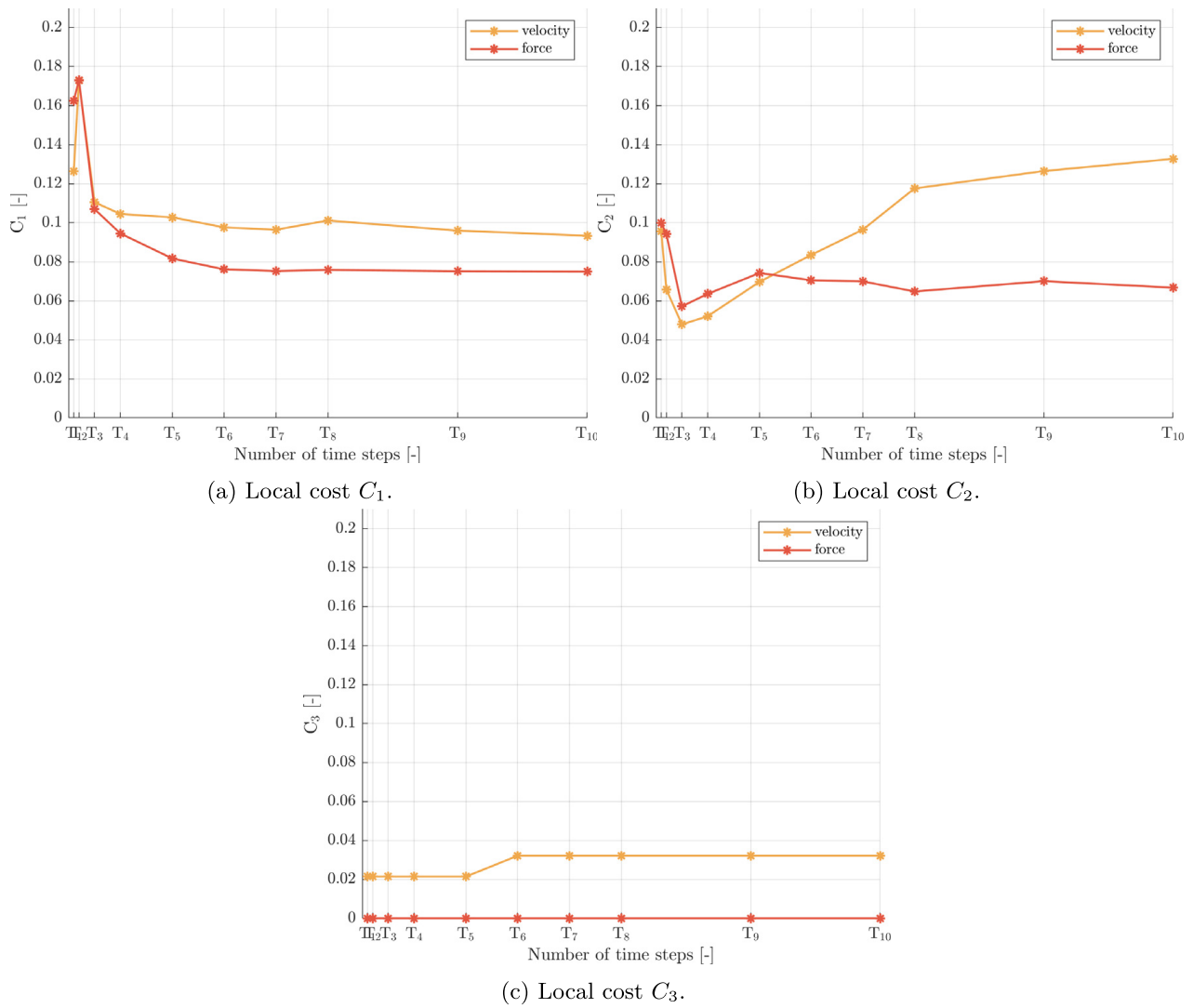


Fig. 16. Local costs $C_1 - C_3$ for both types of loading (TYPE I — nodal velocity, TYPE II — nodal force), 11 nodes loaded with individual signal.

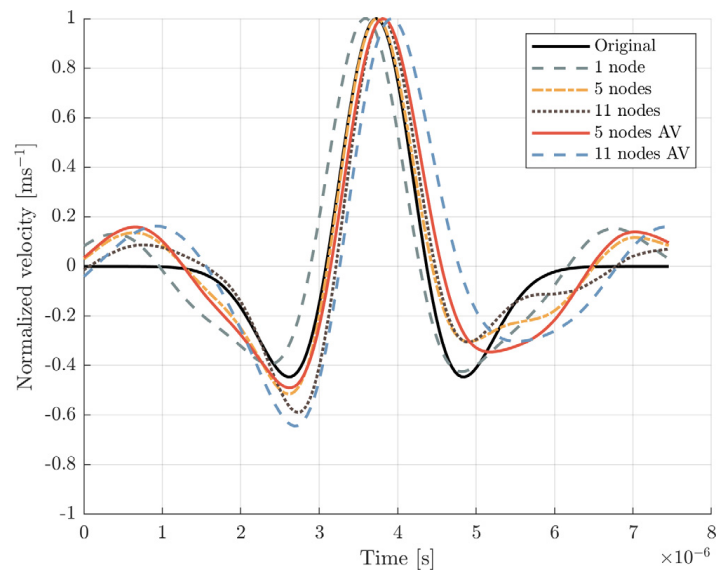


Fig. 17. Reconstructed pulse for time T_{10} , loading of TYPE I - nodal velocities.

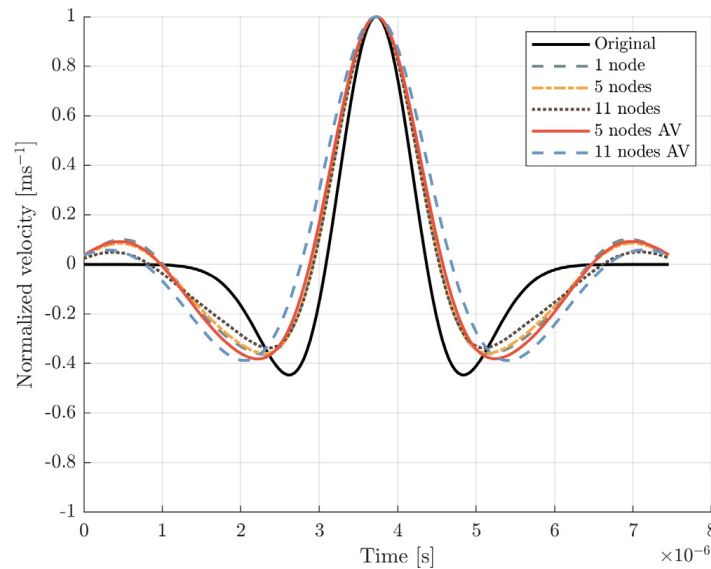


Fig. 18. Reconstructed pulse for time T_{10} , loading of TYPE II — nodal forces.

Table 2
Sensitivity study 1 - input values.

Courant number	Time step size [s]
0.5	$2.673 \cdot 10^{-8}$
(reference) 0.75	$4.009 \cdot 10^{-8}$
0.99	$5.282 \cdot 10^{-8}$

(domain with a hole), and environmental disturbance (background noise) on reconstruction of the original pulse. In each study we focus on the influence of the change of some parameter in reverse task and compare it with the reference one. Again, we use the same FE model as shown in Fig. 1 and Ricker pulse for loading. Eventual changes are commented in description of particular sensitivity study. The computational time for all studies was $T_4 \sim 10,000 \Delta t$. The quality of reconstruction is evaluated only visually here because for the usage of costs we do not perform enough numerical experiments to show some reasonable trend. Following results are more illustrative and show some practical aspects of computational TR.

5.4.1. Sensitivity study 1 - time step size

In Sensitivity study 1 we analyze the influence of the change of the time step size in the reverse problem compared with the frontal problem. We use three different Courant numbers (time step sizes) in the reverse problem. One task is a reference task with the same time step size as in the frontal task, and then one is smaller and the other one is larger than the reference one. See Table 2 for details.

We can state that the change of time steps size has a minor effect on the quality of reconstruction, see Fig. 19. There is only a small time and phase shift apparent which outcome of the temporal-space dispersive behavior of the finite element method depending on time step size, Kolman et al. [27].

5.4.2. Sensitivity study 2 - mesh density

In Sensitivity study 2 we study the effect of changing the FE mesh density in the reverse problem. We use three different meshes in the reverse problem, Courant number $C \doteq 0.75$ in all cases, so the time step size had to be changed. Again, one reverse task is reference with the same mesh as in the frontal task, then one mesh is coarser and the other one is finer. See Table 3 for details.

Very significant impact on the result has the change of FE mesh density, see Fig. 20. Here, the time and phase shift is more apparent than in Sensitivity study 1, though the reconstructed peak is still easily recognizable from the surrounding signal. It can be explained so that the FE model has a dispersive behavior — numerical wave speed

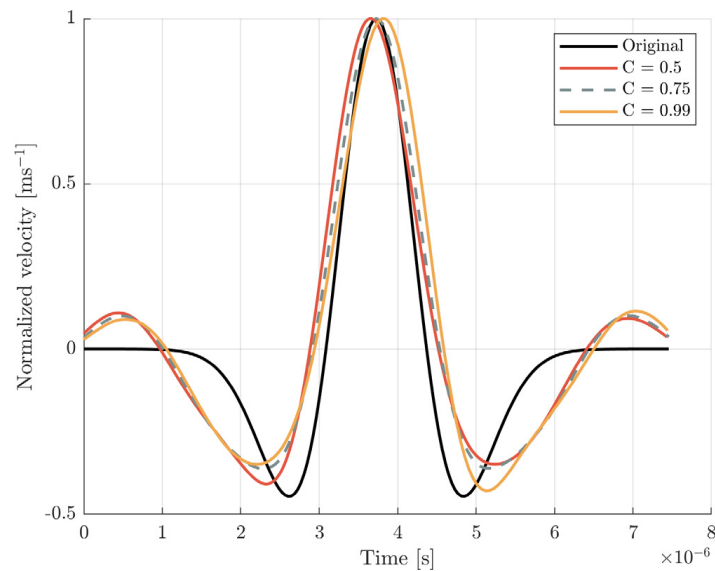


Fig. 19. Sensitivity study 1 - Reconstruction.

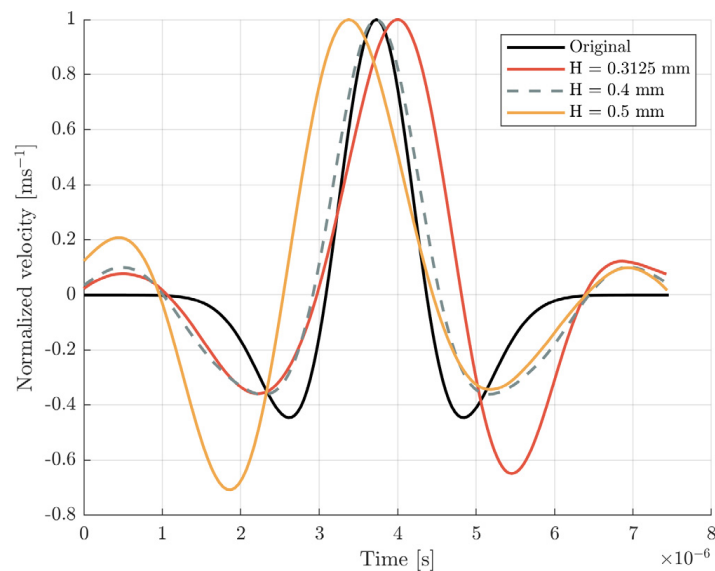


Fig. 20. Sensitivity study 2 - Reconstruction.

Table 3
Sensitivity study 2 - input values.

Element size [mm]	Mesh density	Time step size [s]
0.3125 mm	$320 \times 320 = 102,400$	$3.132 \cdot 10^{-8}$
(reference) 0.4 mm	$250 \times 250 = 62,500$	$4.009 \cdot 10^{-8}$
0.5 mm	$200 \times 200 = 40,000$	$5.011 \cdot 10^{-8}$

depends on the mesh density, see [26], and by change of mesh density this effect is more dominant than the effect of the time step size.

To summarize this sensitivity test, one can see a considerable sensitivity of the TR results on the chosen spatial discretization — mesh size and quality of the finite element mesh. We have to say that the inverse crime, see [9], is coming into our inverse problem in TR. This is a product of the numerical dispersive behavior of the finite element method which depends on the mesh size setting with respect to the wavelength of the propagation elastic waves.

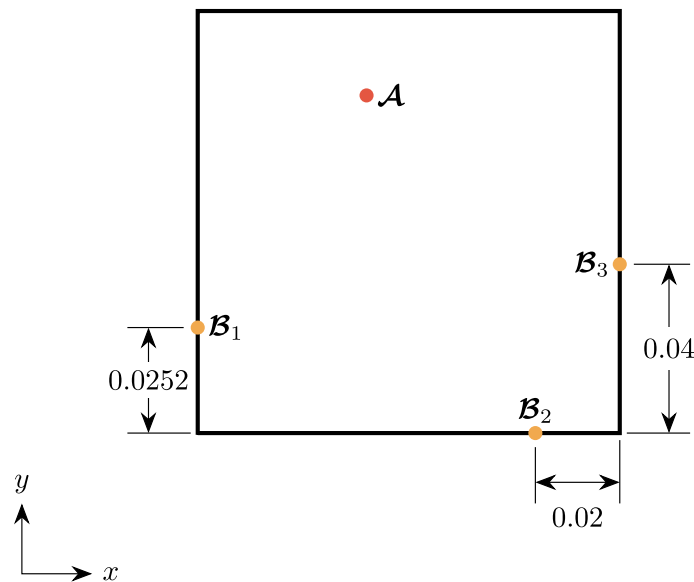


Fig. 21. Sensitivity study 3 - positions of recording points.

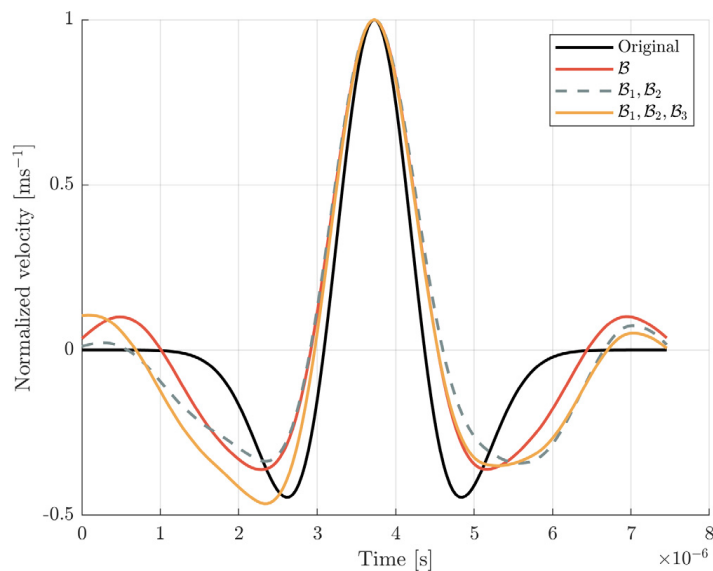


Fig. 22. Sensitivity study 3 - Reconstruction.

5.4.3. Sensitivity study 3 - number of transmitters

In Sensitivity study 3 we study the quality of reconstruction depending on the number of positions used in the frontal problem for recording of the output signals. In these positions the reverse problem is then loaded. The positions are denoted as $\mathcal{B}_1 - \mathcal{B}_3$, and the coordinates are shown in Fig. 21. The positions were chosen randomly. In these three tasks we use step-by-step one (\mathcal{B}_1), two ($\mathcal{B}_1, \mathcal{B}_2$), and three ($\mathcal{B}_1, \mathcal{B}_2, \mathcal{B}_3$) positions of transmitters for recording of the signal used in TR task.

Based on Fig. 22, the number of points \mathcal{B}_i does not cause any time shift. Using more points-transmitters for loading slightly improves the quality of reconstruction.

5.4.4. Sensitivity study 4 - effect of unknown obstacle

Sensitivity study 4 represents a problem where the analyzed domain contains an unknown obstacle. The frontal problem is same as e.g. the reference one in Sensitivity study 1 but besides the reference one we also use a domain with a hole. The dimensions are shown in Fig. 23. See the comparison of velocity wave fields of domains with and

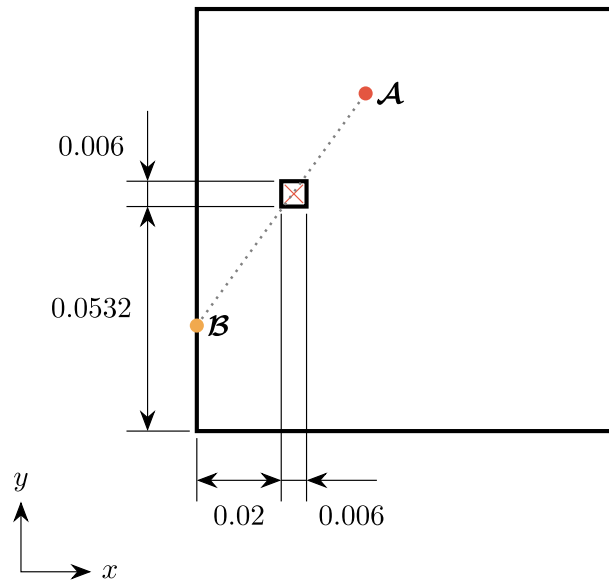
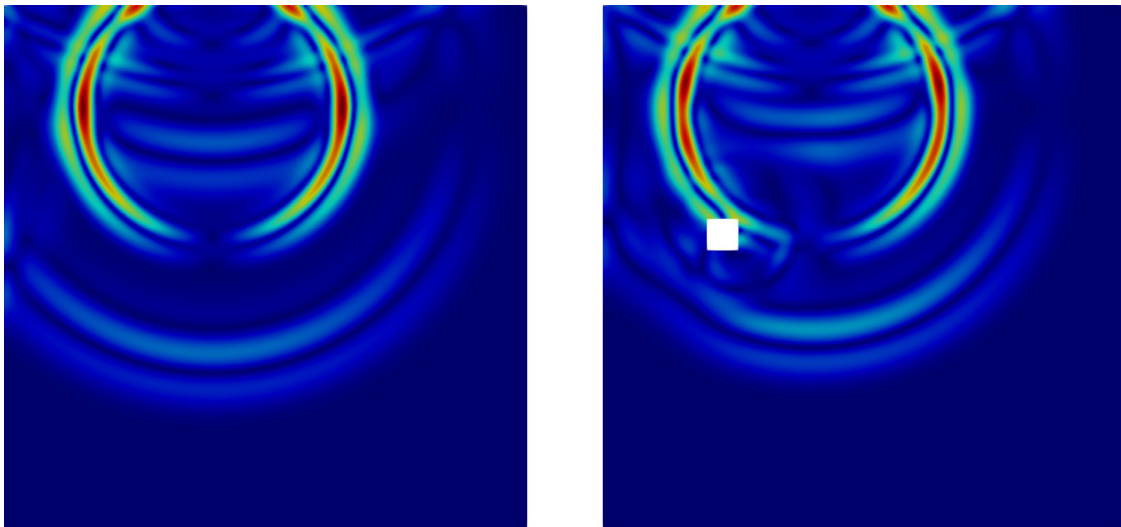


Fig. 23. Sensitivity study 4 - scheme.



(a) A domain without a hole.

(b) A domain with a rectangular hole.

Fig. 24. A snapshot of velocity wave field from the frontal problem for time $300 \Delta t$, comparison of a domain without/with a hole.

without the hole at time $300 \Delta t$, Fig. 24. Both reverse tasks, with reversed signals from domains with and without the hole, are performed on the domain without the hole.

For the successful reconstruction, wave reflections and time of computation play the key role, as says the principal of the TR method. Present obstacle, a small rectangular hole here, behaves as a scatterer and brings another reflections into the domain. This study shows a robustness of TR method and the used approach, as there is only a small difference between reconstructed signals from pure domain and domain with a hole, see Fig. 25.

5.4.5. Sensitivity study 5 - environmental disturbance

In Sensitivity study 5 we study the influence of a preceding disturbance of the system. It is represented by a pseudo random signal, see Fig. 26c, which creates a complex wave field before the Ricker pulse is transmitted. The disturbance signal is a filtered white noise, so that it covers the frequency range of the Ricker pulse and retains zero mean value. This study is designed to test the superposition principle and the robustness of time reversal to

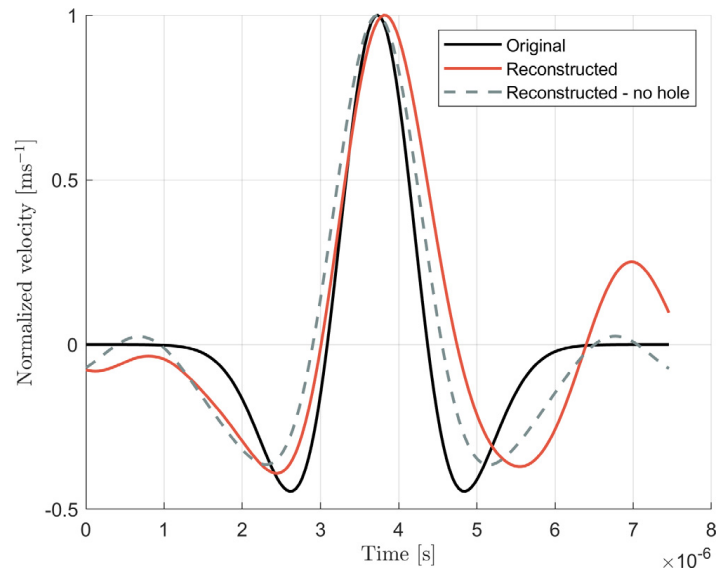
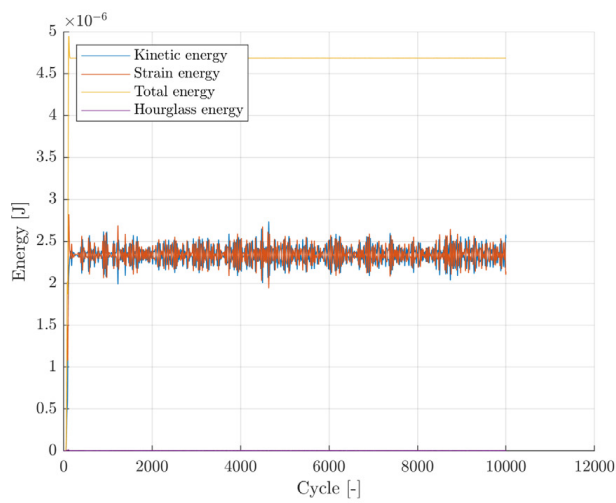
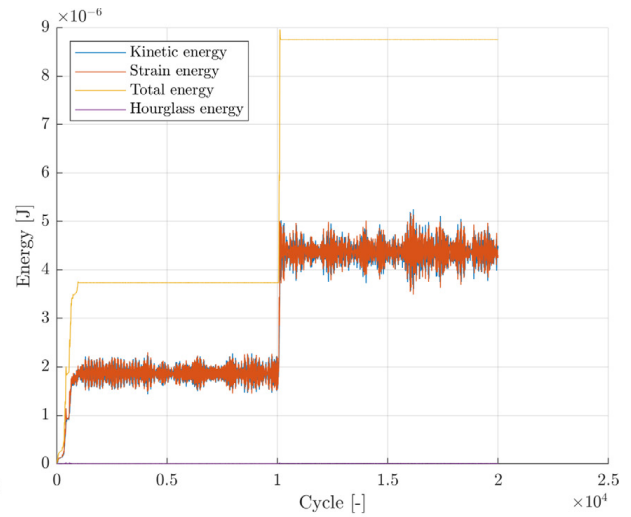


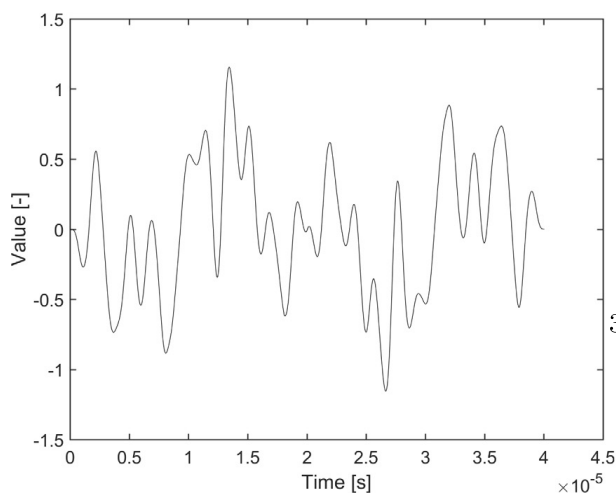
Fig. 25. Sensitivity study 4 - Reconstruction.



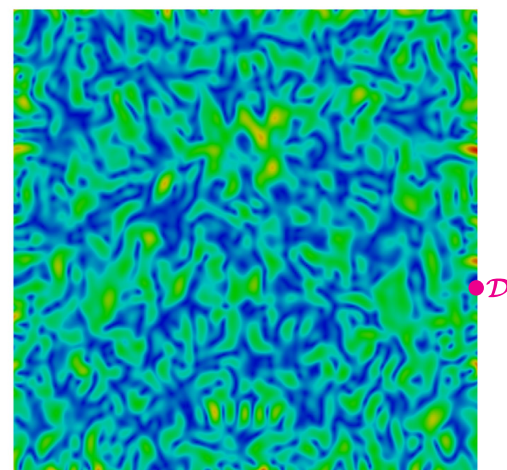
(a) Energy conservation of reference frontal task.



(b) Energy conservation of frontal task with some environmental disturbance.



(c) Pseudo random signal prescribed as an environmental disturbance.



(d) Velocity magnitude distribution at time $10,000\Delta t$ - noise-like wave field.

Fig. 26. Sensitivity study 5 - creation of noise.

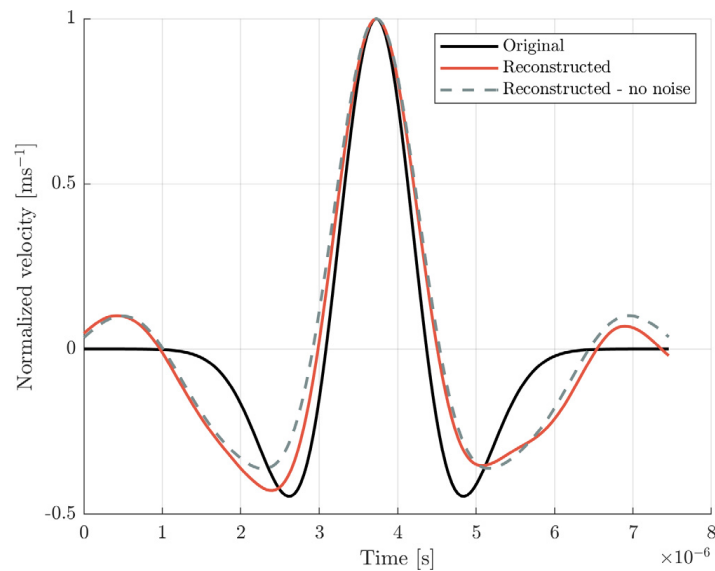


Fig. 27. Sensitivity study 5 - Reconstruction.

environmental disturbances. The computational time is doubled here ($20,000 \Delta t$). At time $t = 0 \Delta t$ the pseudo-random signal is prescribed as a load at arbitrarily chosen location \mathcal{D} , marked in magenta in Fig. 26d. When the classical loading by the Ricker pulse begins at $t = 10,000 \Delta t$, a noise-like wave field is already present in the system, see Fig. 26d. Then only the second half of the output signal is considered as relevant and sent back as a load in the reverse problem. Compare energy conservation on Figs. 26a and 26b for tasks without and with disturbance to see the effect in the total energy. Note that if the task ran until $20,000 \Delta t$, we would see a reconstruction of the disturbance as well.

Result shows, see Fig. 27, that the environmental disturbance does not have any major effect on the quality of reconstruction, which is a well known fact in experimental TR.

6. Conclusions

In this paper, we have proposed an algorithm for practical use of time reversal method in NDT problems in solids. This algorithm, with a set of measured signals corresponding to different types of forming, or excited present defects, should set a path to not only refocusing of energy into the location of some defect, but also to determination of the type of the defect by reconstruction of its time function.

We have suggested a numerical approach based on the explicit finite element method with suitable prescription of reversal boundary conditions. For that, we have performed several numerical tests to compare the behavior of the proposed algorithm, using loading by nodal force, and loading by nodal velocity. For measurement of quality of reconstruction of both types of loading, we have suggested several cost functions. Loading with nodal forces gives more accurate reconstruction of the source and the accuracy increases with length of computation and number of active nodes (size of measurement area). Loading with nodal velocity evinces different trend — reconstruction loses its accuracy when the length of computation increases. On the other hand, both types of loading can be used for localization of the source. In our tests, we have synthesized the measurement data numerically, but the use of our algorithm with real experimental data should lead to correct reconstruction of the time history of the original source, affected mainly by precise assessment of the input parameters. We have also tested the sensitivity of the suggested TR approach to analyze its behavior in simulations of real applications of TR method.

In future work, we plan to employ real experimental data from sensors and use them as input data for TR analysis of localization of cracks and defects in real subjects and structures. Also, we will pay attention to the sensitivity study of material and geometrical parameters in numerical models for reverse tasks.

Acknowledgments

The work was initialized during the bilateral mobility project DAAD-16-12 and Projekt-ID 57219898 funded via DAAD from Federal Ministry of Education and Research, Germany. The work of J. Kober and Z. Převorovský

was supported by the grant projects with No. GA17-22615S of the Czech Science Foundation (CSF) within institutional support RVO:61388998. The work of M. Mračko, R. Kolman and J. Plešek was supported by the Centre of Excellence for Nonlinear Dynamic Behaviour of Advanced Materials in Engineering, Czech Republic CZ.02.1.01/0.0/0.0/15_003/0000493 (Excellent Research Teams) in the framework of Operational Programme Research, Development and Education.

References

- [1] J.D. Achenbach, *Wave Propagation in Elastic Solids*, by J.D. Achenbach, North-Holland Pub. Co.; American Elsevier Pub. Co, Amsterdam, New York, 1973.
- [2] E. Amitt, D. Givoli, E. Turkel, Combined arrival-time imaging and time reversal for scatterer identification, *Comput. Methods Appl. Mech. Engrg.* 313 (2017) 279–302.
- [3] H. Ammari, E. Bretin, J. Garnier, A. Wahab, Time-reversal algorithms in viscoelastic media, *European J. Appl. Math.* 24 (4) (2013) 565–600.
- [4] B.E. Anderson, J. Douma, T.J. Ulrich, R. Snieder, Improving spatio-temporal focusing and source reconstruction through deconvolution, *Wave Motion* 52 (2015) 151–159.
- [5] G. Arfken, *Mathematical Methods for Physicists*, Elsevier, Boston, 2005.
- [6] K.-J. Bathe, *Finite Element Procedures*, Prentice Hall, 1996.
- [7] T. Belytschko, W.E. Bachrach, Efficient implementation of quadrilaterals with high coarse-mesh accuracy, *Comput. Methods Appl. Mech. Engrg.* 54 (3) (1986) 279–301.
- [8] T. Belytschko, W. Liu, B. Moran, K. Elkhodary, *Nonlinear Finite Elements for Continua and Structures*, Wiley, 2013, No Longer used.
- [9] D. Colton, R. Kress, *Inverse Acoustic and Electromagnetic Scattering Theory*, in: *Applied Mathematical Sciences*, No. v. 93, pt. 1, Springer-Verlag, 1992, URL https://books.google.cz/books?id=zbw_vgAACAAJ.
- [10] J.A. Cottrell, T.J.R. Hughes, Y. Bazilevs, *Isogeometric Analysis: Toward Integration of CAD and FEA*, first ed., Wiley Publishing, 2009.
- [11] R. Courant, K. Friedrichs, H. Lewy, Über die partiellen differenzgleichungen der mathematischen Physik, *Math. Ann.* 100 (1928) 32–74.
- [12] S. Dos Santos, Z. Prevorsevsky, Imaging of human tooth using ultrasound based chirp-coded nonlinear time reversal acoustics, *Ultrasonics* 51 (6) (2011) 667–674.
- [13] C. Farhat, F.-X. Roux, A method of finite element tearing and interconnecting and its parallel solution algorithm, *Internat. J. Numer. Methods Engrg.* 32 (6) (1991) 1205–1227.
- [14] C. Felippa, K. Park, The construction of free-free flexibility matrices for multilevel structural analysis, *Comput. Methods Appl. Mech. Engrg.* 191 (2002) 2111–2140.
- [15] M. Fink, Time reversal of ultrasonic fields-part, *IEEE Trans. Ultrason. Ferroelectr. Freq. Control* 39 (5) (1992) 555–566.
- [16] M. Fink, Time-reversal mirrors, *J. Phys. D: Appl. Phys.* 26 (1993) 1333–1350.
- [17] M. Fink, Time reversal and phase conjugation with acoustic waves: industrial and medical applications, in: *Conference on Lasers and Electro-Optics*, Vol. 3, 2005, pp. 2334–2335.
- [18] M. Fink, G. Montaldo, M. Tanter, Time-reversal acoustics in biomedical engineering, *Annu. Rev. Biomed. Eng.* 5 (1) (2003) 465–497.
- [19] D. Givoli, Time reversal as a computational tool in acoustics and elastodynamics, *J. Comput. Acoust.* 22 (03) (2014) 143000.
- [20] D. Givoli, E. Turkel, Time reversal with partial information for wave refocusing and scatterer identification, *Comput. Methods Appl. Mech. Engrg.* (2012) 223–242.
- [21] R. Gonzalez, *Digital Image Processing*, Prentice Hall, Upper Saddle River, N.J, 2008.
- [22] J.O. Hallquist, *LS-Dyna Theory Manual*, Livermore Software Technology Corporation, 2006.
- [23] C. He, Q. Zhang, J. Huang, Passive time reversal communication with cyclic shift keying over underwater acoustic channels, *Appl. Acoust.* 96 (2015) 132–138.
- [24] T.J.R. Hughes, *The Finite Element Method: Linear Static and Dynamic Finite Element Analysis*, Dover Publication, 2000.
- [25] K. Kimoto, K. Nakahata, T. Saitoh, An elastodynamic computational time-reversal method for shape reconstruction of traction-free scatterers, *Wave Motion* 72 (2017) 23–40.
- [26] R. Kolman, J. Plešek, M. Okrouhlík, D. Gabriel, Grid dispersion analysis of plane square biquadratic serendipity finite elements in transient elastodynamics, *Internat. J. Numer. Methods Engrg.* 96 (1) (2013) 1–28.
- [27] R. Kolman, J. Plešek, J. Červ, M. Okrouhlík, P. Pařík, Temporal-spatial dispersion and stability analysis of finite element method in explicit elastodynamics, *Internat. J. Numer. Methods Engrg.* 106 (2) (2016) 113–128.
- [28] Y. Kwak, S.M. Park, J. Lee, J. Park, Rattle noise source localization through the time reversal of dispersive vibration signals on a road vehicle, *Wave Motion* 93 (2020) 102452.
- [29] C.S. Larmat, R.A. Guyer, P.A. Johnson, Time-reversal methods in geophysics, *Phys. Today* 63 (8) (2010) 31–35.
- [30] I. Levi, E. Turkel, D. Givoli, Time reversal for elastic wave refocusing and scatterer location recovery, *J. Comput. Acoust.* 23 (1) (2015) 1450013.
- [31] C. Lopatin, D. Rabinovich, D. Givoli, E. Turkel, Computational time reversal for NDT applications using experimental data, *J. Nondestruct. Eval.* (2017) 36–48.
- [32] A. Love, *A Treatise on the Mathematical Theory of Elasticity*, University Press, 1934.
- [33] W. Mu, J. Sun, G. Liu, S. Wang, High-resolution crack localization approach based on diffraction wave, *Sensors (Basel)* 19 (8) (2019).
- [34] C.G. Panagiotopoulos, Y. Petromichelakis, C. Tsogka, Time reversal and imaging for structures, *Lect. Notes Civ. Eng.* 2 (2017) 159–182.

- [35] H.W. Park, S.B. Kim, H. Sohn, Understanding a time reversal process in lamb wave propagation, *Wave Motion* 46 (7) (2009) 451–467.
- [36] A. Parvulescu, C. Clay, Reproducibility of signal transmissions in the ocean, *Radio Electron. Eng.* 29 (4) (1965) 223–228.
- [37] G. Ribay, S. Catheline, D. Clorennec, R.K. Ing, N. Quieffin, M. Fink, Acoustic impact localization in plates: Properties and stability to temperature variation, *IEEE Trans. Ultrason. Ferroelectr. Freq. Control* 54 (2) (2007) 378–385.
- [38] W. Sachse, K. Yamaguchi, J. Roget, A. (Association), *Acoustic Emission: Current Practice and Future Directions*, ASTM STP 1077, ASTM, 1991.
- [39] G. Strang, *Linear Algebra and Its Applications*, Cengage Learning, 2005.
- [40] Y. Wang, Frequencies of the ricker wavelet, *GEOPHYSICS* 80 (2) (2015) A31–A32.
- [41] G. Zhang, J.M. Hovem, H. Dong, L. Liu, Coherent underwater communication using passive time reversal over multipath channels, *Appl. Acoust.* 72 (7) (2011) 412–419.



Full field computing for elastic pulse dispersion in inhomogeneous bars

A. Berezovski^d, R. Kolman^{a,*}, M. Berezovski^b, D. Gabriel^a, V. Adámek^c

^a Institute of Thermomechanics, v.v.i., The Czech Academy of Sciences, Dolejškova 1402/5, 182 00 Praha 8, Czech Republic

^b Department of Mathematics, Embry-Riddle Aeronautical University, 600 S. Clyde Morris Boulevard, Daytona Beach, FL 32114-3990, USA

^c NTIS – New Technologies for the Information Society, Faculty of Applied Sciences, University of West Bohemia, Technická 8, 301 00 Pilsen, Czech Republic

^d Department of Cybernetics, School of Science, Tallinn University of Technology, Akadeemia 21, 12618 Tallinn, Estonia



ARTICLE INFO

Keywords:

Wave propagation
Wave dispersion
Heterogeneous solids
Finite element method
Finite volume method

ABSTRACT

In the paper, the finite element method and the finite volume method are used in parallel for the simulation of a pulse propagation in periodically layered composites beyond the validity of homogenization methods. The direct numerical integration of a pulse propagation demonstrates dispersion effects and dynamic stress redistribution in physical space on the example of a one-dimensional layered bar. Results of numerical simulations are compared with the analytical solution constructed specifically for the considered problem. The analytical solution as well as numerical computations show the strong influence of the composition of constituents on the dispersion of a pulse in a heterogeneous bar and the equivalence of results obtained by two numerical methods.

1. Introduction

Wave propagation in a slender heterogeneous solid bar is the typical test problem for models of composite materials [1–4, e.g.]. The modeling is necessary because macroscopic properties of composite materials are strongly influenced by the properties of their constituents. The macroscopic properties are usually determined by a homogenization, which yields the effective stresses and strains acting on the effective material.

The basic idea of homogenization consists in a replacement of a heterogeneous solid by a homogeneous one which, from the macroscopic point of view, behaves in the same way, as do its constituents, but with different, effective, values of the appropriate material constants [5]. This idea reappeared many times in the last two centuries, as it is indicated in recent reviews [5–8]. Mathematical details of classical homogenization models can be found in [9].

Layered periodic materials represent the simplest possible pattern of composites from the theoretical point of view. Their modeling also has a rich history [10]. Constitutive models of effective properties for such materials are still under development using either ensemble averaging [11,12], or integration over unit cell [13,14], or scattering response [15]. However, as it is pointed out by Willis [16], "The broad conclusion is that an "effective medium" description of a composite medium provides a reasonable approximation for its response, so long as the predicted "effective wavelength" is larger than two periods of

microstructure – say at least 2.5λ ". This is confirmed recently on the example of Mindlin's microelasticity theory [17]. It is worth therefore to build tools for the analysis of the interaction between layers and waves with the shorter wavelength. The natural choice for such tools is provided by numerical methods due to their flexibility and universality. However, we need to be insured in the accuracy and stability of them. It is well known that numerical simulation of wave propagation even in a homogeneous solid bar under shock loading is under discussion so far both in the context of finite volume [18,19] and finite element methods [20–23]. This is why two different numerical methods – finite element method and finite volume method – are applied in the paper for the simulation of a pulse propagation in a slender heterogeneous solid bar. The pulse propagation is preferable from the practical point of view [24], while theoretically only the behavior of dispersion curves is of interest [25–27] e.g.

It should be repeated, following Zohdi [28] that "solutions to partial differential equations, of even linear material models, at infinitesimal strains, describing the response of small bodies containing a few heterogeneities are still open problems". Fortunately, the analytical solution is constructed specifically for the considered test problem by means of the Laplace transform technique [29].

The objective of the paper is to demonstrate the influence of the composition of alternating layers on the dispersion of a short pulse and to compare results of simulation obtained by two different numerical methods with the analytical solution of the problem.

* Corresponding author.

E-mail addresses: Arkadi.Berezovski@cs.ioc.ee (A. Berezovski), kolman@it.cas.cz (R. Kolman), mihhail.berezovski@erau.edu (M. Berezovski), gabriel@it.cas.cz (D. Gabriel), vadamek@kme.zcu.cz (V. Adámek).

<https://doi.org/10.1016/j.compstruct.2018.07.055>

Received 23 January 2018; Received in revised form 26 June 2018; Accepted 16 July 2018

Available online 29 July 2018

0263-8223/ © 2018 Elsevier Ltd. All rights reserved.

In this paper, we consider the propagation of a finite pulse, the length of which is comparable with the size of heterogeneities. The dispersion of the pulse is provided by the wave reflection and transmission in periodic layered structure where each layer is dispersionless. It is clearly demonstrated that strong dispersion effects depend not only on the size of heterogeneities but also on their mutual position.

2. Formulation of the problem

We consider wave propagation in a bar of a constant cross section. The motion is assumed being one-dimensional and considered within the linear theory of elastodynamics [30, e.g.] It is governed by the balance of linear momentum, which in the absence of body forces has the form

$$\rho \frac{\partial v}{\partial t} - \frac{\partial \sigma}{\partial x} = 0, \tag{1}$$

where ρ is the matter density, v is the particle velocity, σ is the one-dimensional Cauchy stress. In the linear elasticity the Cauchy stress obeys the Hooke law $\sigma = E \varepsilon$, where E is the Young modulus and ε is the one-dimensional strain. The wave speed in a bar is given for one-dimensional case by $c = \sqrt{E/\rho}$, therefore, the Hooke law has the following form

$$\sigma = \rho c^2 \varepsilon. \tag{2}$$

The strain and velocity are related by the compatibility condition

$$\frac{\partial \varepsilon}{\partial t} = \frac{\partial v}{\partial x}. \tag{3}$$

In terms of the displacement, the balance of linear momentum is represented in the form of the wave equation

$$\frac{\partial^2 u}{\partial t^2} = c^2 \frac{\partial^2 u}{\partial x^2}, \tag{4}$$

since the displacement u is connected to the strain and particle velocity by

$$v = \frac{\partial u}{\partial t}, \quad \varepsilon = \frac{\partial u}{\partial x}. \tag{5}$$

It should be noted that the material parameters ρ and c are distinct in different parts of the bar. However, they keep constant values for each computational cell in numerical methods for the bar with a piecewise constant distribution of material parameters such as Young modulus and matter density.

It is assumed that the bar is occupied the interval $0 \leq x \leq L$. Initially, the bar is at rest. The left end of the bar is loaded by the pulse, the shape of which is formed by an excitation of the stress for a limited time period (Fig. 1). Then the stress at the left end is zero. The right end of the bar is fixed.

For convenience, the bar is divided into three parts. The left and the right parts of the bar are supposed to be homogeneous and made from the same stiff material. The central part of the bar contains inhomogeneity provided by inclusions of a more soft materials (see Fig. 2). The solution of system of Eqs. (1)–(3) or Eq. (4) satisfying formulated initial and boundary conditions is obtained by means of analytical and numerical methods in the following sections.

3. Analytical solution

To verify the correctness and the accuracy of numerical results presented in Section 4, the analytical solution of the above described



Fig. 1. A scheme of the test problem - a pulse loaded free-fixed bar.

problem was derived. The main idea of the analytical procedure is based on the fact that the final solution for a bar with a piecewise constant distribution of material properties can be constructed from the solutions derived for each of homogeneous parts of the bar combined through the boundary conditions formulated at their interfaces.

It is clear that the propagation of longitudinal waves in arbitrary i th homogeneous part is formally described by the same equation as (4). The solution for such particular problem with general boundary conditions can be simply derived based on the solution presented in [30]. Applying the Laplace transform in time [29] to (4) with zero initial conditions one obtains a simple ODE the solution of which can be written as

$$\bar{u}_i(x_i, p) = C_{1,i}(p) \sinh\left(\frac{px_i}{c_i}\right) + C_{2,i}(p) \cosh\left(\frac{px_i}{c_i}\right), \tag{6}$$

where p is a complex number. The variable x_i in (6) represents a local coordinate defined for the i th part of the bar, the constant c_i is the wave speed in this part and the function $\bar{u}_i(x_i, p)$ denotes the Laplace transform of the corresponding displacement $u_i(x_i, t)$. The unknown complex functions $C_{1,i}$ and $C_{2,i}$ can then be determined through the boundary conditions of the problem and through the conditions of displacement and stress continuity formulated for each interface between two parts with different material properties. It leads to a system of algebraic equations in complex domain. Substituting its solution into (6) one obtains the final solution of the problem in Laplace domain.

The last step of the analytical procedure consists in the inversion of previously mentioned formulas back to time domain. It can be done analytically by means of the residue theorem in this case or numerically by using a suitable algorithm. Given the low computational demands and the versatility, the latter approach was used in this work. In particular, an algorithm based on FFT and Wynn’s epsilon accelerator was applied to manage the inverse Laplace transform problem. As proved in [29], this algorithm is effective and robust and it gives very precise results for various problems of elastodynamics. The analytical results for specific study cases are presented together with the numerical solutions in Section 5.

4. Numerical procedures

Application of numerical methods suggests a discretization in space and time. For this purpose, the interval $0 \leq x \leq L$ is divided into N elements of the same size. The state of each element is described differently in distinct methods. In this paper, we compare results obtained by the finite element method (FEM) and the finite volume method (FVM) in case of explicit approaches of these methods.

4.1. Finite element method and explicit time integration

In this section, we shortly remind the basic of the finite element method in the one-dimensional case for linear elastodynamics. Spatial discretization of elastodynamics problems by the finite element method leads to the matrix form [31]

$$\mathbf{M}\dot{\mathbf{d}}(t) + \mathbf{K}\mathbf{d}(t) = \mathbf{F}(t), \quad t \in [0, T], \tag{7}$$

$$\mathbf{d}(0) = \mathbf{d}_0, \tag{8}$$

$$\dot{\mathbf{d}}(0) = \dot{\mathbf{d}}_0. \tag{9}$$

Here \mathbf{M} denotes the mass matrix, \mathbf{K} marks the stiffness matrix, \mathbf{F} is the time-dependent load vector, \mathbf{d} , $\dot{\mathbf{d}}$ and $\ddot{\mathbf{d}}$ contain nodal variables, namely, displacements, velocities, and accelerations, respectively, t is the time and dots denote time derivatives. Initial values for displacements and velocities are denoted by \mathbf{d}_0 and $\dot{\mathbf{d}}_0$. The initial acceleration vector should satisfy the equation of motion at the time t_0 : $\mathbf{M}\ddot{\mathbf{d}}_0 + \mathbf{K}\mathbf{d}_0 = \mathbf{F}_0$.

Practically, the stiffness matrix \mathbf{K} and the mass matrix \mathbf{M} are

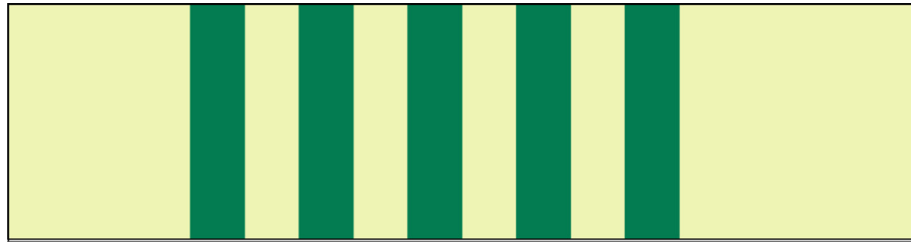


Fig. 2. Distribution of thick periodic layers. Yellow domain corresponds to material 1, green domain – to material 2. (For interpretation of the references to colour in this figure legend, the reader is referred to the web version of this article.)

defined by the relationships

$$\mathbf{K} = \int_{\Omega} \mathbf{B}^T \mathbf{E} \mathbf{B} \, d\Omega, \quad \mathbf{M} = \int_{\Omega} \rho \mathbf{N}^T \mathbf{N} \, d\Omega, \tag{10}$$

and the right hand side is given

$$\mathbf{F} = \int_{\Gamma_N} \mathbf{N}^T h \, d\Gamma - \int_{\Omega} \mathbf{B}^T \mathbf{E} \mathbf{B} \mathbf{g} \, d\Omega - \int_{\Omega} \rho \ddot{\mathbf{g}} \mathbf{N}^T \, d\Omega, \tag{11}$$

where \mathbf{B} is the strain–displacement matrix, \mathbf{N} stores the displacement shape functions, h is the traction prescribed on the boundary Γ_N , \mathbf{g} is the displacement prescribed as the Dirichlet boundary condition.

In this paper, we assume linear shape functions and diagonal mass matrix obtained by row-summing of the consistent mass matrix given by (10). The mass matrix, \mathbf{M} , and the stiffness matrix, \mathbf{K} , are evaluated by the Gauss–Legendre quadrature formula [31].

For time integration, we use the central difference method [31] which is based on the approximate relationships between the nodal displacements \mathbf{d} , velocities \mathbf{v} and accelerations \mathbf{a} so that

$$\mathbf{v}^k = \frac{1}{2\Delta t} (\mathbf{d}^{k+1} - \mathbf{d}^{k-1}), \tag{12}$$

$$\mathbf{a}^k = \frac{1}{(\Delta t)^2} (\mathbf{d}^{k+1} - 2\mathbf{d}^k + \mathbf{d}^{k-1}). \tag{13}$$

Here the superscript k denotes the time level and Δt is the time step size. Substituting relationships (12) and (13) into equations of motion (7) at time t , we get a system of algebraic equations which we can solve for displacements at the next time step $t + \Delta t$

$$\mathbf{M} \mathbf{d}_{n+1} = \mathbf{F}_n (\Delta t)^2 - (\mathbf{K} (\Delta t)^2 - 2\mathbf{M}) \mathbf{d}_n - \mathbf{M} \mathbf{d}_{n-1}. \tag{14}$$

Stress field $\sigma(x, t_{n+1})$ is computed from the approximated displacement field given by \mathbf{d}_{n+1} .

This explicit method is only conditionally stable. The critical time step Δt_{cr} securing the stability of the central difference method for a linear undamped system is $\Delta t_{cr} = 2/\omega_{max}$ [32], where ω_{max} being the maximum eigenfrequency related to the maximum eigenvalue λ_{max} of the generalized eigenvalue problem $\mathbf{K} \mathbf{u} = \lambda \mathbf{M} \mathbf{u}$ by $\omega^2 = \lambda$. In the one-dimensional case with a structured mesh in a homogeneous material, Δt_{cr} is exactly given by $\Delta t_{cr} = h/c$, where h is the finite element size and c is the wave speed in an elastic bar. The time integration by the critical time step produces results without numerical dispersion in 1D case, see [33].

4.2. Finite volume method

In this section, we shortly introduce the finite volume scheme based on the approach presented in [34]. In finite volume methods, the fields of interest (stress and velocity fields) are uniform inside each element [35]. This means that shape functions are piecewise constant. Though this is not a good approximation, it can be interpreted in terms of thermodynamic systems [36]. Since we cannot expect that this thermodynamic system is in equilibrium, its local equilibrium state is described by averaged values of field quantities. Therefore, so-called excess quantities are introduced in the spirit of the thermodynamics of discrete systems

$$\sigma = \bar{\sigma} + \Sigma, \quad v = \bar{v} + \mathcal{V}. \tag{15}$$

Here overbars denote averaged quantity and Σ and \mathcal{V} are the corresponding excess quantities. Excess quantities represent the difference between the values of entire and averaged fields.

Integrating the balance of linear momentum (1) over the computational cell under the assumption of constant material parameters (Young modulus, matter density) per cell we have

$$\rho \frac{\partial}{\partial t} \int_{x_n}^{x_{n+1}} v \, dx = \sigma_n^+ - \sigma_n^- = \bar{\sigma}_n + \Sigma_n^+ - \bar{\sigma}_n - \Sigma_n^- = \Sigma_n^+ - \Sigma_n^-, \tag{16}$$

where superscripts ”+” and ”-” denote values of the quantities at right and left boundaries of the cell, respectively. The corresponding integration of the kinematic compatibility (3) results in

$$\frac{\partial}{\partial t} \int_{x_n}^{x_{n+1}} \varepsilon \, dx = v_n^+ - v_n^- = \bar{v}_n + \mathcal{V}_n^+ - \bar{v}_n - \mathcal{V}_n^- = \mathcal{V}_n^+ - \mathcal{V}_n^-. \tag{17}$$

Averaged quantities are defined as follows:

$$\bar{v}_n = \frac{1}{\Delta x} \int_{x_n}^{x_{n+1}} v(x, t_k) \, dx, \quad \bar{\varepsilon}_n = \frac{1}{\Delta x} \int_{x_n}^{x_{n+1}} \varepsilon(x, t_k) \, dx. \tag{18}$$

Standard approximation of time derivatives in (16) and (17) allows us to write a first-order Godunov-type scheme in terms of averaged and excess quantities

$$(\rho \bar{v})_n^{k+1} - (\rho \bar{v})_n^k = \frac{\Delta t}{\Delta x} (\Sigma_n^+ - \Sigma_n^-), \tag{19}$$

$$\bar{\varepsilon}_n^{k+1} - \bar{\varepsilon}_n^k = \frac{\Delta t}{\Delta x} (\mathcal{V}_n^+ - \mathcal{V}_n^-). \tag{20}$$

Here the superscript k denotes time step and the subscript n denotes the number of the computational cell.

Though excess quantities are determined formally everywhere inside elements, we need to know only their values at the boundaries of the elements, where they describe the interactions between neighboring elements. The values of excess quantities at the boundaries (numerical fluxes) are determined by the continuity of entire fields

$$(\bar{\sigma})_{n-1} + (\Sigma^+)_{n-1} = (\bar{\sigma})_n + (\Sigma^-)_n, \tag{21}$$

$$(\bar{v})_{n-1} + (\mathcal{V}^+)_{n-1} = (\bar{v})_n + (\mathcal{V}^-)_n, \tag{22}$$

and the conservation of the Riemann invariants [36]

$$\rho_n c_n \mathcal{V}_n^- + \Sigma_n^- = 0, \tag{23}$$

$$\rho_{n-1} c_{n-1} \mathcal{V}_{n-1}^+ - \Sigma_{n-1}^+ = 0. \tag{24}$$

The obtained system of linear equations for excess quantities (21)–(24) is solved exactly. Having the values of numerical fluxes, we can update the state of each element for the next time step by means of numerical scheme (19)–(20). The described procedure is in fact the conservative wave-propagation algorithm [34]. As the result, the reflection and transmission of waves at each interface are handled automatically. The scheme is explicit and solved without a matrix solver. The mentioned scheme is conditionally stable for the time step size Δt satisfying the stability condition in the form $\Delta t \leq \Delta x/c$, where Δx is the grid size.

In both mentioned explicit computational methods for wave

propagation in heterogeneous bars, we choose the time step size as $\Delta t = \min(\Delta x_{cell}/c_{0cell})$ over all cells.

5. Results of numerical simulations

In this section, we compare several results of simulations of wave propagation in heterogeneous bars with corresponding analytical solutions.

5.1. Two-phase layered composite

We start with the simulation of a pulse propagation in the so-called two-phase layered composite following the terminology introduced in [14]. This means that the heterogeneity is composed by alternating layers of two different materials. The properties of the matrix material for the test problem are chosen artificially. In the dimensionless setting they are the following: $\rho_1 = 1, c_1 = 1$, with corresponding $E_1 = c_1^2 \rho_1 = 1$. Accordingly, the dimensionless properties of embedded layers are: $\rho_2 = 0.6, c_2 = 0.96$, with $E_2 = 0.55296$. The computational domain is divided into 1500 elements of the same size. Choosing the dimensionless length of the bar equal to 1, we have for the size of a space step $\Delta x = 1/1500$. The choice of the time step is indicated at the end of the previous section. The thickness of each layer is equal to 90 space elements. The alternating layers are placed starting from 300th space step until 1200th space step (Fig. 2). We focus on the propagation of a pulse with finite time duration. Initial pulse is formed by the excitation of stress at the left end of the bar

$$F(t) = \sigma(0, t) = \frac{1}{2}(1 + \cos(\pi(t-20)/20)). \tag{25}$$

The time duration of the initial pulse is set with respect to the size of layers and wave speed in layers. The length of the initial pulse is shorter than the size of layers in this case. Its shape is shown in Fig. 3. Its frequency spectrum is given in the next figure with a zooming of small frequencies area (Fig. 4).

Fig. 5 shows the evolution of the initial pulse in time due to interaction with layers of different materials. In this Fig., vertical lines display the boundaries of distinct layers and arrows indicate the direction of propagation of the main pulse. Now we compare results of numerical simulations with the analytical solution of the pulse propagation problem. We start with FEM simulation. The distribution of the stress at 1400th time step computed by FEM is shown in Fig. 6 together with the initial pulse recorded at 200th time step. As one can see, there is practically no difference in the results computed by FEM and obtained analytically.

Similar great agreement between numerical and analytical results

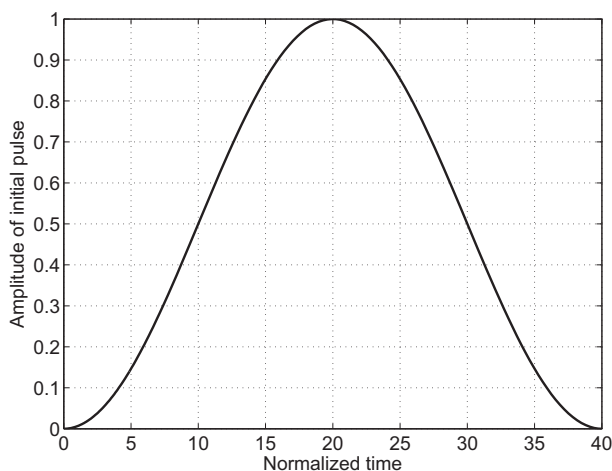


Fig. 3. Initial pulse shape.

have been obtained also in the case of FVM. The corresponding comparison with the analytical solution is presented in Fig. 7. A small distinction in the distribution of the stress close to the left end of the bar is due to a different handling of stress-free conditions in FEM and FVM.

It is clearly visible that in addition to many reflections, two main transmitted stress pulses are formed by the periodic heterogeneity. This demonstrates a strong dispersion provided by the alternating layers. In the considered case, the amplitude of the leading pulse is greater than the amplitude of the following one.

Now we turn to more thin alternating layers to study the influence of the size of the heterogeneity. We apply the same loading as previously, but the thickness of each layer is reduced to 30 space elements. In this case the length of the initial pulse is greater than the size of layers. The periodic heterogeneity is placed in the same position as previously, as it can be seen in Fig. 8.

The comparison of the analytical solution and results of computations by FEM is presented in Fig. 9. As in the previous case, results of computations by FEM coincide with analytical predictions. Calculations performed by means of FVM (Fig. 10) shows small differences from analytical solution in the vicinity of the left end of the bar. This confirms once more the equivalence of finite element and finite volume methods for smooth solutions, as it is pointed out by Idelsohn and Oñate [37]. In contrast to the case of thick layers, here the leading transmitted pulse is smaller in amplitude than the following one. The difference in the shape and position of transmitted pulses for thick and thin alternating layers indicates a strong influence of the size of the heterogeneity on the wave dispersion.

It is clear that there exists an infinite number of relations between the length of the pulse and the size of heterogeneity in layered materials, which are beyond the validity of homogenization methods. As it is shown, all such cases can be computed precisely by means of accurate numerical methods.

5.2. Three-phase layered composite

To illustrate the capabilities of numerical simulations, we consider the so-called three-phase periodic composite. Considering first a symmetric composition, we assume that each thick layer presented in the previous section is divided into three identical parts, and the central part of each thick layer is occupied with the material of properties, which are intermediate between the properties of hard and soft materials (Fig. 11).

Namely, we apply dimensionless values $\rho_3 = 0.8, c_3 = 0.98, E_3 = 0.76832$ for the third material marked by the violet color in Fig. 11. The initial and boundary conditions are the same as in the previous cases. Analytical solution and numerical simulations demonstrate again the strong dispersion manifested in the transformation of the initial pulse into two main transmitted pulses with almost equal amplitudes (Fig. 12).

Now we change the arrangement of the layers keeping the volume fractions of the layers unchanged. We assume that the layer with intermediate properties is moved into the beginning of each thick layer. The resulting new composition is shown in Fig. 13. Analytical solution as well as numerical simulations of the wave propagation under the same loading as in the previous case show a completely different evolution of the stress pulse: only a single transmitted pulse is formed after the heterogeneous zone. Due to the dispersion, the amplitude of the transmitted pulse is decreased in comparison with the initial pulse (Fig. 14).

Of course, there is infinitely many possible arrangements of distinct layers in composites. Each of them produces a specific shape of the transmitted signal. As it is demonstrated, accurate numerical methods are capable to predict any possible wave field in layered composites (at least in the one-dimensional case). Additional examples of one-dimensional wave dispersion in layered composites can be found in [38]. It is worth to note that the change of material properties of the layers also

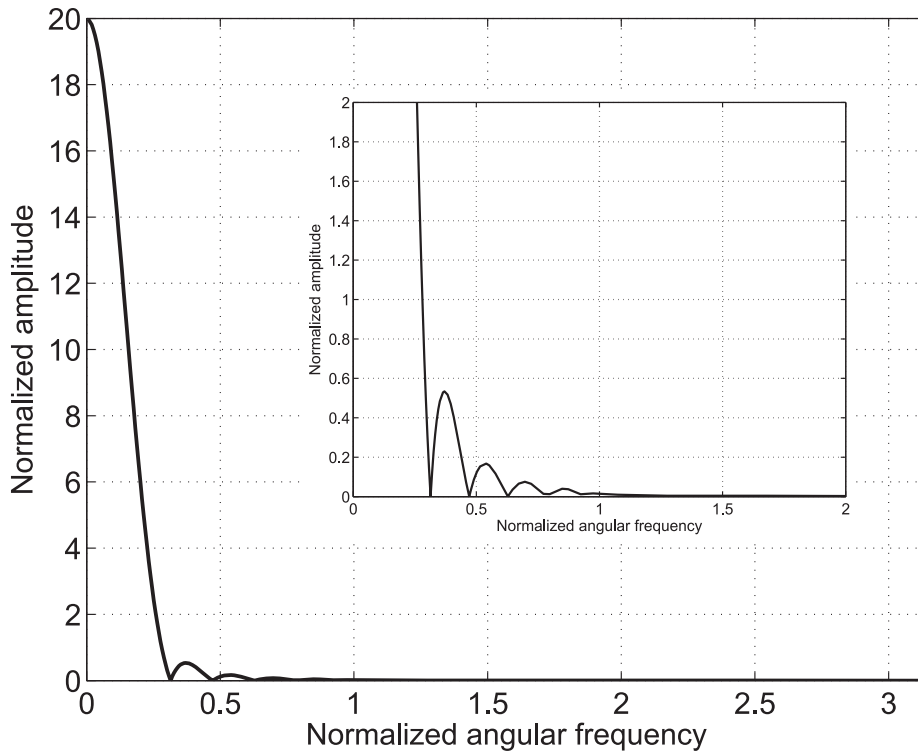


Fig. 4. Frequency spectrum of the initial pulse.

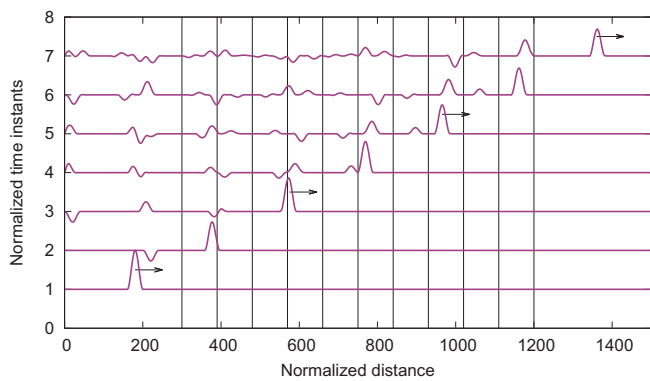


Fig. 5. Stress distribution at distinct time instants.

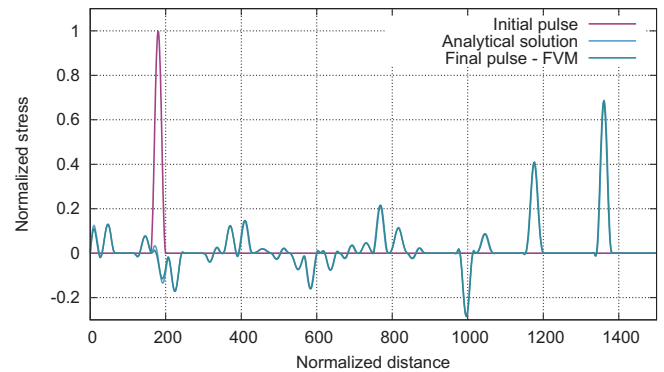


Fig. 7. Stress distribution along the bar at 1400th time step in the case of thick periodic layers.

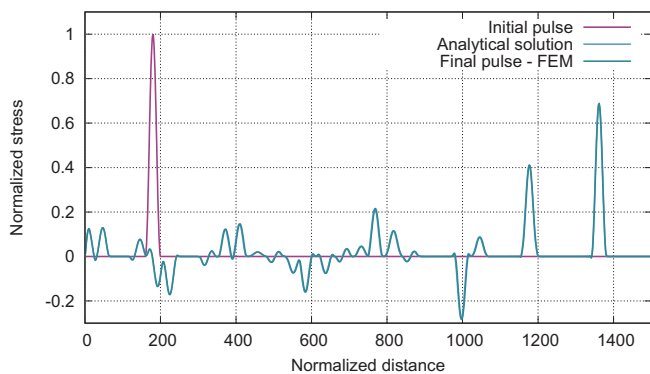


Fig. 6. Stress distribution along the bar at 1400th time step in the case of thick periodic layers.

affects the wave dispersion. This extends the area of possible applications but does not restrict the capabilities of the applied numerical methods.

6. Conclusions

Composite materials are broadly applied in industry because of their excellent designable characteristics. To meet a desired functionality, the microstructure in a composite material can be architected. The recent advancement in additive manufacturing eased the fabrication of complex structures with a very wide range of materials.

Dispersion is a characteristic feature of composites. It manifests itself in the change of the shape and/or of the length of a signal during its propagation through composites or heterogeneous structures. For harmonic waves, dispersion is expressed in the relation between frequency and wave number. While it may be sufficient from the theoretical point of view, it is also helpful to observe directly the transformation of a signal due to heterogeneity in a material. This is why two different numerical methods – FEM and FVM – are used for the simulation of a pulse propagation in periodically layered composites beyond the validity of homogenization methods. The results of simulations of one-dimensional pulse propagation by the two numerical approaches are compared with the analytical solution and practically coincide in all

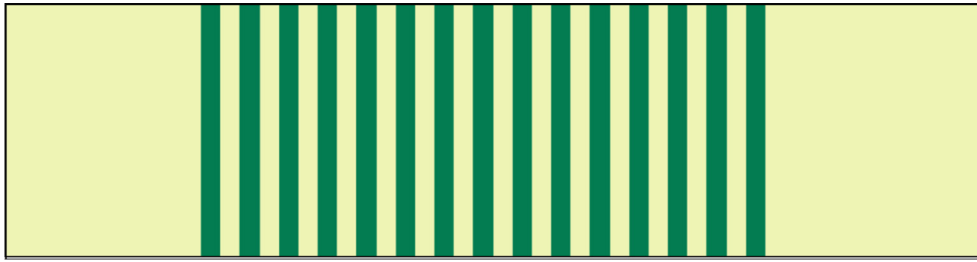


Fig. 8. Distribution of thin periodic layers.

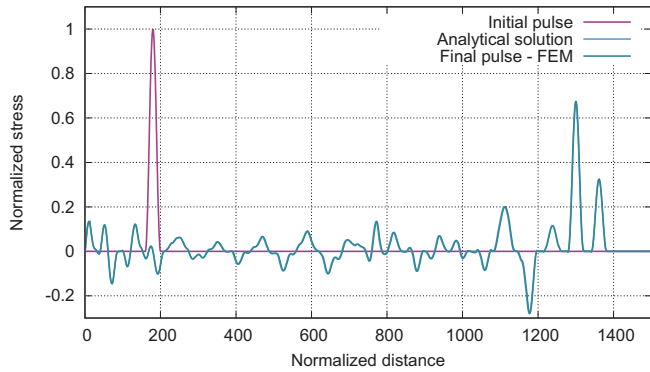


Fig. 9. Stress distribution along the bar at 1400th time step in the case of thin periodic layers.

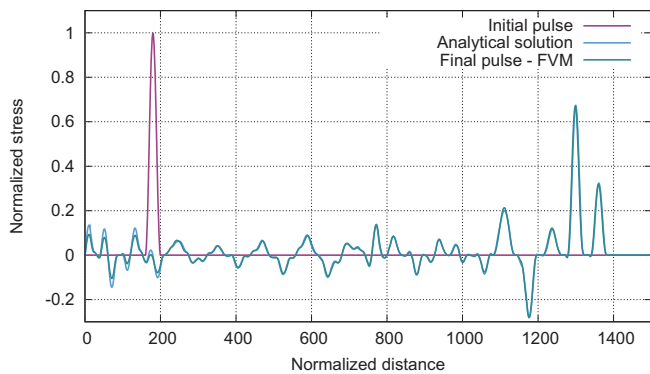


Fig. 10. Stress distribution along the bar at 1400th time step in the case of thin periodic layers.

considered cases. This coincidence with analytical solution ensures the accuracy of the results obtained numerically. As it is shown, even a simple rearrangement of the position of layers provides the possibility of manipulation of the shape of a transmitted pulse. Though this result can be qualitatively expected in advance, it is not easy to predict the shape of the final pulse quantitatively.

Accurate numerical computation of the full-field solution for pulse propagation in layered materials allows to analyze the influence of

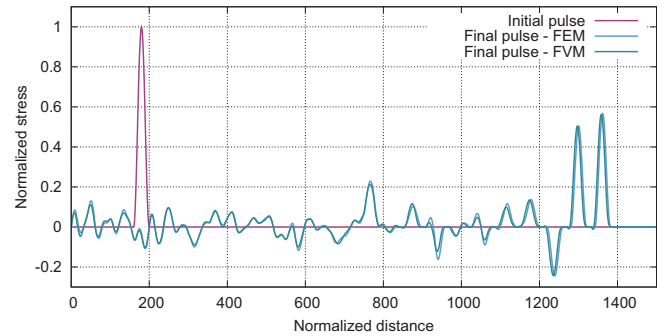


Fig. 12. Stress distribution along the bar at 1400th time step in the case of three-phase symmetric periodic layers. FEM results coincide with analytical solution.

heterogeneity beyond the possibilities of homogenization methods. The difference in the transmitted signals due to a simple change of the positions of the same layers, which is invisible from the point of view of homogenized effective media, is demonstrated clearly.

The full scale direct simulation of wave dispersion in composites has become increasingly feasible with advanced numerical techniques and rapidly enhanced computing power. A major advantage of numerical simulation is its generality, capable of predicting accurate wave fields for any composite with arbitrarily distributed layers of different sizes.

In future work, we will focus on modelling of elastic wave propagation in two- and three-dimensional specimens composed by heterogeneous and anisotropic materials with a special attention on Rayleigh-edge waves [39] and wave propagation in metamaterials [40] and piezomaterials [41].

Acknowledgements

The work of A. Berezovski and D. Gabriel was supported by the Centre of Excellence for Nonlinear Dynamic Behaviour of Advanced Materials in Engineering CZ.02.1.01/0.0/0.0/15.003/0000493 (Excellent Research Teams) in the framework of Operational Programme Research, Development and Education. The work of R. Kolman was supported by the Grant projects with Nos. 17-22615S and 17-12925S of the Czech Science Foundation (CSF) within institutional support RVO:61388998. The work of V. Adánek was supported by the



Fig. 11. Symmetric distribution of three-phase periodic layers. Violet color indicates material 3.

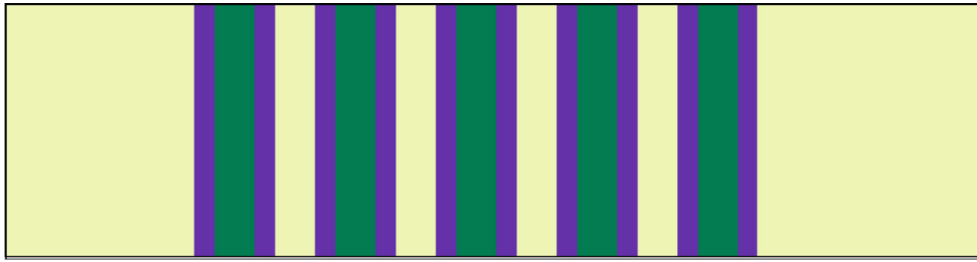


Fig. 13. Another distribution of three-phase periodic layers.

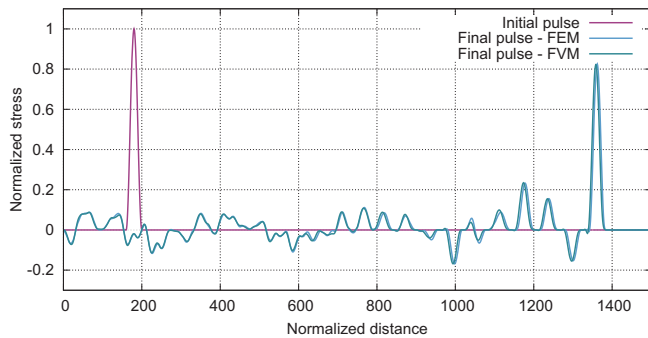


Fig. 14. Stress distribution along the bar at 1400th time step in the case of another arrangement of three-phase symmetric periodic layers. FEM results coincide with analytical solution.

project LO1506 of the Czech Ministry of Education, Youth and Sports. Further, the work has been supported by the bilateral project between the Estonian Academy of Sciences and the Czech Academy of Sciences (project No. ETA-15-03 entitled 'Advanced numerical modelling of dynamic processes in solids').

References

- [1] Clements B, Johnson J, Hixson R. Stress waves in composite materials. *Phys Rev E* 1996;54(6):6876–88.
- [2] Chakraborty A, Gopalakrishnan S. Various numerical techniques for analysis of longitudinal wave propagation in inhomogeneous one-dimensional waveguides. *Acta Mech* 2003;162(1–4):1–27.
- [3] Hussein MI, Hulbert GM, Scott RA. Dispersive elastodynamics of 1d banded materials and structures: design. *J Sound Vib* 2007;307(3):865–93.
- [4] Hui T, Oskay C. A high order homogenization model for transient dynamics of heterogeneous media including micro-inertia effects. *Comput Methods Appl Mech Eng* 2014;273:181–203.
- [5] Markov KZ. Elementary micromechanics of heterogeneous media. *Heterogeneous media*. Springer; 2000. p. 1–162.
- [6] Kanouté P, Boso D, Chaboche J, Schrefler B. Multiscale methods for composites: a review. *Arch Comput Methods Eng* 2009;16(1):31–75.
- [7] Herakovich CT. *Mechanics of composites: a historical review*. Mech Res Commun 2012;41:1–20.
- [8] Reda H, Elnady K, Ganghoffer J, Lakiss H. Wave propagation in pre-deformed periodic network materials based on large strains homogenization. *Compos Struct* 2018;184(Supplement C):860–71.
- [9] Aboudi J. *Mechanics of composite materials: a unified micromechanical approach*. Elsevier; 1991.
- [10] Brillouin L. *Wave propagation in periodic structures: electric filters and crystal lattices*. McGraw-Hill Book Company; 1946.
- [11] Willis J. Exact effective relations for dynamics of a laminated body. *Mech Mater* 2009;41(4):385–93.
- [12] Willis JR. The construction of effective relations for waves in a composite. *CR Méc* 2012;340(4–5):181–92.
- [13] Nemat-Nasser S, Srivastava A. Overall dynamic constitutive relations of layered elastic composites. *J Mech Phys Solids* 2011;59(10):1953–65.
- [14] Srivastava A, Nemat-Nasser S. On the limit and applicability of dynamic homogenization. *Wave Motion* 2014;51(7):1045–54.
- [15] Amirkhizi AV. Homogenization of layered media based on scattering response and field integration. *Mech Mater* 2017;114:76–87.
- [16] Willis J. Some thoughts on dynamic effective properties—a working document, arXiv preprint arXiv:1311.3875.
- [17] Berezovski A. On the Mindlin microelasticity in one dimension. *Mech Res Commun* 2016;77:60–4.
- [18] Boutin B, Chalons C, Lagoutiere F, LeFloch P. A sharp interface and fully conservative scheme for computing nonclassical shocks. *Numerical mathematics and advanced applications*. Springer; 2008. p. 217–24.
- [19] Ketcheson DI, Parsani M, LeVeque RJ. High-order wave propagation algorithms for hyperbolic systems. *SIAM J Sci Comput* 2013;35(1):A351–77.
- [20] Park K, Lim S, Huh H. A method for computation of discontinuous wave propagation in heterogeneous solids: basic algorithm description and application to one-dimensional problems. *Int J Numer Meth Eng* 2012;91(6):622–43.
- [21] Idesman A, Pham D, Foley J, Schmidt M. Accurate solutions of wave propagation problems under impact loading by the standard, spectral and isogeometric high-order finite elements. *Comparative study of accuracy of different space-discretization techniques*. *Finite Elem Anal Des* 2014;88:67–89.
- [22] Kolman R, Cho SS, Park KC. Efficient implementation of an explicit partitioned shear and longitudinal wave propagation algorithm. *International Journal for Numerical Methods in Engineering* 2016;107(7):543–79.
- [23] Kolman R, Okrouhlik M, Berezovski A, Gabriel D, Kopačka J, Plešek J. B-spline based finite element method in one-dimensional discontinuous elastic wave propagation. *Appl Math Model* 2017;46:382–95.
- [24] Dona M, Lombardo M, Barone G. Experimental study of wave propagation in heterogeneous materials. *Proceedings of the fifteenth international conference on civil, structural and environmental engineering computing*, Prague, 1–4 Sept. 2015. *Civil-Comp Limited*; 2015.
- [25] Sun C-T, Achenbach JD, Herrmann G. Continuum theory for a laminated medium. *J Appl Mech* 1968;35(3):467–75.
- [26] Norris AN. Waves in periodically layered media: a comparison of two theories. *SIAM J Appl Math* 1993;53(5):1195–209.
- [27] Carta G, Brun M. A dispersive homogenization model based on lattice approximation for the prediction of wave motion in laminates. *J Appl Mech* 2012;79(2):021019.
- [28] Zohdi TI, Wriggers P. *An introduction to computational micromechanics*. Springer Science & Business Media; 2008.
- [29] Adámek V, Valeš F, Červ J. Numerical Laplace inversion in problems of elastodynamics: Comparison of four algorithms. *Adv. Eng. Softw.* 2017;113:120–9.
- [30] Graff KF. *Wave motion in elastic solids*. Clarendon Press; 1975.
- [31] Hughes T. *The finite element method: linear static and dynamic finite element analysis*. Dover Publications; 2000.
- [32] Park K. Practical aspects of numerical time integration. *Comput Struct* 1977;7(3):343–53.
- [33] Kolman R, Plešek J, Červ J, Okrouhlik M, Pařík P. Temporal-spatial dispersion and stability analysis of finite element method in explicit elastodynamics. *Int J Numer Methods Eng* 2016;106(2):113–28.
- [34] Berezovski A, Engelbrecht J, Maugin GA. *Numerical simulation of waves and fronts in inhomogeneous solids*. World Scientific; 2008.
- [35] Barth T, Ohlberger M. *Finite volume methods: Foundation and analysis*. In: *Encyclopedia of computational mechanics, Vol. 1, Fundamentals*; 2004. p. 439–74.
- [36] Berezovski A. Thermodynamic interpretation of finite volume algorithms. *J Struct Mech (Rakenteiden Mekaniikka)* 2011;44:156–71.
- [37] Idelsohn SR, Oñate E. Finite volumes and finite elements: two 'good friends'. *Int J Numer Meth Eng* 1994;37(19):3323–41.
- [38] Berezovski M, Berezovski A, Soomere T, Viikmäe B. On wave propagation in laminates with two substructures. *Est J Eng* 2010;16(3):228–42.
- [39] Cerv J, Kroupa T, Trnka J. Influence of principal material directions of thin orthotropic structures on Rayleigh-edge wave velocity. *Compos Struct* 2010;92(2):568–77.
- [40] Reda H, Rahali Y, Ganghoffer J, Lakiss H. Wave propagation in 3D viscoelastic auxetic and textile materials by homogenized continuum micropolar models. *Compos Struct* 2016;141(Supplement C):328–45.
- [41] Zhou Y, Chen CLW. Bulk wave propagation in layered piezomagnetic/piezoelectric plates with initial stresses or interface imperfections. *Compos Struct* 2012;94(9):2736–45.



ELSEVIER



Available online at www.sciencedirect.com

ScienceDirect

Mathematics and Computers in Simulation 189 (2021) 126–140



MATHEMATICS
AND
COMPUTERS
IN SIMULATION

www.elsevier.com/locate/matcom

Original articles

A two-layer elastic strip under transverse impact loading: Analytical solution, finite element, and finite volume simulations

V. Adámek^a, A. Berezovski^{b,c}, M. Mračko^c, R. Kolman^{c,*}

^a NTIS - New Technologies for the Information Society, Faculty of Applied Sciences, University of West Bohemia, Technická 8, 301 00 Pilsen, Czech Republic

^b Department of Cybernetics, School of Science, Tallinn University of Technology, Akadeemia 21, 12618 Tallinn, Estonia

^c Institute of Thermomechanics, v.v.i., The Czech Academy of Sciences, Dolejškova 1402/5, 182 00 Praha 8, Czech Republic

Received 4 February 2020; received in revised form 3 October 2020; accepted 13 October 2020

Available online 17 October 2020

Abstract

In this paper, wave propagation in a two-layer composite strip is investigated analytically and numerically. The strip is loaded by a very short transverse stress pulse. Three cases of the strip problem are assumed: (i) isotropic aluminum Al strip and two-layer strips made of (ii) Al and the ceramics Al_2O_3 and (iii) the ceramics Al_2O_3 and Al. The analytical method is based on Laplace and Fourier transform. The in-house finite element algorithm and thermodynamic consistent finite volume scheme are employed for computations, while the explicit time stepping procedure is used in both cases. The comparison of analytical and numerical results determines the degree of the accuracy of calculations, which is important for simulation of complex wave propagation problems in general heterogeneous media.

© 2020 International Association for Mathematics and Computers in Simulation (IMACS). Published by Elsevier B.V. All rights reserved.

Keywords: Wave propagation; Heterogeneous solids; Analytical solution; Finite element method; Finite volume method; Plane stress problem

1. Introduction

Application of elastic wave propagation to inspect the state of real structures and their damage localization is an essential part of structural health monitoring [12]. For instance, acoustic emission testing is completely based on elastic wave phenomena [17]. The acoustic emission testing is the broadly accepted approach for the localization of defects in structures [14,23,27]. The validity of this approach has, however, certain limitations [20]. In fact, the signal arrival time measurement is performed under the assumption that the propagation velocity is constant in all directions (see, e.g., MISTRAS Acousto-Ultrasonics, <https://www.mistrasgroup.com/products/technologies/acousto-ultrasonics.aspx>). The wave propagation from a source to the sensor is supposed to be straight and uninterrupted. These assumptions can be invalid due to various possible inhomogeneity effects that can reduce the accuracy of this technique.

This is only one reason to have effective tools for the prediction of wave propagation in real materials and structures. A key element in wave controlling is the prediction of the wavefield for any composite with

* Corresponding author.

E-mail addresses: vadamek@kme.zcu.cz (V. Adámek), Arkadi.Berezovski@cs.ioc.ee (A. Berezovski), mracko@it.cas.cz (M. Mračko), kolman@it.cas.cz (R. Kolman).

<https://doi.org/10.1016/j.matcom.2020.10.007>

0378-4754/© 2020 International Association for Mathematics and Computers in Simulation (IMACS). Published by Elsevier B.V. All rights reserved.

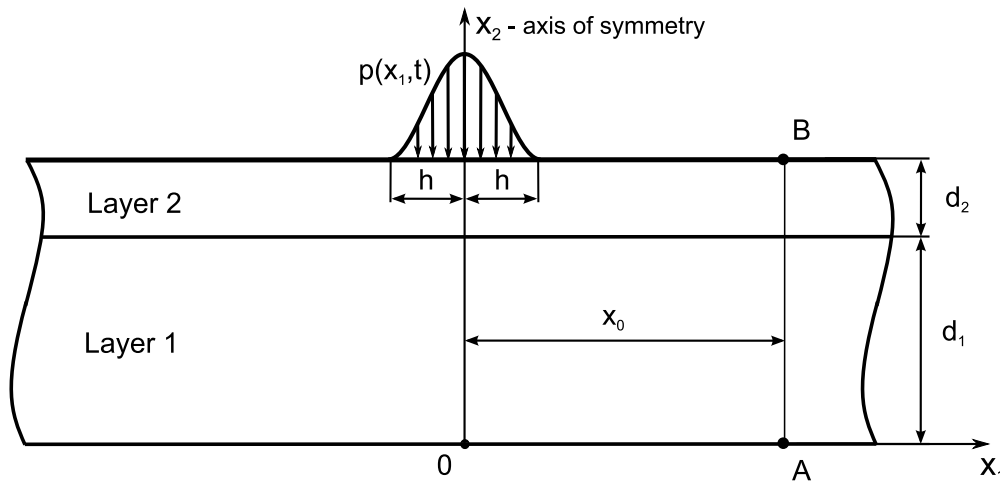


Fig. 1. Sketch of the problem.

Table 1
Values of material properties.

Material	Density ρ [kg/m ³]	Young modulus E [GPa]	Poisson ratio ν	Longitudinal wave speed c_p [m/s]	Shear speed c_s [m/s]	Source
Al	2700	70.6	0.345	6420 (5448)	3040	[34]
Al ₂ O ₃	3970	401	0.24	10911.2 (10352.8)	6381.9	[15]

arbitrarily distributed scatterers of irregular shapes and sizes. It should be noted that classical works in wave propagation [1,16,26] deal with the theoretical description of propagation, reflection, and transmission of elastic waves in simplified situations. More recent works [4,5,25,29,32] demonstrate the applicability of numerical methods to characterize wave propagation in inhomogeneous materials and structures.

This means that if the geometry of inhomogeneities and material properties of constituents are prescribed, then the only problem is in the accuracy of calculations. The accuracy is determined by the comparison of an approximate numerical solution with the true analytical one. However, analytical solutions are usually known for idealized isotropic homogeneous materials and simplified geometry.

It is a great advantage of the paper that the analytical solution can be constructed for the dynamic transverse load of a two-layer infinite strip following [2]. Having an analytical solution, its comparison with numerical solutions can be performed. In the paper, calculations by the finite element method and by the finite volume method are compared with the analytical solution to examine their accuracy on the example of a two-layer strip under dynamic transverse loading. The paper is a continuation of the work performed on one-dimensional wave propagation in layered bars [10].

2. Problem description

We will consider the transient response of a two-layer elastic strip to the transverse impulse loading. The sketch of the problem is shown in Fig. 1. The infinite elastic strip is composed of two homogeneous isotropic layers of different materials. Namely, the bottom layer 1 of the thickness $d_1 = 30$ mm is made from aluminum Al and the upper layer 2 of the thickness $d_2 = 10$ mm is made from aluminum oxide Al₂O₃ (ceramics). The properties of materials are given in Table 1. The corresponding longitudinal and shear wave speeds are also stated there. The values of longitudinal speed c_p in parenthesis correspond to plane stress conditions. It is clear from the values specified in Table 1 that the composite strip is made from two materials with highly different properties.

Initially, the strip is at rest. The stress loading $p(x_1, t)$, as normal pressure, is nonzero only for $x_2 = d_1 + d_2$ and for $x_1 \in [-h, h]$. All other parts of the strip boundaries were stress-free. The shape of the loading $p(x_1, t)$ is a smooth cosine pulse of duration t_0 with the amplitude σ_0 changing according to cosine function in x_1 , namely,

$$p(x_1, t) = \frac{\sigma_0}{2} \cos\left(\frac{\pi x_1}{2h}\right) \left(1 - \cos\frac{2\pi t}{t_0}\right) [H(t) - H(t - t_0)], \tag{1}$$

where $H(t)$ denotes the Heaviside step function. Corresponding parameters contained in (1) were the following: $h = 2 \text{ mm}$, $\sigma_0 = 10^6 \text{ Pa}$, $t_0 = 2 \cdot 10^{-6} \text{ s}$.

3. Governing equations

In this section, basic equations of dynamic problems in solids are specified for 2D case under plane stress conditions. Let $\Omega \subset \mathbb{R}^3$ be an open, bounded domain with a piecewise smooth boundary $\partial\Omega$ and $t \in [0, T]$ is the time range of interest. Neglecting both geometrical and physical nonlinearities, we can write the bulk equations (balance of linear momentum) of homogeneous linear isotropic elasticity in the absence of body forces as follows [6]:

$$\rho \frac{\partial v_i}{\partial t} = \frac{\partial \sigma_{ij}}{\partial x_j}, \quad \text{on } \Omega \times [0, T]. \tag{2}$$

The balance of linear momentum is complemented by the Hooke law in the form

$$\frac{\partial \sigma_{ij}}{\partial t} = \lambda \frac{\partial v_k}{\partial x_k} \delta_{ij} + \mu \left(\frac{\partial v_i}{\partial x_j} + \frac{\partial v_j}{\partial x_i} \right), \tag{3}$$

where t is time, x_i are spatial coordinates, v_i are the velocity components, σ_{ij} denotes the Cauchy stress tensor, ρ is the density, λ and μ are the Lamé coefficients given by $\lambda = E\nu/((1 + \nu)(1 - 2\nu))$ and $\mu = E/(2(1 + \nu))$, E is the Young modulus and ν is the Poisson ratio. We assume that E and ν could be different at each material point.

Since initially the strip is at rest, therefore the initial displacement and velocity fields are of zero values. The Neumann boundary conditions are assumed as the pressure at the boundary $\Gamma_N = [-h, h] \times [x_2 = d_1 + d_2]$ with the space distribution and time history given by Eq. (1). The strip is floating in the space, therefore the Dirichlet boundary conditions is not taken into account.

3.1. Plane stress approximation

For the 2D problem, in our case of the strip geometry, we have $\Omega = (-\infty, \infty) \times [0, d_1 + d_2]$. The strip is supposed to be thin along the x_3 direction then stresses on all parallel x_3 -planes are sufficiently small and can be neglected, i.e.,

$$\sigma_{i3} = 0, \quad i = 1, 2, 3. \tag{4}$$

This approximation is called plane stress approximation. Though the displacement u_3 in the direction of x_3 does not vanish, the others (u_1, u_2) are independent of the coordinate x_3 ; that is,

$$u_i = u_i(x_1, x_2), \quad i = 1, 2. \tag{5}$$

It follows that the strain tensor components, ε_{i3} , are

$$\varepsilon_{i3} = 0, \quad \varepsilon_{33} = -\frac{\nu}{E} \sigma_{ii}, \quad i = 1, 2. \tag{6}$$

Equations of motion (2)–(3) specialized to plane stress conditions have the form

$$\rho \frac{\partial v_1}{\partial t} = \frac{\partial \sigma_{11}}{\partial x_1} + \frac{\partial \sigma_{12}}{\partial x_2}, \tag{7}$$

$$\rho \frac{\partial v_2}{\partial t} = \frac{\partial \sigma_{21}}{\partial x_1} + \frac{\partial \sigma_{22}}{\partial x_2}. \tag{8}$$

Accordingly, strain–velocity relationships are represented as

$$\frac{\partial \varepsilon_{11}}{\partial t} = \frac{\partial v_1}{\partial x_1}, \tag{9}$$

$$\frac{\partial \varepsilon_{12}}{\partial t} = \frac{1}{2} \left(\frac{\partial v_1}{\partial x_2} + \frac{\partial v_2}{\partial x_1} \right), \tag{10}$$

$$\frac{\partial \varepsilon_{22}}{\partial t} = \frac{\partial v_2}{\partial x_2}. \tag{11}$$

3.2. Stress–strain relation

Stress–strain relations (the Hooke law) which close the system of governing equations under plane stress conditions have the form

$$\sigma_{11} = (\bar{\lambda} + 2\mu)\varepsilon_{11} + \bar{\lambda}\varepsilon_{22}, \tag{12}$$

$$\sigma_{12} = \sigma_{21} = 2\mu\varepsilon_{12}, \tag{13}$$

$$\sigma_{22} = (\bar{\lambda} + 2\mu)\varepsilon_{22} + \bar{\lambda}\varepsilon_{11}, \tag{14}$$

where $\bar{\lambda} = 2\mu\lambda/(\lambda + 2\mu)$. Time derivatives of the stress–strain relations together with compatibility conditions determine relationships

$$\frac{\partial\sigma_{11}}{\partial t} = (\bar{\lambda} + 2\mu)\frac{\partial v_1}{\partial x_1} + \bar{\lambda}\frac{\partial v_2}{\partial x_2}, \tag{15}$$

$$\frac{\partial\sigma_{22}}{\partial t} = \bar{\lambda}\frac{\partial v_1}{\partial x_1} + (\bar{\lambda} + 2\mu)\frac{\partial v_2}{\partial x_2}, \tag{16}$$

$$\frac{\partial\sigma_{12}}{\partial t} = \frac{\partial\sigma_{21}}{\partial t} = \mu\left(\frac{\partial v_1}{\partial x_2} + \frac{\partial v_2}{\partial x_1}\right). \tag{17}$$

These equations together with the balance of linear momentum (7)–(8) form the system of equations, which is convenient for the solution.

3.3. Wave speeds

The wave speeds under plane stress conditions are specified for the isotropic case as

$$c_p = \sqrt{\frac{E}{(1 - \nu^2)\rho}}, \quad c_s = \sqrt{\mu/\rho}. \tag{18}$$

In the case of heterogeneous media, material parameters depend on position of material points.

4. Analytical solution

In this Section, we set out the technique used for obtaining the analytical solution of the studied problem.

4.1. Derivation procedure and final formulas for transforms of stress components

To find the analytical solution of the problem formulated in Sections 2 and 3, it is advantageous to introduce a local coordinate system $x_{1,L} - x_{2,L}$ for each L th layer ($L = 1, 2$). The origins of these systems are localized in the geometrical centers of layers, i.e., the domain of the L th layer are defined as $(-\infty, +\infty) \times [-d_L/2, d_L/2]$. Then one can use a procedure for the derivation of desired formulas of stress components similar to that employed in [2]. Taking the Laplace transform in time domain, we transfer the original systems of equations of motion for each layer to spatial boundary value problems with a complex parameter p . The general solutions of obtained systems can then be expressed by means of Fourier integrals. Taking into account the symmetry of the problem, the Laplace transforms of all non-zero stress components denoted hereinafter by a hat are given for $\omega \in \mathbb{R}$ by Fourier integrals having the form

$$\hat{\sigma}_{11,L}(x_{1,L}, x_{2,L}, p) = \frac{1}{\pi} \int_0^\infty \left[(A_{1,L} \sinh(x_{2,L}\lambda_{1,L}) + A_{2,L} \cosh(x_{2,L}\lambda_{1,L})) k_{1,L} - (A_{3,L} \sinh(x_{2,L}\lambda_{2,L}) + A_{4,L} \cosh(x_{2,L}\lambda_{2,L})) k_{2,L} \right] \cos(\omega x_{1,L}) d\omega, \tag{19}$$

$$\hat{\sigma}_{22,L}(x_{1,L}, x_{2,L}, p) = \frac{1}{\pi} \int_0^\infty \left[(A_{1,L} \sinh(x_{2,L}\lambda_{1,L}) + A_{2,L} \cosh(x_{2,L}\lambda_{1,L})) k_{3,L} + (A_{3,L} \sinh(x_{2,L}\lambda_{2,L}) + A_{4,L} \cosh(x_{2,L}\lambda_{2,L})) k_{2,L} \right] \cos(\omega x_{1,L}) d\omega, \tag{20}$$

$$\hat{\sigma}_{12,L}(x_{1,L}, x_{2,L}, p) = -\frac{1}{\pi} \int_0^\infty [(A_{1,L} \cosh(x_{2,L}\lambda_{1,L}) + A_{2,L} \sinh(x_{2,L}\lambda_{1,L})) k_{4,L} + (A_{3,L} \cosh(x_{2,L}\lambda_{2,L}) + A_{4,L} \sinh(x_{2,L}\lambda_{2,L})) k_{5,L}] \sin(\omega x_{1,L}) d\omega. \tag{21}$$

The complex functions involved in (19)–(21) are introduced by the following relations

$$\begin{aligned} \lambda_{1,L} &= \omega \sqrt{1 + \frac{p^2}{\omega^2 c_{p,L}^2}}, \quad \lambda_{2,L} = \omega \sqrt{1 + \frac{p^2}{\omega^2 c_{s,L}^2}}, \quad k_{1,L} = \frac{E_L \nu_L}{1 - \nu_L^2} - \frac{2G_L c_{p,L}^2 \omega^2}{p^2}, \\ k_{2,L} &= \frac{4G_L c_{s,L}^2 \lambda_{2,L} \omega}{p^2}, \quad k_{3,L} = 2 \left(\frac{\omega^2 c_{p,L}^2}{p^2} + 1 \right) G_L + \frac{E_L \nu_L}{1 - \nu_L^2}, \\ k_{4,L} &= \frac{2G_L c_{p,L}^2 \lambda_{1,L} \omega}{p^2}, \quad k_{5,L} = 2 \left(\frac{2c_{s,L}^2 \omega^2}{p^2} + 1 \right) G_L, \end{aligned} \tag{22}$$

where G_L denotes the shear modulus of the material in the L th layer ($L = 1, 2$) and $A_{i,L} = A_{i,L}(\omega, p)$ for $i = 1 \dots 4$ and $L = 1, 2$ represent 8 unknown complex functions which need to be found using the Laplace transform of four boundary conditions of the problem and four conditions defined at the interface of the strip layers. Following the problem description given in Section 2, the Laplace transforms of mentioned conditions can be written as (in order from the upper edge of the strip)

$$\begin{aligned} \hat{\sigma}_{22,2}(x_{1,2}, d_2/2, p) &= \hat{p}(x_{1,2}, p), \quad \hat{\sigma}_{12,2}(x_{1,2}, d_2/2, p) = 0, \\ \hat{u}_{1,1}(x_{1,1}, d_1/2, p) &= \hat{u}_{1,2}(x_{1,2}, -d_2/2, p), \quad \hat{u}_{2,1}(x_{1,1}, d_1/2, p) = \hat{u}_{2,2}(x_{1,2}, -d_2/2, p), \\ \hat{\sigma}_{22,1}(x_{1,1}, d_1/2, p) &= \hat{\sigma}_{22,2}(x_{1,2}, -d_2/2, p), \quad \hat{\sigma}_{12,1}(x_{1,1}, d_1/2, p) = \hat{\sigma}_{12,2}(x_{1,2}, -d_2/2, p), \\ \hat{\sigma}_{22,1}(x_{1,1}, -d_1/2, p) &= 0, \quad \hat{\sigma}_{12,1}(x_{1,1}, -d_1/2, p) = 0. \end{aligned} \tag{23}$$

4.2. Evaluation process and its precision

The evaluation process of derived relationships (19)–(21) is realized in two basic steps. Namely, these are the Fourier integrals evaluation (FIE) and the inverse Laplace transform. The sequence of these steps may also be interchanged due to the properties of the integrands in Eqs. (19)–(21). The first mentioned step was managed by using the standard numerical Simpson rule with a constant integration step in this work. The second step has been resolved by means of an algorithm for numerical inverse Laplace transform (NILT). Specifically, the procedure based on FFT and Wynn’s epsilon algorithm was used (see [13] and [11] for more details).

Although the derived relationships (19)–(21) are exact, it is obvious that their evaluation will suffer from numerical errors. The errors are caused not only by two numerical procedures mentioned above but also by the precision limits of the software used for the evaluation. In this work, a Matlab code with double precision arithmetics has been used. This limitation may come into play when the hyperbolic functions contained in the integrands of derived Laplace transforms need to be evaluated for large arguments, i.e., for large values of the variable ω of the Fourier integrals. The same concerns to the functions $A_{i,L}(\omega, p)$ evaluated from formulas which can be derived exactly in this case of two-layer strip. These issues can be overcome by symbolic calculations of higher precision but it is always redeemed by significantly higher demands on computational time.

The precision of the algorithm used for NILT is discussed in detail in [3]. We focus on the accuracy of FIE process here. Even though there exist very sophisticated algorithms for numerical integration, we used the simple straightforward Simpson rule with constant integration step, as mentioned above. This decision resulted from the analysis of integrands appearing in Eqs. (19)–(21) after the NILT process. As expected, the precision of FIE is principally influenced by the integration step $d\omega$ and by the upper limit of integration ω_{max} . Their right choice is predetermined by the behavior of integrands depending on t, x_1 and x_2 .

We focus on t and x_2 dependence first. For this purpose, we assume the strip mentioned in Section 2, i.e., the strip composed of 30 mm of Al (1st layer) and of 10 mm of Al_2O_3 (2nd layer). The dependencies of σ_{11} integrand on $t \in [0, 50] \mu s$ and $\omega \in [0, 2000] \text{ rad s}^{-1}$ are shown for studied points A and B for $x_0 = 10 \text{ mm}$ (i.e., for different values of x_2) in Fig. 2(a) and Fig. 2(b), respectively. It is obvious that contrary to the point A, the calculation of the response at point B ($x_2 = 40 \text{ mm}$) for very short times requires $\omega_{max} > 2000$ to take into account the integrand

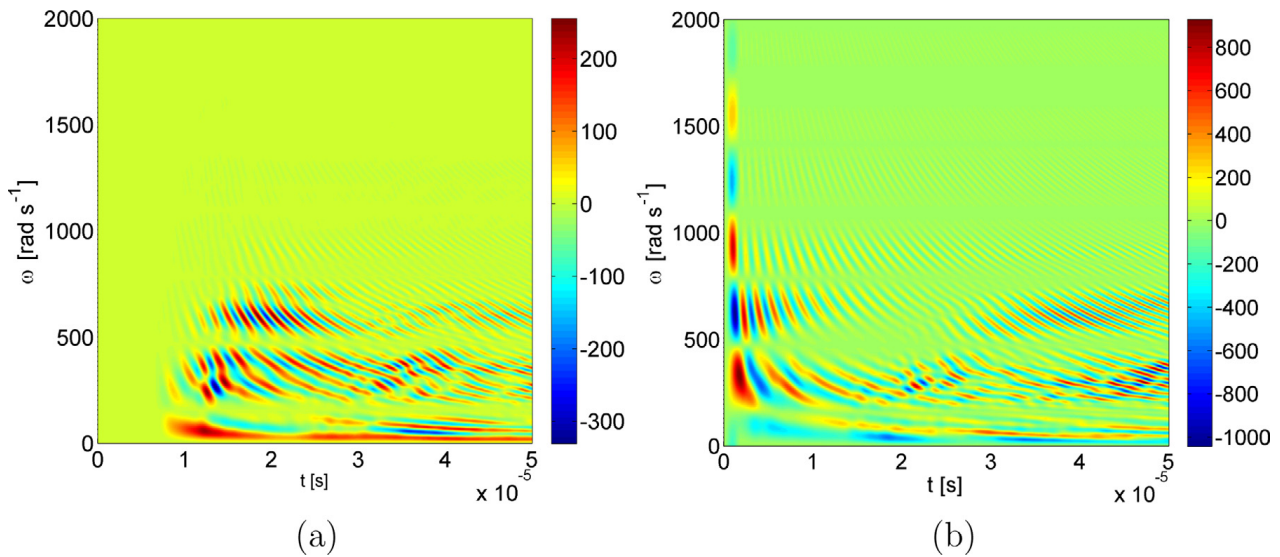


Fig. 2. The dependence of σ_{11} integrand in $[Pa \cdot s]$ on t and ω : (a) point A, (b) point B.

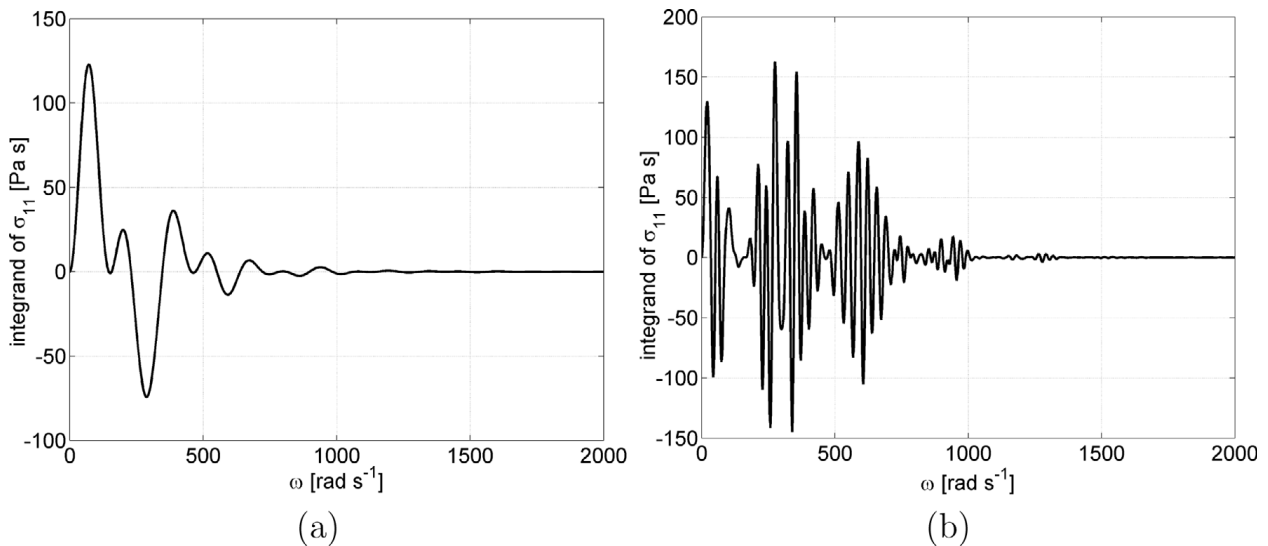


Fig. 3. The dependence of σ_{11} integrand at point A on ω at specific times: (a) $t \doteq 10 \mu s$, (b) $t = 50 \mu s$.

oscillations. On the other hand, to obtain good results for longer times, the values of ω_{max} can be reduced to about 2000 rad s^{-1} at both studied points, i.e., both for $x_2 = 0 \text{ mm}$ and $x_2 = 40 \text{ mm}$.

The specific character of σ_{11} integrand oscillations at point A is obvious from Fig. 3. The curves presented in this figure correspond to vertical cuts of Fig. 2(a) at times $t \doteq 10 \mu s$ and $t = 50 \mu s$. Such oscillations then determine the size of the integration step $d\omega$. It is clear that calculations for larger values of t require smaller $d\omega$. Similar dependence of $d\omega$ on x_1 can be deduced from Eqs. (19)–(21). Since the variables $x_{1,L}$ appear after the NILT process still in the argument of sin or cos functions, the size of $d\omega$ needs to be reduced with increasing x_1 .

It is clear from the previous discussion that the evaluation of Eqs. (19)–(21) is loaded by numerical errors. But if the applied numerical approaches are used wisely, very precise results can be obtained. Their precision can then be verified by means of the exact arrival times of P-waves to the points of interest. In the case of studied points A

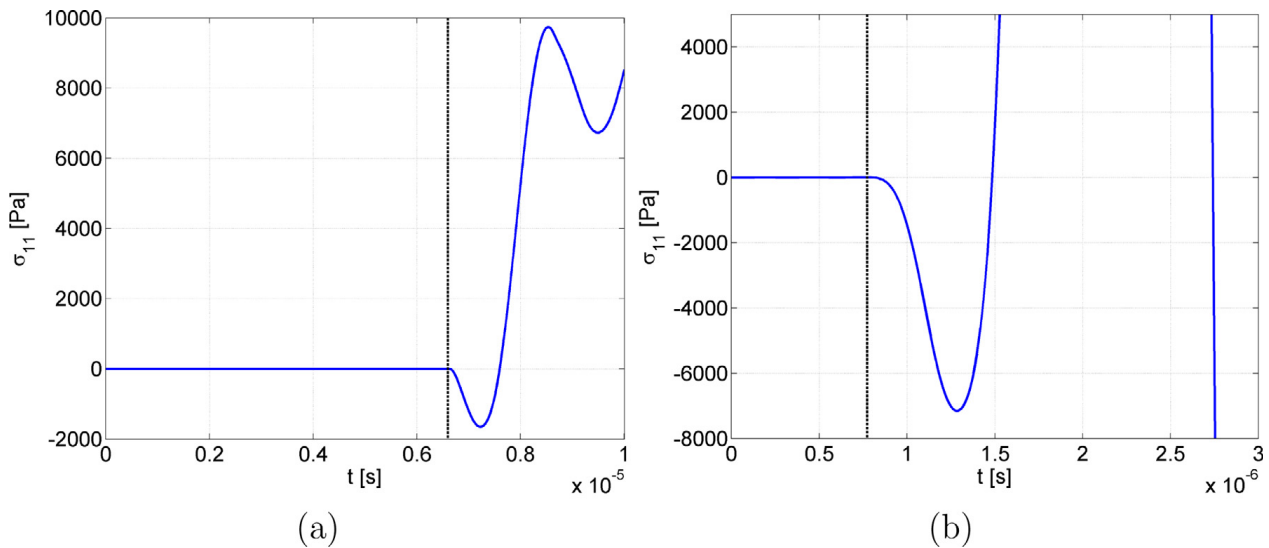


Fig. 4. The detailed views of $\sigma_{11}(t)$ with times of P-wave arrivals to (a) point A and (b) point B.

and B and the $Al-Al_2O_3$ strip, these times can be calculated as

$$t_A = \frac{1}{c_{p,Al_2O_3}} \sqrt{d_2^2 + \left[\frac{(x_0 - h)d_2}{d_1 + d_2} \right]^2} + \frac{1}{c_{p,Al}} \sqrt{d_1^2 + \left[\frac{(x_0 - h)d_1}{d_1 + d_2} \right]^2} \doteq 6.601 \mu s, \tag{24}$$

$$t_B = \frac{x_0 - h}{c_{p,Al_2O_3}} \doteq 0.7727 \mu s.$$

If we make a detailed view of $\sigma_{11}(t)$ at mentioned points, then we find out that the arrival times obtained from the evaluated solution are in very good agreement with the theoretical ones given by Eq. (24). It is clearly visible from Fig. 4 where the stress component σ_{11} at points A and B is shown. The times t_A and t_B are highlighted by vertical dotted lines. Naturally, if one makes a detailed inspection of σ_{11} values calculated at points A and B at times $t < t_A$ and $t < t_B$, respectively, then the values are not exactly equal to zero. The differences from the zero value are more than four (nearly six) orders smaller in magnitude than the maximal values of σ_{11} at point A (point B) on the time interval $[0, 50] \mu s$. It is evident that the results of such precision can be used for the validation of numerical results in the following sections.

5. Finite element procedure with explicit time integration

5.1. Weak formulation and spatial discretization

As the first step, we rewrite the equation of motion (2) in terms of displacements u_i

$$\rho \frac{\partial^2 u_i}{\partial t^2} = \frac{\partial \sigma_{ij}}{\partial x_j}. \tag{25}$$

Next, we represent equation of motion (25) in the weak form by multiplying it by a virtual field $\delta\varphi_i$ and integrating over the domain Ω using Green’s theorem

$$\int_{\Omega} \rho \frac{\partial^2 u_i}{\partial t^2} \delta\varphi_i d\Omega + \int_{\Omega} C_{ijkl} \frac{\partial u_k}{\partial x_l} \frac{\partial \delta\varphi_i}{\partial x_j} d\Omega = \int_{\partial\Omega} t_i^* \delta\varphi_i dS, \tag{26}$$

with a general stress–strain law $\sigma_{ij} = C_{ijkl}\varepsilon_{kl}$ and the traction t_i^* at the boundary $\partial\Omega$.

Applying a spatial discretization

$$u_i = \sum_{a=1}^n N^a q_i^a, \quad \delta\varphi_i = \sum_{a=1}^n N^a \delta\varphi_i^a, \tag{27}$$

we end up with

$$\int_{\Omega} \rho N^b N^a \frac{\partial^2 q_i^b}{\partial t^2} \delta \varphi_i^a d\Omega + \int_{\Omega} C_{ijkl} \frac{\partial N^b}{\partial x_l} \frac{\partial N^a}{\partial x_j} q_k^b \delta \varphi_i^a d\Omega = \int_{\partial\Omega} t_i^* N^a \delta \varphi_i^a dS. \tag{28}$$

Due to the arbitrariness of the virtual field $\delta \varphi_i$, we can represent the latter relationship in the matrix form

$$\mathbf{M}\ddot{\mathbf{q}}(t) + \mathbf{K}\mathbf{q}(t) = \mathbf{f}_{ext}(t), \tag{29}$$

where $\mathbf{q}(t)$ is the nodal displacement vector, $\ddot{\mathbf{q}}(t)$ is the nodal acceleration vector, \mathbf{M} is the mass matrix having the form

$$\mathbf{M} = \int_{\Omega} \rho \mathbf{N}^T \mathbf{N} d\Omega, \tag{30}$$

\mathbf{K} is the stiffness matrix

$$\mathbf{K} = \int_{\Omega} \mathbf{B}^T \mathbf{C} \mathbf{B} d\Omega \tag{31}$$

and \mathbf{f}_{ext} is the load vector

$$\mathbf{f}_{ext} = \int_{\Gamma_N} \mathbf{N}^T \mathbf{t}^* d\Gamma. \tag{32}$$

In linear elastodynamic problems, the matrices \mathbf{K} and \mathbf{M} are constant for each finite element but may differ for distinct elements due to heterogeneous media. \mathbf{C} is the elasticity matrix, \mathbf{B} is the strain–displacement matrix, \mathbf{N} stores the displacement interpolation functions, for details see [21].

For the finite element simulation, we use the standard finite element based on displacement formulation with linear shape functions [21]. The integrals in Eqs. (30)–(32) are evaluated by the Gauss integration procedure. To reduce the integration cost for \mathbf{K} , we use the one-point integration rule with the hourglass control as described in [7]. Elements stiffness matrix \mathbf{K}_{el}^{1gp} obtained by the one-point Gauss integration are complemented by a stabilization stiffness matrix \mathbf{K}_{stab} suppressing hourglass modes, i.e., $\mathbf{K}_{el} = \mathbf{K}_{el}^{1gp} + \mathbf{K}_{stab}$. The mass matrix \mathbf{M} is lumped using row-summing procedure [21], which is preferred in the explicit time integration due to temporal–spatial dispersion [22].

5.2. Explicit time integration in FEM

In this paper, we use the central difference (CD) scheme for explicit time integration as described in the book [8]. The update of nodal velocities at each time step is then split into two half-steps, and the desired values of velocities can be prescribed directly. This approach is also called *leapfrog* integration. It is assumed that quantities $\mathbf{q}(t)$, $\dot{\mathbf{q}}(t)$, $\ddot{\mathbf{q}}(t)$ are known at the time instant t , and the task is to find their values at the next time step $t + \Delta t$. The central difference scheme as the leapfrog integration procedure takes the form presented in Algorithm 1:

Initialize $t^0 = 0$, \mathbf{q}^0 , $\dot{\mathbf{q}}^0$, assemble \mathbf{M} , \mathbf{K} , and compute $\ddot{\mathbf{q}}^0 = \mathbf{M}^{-1} (\mathbf{f}_{ext}^0 - \mathbf{K}\mathbf{q}^0)$

while $t < T$ **do**

setting of the time step size Δt

$\dot{\mathbf{q}}(t + \frac{\Delta t}{2}) = \dot{\mathbf{q}}(t) + \ddot{\mathbf{q}}(t) \frac{\Delta t}{2};$

$\mathbf{q}(t + \Delta t) = \mathbf{q}(t) + \dot{\mathbf{q}}(t + \frac{\Delta t}{2}) \Delta t;$

application of boundary conditions;

$\mathbf{r}(t + \Delta t) = \mathbf{f}_{ext}(t + \Delta t) - \mathbf{K}\mathbf{q}(t + \Delta t);$

$\ddot{\mathbf{q}}(t + \Delta t) = \mathbf{M}^{-1} \mathbf{r}(t + \Delta t);$

$\dot{\mathbf{q}}(t + \Delta t) = \dot{\mathbf{q}}(t + \frac{\Delta t}{2}) + \ddot{\mathbf{q}}(t + \Delta t) \frac{\Delta t}{2};$

application of boundary conditions;

$t = t + \Delta t;$

end

Algorithm 1: The central difference scheme in the *leapfrog* form for direct time integration of elastodynamic problems

It should be noted that the presented scheme is conditionally stable [21]. This means that the value of the time step Δt has to satisfy the stability limit $\Delta t < \Delta t_{cr}$, where Δt_{cr} is the critical limit given as $\Delta t_{cr} = 2/\omega_{max}$. Here

ω_{max} is the maximum angular frequency of the discretized homogeneous system (29). It is known that the maximum eigenfrequency of the assembled finite element mesh is smaller than the maximum value of each separated finite element consisted in the mesh [21], because this value is taken as a maximum over all values as $\omega_{max} \approx \max(\omega_{max}^e)$. Here $\omega_{max}^e = 2c_p^e/h^e$ is the maximum frequency of separated element with longitudinal wave speed c_p^e and length h^e for the case of the lumped mass matrix for regular meshes.

A regular mesh is preferred due to dispersion in the wave propagation problem. Suitable Dirichlet and Neumann boundary conditions and initial conditions should be included for solving the problem. Dirichlet boundary conditions are applied directly to nodal values of the displacement vector, velocity vector, acceleration vector, respectively, at Γ_D . Neumann boundary conditions are applied through the external nodal force $\mathbf{f}_{ext}(t)$. In the case of stress-free boundary conditions, the nodal external force vector is zero for material points at the boundary. It is known that Neumann boundary condition is only an approximation and goes to exact values as convergence properties of FEM with decreasing mesh size. The final results of stress tensor σ_{ij} , computed at integration points inside the finite element domain, are interpolated into the nodal values. This technique is called stress recovering. In the paper, we use the ZZ (Zienkiewicz and Zhu) algorithm for the stress recovery [33], which evaluates the stress tensor σ_{ij} values correctly.

6. Finite volume scheme

In the paper, the standard explicit finite volume scheme is employed following the observation by [19]: "Explicit schemes are often desirable due to their simplicity and efficiency. Furthermore, since the orders of the temporal and the spatial operator are the same for conservation laws, explicit methods are often superior when measured in terms of computational efficiency. For the multi-step schemes, the number of past steps can be very high for an efficient scheme".

For finite volume calculation, governing Eqs. (7)–(8) and (15)–(17) are presented in the conservation form [18]

$$\frac{\partial \mathbf{U}}{\partial t} + \frac{\partial \mathbf{F}}{\partial x_1} + \frac{\partial \mathbf{G}}{\partial x_2} = \mathbf{0}, \tag{33}$$

with the vector of variables \mathbf{U} and fluxes \mathbf{F} and \mathbf{G} defined as

$$\mathbf{U} = \begin{pmatrix} \rho v_1 \\ \rho v_2 \\ \sigma_{11} \\ \sigma_{12} \\ \sigma_{22} \end{pmatrix}, \quad \mathbf{F} = \begin{pmatrix} \sigma_{11} \\ \sigma_{12} \\ (\bar{\lambda} + 2\mu)v_1 \\ \mu v_2 \\ \bar{\lambda} v_1 \end{pmatrix}, \quad \mathbf{G} = \begin{pmatrix} \sigma_{12} \\ \sigma_{22} \\ \bar{\lambda} v_2 \\ \mu v_1 \\ (\bar{\lambda} + 2\mu)v_2 \end{pmatrix}. \tag{34}$$

For the discretization, a regular Cartesian grid of rectangular cells is used in space, and time is discretized by time levels. Variables are approximated by averaged values over cells. The use of cell averages is the standard procedure in the finite-volume method [18,24]. Integrating the governing equations over the control volume results in the Godunov-type numerical scheme [18]

$$\mathbf{U}_{n,m}^{k+1} = \mathbf{U}_{n,m}^k + \frac{\Delta t}{\Delta x_1} (\mathbf{F}_{n+1,m}^k - \mathbf{F}_{n,m}^k) + \frac{\Delta t}{\Delta x_2} (\mathbf{G}_{n,m+1}^k - \mathbf{G}_{n,m}^k). \tag{35}$$

Here the superscript k denotes time level and subscripts n and m indicate the number of cell in horizontal and vertical directions, respectively.

The numerical fluxes $\mathbf{F}_{n,m}^k$ and $\mathbf{G}_{n,m}^k$ are computed by solving Riemann problems at interfaces between cells [18,24]. Various methods have been proposed for the solution of Riemann problems [24,28,30,31]. In the paper, the thermodynamically consistent version of the wave propagation algorithm [9] is applied using jump relations at interfaces between computational cells, which express the continuity of true stresses and velocities. This algorithm provides algebraic procedure for the solution of Riemann problems, second-order accuracy [9], and stability up to values of Courant number close to unity.

6.1. Boundary conditions

To be able to perform the calculation of a particular problem we need to specify initial and boundary conditions. Initial conditions fix the state of each cell at a chosen time instant. We suppose that initially the strip is at rest, which

assumes zero values for all wanted fields. Boundary conditions are imposed by means of ghost cells following [24]. At the loaded upper boundary, the value of the normal stress in each cell and at each time step is given in advance. At the stress-free bottom boundary, the value of the normal stress is zero. Lateral boundary conditions are not specified because the length of the strip is chosen such that the influence of these boundaries is absent.

7. Numerical results and comparison with the analytical solution

In this Section, we present the results of numerical solution of pulse propagation in the homogeneous and heterogeneous strip. The results obtained by the in-house finite element algorithm and by the finite volume scheme specified above are compared to the analytical solution. The comparison of non-dimensional stress component σ_{11}/σ_0 is made at two selected points *A* and *B* for $x_0 = 10$ mm (see the problem sketch in Fig. 1). Note that stress components σ_{22} and σ_{12} have zero values at the points *A* and *B*, therefore only the normal stress σ_{11} is of interest.

We start with the homogeneous case and continue with the heterogeneous case of a layered strip composed by two different materials as specified in Section 2.

7.1. Homogeneous aluminum strip

Based on the geometry of the problem shown in Fig. 1, the values of parameters used for the numerical simulations are chosen as follows:

- Loading size $h = 2$ mm $= 10 \Delta x_1$;
- Strip thickness $d_1 + d_2 = 40$ mm $= 200 \Delta x_1$;
- Strip length $= 120$ mm $= 600 \Delta x_2$;
- Space step (mesh size) $\Delta x_1 = \Delta x_2 = 0.2$ mm;
- Distance $x_0 = 10$ mm $= 50 \Delta x_1$.

The time step Δt for explicit schemes is determined by the maximum of longitudinal velocity in the studied material. For pure aluminum, the value of the longitudinal wave velocity is 5448 m/s (see Table 1), which determines

$$\Delta t = \Delta x_1 / c_p = 2 \cdot 10^{-4} / 5448 = 3.67 \cdot 10^{-8} \text{ s.}$$

Correspondingly, the duration of the loading is

$$t_0 = 200 / 3.67 = 54 \Delta t.$$

The characteristic time T_0 is then

$$T_0 = 0.04 / 5448 = 7.34 \cdot 10^{-6} = 200 \Delta t.$$

Calculations are performed for 500 time steps providing the absence of influence of lateral boundaries of the strip.

The obtained results are shown in Figs. 5–6. Here blue lines correspond to the analytical solution, red lines represent the finite element simulation, and magenta lines denote results obtained by the finite volume calculations. As one can see, there is almost no difference between the results of finite element computations and the analytical solution.

At the same time, results of the finite volume simulation are qualitatively similar but quantitatively have observable distinctions. The reason is in the imposing of boundary conditions. The finite volume calculations are performed with the value of the Courant number less than unity due to stability demand. Keeping the same size for time and space steps as in the finite element computations, we arrive at the delay in the time variation of the loading, as it is demonstrated in Fig. 7. Here the blue line corresponds to the value of the Courant number equal to unity used in the finite element solution and the magenta line shows the representation of the same pulse for $Co = 0.83$ employed in the finite volume calculations. The initial delay in input causes the delay in the response.

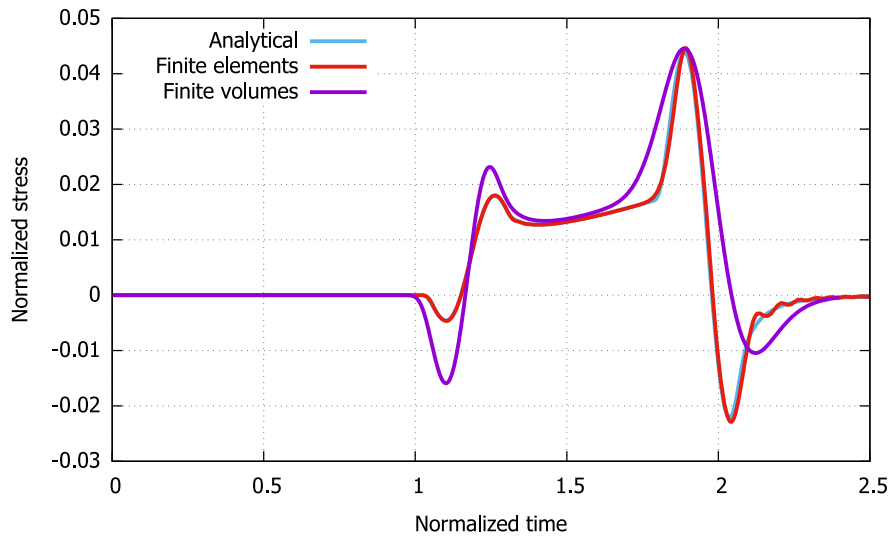


Fig. 5. Time history of the normalized stress σ_{11} at point A in homogeneous aluminum strip.

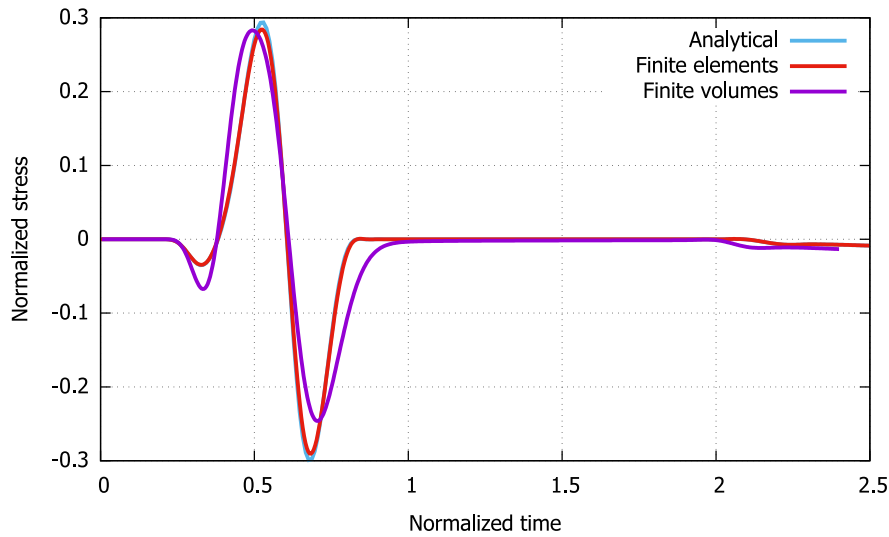


Fig. 6. Time history of the normalized stress σ_{11} at point B in homogeneous aluminum strip.

7.2. Composite strip Al–Al₂O₃

Now we compare the results of numerical simulations with the analytical solution in the case of the layered strip. First, we consider the case where pure aluminum is in the layer 1, and the layer 2 is made from the ceramics Al₂O₃. Since the longitudinal wave speed for Al₂O₃ is 10352.8 m/s, the time step Δt for the simulation is

$$\Delta t = \Delta x / c_p = 2 \cdot 10^{-4} / 10352.8 = 1.93 \cdot 10^{-8} \text{ s.}$$

Accordingly, the duration of the loading is

$$t_0 = 200 / 1.93 = 104 \Delta t,$$

and the characteristic time T_0 is then

$$T_0 = 0.04 / 10352.8 = 3.86 \cdot 10^{-6} = 200 \Delta t.$$

The comparison of numerical and analytical solutions for the time history of the normalized stress σ_{11} at points A and B, in this case, is presented in Figs. 8–9. The finite element and analytical results are practically coincided in the considered case. Even finite volume calculations are closer to analytical and finite element outcomes.

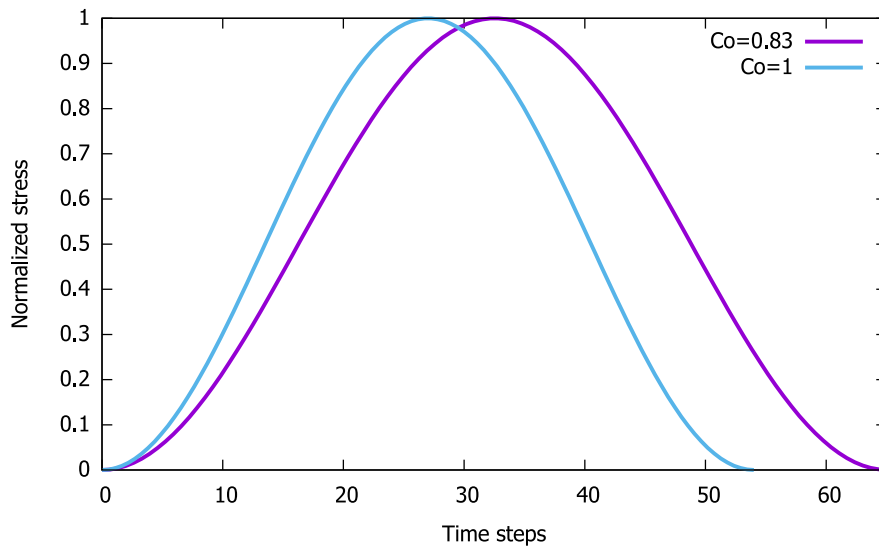


Fig. 7. Time variation of loading pulse along the vertical central line.

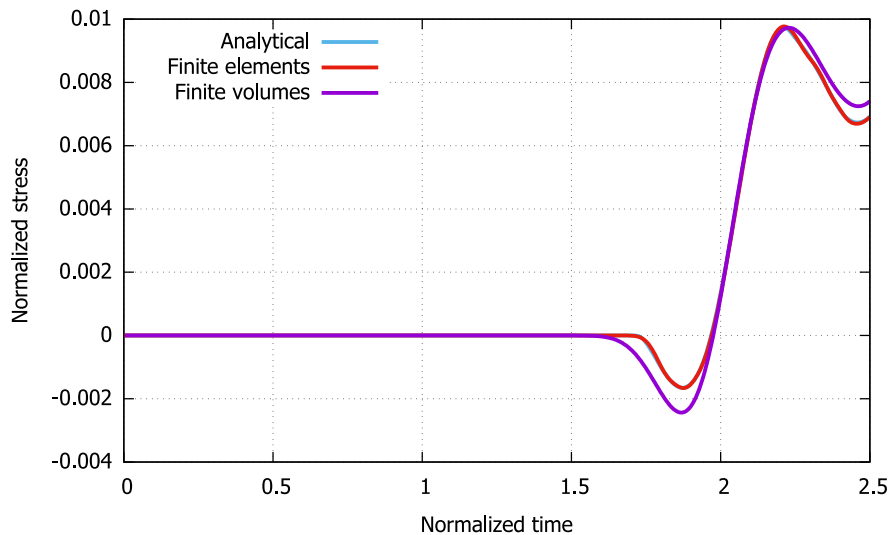


Fig. 8. Time history of the normalized stress σ_{11} at point A in two-layer $Al-Al_2O_3$ strip.

7.3. Composite strip Al_2O_3-Al

Now we alter the placement of the layers to see how this alteration affects the comparison. This means that the layer 1 is made from the ceramic Al_2O_3 and the layer 2 is made from pure aluminum. The parameters used in simulations are the same as in the previous case because the only placement of layers is changed. The comparison of numerical and analytical solutions for the time history of the longitudinal stress at points A and B is presented in Figs. 10–11.

Again, blue lines in mentioned figures still correspond to the analytical solutions, the red ones show the results of finite element computations and the magenta lines denote the results obtained by finite volume calculations. It is clear that the variation of stresses in time is changed, but finite element results are in a perfect agreement with the analytical ones. As before, finite volume calculations provide less accurate results due to the reasons mentioned above.

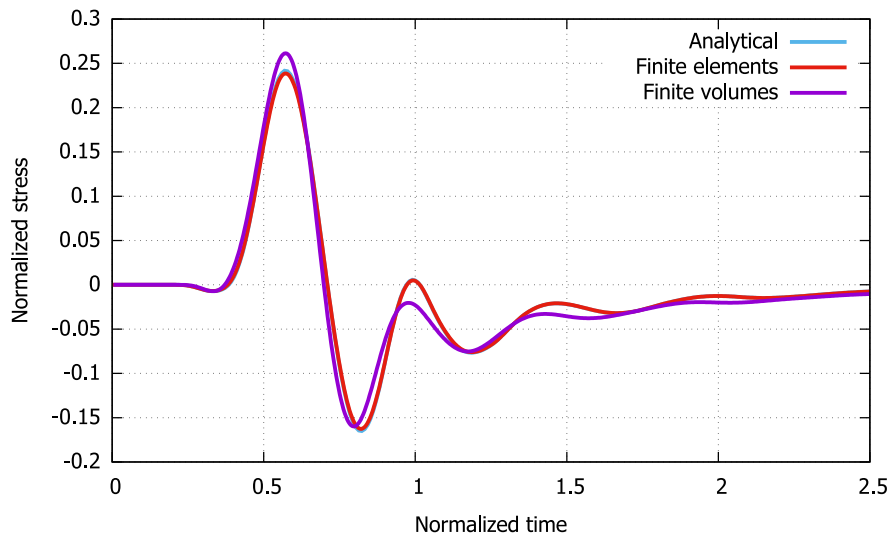


Fig. 9. Time history of the normalized stress σ_{11} at point B in two-layer $Al-Al_2O_3$ strip.

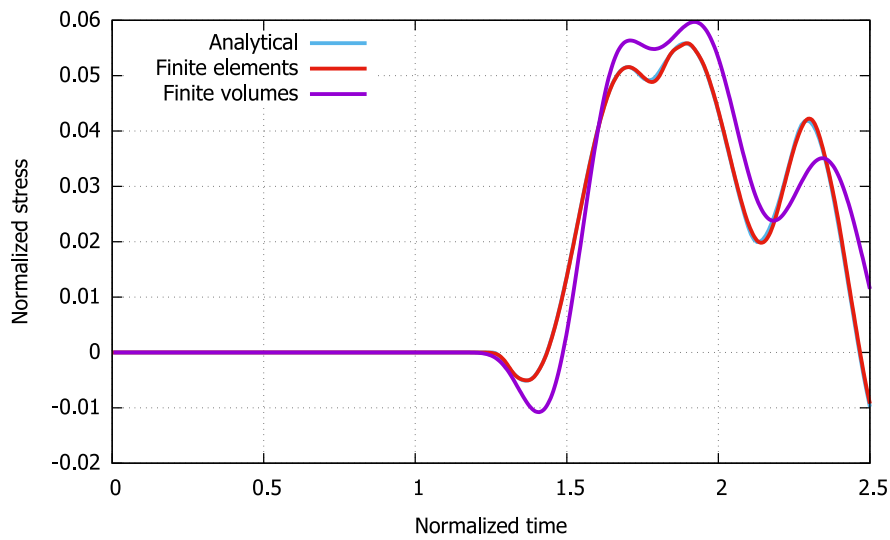


Fig. 10. Time history of the longitudinal stress at point A in two-layer Al_2O_3-Al strip.

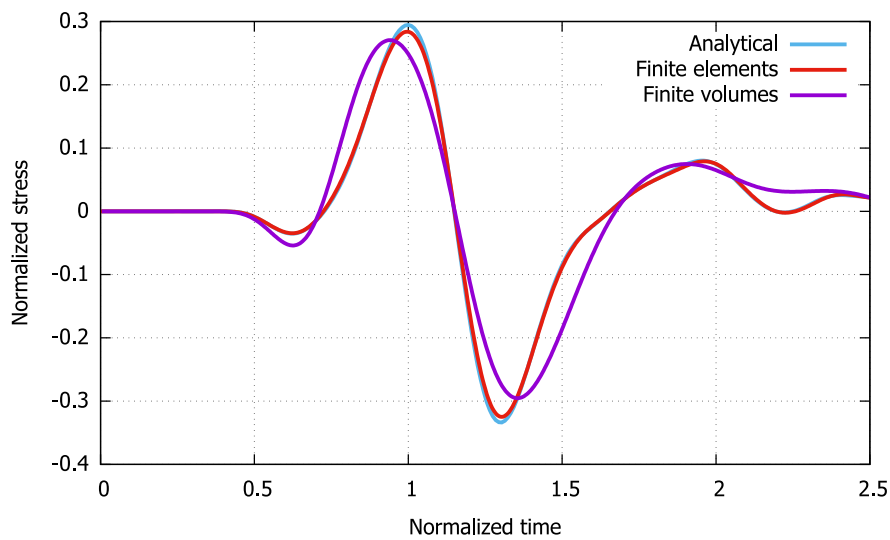


Fig. 11. Time history of the longitudinal stress at point B in two-layer Al_2O_3-Al strip.

8. Conclusions

The main goal of the paper was to examine how accurate are numerical calculations in the comparison with the analytical solution of two-dimensional transverse pulse propagation in a two-layer strip fabricated from materials with highly distinct properties. Time histories of stresses at two different points placed at boundaries of the strip were used for the comparison. It is demonstrated that the in-house finite element algorithm provides the perfect coincidence between analytical and numerical results for all considered examples. The agreement with the results by the finite volume scheme is less definitive due to the distinction in the posing of loading conditions. The main conclusion is that the used numerical algorithms can be applied to the prediction of signal propagation in more complex practical situations.

This work provides the basis for the application of elaborated numerical methods to heterogeneous media with several layers, to graded media, and to media with inclusions. The influence of a microstructure on dispersive behavior of waves in structures can be analyzed by these numerical approaches, where we can control the accuracy. A special attention has to be paid on discontinuous wave propagation in heterogeneous cases which is still an open problem in numerical modeling of composite structures.

Acknowledgments

The research was supported by the Grant project with No. 19-04956S of the Czech Science Foundation (CSF) within institutional support RVO:61388998 (A.B., V.A., R.K.), by the Centre of Excellence for Nonlinear Dynamic Behaviour of Advanced Materials in Engineering, Czech Republic CZ.02.1.01/0.0/0.0/15_003/0000493 (Excellent Research Teams) in the framework of Operational Programme Research, Development and Education (M.M.), by Estonian Research Council under Institutional Research Funding IUT33-24 (A.B.) and by the project LO1506 of the Czech Ministry of Education, Youth and Sports under the program NPU I(V.A.).

References

- [1] J. Achenbach, *Wave Propagation in Elastic Solids*, Elsevier, 1973.
- [2] V. Adánek, The limits of timoshenko beam theory applied to impact problems of layered beams, *Int. J. Mech. Sci.* 145 (2018) 128–137.
- [3] V. Adánek, F. Valeš, J. Červ, Numerical Laplace inversion in problems of elastodynamics: Comparison of four algorithms, *Adv. Eng. Softw.* 113 (2017) 120–129.
- [4] D.G. Aggelis, Wave propagation through engineering materials; assessment and monitoring of structures through non-destructive techniques, *Mater. Struct.* 46 (4) (2013) 519–532.
- [5] H. Aksoy, E. Şenocak, Wave propagation in functionally graded and layered materials, *Finite Elem. Anal. Des.* 45 (12) (2009) 876–891.
- [6] J.R. Barber, *Elasticity*, Springer, 2009.
- [7] T. Belytschko, W.E. Bachrach, Efficient implementation of quadrilaterals with high coarse-mesh accuracy, *Comput. Methods Appl. Mech. Engrg.* 54 (3) (1986) 279–301, [http://dx.doi.org/10.1016/0045-7825\(86\)90107-6](http://dx.doi.org/10.1016/0045-7825(86)90107-6).
- [8] T. Belytschko, W. Liu, B. Moran, K. Elkhodary, *Nonlinear Finite Elements for Continua and Structures*, Wiley, 2013.
- [9] A. Berezovski, J. Engelbrecht, G.A. Maugin, *Numerical Simulation of Waves and Fronts in Inhomogeneous Solids*, World Scientific Singapore, 2008.
- [10] A. Berezovski, R. Kolman, M. Berezovski, D. Gabriel, V. Adánek, Full field computing for elastic pulse dispersion in inhomogeneous bars, *Compos. Struct.* 204 (2018) 388–394, <http://dx.doi.org/10.1016/j.compstruct.2018.07.055>.
- [11] L. Brančík, Programs for fast numerical inversion of Laplace transforms in MATLAB language environment, in: *Proceedings of the 7th Conference MATLAB'99*, 1999, pp. 27–39.
- [12] H.-P. Chen, *Structural Health Monitoring of Large Civil Engineering Structures*, John Wiley & Sons, 2018.
- [13] A. Cohen, *Numerical Methods for Laplace Transform Inversion*, Springer, 2007.
- [14] M.E. De Simone, F. Ciampa, S. Boccardi, M. Meo, Impact source localisation in aerospace composite structures, *Smart Mater. Struct.* 26 (12) (2017) 125026.
- [15] D. Grady, Shock-wave compression of brittle solids, *Mech. Mater.* 29 (3–4) (1998) 181–203.
- [16] K.F. Graff, *Wave Motion in Elastic Solids*, Clarendon Press, 1975.
- [17] C.U. Grosse, M. Ohtsu, *Acoustic Emission Testing*, Springer Science & Business Media, 2008.
- [18] V. Guinot, *Godunov-type Schemes: An Introduction for Engineers*, Elsevier, 2003.
- [19] J.S. Hesthaven, *Numerical Methods for Conservation Laws: From Analysis to Algorithms*, SIAM, 2017.
- [20] K.M. Holford, M.J. Eaton, J.J. Hensman, R. Pullin, S.L. Evans, N. Dervilis, K. Worden, A new methodology for automating acoustic emission detection of metallic fatigue fractures in highly demanding aerospace environments: An overview, *Prog. Aerosp. Sci.* 90 (2017) 1–11.
- [21] T.J.R. Hughes, *The Finite Element Method: Linear Static and Dynamic Finite Element Analysis*, Dover Publication, 2000.

- [22] R. Kolman, J. Plešek, J. Červ, M. Okrouhlík, P. Pařík, Temporal-spatial dispersion and stability analysis of finite element method in explicit elastodynamics, *Internat. J. Numer. Methods Engrg.* 106 (2) (2016) 113–128, <http://dx.doi.org/10.1002/nme.5010>.
- [23] T. Kundu, Acoustic source localization, *Ultrasonics* 54 (1) (2014) 25–38.
- [24] R.J. LeVeque, *Finite Volume Methods for Hyperbolic Problems*, Cambridge University Press, 2002.
- [25] L. Maio, V. Memmolo, F. Ricci, N. Boffa, E. Monaco, R. Pecora, Ultrasonic wave propagation in composite laminates by numerical simulation, *Compos. Struct.* 121 (2015) 64–74.
- [26] A. Nayfeh, *Wave Propagation in Layered Anisotropic Media*, North Holland, 1995.
- [27] W. Ostachowicz, P. Malinowski, T. Wandowski, Damage localisation using elastic waves propagation method. experimental techniques, in: *New Trends in Structural Health Monitoring*, Springer, 2013, pp. 317–371.
- [28] P.L. Roe, Approximate Riemann solvers, parameter vectors, and difference schemes, *J. Comput. Phys.* 43 (2) (1981) 357–372.
- [29] J.L. Rose, *Ultrasonic Waves in Solid Media*, Cambridge University Press, 2004.
- [30] E.F. Toro, *Riemann Solvers and Numerical Methods for Fluid Dynamics: A Practical Introduction*, Springer Science & Business Media, 1997.
- [31] E.F. Toro, *Godunov Methods: Theory and Applications*, Springer Science & Business Media, 2001.
- [32] C. Willberg, S. Duczek, J. Vivar-Perez, Z. Ahmad, Simulation methods for guided wave-based structural health monitoring: a review, *Appl. Mech. Rev.* 67 (1) (2015) 010803.
- [33] O. Zienkiewicz, J. Zhu, The superconvergent patch recovery (SPR) and adaptive finite element refinement, *Comput. Methods Appl. Mech. Engrg.* 101 (1) (1992) 207–224, [http://dx.doi.org/10.1016/0045-7825\(92\)90023-D](http://dx.doi.org/10.1016/0045-7825(92)90023-D).
- [34] B. Zuanetti, T. Wang, V. Prakash, A novel approach for plate impact experiments to determine the dynamic behavior of materials under extreme conditions, *J. Dyn. Behav. Mater.* 3 (1) (2017) 64–75.



ELSEVIER

Contents lists available at ScienceDirect

Applied Acoustics

journal homepage: www.elsevier.com/locate/apacoust

Experimental, analytical, and numerical study of transient elastic waves from a localized source in an aluminium strip

M. Mračko^a, V. Adámek^{b,*}, A. Berezovski^{c,a}, J. Kober^a, R. Kolman^a

^a Institute of Thermomechanics, v.v.i., The Czech Academy of Sciences, Dolejškova 1402/5, 182 00 Praha 8, Czech Republic

^b NTIS – New Technologies for the Information Society, Faculty of Applied Sciences, University of West Bohemia, Technická 8, 301 00 Pilsen, Czech Republic

^c Department of Cybernetics, School of Science, Tallinn University of Technology, Akadeemia 21, 12618 Tallinn, Estonia

ARTICLE INFO

Article history:

Received 26 September 2020

Received in revised form 4 February 2021

Accepted 8 February 2021

Available online 16 March 2021

Keywords:

Wave propagation

Elastic strip

Experimental measurement

Finite element method

Finite volume method

Analytical solution

Plane stress problem

ABSTRACT

Two-dimensional wave propagation in an aluminium strip is examined experimentally, analytically, and numerically in this paper. The high-frequency pulse is generated by a piezoelectric transducer, and the velocity component normal to the strip edge is measured by the non-contact vibrometer system. In-plane waves are then investigated under plane stress conditions using the analytical method based on Laplace and Fourier transforms. For numerical solution, explicit variants of finite element and finite volume solvers are utilized. It is shown that the used numerical algorithms confirm the analytical results and that they are suitable to represent the transient wavefield observed in the experiment including several wave reflections from upper and bottom strip boundaries.

© 2021 Elsevier Ltd. All rights reserved.

1. Introduction

The simplest possible scheme of ultrasonic nondestructive testing (such as presented in Fig. 1) suggests that the signal issued by a transmitter is recorded by a receiver. The difference in the shape and phase between initial and reflected signals can be interpreted as the existence of a defect inside the specimen.

As a rule, the exciting signal is a windowed wave packet centered at certain frequency [19, e.g.], and only first recorded reflection is considered. Much longer records at the receiver are used if a time-reversal procedure is expected [11, e.g.]. In an ideal situation, the wave propagates with constant velocity and its propagation from the transmitter to the sensor is straight and can be interrupted only by the investigated defect. However, even if we restrict ourselves to a two-dimensional strip setting, we cannot find the analytical solution for wave propagation in a finite homogeneous strip. The exact analytical approach is feasible only in the case of an infinite strip as shown by [22] for a strip with distributed transversal excitation and by [8] for a suddenly applied transversal point force. Numerical studies dealing with two-dimensional strip

problems are more common. One can mention for instance the work [23] where the propagation of acoustic emission signal is investigated using the finite element approach.

It should be noted that the strip geometry is closely related to propagation of Lamb waves in thin plates [16,4], which are widely applied to structural health monitoring problems [10]. Modeling of Lamb waves with the desired accuracy, reliability, and efficiency is a valuable part of the methodology, software, and hardware for non-destructive evaluation and structural health monitoring [24]. Various numerical methods have been used for their simulations [16,21,13,18,4, e.g.]. However, as it is demonstrated in [15], the existing computational packages (ANSYS, COMSOL, ABAQUS) are unable to represent wavefield in laminates adequately. The reason is that the commercial software use one-step time schemes which are not able to prescribe wave propagation in heterogeneous media accurately due to spatial dispersion and transmission/reflection effects on interfaces.

It is, therefore, highly desired to have correct descriptive and computational tools for the prediction of wave propagation in a basic setting. The paper presents the results of the experimental, theoretical, and computational study of the propagation of transient elastic waves from a localized source in a homogeneous aluminium strip. The main goal is to examine and verify the suitability of numerical procedures to represent the transient wavefield observed during the experiment. Section 2 is devoted to the

* Corresponding author.

E-mail addresses: mracko@it.cas.cz (M. Mračko), vadamek@kme.zcu.cz (V. Adámek), Arkadi.Berezovski@cs.ioc.ee (A. Berezovski), kober@it.cas.cz (J. Kober), kolman@it.cas.cz (R. Kolman).

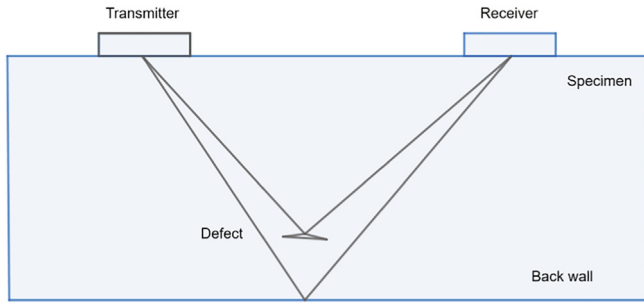


Fig. 1. Transmitter – receiver scheme for structural health monitoring.

description of the experimental setup and procedure. Governing equations corresponding to linear elasticity are presented in Section 3. Analytical solution and numerical methods are shortly described in Section 4. In Section 5, the comparison of analytical, numerical, and experimental results are presented. Conclusions and discussion are included in the last Section.

2. Experimental setup

Measurements of wave propagation in an elastic strip of finite length were done in the Laboratory of Non-Destructive Testing of the Institute of Thermomechanics of the Czech Academy of Sciences. The elastic strip was made from a homogeneous isotropic Al alloy D16-ATV. Material parameters that are necessary for wave investigation in such a medium are summarized in Table 1. The value of longitudinal speed c_p corresponds to plane stress conditions.

Dimensions of the strip suspended on thin UHMWPE Dyneema filaments were $399 \times 50 \times 1.35$ mm. To induce a loading pulse, the piezoelectric transducer Dakel IDK09 of diameter 6mm was glued in the middle of the strip from the bottom side (see Fig. 2). The NI PXI test system includes NI PXI 5105 digitizer and NI PXI 5412 generator connected with a custom power pulse amplifier. For the non-contact vibration record, the Polytec vibrometer system was

Table 1
Material properties of the strip under investigation.

Material	Density	Young modulus	Poisson ratio	Longitudinal speed	Shear speed
	ρ (kg/m ³)	E (GPa)	ν	c_p (m/s)	c_s (m/s)
Al alloy D16-ATV	2770	72	0.333	5401	3126

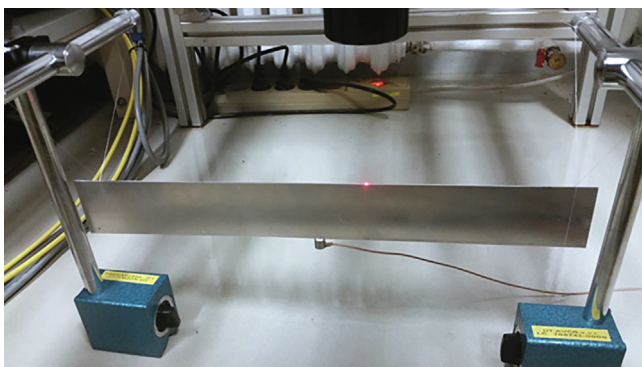


Fig. 2. Experimental setup.

used. The OFV-5000 controller decodes the sensor OVF-505 head's signals in real time. The automated ultrasonic Starmans scanning stage DIO 200 system was applied for the signal inspection. The mentioned device enabled the lengthwise scanning along the upper edge at points of a regular grid with the step of 1mm. The response measured up to 750 μ s was represented by 15 000 samples at frequency 20MHz, i.e. the sampling time step was $\Delta t = 5 \cdot 10^{-8}$ s.

The input signal to the transducer causing the strip loading corresponds to a smooth pulse of duration $t_0 = 9 \mu$ s with maximal amplitude $\sigma_0 = 0.72$ MPa. Its amplitude changes according to cosine train 333kHz with 0.25 cosine window. This pulse can be expressed as

$$\sigma(t) = \begin{cases} \frac{\sigma_0}{2} \cos\left(\frac{\pi t}{30}\right) \left(1 - \cos\left(\frac{\pi t}{22}\right)\right) & \text{for } t \leq 23\Delta t, \\ \sigma_0 \cos\left(\frac{\pi t}{30}\right) & \text{for } 23\Delta t \leq t \leq 157\Delta t, \\ \frac{\sigma_0}{2} \cos\left(\frac{\pi t}{30}\right) \left(1 - \cos\left(\frac{\pi(180-t)}{22}\right)\right) & \text{for } 157\Delta t \leq t \leq 180\Delta t, \\ 0 & \text{for } t \geq 180\Delta t. \end{cases}$$

The time history of this input signal is shown in Fig. 3 (curve *Ideal pulse*). The more precise experimental investigation shows that the input signal does not correspond to the real signal exciting the strip (see Fig. 3, curve *Real pulse*). This real pulse is the result of the normal velocity measurement in the center of the transducer surface using a vibrometer. The difference between the ideal pulse (input electric signal into the transducer) and real pulse (corresponding to the normal velocity measured on the transducer surface) is due to complex wave processes inside the transducer, piezo-electric response, and piezo-electric/mechanical coupling. Moreover, the information about the time history of the normal velocity on the transducer surface can be implemented into the finite element model as a time-varying Dirichlet boundary condition. In parallel, the normal stress loading will be applied via Neumann boundary conditions.

In reality, one has to think also about a non-ideal connection between the transducer and the strip under investigation. This effect is neglected both in numerical and analytical solutions of the problem, so an ideal connection between the transducer and the strip is assumed.

3. Model description and mathematical formulation

The problem lies in the investigation of the transient response of an elastic strip to a transversal loading, as mentioned previously. The sketch of the model corresponding to the described measured problem is shown in Fig. 4.

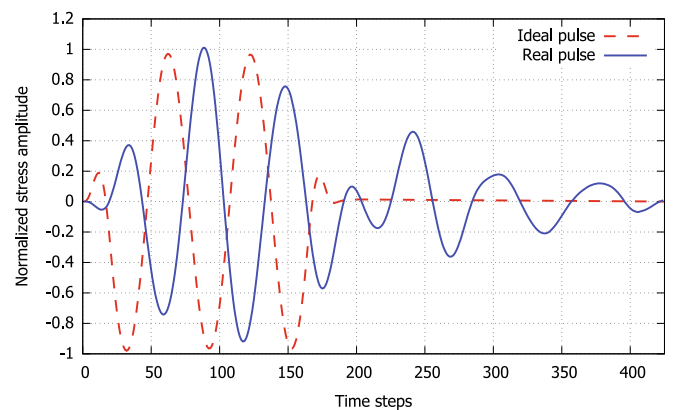


Fig. 3. Shape of ideal and real loading pulses.

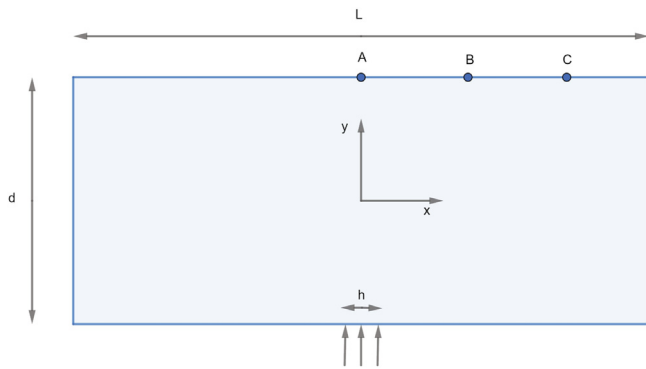


Fig. 4. Sketch of the problem.

According to the introduced coordinate system and to the experiment description given in Section 2, the stress loading $p(x, t)$ is nonzero only for $y = -d/2$ and $x \in [-h/2, h/2]$. It will be approximated by $p(x, t) = (H(x + h/2) - H(x - h/2))\sigma(t)$, where $H(x)$ denotes the Heaviside function in x and $\sigma(t)$ stands for the ideal or real pulse from Fig. 3. The problem was solved as the symmetric one and the evaluation of vertical velocity component up to time $t_{max} = 750\mu s$ was primarily made at points A, B, and C for comparison with experimental data. The position of these points is shown in Fig. 4 and the distance between them is 13.5 mm each.

The problem is considered in the framework of small strain elasticity theory. For thin strip, we use the plane stress approximation suggesting that stress normal to the strip plane and appropriate shear stresses can be neglected, i.e.,

$$\sigma_{i3} = 0, \quad i = 1, 2, 3. \quad (1)$$

The governing equations of homogeneous linear isotropic elasticity in the absence of body forces specialized to plane stress conditions have the form [20]

$$\rho \frac{\partial v_1}{\partial t} = \frac{\partial \sigma_{11}}{\partial x} + \frac{\partial \sigma_{12}}{\partial y}, \quad (2)$$

$$\rho \frac{\partial v_2}{\partial t} = \frac{\partial \sigma_{21}}{\partial x} + \frac{\partial \sigma_{22}}{\partial y}, \quad (3)$$

where t is time, v_i are the components of the velocity vector, σ_{ij} is the Cauchy stress tensor and ρ is the density.

Accordingly, compatibility conditions for strains are represented as

$$\frac{\partial \varepsilon_{11}}{\partial t} = \frac{\partial v_1}{\partial x}, \quad (4)$$

$$\frac{\partial \varepsilon_{12}}{\partial t} = \frac{1}{2} \left(\frac{\partial v_1}{\partial y} + \frac{\partial v_2}{\partial x} \right), \quad (5)$$

$$\frac{\partial \varepsilon_{22}}{\partial t} = \frac{\partial v_2}{\partial y}. \quad (6)$$

The Hooke law defining the stress–strain relation is modified as follows [20]:

$$\sigma_{11} = (\bar{\lambda} + 2\mu)\varepsilon_{11} + \bar{\lambda}\varepsilon_{22}, \quad (7)$$

$$\sigma_{12} = \sigma_{21} = 2\mu\varepsilon_{12}, \quad (8)$$

$$\sigma_{22} = (\bar{\lambda} + 2\mu)\varepsilon_{22} + \bar{\lambda}\varepsilon_{11}, \quad (9)$$

where $\bar{\lambda} = 2\mu\lambda/(\lambda + 2\mu)$ and λ and μ are the Lamé coefficients. Compatibility conditions (4)–(6) allow to eliminate strains in time derivatives of stress–strain relations

$$\frac{\partial \sigma_{11}}{\partial t} = (\bar{\lambda} + 2\mu) \frac{\partial v_1}{\partial x} + \bar{\lambda} \frac{\partial v_2}{\partial y}, \quad (10)$$

$$\frac{\partial \sigma_{22}}{\partial t} = \bar{\lambda} \frac{\partial v_1}{\partial x} + (\bar{\lambda} + 2\mu) \frac{\partial v_2}{\partial y}, \quad (11)$$

$$\frac{\partial \sigma_{12}}{\partial t} = \frac{\partial \sigma_{21}}{\partial t} = \mu \left(\frac{\partial v_1}{\partial y} + \frac{\partial v_2}{\partial x} \right). \quad (12)$$

Together with the balance of linear momentum (2)–(3), latter equations form the system of equations, which is convenient for the solution.

4. Solution methods

4.1. Analytical solution

As mentioned in Section 1, there exists the analytical solution of an infinite elastic strip problem derived by [22]. In our study, we generalized this solution to an arbitrary type of external loading even in the variable x_1 , see Fig. 4. Analogously to [1], the Laplace transform of the vertical velocity component v_2 can be written as

$$\bar{v}_2(x, y, p) = -\frac{p}{\pi} \int_0^\infty [(C_1 \sinh(\lambda_1 y) + C_2 \cosh(\lambda_1 y))k_1 + (C_3 \cosh(\lambda_2 y) + C_4 \sinh(\lambda_2 y))k_2] \cos(\omega x) d\omega, \quad (13)$$

where $p \in \mathbb{C}$ denotes the variable of Laplace transform and the relevant complex functions are defined by

$$\lambda_1(\omega, p) = \sqrt{\omega^2 + \frac{p^2}{c_p^2}}, \quad \lambda_2(\omega, p) = \sqrt{\omega^2 + \frac{p^2}{c_s^2}}, \quad (14)$$

$$k_1(\omega, p) = \frac{c_p^2 \lambda_1(\omega, p)}{p^2}, \quad k_2(\omega, p) = \frac{2c_s^2 \omega}{p^2}. \quad (15)$$

The complex unknowns $C_i(\omega, p)$ for $i = 1, \dots, 4$ in (13) can be determined using the boundary conditions of the problem. The evaluation procedure of the formula (13) is similar to that presented in the work [1]. This two-step procedure involves the inverse Laplace transform and the evaluation of Fourier integral. The latter one issue is addressed by classical Simpson's rule with a regular integration grid while the first one is resolved by the application of an algorithm based on fast Fourier transform and Wynn's epsilon accelerator. This accelerator is used to speed up the summation of infinite series involved in the inversion process, see [7]. The precision and the stability of this procedure is discussed in detail in [2].

4.2. Finite volume computations

Among finite volume methods, the most suitable for our purpose is the wave propagation algorithm [17]. Its two-dimensional implementation is applied for the simulation of wave propagation in the finite elastic strip. The thermodynamically consistent version of the algorithm [6] is employed with values of the Courant number close to unity. The applied method is second-order accurate on smooth solutions [3]. Boundary conditions are imposed using ghost cells following [17].

4.3. Finite element computations

In the finite element computations based on an in-house code, we use the displacement formulation with linear shape functions [12], which are preferred in explicit time integration with the lumped mass matrix. The central difference method for direct time integration is employed, therefore the stability limit according to the Courant–Friedrichs–Lewy condition should be satisfied, see [9]. For evaluation of the stiffness matrix, the one-Gauss point inte-

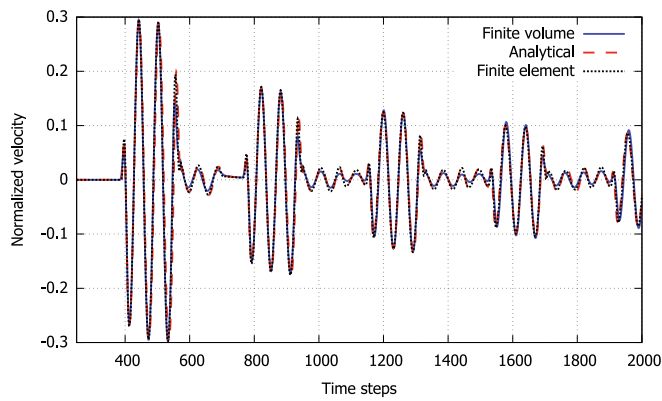


Fig. 5. The response to the ideal pulse: analytical solution vs numerical simulations.

gration with the hourglass stabilization [5] is utilized. For the maximum frequency contained in the loading pulse, the length of the finite element edge is set to 0.25mm due to the spatial dispersion of the finite element method [14]. The time step size corresponds to the Courant number $Co = 0.97$.

5. Infinite strip

To validate the accuracy of both numerical methods, it is instructive to start with the problem of an infinite strip for which the analytical solution exists. According to the experimental setup, the time step $\Delta t = 5 \cdot 10^{-8} s$ and the ideal pulse of duration $t_0 = 180 \Delta t = 9 \mu s$ are used at first. Space step for explicit schemes corresponds to the Courant number $Co = 1$ determined by the maximum of longitudinal velocity in material. In the case of Al alloy D16-ATV, the longitudinal wave velocity is equal to 5401 m/s which means that $\Delta x = c_p \cdot \Delta t = 0.27 \text{ mm}$. It follows then that the strip width $d = 50 \text{ mm} = 185 \Delta x$ and the loading length $h = 6 \text{ mm} = 22 \Delta x$.

Using these values, the computation of wave propagation in the strip under ideal loading via the normal stress shown in Fig. 3 was performed analytically and by finite volume and finite element methods. Results of numerical simulations and analytical solution are compared at all three points. The comparison at point A that corresponds to the middle of the strip is presented in Fig. 5. As one can see, the results of simulations by finite volume and finite element methods are almost coinciding with the analytical solution up to 2000 time steps (100 μs), i.e., at early stages of the signal propagation. Similar results have been obtained also for points B and C. After 2000 time steps, the results start to diverge due to the influence of lateral vertical boundaries of the strip used in numerical models. Based on this comparison, we can conclude that the chosen finite element and finite volume methods are suitable for the elastic wave propagation problem in the strip.

The same coincidence between the analytical and numerical solutions was achieved also for the real pulse excitation. Making such verification of applied approaches, the obtained results can be compared with the measured strip response to the real pulse. This comparison is presented in Fig. 6, Fig. 7, Fig. 8 for all three studied points. Due to the mentioned coincidence between analytical and numerical solutions, only analytical and experimental results are shown.

It is seen that the very good agreement with the measured data occurs for the first 1000 time steps (i.e. up to time 50 μs), especially at point B (see Fig. 7). Considering the time history for the vertical velocity at point C (Fig. 8), we cannot say that the agreement with the experiment is as good as at the previous points even for the short time simulations. Also for longer times, the dispersion

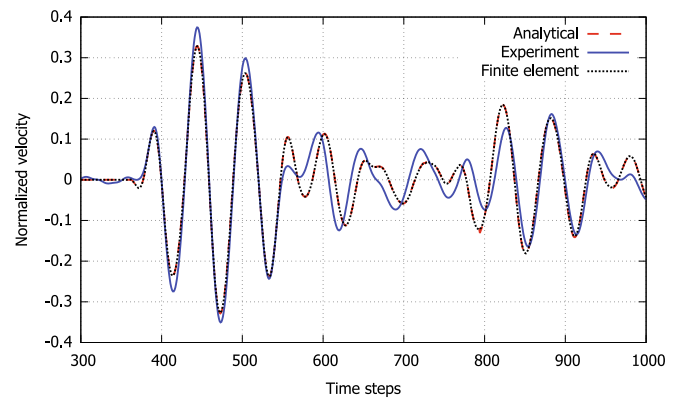


Fig. 6. The response to the real pulse at point A: analytical and numerical solution vs experimental data.

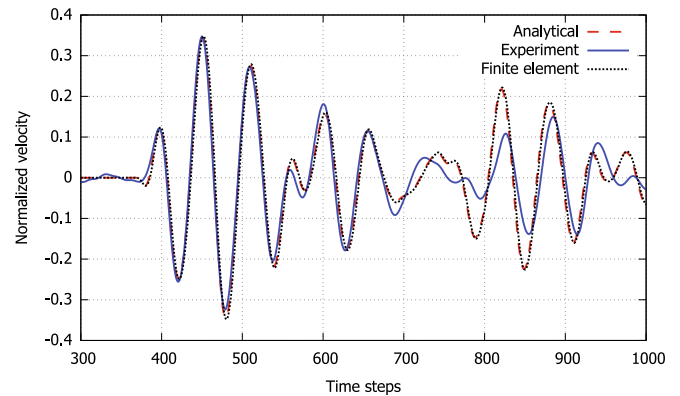


Fig. 7. The response to the real pulse at point B: analytical and numerical solution vs experimental data.

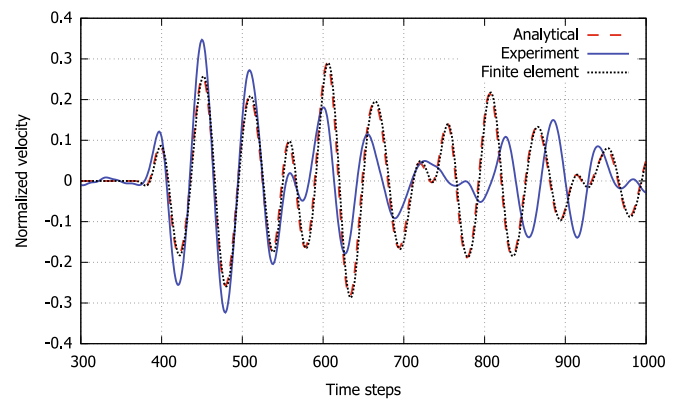


Fig. 8. The response to the real pulse at point C: analytical and numerical solution vs experimental data.

properties of the real strip and the real structure of the strip material make the differences between both responses more significant at all three points.

The application of the Dirichlet boundary condition for the normal velocity is also checked in the finite element simulations. The results of the time history of the normal velocity at the point B are depicted in Fig. 9 as an example. One can see that the results for Dirichlet and Neumann boundary conditions are very close to each other. So it can be said that both types of boundary conditions can be used for correct representation of transducer loading.

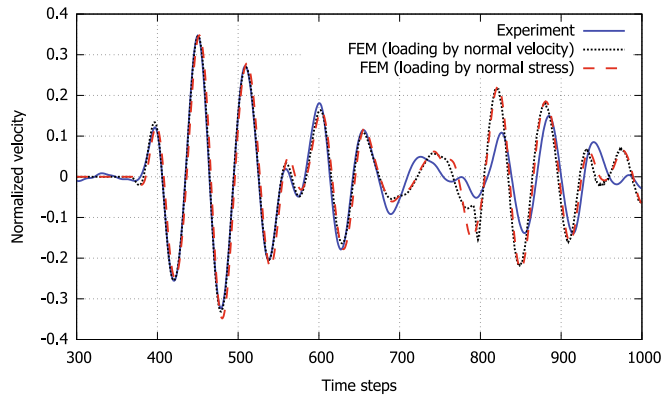


Fig. 9. The response to the real pulse at point B obtained by the stress and velocity loading.

Having the verified analytical and numerical models for short time response of the real strip, one can use these models to visualize the wavefield the consequences of which have been measured at the strip edge. For this purpose, the snapshots of the mean velocity $\sqrt{v_1^2 + v_2^2}$ at various time instants obtained by the analytical solution are shown in Fig. 10. This picture demonstrates how the wave field is varied due to reflections from upper and bottom boundaries and internal interferences. A clear separation between the longitudinal wave and the pattern of remaining wave interference is observed.

6. Finite strip

In the case of finite strip, we need to take into account the reflections from the lateral vertical boundaries. It requires computations for a longer time. The comparison of experimental data with analytical solution and numerical results obtained by the finite element method is shown in Fig. 11. The results of finite volume simulation are not presented because they are nearly identical to analytical ones up to about 2000 time steps and for longer times they do not conserve the total energy of the signal. It is clear from Fig. 11 that all results coincide quite well up to about 2500 time

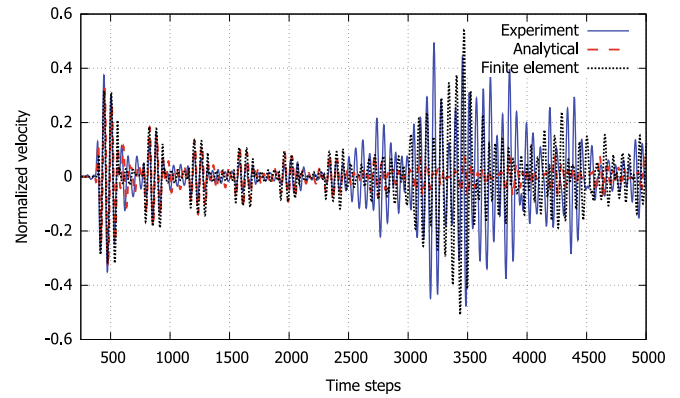


Fig. 11. Measured response vs analytical solution and finite element computation for longer time.

steps. After this time instant, the analytical solution does not represent the real response due to the absence of lateral strip boundaries influence. The results of finite element computations take the reflections from lateral boundaries into account, but uncertainties in experimental setup prevent the detailed coincidence.

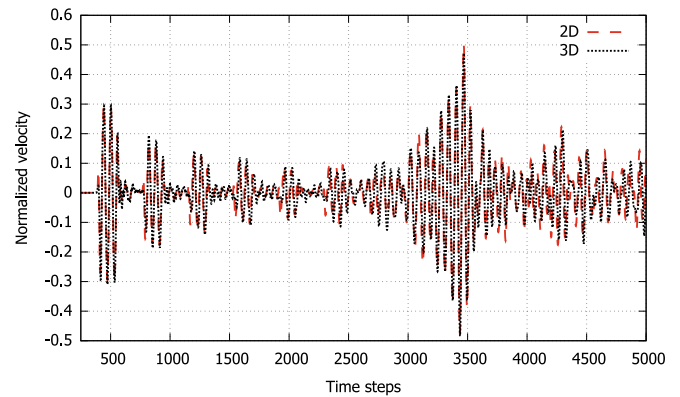


Fig. 12. Comparison of results for finite element 2D and 3D simulation.

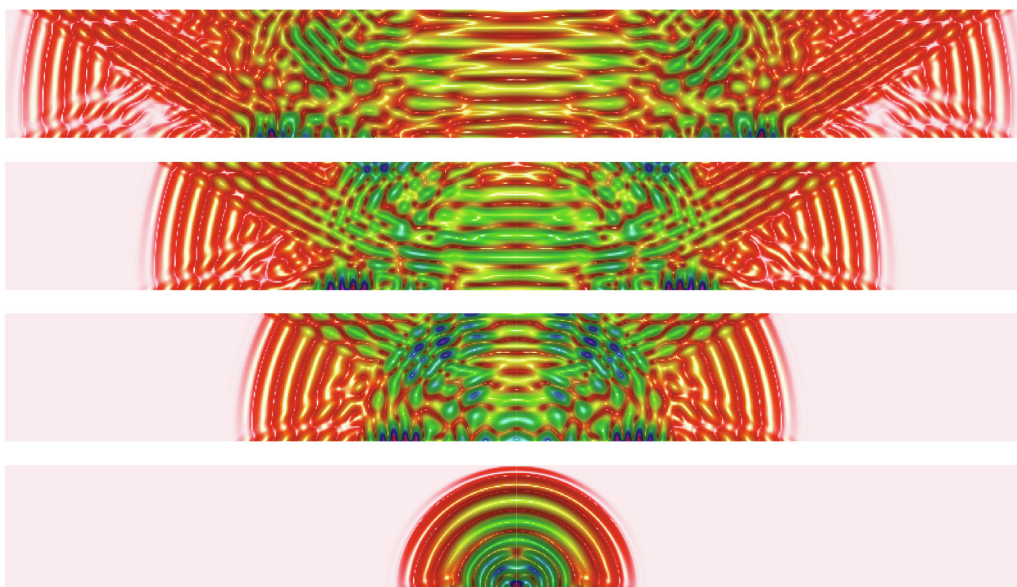


Fig. 10. Distribution of the mean velocity $\sqrt{v_1^2 + v_2^2}$ inside the strip. Snapshots of the analytical solution for $t = \{186\Delta t, 420\Delta t, 561\Delta t, 753\Delta t\}$.

In an attempt to improve the agreement between numerical simulations and experimental data, the 3D computation of the problem was performed using the in-house finite element code. Unfortunately, the results of 3D calculation differ from those in 2D only slightly, as it can be clearly seen in Fig. 12. From one side, it confirms that the applied plane stress approximation is applicable for the considered problem. From another side, it does not assure that 3D computing will improve the results of numerical modeling significantly.

7. Conclusions

Experimental measurements and numerical simulations were performed to examine the accuracy of the plane stress approximation in the description of elastic waves in a finite strip. The comparison of experimental data with the analytical solution and numerical simulations demonstrates the ability of standard numerical methods to reproduce the signal propagation in a homogeneous strip only for short time computations. The obtained results confirm the suitability of existing nondestructive evaluation methods and pose certain questions concerning the time-reversal technique using long-time computing. All the results presented in this study can be used as a benchmark data for the investigation of transient waves in a two-dimensional elastic medium to validate other numerical or semi-analytical methods.

Declaration of Competing Interest

The authors declare that they have no known competing financial interests or personal relationships that could have appeared to influence the work reported in this paper.

Acknowledgments

The work was supported by the grant projects with No. 19-04956S of the Czech Science Foundation (CSF) within institutional support RVO:61388998, by the Centre of Excellence for Nonlinear Dynamic Behaviour of Advanced Materials in Engineering CZ.02.1.01/0.0/0.0/15_003/0000493 (Excellent Research Teams) in the framework of Operational Programme Research, Development and Education and by the project LO1506 of the Czech Ministry of Education, Youth and Sports under the program NPU I. A.B. acknowledges the support by the Estonian Research Council under Institutional Research Funding IUT33-24.

References

- [1] Adámek V, Valeš F. Analytical solution for transient response of an infinite viscoelastic strip. *J Vib Eng Technol* 2015;3:699–710.
- [2] Adámek V, Valeš F, Červ J. Numerical Laplace inversion in problems of elastodynamics: Comparison of four algorithms. *Adv Eng Softw* 2017;113:120–9.
- [3] Bale DS, LeVeque RJ, Mitran S, Rossmanith JA. A wave propagation method for conservation laws and balance laws with spatially varying flux functions. *SIAM J Sci Comput* 2003;24:955–78.
- [4] Barouni AK, Saravanos DA. A layerwise semi-analytical method for modeling guided wave propagation in laminated and sandwich composite strips with induced surface excitation. *Aerosp Sci Technol* 2016;51:118–41.
- [5] Belytschko T, Bachrach WE. Efficient implementation of quadrilaterals with high coarse-mesh accuracy. *Comput Methods Appl Mech Eng* 1986;54:279–301.
- [6] Berezovski A, Engelbrecht J, Maugin GA. *Numerical Simulation of Waves and Fronts in Inhomogeneous Solids*. World Scientific Singapore; 2008.
- [7] Brezinski C. *History of Continued Fractions and Padé Approximants*. Springer-Verlag; 1991.
- [8] Brock L. The transient field under a point force acting on an infinite strip. *J Appl Mech* 1986;53:321–5.
- [9] Courant R, Friedrichs K, Lewy H. Über die partiellen differenzgleichungen der mathematischen. *Physik Math Ann* 1928;100:32–74.
- [10] Croxford A, Wilcox P, Drinkwater B, Konstantinidis G. Strategies for guided-wave structural health monitoring. *Proc R Soc A: Math, Phys Eng Sci* 2007;463:2961–81.
- [11] Givoli D. Time reversal as a computational tool in acoustics and elastodynamics. *J Comput Acoustics* 2014;22:1430001.
- [12] Hughes TJR. *The Finite Element Method: Linear Static and Dynamic Finite Element Analysis*. Dover Publication; 2000.
- [13] Kluska P, Staszewski W, Leamy M, Uhl T. Cellular automata for Lamb wave propagation modelling in smart structures. *Smart Mater Struct* 2013;22:085022.
- [14] Kolman R, Plešek J, Červ J, Okrouhlík M, Pařík P. Temporal-spatial dispersion and stability analysis of finite element method in explicit elastodynamics. *Int J Numer Methods Eng* 106:2016;113–128.
- [15] Leckey CA, Wheeler KR, Hafiychuk VN, Hafiychuk H, Timuçin DA. Simulation of guided-wave ultrasound propagation in composite laminates: Benchmark comparisons of numerical codes and experiment. *Ultrasonics* 2018;84:187–200.
- [16] Lee B, Staszewski W. Lamb wave propagation modelling for damage detection: I. two-dimensional analysis. *Smart Mater Struct* 2007;16:249–59.
- [17] LeVeque RJ. *Finite Volume Methods for Hyperbolic Problems*. vol. 31. Cambridge University Press; 2002.
- [18] Maio L, Memmolo V, Ricci F, Boffa N, Monaco E, Pecora R. Ultrasonic wave propagation in composite laminates by numerical simulation. *Compos Struct* 2015;121:64–74.
- [19] Rose JL. *Ultrasonic Guided Waves in Solid Media*. Cambridge University Press; 2014.
- [20] Sadd MH. *Elasticity: Theory, Applications, and Numerics*. 2nd ed. Elsevier, Academic Press; 2009.
- [21] Sundararaman S, Adams DE. Accuracy and convergence using a local interaction simulation approach in one, two, and three dimensions. *J Appl Mech* 2009;76:031008.
- [22] Valeš F, Šebková H. The state of stress in non-stationary loaded thin belt. *Acta Technica ČSAV* 1976;4:439–58.
- [23] Červ J, Landa M, Převorovský Z. Numerical modelling of acoustic emission signal propagation in a strip. *Appl Mech Rev* 1993;49(4–6):6A182.
- [24] Willberg C, Duczek S, Vivar-Perez J, Ahmad Z. Simulation methods for guided wave-based structural health monitoring: A review. *Appl Mech Rev* 2015;67:010803.

Available online at www.sciencedirect.com

jmr&t
Journal of Materials Research and Technology
www.jmrt.com.br



Review Article

Residual stress analysis of additive manufacturing of metallic parts using ultrasonic waves: State of the art review

R. Acevedo^{a,*}, P. Sedlak^b, R. Kolman^b, M. Fredel^a^a Federal University of Santa Catarina, Mechanical Engineering Center, Campus David Ferreira Lima, Florianopolis, SC, Brazil^b Institute of Thermomechanics, Academy of Sciences of the Czech Republic, Dolejskova, 1402/5, Praha, Czech Republic

ARTICLE INFO

Article history:

Received 21 October 2019

Accepted 24 May 2020

Available online 10 June 2020

Keywords:

Residual Stress (RS)

Additive Manufacturing (AM)

Non-destructive Testing (NDT)

Ultrasonic Testing (UT)

ABSTRACT

Additive manufacturing has become a major growing field in materials engineering, following a new tendency for custom, high precision and on-demand fabrication. Residual stresses are prone to appear in any production technique, which remain a challenge to be measured. These stresses can lead to a reduction on mechanical performance and even cause premature failure. Thus, a wide understanding of residual stress is critical for greater part reliability. Among Non-destructive Testing (NDT) techniques, acoustic and ultrasonic waves remain widely used to determine stresses, voids and defects in a wide array of parts. In this contribution, Ultrasonic Testing (UT) is highlighted as an alternative for measuring residual stress both during and after fabrication.

© 2020 Published by Elsevier B.V. This is an open access article under the CC BY-NC-ND license (<http://creativecommons.org/licenses/by-nc-nd/4.0/>).



R. Acevedo Currently, I hold a PhD position at the Federal University of Santa Catarina (UFSC). My research field is on Materials Engineering, more specifically in the Additive Manufacturing of auxetic samples made from a Titanium alloy - Ti6Al4V.

I started my studies of Physics in Brazil at the UFSC with a grant from the National Council of Scientific Research (CNPq) under the direction of Mrs. Menezes on the theme of nuclear physics. Wishing to

open up to the international and interested in particular applications in the field of nanotechnology, I followed the Master

2 Research - Nanosciences, Nanocomponents, Nanomeasurements of the UniversitPaul Sabatier in Toulouse. My internship at LAAS-CNRS under the direction of Mr. Coccetti then allowed me to gain experience in modeling and electrical characterization of ferroelectric materials (BST) for wireless architectures.

The internship realized at LAAS made me discover the field of materials, in which I wished to gain more knowledge through specific studies in the Materials Science field. During the Master in Materials Science, I carried out two research internships at CIRIMAT - UPS. The first, in the framework of the Master 1 Materials Science of UPS, concerned the synthesis of carbon nanotubes. The second, conducted as part of the Master 2 Research Science Materials, Nanomaterials, Multimaterials (SMNM) of UPS, focused on the production of energy nanomaterials based on carbon nanotubes. Through these periods, I was able to develop a sense of analysis necessary in the realization of many experiments.

* Corresponding author.

E-mail: ruben.acevedo@rocketmail.com (R. Acevedo).<https://doi.org/10.1016/j.jmrt.2020.05.092>2238-7854/© 2020 Published by Elsevier B.V. This is an open access article under the CC BY-NC-ND license (<http://creativecommons.org/licenses/by-nc-nd/4.0/>).

Furthermore, as the master period ended, I engaged myself in a Doctoral programme at UFSC, but, this time, in the field of Materials Science and Engineering. My subject of research is the fabrication of auxetic Ti6Al4V samples using Selective Laser Melting (SLM) aiming ballistic applications. Part of my research was performed with the collaboration of two institutions: SENAI-Laser from Brazil, in which the research samples were produced; and, IT-CAS, where an important simulation work and several experiments on mechanical behavior of auxetic Ti6Al4V samples were done.



P. Sedlak Graduate and MSc. (Ing.) degree in Physical Engineering at Czech Technical University of Prague. Ph.D. degree in Physical Engineering, FNSPE, Czech Technical University of Prague. At present works as senior researcher at the Thermomechanics Institute of the Czech Academy of Sciences, with emphasis on the development of ultrasonic methods for elastic properties measurement, and development of phenomenological models for SMA.

els for SMA.



R. Kolman Graduate in Mechanical Engineering at the Czech Technical University of Prague, speciality Applied Mechanics and Ph.D at the Faculty of Mechanical Engineering, CTU Prague, speciality Mechanics of Solids, Deformable Bodies and Continua. Currently works at the Thermomechanics Institute of the Czech Academy of Sciences, as a research scientist in the field of computational mechanics and wave propagation in solids.

solids.



M. Fredel Graduate at Mechanical Engineering from Universidade Federal de Santa Catarina/BR (1986), Master's at Mechanical Engineering from Universidade Federal de Santa Catarina/BR (1990) and Ph.D. at the Rheinische-Westfaelische Technische Hochschule Aachen/DE (1995). Has experience in Materials Science and Mechanical Engineering on Near Net Shape Powder-based Manufacturing mainly with oxides, PIM, biomaterials, surface and interfacial energy; processing and mechanical behavior of ceramics and composites.

biomaterials, surface and interfacial energy; processing and mechanical behavior of ceramics and composites.

1. Introduction

According to a joint effort between the International Organization for Standardization (ISO) and the American Society for Testing and Materials (ASTM), standard 52900 (substituting previous norm ASTM F42), Additive Manufacturing (AM) is defined as “the process of joining materials to make parts from 3D model data, usually layer upon layer, as opposed to subtractive manufacturing and formative manufacturing technologies” [1]. This process is regarded as one of the major forces in the so-called 4th Industrial Revolution, in which connected machines, complex shapes, topological optimization, and on-demand fabrication are brought together in new innovative processes. Even so, just as in conventional manu-

facturing methods, AM produces residual stresses (RS) in the fabricated parts.

Using sound to characterize and identify materials, however, has been a common practice since early ages. For instance, manufacturers of ceramic materials could detect the presence of voids and defects by producing a sound on two different parts of the ceramic. This method was later used to create devices such as the tuning fork. In the past 100 years, major developments were observed in sound-based Non-Destructive Testing (NDT) techniques, such as its application in the industrial field for testing casting, as proposed by Sokolov [2]. Hellier [3] cited the following historical developments: after WWII, several companies and researchers entered the Ultrasonic NDT field, such as Siemens, Lehfeldt, Kretztechnik, Krautkrämer, Sonatest, Karl Deutsch, Gilardoni, and Mitsubishi; in 1947, D. Sproule created a transducer capable of generating shear waves in materials, paving the way for weld inspection and other applications; later on, during the 1950s, J. Kaiser did an important contribution in the field with the introduction of Acoustic Emission (AE) as a new NDT method. Currently, those enterprises and new players compete to provide advanced solutions to improve industrially produced parts [4].

RS can be artificially introduced in materials. For instance, in tempered glass, one side of the material receives a thermal shock, creating a compressive stress zone that significantly toughens it [5]. On the other hand, RS can produce similar effects to those created by stress concentration that are critical to the life cycle of components. In welded parts, the presence of RS combined with further loading stresses can significantly reduce fatigue resistance and cause distortion (Fig. 1a) as well as delamination, cracks (Fig. 1b), and other structural failures [6–9].

To save resources, time, and improve quality control, there is a growing need to integrate online characterization of AM parts. Still, as pointed out by Everton et al. [11], further developments are required. Even if laser-based ultrasonic waves (UW) are effective in monitoring defects in AM, there is another challenge for optimizing process parameters: a wider communication/data exchange between ultrasonic wave generator devices and AM machines. Besides, complex part geometry, microstructure and surface condition are important influencing factors for UT of AM parts. By successfully meeting all these requirements, it would be possible to correct and minimize RS and defects before the part is finished.

Different fabrication methods used in AM are summarized in Table 1. Powder Bed Fusion methods – Laser (L-PBF) and Electron beam (E-PBF) – have similar functioning principles and account for 80% of all metal AM systems worldwide [12]. A modulable energy source (laser or electron beam) is used to sinter and locally melt powder particles, layer by layer, until the designed part is finished, as shown in Fig. 2. Typically, productivity and roughness are lower than in the Directed Energy Deposition (DED) methods, but dimensional accuracy and processing time are higher. In the case of Powder (P-DED) and Wire (W-DED), several energy sources can be applied: laser, electron beam, or electric discharge (Fig. 2). In comparison with PBF, all DED processes have higher productivity, can form bigger parts, and can be used to perform repair and coating on several mate-

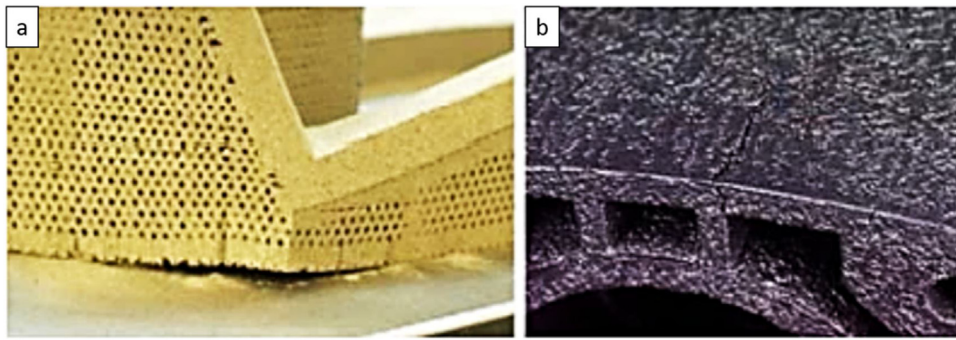


Fig. 1 – Direct consequences of residual stresses in AM parts - (a) distortion and separation from the base plate; (b) crack formation [10].

Table 1 – Fabrication methods in Additive Manufacturing (adapted from Ref. [5,6]).

ASTM designation	Terminology	Commercial name	Manufacturer(s)
Powder Bed Fusion (PBF)	Laser PBF (L-PBF)	Direct Metal Laser Sintering (DMLS)	EOS
		LaserCusing	ConceptLaser
		Laser Metal Fusion (LMF)	Sisma Group
		Selective Laser Melting (SLM)	Matsuura/MTT/Phenix/ Renishaw/ Realizer/SLM Solutions
Directed Energy Deposition (DED)	Electron beam PBF (E-PBF)	Electron beam melting (EBM)	Arcam
	Powder DED (P-DED)	Direct Metal Deposition (DMD)	POM
		Laser Engineer Net Shaping (LENS)	Optomec
		Laser consolidation	Accufusion
	Wire DED (W-DED)	Laser deposition/cladding/ Laser Metal Deposition (LMD)	Huffman/Irepa/ Trumpf
			Sciaky
		Electron Beam Direct Melting (EBDM)	Honeywell
		Ion Fusion Formation (IFF)	MER
	Plasma Transferred Arc Selected (PTAS -FFF)	Rapid Plasma Deposition (RPD)	Norsk Titanium
			Rolls-Royce
Shape Metal Deposition (SMD)			

rials. However, they produce higher surface roughness, as well as more defects and voids. On both PBF and DED processes, thermal stresses are elevated due to the rapid heat transfer between the energy source and the material (in powder or wire form), producing a complex state of RS in the finished part. Each process will, however, create a different type and distribution of RS. When a material is processed by two different techniques, namely SLM and DMLS, RS profiles will be completely different in each case [13].

The present work aims at creating an updated state of the art on acoustic waves NDT applied to AM metallic parts. Different measurement techniques are compared to ultrasonic waves non-destructive testing (UT) regarding both their capa-

bilities and limitations. Also, fundamental aspects of RS and UT are discussed in-depth.

2. Residual stress (RS)

Residual stresses are self-equilibrating stresses which remain in the part after its manufacture even without supplementary thermal gradient and external forces. These stresses arise from misfits in the shape of parts of both different regions and different phases within a part, or even because of local variations in elastic constants, or thermal and mechanical properties [14]. RS can result in several undesirable consequences on the part's properties, such as poor fatigue resistance, critical failure during operation, lower chemical

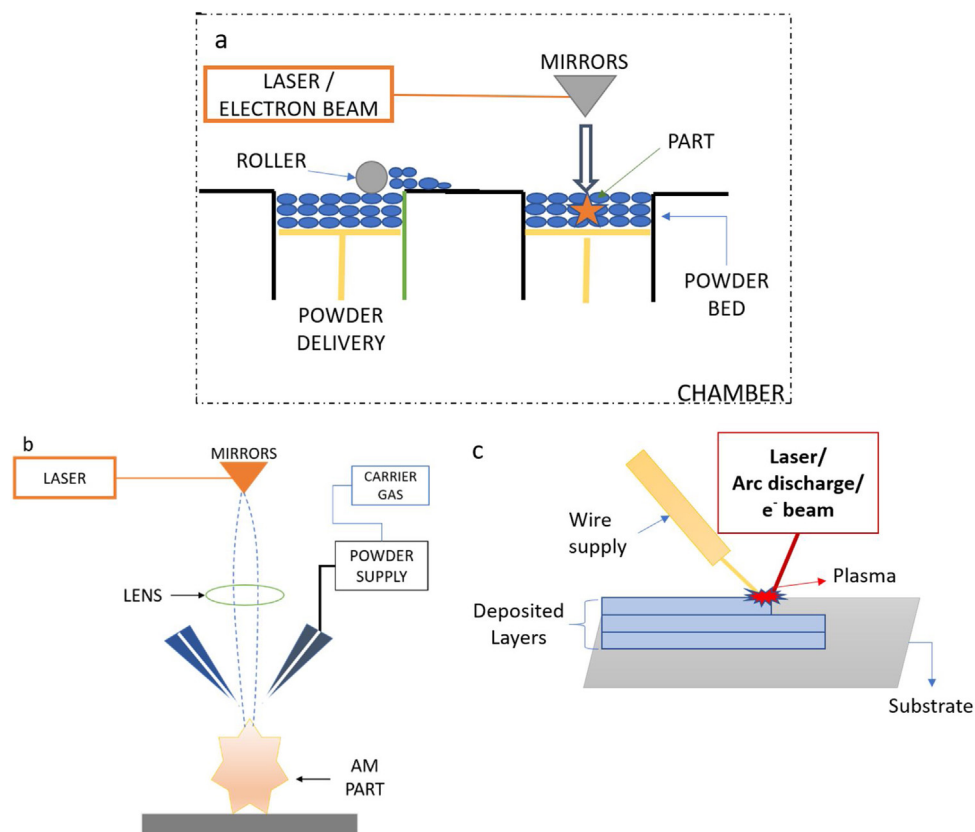


Fig. 2 – Additive Manufacturing methods - (a) Powder Based Fusion (laser/electron beam); Direct Energy Deposition (b) powder & (c) wire.

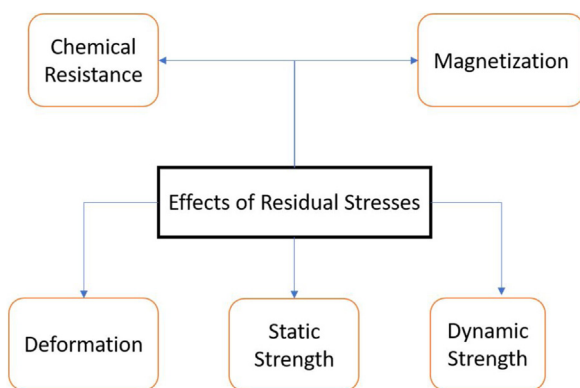


Fig. 3 – Effects of Residual Stress in materials (adapted from Ref. [15]).

resistance, lower magnetization, lower resistance to deformation, and diminished static and dynamic strength, as summarized in Fig. 3 [15].

Service loading can also lead to the creation of RS and, consequently, originate inhomogeneous plastic deformation. These stresses can be found not only in the finished parts but in the unprocessed raw material. The origin of RS can be classified into four main categories [16]:

- Differential plastic flow

- High cooling/heating rates
- Phase transformations with a volume change
- Chemical-induced misfits

In most of the additive manufacturing processes, the rapid heating due to the power source (laser/electron/plasma) leads to the sintering/melting and further solidification of the metal/alloy (powder or wire-based). Repeated heating and cooling affects the local structure and properties of the components [17]. Because of such high cooling and heating rates, RS are produced and may cause deformation, cracks, and limit the performance of the materials produced by AM. Also, another direct consequence of RS is the strong anisotropic behavior created in these materials [16]. The origins of RS in AM can be explained by the Temperature Gradient Mechanism (TGM), shown in Fig. 4. Upon heating, the power source creates a series of local elastoplastic deformations (represented by ϵ_{pl} , ϵ_{el} and σ_{yield}) and further tensile stress in the irradiated zone. During the cooldown of the molten top layers, thermal contraction causes shrinkage and leads to the creation of tensile and compressive RS regions (upper and lower layers, respectively) [17,18]. Since the AM process is very complex, TGM model represents only a simplification of how RS are generated [18]. Many factors affect the intensity and creation of RS: material properties (grain size, heat capacity, porosity/voids, phase composition), geometry of specimens, support structure (when required), and process parameters (laser/electron beam power, preheating type, scan strategies and speed, and

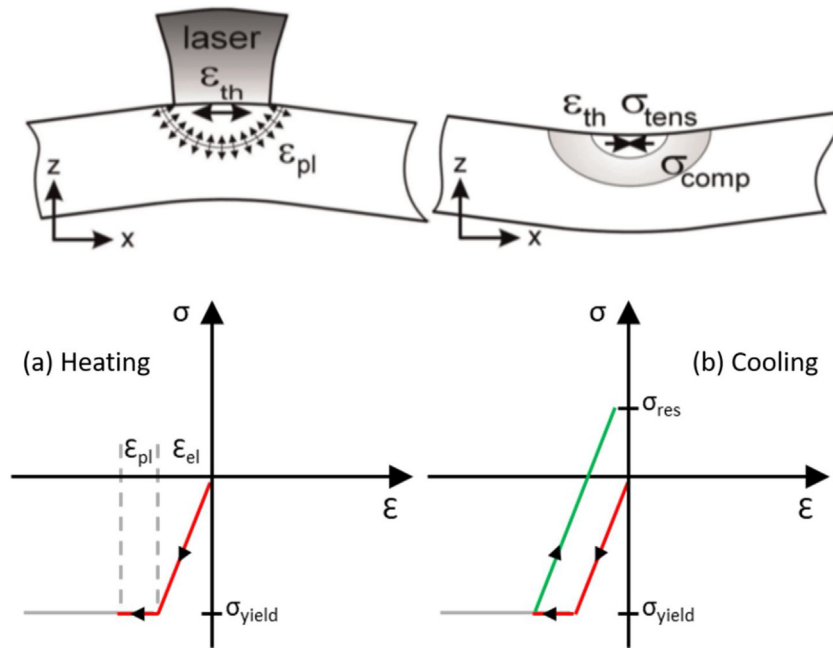


Fig. 4 – Temperature Gradient Mechanism (TGM). Stresses and deformation during heating (a) and cooling down (b) in the irradiated zone [18].

Table 2 – Sources of error in the measurement of RS [19].

Sources of uncertainties and accuracy of calculation of Residual Stresses	Elastic constants Nonlinearity due to texture Stress gradients with depth Microstresses due to plastic deformation or grain interactions
---	---

layer thickness) [16,18]. Furthermore, many factors — summarized in Table 2 — influence the estimation of RS [19].

RS can be classified according to the length scale on which they occur [20]:

- Type I: Macro RS, which equilibrate over large distances and deform the part if boundary conditions are changed.
- Type II: Micro RS, that occur over the grain scale because of the formation of different phases in the structure. They are frequently observed in a polycrystalline material because of the different grain orientation and the anisotropy of a crystal structure.
- Type III: Micro RS inside a grain (over atomic dimensions), which occur because of defects such as dislocations, vacancies, or alien atoms distorting the crystal lattice in the crystal structure.

In DED and PBF methods, some in-process strategies can be implemented to minimize RS (see Section 2.3). By pre-heating the powder/wire, thermal gradients are minimized [18]. Another alternative is to reduce scan tracks or optimize scanning paths (in the case of laser or electron beam), leading to smaller thermal gradients [17,18,21]. This has a significant – direct or indirect – influence on RS distribution [13].

Table 3 – In-process techniques for relieving of RS.

	Strategy	Authors
Mechanisms of reduction /redistribution /elimination of Residual Stresses (in-process)	Reduction of scan tracks	[17,18]
	Optimization of scanning paths using the inherent strain method	[21]
	Pre-heating of powder/wire treatment	[22]
	Laser Shock Peening (LSP)	[23]

Table 3 summarizes the existing in-process strategies available to reduce the influence of RS.

Carlsson et al. [24,25] proposed a power-law relation – Eq. (1) for residual surface stress (uniaxial stress-strain), considering both theoretical and experimental analysis. This equation was tested for aluminum alloy Al4120-14 and vessel steel A508B and proved to be in good agreement with experimental results [25].

$$\sigma_{RS} = k\varepsilon^n \tag{1}$$

For each AM process and material there is a specific distribution of RS. Therefore, two samples from the same material produced by different techniques, e.g. EBM and SLM, will not have a similar distribution of RS [13]. Those processes create complex distributions of stress fields, creating high anisotropy of RS. Additionally, as most of the material properties are not constant and isotropic through the volume, RS distribution and magnitudes are also concerned. Besides, microstructure is another source of anisotropy: typically, due to the fabrication

Table 4 – Post-processing techniques for relieving of Residual stresses.

	Strategy	Authors
Mechanisms of reduction /redistribution /elimination of RS (post-process)	Peening: ultrasonic, laser shock,	[35]
	hammer, shot, heat treatment	
	Machining	[36]
	Explosive treatment	[36]
	Annealing	[28]

of parts by superposition of layers, AM parts have predominantly columnar grains with a mix of cellular dendrites; as the grains grow in the build direction, more anisotropy and micro RS are created in the part [26]. Common strategies to minimize undesired anisotropic effects include the superposition of layers in different build directions such as [0, 45°, 90°, 135°, ... 315°], bidirectional scan strategies regarding one axis and two axes [27]; as well as annealing treatments at higher temperatures (1160 °C during four hours – Inconel 718 samples made by L-PBF method) [28].

Furthermore, during fabrication, phase transformation strains, microstructural evolution and material properties can drastically influence RS. In this sense, a low material thermal diffusivity implies in high magnitude of strains [29]. Thermal diffusivity is affected by material density (ρ), thermal conductivity (k) and specific heat (c); besides, it can be presented as in Eq. (2):

$$D_t = \frac{k}{\rho c} \quad (2)$$

If thermal conductivity (k) is low, and the product ρc has a high value, residual strains are incremented. Complementarily, high thermal expansion coefficient (α) also increases the distribution of strain and stress [29]. Bartlett et al. [30] discovered that RS have a linear relation with D_t and k , which was expected from solidification theory. Finally, some AM process parameters can be strongly affected by material-dependent properties: Kruth et al. [18] performed layer post-scanning in Ti6Al4V and 316 L SLM samples: as a result, Ti parts presented 8% less distortion whilst no reduction was observed in 316 L samples. Thus, the complex nature of material and process parameters relationships require more theoretical and experimental developments.

In AM fabrication, stresses are higher in the perpendicular direction than in the scanning direction, by a factor between 1.5–2.5 [31–34], which could be related to the anisotropy induced by AM processing and material properties. In processes that Electrical Discharge Machining (EDM) cutting is required (especially in SLM and EBM), strong tensile stresses are introduced in the depth of around 40 μm from the cut surface [14]. Post-processing techniques, however, can be applied to reduce, redistribute, or even eliminate RS. These methods are described in Table 4 and are further discussed in Section 2.4.

Part geometry is also a feature that influence distribution and magnitude of RS. Salmi et al. [37] performed a series of RS measurement using Hole Drilling (HD) method in AlSi10Mg parts made by SLM process. Several geometries were pro-

duced, comprising flat (plates and hollow square cylinder) and curved (circular and semi-circular hollow cylinders). It was found that RS were slightly higher in curved walls than in flat walls, which is probably due to lower hatch spacing. Moreover, in open geometries, RS can be dissipated with more ease than in the closed geometries cases. Complementarily, support structures play a significant role, by allowing heat transfer during the build, and progressively decreasing the stress state. Thus, an optimization of supports is an important tool to mitigate and control RS.

PBF process variables that affect RS are brought together in Fig. 5. Beam/laser parameters and scan strategy can be adjusted during fabrication. On the other hand, some process conditions can not be easily modified in-situ, such as part geometry and supports. Among these variables, powder bed pre-heating is one of the most important factors since it significantly diminishes thermal gradients part distortion, improve dimensional accuracy, density and enhance mechanical properties [38]. Still, this parameter has to be balanced with other variables to avoid undesired effects such as excessive grain growth, recrystallization and precipitation [30]. Beam power and scan speed also have dominant roles in the mitigation of RS, regardless of the material: higher beam power increases RS [39–41]; in the other hand, greater scan speed diminishes RS [39–44]. Finally, scan strategy and related parameters (Fig. 5) result in complex effect on stress, both regarding its distribution and direction but also its magnitude [30]. Nevertheless, these effects are different for single and multiple layers (RS in-plane anisotropy) and build direction (variations in strain/stress) [45].

Along with the rise of RS, several defects can also be observed: balling, cracks, inclusions, microstructural anomalies, porosity, etc. [46]. Typically, porosity (designed or undesired) is the most frequent defect observed in AM. Excessive porosity can lead to failure and produce detrimental changes in mechanical properties of the manufactured component. There are two main origins for this undesired porosity: lack of fusion (LOF) and trapped gas in the material. LOF porosity (irregular pores) occurs due to an inadequate set of processing parameters, which leads to a partial melting of the material and lower densification of the part. On the other hand, gas porosity (spherical pores) is due to the presence of gas trapped in the raw material or trapped inert gas (nitrogen, argon, helium) during fabrication [47]. Despite not being as frequent as the former porosity types, keyhole porosity is also a concern in AM. During fabrication, if a threshold of processing parameters (laser power, scanning speed and beam size) is reached, this could lead to the evaporation of metal and formation of plasma. In the following, a vapor cavity is created with greater laser absorptivity, that enables the laser beam to reach deeper sections of the melting pool and form voids as the cavities collapse [48]. This type of porosity has been studied in SLM [48–50], in laser or electron beam welding [51] and other single-track L-PBF process combined with Finite Volume Method [52].

Several strategies can be applied to eliminate or attenuate the presence of these porosities in AM processes: processing parameters optimization (laser power, scanning speed, laser spot size, hatch distance); pre-heating of the powder mate-

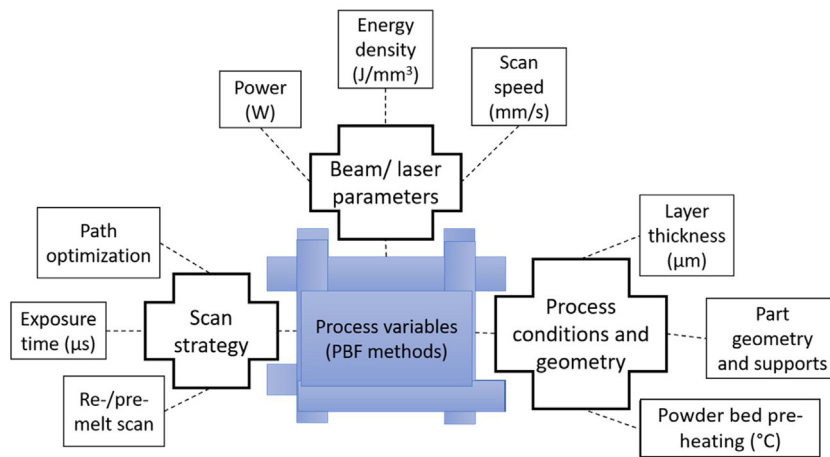


Fig. 5 – Process variables (PBF methods) influencing RS (adapted from Ref. [30]).

rial – some of the available SLM and EBM equipment present this feature and are able to keep chamber heated at temperature ranges of 100–500 °C and 300–1100 °C, respectively [53–55]. Consequently, EBM parts show much lower RS than SLM specimens, which is due to lower thermal gradients [30].

Temperature of pre-heating is dependent on the powder properties and type (pure metal or alloy) [55]. Cooling rate is an important feature that can also be controlled, with higher precision in EBM, enabling to process brittle materials such as TiAl and hard intermetallics [54]; in the other hand, heat treatment of the part, is a post-processing step performed under vacuum to avoid material oxidation [47].

2.1. Predictive models of RS in AM

A significant effort has been put out by the scientific community to create and enhance models capable of describing the dynamics of RS in AM processes. A great number of computer models based on Finite Element Method (FEM) are reported in the literature, including a series of different approaches intended to optimize computational expense [30]:

- Grouping many thin layers into a small quantity of thicker layers: this results in fast calculation of RS with the expense of 10% deviation from experimental data [56].
- Single-pass beam scanning models: this model ignore multilayer effects and focus on the analysis of the influence of scanning strategies, scan speed and beam power on RS [40].
- Uniformly heated layers without beam motion: this model considers multilayer effects, also, it is effective to estimate average RS and stresses in the build direction. Nevertheless, in-plane anisotropy is not considered [57].
- Simulation of few-layer builds for multilayer effects: in this model a total of 8 scanning strategies were employed to build 3-layer parts. Among all scanning strategies, the use of the 45° inclined line case produced the greatest reduction of RS in both X and Y directions [58].
- Multiscale models: these models are divided in four main categories – micro-scale (follows the microstructure evolution); particle-scale (laser-powder interaction); meso-scale (simulation of one or many layers); meso-scale (simulation

of the whole process). Despite that great computational resources are required and scaling difficulties may appear, crucial and accurate information on distortion, microstructure, porosity, RS and temperature history can be obtained with the use of one or more models [26,59,60].

Furthermore, analytical and semi-analytical models can also be coupled to computer models in the prediction of RS in AM. A common approach is the use of linear stress profiles in each layer height [43,61]. These estimations of RS (stress distributions are easier to assess than stress values) are quite accurate compared with numerical simulation and experimental results. Finally, commercial software which use multi-approach models such as Ansys, ABAQUS, Autodesk, Simufact are developing and enhancing tools to predict RS in AM parts.

2.2. RS measurement methods

Fundamentally, RS measurement methods can be divided into three major groups: non-destructive, semi-destructive, and destructive. Some examples of each type are presented in Fig. 6. The measurement process introduces a perturbation in the stress state of a sample, which is especially pronounced in destructive and semi-destructive testing. In all cases, residual strain is measured and then, by linear elastic theory for homogeneous isotropic solids, residual stresses are obtained [62].

In non-destructive methods (NDT), such as neutron diffraction and XRD (Fig. 6), the crystal lattice strain is measured. Then, the corresponding RS are estimated using elastic constants, assuming linear elastic deformation of the crystal lattice. NDT techniques can provide information on a series of material properties: tensile modulus, fracture toughness, microstructure and defects, etc. (Table 5). Typically, these methods bring great flexibility of use and repeatability, besides of high accuracy. Nevertheless, there are some disadvantages: such as limited penetration and reflection of waves/rays and resolution, as observed in UT, detailed in Section 3. Additionally, sample size can be critical in some cases and operation

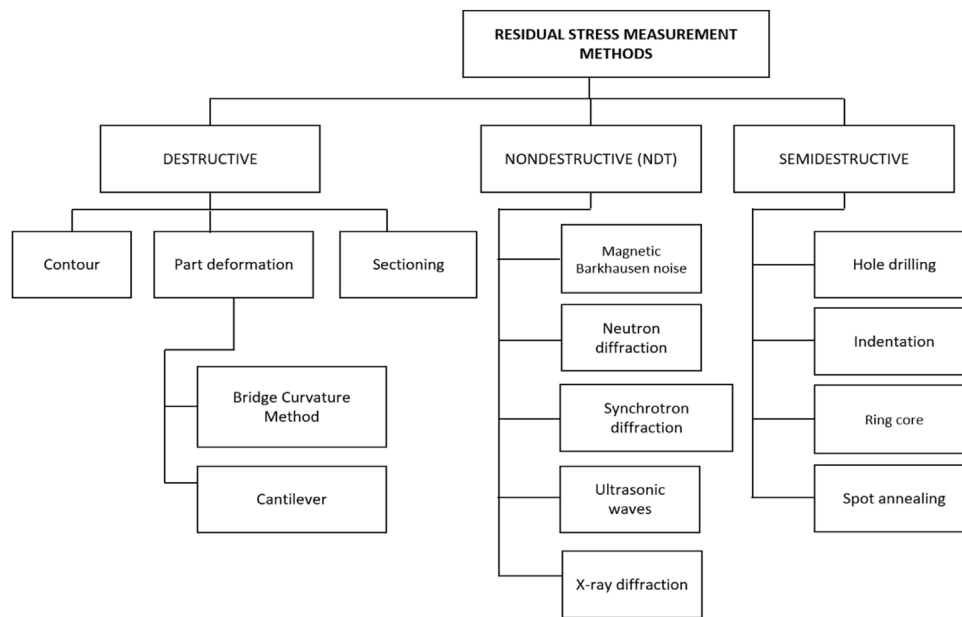


Fig. 6 – Residual Stress measurement techniques.

Table 5 – Field of application for NDT in materials characterization (adapted from Ref. [64]).

Mechanical properties	Physical properties
Tensile modulus	Microstructure
Shear modulus	Grain size
Tensile strength	Phase composition
Yield strength	Porosity/voids
Fracture toughness	Inclusions
Hardness	Anisotropy
	Hardening depth
	Residual stress
	Thermal history

cost is a major concern, especially regarding neutron diffraction [63].

Destructive methods, such as sectioning, consist of removing specific portions of a sample to relieve RS. Then, deformations are created and the corresponding stresses can be determined. Typically, these methods require Finite Element Method (FEM) tools to analyze deformation behavior and, then, obtain RS values [63]. As an intermediary case, semi-destructive methods (Fig. 5) induce fewer properties modifications than destructive methods. Among those, hole drilling (HD) is the most used. It consists of cutting a portion (hole) of a part and installing strain gauges to measure stress profiles. In most modern approaches, Digital Image Correlation (DIC) can be coupled to HD and provide more precise information on the stress behavior [65]. As a complementary method to acquire knowledge on RS, FEM simulations can be used. Different authors [32,66,67] compared the results obtained by experiments with a linear elastic model created on a specific FEM software. In the majority of cases, it was considered that most of the properties of the materials are temperature-dependent. Using specific models from ABAQUS and ANSYS software, thermally-induced stresses can be created, and the correlated effect on the part can be modeled.

Currently, most of the RS measurement in AM is performed by HD and X-rays diffraction (XRD), which is due to the easiness of measurement, high number of standardized norms (ASTM, ISO, etc.) and availability of equipment. Despite both methods have good accuracy and reliability, there are some limitations: in the case of XRD, samples are limited in size and surface roughness (polished surfaces are optimal for measurements), and penetration of X-rays is limited to a few micrometers [39]. In the other hand, HD is a semi-destructive technique which suffers from errors due to plasticity effects of the material and stress concentration around the hole, and, in the Incremental Hole-drilling variant (IHD) there is an error correlated to each increment depth and a major difficulty to correctly assess RS at the surface [68].

In recent years, a significant effort has been performed to develop UT of RS and defects. This will be detailed in the Section 3.3.

2.3. RS in-process control

Several methods, summarized in Table 6, can be used to reduce or even eliminate RS. According to Li et al. [69], preheating the powder at temperatures higher than 570 °C could eliminate RS and create beneficial compressive stresses. On the other hand, when the base plate was heated at 160 °C, only a 40% reduction of RS was observed [70]. Yet, in another study by Buchbinder et al. [22], a preheating temperature of 250 °C was employed in AlSi10Mg cantilevers made by SLM, which resulted in no defects or distortions. Also, because of lower thermal gradients, fewer RS were formed in these parts. Following that, Ali et al. [71] used preheating temperatures in the range of 370–770 °C and found that in SLM part production, the minimal quantity of RS was found around 570 °C. At preheating temperatures of 570–770 °C, compressive RS were observed in several samples, including I beam geometries [72]. Moreover, cooling

Table 6 – Strategies of in situ RS reduction (adapted from Ref. [69]).

	Mechanical control	Laser Shock Peening (LSP) Rolling
Mechanisms of RS reduction (in situ)	Thermal control Scan strategy control Feedback control	Preheating of powder bed Algorithms (LaserCUSING®) IR cameras

rates were diminished during fabrication and, consequently, high yield strength (1176 MPa) parts were obtained.

Ali [73] produced a series of I beam geometries by SLM using different layer thicknesses of 25, 50 and 75 μm . In this investigation, different values of exposure time, laser power and pre-heating of powder bed were combined with the aforementioned layer thicknesses. This author discovered that parts produced with thicker layer (75 μm) coupled with 133 μs of exposure time, 150 W of laser power, and 570 °C of powder bed pre-heating, presented fewer RS than thinner layer thicknesses using similar fabrication parameters.

The control of thermal gradients can tailor the formation of RS. Some solutions can be applied, including specific algorithms that optimize scan trajectories to reduce thermal stresses, such as LaserCusing®, developed by ConceptLaser. Similarly, rescanning each layer promotes a 55% relief on RS [43]. Lu et al. [74] used a novel scanning strategy called “island” to create Inconel 718 parts by SLM, and, to understand how this parameter affects the microstructure, mechanical properties, and RS. This particular scanning strategy consists in separating one layer in many small portions – islands – and then randomly melting shorter scan tracks through the melt pool (Fig. 7 a–c). It was found that parts made by $2 \times 2 \text{ mm}^2$ islands presented less RS than other strategies, followed by 5×5 , 7×7 , and $3 \times 3 \text{ mm}^2$ islands. Another approach to control and mitigate RS is the use of Laser Shock Peening (LSP), creating compressive stresses to cancel out preexisting ones. This method can be implemented during AM processing: as each layer is finished, LSP is performed on the present layer, reducing the effect of thermal stresses. By controlling laser power and focus, the RS field can be modified: higher laser power creates non-equi-biaxial RS, while lower laser power generates equi-biaxial RS. Besides, small laser focus implies in higher compressive RS at the surface [75].

In PBF routes, as powder layers are deposited, a stress redistribution is observed. Consequently, the highest tensile stresses are detected in the last deposited layers [76]. Thus, finer control of layer deposition can effectively reduce RS. In W-DED routes, rolling can be implemented to reduce RS. Martina et al. [77] showed that Ti6Al4V samples produced by Wire Arc Additive Manufacturing (WAAM), when combined with high pressure rolling of each layer, had lower tensile RS than unrolled specimens. Peaks of tensile stress were 200 MPa and 500 MPa, respectively. Also, compressive RS zones were generated in rolled specimens, which were 150 and 250 MPa higher than in the unrolled ones [77].

Chen et al. [21] performed a numerical study of scanning path optimization in AM processes. Using Adaptive Level Set Adjustment (ALSA) strategy, stress distributions can be minimized and this accurate model is scalable to complex geometries composed of multiple layers. Still, phenomena such as LOF and porosities are problematic to treat due to gaps in the scanning path algorithm. This type of path optimization

- combined with preheating of powder bed - has a great potential to be used in many AM processes and improve control on RS.

Current SLM systems are able to predict and quickly change processing parameters for support structures and their outer surface. In contrast, for anticipated geometry-related stresses and sensitive zones within a part, there is no possible adaptation. Further developments through software and in-situ measurement would allow to increase process reactivity (swift parameter change), reduction of RS and improvement of fabrication quality [72].

An alternative approach to reduce the effect of RS is through the development of Metal Matrix Nanocomposites (MMNC) materials for AM processes. This topic has been extensively discussed in a review by Yu et al. [78]. Since nanoparticles ensure the refinement of the powder structure and there are strengthening-related mechanisms, fabrication of MMNC parts by SLM could bring several advantages such as more resistance to crack propagation and improved strength. Several alloys available in AM have been tested with different nanoparticles: 316L steel matrix reinforced with TiC nanoparticles; AlSi10Mg matrix reinforced with WC nanoparticles; Ti6Al4V matrix reinforced with ZrH₂ nanoparticles and pure Ti matrix reinforced with TiC nanoparticles. Still, due to the inherent tendency of agglomeration by nanoparticles, which creates an inhomogeneous distribution of reinforcement phases throughout the matrix, challenging limitations appear in the repeatability of microstructure. Besides, wettability between matrix and reinforcement phase is also a critical issue. Research in the field of MMNC fabricated by AM is very promising but requires much more advancements concerning both theoretical and technological matters.

Lastly, through thermography (infrared – IR – or near-infrared), specific cameras can be installed inside the build chamber to monitor temperature during fabrication. By this method, lack or excess of fusion and homogenization of thermal gradients can be determined. This method results in high speed, good spatial resolution and can be used to analyze parts immersed in fluids [79]. Still, it has limited penetration (few millimeters) and needs a detailed calibration. When combined with high-speed image analysis, IR and near-IR sensors allow the accurate detection of defects [80,81].

2.4. RS post-process control

A common solution to reduce RS is to perform a heat treatment after part fabrication, which helps to homogenize the microstructure. In AM parts, this post-process step can reduce RS up to 70% when the treatment is performed in the 600–700 °C range [82]. Annealing promotes a redistribution of stresses and homogenization of microstructure. Besides, several other properties can be tailored, such as tensile strength, ductility, and hardness [71]. Newell et al. [28] performed a

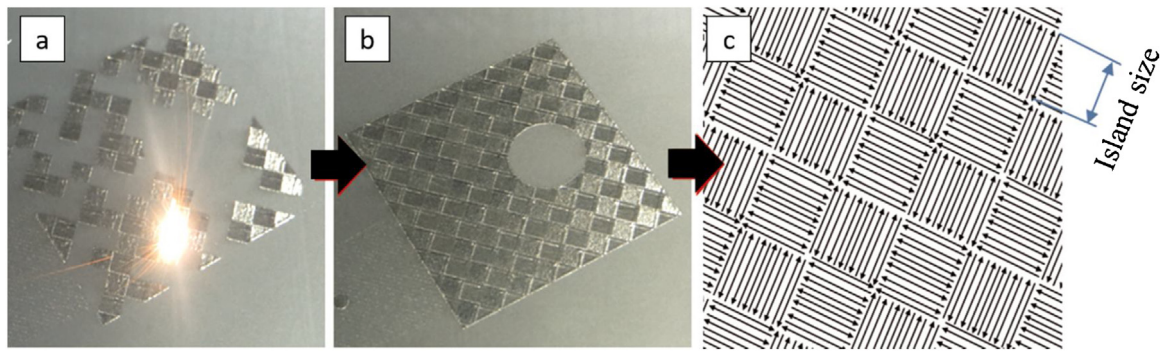


Fig. 7 – Island scanning strategy for Inconel 718 parts (adapted from Ref. [74]).

series of heat treatments in Inconel 718 to promote reduction of RS: it was discovered that heating the nickel-based superalloy at 1160 °C during four hours produced a significant reduction in RS, through recrystallization and grain growth.

Moreover, several other strategies can be employed to diminish RS. Machining (e.g., grinding and hard turning) promotes a redistribution of stress by creating compressive RS on the machined subsurface and surface, resulting in a significant reduction of RS [83,84]. Parameters such as cutting speed and feed rate have a significant influence on the final RS: Tang et al. [85] discovered that higher cutting speeds result in shallower RS layers. On the other hand, changes in the feed rate presented fewer variations in RS. By combining heat treatment and machining, Oyelola et al. [86] discovered that a 22% increase in compressive surface RS could be obtained in the case of Ti6Al4V produced by DED. An innovative solution pointed out by Yamaguchi et al. [87] uses a magnetic field to finish SLM parts and diminish RS: through motion control of the magnetic tool, RS can be eliminated, mitigating the stresses created by the laser during the SLM process.

Another mechanical post-process to control and minimize the effect of RS is the Surface Mechanical Attrition Treatment (SMAT), a technique similar to LSP. However, in SMAT, the impacting balls travel in multiple directions and not only normal to the surface as in LSP. Portella et al. [88] measured RS in 316L stainless steel samples after SMAT and noted that regions of compressive RS were created. These stresses were in the range of -170 to -280 MPa, values lower than the tensile RS observed in 316L parts without SMAT, which ranged from 90 to 140 MPa [88]. Compared to LSP, SMAT generates deeper compressive RS zones [89]. Ultrasonic waves can also be employed to modify the stress profile of samples: in a study by Gao et al. [90], structural steel samples were treated by Ultrasonic Impact Treatment (UIT). As a direct consequence, RS were redistributed and softened, with more pronounced effect in deformed regions (stress concentration zones). Also, it was stated that ultrasonic waves modify RS in depth up to 16 mm.

Hybrid methods that combine production and stress relief process can also be employed, as mentioned by Kalentics et al. [91,92]. First, LSP was used on the surface of the SLM part during the fabrication process. Then, RS was significantly reduced by switching tensile to compressive RS in a depth of 1 mm from the part's surface [92]. Additionally, low energy pulsed lasers with high frequency and small spot size are well suited

to optimize compressive RS, both in depth and in magnitude [91].

3. Ultrasonic waves

Ultrasonic waves (UW) testing uses mechanical waves, which are oscillations of material particles that need a material medium to propagate [93]. These waves are used in many fields of application: medical, mechanical structural measurement (NDT), sensors, sonars, and weapons. Typically, UW have a frequency higher than 20 kHz, corresponding to the upper limit of the human hearing range (high pitch). Its utilization in NDT has several advantages, such as good accuracy, high speed, reliability, repeatability, affordability and capability to use in several environments such as liquids [94]. Also, it is non-destructive and does not require direct contact with the part being tested, which makes it suitable for in-situ monitoring systems in AM. Finally, there is no limitation in terms of the type of material being tested or its geometric complexity (thin films or large components), and it is minimally influenced by temperature [16,95]. Still, UT has some challenges to be overcome: as such, it has limited spatial resolution when compared to other RS measurement methods (Fig. 8), and it is difficult to separate multi-axial stresses, measure RS in the whole volume of the part, which makes it more suitable for macro-stresses (RS Type I) [16,96–98].

Several aspects can be characterized by employing acoustic and ultrasonic waves: microstructure, defects (cracks, voids, inclusions, impurities, and porosity), mechanical properties, geometric accuracy, phase transition, acoustoelastic parameters, surface roughness, and RS [99–102]. Nevertheless, there are limitations for each method, as shown in Table 7 [103].

According to the frequency and the correlated wavelength of UT, some characterization aspects will provide limited information, especially on cracks, porosity, and voids. Typically, if the average dimensions of these defects are below 1 mm, several difficulties can appear in their detection. Besides, there is a significant surface effect which influence all the properties listed in Table 7: an irregular surface brings a major challenge in the signal acquisition of backscattered UW.

The basis of acoustic and ultrasonic wave NDT (UT) is the laws of acoustoelastic theory, which states that the velocity of elastic wave propagation depends on mechanical stress, and of wave propagation in bodies with initial stresses [a].

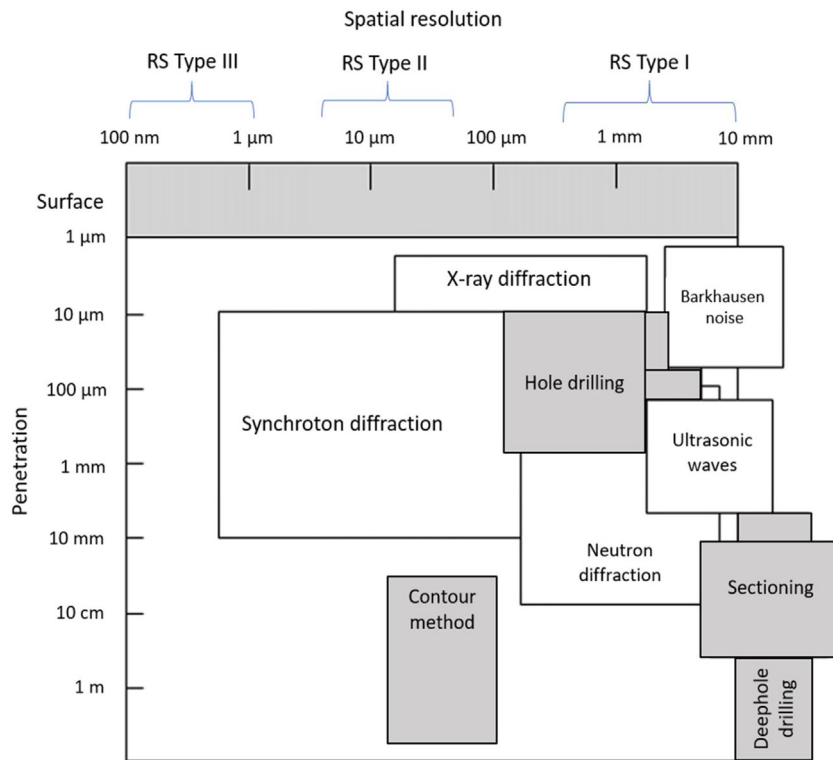


Fig. 8 – Spatial resolution and penetration of RS measurement techniques (adapted from Ref. [16]).

Table 7 – Ultrasonic and acoustic waves characterization fields (Adapted from Ref. [103]).

	Microstructure	Cracks, porosity, voids	Mechanical properties	Geometric accuracy	Surface roughness	Residual stress
Ultrasonic waves	App.	SS, I	App.	App.*	NApp.	App.*
Acoustic waves	App.	App.*	App.	App.*	App.*	App.*

App.: Applicable (* with restrictions).
 SS: surface sensitive.
 I: internal or through thickness.
 NApp.: not applicable.

Table 8 – UT evaluation of material properties [64].

Material property	Ultrasonic measurement	Applicable materials
Longitudinal modulus	Longitudinal velocity	Most engineering solids
Grain size, microstructure	Attenuation	Polycrystalline metals, ceramics
Porosity, voids	Velocity, attenuation	Fiber composites, ceramics
Residual stress	Velocity	Most engineering solids
Yield strength	Frequency-dependent attenuation	Polycrystalline metals

This theory corresponds to the third-order effect. Since the acoustoelastic effect is a weak nonlinear phenomenon, there are many influencing factors in acoustic NDT: temperature, roughness, plasticity, anisotropy, and micro-inhomogeneity [104]. Also, material properties have a significant role in the wave propagation velocity [105] and, as a consequence, several material properties can be obtained by using specific ultrasonic measurements, as specified in Table 8 [64]. It is worth noting that the measurement of ultrasonic waves speed can be used to analyze RS in most of the engineering solids.

Murnaghan [106] developed a study on elasticity theory applied to solids. In his paper, a finite deformation theory is proposed for the case of a unidirectional deformed isotropic solid. A new set of constants, called the third-order elastic constants, was proposed. Later, Crecraft [107] improved the mathematical formulation and Takahashi et al. [108–111] explored the engineering applications of the third-order elastic constants proposed in Murnaghan’s papers. After intense mathematical analysis, the relations between the velocity of elastic wave propagation and the localized stress of a solid were introduced. To measure the velocity of wave propagation,

a specimen undergoing tensile testing was used. Transducers were mounted to evaluate transverse and longitudinal elastic waves in the specimen. After applying several mathematical operations and considering wave propagation, Eq. (3) was proposed [110]:

$$V_{ij} = V_0(1 + \alpha_{ij} \frac{T_{11}}{E}) \quad (3)$$

According to this equation, the propagation velocity of elastic waves depends on the ratio $\frac{T_{11}}{E}$ and the second or the third-order elastic modulus. The element $T_{ij} = J_{i\alpha} \frac{\partial(\rho_0\varphi)}{\partial m_{\alpha j}}$ is the static stress and it is linked to strain ($n_{\alpha j}$), the free energy per unit of volume of deformed isotropic solid ($\rho_0\varphi$) and the Jacobian matrix ($J_{i\alpha}$). V_0 is the propagation velocity of the non-loaded object and α_{ij} corresponds to the strain dependence coefficient. Employing simple calculations, coefficients α_{11} , α_{22} , α_{23} can be obtained by measuring V_{ij} , V_0 . Then, Mur-naghan's third-order elastic constants l , m , and n (TOEC) can be calculated. Those constants, when combined with the measurement of elastic wave propagation times, allow the estimation of the stress in various locations through the material [110].

The Time of flight (TOF) has a linear relationship with the material stress. In the case of a CRLW wave, TOF (t_0) is linked with stress by Eq. (4) [69]:

$$\sigma = B(t_0 - t) \quad (4)$$

Where B is a constant defined as Stress to Acoustic Time Difference (SATD). B is composed of several factors: material density, 2nd and 3rd order elastic constants of material. The combination of acoustoelastic constant (K) and TOF (t_0) results in the mathematical definition of B : $B = 1/Kt_0$. Moreover, B can be obtained from experimental data fitting, typically from strain gauges [69].

Li et al. [69], used CRLW method and Eq. (4) cited above to study structural steel samples. Further on, the reliability of the CRLW method was validated with the strain gauge method and the measured difference was within 5% in all samples. Nevertheless, a detailed calibration is critical to have accurate and reproducible results.

3.1. Ultrasonic waves types

Different types of ultrasonic waves can be employed to measure internal stress. Typically, the frequency range of ultrasound is between 20 kHz and 5 GHz, when propagating in air. Those waves can be combined in several modes to characterize stress:

1 TOF method: In this group, the time of flight (TOF) is directly considered focusing on longitudinal waves. From experimental results, it was discovered that ultrasonic wave velocity has an inverse correlation with stress. This method is more accurate since it uses only the value of the axial load calculated from the ratio of TOF in the stressed state. Nevertheless, many factors influence its efficiency, such as microstructure, noise, and bonding layer thickness [108].

2 Longitudinal and transverse waves combination: In this method, stress is measured using a birefringence approach. TOF of both longitudinal and shear waves traveling perpendicularly to the acoustic stress field are measured. Still, there are some disadvantages: Implementation of this technique is difficult and time-consuming, there is information only on the mean stress value of the measured part, and there is no available information on variations of stress in the material [108].

3 Critically refracted longitudinal waves (CRLW): The main advantage of this technique is a higher sensitivity for stress changes due to the greater variations on CRLW velocity when compared to other wave types. Besides, there is no need to measure second and third-order constants. Nevertheless, there are some limitations: first, the measured stress is an average value in a given wave path, which results in poor information on regions far away from the travel path; second, the measurement's accuracy can be affected by many factors, such as temperature, grain size, and material texture. Third, when $\theta_r = 90^\circ$, the refracted wave corresponds to the CRLW [112]. Finally, this wave is a combination of shear, longitudinal, Rayleigh, and incident components (see Fig. 9) [108].

4 Lamb/plate waves: guided waves produced in thin metal whose thickness is comparable to the wavelength of ultrasonic wave (smaller than 1.9 cm). Unlike bulk waves, the acoustoelastic behavior of plate waves is frequency-dependent. Besides, lamb waves propagate over longer distances than other bulk waves (longitudinal, transverse, Rayleigh) and, still, are sensitive to damage, stress, surface condition and temperature changes [113–117]. As pointed out in a paper by Gandhi et al [118], the use of several Lamb wave modes and frequencies for a uniaxial loaded aluminum plate resulted in an experimental data set in good agreement with theoretical predictions. Still, more work in third order constant calculation for specific materials would be helpful to reduce the gap between theoretical predictions and experimental results [118].

Among these three methods, the TOF is the most used one, followed by CRLW. The longitudinal and transverse waves combination is still not achievable in practice. Another possibility is the measurement of acoustoelastic birefringence, schematically shown in Fig. 10. In this case, there is one P-wave (longitudinal) and two T-waves (transversal) with orthogonal polarizations propagating at different velocities [110]. The acoustoelastic birefringence is based on the double refraction of waves. The phenomenon is also observed in optics, where rays of incident light split in two as they pass through certain types of materials [119].

3.2. Ultrasonic waves sources

A laser source can generate both acoustic and ultrasonic waves, according to the frequency of the signal. The functioning principle of this device, as illustrated in Fig. 11a, at first there is a pulsed laser – typically represented by Nd:YAG apparatus using a 1064 nm wavelength [120] - that creates an ultrasonic wave directed to the sample. Then, a separate continuous wave (CW) laser ultrasonic receiver detects this

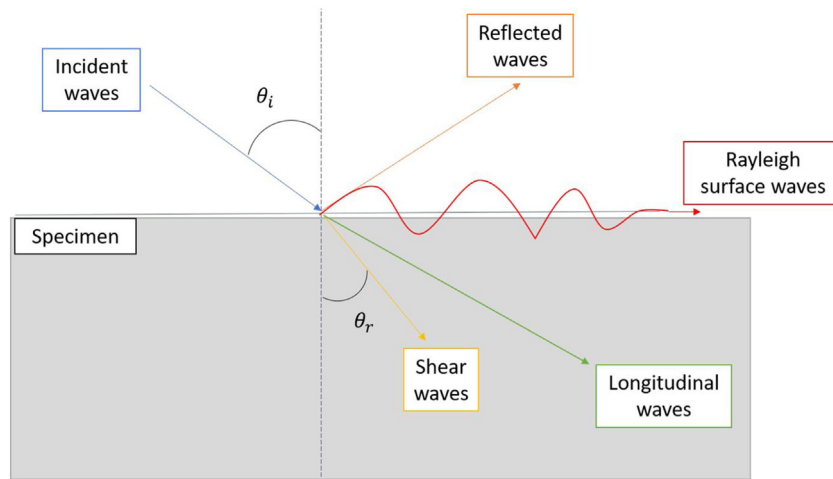


Fig. 9 – Wave components in a specimen (adapted from Ref. [112]).

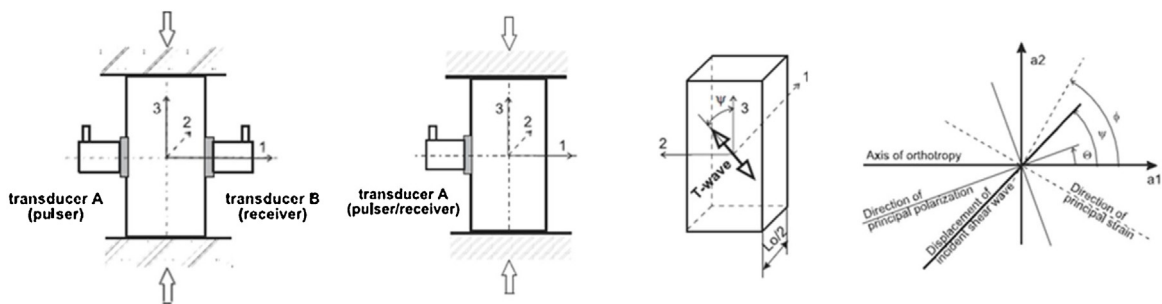


Fig. 10 – Schematics of acoustoelastic birefringence measurements using P-wave and two T-waves [109].

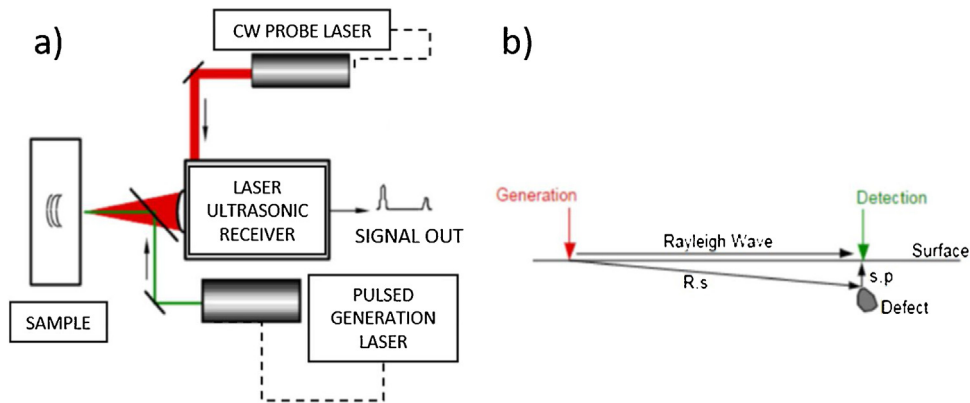


Fig. 11 – Schematics of Laser Ultrasound generator (adapted from Ref. [121]).

generated wave as it scatters from the surface of the sample [121]. Fig. 11b illustrates how Rayleigh surface waves can locate a shallow defect: Rayleigh (R) and Shear (s) waves are generated on the left of the surface and travel through the material until a defect is found. Then, after partially scattering from the defect, Shear (s) and compressional (p) waves are created and reach the surface on which they are detected [121]. Combining surface R waves with Volume waves allows the measurement of more complex fields of RS [122]. The processed signal allows the detection of internal defects such as voids, cracks, and

pores. In laser-based ultrasound, the signal of interest is oscillating bursts. One of the advantages of using laser is its greater flexibility, which allows performing measurements on curved or recessed surfaces [121]. Since laser ultrasound was successfully implemented for the detection of shallow pores or voids [121], a similar analysis could be performed to study RS.

In ultrasonic waves applied to NDT, Critically Refracted Longitudinal Wave (CRLW) method is the most used. After calibration and further calculation of acoustoelastic coefficients, the wave traveling speed (longitudinal and transverse) is mea-

sured. Then, using Eqs. (5), macro stresses can be determined along the wave path over large volumes of material, typically a few cubic millimeters [20].

$$\frac{V_{pp} - V_L^0}{V_L^0} = k_1\sigma_p + k_2(\sigma_q + \sigma_s) \frac{V_{pq} - V_T^0}{V_T^0} = k_3\sigma_p + k_4\sigma_q + k_5\sigma_s \quad (5)$$

V_{ij} is the wave velocity in the direction i and polarized in j . V_L^0 and V_T^0 are the isotropic longitudinal and transverse speeds, respectively. Directions p (longitudinal), s (shear), and q are orthogonal. Finally, k_n ($n = 1 \dots 5$) are coupling constants. As the wave propagates parallel to stress, more data is obtained. This method has high efficiency because wave velocity depends on microstructural inhomogeneities. As a consequence, voids, defects, or RS imply in different signal intensity and pattern [20,45].

Yan et al. [123] considered the measurement of stress in SLM-made 316 L stainless steel samples using the CRLW method. The UT test setup consisted in a set of transducers – transmitter and receiver (bandwidth: 2,7 – 7,5 MHz; diameter: 6 mm; central frequency: 5 MHz); an ultrasonic pulse transmitting instrument and an oscilloscope (sampling frequency: 2,5 GHz). As AM parts are highly anisotropic, one of the main concerns of their work was regarding the reliability of this UT method. Authors found that as each of the samples is scanned, the acoustoelastic coefficients are linked to the SLM scanning strategy. Besides, anisotropic microstructure will produce small changes in the acoustic time, which can lead to significant fluctuations in stress measurement. In this sense, it is necessary to consider a correction factor in the linear acoustoelastic formula when using CRLW method for the stress analysis of SLM samples.

Another method to generate acoustic waves for NDT is the Impulsive Stimulated Thermal Scattering (ISTS). It consists of the optical excitation of a material using a YAG:Nd laser in the infrared range and detection of the narrowband Surface Acoustic Waves (SAW). This technique can be widely implemented for repeated measurements in a single point of a sample since there is no local ablation and low surface heating by the action of the laser [95].

3.3. UT assessment of RS in AM processes

In a study by Guz' et al. [46], parts were analyzed using UT, with an emphasis on biaxial RS measurement. A long strip made of aluminum alloy AMG6 (Al - 6% Mg) was evaluated under the influence of different additional machining, aiming for RS relieving (Fig. 12). Initially, a measurement of RS – at a frequency of 5 MHz [122] – is made right after the deposition of a bead along the edge of the strip (curve 1). Then, the part is subjected to a stress of 50 % σ_y - yield stress (curve 2, first machining step) and, finally, a stress of 100% σ_y (curve 3, second machining step). Considering all measured RS curves (Fig. 12), it can be stated that further machining processes decrease RS. In analogous cases, parts were subjected to heat and explosive treatments and were then analyzed by UT. Measurements indicated a significant reduction of RS (both biaxial and triaxial). Nevertheless, RS measurement accuracy and error are around 10^{-5} [36].

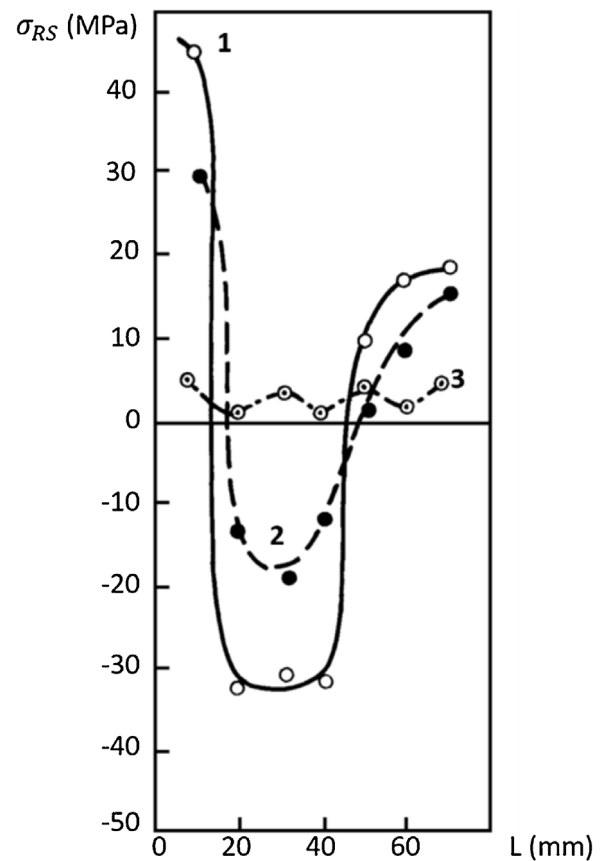


Fig. 12 – RS measurement of samples by ultrasonic-based NDT (adapted from Ref. [36]).

As most of the measurements occur in finished parts, Cerniglia et al. [124] performed an analysis of defects in Laser Metal Deposition (LMD) Inconel components. By combining FEM with laser ultrasonic measurements, near surface and surface defects with a size greater than 100 μm and depth up to 700 μm were successfully characterized. This same approach could be applied to study RS – type I – macrostresses (Fig. 8), including high precision analysis.

Spatially Resolved Acoustic Spectroscopy (SRAS) is a fast and high-resolution NDT method, based on laser ultrasound. Typically, SRAS apparatus uses two separate lasers (Fig. 13): one for thermoelastic generation of a SAW onto a specific sample and the other for the measurement of corresponding signal, making it able to detect surface and near subsurface features [125]. This technique is applicable to samples of any size, including varying degrees of surface finish and in different depths, typically in the 10–100 μm range. Recent research in the field is enhancing SRAS capability to treat rougher surfaces, one of such advances is the inclusion of a Fabry-Pierot interferometer and a broad array of sensors in the SRAS hardware. Since this method allows the monitoring of grain structures and has good spatial resolution (typically around 50 μm) [126], in principle, RS could be monitored by acoustic background correlation.

Finally, SRAS has great potential to become an in-situ NDT tool in AM processes, due to its compact size, good spatial capability, and reliability. Still, as pointed out by authors

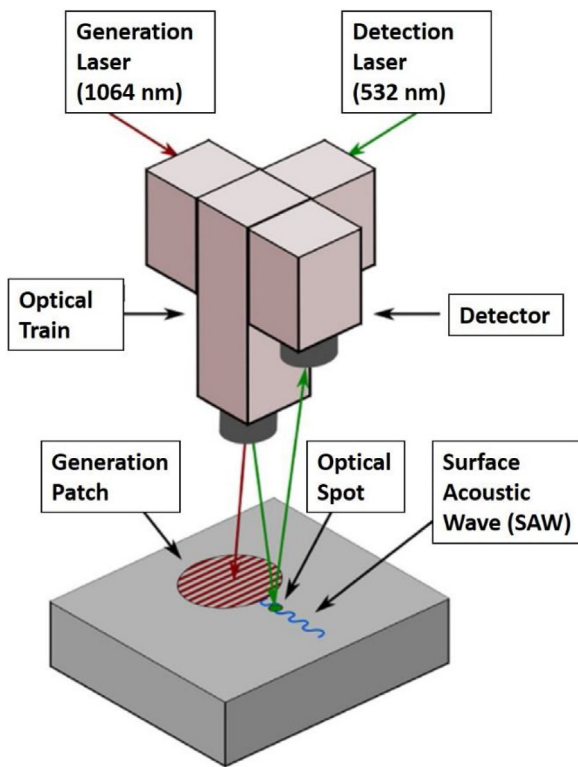


Fig. 13 – Typical SRAS apparatus configuration (adapted from Ref. [125]).

Hirsch et al. [125] and Smith et al. [127], SRAS measurement speeds, effects of surface roughness and data exchange between AM machine and SRAS are the most critical issues that require further work to obtain a competitive in-situ method for RS and defects monitoring.

Another alternative to assess RS is the hybrid method proposed by Bescond et al. [128,129], which results from the combination of a SAW with Laser-generated Surface Skimming Longitudinal Wave (LSSLW), which is more sensible to RS. By this method - based on monitoring the small ultrasonic velocity changes - RS of shot peened samples were determined and were found to be in good agreement with X-ray experiment. Still, as measurements were performed, the surfaces of the samples were damaged.

In two recent studies by Zhan et al. [130,131], RS of TC4 Ti alloy and 7075-Al alloy samples are assessed by a laser ultrasonic technique and hole-drilling method. As in the previous study by [129], the functioning principle of the laser ultrasonic system is based on the measurement of small velocity changes of laser-generated SAW.

Concerning the investigation on RS of TC4 Ti parts [131], the laser ultrasonic system setup has some of the features observed in Fig. 13: a laser generator of ultrasonic waves and a laser vibrometer for signal detection, with the inclusion of a pre-stress loading device – for acoustoelastic constant measurement and creation of stress fields in the samples. Then, RS is measured by laser ultrasound and compared with experimental data from hole-drilling method which proved to be equivalent. The influence of process parameters – heat input, welding speed and heat treatment – in the RS was observed.

The results showed that heat input has major influence on the RS of TC4 Ti parts.

As for the study on 7075 aluminum parts [130], a similar experimental setup from [131] was used. As in the previous study, the influence of process parameters on the RS was analyzed and showed that welding speed is the most relevant factor. Finally, RS experimental results from laser ultrasound and hole drilling methods presented small differences, highlighting the capability of the ultrasonic technique.

Rieder et al. [132] proposed an online monitoring tool for SLM process (which share the same functioning principle as DMLS). Several types of defects, such as voids and cracks can be determined during SLM part fabrication: as each layer is scanned by acoustic waves, spectra are obtained and perturbations can reveal the presence of anomalies (Fig. 14). Moreover, a qualitative evaluation seems to be possible on the RS – with the proper setup [132].

Complementarily, Cerniglia et al. [133] proposed an in-line UT inspection device of Laser Powder Deposition (LPD, similar to the DMD process) components. The authors coupled an Nd: YAG pulsed laser (source of acoustic waves) and an interferometric unit (laser receiver) to an LPD machine. During fabrication of Inconel parts, several induced flaws were accurately detected using UW (Rayleigh) up to 30 MHz and corresponding shortest wavelength of 9.6 μm . The prototype proved to be competitive with X-Ray computed tomography, with the additional advantage of inspecting each layer immediately after solidification. Still, some challenges need to be overcome, especially in the surface roughness effect and automated data exchange and analysis.

In another study by Cerniglia et al. [134], a new laser ultrasound device is evaluated to observe defects in LMD-Inconel 600 components. At first, sample 1 was analyzed only by laser ultrasound (wavelength: 532 nm; detection bandwidth: 1–50 MHz and laser spot: 200 micrometers), resulting in a total of four defects detected, whose diameter range is [420, 640] (micrometer) and depth range is [0.6, 1.3] (mm). In the following, sample 1 was analyzed using Laser Thermography, resulting in similar experimental data as observed in Laser Ultrasound. Then, both techniques were used to analyze sample 2, and three defects were spotted. The diameter range is [200, 490] (micrometer) and depth range is [0, 0.3] (millimeter). As such, this new technique allows more accurate evaluation of defects (through B-scan image analysis), higher sensitivity and wide detection bandwidth. Still, there are limitations regarding the range of defect size/depth ratio combination, high cost of equipment hardware and software, and, signal-to-noise is relied to the light collected

In recent work by Bond et al. [135], an ultrasonic in-situ system is tested for monitoring Directed Energy Deposition (DED) process. During the DED fabrication, acoustic signals were obtained from piezoelectric acoustic sensors coupled to the build plate. These signals were found in the 150 kHz to 2 MHz range. Further on, a spectral feature-based clustering method was used to analyze acoustic signals and create a specific signature for different DED processing conditions. This method has potential to detect anomalies such as defects and fabrication faults, and, can be implemented for parameter optimization and control.

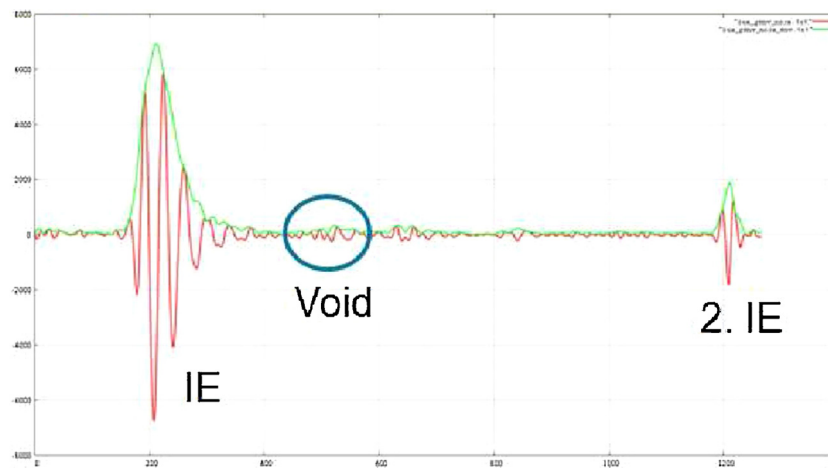


Fig. 14 – Defect detection using ultrasonic signals [132].

A novel approach to monitor AM parts during fabrication has been outlined by Xu et al. [96]: instead of scanning a single layer from a part, as performed in the publications cited above, Xu et al. focused on the spectral characteristics of ultrasonic elastic wave propagation, such as sample frequency and wave speed. Using an ultrasonic testing instrument and a series of transducers, a series of periodic phononic crystal artifact (PCA) – Polylactic Acid samples produced by Fused Filament Fabrication (FFF) were studied. This specific type of structure reproduces the complexities of the build and reveal some of the features present in AM processes and materials, such as defects and roughness. Finally, authors stated that this methodology can be implemented in any AM available technologies; monitor defects, mechanical characteristics and material internal structures [136]; and, it is able to perform process corrections in real time.

Further developments are required to enhance exchange between manufacturing units and ultrasonic systems. Lastly, the effect of the surface is critical: excessive surface roughness and poor surface finish increase signal noise and attenuation, ultrasonic wave dispersion, besides of not producing further relevant information and lowering the quality of ultrasonic signals [137,138]. Thus, UT is being more intensively applied in parts with lower surface roughness (10–20 μm), produced with PBF methods rather than DED process (average roughness around 80 μm).

4. Summary and perspectives

In this study, the advantages and limitations of UT were presented. This method has great potential to be employed in the next generation of metal-AM machines, focusing on the measurement of RS, voids, roughness, and defects. The most remarkable challenges remain in the field of data exchange, surface effects and spatial resolution [11,139]. Namely, the optimization of the link between UT apparatus and the AM hardware is required.

The complexity of AM parts brings another challenge to UT, since it is limited to simple geometries. Moreover, detected sound signatures have to be compared to a reference sound

signature and, there is any precise information on the origin of sound signature changes (microstructure, stresses, material properties change) [79].

Existing in-situ monitoring tools for commercial systems are quickly evolving: EOSTATE Meltpool[®] is able to monitor the entire building process through four separate and independent modules (Base, PowderBed, Meltpool, Exposure OT), increasing control on machine parameters and part quality. Besides, in a recent development with MTU Aero, a promising contact UT device was created including high spatial resolution (40 μm) and capability to measure porosities [140]. Furthermore, ARCAM LayerQam[®] allow to monitor porosity and defects up to 100 μm over all build chamber regarding before and after each layer. Another interesting tool is ARCAM xQam, an X-ray automated detector employed to calibrate the electron beam of EBM machines and it has the potential to be used in material characterization [141]. At present, most of these solutions are based on high-speed and high-resolution cameras, IR/near IR cameras and X-ray backscatter sensors. Nevertheless, UT-based alternatives such as Surface Resolved Acoustic Spectroscopy (SRAS), backscatter ultrasound, and Surface Resolved Acoustic Microscopy (SRAM) are under intense development, enhancing their features and are expected to meet higher standards in the short to medium term [142].

As abnormalities - voids, defects, and excessive RS - are detected during fabrication, AM machine parameters have to be quickly updated and their effects (individually or combined) on RS have to be understood. Also, discerning the relationship between multiple variables such as material properties and AM parameters is crucial to a more precise analysis and control of RS [30]. Solving this issue is critical to increase quality and accuracy (DED methods), and productivity (PBF methods).

Table 9 summarizes actual UT capabilities, regarding accuracy, frequencies and spatial resolution.

Research in the field of RS is advancing. Nevertheless, many aspects require attention, such as the influence of RS on the properties (durability and fatigue, creep, and corrosion resistance) of AM parts. In this sense, the development of a broad thermomechanical model in good agreement with experimental data would enhance the control and mitigation of these

Table 9 – UT techniques and respective capabilities.

Technique	Wave frequency (MHz)	Accuracy	Resolution (micrometer)	Reference
LSSLW	150	5×10^{-4}	–	[127]
SRAS	14	Speed-dependent	20	[124]
UT based on Nd:YAG pulsed laser	30	10^{-5}	100–800	[123]

stresses, especially in the field of AM [143]. Moreover, there is a growing need of finer control of these stresses in AM technologies: new developments such as hybrid instrumentation, involving different NDT methods, could bring more information on part abnormalities and increase production speed [11].

A specific set of norms for NDT of AM parts is in progress under the ISO/ASTM – DTR 52905 initiative. This will bring more knowledge on how to perform NDT in AM parts, with high levels of accuracy and repeatability, considering the intricate nature of AM.

Conflicts of interest

We wish to confirm that there are no known conflicts of interest associated with this publication and there has been no significant financial support for this work that could have influenced its outcome. We confirm that the manuscript has been read and approved by all named authors and that there are no other persons who satisfied the criteria for authorship but are not listed. We further confirm that the order of authors listed in the manuscript has been approved by all of us. We confirm that we have given due consideration to the protection of intellectual property associated with this work and that there are no impediments to publication, including the timing of publication, with respect to intellectual property. In so doing we confirm that we have followed the regulations of our institutions concerning intellectual property. We further confirm that any aspect of the work covered in this manuscript that has involved either experimental animals or human patients has been conducted with the ethical approval of all relevant bodies and that such approvals are acknowledged within the manuscript. We understand that the Corresponding Author is the sole contact for the Editorial process (including Editorial Manager and direct communications with the office). He is responsible for communicating with the other authors about progress, submissions of revisions and final approval of proofs. We confirm that we have provided a current, correct email address which is accessible by the Corresponding Author and which has been configured to accept email from ruben.acevedo@rocketmail.com.

Acknowledgments

The work of Ruben Acevedo was supported by the Centre of Excellence for Nonlinear Dynamic Behavior of Advanced Materials in Engineering CZ.02.1.01/0.0/0.0/15_003/0000493 (Excellence Research Teams) in the framework of Operational Program Research, Development and Education. The work of R. K. was supported by the grant projects with No. 19-04956S of the Czech Science Foundation (CSF) within institutional support RVO: 61388998.

Author R.A. would like to thank CAPES and PGMAT - UFSC (Brazil) for their support.

REFERENCES

- [1] ISO/ASTM 52900. Additive manufacturing technologies: general principles and terminology; 2018.
- [2] Sokolov SY. Ultrasonic oscillations and their applications. *Tech Phys* 1935;2:1–23.
- [3] Hellier CJ. <https://app.aws.org/itrends/2005/07/021/>, 2005.
- [4] Deutsch V. <https://www.ndt.net/article/wcndt00/papers/idn378/idn378.htm>, 2000.
- [5] Black JT, Kohser RA. *Materials and process in manufacturing*. 11th edition John Wiley & Sons; 2012.
- [6] Frazier WE. Metal additive manufacturing: a review. *J Mater Eng Perform* 2014;23(6):1917–28.
- [7] Trufiyakov V, Mikheev P, Kudryavtsev Y. Fatigue strength of welded structures. In: *Residual stresses and improvement treatments*. Harwood Academic Publishers; 1995.
- [8] Kudryavtsev Y. Effect of residual stresses on the endurance of welded joints. *International Institute of Welding*; 1994. p. 1568–94. IIW Doc. XIII.
- [9] Gu DD, Meiners W, Wissenbach K, Poprawe R. Laser additive manufacturing of metallic components: materials, processes and mechanisms. *Int Mater Rev* 2012;57(3):133–64.
- [10] Zaeh MF, Branner G. Investigations on residual stresses and deformations in selective laser melting. *Prod Eng* 2009;4(1):35–45.
- [11] Everton SK, Hirsch M, Stravroulakis P, Leach RK, Clare AT. Review of in-situ process monitoring and in-situ metrology for metal additive manufacturing. *Mater Des*, Elsevier 2016;95:431–45.
- [12] SmarTech Analysis. Additive manufacturing with metal powders report; 2019.
- [13] Sochalski-Kolbus LM, Payzant EA, Cornwell PA, Watkins TR, Babu SS, Dehoff RR, et al. Comparison of residual stresses in inconel 718 simple parts made by electron beam melting and direct metal laser sintering. *Metall Mater Trans A* 2015;46(3):1419–32.
- [14] Mercelis P, Kruth JP. Residual stresses in selective laser sintering and selective laser melting. *Rapid Prototyp J* 2006;12(5):254–65.
- [15] Brinksmeier E, Cammett JT, König W, Leskovic P, Peters J, Tonshoff HK. Residual stresses-measurement and causes in machining processes. *Ann CIRP* 1982;31(2):491–510.
- [16] Rossini NS, Dassisti M, Benyounis KY, Olabi AG. Methods of measuring residual stresses in components. *Mater Des* 2012;35:572–88.
- [17] Kruth JP, Froyen L, Van Vaerenbergh J, Mercelis P, Rombouts M, Lauwers B. Selective laser melting of iron-based powder. *J Mater Process Technol* 2004;149(1–3):616–22.
- [18] Kruth JP, Deckers J, Yasa E, Wauthele R. Assessing and comparing influencing factors of residual stresses in selective laser melting using a novel analysis method. *Proc Inst Mech Eng B J Eng Manuf* 2012;226(6):1–12.

- [19] Zyl I, Yadroitsava I, Yadroitsev I. Residual stress in Ti6Al4V objects produced by direct metal laser sintering. *South Afr J Ind Eng* 2016;27(4):134–41.
- [20] Withers PJ, Bhadeshia HK. Residual stress overview. Part 1 measurement techniques. *Mater Sci Technol* 2001;17:355–64.
- [21] Chen Q, Liu J, Liang X, Albert C. A level-set based continuous scanning path optimization method for reducing residual stress and deformation in metal additive manufacturing. *Comput Methods Appl Mech Eng* 2019;360:112719.
- [22] Buchbinder D, Meiners W, Pirch N, Wissenbach K, Schrage J. Investigation on reducing distortion by preheating during manufacture of aluminum components using selective laser melting. *J Laser Appl* 2014;26(1):012004.
- [23] Li C, Liu JF, Guo YB. Prediction of residual stress and part distortion in selective laser melting. *Procedia Cirp* 2016;45:171–4.
- [24] Carlsson S, Larsson PL. On the determination of residual stress and strain fields by sharp indentation testing: part I – theoretical and numerical analysis. *Acta Mater* 2001;49(12):2179–91.
- [25] Carlsson S, Larsson PL. On the determination of residual stress and strain fields by sharp indentation testing: part II – experimental investigation. *Acta Mater* 2001;49(12):2193–203.
- [26] Tan JHK, Sing SL, Yeong WY. Microstructure modelling for metallic additive manufacturing: a review. *Virtual Phys Prototyp* 2019;15(1):1–19.
- [27] Bhardwaj T, Shukla M. Effect of laser scanning strategies on texture, physical and mechanical properties of laser sintered maraging steel. *Mater Sci Eng A* 2018;734:102–9.
- [28] Newell DJ, O'Hara RP, Cobb GR, Palazotto AN, Kirka MM, Burggraf LW, et al. Mitigation of scan strategy effects and material anisotropy through supersolvus annealing in LPBF IN718. *Mater Sci Eng A* 2019;764:138230.
- [29] Dieter GE. Mechanical metallurgy. Metallurgy and metallurgical engineering series. McGraw-Hill; 1961.
- [30] Bartlett JL, Li X. An overview of residual stresses in metal powder bed fusion. *Addit Manuf* 2019;27:131–49.
- [31] Gusarov AV, Pavlov M, Smurov I. Residual stresses at laser surface remelting and additive manufacturing. *Phys Proc* 2011;12:248–54.
- [32] Parry L, Ashcroft IA, Wildman RD. Understanding the effect of laser scan strategy on residual stress in selective laser melting through thermo-mechanical simulation. *Addit Manuf* 2016;12:1–15.
- [33] Robinson J, Ashton I, Fox P, Jones E, Sutcliffe C. Determination of the effect of scan strategy on residual stress in laser powder bed fusion additive manufacturing. *Addit Manuf* 2018;23:13–24.
- [34] Yadroitsava I, Grewar S, Hattings D, Yadroitsev I. Residual stress in SLM Ti6Al4V alloy specimens. *Mater Sci Forum* 2015;828–829:305–10.
- [35] Kudryavtsev Y, Kleiman J. Residual stress management: measurement, fatigue analysis and beneficial redistribution. In: *Conference Proceedings for the Society for Experimental Mechanics Series*. 2011. p. 119–29.
- [36] Guz' AN, Makhort FG. The physical fundamentals of the ultrasonic nondestructive stress analysis of solids. *Int Appl Mech*, Springer 2000;36(9):1119–49.
- [37] Salmi A, Atzeni E. Residual stress analysis of thin AlSi10Mg parts produced by laser powder bed fusion. *Virtual Phys Prototyp* 2019;15:49–61.
- [38] Zhang B, Dembinski L, Coddet C. The study of the laser parameters and environment variables effect on mechanical properties of high compact parts elaborated by selective laser melting 316L powder. *Mater Sci Eng A* 2013;584:21–31.
- [39] Simson T, Emmel A, Dwars A, Böhm J. Residual stress measurements on AISI 316L samples manufactured by selective laser melting. *Addit Manuf* 2017;17:183–9.
- [40] Vastola G, Zhang G, Pei QX, Zhang YW. Controlling of residual stress in additive manufacturing of Ti6Al4V by finite element modeling. *Addit Manuf* 2016;12:231–9.
- [41] Mukherjee T, Manvatkar V, De A, DebRoy T. Mitigation of thermal distortion during additive manufacturing. *Scr Mater* 2017;127:79–83.
- [42] Hussein A, Hao L, Yan C, Everson R. Finite element simulation of the temperature and stress fields in single layers built without-support in selective laser melting. *Mater Des (1980-2015)* 2013;52:638–47.
- [43] Shiomi M, Osakada K, Nakamura K, Yamashita T, Abe F. Residual stress within metallic model made by selective laser melting process. *CIRP Ann Manuf Technol* 2004;53(1):195–8.
- [44] Loh L-E, Chua C-K, Yeong W-Y, Song J, Mapar M, Sing S-L, et al. Numerical investigation and an effective modelling on the selective laser melting (SLM) process with aluminium alloy 6061. *Int J Heat Mass Transf* 2015;80:288–300.
- [45] Withers PJ, Bhadeshia HK. Residual stress overview. Part 2 nature and origins. *Mater Sci Technol* 2001;17:366–75.
- [46] Taheri H, Shoaib MRM, Koester L, Bigelow TA, Collins PC, Bond LJ. Powder based additive manufacturing – a review of types of defects, generation mechanisms, detection property evaluation and metrology. *Int J Addit Subtractive Manuf* 2017;1(2):172–209.
- [47] Kim FH, Moylan SP. Literature review of metal additive manufacturing defects. *NIST Adv Manuf Ser* 2018:100–16.
- [48] King WE, Barth HD, Castillo VM, Gallegos GF, Gibbs JW, Hahn DE, et al. Observation of keyhole-mode laser melting in laser powder-bed fusion additive manufacturing. *J Mater Process Technol* 2014;214(12):2915–25.
- [49] Rombouts M, Kruth JP, Froyen L, Mercelis P. Fundamentals of selective laser melting of alloyed steel powders. *CIRP Ann* 2006;55(1):187–92.
- [50] Verhaeghe F, Craeghs T, Heulens J, Pandelaers L. A pragmatic model for selective laser melting with evaporation. *Acta Mater* 2009;57(20):6006–12.
- [51] Panwisawas C, Perumal B, Ward RM, Turner N, Turner RP, Brooks JW, et al. Keyhole formation and thermal fluid flow-induced porosity during laser fusion welding in titanium alloys: experimental and modelling. *Acta Mater* 2017;126:251–63.
- [52] Bayat M, Thanki A, Mohanty S, Witvrouw A, Yang S, Thorborg J, et al. Keyhole-induced porosities in laser-based powder bed fusion (L-PBF) of Ti6Al4V: high-fidelity modelling and experimental validation. *Addit Manuf* 2019;30:100835.
- [53] Rafi HK, Karthik NV, Gong H, Starr TL, Stucker BE. Microstructures and mechanical properties of Ti6Al4V parts fabricated by selective laser melting and Electron beam melting. *J Mater Eng Perform* 2013;22(12):3872–83.
- [54] Gokuldoss PK, Kolla S, Eckert J. Additive manufacturing processes: selective laser melting, electron beam melting and binder jetting—selection guidelines. *Materials* 2017;10(6):672.
- [55] Körner C. Additive manufacturing of metallic components by selective electron beam melting — a review. *Int Mater Rev* 2016;61(5):361–77.
- [56] Williams RJ, Davies CM, Hooper PA. A pragmatic part scale model for residual stress and distortion prediction in powder bed fusion. *Addit Manuf* 2018;22:416–25.
- [57] Prabhakar P, Sames WJ, Dehoff R, Babu SS. Computational modeling of residual stress formation during the electron beam melting process for inconel 718. *Addit Manuf* 2015;7:83–91.

- [58] Cheng B, Shrestha S, Chou K. Stress and deformation evaluations of scanning strategy effect in selective laser melting. *Addit Manuf* 2016;12:240–51.
- [59] Li C, Liu JF, Fang XY, Guo YB. Efficient predictive model of part distortion and residual stress in selective laser melting. *Addit Manuf* 2017;17:157–68.
- [60] Bertini L, Bucchi F, Frenzo F, Moda M, Monelli BD. Residual stress prediction in selective laser melting. *Int J Adv Manuf Technol* 2019;105:609–36.
- [61] Ding J, Colegrove P, Mehnen J, Ganguly S, Almeida PMS, Wang F, et al. Thermo-mechanical analysis of wire and arc additive layer manufacturing process on large multi-layer parts. *Comput Mater Sci* 2011;50(12):3315–22.
- [62] Green RE. Ultrasonic measurement of residual stress. *Proceedings of the First International Symposium on Ultrasonic Materials Characterization*, vol. 596. National Bureau of Standards Special Publication; 1978. p. 173–7.
- [63] Wu AS, Brown DW, Kumar M, Gallegos GF, King WE. An experimental investigation into additive manufacturing-induced residual stresses in 316L stainless steel. *Metall Mater Trans A* 2014;45(13):6260–70.
- [64] Vary A. Quantitative ultrasonic evaluation of mechanical properties of engineering materials. *Proceedings of the First International Symposium on Ultrasonic Materials Characterization*, vol. 596. National Bureau of Standards Special Publication; 1978. p. 41–53.
- [65] Baldi A. Residual stress measurement using hole drilling and integrated digital image correlation techniques. *Exp Mech* 2013;54(3):379–91.
- [66] Protasov CE, Safronov VA, Kotoban DV, Gusarov AV. Experimental study of residual stresses in metal parts obtained by selective laser melting. *Phys Procedia* 2016;83:825–32.
- [67] Alderson NA. Thermal modeling and simulation of electron beam melting for rapid prototyping on Ti6Al4V alloys. North Carolina State University; 2012.
- [68] Nobre JP, Kornmeier M, Dias AM, Scholtes B. Use of the hole-drilling method for measuring residual stresses in highly stressed shot-peened surfaces. *Exp Mech* 2000;40(3):289–97.
- [69] Li Z, He J, Teng J, Wang Y. Internal stress monitoring of in-service structural steel members with ultrasonic method. *MDPI Mater J* 2016;9:223.
- [70] Li C, Liu ZY, Fang XY, Guo YB. Residual stress in metal additive manufacturing. In: 4th CIRP Conference on Surface Integrity. 2018. p. 348–53.
- [71] Ali H, Ma L, Ghadbeigi H, Mumtaz K. In-situ residual stress reduction, martensitic decomposition and mechanical properties enhancement through high temperature powder bed pre-heating of selective laser melted Ti6Al4V. *Mater Sci Eng A* 2017;695:211–20.
- [72] Ali H, Ghadbeigi H, Hosseinzadeh F, Oliveira J, Mumtaz K. Effect of pre-emptive in situ parameter modification on residual stress distributions within selective laser-melted Ti6Al4V components. *Int J Adv Manuf Technol* 2019;103:4467–79.
- [73] Ali H. Evolution of residual stress in Ti6Al4V components fabricated using selective laser melting. PhD thesis. University of Sheffield; 2017.
- [74] Lu Y, Wu S, Gan Y, Huang T, Yang C, Junjie L, et al. Study on the microstructure, mechanical property and residual stress of SLM inconel-718 alloy manufactured by differing island scanning strategy. *Opt Laser Technol* 2015;75:197–206.
- [75] Keller S, Chupakhin S, Staron P, Maawad E, Kashaev N, Klusemann B. Experimental and numerical investigation of residual stresses in laser shock peened AA2198. *J Mater Process Technol* 2018;255:294–307.
- [76] Kromm A, Cabeza S, Mishurova T, Nadammal N, Thiede T, Bruno G. Residual stresses in selective laser melted samples of a nickel-based superalloy. *Mater Res Proc* 6, ECRS 2018;10:259–64.
- [77] Martina F, Roy MJ, Szost BA, Terzi S, Colegrove PA, Williams SW, et al. Residual stress of as-deposited and rolled wire+arc additive manufacturing Ti-6Al-4V components. *Mater Sci Technol* 2016;32(14).
- [78] Yu WH, Sing SL, Chua CK, Kuo CN, Tian XL. Particle-reinforced metal matrix nanocomposites fabricated by selective laser melting: a state of the art review. *Prog Mater Sci* 2019;104:330–79.
- [79] Lu QY, Wong CH. Additive manufacturing process monitoring and control by non-destructive testing techniques: challenges and in-process monitoring. *Virtual Phys Prototyp* 2017;13(2):39–48.
- [80] Boone N, Zhu C, Smith C, Todd I, Willmott JR. Thermal near infrared monitoring system for electron beam melting with emissivity tracking. *Addit Manuf* 2018;22:601–5.
- [81] Moylan S, Whitenon E, Lane B, Slotwinski J. Infrared thermography for laser-based powder bed fusion additive manufacturing processes. *ResearchGate*; 2014.
- [82] Aba-Perea PE, Pirling T, Preuss M. In-situ residual stress analysis during annealing treatments using neutron diffraction in combination with a novel furnace design. *Mater Des* 2016;110(15):925–31.
- [83] Matsumoto Y, Hashimoto F, Lahoti G. Surface integrity generated by precision hard turning. *CIRP Ann Manuf Technol* 1999;48(1):59–62.
- [84] Guo YB, Li W, Jawahir IS. Surface integrity characterization and prediction in machining of hardened and difficult-to-machine alloys: a state-of-art research review and analysis. *Mach Sci Technol* 2009;13:437–70.
- [85] Tang ZT, Liu ZQ, Wan Y, Ai X. Study on residual stresses in milling aluminum alloy 7050-T7451. In: *Advanced design and manufacture to gain a competitive edge*. Springer; 2008. p. 169–78.
- [86] Oyelola O, Crawforth P, Saoubi R, Clare AT. On the machinability of directed energy deposited Ti6Al4V. *Addit Manuf* 2017;245.
- [87] Yamaguchi H, Fergani O, Wu PY. Modification using magnetic field-assisted finishing of the surface roughness and residual stress of additively manufactured components. *CIRP Ann Manuf Technol* 2017;1642.
- [88] Portella Q, Chemkhi M, Reira D. Residual stresses in analysis in AISI 316L processed by Selective Laser Melting (SLM) treated by mechanical post-processing treatments. *Mater Res Proc* 2018;6:271–6. ECRS-10.
- [89] Galitelli D, Reira D, Rouhaud E. Comparison between conventional shot peening (SP) and surface mechanical attrition treatment (SMAT) on a titanium alloy. *Adv Mater Res* 2014;996:964–8.
- [90] Gao H, Dutta RK, Huizenga RM, Amirthalangam M, Hermans MJM, et al. Stress relaxation due to ultrasonic impact treatment on multi-pass welds. *Sci Technol Weld Join* 2014;19(6).
- [91] Kalentics N, Boillat E, Peyre P, Ciric S, Bogojevic N, Logev R. Tailoring of residual stress profile of selective melted parts by laser shock peening. *Addit Manuf*, Elsevier 2017;16:90–7.
- [92] Kalentics N, Boillat E, Peyre P, Gorny C, Kenel C, Leinenbach C, et al. 3D Laser shock peening – a new method for the 3D control of residual stresses in selective laser melting. *Mater Des* 2017;130:350–6.
- [93] Krautkramer J, Krautkramer H. *Ultrasonic testing of materials*. 4th edition Springer-Verlag; 1990.
- [94] Rizzo P, Pistone E, Werntges P, Han J, Ni X. Inspection of underwater metallic plates by means of laser ultrasound.

- Nondestructive testing of materials and structures, vol. 6. Rilem Bookseries, Springer; 2011. p. 675–80.
- [95] Grabec T, Sedlak P, Stoklasova P, Thomasova M, Shilo D, Kabla M, et al. In situ characterization of local elastic properties of thin shape memory films by surface acoustic waves. *Smart Mater Struct* 2016;25:127002.
- [96] Xu X, Vallabh CKP, Krishnan A, Volk S, Cetinkaya C. In-process thread orientation monitoring in additive manufacturing. *3D Print Addit Manuf* 2019;6(1):21–30.
- [97] Hübschen G. Ultrasonic techniques for materials characterization. In: *Materials characterization using nondestructive evaluation (NDE) methods*; 2016. p. 177–224.
- [98] Hauk V. Definition of macro- and microstresses and their separation. In: *Structural and residual stress analysis by nondestructive methods*; 1997. p. 129–215.
- [99] Nejezchlebová J, Seiner H, Sedlák P, Landa M, Šmilauerová J, Aeby-Gautier E, et al. On the complementarity between resistivity measurement and ultrasonic measurement for in-situ characterization of phase transitions in Ti-alloys. *J Alloys Compd* 2018;762:868–72.
- [100] Sevcik M, Grabec t, Stoklasova P, Janovska M, Zoubkova K, Sedlak P, et al. Non-contact characterization of acoustoelastic parameters of advanced materials by laser-ultrasound. *Acta Phys Pol A* 2017;134(3). ISPMA 14.
- [101] Thomasová M, Sedlák P, Seiner H, Janovská M, Kabla M, Shilo D, et al. Young's moduli of sputter-deposited NiTi films determined by resonant ultrasound spectroscopy: austenite, R-phase, and martensite. *Scr Mater* 2015;101:24–7.
- [102] Seiner H, Sedlák P, Bodnárová L, Kruisová A, Landa M, Pablos A, et al. Sensitivity of the resonant ultrasound spectroscopy to weak gradients of elastic properties. *J Acoust Soc Am* 2012;131(5):3775–85.
- [103] Prevorovsky Z, Krofta J, Kober J, Chlada M, Kirschner A. Nonlinear ultrasonic spectroscopy of 3D printed metallic samples. In: *12th European Conference on Non-Destructive Testing (ECNDT)*. 2018.
- [104] Landa M, Plesek J. Ultrasonic techniques for non-destructive evaluation of internal stresses. *15th World Conf. NDT* 2000;385.
- [105] Kudryavtsev Y, Kleiman J, Guschka O, Smilenko V, Brodovoy V. Ultrasonic technique and device for residual stress measurement. *ResearchGate*; 2004.
- [106] Murnaghan FD. Finite deformations of an elastic solid. *Am J Math* 1937;59:235–60.
- [107] Crecraft DI. The measurement of applied and residual stresses in metals using ultrasonic waves. *J Sound Vib* 1967;5:173–92.
- [108] Takahashi S. Japan patent 5033739. In: *Stress measurement method and its apparatus*; 2012.
- [109] Takahashi S. Measurement of third-order elastic constants and stress dependent coefficients for steels. *Mech Adv Mater Mod Process* 2018;4(2). SpringerOpen.
- [110] Takahashi S, Motegi R. Measurement of third-order elastic constants and applications to loaded structural materials. *SpringerPlus* 2015;4:325.
- [111] Takahashi, S. U.S. Patent No.11/312, 516 (2007).
- [112] Ramasamy R, Ibrahim Z, Chai HK. Numerical investigations of internal stresses on carbon steel based on ultrasonic LCR waves. *J Phys Conf Ser* 2017;908:012044.
- [113] Croxford AJ, Moll J, Wilcox PD, Michaels JE. Efficient temperature compensation strategies for guided wave structural health monitoring. *Ultrasonics* 2010;50: 517–28.
- [114] Dalton RP, Cawley P, Lowe MJS. The potential of guided waves for monitoring large areas of metallic aircraft fuselage structure. *J Nondestruct Eval* 2001;20(1):29–46.
- [115] Lu Y, Michaels JE. Feature extraction and sensor fusion for ultrasonic structural health monitoring under changing environmental conditions. *IEEE Sens J* 2009;9(11):1462–71.
- [116] Michaels JE, Lee SJ, Michaels TE. Effects of applied loads and temperature variations on ultrasonic guided waves. In: *Proceedings of the 2010 European Workshop on Structural Health Monitoring*. Lancaster, PA: DEStech Publications, Inc.; 2010. p. 1267–72.
- [117] Rose JL. Guided wave nuances for ultrasonic nondestructive evaluation. *IEEE Trans Ultrason Ferroelectr Freq Control* 2000;47(3):575–83.
- [118] Gandhi N, Michaels JE, Lee SJ. Acoustoelastic lamb wave propagation in biaxially stressed plates. *J Acoust Soc Am* 2012;132(3):1284–93.
- [119] Douplik A, Saiko G, Schelkanova I, Tuchin VV. The response of t to laser light. In: *Lasers for medical applications*. Woodhead Publishing; 2013. p. 47–109.
- [120] Liu IH, Yang CH. A quantitative laser ultrasound visualization system for investigating the interaction of wedge waves with a defect. *Nondestructive testing of materials and structures, 6. Rilem Bookseries, Springer*; 2011. p. 25–30.
- [121] Klein M, Sears J. Laser ultrasonic inspection of laser clad 316LSS and Ti-6-4. In: *23rd International Congress on Applications of Lasers and Electro-Optics*; 2004.
- [122] Guz' AN. Elastic waves in compressible materials with initial stresses and a nondestructive ultrasonic method for the determination of biaxial residual stresses. *Int Appl Mech* 1994;30(1):1–14.
- [123] Yan X, Xu X, Pan Q. Study on the measurement of stress in the surface of selective laser melting forming parts based on the critical refraction longitudinal wave. *Coatings* 2019;10(1):5.
- [124] Cerniglia D, Scafidi M, Pantano A, Rudlin J. Inspection of additive-manufactured layered components. *Ultrasonics* 2015;62:292–8.
- [125] Hirsch M, Patel R, Li W, Guan G, Leach RK, Sharples SD, et al. Assessing the capability of in-situ nondestructive analysis during layer based additive manufacture. *Addit Manuf* 2016;13:135–42.
- [126] Smith RJ, Wenqi L, Coulson J, Clark M, Somekh MG, Sharples SD. Spatially resolved acoustic spectroscopy for rapid imaging of material microstructure and grain orientation. *Meas Sci Technol* 2014;25:055902.
- [127] Smith RJ, Hirsch M, Patel R, Li W, Clare AT, Sharples SD. Spatially resolved acoustic spectroscopy for selective laser melting. *J Mater Process Technol* 2016;236:93–102.
- [128] Bescond C, Monchalain J-P, Levesque D, Gilbert A, Talbot R, Ochiai M. Determination of residual stresses using laser-generated surface skimming longitudinal waves. In: *Nondestructive evaluation and health monitoring of aerospace materials, composites, and civil infrastructure IV*; 2005.
- [129] Bescond C, Lévesque D, Lord M, Monchalain J-P, Forgues S. Laser-generated surface skimming longitudinal wave measurement of residual stress in shot peened samples. *AIP Conf Proc* 2006;820(1):1426.
- [130] Zhan Y, Li Y, Zhang E, Ge Y, Liu C. Laser ultrasonic technology for residual stress measurement of 7075 aluminum alloy friction stir welding. *Appl Acoust* 2019;145:52–9.
- [131] Zhan Y, Zhang E, Ge Y, Liu C. Residual stress in laser welding of TC4 titanium alloy based on ultrasonic laser technology. *Appl Sci* 2018;8(10).
- [132] Rieder H, Dillhofer A, Spies M, Bamberg J, Hess T. Online monitoring of additive manufacturing processes using ultrasound. In: *11th European Conference on Non-Destructive Testing (ECNDT), NDT.net : 2014-12*. 2014.

- [133] Cerniglia D, Scafidi M, Pantano A, Lopatka R. Laser ultrasonic technique for laser powder deposition inspection. In: 13th International Symposium on Nondestructive Characterization of Materials. 2013.
- [134] Cerniglia D, Montinaro N. Laser ultrasound for the evaluation of additive manufactured parts. In: 3rd International Workshop on Laser Ultrasound for Metals. 2017.
- [135] Bond LJ, Koester LW, Taheri H. NDE in-process for metal parts fabricated using powder based additive manufacturing. In: Proceedings of SPIE 10973, Smart Structures and NDE for Energy Systems and Industry 4.0,1097302. 2019.
- [136] Xu X, Vallabh CKP, Cleland ZJ, Cetinkaya C. Phononic crystal artifacts for real-time in-situ quality monitoring in additive manufacturing. *J Manuf Sci Eng* 2017;139(9):3–12, 091001.
- [137] Everton S, Dickens P, Tuck C, Dutton B. Using laser ultrasound to detect subsurface defects in metal laser powder bed fusion components. *J Miner Met Mater Soc* 2018;70(3):378–83.
- [138] Lu QY, Wong CH. Applications of non-destructive testing techniques for post-process control of additively manufactured parts. *Virtual Phys Prototyp* 2017;12(4):301–21.
- [139] Lopez A, Bacelar R, Pires I, Santos TG, Sousa JP, Quintino L. Non-destructive testing application of radiography and ultrasound for wire and arc additive manufacturing. *Addit Manuf* 2018;21:298–306.
- [140] Rieder H, Spies M, Bamberg J, Henkel B. On- and offline ultrasonic inspection of additively manufactured components. In: 19th World Conference on Non-Destructive Testing - WCNDT. 2016.
- [141] Arcam Just Add Brochure. <http://www.arcam.com/wp-content/uploads/justaddbrochure-web.pdf>.
- [142] Koester L, Taheri H, Bigelow T, Collins P, Bond L. Nondestructive testing for metal parts fabricated using powder-based additive manufacturing. *Mater Eval* 2018;76(4).
- [143] Ganeriwala RK, Strantz M, King WE, Clausen B, Phan TQ, Levine LE, et al. Evaluation of a thermomechanical model for prediction of residual stress during laser powder bed fusion of Ti-6Al-4V. *Addit Manuf* 2019;27:489–502.
- CRLW: Critically Refracted Longitudinal Wave
 CW: Continuous Wave
 DED: Directed Energy Deposition
 DMLS: Direct Metal Laser Sintering
 DIC: Digital Image Correlation
 DMLS: Direct Metal Laser Sintering
 EBDM: Electron Beam Direct Melting
 EBM: Electron Beam Melting
 EDM: Electrical Discharge Machining
 E-PBF: Electron Powder Bed Fusion
 FEM: Finite Element Method
 HD: Hole Drilling
 IFF: Ion Fusion Formation
 IR: Infrared
 L-DED: Laser-based Directed Energy Deposition
 LENS: Laser Engineering Net Shaping
 LMD: Laser Metal Deposition
 LMF: Laser Metal Fusion
 L-PBF: Laser-based Powder Bed Fusion
 LPD: Laser Powder Deposition
 LSSLW: Laser-generated surface skimming longitudinal wave
 LSP: Laser Shot Peening
 NDT: Non-Destructive Testing
 Nd:YAG: Neodimium-doped Yttrium Aluminum garnet
 PBF: Powder Bed Fusion
 P-DED: Powder Direct Energy Deposition
 PTAS FFF: Plasma Transferred Arc Selected Free Form Fabrication
 RPD: Rapid Plasma Deposition
 RS: Residual Stress
 SATD: Stress to Acoustic Time Difference
 SAW: Surface Acoustic Waves
 SLM: Selective Laser Melting
 SMAT: Surface Mechanical Attrition Treatment
 SMD: Shape Metal Deposition
 SRAS: Spatially Resolved Acoustic Spectroscopy
 TGM: Temperature Gradient Mechanism
 TOEC: Third-Order Elastic Constant
 TOF: Time of Flight
 UIT: Ultrasonic Impact Treatment
 UT: Ultrasonic Testing
 UW: Ultrasonic Waves
 WAAM: Wire Arc Additive Manufacturing
 W-DED: Wire Direct Energy Deposition
 XRD: X-Ray Diffraction



Glossary

Glossary

AM: Additive Manufacturing
 AW: Acoustic Waves

RESEARCH ARTICLE

Inverse mass matrix via the method of localized lagrange multipliers

José A. González¹  | R. Kolman²  | S. S. Cho³ | C. A. Felippa⁴ | K. C. Park⁴

¹Escuela Técnica Superior de Ingeniería, Universidad de Sevilla, Camino de los Descubrimientos s/n Sevilla, E-41092, Spain

²Institute of Thermomechanics, The Czech Academy of Sciences, Dolejškova 5 Prague, 182 00, Czech Republic

³Reactor Mechanical Engineering Division, Korea Atomic Energy Research Institute, Daejeon, 305-353, 999-111 Daedeok-Daero, Yuseong-gu, Republic of Korea

⁴Department of Aerospace Engineering Sciences, University of Colorado at Boulder, Boulder, 80309-429, CO, USA

Correspondence

K. C. Park, Department of Aerospace Engineering Sciences, University of Colorado at Boulder, Boulder, CO 80309-429, USA.
Email: kcpark@colorado.edu

Funding information

Centre of Excellence; Operational Program Research, Development and Education; Czech Science Foundation, Grant/Award Number: 17-22615S, RVO:61388998; Nuclear Safety Research Program; Korea Foundation of Nuclear Safety (KOFONS); Nuclear Safety and Security Commission (NSSC), Republic of Korea, Grant/Award Number: 1503003

Summary

An efficient method for generating the mass matrix inverse of structural dynamic problems is presented, which can be tailored to improve the accuracy of target frequency ranges and/or wave contents. The present method bypasses the use of biorthogonal construction of a kernel inverse mass matrix that requires special procedures for boundary conditions and free edges or surfaces and constructs the free-free inverse mass matrix using the standard FEM procedure. The various boundary conditions are realized by the the method of localized Lagrange multipliers. In particular, the present paper constructs the kernel inverse matrix by using the standard FEM elemental mass matrices. It is shown that the accuracy of the present inverse mass matrix is almost identical to that of a conventional consistent mass matrix or a combination of lumped and consistent mass matrices. Numerical experiments with the proposed inverse mass matrix are conducted to validate its effectiveness when applied to vibration analysis of bars, beams, and plain stress problems.

KEYWORDS

explicit time integration, inverse mass matrix, localized Lagrange multipliers, partitioned analysis

1 | INTRODUCTION

Recently, improvements of FEM mass matrices have been receiving an intense attention in the computational mechanics community.¹⁻⁵ The need for mass matrix improvements comes from 2 distinct motivations: efficient large explicit time integration step lengths for the analysis of highly nonlinear transient structural dynamics and dispersion accuracy improvements for wave propagation analysis.⁶⁻¹⁰ The first one has been addressed by adopting lumped mass matrices that improves computational efficiency and at the same time decreases the highest frequency (often equalling to the highest mesh frequency). The second need arises from the requirements of high accuracy in the transmitting forces with

high-frequency stress waves. This is where a diagonalized mass matrix may not yield sufficiently accurate results, hence the search for nondiagonal mass matrix continues to date.

Ideally, an inverse mass matrix should possess the following properties:

1. It should accurately capture both low and intermediate-frequency response components.
2. Except for discontinuous wave propagation problems, its numerically stable explicit integration step size should be much larger than using the standard mass matrix.
3. Its inverse should be inexpensive to generate, preferably without factorization computations.

Recently, Tkachuk and Bischoff⁵ presented an innovative method for constructing an inverse mass matrix based on Hamilton's principle with momentum and displacement (\mathbf{p}, \mathbf{u}) variables. A key idea in their work is the discretization of the momentum-based kinetic energy in terms of a set of biorthogonal basis functions corresponding to the displacement basis functions. The method proposed in Tkachuk and Bischoff⁵ resorts to nonstandard finite element construction with special tailoring for treating the Dirichlet boundary terms. Hence, considerable modifications of the existing finite element software modules are required. When one contemplates element-by-element construction of the inverse of the global mass matrix, many degrees of freedom belong to the cross points and boundary nodes, which implies that one has to replace the existing mass matrix routines by specially constructed mass matrix inverse.

The present method, while using the same momentum-velocity formulation as adopted in Tkachuk and Bischoff⁵ only as a formulation vehicle, uses standard FEM procedures, thus alleviates the special treatments associated the use of biorthogonal construction and mass matrix modification via a penalty procedure. Specifically, we outline the present method as follows:

First, we abandon the biorthogonal generation of the elemental kernel inverse mass matrix. Instead, we use the standard FEM mass matrix with a diagonalized mass-like matrix to construct the elemental kernel inverse matrix.

Second, the present proposed method does not require the penalty insertion to improve the accuracy of the procedure presented in Tkachuk and Bischoff.⁵ It is shown that the accuracy of the present method is almost identical to that of a weighted elemental mass matrix of a lumped and consistent elemental mass matrix.

Third, boundary conditions are enforced by the method of localized Lagrange multipliers,¹¹⁻¹⁴ hence the present method needs only free-free inverse matrices. This makes the present method applicable to all the existing element types. Since the number of boundary degrees of freedom is usually substantially smaller than the those of the resulting size of the unknown equations, the cost associated with the enforcement of the boundary conditions via the localized method of Lagrange multipliers is insignificant as will be shown subsequently.

The paper is organized as follows. Section 2 derives from Hamilton's principle the (\mathbf{p}, \mathbf{u}) mixed equations of elastodynamics and describes the direct construction of inverse mass matrices through biorthogonal basis functions. The incorporation of boundary conditions into the inverse mass matrix is described in Section 3, together with its mathematical formalization through the use of a projector. Furthermore, a new method for selective mass scaling that reduces the maximum frequencies is described in Section 4. In Section 5, a series of numerical examples is solved and compared with analytical solutions to demonstrate the accuracy of the proposed methodology. Finally, Section 6 closes with some concluding remarks.

2 | BASIS FOR CONSTRUCTING INVERSE MASS MATRIX VIA THE LOCALIZED LAGRANGE MULTIPLIERS

The prevailing practice for computing the mass matrix \mathbf{M} in the finite element method is to use a bilinear form of the system kinetic energy T , viz,

$$T = \int_{\Omega} \frac{1}{2} \rho \mathbf{v}(\mathbf{x}, t) \cdot \mathbf{v}(\mathbf{x}, t) d\Omega \approx \frac{1}{2} \dot{\mathbf{u}}(t)^T \mathbf{M} \dot{\mathbf{u}}(t), \quad (1)$$

where $\mathbf{v}(\mathbf{x}, t)$ and $\dot{\mathbf{u}}(t)$ are the continuum velocity and discrete approximate velocity, respectively. Since our objective is to generate the inverse mass matrix directly, instead of using matrix inversion, we use a dual form of the kinetic energy:

$$T = \int_{\Omega} \frac{1}{2\rho} \mathbf{p}(\mathbf{x}, t) \cdot \mathbf{p}(\mathbf{x}, t) d\Omega \approx \frac{1}{2} \mathbf{p}(t)^T \mathbf{C} \mathbf{p}(t), \quad (2)$$

where $\mathbf{p}(\mathbf{x}, t)$ and $\mathbf{p}(t)$ are, respectively, the continuum and discrete approximate momentum vectors, and \mathbf{C} is defined as the reciprocal mass matrix (RMM).

It will be shown that an inverse of the mass matrix can be obtained via

$$\mathbf{M}^{-1} = \mathbf{A}^{-\top} \mathbf{C} \mathbf{A}^{-1}, \quad (3)$$

where \mathbf{A} is the dual-base projection matrix, that can be transformed into a diagonal area/volume-like matrix, hence the computational simplicity of obtaining an inverse of the mass matrix via this new route.

To this end, we invoke Hamilton's principle for constrained elastodynamic problems. This principle states that "the path followed by a dynamic system is the one which minimizes the action integral of the Lagrangian" condition that can be expressed using the following three-field variational form:

$$\delta H(\mathbf{u}, \mathbf{p}, \ell) = \int_{t_1}^{t_2} \delta \{T(\dot{\mathbf{u}}, \mathbf{p}) - U(\mathbf{u}, \ell) + W(\mathbf{u})\} dt = 0, \quad (4)$$

where δT is the virtual kinetic energy, δU the virtual elastic energy, and δW the virtual work done by the external loads, magnitudes that can be expressed:

$$\delta T = \int_{\Omega} \delta \left(\frac{1}{2} \mathbf{p} \cdot \dot{\mathbf{u}} \right) d\Omega, \quad (5)$$

$$\delta U = \int_{\Omega} \delta \boldsymbol{\varepsilon} : \boldsymbol{\sigma} d\Omega + \int_{\Gamma} \delta \{ \ell \cdot (\mathbf{u} - \mathbf{u}_b) \} d\Gamma, \quad (6)$$

$$\delta W = \int_{\Omega} \delta \mathbf{u} \cdot \mathbf{f} d\Omega \quad (7)$$

with known displacement boundary conditions \mathbf{u}_b imposed at interface Γ by using a field of localized Lagrange multipliers ℓ and external body forces per unit volume \mathbf{f} acting on Ω .

By making use of the momentum-velocity relation ($\mathbf{p} = \rho \dot{\mathbf{u}}$) in the following identity:

$$\frac{1}{2} \mathbf{p} \cdot \dot{\mathbf{u}} = \mathbf{p} \cdot \dot{\mathbf{u}} - \frac{1}{2\rho} \mathbf{p} \cdot \mathbf{p}, \quad (8)$$

we can obtain an equivalent expression for the virtual kinetic energy per unit volume:

$$\delta \left(\frac{1}{2} \mathbf{p} \cdot \dot{\mathbf{u}} \right) = \delta \dot{\mathbf{u}} \cdot \mathbf{p} + \delta \mathbf{p} \cdot \left(\dot{\mathbf{u}} - \frac{1}{\rho} \mathbf{p} \right) \quad (9)$$

and finally performing an integration by parts of the second term of the last equation yields:

$$\int_{t_1}^{t_2} \delta \dot{\mathbf{u}} \cdot \mathbf{p} dt = - \int_{t_1}^{t_2} \delta \mathbf{u} \cdot \dot{\mathbf{p}} dt \quad (10)$$

relation that can be used to eliminate the virtual velocity field from the formulation.

Introducing previous identities, (9) and (10), into the principle of stationary action 4, we obtain the final 3-field variational form of the Hamilton principle for constrained elastodynamics:

$$\begin{aligned} \delta H(\mathbf{u}, \mathbf{p}, \ell) = \int_{t_1}^{t_2} \left\{ \int_{\Omega} \delta \mathbf{p} \cdot \left(\dot{\mathbf{u}} - \frac{1}{\rho} \mathbf{p} \right) d\Omega - \int_{\Omega} (\delta \mathbf{u} \cdot \dot{\mathbf{p}} + \delta \boldsymbol{\varepsilon} : \boldsymbol{\sigma}) d\Omega + \int_{\Omega} \delta \mathbf{u} \cdot \mathbf{f} d\Omega \right. \\ \left. + \int_{\Gamma} \delta \mathbf{u} \cdot \ell d\Gamma - \int_{\Gamma} \delta \ell \cdot (\mathbf{u} - \mathbf{u}_b) d\Gamma \right\} dt = 0, \end{aligned} \quad (11)$$

expression that will be used to derive the equations of motion.

Discretization in space of this mixed form is performed by using independent shape functions for displacements, momenta, and Lagrangian multipliers. We conduct then a standard mixed FEM discretization with independent shape functions for the 3 fields:

$$\mathbf{u} = \mathbf{N}_u \mathbf{u}, \quad \mathbf{p} = \mathbf{N}_p \mathbf{p}, \quad \ell = \mathbf{N}_\lambda \lambda, \quad (12)$$

and introducing these approximations in (11), one obtains the following set of semidiscrete equations:

$$\mathbf{A}^\top \dot{\mathbf{u}} - \mathbf{C}\mathbf{p} = \mathbf{0} \quad \text{Momentum equation,} \quad (13)$$

$$\mathbf{A}\dot{\mathbf{p}} + \mathbf{B}\boldsymbol{\lambda} = \mathbf{r} \quad \text{Equilibrium equation,} \quad (14)$$

$$\mathbf{B}^\top \mathbf{u} - \mathbf{L}_b \mathbf{u}_b = \mathbf{0} \quad \text{Boundary (and interface) constraints,} \quad (15)$$

$$-\mathbf{L}_b^\top \boldsymbol{\lambda} = \mathbf{0} \quad \text{Newton's 3rd law on the boundaries,} \quad (16)$$

where vector $\mathbf{r} = \mathbf{f} - \mathbf{f}^{int}$ is the external-internal forces residual, and the matrix components are expressed:

$$\mathbf{A} = \int_{\Omega} \mathbf{N}_u^\top \mathbf{N}_p \, d\Omega, \quad (17)$$

$$\mathbf{C} = \int_{\Omega} \frac{1}{\rho} \mathbf{N}_p^\top \mathbf{N}_p \, d\Omega, \quad (18)$$

$$\mathbf{B} = \int_{\Gamma} \mathbf{N}_u^\top \mathbf{N}_\lambda \, d\Gamma, \quad (19)$$

$$\mathbf{L}_b = \int_{\Gamma} \mathbf{N}_\lambda^\top \mathbf{N}_{ub} \, d\Gamma, \quad (20)$$

where \mathbf{A} is the global projection matrix, \mathbf{C} the global reciprocal mass matrix, \mathbf{B} the boundary assembly operator, and \mathbf{L}_b is the Localized multipliers assembly matrix.

Eliminating symbolically the momentum variable (\mathbf{p}) from (13) and (14), one obtains the classical equation of motion expressed in terms of displacements:

$$(\mathbf{A}\mathbf{C}^{-1}\mathbf{A}^\top) \ddot{\mathbf{u}} + \mathbf{B}\boldsymbol{\lambda} = \mathbf{r} \quad (21)$$

with the mass matrix approximated as

$$\mathbf{M} = \mathbf{A}\mathbf{C}^{-1}\mathbf{A}^\top \quad (22)$$

and observe that there must exist an inverse mass matrix (denoted as \mathbf{M}^{-1}) given by:

$$\mathbf{M}^{-1} = \mathbf{A}^{-\top} \mathbf{C} \mathbf{A} \quad (23)$$

assuming that the global projection matrix is invertible.

Since the objective of the present paper is to obtain inverse mass matrices in efficient and accurate ways, one must insist on easily to invert *diagonal* or narrowly banded projection matrices. This can be accomplished by diagonalizing the projection \mathbf{A} -matrix given in (17), leaving the task of constructing the reciprocal \mathbf{C} -matrix efficiently and accurately.

2.1 | Biorthogonal basis functions

Observing (17) and (23), we realize that a careful selection of the basis functions can simplify the calculation of the mass matrix inverse. For this task, Tkachuk et al⁵ proposed the use of biorthogonal basis functions¹⁵ because they produce a diagonal projection matrix in the form:

$$\mathbf{A}_e = \int_{\Omega_e} \mathbf{N}_u^\top \mathbf{N}_p \, d\Omega, \quad \text{where } [\mathbf{A}_e]_{ij} = 0 \text{ for } i \neq j \quad (24)$$

with a trivial inverse that permits to compute the inverse mass matrix directly from the RMM. We exemplify this in the following simple example.

Example 1. Evaluate the projection matrix and the reciprocal mass matrix for a 1-D 2-node linear bar element of length L_e and density per unit length ρ_e .

For a 2-node linear element with one DOF per node, the basis functions are expressed:

$$\mathbf{N}_u = \left[\frac{1}{2}(1 - \xi) \quad \frac{1}{2}(1 + \xi) \right],$$

and their associated biorthogonal basis functions are given by

$$\mathbf{N}_p = \left[\frac{1}{2}(1 - 3\xi) \quad \frac{1}{2}(1 + 3\xi) \right],$$

hence the projection matrix 17 is evaluated as

$$\mathbf{A}_e = \int_{-1}^1 \begin{bmatrix} \frac{1}{4}(1 - \xi)(1 - 3\xi) & \frac{1}{4}(1 - \xi)(1 + 3\xi) \\ \frac{1}{4}(1 + \xi)(1 - 3\xi) & \frac{1}{4}(1 + \xi)(1 + 3\xi) \end{bmatrix} \frac{L_e}{2} d\xi = \frac{L_e}{2} \begin{bmatrix} 1 & 0 \\ 0 & 1 \end{bmatrix},$$

where we observe that the projection matrix \mathbf{A}_e is diagonal (by design) and indeed equal to the lumped mass matrix (LMM) computed with unit density. Next, we evaluate analytically the reciprocal mass matrix from its definition 18:

$$\mathbf{C}_e = \int_{-1}^1 \frac{1}{\rho_e} \begin{bmatrix} \frac{1}{4}(1 - 3\xi)^2 & \frac{1}{4}(1 - 3\xi)(1 + 3\xi) \\ \frac{1}{4}(1 + 3\xi)(1 - 3\xi) & \frac{1}{4}(1 + 3\xi)^2 \end{bmatrix} \frac{L_e}{2} d\xi = \frac{L_e}{2\rho_e} \begin{bmatrix} 2 & -1 \\ -1 & 2 \end{bmatrix}$$

and finally use expression 23 to obtain the inverse mass matrix:

$$\mathbf{M}_e^{-1} = \mathbf{A}_e^{-T} \mathbf{C}_e \mathbf{A}_e^{-1} = \frac{2}{\rho_e L_e} \begin{bmatrix} 2 & -1 \\ -1 & 2 \end{bmatrix}$$

to confirm that this is exactly the analytical inverse of the consistent mass matrix (CMM). From this simple example, we conclude that it is possible to compute the inverse of the mass matrix without expensive matrix inversions and that, at least for simple linear elements, the result is exact. At the same time, we realize that the projection matrix can be effectively computed from the LMM.

However, in presence of Dirichlet boundary conditions or cross points, things get more complicated because the diagonalization property of the biorthogonal basis functions is lost for the constrained DOFs and the biorthogonal bases need to be modified accordingly.¹⁵ This problem has been extensively studied by Tkachuk et al⁵ that proposed a solution using the following velocity-momentum relation:

$$\mathbf{u} = \begin{Bmatrix} \mathbf{u}_f \\ \bar{\mathbf{u}} \end{Bmatrix} \rightarrow [\mathbf{I} \quad \mathbf{A}_d^T] \begin{Bmatrix} \dot{\mathbf{u}}_f \\ \dot{\bar{\mathbf{v}}} \end{Bmatrix} = \mathbf{C}\mathbf{p}, \quad (25)$$

where the total displacements \mathbf{u} have been partitioned into free \mathbf{u}_f and fixed $\bar{\mathbf{u}}$. The constrained DOFs produce a populated matrix \mathbf{A}_d that requires special construction, depending upon the element types used and the BC configuration.

Reference⁵ discusses various ways of constructing matrices \mathbf{A}_d and \mathbf{C} this way, namely, by using biorthogonal shape functions and inserting penalty terms with adjustable parameters together with somewhat complicated ways of accounting for boundary conditions, etc. This process complicates enormously the formulation. Hence, it is not possible to use, in a straightforward manner, the existing FEM software without considerable modifications. In the present paper, we bypass this procedure and use standard FEM data structure.

2.2 | An alternative method

For the calculation of the inverse mass matrix, biorthogonal basis functions must be first build for each particular finite element. However, basis functions are known for a limited number of elements, such as line, triangular, quadrilateral, and tetrahedral elements. Therefore, we propose a different route for the evaluation of the mass matrix inverse that bypasses this necessity through the following steps:

1. Consider all the structures as free-floating.
2. Approximate the element projection matrix \mathbf{A}_e by a lumping of the element mass matrix.
3. Compute the element reciprocal mass matrix \mathbf{C}_e from a direct inversion of the element mass matrix.
4. Assemble the global projection and reciprocal matrices and compute the global mass matrix inverse.
5. Impose boundary conditions using localized Lagrange multipliers.

The first 4 steps of this process are described next and the last step, which is a little bit more involved, will be analyzed in the next section.

First, we consider an element at a time by using the element mass matrices existing in standard FEM software systems. Second, we use the element mass matrix to approximate the element projection matrix by diagonalization, viz,

$$[\mathbf{A}_e]_{ii} = \frac{1}{\rho_e} \sum_j [\mathbf{M}_e]_{ij}, \quad (26)$$

assuming that the density is constant inside the element. Third, the elemental reciprocal mass matrix is evaluated inverting numerically the element mass matrix:

$$\mathbf{C}_e = \mathbf{A}_e^T \mathbf{M}_e^{-1} \mathbf{A}_e, \quad (27)$$

where $(\mathbf{A}_e, \mathbf{C}_e, \mathbf{M}_e)$ are elemental matrices, and particularly, \mathbf{A}_e is a diagonalized matrix.

Finally, we proceed with the assembly of the global reciprocal mass matrix:

$$\mathbf{C} = \sum_{e=1}^{n_e} \mathbf{C}_e, \quad (28)$$

and the global projection matrix

$$\mathbf{A} = \sum_{e=1}^{n_e} \mathbf{A}_e, \quad (29)$$

observing that as long as the elemental \mathbf{A}_e is diagonal, so is the assembled matrix \mathbf{A} and its inverse. These steps permit to evaluate the inverse of the global mass matrix through expression 23 in an efficient way.

3 | INCORPORATION OF BOUNDARY CONDITIONS

As we mentioned, in presence of Dirichlet boundary conditions, a direct computation of the mass inverse requires complicated modifications of the biorthogonal shape functions. We eliminate the necessity of these modifications by considering the structures as free-floating and applying the boundary conditions through localized Lagrangian multipliers.¹¹⁻¹⁴ To explain the enforcement of boundary conditions, we reorganize the semidiscrete equations of motions 13 to (16) to obtain the following partitioned equation set:

$$\begin{bmatrix} \mathbf{M} & \mathbf{B} & \mathbf{0} \\ \mathbf{B}^T & \mathbf{0} & -\mathbf{L}_b \\ \mathbf{0} & -\mathbf{L}_b^T & \mathbf{0} \end{bmatrix} \begin{Bmatrix} \ddot{\mathbf{u}} \\ \lambda \\ \ddot{\mathbf{u}}_b \end{Bmatrix} = \begin{Bmatrix} \mathbf{r} \\ \mathbf{0} \\ \mathbf{0} \end{Bmatrix}, \quad (30)$$

where the second equation is simply twice time-differentiated expression of (15).

Let us assume now that the boundary acceleration vector $(\ddot{\mathbf{u}}_b)$ consists of entirely the prescribed boundary quantities, regardless whether they are zero or nonzero (eg, ground excitations of earthquakes or car tires rolling on the road). In this case, we obtain the accelerations $(\ddot{\mathbf{u}})$ from the first equation of (30) as

$$\ddot{\mathbf{u}} = \mathbf{M}^{-1} (\mathbf{r} - \mathbf{B}\lambda), \quad (31)$$

in which once again we emphasize that the computation of $\mathbf{M}^{-1} = \mathbf{A}^{-T} \mathbf{C} \mathbf{A}^{-1}$ does not require additional computational effort because the global projection matrix \mathbf{A} is diagonal.

Then, substitute the accelerations obtained above into the second equation of (30):

$$\mathbf{B}^T \mathbf{M}^{-1} (\mathbf{r} - \mathbf{B}\lambda) - \mathbf{L}_b \ddot{\mathbf{u}}_b = \mathbf{0} \quad (32)$$

to compute the Lagrange multipliers

$$\lambda = [\mathbf{B}^T \mathbf{M}^{-1} \mathbf{B}]^{-1} (\mathbf{B}^T \mathbf{M}^{-1} \mathbf{r} - \mathbf{L}_b \ddot{\mathbf{u}}_b) \quad (33)$$

and substitute them back in (31) to obtain the final accelerations

$$\ddot{\mathbf{u}} = \mathbf{M}_b^{-1} \mathbf{r} + \mathbf{M}^{-1} \mathbf{B} [\mathbf{B}^T \mathbf{M}^{-1} \mathbf{B}]^{-1} \mathbf{L}_b \ddot{\mathbf{u}}_b \quad (34)$$

with a constrained inverse mass matrix:

$$\mathbf{M}_b^{-1} = \mathbf{M}^{-1} - \mathbf{M}^{-1} \mathbf{B} [\mathbf{B}^T \mathbf{M}^{-1} \mathbf{B}]^{-1} \mathbf{B}^T \mathbf{M}^{-1}, \quad (35)$$

defined as the inverse mass matrix incorporating the applied boundary conditions. Once again, since the size of $[\mathbf{B}^T \mathbf{M}^{-1} \mathbf{B}]$ is small, pertaining to the boundary degrees of freedom, its inversion is trivial. Notice that when the structure is free-free, one has $\mathbf{B} = \mathbf{0}$ so that \mathbf{M}_b^{-1} is simply the inverse mass matrix.

It is also noted that the degrees of freedom for $\ddot{\mathbf{u}}$ consists of not only the interior ones but also the constrained boundary displacements. Consequently, \mathbf{M}_b^{-1} would be singular corresponding to the constrained boundary degrees of freedom. One way to eliminate the almost singular mass matrix is simply to eliminate the rows and columns of \mathbf{M}_b^{-1} corresponding to the boundary degrees of freedom. Its justification will be examined next.

3.1 | Projection of the mass matrix

The proposed element-independent and biorthogonal-free derivation of the global inverse mass matrix described in section 2.2 and subsequent evaluation of final accelerations through (34) can be elegantly expressed as

$$\ddot{\mathbf{u}} = \mathbf{M}_b^{-1} \mathbf{r} + (\mathbf{I} - \mathcal{P}) \mathbf{L}_b \ddot{\mathbf{u}}_b, \quad (36)$$

where we understand the constrained inverse 35 as a projection of the free-floating inverse mass matrix on a subspace incorporating the boundary constrains, ie,

$$\mathbf{M}_b^{-1} = \mathcal{P} \mathbf{M}^{-1}, \quad (37)$$

with an operator

$$\mathcal{P} = \mathbf{I} - \mathbf{M}^{-1} \mathbf{B} [\mathbf{B}^T \mathbf{M}^{-1} \mathbf{B}]^{-1} \mathbf{B}^T \quad (38)$$

that projects any acceleration vector on the subspace of accelerations, automatically fulfilling the zero boundary conditions ($\ddot{\mathbf{u}}_b = \mathbf{0}$).

Projector 38 presents the following 2 interesting properties:

$$\mathbf{B}^T \mathcal{P} = \mathbf{0}, \quad (39)$$

$$\mathcal{P} \mathbf{M}^{-1} \mathbf{B} = \mathbf{0} \quad (40)$$

that will be used next to derive some important conclusions.

Proposition 2. *The rows and columns of \mathbf{M}_b^{-1} corresponding to constrained DOFs are identically zero.*

Proof. Note that premultiplication and postmultiplication by the boundary extraction operator \mathbf{B} selects the rows and columns corresponding to constrained DOF positions. Thanks to properties 39 and 40 we find that

$$\mathbf{B}^T \mathcal{P} \mathbf{M}^{-1} \mathbf{B} = \mathbf{0}. \quad \square$$

Proposition 3. *Projector \mathcal{P} applied to the free-floating body accelerations of the system $\mathbf{a}_{free} = \mathbf{M}^{-1} \mathbf{r}$, imposes zero Dirichlet boundary conditions to the constrained DOFs.*

Proof. Note from (36) that, if the boundary conditions are zero ($\ddot{\mathbf{u}}_b = \mathbf{0}$), the final accelerations can be written as

$$\ddot{\mathbf{u}} = \mathcal{P} \mathbf{a}_{free},$$

and thanks to property 40 we also observe that the projector filters out the unbalanced-force components ($\mathbf{B} \mathbf{r}$) associated to the fixed DOFs, ie,

$$\ddot{\mathbf{u}} = \mathcal{P} \mathbf{M}^{-1} [\mathbf{B} \mathbf{r} + (\mathbf{I} - \mathbf{B}) \mathbf{r}] = \mathcal{P} \mathbf{M}^{-1} (\mathbf{I} - \mathbf{B}) \mathbf{r},$$

where $(\mathbf{I} - \mathbf{B}) \mathbf{r}$ is the external-internal residual forces of the free DOFs. □

As a summary, the complete process followed to obtain the inverse mass matrix \mathbf{M}^{-1} and the projector \mathcal{P} is contained in Table 1. Note that in dynamic analyses, the product of these 2 matrices \mathbf{M}_b^{-1} is never evaluated explicitly. Hence, the

TABLE 1 Procedure for the computation of the constrained inverse mass matrix \mathbf{M}_b^{-1} **Step 1:** Assemble diagonal projection matrix:

$$[\mathbf{A}_e]_{ii} = \frac{1}{\rho_e} \sum_j [\mathbf{M}_e]_{ij} \rightarrow \mathbf{A} = \sum_{e=1}^{n_e} \mathbf{A}_e$$

Step 2: Assemble reciprocal mass matrix:

$$\mathbf{C}_e = \mathbf{A}_e^T \mathbf{M}_e^{-1} \mathbf{A}_e \rightarrow \mathbf{C} = \sum_{e=1}^{n_e} \mathbf{C}_e$$

Step 3: Evaluate free-floating inverse mass matrix:

$$\mathbf{M}^{-1} = \mathbf{A}^{-T} \mathbf{C} \mathbf{A}^{-1}$$

Step 4: Compute projector:

$$\mathcal{P} = \mathbf{I} - \mathbf{M}^{-1} \mathbf{B} [\mathbf{B}^T \mathbf{M}^{-1} \mathbf{B}]^{-1} \mathbf{B}^T$$

Step 5: Apply boundary conditions by projection:

$$\mathbf{M}_b^{-1} = \mathcal{P} \mathbf{M}^{-1}$$

Step 6: Eliminate rows and columns of \mathbf{M}_b^{-1} .

2-step solution process consists of multiplying the residual by the mass inverse to compute free-floating body accelerations and later by the projector to apply boundary conditions. Multiplication of the projector times a vector requires also the factorization of $\mathbf{B}^T \mathbf{M}^{-1} \mathbf{B}$, but this is a small matrix of size equal to the number of BCs.

4 | SELECTIVE MASS SCALING

In classical explicit time-integration methods, maximum time-step size for stability is controlled by the highest natural frequency of the system.¹⁶ The basic idea behind selective mass scaling¹⁷⁻²¹ is to alter the mass matrix artificially to reduce the high frequencies of the dynamical system without affecting the low-mid frequencies.

In this section, we propose a simple method to reduce the highest frequencies of the system that can be combined with the proposed mass matrix inverse method for best efficiency. The mass scaling process is applied element by element. To start, the original mode shapes of the element are first computed by solving the eigenvalue problem:

$$\mathbf{K}_e \mathbf{X}_e = \mathbf{M}_e \mathbf{X}_e \Lambda_e, \quad (41)$$

where \mathbf{X}_e is the matrix containing the orthogonal mode shapes of the element and the diagonal matrix $\Lambda_e = \mathbf{X}_e^T \mathbf{K}_e \mathbf{X}_e$ contains the original eigenfrequencies of the problem.

The n orthogonal mode shapes of the element can be separated into high- and low-frequency modes in the form

$$\mathbf{X}_e = [\Phi_l, \Phi_h], \quad (42)$$

where we have r retained low-frequency modes Φ_l and $s = n - r$ scaled high-frequency modes Φ_h .

To scale only the high-frequency modes of the element, without affecting the low frequency modes at the same time, we define a new projector:

$$\mathcal{P}_e = \mathbf{I} - \Phi_l [\Phi_l^T \Phi_l]^{-1} \Phi_l^T, \quad (43)$$

with the following filtering property

$$\mathcal{P}_e \mathbf{X}_e = [\mathbf{0}, \Phi_h], \quad (44)$$

and then modify the element mass matrix in the form

$$\mathbf{M}_e^\alpha = \mathbf{M}_e + \alpha \mathcal{P}_e^T \mathbf{M}_e \mathcal{P}_e, \quad (45)$$

where $\alpha \geq 0$ is a mass scaling parameter.

Proposition 4. *With the mass scaled matrix \mathbf{M}_e^α , the high frequencies of the element are scaled by a factor $(1 + \alpha)^{-1}$ maintaining the element low frequencies unaffected, ie, the new element eigenvalues are given by the diagonal matrix:*

$$\Lambda_e^\alpha = \begin{bmatrix} \mathbf{I}_r & \mathbf{0} \\ \mathbf{0} & (1 + \alpha)^{-1} \mathbf{I}_s \end{bmatrix} \Lambda_e,$$

with the same modes \mathbf{X}_e than the original element.

Proof. It is very simple to demonstrate that the new scaled-mass eigenvalue problem

$$\mathbf{K}_e \mathbf{X}_e = (\mathbf{M}_e + \alpha \mathcal{P}_e^T \mathbf{M}_e \mathcal{P}_e) \mathbf{X}_e \Lambda_e^\alpha$$

has exactly the same eigenvectors than the original one, with the same r low frequencies and s reduced high frequencies. This is demonstrated premultiplying by \mathbf{X}_e^T that produces, thanks to property 44, the new eigenvalues

$$\Lambda_e = (\mathbf{I}_n + \alpha [\mathbf{0}, \Phi_n]^T \mathbf{M}_e [\mathbf{0}, \Phi_n]) \Lambda_e^\alpha = \left(\mathbf{I}_n + \begin{bmatrix} \mathbf{0}_r & \mathbf{0} \\ \mathbf{0} & \alpha \mathbf{I}_s \end{bmatrix} \right) \Lambda_e^\alpha,$$

from where we can obtain Λ_e^α inverting a simple diagonal matrix. \square

It remains the selection of appropriated values for the scaling parameter α and the number of modes to scale s that will be analyzed in the next section.

It is important to mention that, although different mass-scaling methods have been proposed by other authors,²²⁻²⁴ the proposed mass-scaling technique is defined as selective in the sense that we can choose the number of modes to scale, and this scaling is performed at the element level.

5 | NUMERICAL EXPERIMENTS

Although the proposed techniques for mass matrix inversion and scaling can be equally applied to linear and nonlinear constitutive models, we will assume linear-elastic materials in our numerical experiments with internal forces simply given by the linear relation $\mathbf{f}^{int} = \mathbf{K}\mathbf{u}$. We have assessed the performance of the present mass matrix inverse for bar, beam, solid, and shell structural elements, in both free-free states and cantilevered conditions. In so doing, for the derivation of elemental reciprocal mass matrix \mathbf{C}_e , we have used a parametrized elemental mass matrix expressed in the form

$$\mathbf{M}_e = (1 - \beta) \mathbf{M}_e^c + \beta \mathbf{M}_e^l, \quad (46)$$

in which a parameter $\beta \in [0, 1]$ is used to balance between the consistent element mass matrix \mathbf{M}_e^c and the lumped element mass matrix \mathbf{M}_e^l . Using $\beta = \{0, 0.5, 1\}$, the element mass matrix is then easily reduced, respectively, to the CMM, averaged mass matrix (AMM), and LMM. Unless otherwise stated, in the following numerical experiments, we use AMM as a reference and compute the mass matrix inverse using RMM with $\beta = 0.5$ to test the proposed methodology. There are several ways to parametrize mass matrices, for example, see Felippa et al⁴ for an exhaustive classification. Among them, spectral parametrization 45 and matrix-weighted linear parametrization 46 are the simplest choices.

For vibration analyses, we seek for an harmonic solutions that satisfy the EOM and fulfill the boundary conditions $\mathbf{u}_b = \mathbf{0}$. These solutions are obtained by solving the following eigenvalue problem:

$$[\mathbf{M}_b^{-1} \mathbf{K}_b - \omega^2 \mathbf{I}] \boldsymbol{\phi} = \mathbf{0}, \quad (47)$$

where \mathbf{M}_b^{-1} is the inverse mass matrix computed as described in Section 3 and \mathbf{K}_b is the stiffness matrix incorporating the applied boundary conditions. From the solution of this eigenvalue problem, we obtain the vibration frequencies ω_i of the system and its associated mode shapes $\boldsymbol{\phi}_i$ for mode number $i = 1, \dots, n$.

In time-domain analyses, for time integration of the semidiscrete equations of elastodynamics, we use the classical explicit central difference scheme.²⁵⁻²⁷ This method is among the most popular explicit methods in computational mechanics²⁸ and can be summarized in the following steps:

1. Knowing from previous time \mathbf{u}^n and $\dot{\mathbf{u}}^{n-\frac{1}{2}}$.
2. Evaluate the forces residual $\mathbf{r}^n = \mathbf{f}^n - \mathbf{K}_b \mathbf{u}^n$.
3. Compute accelerations $\ddot{\mathbf{u}}^n = \mathbf{M}_b^{-1} \mathbf{r}^n$.
4. Update nodal velocities $\dot{\mathbf{u}}^{n+\frac{1}{2}} = \dot{\mathbf{u}}^{n-\frac{1}{2}} + \Delta t \ddot{\mathbf{u}}^n$.
5. Update nodal displacements $\mathbf{u}^{n+1} = \mathbf{u}^n + \Delta t \dot{\mathbf{u}}^{n+\frac{1}{2}}$.
6. Advance time $n \leftarrow n + 1$.

repeating these basic steps until the total simulation time has been reached.

It is well known that the explicit central difference scheme in linear dynamics is conditionally stable, so the time-step Δt must be chosen below a critical value $\Delta t_{crit} = 2/\omega_{max}$, where ω_{max} is the maximum frequency of the system. Selective mass scaling techniques, like the one proposed in Section 4, permits a localized reduction of the highest eigenvalues of

the system by a certain factor. This reduction automatically increases the critical time step, improving computational efficiency.

5.1 | Frequencies of a free-free and a fixed-free bar

In this first example, we consider a long bar of length $L = 1\text{ m}$ with a rectangular section of width $b = 0.05\text{ m}$ and thickness $h = 0.01\text{ m}$. The material of the bar is linear elastic, with Young modulus $E = 69\text{ GPa}$ and a constant density $\rho = 2700\text{ kg/m}^3$. We discretize the bar using a uniform mesh of 40 two-node linear bar elements and compute the vibration modes of the structure with different approximations for the mass matrix inverse. In particular, we investigate differences in the use of the LMM, AMM, and the proposed mass matrix inverse computed through RMM with $\beta = 0.5$.

The results of the eigenvalue analysis are presented in Figure 1 for 2 different boundary conditions, free-free case (left) and fixed-free case (right). We start with the free-free case, by comparing the numerical frequencies with the exact solution obtained from continuum theory. The exact frequencies of this problem are $\omega_i^{exact} = \sqrt{E/\rho}(\pi/L)(i - 1)$ rad/second for mode number $i = 1, \dots, n$, and the first eigenfrequency is zero, corresponding to the horizontal rigid body motion. We observe that the present method, using the RMM, yields far better accuracy than the LMM and approximates very well to the AMM results for all frequencies.

For the fixed-free case, we obtain very similar results. The only difference now is in the restriction of the rigid body motion and the shift of exact frequencies to $\omega_i^{exact} = \sqrt{E/\rho}(\pi/L)(i - 1/2)$ rad/second for mode number $i = 1, \dots, n$. We corroborate that the AMM and its approximation through the RMM with $\beta = 0.5$ provide exactly the same result. This means that the present method using the inverse mass matrix yields far better accuracy than the LMM with similar computational effort.

It can also be observed that LMM produces a maximum frequency around 20% lower than AMM, so the critical time-step for explicit time integration can be reduced by the same amount using a diagonal mass matrix. As we will see later, even higher gains can be obtained with the selective mass-scaling technique proposed in Section 4, maintaining at the same time the advantages in terms of accuracy of using a nondiagonal mass matrix.

5.1.1 | Free-free heterogeneous bar

The effect of material heterogeneity in the accuracy of the direct mass inverse is next investigated by dividing the free-free bar into 2 segments of different density; see Figure 2 (left) for a description of the new configuration. The exact angular frequencies for this new case are obtained from the equation $(c_2 E_1 A_1) \sin(k_1 L_1) \cos(k_2 L_2) + (c_1 E_2 A_2) \sin(k_2 L_2) \cos(k_1 L_1) = 0$ where $k_j = \omega_j/c_j$ and $c_j = \sqrt{E_j/\rho_j}$ with $j = 1, 2$ respectively are the wave number and the velocity of compressional waves in material j .

A relatively coarse regular mesh of 5 elements is selected to discretize each part of the bar, and the frequencies are recalculated first using AMM and RMM ($\beta = 0.5$) without partitioning the domain. The results are represented in Figure 2 (right) together with the numerical values contained in Table 2. In general, the accuracy of the 6 first nonzero modes is

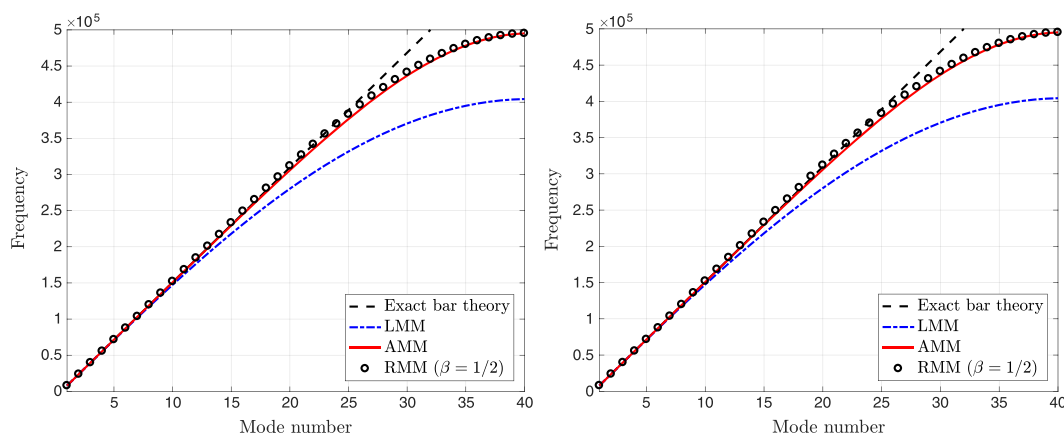


FIGURE 1 Bar vibration problem. Frequencies for the free-free (left) and fixed-free (right) cases. Comparison of exact frequencies and numerical frequencies obtained with: lumped mass matrix (LMM), average mass matrix (AMM), and the proposed inverse mass matrix (RMM, $\beta = 0.5$)

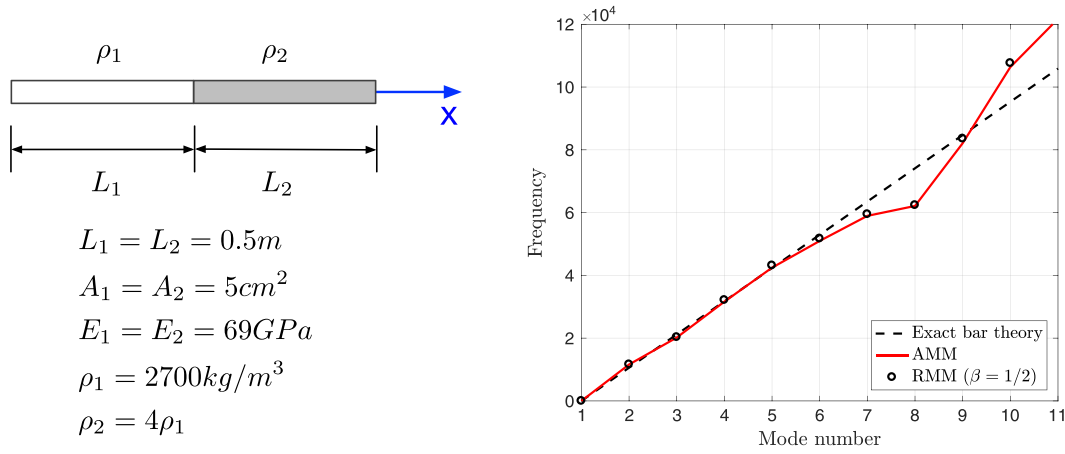


FIGURE 2 Heterogeneous bar problem. Setup of the free-free bimaterial bar (left). Comparison of the exact angular frequencies with numerical frequencies computed using the average mass matrix (AMM) and the proposed inverse mass matrix (RMM, $\beta = 0.5$) without partitioning the domain (right)

TABLE 2 Free-free 2 material rod. Frequencies of the first 6 nonzero modes obtained with the AMM and the proposed RMM using one domain and partitioning the bar into 2 subdomains

Frequency (Hz) $\times 10^{-4}$	Mode 2	Mode 3	Mode 4	Mode 5	Mode 6	Mode 7
AMM	0.1848	0.3213	0.5033	0.6757	0.8112	0.9383
RMM no partitioning	0.1853	0.3235	0.5116	0.6871	0.8234	0.9468
RMM partitioning	0.1853	0.3233	0.5114	0.6851	0.8224	0.9468

Abbreviations: AMM, average mass matrix; RMM, proposed reciprocal mass matrix.

very good, but a congruent application of the proposed methodology to this case requires a partitioning the domain into different homogenous subdomains interconnected using localized Lagrange multipliers. In this case, a computation of frequencies with RMM ($\beta = 0.5$) partitioning the problem into 2 different subdomains produces exactly the same global frequencies, contained in the third row of Table 2.

5.2 | Frequencies of a free-free and a fixed-free beam

In this second case, we consider the same geometry of the previous example, but now, it is discretized using 20 Euler-Bernoulli beam elements with two DOFs per node, ie, deflection and rotation. We know that the shape functions for the Euler-Bernoulli beam require C^1 -continuity for deflections and rotations, hence cubic Hermite polynomials are used as interpolation functions. This means that we would need to derive biorthogonal basis functions for the Hermite cubic shape functions to compute the reciprocal mass matrix \mathbf{C}_e from its definition 18. As previously described, we bypass this complex derivation obtaining the projection matrix \mathbf{A}_e from the diagonalization of the element mass matrix.

In Figure 3 (left), we analyze the frequencies obtained for the free-free beam case. The exact frequencies of this problem obtained from continuum theory are $\omega_i^{exact} = \sqrt{EI/\rho A}(c_i/L)^2$ rad/second with $c = \{0, 0, 4.73, 7.853, 10.996, 14.137, 17.279, \dots\}$ for mode number $i = 1, \dots, n$ and 2 zero frequencies corresponding to the displacement and rotation rigid-body motions. We solve again the problem with exact LMM and AMM inverse mass matrices and then using the proposed RMM with $\beta = 0.5$. Results illustrate, first, that the consistent AMM gives far better accuracy than diagonal LMM for this particular case, specially in the high-frequency range, and, second, that the present RMM method using the inverse mass matrix yields the same accuracy than the consistent AMM.

The results for the fixed-free alternative of this problem are represented in Figure 3 (right). The exact frequencies of this case is $\omega_i^{exact} = \sqrt{EI/\rho A}(c_i/L)^2$ rad/second with $c = \{1.875, 4.694, 7.854, 10.995, 14.131, 17.278, \dots\}$. Exactly the same precision is observed in the free-free and fixed-free solutions. This convinces us to the conclusion that the described method for generating the inverse of mass matrices \mathbf{M}_b^{-1} , yields almost the same resonant frequencies as those obtained by the consistent mass matrices, as evidenced from Figure 3, thus confirming the validity of the present formulation.

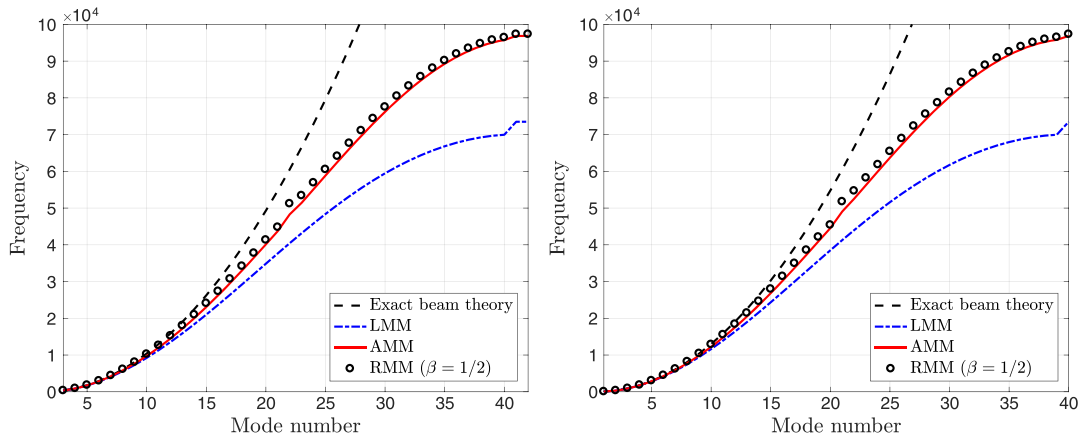


FIGURE 3 Beam vibration problem. Frequencies for the free-free (left) and fixed-free (right) cases. Comparison of exact frequencies and numerical frequencies obtained with lumped mass matrix (LMM), average mass matrix (AMM), and the proposed inverse mass matrix (RMM, $\beta = 0.5$)

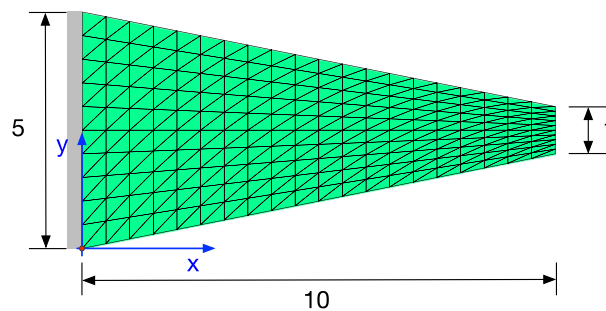


FIGURE 4 NAFEMS benchmark case FV32. Geometry, mesh, and dimensions in meters. The thickness of the plate is $t = 0.05$ m and zero boundary displacements are imposed on the lateral side

5.3 | Frequency analysis of a cantilevered tapered plate

Our third example is a plane-stress test proposed by the National Agency for Finite Element Methods and Standards.²⁹ In particular, the dynamic case FV32, where the natural frequencies of a trapezoidal elastic plate are analyzed. The geometry and dimensions of the plate are represented in Figure 4 together with the boundary conditions. A linear elastic material with Young modulus $E = 200$ GPa, Poisson ratio $\nu = 0.3$, and density $\rho = 8000\text{kg/m}^3$ is assumed. The plate is discretized using a regular mesh composed of 231 nodes and 400 triangular linear finite elements, constraining the horizontal and vertical displacements of the 11 nodes located at $x = 0$, a lateral side of the plate. Note that this is a more refined mesh than the one proposed in the original NAFEMS benchmark case, which uses quadrilateral elements instead of triangles and doubles the element size.

We perform a frequency analysis solving the eigenvalue problem 47 using different mass matrices. In particular, we consider the CMM and the average mass matrix AMM, which are compared with their equivalent RMMs obtained with $\beta = 0$ and $\beta = 0.5$.

The first 6 mode shapes of the plate are illustrated in Figure 5, and their associated frequencies, obtained with the different mass matrices, arranged in Table 3. Notice that, in the original NAFEMS results, mode shapes 5 and 6 are interchanged. In our case, mode 5 appears at a little higher frequency because it is a pure longitudinal symmetric mode and our mesh made of triangles is not symmetric.

Tkachuk et al⁵ solved this problem using the same mesh and the RMM. When comparing with their results, the maximum difference is obtained in the sixth frequency with an error below 2% while the best fit is obtained for RMM with $\beta = 0.5$. On the other hand, comparing the frequencies obtained using our exact implementation of the CMM with the reciprocal mass-inverse RMM technique, errors reduce to the second decimal digit. It is also observed that averaging the mass matrix increases slightly the error to a 0.6% in the sixth mode. In general, it is verified that the proposed mass-inversion process gives very accurate approximations of the CMM and AMM inverses.

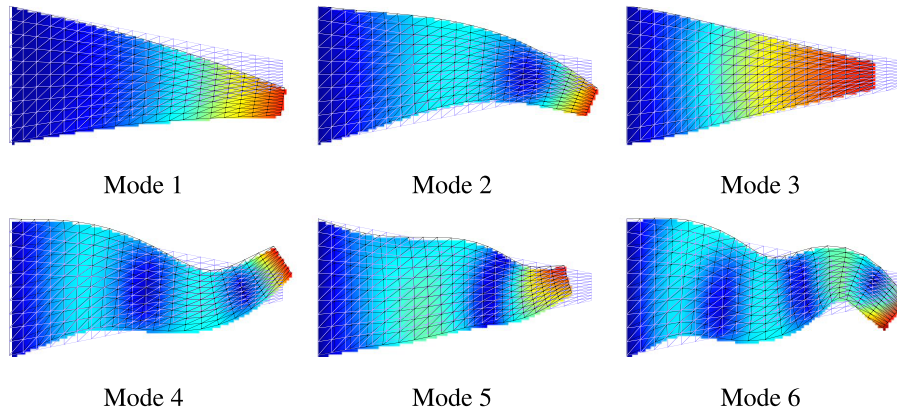


FIGURE 5 NAFEMS benchmark case FV32. Representation of the 6 lowest vibration modes occurring at frequencies contained in Table 3. Results correspond to proposed reciprocal mass matrix with $\beta = 0.5$

TABLE 3 Plane-stress case from NAFEMS

Frequency (Hz)	Mode 1	Mode 2	Mode 3	Mode 4	Mode 5	Mode 6
NAFEMS	44.623	130.03	162.70	246.05	379.90	391.44
Tkachuk et al. ⁵	45.499	133.55	162.89	255.37	393.16	398.56
CMM	45.42	132.60	162.73	251.40	387.40	391.16
RMM ($\beta = 0$)	45.42	132.60	162.73	251.40	387.40	391.18
AMM	45.46	133.08	162.81	253.36	391.72	393.32
RMM ($\beta = 0.5$)	45.48	133.33	162.85	254.37	392.56	395.68

Six lowest frequencies obtained with different mass matrices.

Abbreviations: AMM, averaged mass matrix; CMM, consistent mass matrix; RMM, proposed reciprocal mass matrix.

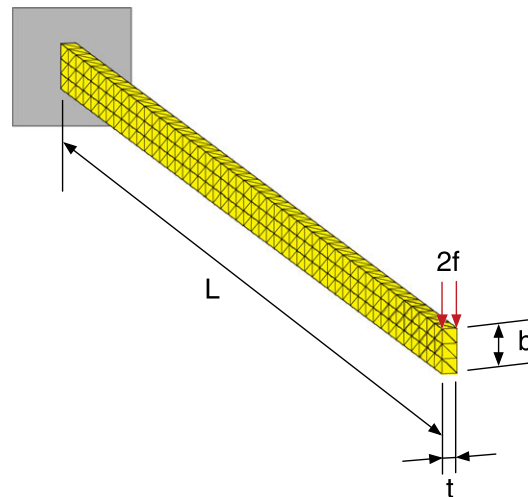


FIGURE 6 Cantilever beam with tip load. Geometry, mesh, and dimensions

5.4 | Transient analysis of a cantilever beam under tip load

To test the solid tetrahedral element, we use the cantilever beam with vertical load proposed by Olovsson et al.¹⁹ also studied by Tkachuk et al.⁵ to investigate the accuracy of direct mass-inverse methods. The geometrical definition of the problem is shown in Figure 6, where a cantilever beam of length $L = 0.1$ m and section height $b = 0.003$ m with thickness $t = 0.001$ m is considered. Material properties of the beam are $E = 207$ GPa, $\nu = 0.3$, and $\rho = 7800$ kg/m³.

The beam is discretized using a regular mesh of 408 nodes and 900 tetrahedral elements, with $50 \times 3 \times 1$ divisions per side. One end of the beam is completely fixed, and the other side has 2 vertical point loads of value $f = -1$ N.

In this case, we perform a time-domain analysis integrating in time the response of the beam using the explicit central difference method. Initial conditions of the beam are assumed to be zero displacements and velocities, applying the tip load completely at the initial time step. We have selected for comparison the exact AMM and the proposed inverse through RMM computed with $\beta = 0.5$.

The results are shown in Figure 7, where it is represented the evolution of the tip deflection of the beam obtained with both mass matrices (left). We also compare the time evolution of total internal U , external W , and kinetic T energies of the beam (right).

Figure 8 (left) represented the relative error $(u - u_{exact})/|u_{exact}|$ of the tip displacement, computing u with the RMM inverse mass matrix and u_{exact} with the exact AMM. The error remains under 0.003% during the 0.002 seconds of simulation, indicating a perfect agreement. Displacement contours obtained with both methods at time $t = 1.16$ ms are represented in Figure 8 (right). Differences between RMM displacements (top) and AMM displacements (bottom) can not be perceived. It is also noted that, although the problem is perfectly symmetric, a small lateral displacement appears in the solution due to the asymmetry introduced by the mesh.

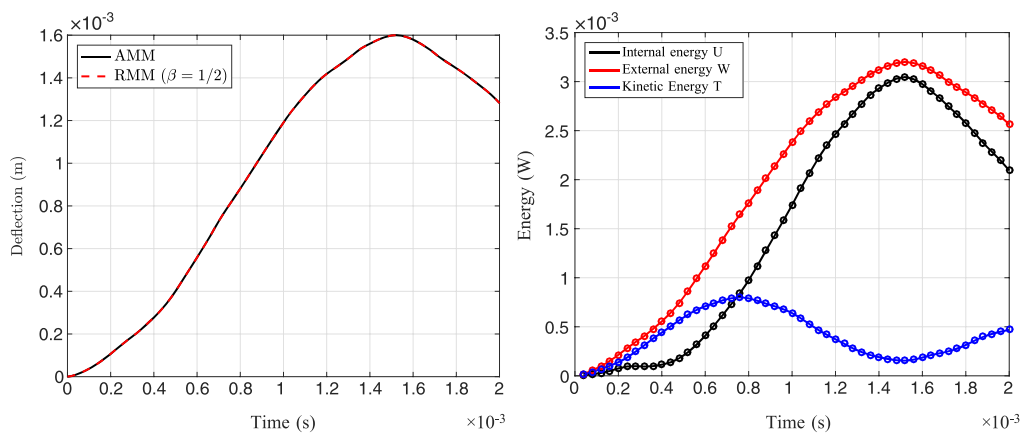


FIGURE 7 Results of the tip-loaded cantilever beam. Tip deflection $|u_z|$ computed with the exact averaged mass matrix (AMM) and the reciprocal mass matrix (RMM) ($\beta = 0.5$) (left). Evolution of the internal, external, and kinetic energies in the beam (right). Solutions obtained using the proposed RMM inverse matrix are represented with dots

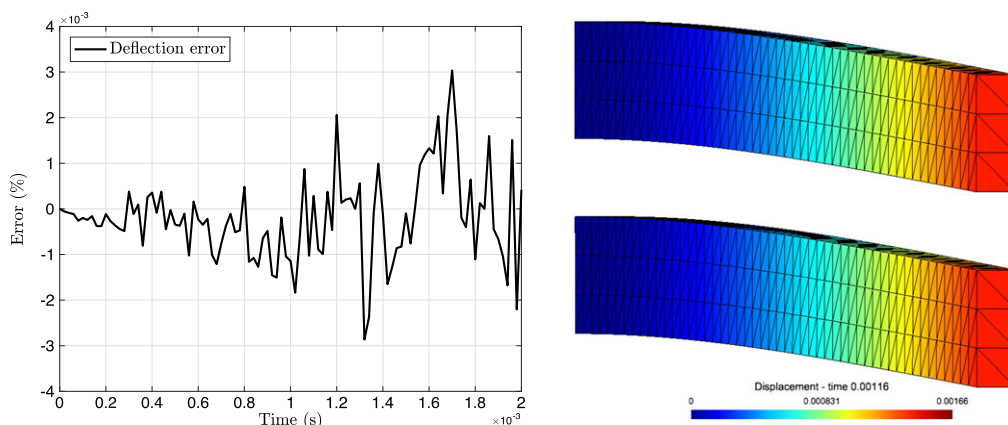


FIGURE 8 Error of the cantilever beam solution. Error evolution of the beam tip deflection computed with proposed reciprocal mass matrix (RMM) ($\beta = 0.5$) compared to average mass matrix (AMM). Displacement contours at $t = 0.00116$ s (right), computed with the exact AMM (bottom) and the RMM ($\beta = 0.5$) (top)

5.5 | Transient analysis of a panel

In this example, we analyze the inverse mass matrix of a structural 3-node shell element with 6 DOFs per node. The CMM of the 18 DOF shell element is computed by separating membrane and bending contributions, where the membrane component is obtained from the plane triangular linear element while the normal and bending mass from three equivalent fictitious beams located on the element edges. Therefore, we are applying the proposed mass-inverse methodology to a complicated structural mass matrix that would be difficult to invert by other means.

The selected test problem is represented in Figure 9, a simply supported plate constructed using a square plate of side length $L = 1$ m and 4 longitudinal stiffeners separated a constant distance $B = 0.2$ m. The stiffeners, attached on one side the plate, have a section height $a = 0.05$ m, and all components have the same thickness $t = 0.01$ m. For the material properties, we consider a steel with Young modulus $E = 207$ GPa, Poisson coefficient $\nu = 0.3$, and density $\rho = 7850$ kg/m³.

The plate is modeled using a regular mesh of $20 \times 20 \times 2$ elements and each stiffener has $20 \times 2 \times 2$ elements, with a total number of 1120 shell elements and 609 nodes. All the boundary nodes of the plate have restricted displacements in the 3 directions, and the panel is loaded by a transversal constant line load of value $q = 200$ N/m that is abruptly applied at time zero.

An explicit time integration of the problem is performed for 10 ms using the central difference method. The results are shown in Figure 10 (left) where it is compared the deflection in the center of the plate obtained with the AMM and the reciprocal mass matrix (RMM) inverse with $\beta = 0.5$. Figure 10 (right) represents the evolution of the total kinetic, internal, and external energies computed with both methods.

In this case, although some small differences are observed in the solutions, the error is perfectly acceptable for engineering purposes. The deflection errors obtained in the center of the plate, see Figure 11 (left), remain under 0.6% during the simulation period, and the structural deformations obtained with AMM and RMM inverses are completely indistinguishable, as demonstrated by the contour solutions at time $t = 5$ ms compared side by side in Figure 11 (right).

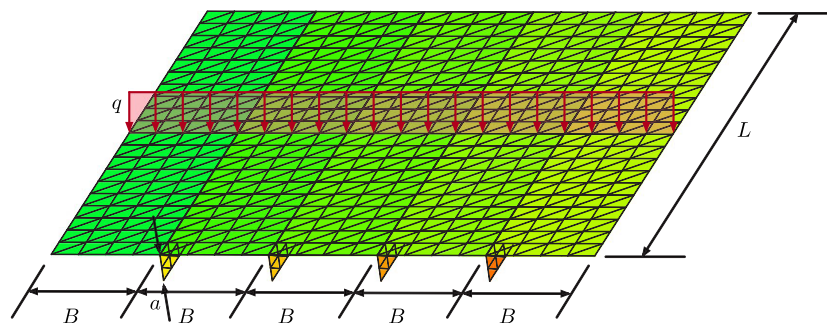


FIGURE 9 Geometrical definition of a simply supported plate with 4 stiffeners and loaded by a constant line load at the center of the plate

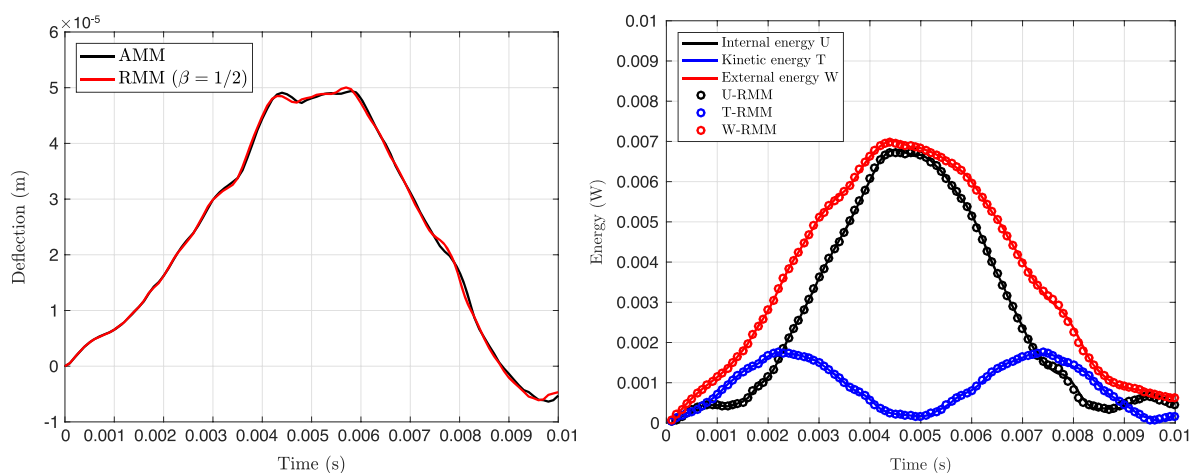


FIGURE 10 Results of the stiffened plate problem. Deflection at the center of the plate (left) and evolution of the total kinetic, internal and external energies (left) computed with the average mass matrix (AMM) and the reciprocal mass matrix (RMM) inverse

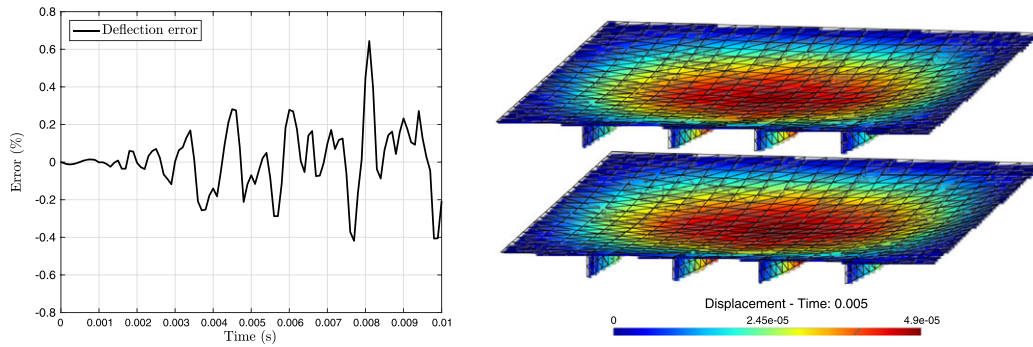


FIGURE 11 Error in the deflection obtained with exact mass matrix and using proposed inverse mass (right). Displacement contours at $t = 5$ ms (right) obtained with exact average mass matrix (bottom) and using proposed inverse through the consistent mass matrix (top)

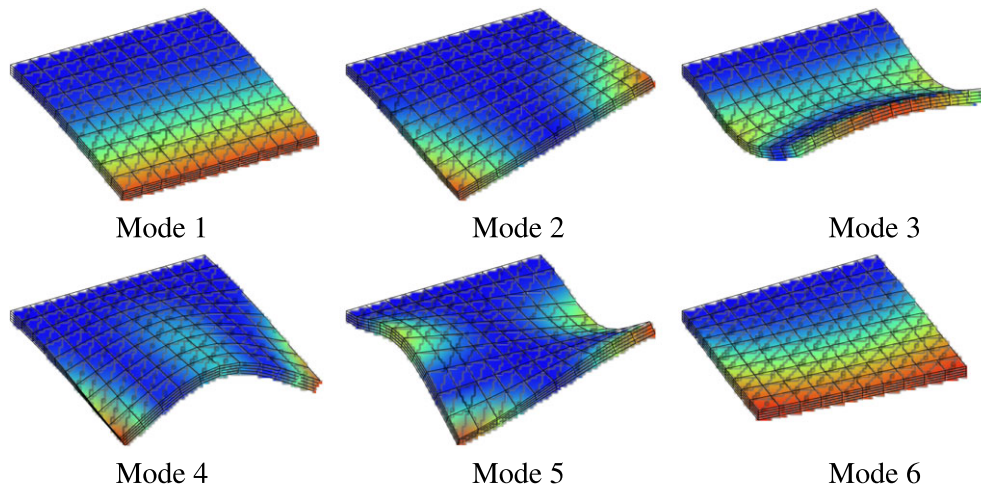


FIGURE 12 First six mode shapes of the 3-D cantilever plate model. Representation of the 6 lowest vibration modes occurring at frequencies contained in Table 4. Results correspond to proposed reciprocal mass matrix with 18-scaled modes and a scaling parameter $\alpha = 100$

TABLE 4 Cantilever plate model

Frequency (Hz)	Mode 1	Mode 2	Mode 3	Mode 4	Mode 5	Mode 6
No scaling	6.7703	12.0809	42.0886	47.7580	50.3711	54.6703
Scaling ($\alpha = 1$)	6.8151	12.3473	43.7787	50.6586	53.0128	54.9494
Scaling ($\alpha = 10$)	6.8147	12.3399	43.7571	50.5726	52.8431	54.8953
Scaling ($\alpha = 100$)	6.8141	12.3356	43.7325	50.5274	52.7784	54.8702

Effect of mass scaling on the first 6 natural frequencies of the system.

These results correspond to the case $s = 12$ scaled modes, represented in Figure 13 (right).

5.6 | Mass scaling of a cantilever plate

The purpose of this last example is to test the selective mass-scaling technique proposed in Section 4. For that, we consider a square cantilever plate of side length $L = 10$ m and thickness $t = 0.5$ m, made of a structural steel with Young modulus $E = 207$ GPa, Poisson coefficient $\nu = 0.3$ and $\rho = 7800$ kg/m³.

The plate is discretized with 3-dimensional 8-node solid elements, using a structured mesh of 10 elements per side and 4 elements across the thickness, with a total of 400 brick elements and 605 nodes. Zero displacement boundary conditions are imposed in the 3 directions to all the nodes lying on one side of the plate, and the eigenvalue problem 47 is solved for all the frequencies with a scaled mass matrix. The vibration mode shapes of the plate are represented in Figure 12 for the 6 lowest frequencies, and their associated frequencies are contained in the first row of Table 4.

With the intention of reducing the highest frequencies of the resulting FEM equations, corresponding to the so-called mesh frequencies, without affecting the lower physical frequencies, we proceed with a scaling of the mass matrix increas-

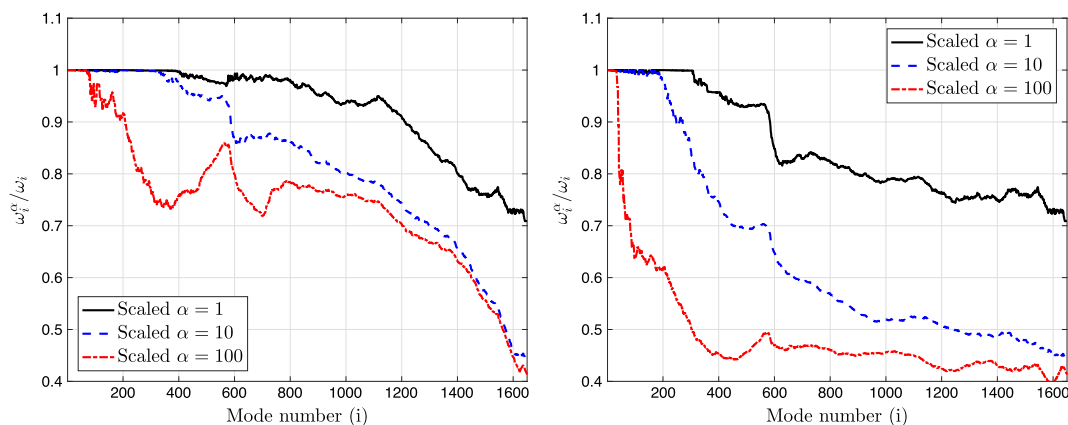


FIGURE 13 Relation of scaled/exact frequencies for the cantilever plate model. Effect of the scaling parameter α and the number of scaled modes s on the complete range of system frequencies. Number of scaled element modes are $s = 6$ (left) and $s = 12$ (right) and the highest element modes are scaled by a factor $(1 + \alpha)^{-1}$

ing the values of the scaling parameter to $\alpha = \{1, 10, 100\}$. This is made for 2 different cases by scaling $s = 6$ and $s = 12$ of the highest element modes.

Independently of the number of element frequencies scaled, we demonstrate in Table 4 that the lowest structural frequencies of the plate are not considerably affected. Observing the complete range of frequencies in Figure 13, we deduce that a mass scaling factor $\alpha = 10$ reduces the maximum frequency in the order of 2.5, speeding the computational cost for explicit dynamics more than 50%. However, there exists a saturation limit in the scaling with this methodology, since a further increase of the scaling parameter, compare $\alpha = 10$ and $\alpha = 100$ in Figure 13, does not improve the benefit and will start to produce an ill-conditioning of the mass matrix.

Another important effect to observe in Figure 13 is the influence of the number of scaled element modes s on the frequencies. Increasing the number of scaled modes for a fixed α does not affect the gain in the highest frequency but can degrade significantly the approximation in the mid frequency range. We conclude that we should use a minimum number of scaled modes to improve the accuracy.

Finally, it is important to mention that similar gains have been obtained by other scaling techniques proposed in the literature.^{5,22} But in these references, the mass scaling is made by augmentation of the RMM without discriminating higher and lower element modes. In fact, this separation has been found to be important to improve the approximation of the mid frequency range.

6 | CONCLUSIONS

A new methodology for direct generation of the inverse mass matrix for discrete finite element equations of elastodynamics is presented, which is completely element-independent and does not require any special treatment of the elements adjacent to Dirichlet boundaries. In the present method, the Dirichlet boundary conditions are handled by the method of localized Lagrange multipliers. This process is found to be computationally efficient, because matrices are sparse and only the factorization of a small matrix associated with the constrained DOFs is required. In structural dynamics, classical explicit time-integration methods equipped with a direct solver require an initial factorization of the mass matrix and the solution of a new free term every time step. If we choose Cholesky factorization, for example, the total cost is around $\frac{1}{3}n^3$ flops plus $2n^2$ operations per time step for each forward-backward substitution. With the proposed direct mass matrix inverse, factorization is not needed and operation count per time step is reduced to a sparse-matrix vector multiplication with nm flops, where m is the average number of nonzero entries per row.

The proposed inverse mass matrices have been tested for rod, beam, solid, and shell elements, demonstrating excellent accuracy in terms of frequencies and time evolution of the DOFs obtained with explicit time-integration methods.

In addition, a new mass-scaling technique is offered, which can be applied element-by-element and is frequency selective. Usage of scaled mass matrices reduces the maximum frequency of the system and thus increases the critical time step. Preliminary results demonstrate that the proposed selective mass scaling can attain reductions up to 40% in the high-

est frequencies without significantly affecting the low-mid frequency ranges. Further work along the line of the scaling technique will bring about a significant reduction of explicit transient analysis time. Work in this direction is underway.

ACKNOWLEDGMENTS

The work of R. Kolman was supported by the Centre of Excellence for nonlinear dynamic behavior of advanced materials in engineering CZ.02.1.01/0.0/0.0/15 003/0000493 (Excellent Research Teams) in the framework of Operational Program Research, Development and Education, and the grant project of the Czech Science Foundation, 17-22615S, within institutional support RVO:61388998. S.S. Cho was partially supported by the Nuclear Safety Research Program through the Korea Foundation of Nuclear Safety (KOFONS), granted financial resource from the Nuclear Safety and Security Commission (NSSC), Republic of Korea (No. 1503003).





REFERENCES

- Hinton E, Rock T, Zienkiewicz OC. A note on mass lumping and related processes in the finite element method. *Earthquake Eng Struct Dyn*. 1976;4(3):245-9.
- Lombardo M, Askes H. Lumped mass finite element implementation of continuum theories with micro-inertia. *Int J Numer Methods Eng*. 2013;96(7):448-466.
- Hetherington J, Askes H. A mass matrix formulation for cohesive surface elements. *Theor Appl Fract Mech*. 2014;69:110-117.
- Felippa CA, Guo Q, Park KC. Mass matrix templates: general description and 1D examples. *Arch Comput Methods Eng*. 2015;22:1-65.
- Tkachuk A, Bischoff M. Direct and sparse construction of consistent inverse mass matrices: general variational formulation and application to selective mass scaling. *Int J Numer Methods Eng*. 2015;101:435-469.
- Krenk S. Dispersion-corrected explicit integration of the wave equation. *Comput Methods Appl Mech Eng*. 2001;191(8-10):975-987.
- Gravouil A, Elguedj T, Maigre H. An explicit dynamics extended finite element method. Part 2: element-by-element stable-explicit/explicit dynamic scheme. *J Comput Appl Math*. 2009;198:2318-2328.
- Idesman A, Schmidt M, Foley J. Accurate finite element modeling of linear elastodynamics problems with the reduced dispersion error. *Comput Mech*. 2011;47(5):555-572.
- Park KC, Lim SJ, Huh H. A method for computation of discontinuous wave propagation in heterogeneous solids: basic algorithm description and application to one-dimensional problems. *Int J Numer Methods Eng*. 2012;91:622-643.
- Cho SS, Park KC, Huh H. A method for multidimensional wave propagation analysis via component-wise partition of longitudinal and shear waves. *Int J Numer Methods Eng*. 2013;95:212-237.
- Park KC, Felippa CA. A variational framework for solution method developments in structural mechanics. *J Appl Mech*. 1998;65(1):242-249.
- Park KC, Felippa CA. A variational principle for the formulation of partitioned structural systems. *Int J Numer Methods Eng*. 2000;47:395-418.
- Park KC, Felippa CA, Gumaste UA. A localized version of the method of Lagrange multipliers and its applications. *Comput Mech*. 2000;24(6):476-490.
- Gonzalez JA, Park KC, Felippa CA, Abascal R. A formulation based on localized Lagrange multipliers for BEM-FEM coupling in contact problems. *Comput Methods Appl Mech Eng*. 2007;197(6-8):623-640.
- Wohlmuth B. A mortar finite element method using dual spaces for the Lagrange multiplier. *SIAM J Numer Anal*. 2000;38:989-1012.
- Courant R, Friedrichs K, Lewy H. On the partial difference equations of mathematical physics. *IBM Journal of Research and Development*. 1967;11(2):215-234. English translation of the 1928 German original, Courant R, Friedrichs K, Lewy H. Über die partiellen Differenzgleichungen der mathematischen Physik. doi:10.1147/rd.112.0215.
- Macek RW, Aubert BH. A mass penalty technique to control the critical time increment in explicit dynamic finite element analyses. *Earthquake Eng Struct Dyn*. 1995;24(10):1315-1331.
- Olovsson L, Unosson M, Simonsson K. Selective mass scaling for thin walled structures modeled with tri-linear solid elements. *Comput Mech*. 2004;34:134-136.
- Olovsson L, Simonsson K, Unosson M. Selective mass scaling for explicit finite element analyses. *Int J Numer Methods Eng*. 2005;63(10):1436-1445.
- Askes H, Nguyen D, Tyas A. Increasing the critical time step: micro-inertia, inertia penalties and mass scaling. *Comput Mech*. 2011;47:657-667.
- Cocchetti G, Pagani M, Perego U. Selective mass scaling and critical time-step estimate for explicit dynamics analyses with solid-shell elements. *Comput Struct*. 2013;127:39-52.
- Tkachuk A, Bischoff M. Variational methods for selective mass scaling. *Comput Mech*. 2013;52:563-570.
- Tkachuk A, Bischoff M. Local and global strategies for optimal selective mass scaling. *Comput Mech*. 2014;53(6):1197-1207.
- Frias G, Aquino W, Pierson K, Heinstejn M, Spencer B. A multiscale mass scaling approach for explicit time integration using proper orthogonal decomposition. *Int J Numer Methods Eng*. 2014;97:799-818.
- Park KC. Practical aspects of numerical time integration. *Comput Struct*. 1977;7:343-353.

26. Hulbert G, Chung J. Explicit time integration algorithms for structural dynamics with optimal numerical dissipation. *Comput Methods Appl Mech Eng*. 1996;137:175-188.
27. Chang SY. An explicit method with improved stability property. *Int J Numer Methods Eng*. 2008;77(8):1100-1120.
28. Belytschko T, Liu WK, Moran B, Elkhodary K. *Nonlinear Finite Elements for Continua and Structures*, Chichester, West Sussex, UK: John Wiley & Sons, Ltd; 2014.
29. NAFEMS. The standard NAFEMS benchmarks. *National Agency for Finite Element Methods & Standards*. East Kilbride, Glasgow, UK: NAFEMS; 1990.

How to cite this article: González JA, Kolman R, Cho SS, Felippa CA, Park KC. Inverse mass matrix via the method of localized lagrange multipliers. *Int J Numer Meth Engng*. 2018;113:277–295. <https://doi.org/10.1002/nme.5613>

Inverse mass matrix for isogeometric explicit transient analysis via the method of localized Lagrange multipliers

José A. González¹  | J. Kopačka² | R. Kolman²  | S. S. Cho³  | K. C. Park⁴ 

¹Escuela Técnica Superior de Ingeniería, Universidad de Sevilla, Seville, Spain

²Institute of Thermomechanics, The Czech Academy of Sciences, Prague, Czech Republic

³Reactor Mechanical Engineering Division, Korea Atomic Energy Research Institute, Daejeon, Republic of Korea

⁴Department of Aerospace Engineering Sciences, University of Colorado at Boulder, Boulder, Colorado

Correspondence

José A. González, Escuela Técnica Superior de Ingeniería, Universidad de Sevilla, Camino de los Descubrimientos s/n, 41092 Seville, Spain.
Email: japerez@us.es

Present Address

José A. González, Camino de los Descubrimientos s/n, 41092 Seville, Spain.

Funding information

Centre of Excellence for Nonlinear Dynamic Behaviour of Advanced Materials in Engineering, Grant/Award Number: CZ.02.1.01/0.0/0.0/15 003/0000493; Czech Science Foundation, Grant/Award Number: 17-22615S, 17-12925S, and 16-03823S; Nuclear Safety Research Program through the Korea Foundation of Nuclear Safety (KOFONS), Grant/Award Number: 1503003

Abstract

A variational framework is employed to generate inverse mass matrices for isogeometric analysis (IGA). As different dual bases impact not only accuracy but also computational overhead, several dual bases are extensively investigated. Specifically, locally discontinuous biorthogonal basis functions are evaluated in detail for B-splines of high continuity and Bézier elements with a standard C^0 continuous finite element structure. The boundary conditions are enforced by the method of localized Lagrangian multipliers after generating the inverse mass matrix for completely free body. Thus, unlike inverse mass matrix methods without employing the method of Lagrange multipliers, no modifications in the reciprocal basis functions are needed to account for the boundary conditions. Hence, the present method does not require internal modifications of existing IGA software structures. Numerical examples show that globally continuous dual basis functions yield better accuracy than locally discontinuous biorthogonal functions, but with much higher computational overhead. Locally discontinuous dual basis functions are found to be an economical alternative to lumped mass matrices when combined with mass parameterization. The resulting inverse mass matrices are tested in several vibration problems and applied to explicit transient analysis of structures.

KEYWORDS

Bézier extraction, explicit transient analysis, free vibration, inverse mass matrix, isogeometric analysis, localized Lagrange multipliers

1 | INTRODUCTION

Efficient explicit time integration of structural dynamics equations calls for the availability of diagonal mass matrices. This is because the computational cost associated with the use of consistent/nondiagonal mass matrices in an explicit integration is equivalent with that of implicit time integration procedures, whose time step sizes can be chosen much larger than for explicit integration procedures. Specifically, explicit time integration methods in transient dynamics require a repeated application of the inverse mass matrix to obtain accelerations at every time step. For example, computing the inverse of a consistent mass matrix (CMM) requires $\mathcal{O}(n^3)$ flops. This has led to the adoption of the diagonalized lumped mass matrix

(LMM) that is typically obtained by a row sum of the CMM. However, even though the accuracy of LMM is acceptable for capturing low-frequency response components, it is unable to track high-frequency components.¹⁻⁵ Another shortcoming of LMM for higher-order elements is that most of the mass is lumped at the center node, causing very strange behavior when high-order modes are excited. These deficiencies motivated researchers to find ways of generating the inverse of CMM in a consistent and efficient way.⁶⁻⁸

From the viewpoint of principles in dynamics, there are two ways for computing the mass matrices, which need to be inverted for efficient explicit time integration. One approach is to directly discretize system kinetic energy. The second is to exploit Hamilton's principle (or Hamilton's equations) that require discretization of both momentum (\mathbf{p}) and displacement (\mathbf{u}). In this case, the inverse mass matrix (\mathbf{M}^{-1}) is obtained as a second-order tensor product, where only a diagonalized projection operator (\mathbf{A} which will be detailed later in this paper) needs to be inverted, viz,

$$\left(\int_{\Omega} \frac{1}{\rho} \delta \mathbf{p} \cdot \mathbf{p} \, d\Omega \approx \delta \mathbf{p} \mathbf{C} \mathbf{p}, \quad \int_{\Omega} \delta \mathbf{p} \cdot \mathbf{u} \, d\Omega \approx \delta \mathbf{p} \mathbf{A}^T \mathbf{u} \right) \Rightarrow \mathbf{M}^{-1} = \mathbf{A}^{-T} \mathbf{C} \mathbf{A}^{-1}, \quad (1)$$

where \mathbf{C} is labeled as a momentum matrix, \mathbf{p} denotes discretized momentum vector. Hence, inversion of mass matrix is accomplished via the generation of the momentum matrix (\mathbf{C}) followed by a *push-forward* projection operation.

Thus, an efficient generation of consistent inverse mass matrices depends on how efficiently the projection operator (\mathbf{A}) can be generated and inverted. This, in turn, requires that the interpolation functions for the momentum must be biorthogonal with respect to the displacement interpolation functions so that the resulting projection matrix (\mathbf{A}) becomes diagonal. While derivations of biorthogonal basis functions are straightforward for most interpolation functions for the interior elements, for the elements bordering the boundaries, special biorthogonal basis functions need to be constructed. This construction has to be performed for each of the corresponding \mathbf{u} -interpolation functions. It should be noted that, by the very nature of finite element method, elements bordering the boundaries do not need to be specialized.

The preceding complications in generating biorthogonal basis functions for the momentum vector in treating the boundary conditions were alleviated in the work of González et al⁹ for FEM by introducing the method of localized Lagrange multipliers (LLMs).¹⁰⁻¹³ In that work, the system is considered completely free floating such that no special treatment is required for generating the biorthogonal interpolation of the momentum vector. Enforcement of boundary conditions is simply accomplished via constraining the boundary conditions. We believe that the same ideas used for the obtention of FEM inverse mass matrices can be extended to the more general framework of isogeometric analysis (IGA).

Particularly for IGA, different approaches have been proposed in the literature to address this difficulty present in the mass matrix inversion. First contributions in explicit dynamics were developed for B-spline collocation methods, treating the equations of motion (EOMs) in strong form and obtaining one-point quadrature mass matrices.^{14,15} Solutions to the mass inversion problem were then suggested at the time-integration solution algorithm level, introducing a *predictor multicorrector* scheme that predicts accelerations with LMM on the left-hand side of the linear system and corrects the residual using the CMM. This method is iterative in essence and energy stability is not guaranteed.

Other methods benefit from the regularity of the reference patches used in IGA, taking advantage of the tensor product separable form of the mass matrix associated to these structured meshes. For example, at the linear solver level with a CMM, Gao and Calo¹⁶ proposed using a *preconditioned conjugate gradient* method with special preconditioners that achieves a complexity of $\mathcal{O}(n)$ flops. However, this procedure is not completely general and nonseparable mass matrices require a carefully designed preconditioner that adds significant complexity and computational cost to the linear solver. New preconditioning and multigrid techniques with linear cost¹⁷⁻¹⁹ could also be considered for that task.

In the context of multipatch discontinuous Galerkin IGA for acoustic wave propagation and linear advection, a recent work of Chan and Evans²⁰ aims to approximate the mass matrix inverse by a computable *weight-adjusted mass matrix* that is pre-post multiplied by an easily invertible affine mass matrix obtained from the tensor product of one-dimensional (1D) inverses. Although not derived from energy principles, the proposed algebraic approximation is demonstrated to be high-order accurate only for sufficiently regular discretizations.

A different approach, the methodology used in this paper belongs to this last group, tries to derive a reciprocal mass matrix (RMM) directly from *parameterized variational principles* and dual-space shape functions.²¹ The idea here is to derive variationally consistent RMMs from a parameterized functional and adjust the value of these parameters to construct customizable RMMs with desired properties, like high accuracy on certain frequency ranges or extending the critical time step needed for time integration stability.

The objective of the present paper is to extend the procedure for generating FEM inverse mass matrices presented in the work of González et al⁹ for explicit transient analysis by utilizing existing IGA capabilities.²²⁻²⁵ To this end, this paper

is organized as follows. Section 2 briefly reviews some basic concepts on B-splines, NURBS, and Bézier elements interpolation. Section 3 derives the displacement-momentum mixed equations of elastodynamics from Hamilton's principle, and Section 4 describes the direct construction of inverse mass matrices through biorthogonal basis functions. Sections 5 and 6 categorize and analyze the construction of dual basis functions. Section 7 discusses the incorporation of boundary conditions into the inverse mass matrix via the method of LLMs. Finally, in Section 8, we present several numerical examples, where we test the accuracy of the proposed mass matrix inverse in vibration and transient analyses, and Section 9 closes with the conclusions.

2 | A BRIEF REVIEW OF BASICS OF IGA

In this section, we review the basic concepts of the IGA techniques that will be used to construct the proposed RMMs. We start with the classical B-spline and NURBS approximation and next outline the basics of the Bézier extraction technique. This last technique is utilized to produce a finite element data structure of the geometry with the same approximation than the B-spline basis functions.

2.1 | B-splines and NURBS-based functions

In NURBS-based Galerkin IGA, the approximation of a displacement field $\mathbf{u}(\mathbf{x})$ uses the same mathematical representation than the geometry based on spline-like approximation techniques.²⁶ For three-dimensional (3D) problems in particular, the geometry of a domain $\Omega \in \mathbb{R}^3$ is described by the tensor product formula

$$\mathbf{x}(\xi, \eta, \zeta) = \sum_{i=1}^n \sum_{j=1}^m \sum_{k=1}^l R_{i,j,k}^{p,q,r}(\xi, \eta, \zeta) \mathbf{P}_{i,j,k}, \quad (2)$$

where $\mathbf{x} \in \Omega$ marks the position of point of interest in the physical space, (ξ, η, ζ) are its associated coordinates in the parametric space, $R_{i,j,k}^{p,q,r}$ are NURBS basis functions of orders (p, q, r) on each dimension, and $\mathbf{P}_{i,j,k}$ with $i = 1, \dots, n, j = 1, \dots, m, k = 1, \dots, l$ is a matrix with the three coordinates of the control points defining the geometry.

An associated displacement field $\mathbf{u}(\mathbf{x})$ is then approximated as follows:

$$\mathbf{u}(\mathbf{x}(\xi, \eta, \zeta)) = \sum_{i=1}^n \sum_{j=1}^m \sum_{k=1}^l R_{i,j,k}^{p,q,r}(\xi, \eta, \zeta) \mathbf{u}_{i,j,k}^p, \quad (3)$$

where $\mathbf{u}_{i,j,k}^p$ are now the displacements corresponding to the control point indicated by indices i, j, k .

For NURBS solids, the shape functions are described by the tensor product as

$$R_{i,j,k}^{p,q,r}(\xi, \eta, \zeta) = \frac{N_i^p(\xi)N_j^q(\eta)N_k^r(\zeta)w_{i,j,k}}{\sum_{\hat{i}=1}^n \sum_{\hat{j}=1}^m \sum_{\hat{k}=1}^l N_{\hat{i}}^p(\xi)N_{\hat{j}}^q(\eta)N_{\hat{k}}^r(\zeta)w_{\hat{i},\hat{j},\hat{k}}}, \quad (4)$$

where $w_{i,j,k}$ is referred to as the i th, j th, k th *weight* corresponding to the i th, j th, k th control point, and $N_i^p(\xi), N_j^q(\eta), N_k^r(\zeta)$ are univariate B-spline basis functions of orders $p, q,$ and r corresponding to the knot vectors $\Xi, \mathcal{H}, \mathcal{Z}$, respectively.²⁷

Let us define a knot vector in 1D case as a nondecreasing set of coordinates in the parametric space, written as $\Xi = \{\xi_1, \xi_2, \dots, \xi_{m_k}\}$, where $\xi_i \in \mathbb{R}$ is the i th knot, i is the knot index, $i = 1, 2, \dots, m_k$, number of knots $m_k = n + p + 1$, order p is the polynomial degree, and n is the number of basis functions (control points) used to construct the B-spline curve. Associated B-spline basis functions $N_i^p(\xi)$, see Figure 1, are C^{p-k} continuous piecewise polynomials defined by the Cox-de Boor recursion formula.²⁸ Observe that N_i^p are C^{p-k} continuous piecewise polynomials, where k is the knot multiplicity and that continuity can be controlled by the multiplicity of a knot in the knot vector Ξ .

Finally, the NURBS-based interpolation in \mathbb{R}^3 of a displacement field $\mathbf{u}(\mathbf{x})$ can then be expressed in matrix form as

$$\mathbf{u}(\xi) = \sum_{i=1}^n \mathbf{N}_i^p(\xi) \mathbf{u}_i^p = \mathbf{N}_u(\xi) \mathbf{u}, \quad (5)$$

where the matrix of interpolation functions $\mathbf{N}_u(\xi)$ is constructed by using B-spline basis functions of a given degree p and vector \mathbf{u} groups the unknown discrete values at the control points.

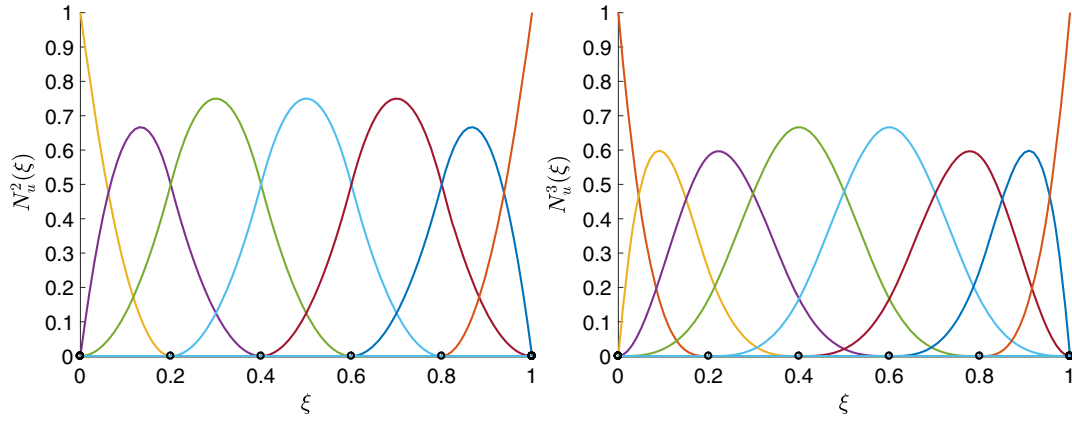


FIGURE 1 Standard one-dimensional quadratic $p=2$ (left) and cubic $p=3$ (right) B-spline basis functions $N_u^p(\xi)$ in the normalized parameter space for an open knot vector with internal values $\Xi = \{0, 0.2, 0.4, 0.6, 0.8, 1\}$ [Colour figure can be viewed at wileyonlinelibrary.com]

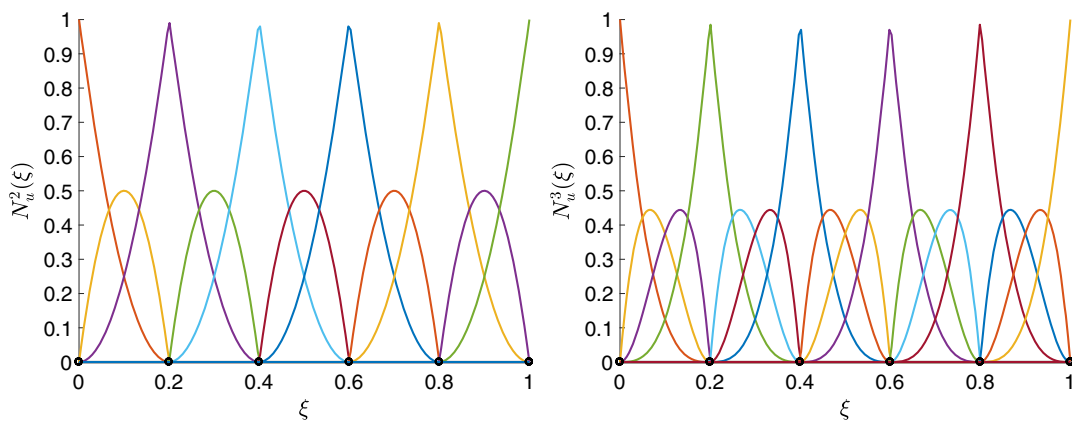


FIGURE 2 Result of the application of the Bézier extraction process to the original quadratic $p=2$ (left) and cubic $p=3$ (right) B-spline basis functions represented in Figure 1. After knot insertion, $\Xi = \{0, 0.2, 0.2, 0.4, 0.4, 0.6, 0.6, 0.8, 0.8, 1\}$ for $p = 2$, the original B-spline basis functions can be expressed as a linear combination of the new Bézier interpolation functions with compact support [Colour figure can be viewed at wileyonlinelibrary.com]

2.2 | Bézier extraction: transformation of NURBS-based mesh into Bézier-based mesh

As mentioned in the previous section, the support of a B-spline basis function N_i^p is compact and contained over $p + 1$ knot spans in the interval $[\xi_i, \xi_{i+p+1}]$. As a result (see Figure 2), it is not possible to use the concept of a single parent finite element with locally defined shape functions that is mapped onto individual knot intervals, complicating the implementation. One solution to circumvent this difficulty is the Bézier's extraction process.²⁹

In the same way that NURBS are a generalization of B-Splines, B-Splines represent the generalization of Bézier splines (based on Bernstein polynomials), and as such, the Bézier representation of a domain can be written in the form

$$\mathbf{x}(\xi, \eta, \zeta) = \sum_{i=1}^n \sum_{j=1}^m \sum_{k=1}^l B_{i,j,k}^{p,q,r}(\xi, \eta, \zeta) \mathbf{P}_{i,j,k}^B, \quad (6)$$

where $\mathbf{P}_{i,j,k}^B$ are new coordinates of control points for a Bézier-based representation and $B_{i,j,k}^{p,q,r}$ are the shape functions based on the Bernstein polynomials of order p, q, r .

By Bézier extraction, it is meant the construction of a mesh of isogeometric Bézier elements from a NURBS representation. This process provides a local element support structure for IGA that can be easily incorporated into existing finite element codes, see Figure 3. Following this technique, the B-spline functions $\mathbf{N}(\xi)$ can be unambiguously written as linear combination of Bernstein polynomials $\mathbf{B}(\xi)$, expressed in matrix form

$$\mathbf{N}(\xi) = \mathbf{C}_B \mathbf{B}(\xi), \quad (7)$$

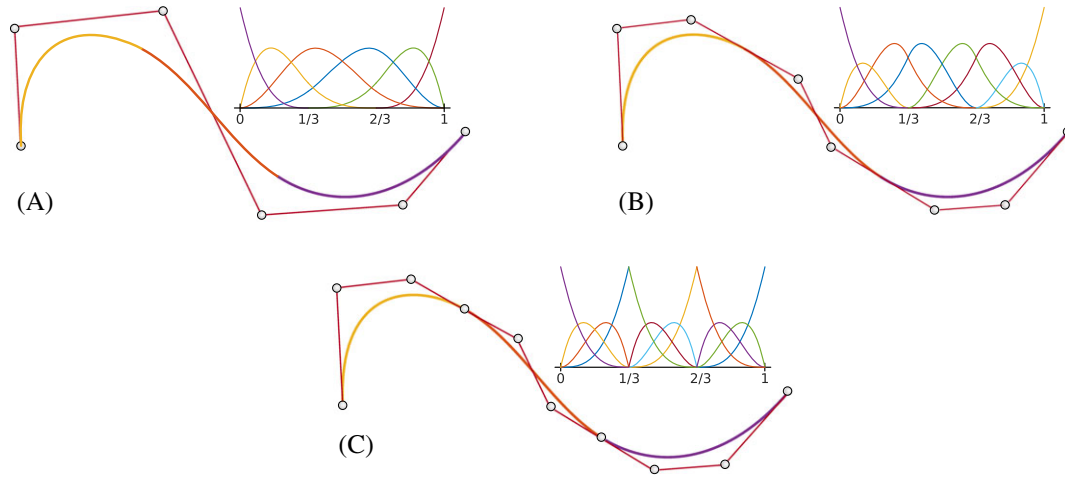


FIGURE 3 Bézier extraction operation performed in a two-dimensional cubic ($p = 3$) B-spline curve. The shape of the initial C^2 continuous curve (A) is defined by six control points and six basis functions, and its associated knot vector is $\Xi = \{0, 0, 0, 0, 1/3, 2/3, 1, 1, 1, 1\}$. After a first repetition of knot values, one gets the curve with C^1 continuity (B) with eight control points/basis functions and knot vector $\Xi = \{0, 0, 0, 0, 1/3, 1/3, 2/3, 2/3, 1, 1, 1, 1\}$. Finally, p repetitions of the knot values results in the C^0 continuous curve (C) with 10 control points/basis functions and knot vector $\Xi = \{0, 0, 0, 0, 1/3, 1/3, 1/3, 2/3, 2/3, 2/3, 1, 1, 1, 1\}$. Now, the basis functions are the same for all the knot intervals; therefore, the curve can be constructed through a systematic assembling of Bézier elements with Bernstein polynomials as shape functions [Colour figure can be viewed at wileyonlinelibrary.com]

where matrix \mathbf{C}_B is the extraction operator that is uniquely associated to a particular knot vector.²⁹

Technically, the new mesh is constructed step-by-step repeating all the knots contained in the original knot vector up to multiplicity $p + 1$, reducing at the same time continuity to C^0 , by following the process described in Figure 3. Then, for each B-spline segment, an expression like (7) can be expressed in local form. Furthermore, new position and weights of the Bézier mesh, \mathbf{P}^B and \mathbf{w}_B , can be computed directly from the position of control points and weights, \mathbf{P} and \mathbf{w} , corresponding to the NURBS mesh as

$$\mathbf{P}^B = \mathbf{W}_B^{-1} \mathbf{C}_B^T \mathbf{W} \mathbf{P}, \quad \mathbf{w}_B = \mathbf{C}_B^T \mathbf{w}, \quad (8)$$

where matrices \mathbf{W}_B and \mathbf{W} are diagonal matrices storing the weight vectors \mathbf{w}^b and \mathbf{w} , for more details, see the work of Borden et al.²⁹

In a typical two-dimensional (2D) case, like the one represented in Figure 4, Bézier analysis starts with an IGA mesh. Then, one can use the previous transformations to convert step-by-step the NURBS-based mesh into a Bézier mesh by repeating knots in the two parametric directions. Finally, a finite element mesh is obtained with C^0 continuity of neighboring elements with Bernstein polynomials as shape functions.

3 | HAMILTON'S PRINCIPLE WITH THE METHOD OF LOCALIZED LAGRANGE MULTIPLIERS

We consider the evolution in time of the displacement and momentum fields $\mathbf{u}, \mathbf{p} \in \mathbb{R}^d$, where $d = 1, 2, 3$ is the number of space dimensions, of a body with domain Ω and boundary Γ for a total time T . The body is subjected to prescribed interface displacements \mathbf{u}_b on part of its boundary Γ_b , to the traction \mathbf{t} on the rest of its boundary Γ_t and to a body force \mathbf{b} per unit volume. Initial conditions that are compatible with the boundary conditions define the displacement and velocity field, respectively, at time $t = 0$. The initial boundary value problem of elastodynamics expressed in strong form can be formulated as follows:

$$\begin{aligned} \nabla \cdot \boldsymbol{\sigma} + \mathbf{b} &= \dot{\mathbf{p}} & \text{in } \Omega \times [0, T], \\ \mathbf{u} &= \mathbf{u}_b & \text{on } \Gamma_b \times [0, T], \\ \boldsymbol{\sigma} \cdot \mathbf{n} &= \mathbf{t} & \text{on } \Gamma_t \times [0, T], \\ \mathbf{u}|_{t=0} &= \mathbf{u}^0 & \text{in } \Omega, \\ \dot{\mathbf{u}}|_{t=0} &= \dot{\mathbf{u}}^0 & \text{in } \Omega, \end{aligned} \quad (9)$$

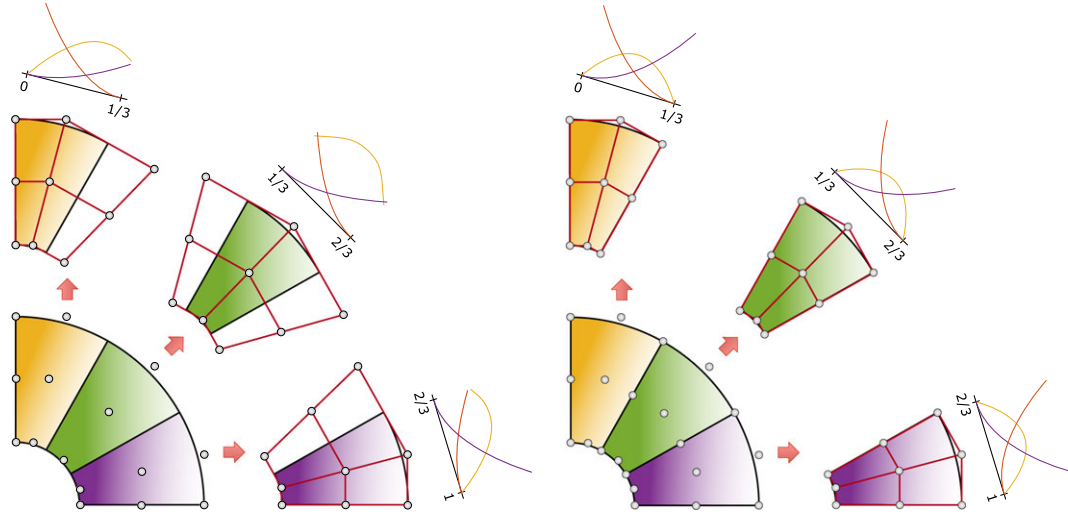


FIGURE 4 Illustration of the Bézier extraction operation performed in a two-dimensional patch of quadratic B-splines. The Bézier extraction operator maps a piecewise Bernstein polynomials basis (right) onto a B-spline basis (left). This transformation makes it possible to create Bézier elements as the finite element representation of B-splines or NURBS [Colour figure can be viewed at wileyonlinelibrary.com]

where $\mathbf{p} = \rho \dot{\mathbf{u}}$ is the momentum per unit volume and $\boldsymbol{\sigma}$ is the stress tensor that, in the case of linear elasticity is linearly related with the deformation tensor $\boldsymbol{\varepsilon} = \frac{1}{2}[\nabla \mathbf{u} + \nabla \top \mathbf{u}]$ by the fourth-order constitutive tensor \mathbf{C} through the constitutive relation $\boldsymbol{\sigma} = \mathbf{C} : \boldsymbol{\varepsilon}$. This is an initial value problem to be solved for all time t in the interval $[0, T]$.

The strong form of the of the initial value problem (9) can be transformed into an equivalent weak variational form. To this end, we invoke Hamilton's principle for constrained elastodynamic problems. This principle states that *the path followed by a dynamic system is the one which minimizes the action integral of the Lagrangian*; condition that can be expressed using the following three-field variational form:

$$\delta H(\mathbf{u}, \mathbf{p}, \boldsymbol{\ell}) = \int_{t_1}^{t_2} \delta \{T(\dot{\mathbf{u}}, \mathbf{p}) - U(\mathbf{u}, \boldsymbol{\ell}) + W(\mathbf{u})\} dt = 0, \tag{10}$$

where δT is the virtual kinetic energy, δU is the virtual elastic energy, and δW is the virtual work done by the external loads, magnitudes that can be expressed

$$\delta T = \int_{\Omega} \delta \left(\frac{1}{2} \mathbf{p} \cdot \dot{\mathbf{u}} \right) d\Omega, \tag{11}$$

$$\delta U = \int_{\Omega} \delta \boldsymbol{\varepsilon} : \boldsymbol{\sigma} d\Omega + \int_{\Gamma_b} \delta \{ \boldsymbol{\ell} \cdot (\mathbf{u} - \mathbf{u}_b) \} d\Gamma, \tag{12}$$

$$\delta W = \int_{\Omega} \delta \mathbf{u} \cdot \mathbf{b} d\Omega, \tag{13}$$

with known displacement boundary conditions \mathbf{u}_b imposed at interface Γ by using a field of LLMs $\boldsymbol{\ell}$ and external body forces per unit volume \mathbf{b} acting on Ω .

By making use of the momentum-velocity relation ($\mathbf{p} = \rho \dot{\mathbf{u}}$) in the following identity:

$$\frac{1}{2} \mathbf{p} \cdot \dot{\mathbf{u}} = \mathbf{p} \cdot \dot{\mathbf{u}} - \frac{1}{2\rho} \mathbf{p} \cdot \mathbf{p}, \tag{14}$$

we can obtain an equivalent expression for the virtual kinetic energy per unit volume

$$\delta \left(\frac{1}{2} \mathbf{p} \cdot \dot{\mathbf{u}} \right) = \delta \dot{\mathbf{u}} \cdot \mathbf{p} + \delta \mathbf{p} \cdot \left(\dot{\mathbf{u}} - \frac{1}{\rho} \mathbf{p} \right), \tag{15}$$

and finally, performing an integration by parts of the second term of the last equation yields:

$$\int_{t_1}^{t_2} \delta \dot{\mathbf{u}} \cdot \mathbf{p} dt = - \int_{t_1}^{t_2} \delta \mathbf{u} \cdot \dot{\mathbf{p}} dt, \quad (16)$$

relation that can be used to eliminate the virtual velocity field from the formulation.

Introducing previous identities, (15) and (16), into the principle of stationary action (10), we obtain the final the three-field variational form of the Hamilton's principle for constrained elastodynamics

$$\begin{aligned} \delta H(\mathbf{u}, \mathbf{p}, \ell) = \int_{t_1}^{t_2} \left\{ \int_{\Omega} \delta \mathbf{p} \cdot \left(\dot{\mathbf{u}} - \frac{1}{\rho} \mathbf{p} \right) d\Omega - \int_{\Omega} (\delta \mathbf{u} \cdot \dot{\mathbf{p}} + \delta \boldsymbol{\varepsilon} : \boldsymbol{\sigma}) d\Omega + \int_{\Omega} \delta \mathbf{u} \cdot \mathbf{b} d\Omega \right. \\ \left. + \int_{\Gamma_b} \delta \mathbf{u} \cdot \boldsymbol{\ell} d\Gamma - \int_{\Gamma_b} \delta \boldsymbol{\ell} \cdot (\mathbf{u} - \mathbf{u}_b) d\Gamma \right\} dt = 0, \end{aligned} \quad (17)$$

expression that will be used to derive the discrete EOMs.

Remark 1. Through the use of a parameterized form of the kinematic energy with three free parameters (C_1, C_2, C_3), Schaeuble et al²¹ proposed a general template for obtaining variationally scaled and customized consistent and RMMs. Variational equation (17) can be considered a particular case of their general template form for $\{C_1 = -1, C_2 = 0, C_3 = 0\}$. An important difference with that work lies on the use of a volume-specific linear momentum instead of a mass-specific linear momentum and the consistent-lumped parameterization of the mass matrix that will be introduced later.

4 | CONSTRUCTING INVERSE MASS MATRIX VIA THE LOCALIZED LAGRANGE MULTIPLIERS

Discretization in space of the mixed variational form (17) is performed by using independent interpolation functions for displacements, momenta, and Lagrangian multipliers. For this purpose, we carry out a standard IGA discretization (5) with independent B-spline shape functions for the three fields

$$\mathbf{u}(\xi) = \mathbf{N}_u(\xi)\mathbf{u}, \quad \mathbf{p}(\xi) = \mathbf{N}_p(\xi)\mathbf{p}, \quad \boldsymbol{\ell}(\xi) = \mathbf{N}_\lambda(\xi)\boldsymbol{\lambda}, \quad (18)$$

and we introduce these discrete approximations in the variational form (17) to obtain, after imposing the stationarity condition, the following set of semidiscrete equations:

$$\mathbf{A}\dot{\mathbf{p}} + \mathbf{B}\boldsymbol{\lambda} = \mathbf{r} \quad \text{Equilibrium equation}, \quad (19)$$

$$\mathbf{A}^\top \dot{\mathbf{u}} - \mathbf{C}\mathbf{p} = \mathbf{0} \quad \text{Momentum equation}, \quad (20)$$

$$\mathbf{B}^\top \mathbf{u} - \mathbf{L}_b \mathbf{u}_b = \mathbf{0} \quad \text{Boundary (and interface) constraints}, \quad (21)$$

$$-\mathbf{L}_b^\top \boldsymbol{\lambda} = \mathbf{0} \quad \text{Newton's third law on the boundaries}, \quad (22)$$

where vector $\mathbf{r} = \mathbf{f} - \mathbf{f}^{\text{int}}$ is the external-internal forces residual, \mathbf{A} is the global projection matrix, \mathbf{C} is the global RMM, \mathbf{B} the boundary assembly operator, and \mathbf{L}_b is the localized multipliers assembly matrix. These matrices are constituted by an element-by-element assembly of the element matrices

$$\mathbf{A}_e = \int_{\Omega_e} \mathbf{N}_u^\top \mathbf{N}_p d\Omega, \quad \mathbf{C}_e = \int_{\Omega_e} \frac{1}{\rho} \mathbf{N}_p^\top \mathbf{N}_p d\Omega, \quad (23)$$

$$\mathbf{B}_e = \int_{\Gamma_e} \mathbf{N}_u^\top \mathbf{N}_\lambda d\Gamma, \quad \mathbf{L}_e = \int_{\Gamma_e} \mathbf{N}_\lambda^\top \mathbf{N}_u d\Gamma, \quad (24)$$

the first two needed for the construction of the element reciprocal mass and the last ones used to enforce interface compatibility and equilibrium. Moreover, it is important to mention that we assume constant mass density along every physical patch.

Going one step forward by eliminating symbolically the momentum variable \mathbf{p} from (19) and (20), one obtains the classical equation of motion expressed in terms of displacements

$$(\mathbf{A}\mathbf{C}^{-1}\mathbf{A}^T)\ddot{\mathbf{u}} + \mathbf{B}\lambda = \mathbf{r} \quad (25)$$

with the mass matrix approximated as

$$\mathbf{M} = \mathbf{A}\mathbf{C}^{-1}\mathbf{A}^T \quad (26)$$

and observe that there must exist an inverse mass matrix (denoted by equivalence as \mathbf{M}^{-1}) given by

$$\mathbf{M}^{-1} = \mathbf{A}^{-T}\mathbf{C}\mathbf{A}^{-1} \quad (27)$$

assuming that the global projection matrix is invertible.

Since the objective of the present paper is to obtain inverse mass matrices for IGA in efficient and accurate ways, one must seek for easily to invert *diagonal* or narrowly banded projection matrices. This certainly can be accomplished in (27) with a diagonal projection \mathbf{A} -matrix, leaving only the task of constructing the reciprocal \mathbf{C} -matrix efficiently and accurately.

5 | DUAL BASIS FUNCTIONS

Observing again the expression obtained for the mass matrix inverse (27), we realize that a careful selection of the basis functions can simplify its calculation. Dual bases can be *local* or *global*, *continuous* or *discontinuous*, and satisfy exactly the orthogonality condition or not. In particular, by using displacement and momentum biorthogonal interpolation functions, we are able to construct a diagonal projection matrix in the form

$$[\mathbf{A}_e]_{ij} = \int_{\Omega_e} \mathbf{N}_{u_i}^T \mathbf{N}_{p_j} d\Omega = d_i \delta_{ij}, \quad \text{where } [\mathbf{A}_e]_{ij} = 0 \text{ for } i \neq j, \quad (28)$$

with a trivial inverse that permits to compute the inverse mass matrix directly from the momentum matrix. Different local and global dual interpolation functions of this kind, originally designed and tested for mortar methods, have been recently proposed in the literature³⁰⁻³² for NURBS and B-spline interpolations. Specifically for the construction of RMMs, biorthogonal basis functions have been proposed under the framework of FEM^{8,9} and also IGA.²¹ The different options available for the construction of dual bases are discussed next.

5.1 | Local dual bases

These dual basis functions entail minimal support, ie, the support of the dual basis is equal to the support of the original B-spline basis, that for the case of B-splines covers $p + 1$ knot spans. Analytical expressions for the construction of local continuous (LC) biorthogonal dual basis exist in the literature for 1D B-splines,³²⁻³⁴ but they are difficult to generalize for multidimensions, restricting their application to our case.

For higher dimensions, the simplest alternative is the use of a local discontinuous (LD) biorthogonal dual basis^{31,35} obtained via an elementwise linear combination of the primal shape functions, providing discontinuous reciprocal basis functions that fulfill the partition of unity with the same support than their primal counterparts. A dual basis $\mathbf{N}_p(\xi)$ of this type, orthogonal to the B-spline displacement interpolation functions $\mathbf{N}_u(\xi)$, can be written in matrix form as

$$\mathbf{N}_p(\xi) = \mathbf{N}_u(\xi)\mathbf{M}_e^{-1}\mathbf{M}_e^L \quad (29)$$

constructed by using the knot intervals as independent elements and where \mathbf{M}_e is an element-by-element constructed mass matrix, with $\mathbf{M}_e^L = \text{diag}(\sum_j [\mathbf{M}_e]_{ij})$ being the LMM obtained by row sum of its components.

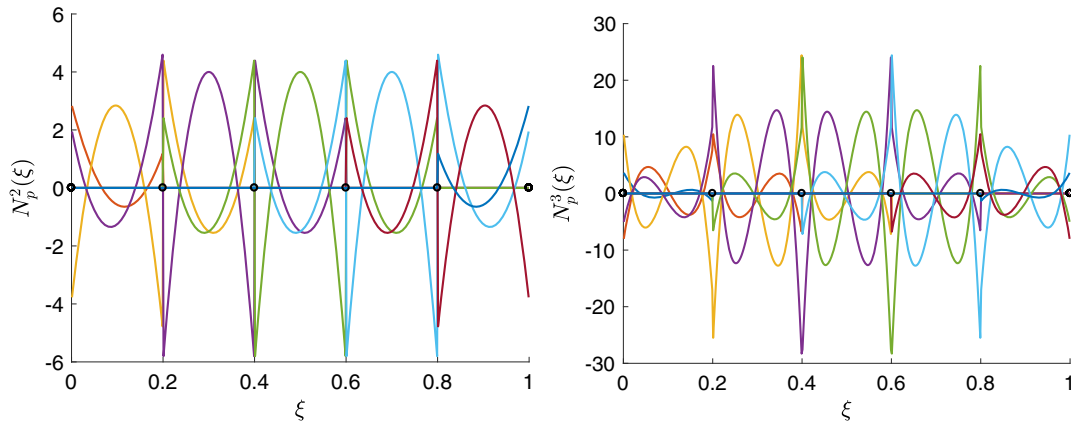


FIGURE 5 Representation of local discontinuous quadratic $p = 2$ (left) and cubic $p = 3$ (right) orthogonal B-spline basis functions $N_p^p(\xi)$ in the normalized parameter space for an open knot vector with internal values $\Xi = \{0, 0.2, 0.4, 0.6, 0.8, 1\}$. These dual interpolation functions are locally orthogonal to the basis $N_u^p(\xi)$ represented in Figure 1 [Colour figure can be viewed at wileyonlinelibrary.com]

Orthogonality of these interpolation functions is easily demonstrated evaluating the projection matrix (28) at the element level

$$\mathbf{A}_e = \int_{\Omega_e} \mathbf{N}_u^T \mathbf{N}_p d\Omega = \left\{ \int_{\Omega_e} \mathbf{N}_u^T \mathbf{N}_u d\Omega \right\} \mathbf{M}_e^{-1} \mathbf{M}_e^L = \frac{1}{\rho} \mathbf{M}_e^L \quad (30)$$

obtaining by design a diagonal projection matrix \mathbf{A}_e that is equal to the lumped element mass matrix computed with unit density. As an example, Figure 5 represents the discontinuous interpolation functions $N_p^p(\xi)$ locally orthogonal to the B-spline basis $N_u^p(\xi)$ contained in Figure 1 for quadratic ($p = 2$) and cubic ($p = 3$) B-spline interpolations.

Finally, we can evaluate analytically the elemental momentum mass matrix from its definition (23), by substituting (29) and considering (30), with a very simple expression

$$\mathbf{C}_e = \int_{\Omega_e} \frac{1}{\rho} \mathbf{N}_p^T \mathbf{N}_p d\Omega = \mathbf{A}_e^T \mathbf{M}_e^{-1} \mathbf{A}_e, \quad (31)$$

confirming that it is possible to compute an RMM element by element without expensive operations.

Remark 2. Expression (30), with the element projection matrix \mathbf{A}_e equal to the lumped element mass matrix, was originally proposed by González et al⁹ for the construction of RMMs in the context of FEM. The same projection matrix was later employed by Schaeuble et al²¹ to construct variationally consistent masses and reciprocal masses for IGA, eliminating the density inverse from its definition by introducing a momentum velocity field instead of a pure momentum field.

A similar elementwise construction process can be applied to Bézier elements, obtaining a basis with compact support restricted to the knot intervals that presents C^0 continuity at the element interfaces. In this case, see Figure 6, the local dual basis presents the same support than the original basis and the element-by-element compact support is well defined.

5.2 | Global dual bases

On the contrary, global dual basis functions present complete support along the parametric space. A common technique to compute global continuous (GC) bases is to write the dual functions as linear combination of the primal shape functions, finding the coefficients by enforcing the orthogonality condition. Accelerated algorithms³⁶ exist for this task, exploiting the mathematical properties of the dual bases that can reduce the algorithm complexity, from $\mathcal{O}(n^3)$ flops needed to compute a full inverse, to $\mathcal{O}(n^2)$ flops.

Another possibility to determine GC dual basis functions for B-spline basis functions is the inversion of the *Gram* matrix.^{32,37} In this case, the first step in the calculation of the dual basis requires the computation of the Gramian matrix

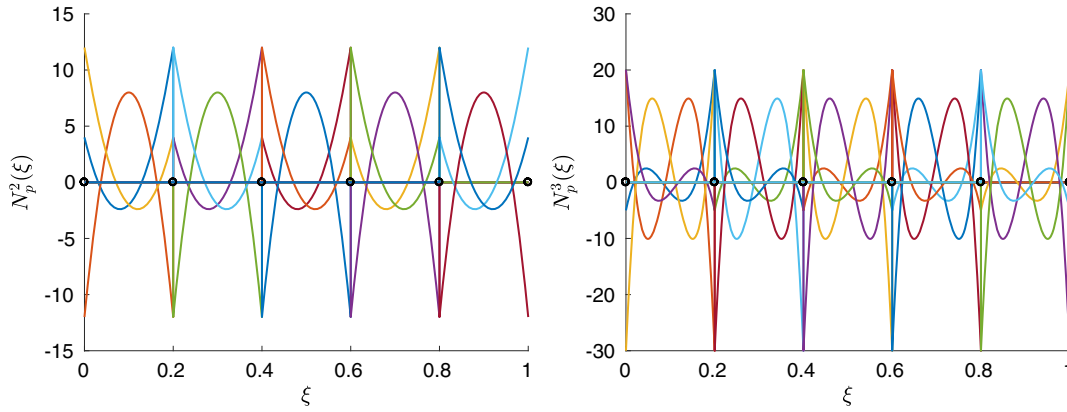


FIGURE 6 Form of the quadratic $p = 2$ (left) and cubic $p = 3$ (right) local discontinuous dual basis functions $N_p(\xi)$ locally orthogonal to the Bézier element basis $N_u^p(\xi)$ represented in Figure 2 [Colour figure can be viewed at wileyonlinelibrary.com]

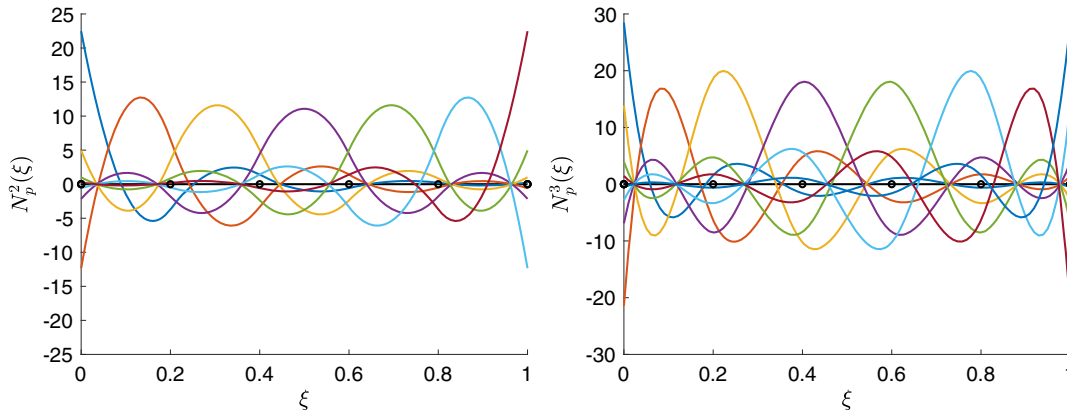


FIGURE 7 Representation of quadratic $p = 2$ (left) and cubic $p = 3$ (right) B-spline global continuous dual basis functions $N_p^p(\xi)$ in the normalized parameter space for an open knot vector with internal values $\Xi = \{0, 0.2, 0.4, 0.6, 0.8, 1\}$. These interpolation functions are orthogonal to the basis $N_u^p(\xi)$ represented in Figure 1 [Colour figure can be viewed at wileyonlinelibrary.com]

for the primal basis

$$\mathbf{G}_{N_u, N_u} = \left[\int_{\xi_1}^{\xi_{n+p+1}} N_{u_i}(\xi) N_{u_j}(\xi) ds \right]_{(i=1, \dots, n; j=1, \dots, n)} \quad (32)$$

that integrates cross products of primal B-spline functions along the complete parametric space. The resulting Gram matrix is symmetric, block-diagonal, and always invertible. Then, the Gram matrix needs to be efficiently inverted to obtain the dual basis

$$\mathbf{N}_p(\xi) = \mathbf{G}_{N_u, N_u}^{-1} \mathbf{N}_u(\xi), \quad (33)$$

where a full populated inverse $\mathbf{G}_{N_u, N_u}^{-1}$ produces a dual basis with global support. The resulting GC biorthogonal basis functions yield the optimal reproduction degree but increase the number of operations and storage needed to compute the inverse mass matrix due to their full support, see Figure 7.

Compared to local reciprocal bases, global dual basis functions produce full RMMs that are computationally more expensive. In particular, the RMM computed with the inverse of the *Gram* dual basis (33) yields very accurate numerical results, but at significantly higher computational cost than local dual bases.

5.3 | Convenient dual bases

We incorporate into this final category bases that are not strictly orthogonal but can simplify the computation of the mass inverse due to the exploitation of a convenient property. One example is the *approximate dual basis* based on wavelets

proposed in the work of Dornisch et al³² for mortar coupling methods that are able to produce semicompact approximations of an orthogonal basis.

Another example is the inverse mass matrix approximation proposed by Chan and Evans,²⁰ in the context of discontinuous Galerkin IGA for wave propagation, where an approximated *weight-adjusted* RMM is derived empirically. It is interesting to note that the same inverse mass matrix is obtained if we apply the proposed variational framework to the LC ansatz basis

$$\mathbf{N}_p(\xi) = \mathbf{N}_u(\xi)J^{-1}(\xi), \quad (34)$$

where $J(\xi)$ is the Jacobian determinant of the physical to parametrical domain transformation and $\hat{\Omega}$ represents the parametric domain. This basis is not biorthogonal, but a simple scaling of the primal basis and its advantage resides in the elimination of the physical domain influence from the projection matrix (23),

$$\mathbf{A} = \int_{\Omega} \mathbf{N}_u^T \mathbf{N}_p d\Omega = \int_{\hat{\Omega}} \mathbf{N}_u^T \mathbf{N}_u d\hat{\Omega} = \mathbf{M}_{\hat{\Omega}} \quad (35)$$

a mass matrix that is not diagonal but is constant for a particular patch and its inversion can be automatized for regular structured patches or affine transformations. The associated momentum matrix is then computed as

$$\mathbf{C} = \int_{\Omega} \mathbf{N}_u^T \mathbf{N}_u J^{-1}(\xi) d\Omega, \quad (36)$$

and from (27), the inverse mass matrix presents the form

$$\mathbf{M}^{-1} = \mathbf{M}_{\hat{\Omega}}^{-1} \mathbf{C} \mathbf{M}_{\hat{\Omega}}^{-1}, \quad (37)$$

where the mass inverse of the parametric domain can be written as the tensor product

$$\mathbf{M}_{\hat{\Omega}}^{-1} = \mathbf{M}_{1D}^{-1} \otimes \cdots \otimes \mathbf{M}_{1D}^{-1}, \quad (38)$$

when the parametric domain $\hat{\Omega}$ is regular with the same structure on each dimension. In this specific case, the inverse mass matrix in one direction \mathbf{M}_{1D}^{-1} is very cheap to compute and the complete patch inverse presents a Kronecker delta structure.

6 | ASSESSMENT OF LOCAL DISCONTINUOUS DUAL BASES

From all the possible dual basis functions discussed in Section 5, the elementwise computation of an LD biorthogonal basis seems a perfect candidate, due to its simplicity and good results demonstrated in FEM and IGA mortar methods. LD biorthogonal bases produce diagonal projection matrices and sparse inverse mass matrices. In this section, we describe in detail its implementation and integration into the proposed variational framework. It also performed a dispersion study that reveals the weakness of this type of basis under certain conditions, together with a parameterization method of the mass matrix that palliates this defect.

6.1 | Procedure to obtain IGA RMMs

The procedure used for the evaluation of the inverse mass matrix for IGA can be summarized in the following steps.

1. Consider all the open patches independently as free-floating substructures.
2. Compute element by element a parameterized mass matrix \mathbf{M}_e using (43) for example.
3. Approximate the element projection matrix \mathbf{A}_e by lumping the element mass matrix.
4. Compute the element RMM \mathbf{C}_e from a direct inversion of the element mass matrix.
5. Assemble the global projection and reciprocal matrices and compute the global mass matrix inverse.
6. Impose boundary conditions between patches using LLMs.

The first four steps of this process are described next, and the last step, which is a little bit more involved, will be analyzed in Section 7.

First, we consider an element of the patch at a time and compute the parameterized element mass matrix. Second, we use the element LMM to obtain the element projection matrix by diagonalization, viz,

$$\mathbf{A}_e = \frac{1}{\rho} \mathbf{M}_e^L \quad (39)$$

assuming that the density is constant in the patch. Third, the elemental RMM is evaluated inverting numerically the element mass matrix

$$\mathbf{C}_e = \mathbf{A}_e^\top \mathbf{M}_e^{-1} \mathbf{A}_e, \quad (40)$$

where $(\mathbf{A}_e, \mathbf{C}_e, \mathbf{M}_e)$ are elemental matrices, and particularly, \mathbf{A}_e is a diagonal matrix, so this operation is very cheap.

Finally, we proceed with the assembly of the global RMM

$$\mathbf{C} = \mathbf{A} \mathbf{C}_e \quad (41)$$

and the global projection matrix

$$\mathbf{A} = \mathbf{A}_e \quad (42)$$

observing that as long as the elemental \mathbf{A}_e is diagonal, so is the assembled matrix \mathbf{A} and its inverse. These steps permit to evaluate the inverse of the global mass matrix through expression (27) in an efficient way.

Remark 3. The same process can be applied to obtain RMMs for the FEM. The details of the methodology, as well as its application to solid and structural elements, were investigated by the authors⁹ in a previous paper.

6.2 | Mass matrix parameterization

A family of RMMs can be constructed by incorporating mass matrix parameterization^{7,8,38} into the previous process. Introducing free parameters, we can create a family of inverses and later select the members of this family with best properties for different applications. There exist several ways to parameterize mass matrices at the element level, see the work of Felippa et al³⁹ for an exhaustive classification,³⁹ being a consistent-lumped linear combination the simplest choice

$$\mathbf{M}_e = (1 - \beta) \mathbf{M}_e^C + \beta \mathbf{M}_e^L, \quad (43)$$

in which a parameter $\beta \in [0, 1]$ is used to balance between the element CMM \mathbf{M}_e^C and LMM \mathbf{M}_e^L . For example, using $\beta = \{0, 1/2, 1\}$, the element mass matrix is then easily reduced respectively to the CMM, averaged mass matrix, and LMM.

In particular, the case $\beta = 1$ is of no interest because it reduces the reciprocal matrix to the common diagonal LMM with a trivial inverse. LMM computed for IGA by the row-sum technique is very popular in explicit dynamics.¹⁵ Unfortunately, the LMM does not maintain the accuracy of the CMM for high frequencies and finding better options would suppose an important advantage for explicit dynamics. It is well known that the frequencies by CMM converge from above, whereas the frequencies by LMM converge from below. Then, it remains the task of selecting an appropriated parameter β for B-spline interpolations of different degree with the objective of beating the LMM accuracy with equivalent computational costs. This point will be addressed in the following section.

6.3 | Dispersion analysis

The introduction of a consistent LMM parameterization in the RMM makes it possible to tune the free parameter β for different objectives, like maximum accuracy for certain frequency ranges. The tool used for evaluating the accuracy of a particular reciprocal mass is Fourier analysis.^{39,40} For this task, we assume a monochromatic compressive steady wave of frequency ω traveling in a uniform and infinite 1D bar.

The governing equation for longitudinal vibration in an elastic bar has the form

$$\frac{\partial}{\partial x} \left(EA \frac{\partial u}{\partial x} \right) - \rho A \frac{\partial^2 u}{\partial t^2} = 0, \quad (44)$$

where $u(x, t)$ is the axial displacement, $x \in (-\infty, \infty)$ is the axial coordinate, $t \geq 0$ denotes the time, ρ is the mass density, A is the area of a cross-section, and E denotes the Young's modulus. The exact speed of longitudinal waves in an elastic

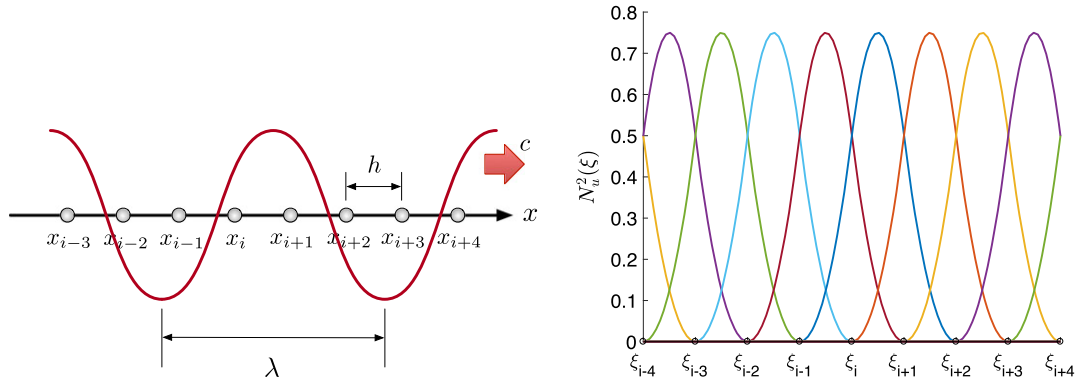


FIGURE 8 A compression wave with velocity c and length λ is assumed to travel in a discretized uniform bar. Infinite one-dimensional lattice of equidistant control points (left) and associated quadratic B-spline interpolation functions (right) used for dispersion analysis [Colour figure can be viewed at wileyonlinelibrary.com]

bar⁴¹ is $c_0 = \sqrt{E/\rho}$. Then, we discretize the problem with a uniform infinite mesh of equidistant knots, see Figure 8, to study the effect of IGA discretization and parameterization in the numerically calculated wave speed c for different wave numbers k .

Assuming an interpolation of B-spline functions of order p in an infinite patch, with uniformly distributed knots and characteristic element length h , we can compute analytically the stiffness and mass matrices and later use expression (40) to obtain the elemental momentum matrix. This process starts obtaining the element matrices, for example, for the linear case

$$\boxed{\text{Linear } (p = 1)}$$

$$\mathbf{K}_e = \frac{EA}{h} \begin{bmatrix} 1 & -1 \\ -1 & 1 \end{bmatrix}, \quad \mathbf{M}_e^C = \frac{\rho Ah}{6} \begin{bmatrix} 2 & 1 \\ 1 & 2 \end{bmatrix}, \quad \mathbf{M}_e^L = \frac{\rho Ah}{2} \begin{bmatrix} 1 & 0 \\ 0 & 1 \end{bmatrix} \quad (45)$$

$$\mathbf{A}_e = \frac{Ah}{2} \begin{bmatrix} 1 & 0 \\ 0 & 1 \end{bmatrix}, \quad \mathbf{C}_e = \frac{Ah}{2(1+2\beta)\rho} \begin{bmatrix} (\beta+2) & (\beta-1) \\ (\beta-1) & (\beta+2) \end{bmatrix} \quad (46)$$

and for quadratic B-splines

$$\boxed{\text{Quadratic } (p = 2)}$$

$$\mathbf{K}_e = \frac{EA}{6h} \begin{bmatrix} 2 & -1 & -1 \\ -1 & 2 & -1 \\ -1 & -1 & 2 \end{bmatrix}, \quad \mathbf{M}_e^C = \frac{\rho Ah}{120} \begin{bmatrix} 6 & 13 & 1 \\ 13 & 54 & 13 \\ 1 & 13 & 6 \end{bmatrix}, \quad \mathbf{M}_e^L = \frac{\rho Ah}{6} \begin{bmatrix} 1 & 0 & 0 \\ 0 & 4 & 0 \\ 0 & 0 & 1 \end{bmatrix} \quad (47)$$

$$\mathbf{C}_e = \frac{Ah}{12(1+3\beta)(1+39\beta)\rho} \begin{bmatrix} 39\beta^2 + 250\beta + 31 & 52(3\beta+1)(\beta-1) & (39\beta-23)(\beta-1) \\ 52(3\beta+1)(\beta-1) & 16(3\beta+1)(13\beta+7) & 52(3\beta+1)(\beta-1) \\ (39\beta-23)(\beta-1) & 52(3\beta+1)(\beta-1) & 39\beta^2 + 250\beta + 31 \end{bmatrix} \quad (48)$$

with the momentum matrix expressed as a function of the weighting parameter β , used to interpolate between CMM and LMM.

These element matrices are then used to assemble the discrete EOMs, obtained from momentum (20) and equilibrium (19) equations, particularized for the infinite lattice in the form

$$\left. \begin{array}{l} \mathbf{A}\dot{\mathbf{p}} + \mathbf{K}\mathbf{u} = \mathbf{0} \\ \mathbf{A}^\top \dot{\mathbf{u}} - \mathbf{C}\mathbf{p} = \mathbf{0} \end{array} \right\} \rightarrow (\mathbf{A}^{-\top} \mathbf{C} \mathbf{A}^{-1} \mathbf{K}) \mathbf{u} - \ddot{\mathbf{u}} = \mathbf{0} \quad (49)$$

from where we have eliminated the momentum variable to finally write the dynamic equilibrium only in terms of displacements.

Next, we force a harmonic solution for the axial displacement in the form

$$u(x, t) = U e^{i(kx - \omega t)} = U e^{i(\kappa \xi - \Omega c_0 t)/h} \quad (50)$$

with the dimensionless wavenumber κ and frequency Ω respectively defined as $\kappa = kh$ and $\Omega = \omega h/c_0$. Then, we particularize it at the control point coordinates $x_i = \{ \dots, -2h, -h, 0, h, 2h, \dots \}$ and substitute back in the equilibrium

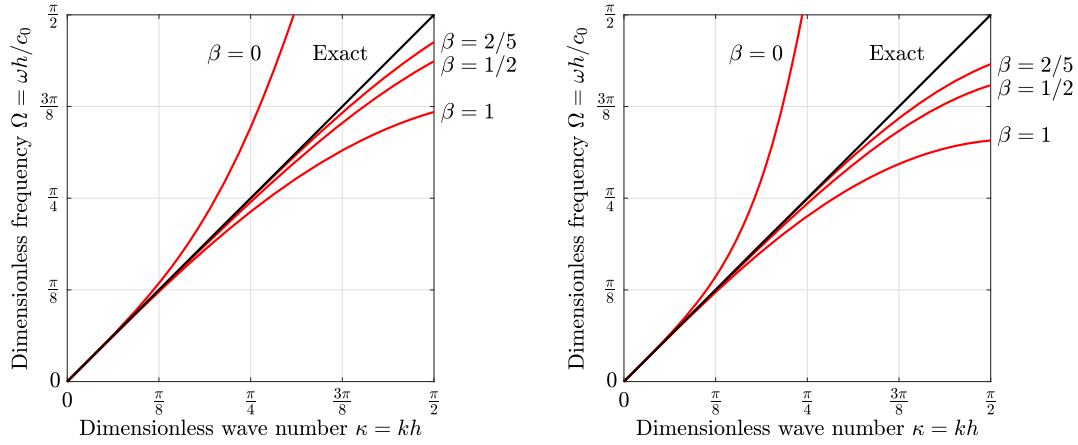


FIGURE 9 Analytical dispersion diagrams for an infinite bar modeled with quadratic $p = 2$ B-splines (left) and cubic $p = 3$ B-splines (right) using different mass scaling parameters. Note that $\kappa = \frac{\pi}{2}$ corresponds to a resolution of four elements per wave length. Divergence is observed for $\beta = 0$ and a minimum dispersion error is obtained for $\beta = 2/5$ [Colour figure can be viewed at wileyonlinelibrary.com]

equation (49) to obtain

$$\left[\mathbf{A}^{-\top} \mathbf{C} \mathbf{A}^{-1} \mathbf{K} - \left(\frac{\Omega c_0}{h} \right)^2 \mathbf{I} \right] \mathbf{u}^h = \mathbf{0} \tag{51}$$

with a discrete solution vector for displacements

$$\mathbf{u}^h = U \left[\dots e^{-2i\kappa} e^{-i\kappa} 1 e^{i\kappa} e^{2i\kappa} \dots \right]^\top \tag{52}$$

obtaining a discrete system that repeats the same equilibrium equation at each location x_i of the lattice.

Finally, the extraction of i th row of system (51) provides us with the sought dispersion equation, relating the dimensionless numerical frequency Ω with the wave number κ and parameter β . This relation is represented in Figure 9 for quadratic (left) and cubic (right) B-spline interpolations and compared with the exact solution for an infinite elastic bar. We observe a divergent result for $\beta = 0$ (CMM), which invalidates the use of that particular RMM for practical purposes. However, it is also observed that convergence is recovered for some positive values of the mass averaging parameter ($\beta > 0$). In particular, a good low-mid frequency fitting is obtained for $\beta = 1/2$, clearly outperforming the accuracy of the LMM ($\beta = 1$).

In order to investigate this divergence issue, we perform a Taylor series expansion of (51) around $\kappa = 0$. For $p = 1$, traditional C^0 linear finite element shape functions, Fourier analysis using element matrices (45) and (46) yields the dispersion relation

$$\Omega^2 = \kappa^2 + \frac{5 - 8\beta}{12(1 + 2\beta)} \kappa^4 + \mathcal{O}(\kappa^6) \tag{53}$$

revealing that, for lower frequencies, the RMM obtained with mass parameterization diverges for $\beta \in [0, 5/8)$. In particular, it is fourth-order accurate for $\beta = 5/8$ and produce acceptable results for $\beta \in [5/8, 1]$.

Similarly, for quadratic B-splines, with element matrices given by (47) and (48), the Taylor expansion with respect to wavenumber κ yields the dispersion relation

$$\Omega^2 = \kappa^2 + \frac{3 - 7\beta}{4(1 + 3\beta)} \kappa^4 + \mathcal{O}(\kappa^6), \tag{54}$$

where it is observed that fourth-order approximation can be achieved by using $\beta = 3/7$ and the admissible interval of the averaging parameter is extended to $\beta \in [3/7, 1]$. Moreover, an optimization of parameter β for higher frequencies, see Figure 9, reveals that the best approximation is obtained for $\beta = 2/5$. Using $\beta = 2/5$ is a compromise to improve accuracy for the higher frequencies, maintaining second-order approximation for the lower frequencies. This value has been obtained empirically, minimizing by numerical experiment the dispersion error at $\kappa = \pi/2$.

Remark 4. For B-splines, the RMM obtained with an elementwise LD dual basis is very cheap to compute but should be used with care. It diverges for $\beta = 0$ (CMM) and is not able to provide accurate results. However, the use of mass parameterization with $\beta \in [2/5, 1)$ always provides a better approximation than the LMM diagonal mass inverse, although p -convergence property is not preserved.

It is worthy to mention that this type of LD B-spline dual basis has also been studied mathematically in the context of IGA mortar methods for contact problems by Seitz et al,³¹ observing that LD bases generated elementwise only guarantee partition of unity, and consequently, the *global* approximation order is limited to one in the L^2 -norm, independently of the *local* approximation order. This defect in the approximation order of the B-spline dual basis causes that optimal convergence rates cannot be guaranteed. Obviously, our elementwise dual basis reproduce the same convergence problems when utilized for inverse mass matrix computations, but these difficulties can be palliated with mass matrix parameterization techniques.²¹ Finally, it has been also investigated the use of sixth-order accurate element mass matrices⁴²⁻⁴⁴ instead of the fourth-order approximation given by (43) for $\beta = 0$. By adopting these high-order mass matrices, it is possible to increase the accuracy of the RMM, but the improvement is still not enough for its practical use with LD dual bases.

Remark 5. Because the RMM \mathbf{C} is by definition positive definite, the unsymmetric eigenvalue problem $[\mathbf{A}^{-\top}\mathbf{C}\mathbf{A}^{-1}\mathbf{K} - \omega_i^2\mathbf{I}] \boldsymbol{\phi}_i = 0$ represented by Equation (51) can be converted into a symmetric eigenvalue problem by a Cholesky decomposition of the RMM with $\mathbf{C} = \mathbf{L}\mathbf{L}^\top$, where \mathbf{L} is a lower triangular matrix. Then, the equivalent symmetric eigenvalue problem is obtained

$$[\mathbf{L}^\top\mathbf{A}^{-1}\mathbf{K}\mathbf{A}^{-\top}\mathbf{L} - \omega_i^2\mathbf{I}] \boldsymbol{\phi}_i = 0, \quad (55)$$

which has different eigenvectors but the same eigenvalues as the original unsymmetric problem.

7 | INCORPORATION OF BOUNDARY CONDITIONS WITH LAGRANGE MULTIPLIERS

As we mentioned earlier, in the connection with other patches or presence of Dirichlet boundary conditions, a direct computation of the mass inverse requires complicated modifications of the biorthogonal shape functions. We eliminate the necessity of these modifications by considering the patches as free-floating substructures and applying the boundary conditions through localized Lagrangian multipliers.¹⁰⁻¹³ To explain the enforcement of boundary conditions, we reorganize the semidiscrete EOMs (20)-(22) to obtain the following partitioned equation set:

$$\begin{bmatrix} \mathbf{M} & \mathbf{B} & \mathbf{0} \\ \mathbf{B}^\top & \mathbf{0} & -\mathbf{L}_b \\ \mathbf{0} & -\mathbf{L}_b^\top & \mathbf{0} \end{bmatrix} \begin{Bmatrix} \ddot{\mathbf{u}} \\ \lambda \\ \ddot{\mathbf{u}}_b \end{Bmatrix} = \begin{Bmatrix} \mathbf{r} \\ \mathbf{0} \\ \mathbf{0} \end{Bmatrix}, \quad (56)$$

where the second equation is simply twice time-differentiated expression of (21).

Let us assume now that the boundary acceleration vector ($\ddot{\mathbf{u}}_b$) consists of entirely the prescribed boundary quantities, regardless whether they are zero or nonzero. In this case, we obtain the accelerations ($\ddot{\mathbf{u}}$) from the first equation of (56) as

$$\ddot{\mathbf{u}} = \mathbf{M}^{-1}(\mathbf{r} - \mathbf{B}\lambda), \quad (57)$$

in which, once again, we emphasize that the computation of $\mathbf{M}^{-1} = \mathbf{A}^{-\top}\mathbf{C}\mathbf{A}^{-1}$ does not require additional computational effort because the global projection matrix \mathbf{A} is diagonal.

Then, substitute the accelerations obtained above into the second equation of (56)

$$\mathbf{B}^\top\mathbf{M}^{-1}(\mathbf{r} - \mathbf{B}\lambda) - \mathbf{L}_b\ddot{\mathbf{u}}_b = \mathbf{0} \quad (58)$$

to compute the Lagrange multipliers

$$\lambda = [\mathbf{B}^\top\mathbf{M}^{-1}\mathbf{B}]^{-1}(\mathbf{B}^\top\mathbf{M}^{-1}\mathbf{r} - \mathbf{L}_b\ddot{\mathbf{u}}_b) \quad (59)$$

as a function of the forces residual and the boundary conditions. Finally, substitute the multipliers back in the equilibrium equation (57) to obtain the final accelerations

$$\ddot{\mathbf{u}} = \mathbf{M}_b^{-1}\mathbf{r} + \mathbf{M}^{-1}\mathbf{B}[\mathbf{B}^\top\mathbf{M}^{-1}\mathbf{B}]^{-1}\mathbf{L}_b\ddot{\mathbf{u}}_b \quad (60)$$

with a constrained inverse mass matrix

$$\mathbf{M}_b^{-1} = \mathbf{M}^{-1} - \mathbf{M}^{-1}\mathbf{B}[\mathbf{B}^\top\mathbf{M}^{-1}\mathbf{B}]^{-1}\mathbf{B}^\top\mathbf{M}^{-1} \quad (61)$$

incorporating the applied boundary conditions. This transformation can also be understood as a projection of the free-floating mass matrix inverse.⁹

Once again, since the size of $[\mathbf{B}^T \mathbf{M}^{-1} \mathbf{B}]$ is small, pertaining only to the constrained degrees of freedom, its inversion is very cheap. It is also noted that $\ddot{\mathbf{u}}$ contains not only the interior but also the constrained degrees of freedom, and the imposition of boundary conditions will produce zeros in the associated rows and columns of \mathbf{M}_b^{-1} making it singular. These zero rows and columns, corresponding to restricted degrees of freedom, can be simply eliminated.

Algorithm 1 Procedure for the computation of the constrained inverse mass matrix \mathbf{M}_b^{-1}

for e **do** $1, \dots, N_e$ (elements)

 Compute parametrized element mass matrix:

$$\mathbf{M}_e = (1 - \beta) \mathbf{M}_e^C + \beta \mathbf{M}_e^L$$

 Assemble diagonal projection matrix:

$$\mathbf{A}_e = \frac{1}{\rho} \mathbf{M}_e^L \quad \longrightarrow \quad \mathbf{A} = \underset{e=1}{\overset{N_e}{\mathbf{A}}} \mathbf{A}_e$$

 Assemble reciprocal mass matrix:

$$\mathbf{C}_e = \mathbf{A}_e^T \mathbf{M}_e^{-1} \mathbf{A}_e \quad \longrightarrow \quad \mathbf{C} = \underset{e=1}{\overset{N_e}{\mathbf{A}}} \mathbf{C}_e$$

end for

 Compute the free-floating inverse mass matrix:

$$\mathbf{M}^{-1} = \mathbf{A}^{-T} \mathbf{C} \mathbf{A}^{-1}$$

 Obtain the projector:

$$\mathbf{P} = \mathbf{I} - \mathbf{M}^{-1} \mathbf{B} [\mathbf{B}^T \mathbf{M}^{-1} \mathbf{B}]^{-1} \mathbf{B}^T$$

 Apply boundary conditions by projection:

$$\mathbf{M}_b^{-1} = \mathbf{P} \mathbf{M}^{-1}$$

 Eliminate the rows and columns of \mathbf{M}_b^{-1} with applied boundary conditions

8 | NUMERICAL TESTS

In the following examples, for vibration analyses, we seek for an harmonic solutions that satisfy the EOM and fulfill the boundary conditions $\mathbf{u}_b = \mathbf{0}$. These solutions are obtained by solving the following eigenvalue problem:

$$[\mathbf{M}_b^{-1} \mathbf{K}_b - \omega^2 \mathbf{I}] \boldsymbol{\phi} = \mathbf{0}, \quad (62)$$

where \mathbf{M}_b^{-1} is the inverse mass matrix computed as described in Section 7 and \mathbf{K}_b is the stiffness matrix incorporating the applied boundary conditions. From the solution of this eigenvalue problem, we obtain the vibration frequencies ω_i of the system and its associated mode shapes $\boldsymbol{\phi}_i$ for mode number $i = 1, \dots, n$.

In time-domain analyses, for time integration of the semidiscrete equations of elastodynamics, we use the classical explicit central difference scheme.⁴⁵⁻⁴⁷ This method is among the most popular explicit methods in computational mechanics,⁴ based on a repetition of the basic steps summarized in Algorithm 2 until the total simulation time has been reached.

Algorithm 2 Explicit time integration by central difference scheme

Solve time $t = 0$:

$$\ddot{\mathbf{u}}^0 = \mathbf{M}_b^{-1} \mathbf{r}^0$$

for n **do** $1, \dots, n$ (time steps)

 Evaluate the forces residual:

$$\mathbf{r}^n = \mathbf{f}^n - \mathbf{K}_b \mathbf{u}^n$$

 Compute accelerations:

$$\ddot{\mathbf{u}}^n = \mathbf{M}_b^{-1} \mathbf{r}^n$$

 Update nodal velocities:

$$\dot{\mathbf{u}}^{n+\frac{1}{2}} = \dot{\mathbf{u}}^{n-\frac{1}{2}} + \Delta t \ddot{\mathbf{u}}^n$$

 Update nodal displacements:

$$\mathbf{u}^{n+1} = \mathbf{u}^n + \Delta t \dot{\mathbf{u}}^{n+\frac{1}{2}}$$

end for

It is well known that the explicit central difference scheme in linear dynamics is conditionally stable, so the time step Δt must be chosen below a critical value $\Delta t_{\text{crit}} = 2/\omega_{\text{max}}$, where ω_{max} is the maximum frequency of the system. We have seen that the proposed RMM with parameterization, obtained following the process described in Section 4, is able to retain the accuracy for lower frequencies reducing highest frequencies at the same time. This reduction automatically increases the critical time step, allowing the use of larger time steps and improving the computational efficiency.

To evaluate all element matrices we have used a Gauss-Legendre quadrature formula¹ of degree $p + 1$ over the knot intervals, where p is the order of the used B-spline or Bézier interpolation function. For the presentation of results, we have adopted the following nomenclature. Plots with labels IGA and IGA-BE are used as a reference, indicating results obtained with the exact IGA mass matrix inverse, computed respectively with B-splines or Bézier extraction. The proposed reciprocal matrix is referred as RMM and RMM-BE depending on the interpolation functions, B-splines or Bézier elements, respectively.

8.1 | Free vibration of a bar

In this first example, we analyze the accuracy of the proposed method for direct computation or RMMs by analyzing the free vibration of elastic bars. For this purpose, we consider we consider a long bar of length $L = 1$ m of uniform section. The material of the bar is linear elastic, with Young's modulus $E = 69$ GPa and constant volumetric mass density $\rho = 2700$ kg/m³.

The bar is discretized using a linear parameterization of 43 control points to investigate the accuracy of the RMM for quadratic and cubic $p = 2, 3$ orders of longitudinal displacement discretization. In particular, we investigate differences in the use of exact IGA inverses of the CMM and LMM matrices and the proposed approximation of the mass matrix inverse RMM computed with an optimized β .

8.1.1 | Free-free case

We start with the free-free case, by comparing the numerical frequencies with exact solutions obtained from continuum theory. The exact frequencies of this problem are $\omega_n^{\text{exact}} = (n - 1)c_0\pi/L$ rad/s for mode number $n = 1, 2, \dots$, where $c_0 = \sqrt{E/\rho}$ is the wave speed of compressive waves and $n = 0$ provides a zero eigenfrequency corresponding to the free rigid body motion.

Results for this case are presented in Figure 10 for two orders of approximation, quadratic $p = 2$ on the left and cubic $p = 3$ on the right, and two different discretization methods, B-splines on the top and Bézier extraction at the bottom. We include frequencies for the exact inverse of the IGA mass matrix, for CMM $\beta = 0$, optimized $\beta = 2/5$ and LLM $\beta = 1$ cases. For comparison, the RMM computed with the proposed method and optimized parameter $\beta = 2/5$ is also included.

It is well known^{27,48} and evident from inspection of Figure 10 (top) that, by increasing the order p of the LMM inverse, higher-order accuracy is not achieved. We also observe that the present method, using the RMM with $\beta = 2/5$, yields far better accuracy than the LMM for all frequencies. With quadratic B-splines, the optimized RMM is able to approximate almost half of the spectrum with good accuracy, first 20 modes are below 5% error, while for cubic order, it is reduced to the 15 first modes approximately. However, in general, increasing the approximation order either for B-spline or Bézier approximations, expands the nonzero elements of the banded mass matrix and reduces the accuracy in the mid and high frequency range.

The RMM for Bézier elements, on the contrary, is completely stable for $\beta = 0$ conserving the p -convergence property, see Figure 10 (bottom) for cases $p = 2, 3$. It can also be observed that although Bézier extraction introduces higher branching in the spectrum,⁴⁹ its accuracy is very close to the B-splines approximation. This branching is caused by the two distinct types of equations for the Bézier-based elements: those corresponding to nodes located at the element boundaries, and those corresponding to the internal nodes located inside the element.²⁷ Note that the number of branches coincide with the Bézier element degree.

Moreover, RMM produces a maximum frequency around 40% lower than the exact IGA consistent matrix (IGA $\beta = 0$), so the critical time step for explicit time integration with the RMM can be reduced by the same amount. This is close to the 55% reduction of the diagonal LMM but without so much degradation of the accuracy for the low frequencies.

Finally, we explore the accuracy of GC dual bases in the bar frequencies. In particular, we use the inverse *Gram* matrix and the *weight-adjusted* to compute the RMM for different B-spline basis orders. The results are shown in Figure 11, where

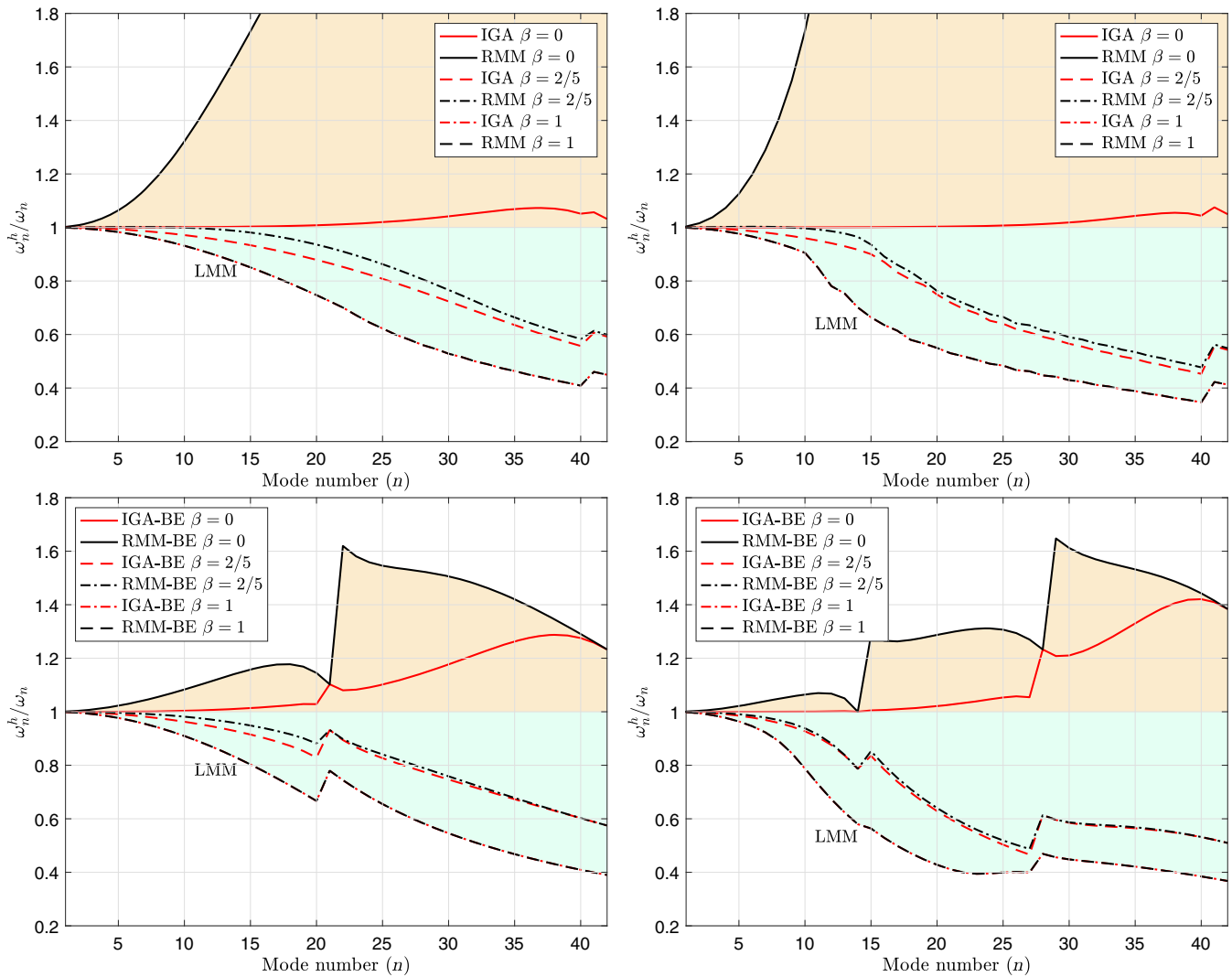


FIGURE 10 Free-free bar vibration problem computed with local discontinuous dual basis. Error in the frequencies for quadratic $p = 2$ (left) and cubic $p = 3$ (right) orders using B-splines (top) and Bézier extraction discretizations (bottom). The RMM with $\beta = 0$ (CMM) produces divergent results for B-splines and p -convergent behaviour for Bézier elements. In all cases, RMM with an optimized parameter $\beta = 2/5$ are able to capture correctly the low frequency band providing higher accuracy than LMM ($\beta = 1$) for the full frequency spectrum. CMM, consistent mass matrix; IGA, isogeometric analysis; LMM, lumped mass matrix; RMM, reciprocal mass matrix

it is observed that the frequency error is totally equivalent to the IGA mass matrix and p -converge is maintained. Once again, note that the evaluation of these two reciprocal bases requires two costly operations, invert the Gramian matrix (left) and invert the mass matrix of the parametric domain (right), but, nevertheless, these operations are cheaper than the inversion of the original mass matrix.

8.1.2 | Fixed-free bar

Now, to test the proposed technique for applying boundary conditions using LLMs described in Section 7, we proceed to fix the displacement of the first control point located on the left side of the bar. In terms of frequencies, the only difference with the free-free case is in the restriction of the rigid body motion of the bar and the shift of exact frequencies to $\omega_n^{\text{exact}} = (n - 1/2)c_0\pi/L$ for mode number $n = 1, 2, \dots$

Figure 12 contains the results obtained for this case. We corroborate that accuracy is not affected by the imposition of boundary conditions through LLMs and the results are completely equivalent. In this case, we have tested the RMM

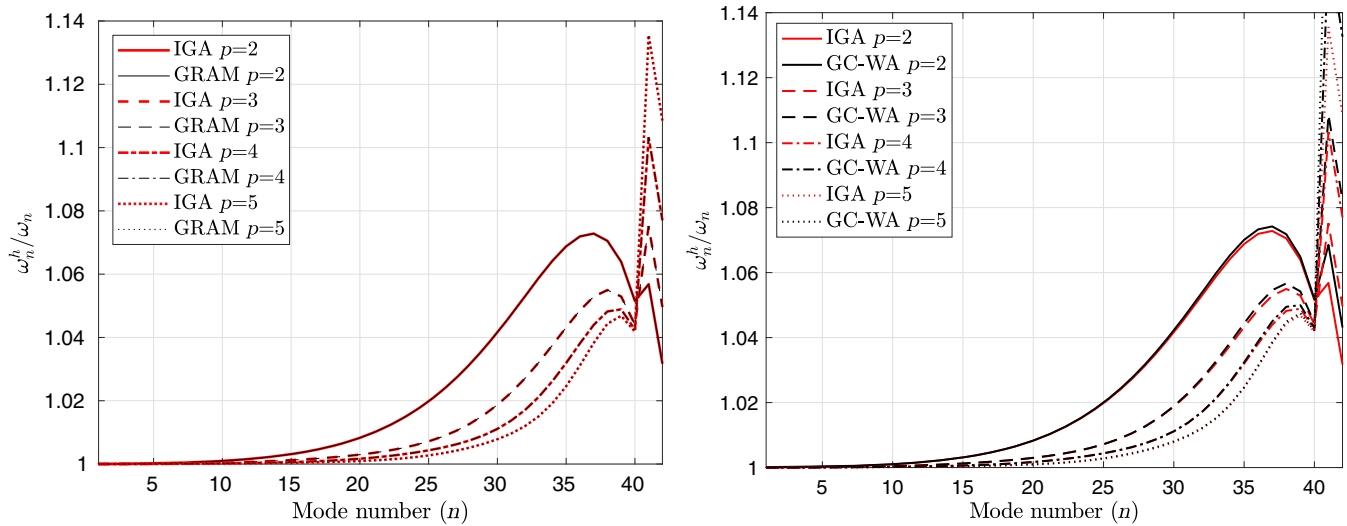


FIGURE 11 Error in the natural frequencies of a free-free bar computed using GC dual bases. The inverse *Gram* matrix (left) and the *weight-adjusted* (GC-WA) basis (right) produce p -convergent approximations. These GC bases provide high accuracy, but at the price of elevated computational cost in the case of the *Gram* matrix and loss of generality for the *weight-adjusted* basis. GC, global continuous; IGA, isogeometric analysis

with $\beta = 2/5$ that provides very similar approximation of the bar frequencies. The results confirm that using the present method to approximate the inverse mass matrix yields much better accuracy than the LMM with similar computational effort.

8.2 | Free vibration of a cantilevered tapered plate: FV32 test

This example is a plane-stress test proposed by the National Agency for Finite Element Methods and Standards.⁵⁰ In particular, the dynamic case FV32 for checking the accuracy of flexural and longitudinal modes, where the natural frequencies of a trapezoidal elastic plate are analyzed. The geometry and dimensions of the plate are represented in Figure 13 together with the boundary conditions. It is assumed a linear elastic material with Young's modulus $E = 200$ GPa, Poisson's ratio $\nu = 0.3$, and density $\rho = 8000$ kg/m³.

First, the plate is discretized using a single patch with a regular mesh of 10×10 control points and quadratic isogeometric NURBS-based elements, constraining the horizontal and vertical displacements of the 10 control points located at $x = 0$, a lateral side of the plate. The knot points vector $\Xi = \{0, 0, 0, 0.125, 0.25, 0.375, 0.5, 0.625, 0.75, 0.875, 1, 1, 1\}$ is used in each direction to construct a regular 2D patch $\Xi \times \Xi$ with B-splines of order $p = 2$.

Next, the Bézier extraction process is applied to the patch of quadratic B-splines, see Figure 14, producing a mesh of 5×5 Bézier elements with 11×11 nodes. Note that, in both cases, these are more refined meshes than the one proposed in the original NAFEMS benchmark case that uses quadrilateral finite elements.

This is a particular example where the *weight-adjusted* dual basis (34) is readily applicable, because the parametric domain is completely regular and the parametrical-to-physical geometrical transformation is an affine mapping, hence Jacobian of the transformation is constant.

The first nine mode shapes of the plate are illustrated in Figure 15 and their associated frequencies, obtained with different mass matrix inverses, arranged in Table 1. As a reference, we use the frequencies computed with the original mass matrix, IGA or IGA-BE (CMM). These frequencies are very close to the NAFEMS test for FEM and results from other authors obtained with different RMM proposals.

First, we note that GC-Gram and GC-WA bases produce exactly the same frequencies and are able to approximate the correct values with negligible error, confirming once again the superiority of these GC bases over the LD ones. Nevertheless, the LD-RMM computed with $\beta = 2/5$ provides a very good fit, with maximum difference obtained respectively in the fourth mode with 1.8% error and the fifth mode with 4.9% error. Note that they correspond to flexural modes that are more difficult to capture than extension modes, see Figure 15. For Bézier elements, maximum errors correspond to the same flexural modes with values under 8%.

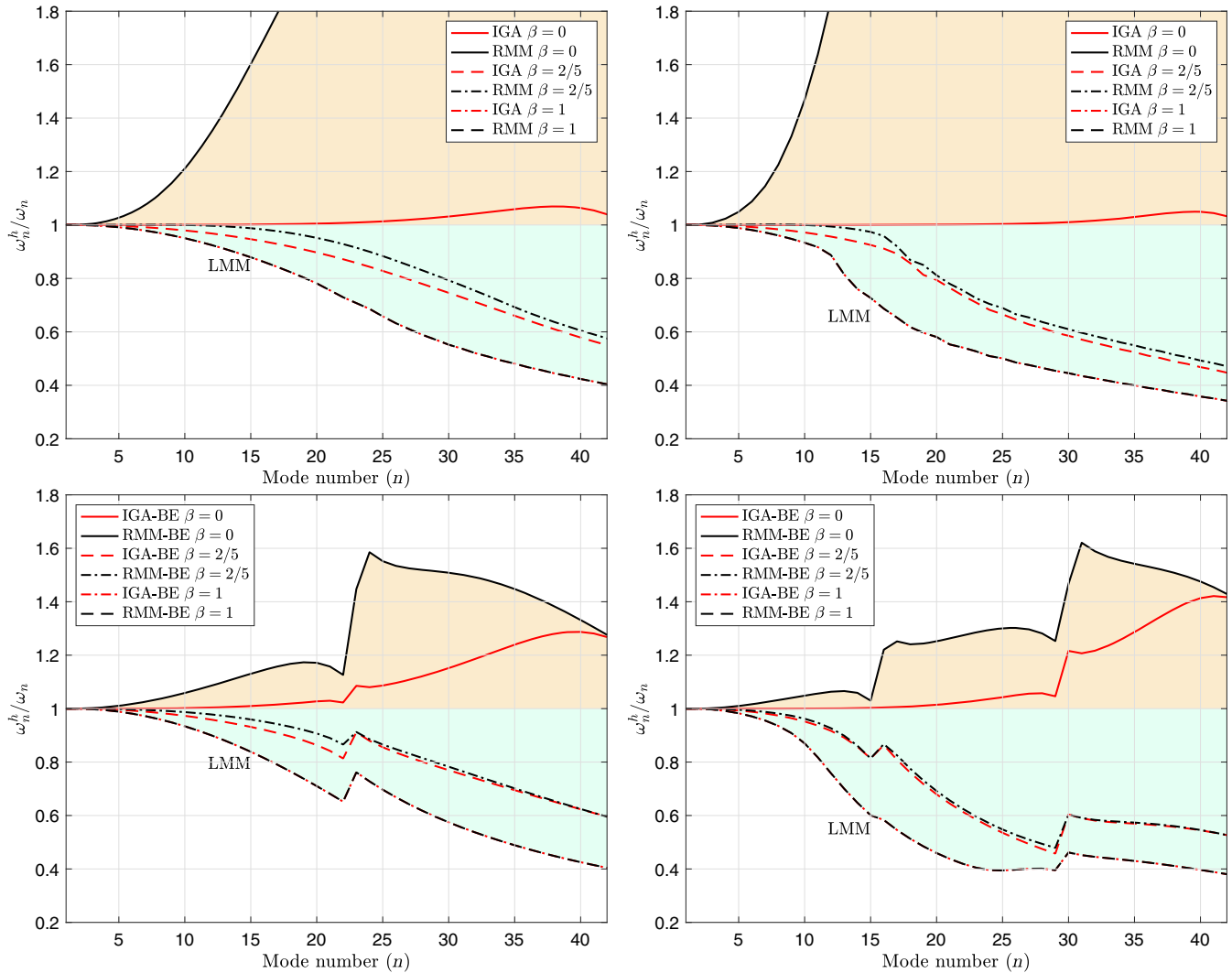


FIGURE 12 Fixed-free bar problem computed with local discontinuous dual basis. Error in the frequencies for quadratic $p = 2$ (left) and cubic $p = 3$ (right) orders using B-splines (top) and Bézier extraction discretizations (bottom). We observe that RMM with $\beta = 0$ (CMM) produces divergent results for B-splines and p -convergent behaviour for Bézier elements. In all cases, RMM with an optimized parameter $\beta = 2/5$ are able to capture correctly the low frequency band providing higher accuracy than LMM ($\beta = 1$) for the full frequency spectrum. CMM, consistent mass matrix; IGA, isogeometric analysis; LMM, lumped mass matrix; RMM, reciprocal mass matrix

In general, it is verified that the proposed RMM obtained with LD bases and mass matrix parameterization is a better alternative than the LMM for all modes.

8.3 | Free vibration of a clamped thin circular plate

This numerical example is inspired by the work of Cottrell et al.,²² where the problem of free vibration of a thin circular plate is solved. The purpose of this example is to show the behavior of the proposed method also for a domain with a curved boundary. The circular plate has a radius $r = 2$ m and thickness $t = 0.02$ mm. Although it would seem natural to model the plate using shell finite elements, we follow the aforementioned work²² and model the circular plate as a 3D body. Material of the plate is considered to be linear elastic with Young's modulus $E = 30$ GPa, Poisson's ratio $\nu = 0.2$, and density $\rho = 2320$ kg/m³.

Similar to the preceding example, the plate is first discretized using a single patch with a regular mesh of $18 \times 18 \times 3$ control points and quadratic isogeometric NURBS-based elements, clamping of the control points located at $x^2 + y^2 = r^2$ as represented in Figure 16. The knot vectors $\Xi_1 = \Xi_2 = \{0, 0, 0, 1/16, 2/16, \dots, 15/16, 1, 1, 1\}$ and $\Xi_3 = \{0, 0, 0, 1, 1, 1\}$

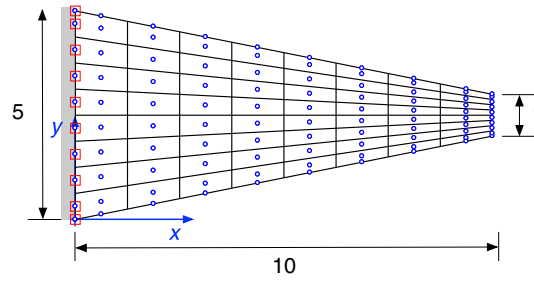


FIGURE 13 NAFEMS benchmark case FV32. Geometry with dimensions in meters and zero boundary displacements imposed on the lateral side of the plate at $x = 0$. The isogeometric analysis regular mesh presents $l \times m = 10 \times 10$ control points, indicated in blue, and uses quadratic B-spline interpolation functions in both directions

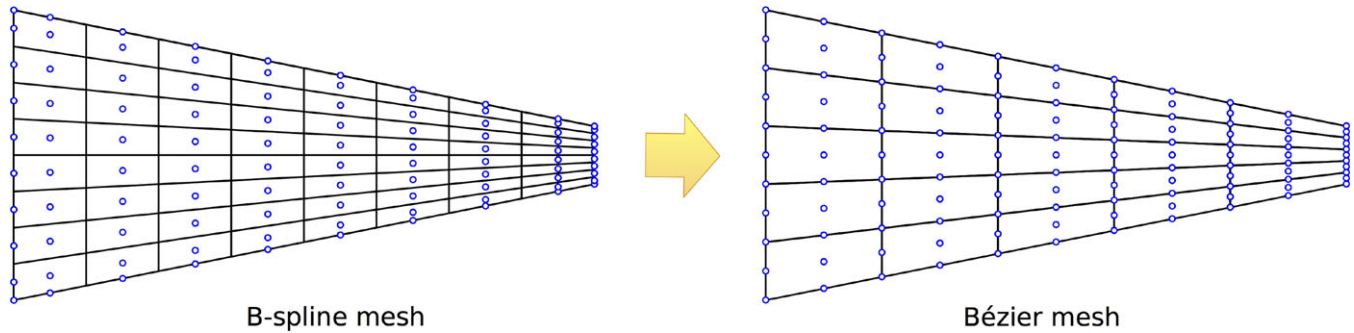


FIGURE 14 A computational isogeometric analysis mesh based on B-spline shape functions (on the left) and based on Bézier shape functions after Bézier extrapolation (on the right) [Colour figure can be viewed at wileyonlinelibrary.com]

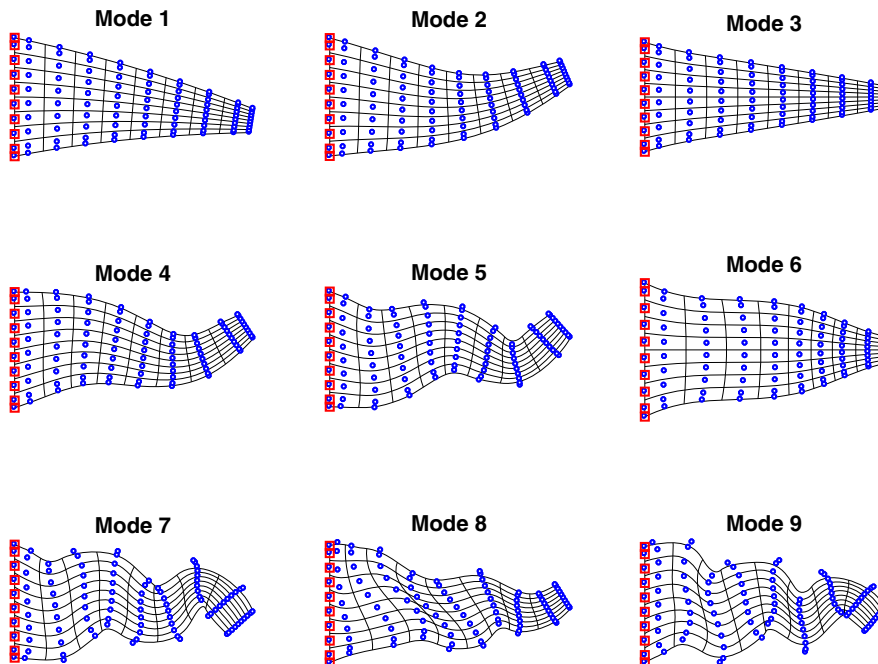


FIGURE 15 NAFEMS benchmark case FV32. Representation of the nine lowest vibration modes occurring at frequencies contained in Table 1. Results correspond to the proposed reciprocal mass matrix with parameter $\beta = 2/5$ computed with quadratic B-splines [Colour figure can be viewed at wileyonlinelibrary.com]

are used in each parametric direction to construct a 3D patch $\Xi_1 \times \Xi_2 \times \Xi_3$ with NURBS of order $p = 2$. Details regarding the used parameterization can be found in the work of Anděl et al.⁵¹

TABLE 1 Plane-stress case FV-32 from NAFEMS. Six lowest frequencies obtained with different mass matrices

Frequency (Hz)	Mode 1	Mode 2	Mode 3	Mode 4	Mode 5	Mode 6
NAFEMS ⁵⁰ (FEM)	44.623	130.03	162.70	246.05	379.90	391.44
Tkachuk and Bischoff ⁸ (FEM)	45.499	133.55	162.89	255.37	393.16	398.56
Schaeuble et al ²¹ (IGA) VSRMS [†]	44.615	128.489	162.860	235.104	335.874	385.989
IGA $\beta = 0$ (CMM)	44.634	130.107	162.709	246.639	382.937	391.525
IGA $\beta = 1$ (LMM)	44.022	122.936	161.413	218.492	308.210	373.077
LD-RMM $\beta = 2/5$	44.645	129.581	162.720	241.956	363.728	390.592
GC-Gram	44.634	130.107	162.709	246.639	382.937	391.525
GC-WA	44.634	130.107	162.709	246.641	382.961	391.526
IGA-BE $\beta = 0$ (CMM)	44.651	130.343	162.730	248.396	389.846	391.848
IGA-BE $\beta = 1$ (LMM)	44.096	123.304	161.532	219.363	309.573	374.468
LD-RMM-BE $\beta = 2/5$	44.544	128.531	162.489	238.999	358.320	387.791

The cited references use different meshes and methods.

[†]Variationally scaled consistent inverse mass matrices.

Abbreviations: CMM, consistent mass matrix; GC, global continuous; IGA, isogeometric analysis; LD, local discontinuous; LMM, lumped mass matrix; RMM, reciprocal mass matrix; WA, weight-adjusted.

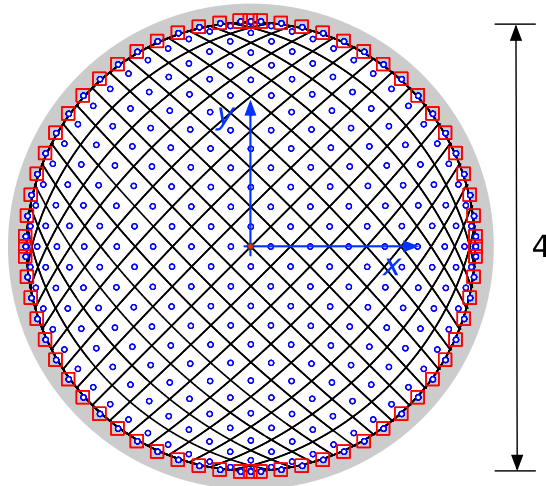


FIGURE 16 Clamped thin circular plate. Geometry with diameter in meters and zero boundary displacements imposed on the lateral side of the plate at $x^2 + y^2 = 4$. The isogeometric analysis mesh presents $l \times m \times n = 18 \times 18 \times 3$ control points, indicated in blue, and uses quadratic NURBS interpolation functions in all three directions

Again, the Bézier extraction process is applied to the patch of quadratic B-splines, see Figure 17, producing a mesh of $8 \times 8 \times 1$ Bézier elements with $17 \times 17 \times 3$ control points.

The three first symmetric ω_{01} , ω_{11} and antisymmetric ω_{02} eigenmodes²² are illustrated in Figure 18, and their associated frequencies, obtained with different mass matrix inverses, are summarized in Table 2. Classical IGA with CMM gives the first three eigenmodes at frequencies $\omega_{01} = 57.636$ rad/s, $\omega_{11} = 127.061$ rad/s, and $\omega_{02} = 260.913$ rad/s that are used as a reference. Note that GC-Gram basis produces again a perfect approximation. As predicted by dispersion analysis, the LD-RMM with best fit is obtained for $\beta = 2/5$, see IGA RMM results in Table 2, presenting discrepancies of 0.05%, 0.04%, and 0.2%, respectively.

Observing now the IGE-BE (CMM) solution, a slightly poorer approximation is obtained for the Bézier extraction results, compared to IGA with NURBS basis functions. The average relative errors for the Bézier extraction for eigenfrequencies ω_{01} , ω_{11} , and ω_{02} are 0.3%, 0.8%, and 2%, respectively. It is important to mention again that the accuracy of the results for LC-RMM crucially depends on the selection of an appropriated value for the parameterization factor β . Its value has been derived from 1D dispersion analyses and its optimization for 2D cases deserves further study.

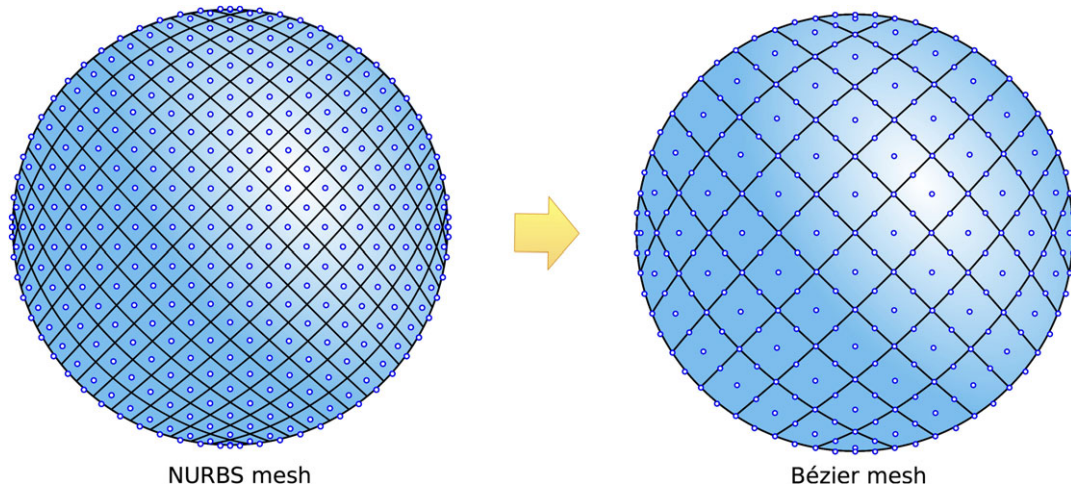


FIGURE 17 A computational isogeometric analysis mesh based on NURBS basis functions (on the left) and based on Bézier shape functions after Bézier extrapolation (on the right) [Colour figure can be viewed at wileyonlinelibrary.com]

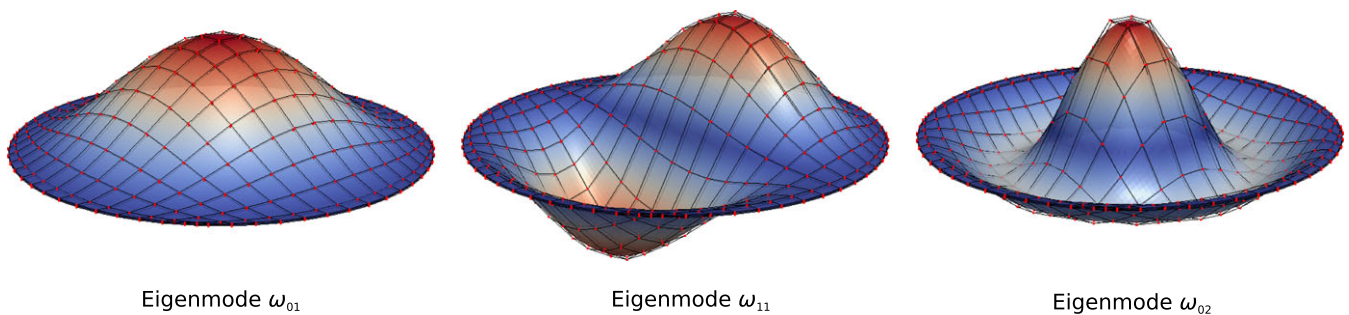


FIGURE 18 Clamped thin circular plate. Two symmetric and one antisymmetric vibration modes corresponding respectively to frequencies ω_{01} , ω_{02} , and ω_{11} [Colour figure can be viewed at wileyonlinelibrary.com]

TABLE 2 Clamped thin circular plate. Three lowest eigenfrequencies obtained with different mass matrices

Frequency (rad/s)	IGA			Bézier Extraction		
	ω_{01}	ω_{11}	ω_{02}	ω_{01}	ω_{11}	ω_{02}
IGA $\beta = 0$ (CMM)	57.636	127.061	260.913	55.933	119.250	231.591
IGA $\beta = 1$ (LMM)	56.947	123.291	245.604	55.022	114.317	211.815
LD-RMM $\beta = 2/5$	57.666	127.114	260.358	55.774	118.274	226.896
GC-Gram	57.636	127.061	260.914	-	-	-

Abbreviations: CMM, consistent mass matrix; GC, global continuous; IGA, isogeometric analysis; LD, local discontinuous; LMM, lumped mass matrix.

8.4 | Transient analysis of a cantilever beam under self weight

Finally, to test the RMM with a transient case, we consider a 3D cantilever beam under self weight with a sudden application of the gravity load at time $t = 0$ seconds. The geometrical definition of the problem is shown in Figure 19 (left), where a cantilever beam of length $L = 10$ m and section width $b = 4$ m with height $h = 2$ m are considered. The elastic material properties of the beam are $E = 10$ MPa, $\nu = 0.3$, and density $\rho = 100$ kg/m³ with a gravity acceleration $g = 9.81$ m/s².

The parametric domain is defined by a 3D patch constructed with knot spans on each direction $\Xi_1 = \{\xi_1, \dots, \xi_{l+p+1}\}$ with $\Delta\xi = 1/19$, $\Xi_2 = \{\eta_1, \dots, \eta_{m+p+1}\}$ with $\Delta\eta = 1/5$, and $\Xi_3 = \{\mu_1, \dots, \mu_{n+p+1}\}$ with $\Delta\mu = 1/3$. Quadratic B-splines with $p = 2$ are used in the three directions. Elements are defined in the parametric space $\Xi_1 \times \Xi_2 \times \Xi_3$ as nonzero knot spans, $[\xi_i, \xi_{i+1}] \times [\eta_i, \eta_{i+1}] \times [\mu_i, \mu_{i+1}]$ and elements in the physical space are images of their parametric counterparts.

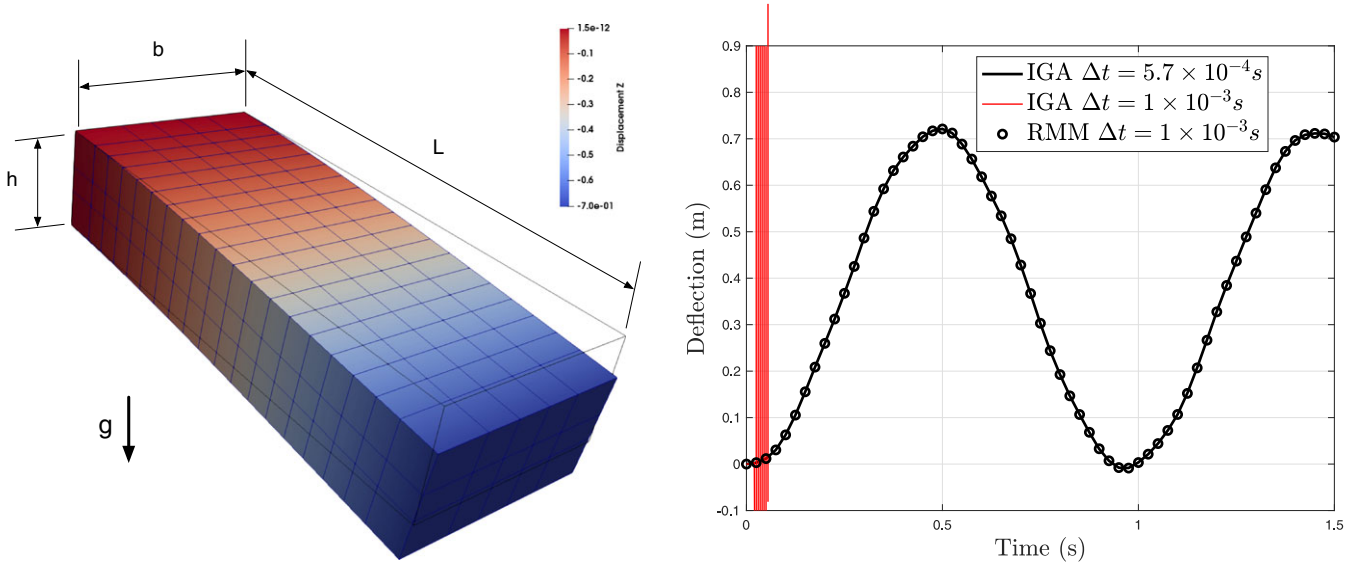


FIGURE 19 Cantilever beam under sudden gravity load. Geometry, dimensions, and mesh with elements defined in the physical space. Deformation with contours of vertical displacement at time $t = 1.5$ seconds computed with the reciprocal mass matrix (RMM) (left). Comparison of tip deflections $|u_z|$ obtained with explicit isogeometric analysis (IGA) and critical time step, IGA with large time step and the reciprocal mass matrix RMM with $\beta = 2/5$ (right)

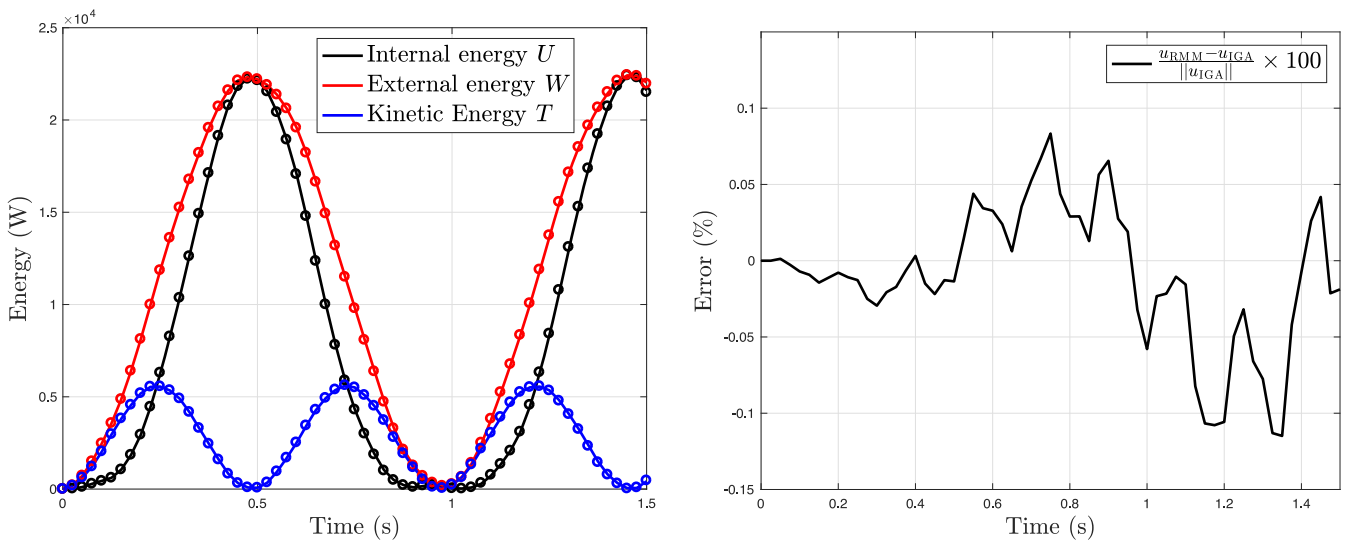


FIGURE 20 Results of the tip loaded cantilever beam. Evolution of the internal, external and kinetic energies in the beam (left). Solutions obtained using the proposed reciprocal mass matrix (RMM) inverse matrix are represented with dots. Error evolution of the beam tip deflection computed with RMM $\beta = 2/5$ (right)

This patch describes the physical domain with a mesh of $l \times m \times n = 21 \times 7 \times 5 = 735$ control points, producing a total number of $735 \times 3 = 2205$ unknowns except for those control points located at the plane $x = 0$ that are restricted in the three directions of space.

An exact eigenvalue analysis of the problem with a CMM reveals that the maximum frequency of the structure is $\omega_{\max} = 3510.5$ rad/s; hence, the critical time step for stability of the central difference scheme is $\Delta t_{\text{crit}}^{\text{IGA}} = 5.7 \times 10^{-4}$ seconds. This critical time step is utilized to compute the reference solution of the problem. The use of RMM with $\beta = 2/5$ reduces the maximum frequency to $\omega_{\max} = 1554.8$ rad/s, increasing the critical time step to $\Delta t_{\text{crit}}^{\text{RMM}} = 0.0013$ seconds, ie, 2.3 times larger than the initial critical time step. Then, a time step $\Delta t = 0.001$ seconds is selected to perform time-domain analysis, integrating in time the response of the beam with the explicit central difference method described in Algorithm 2. It is observed in Figure 19 (right) that this large time step $\Delta t \gg \Delta t_{\text{crit}}^{\text{IGA}}$ produces unstable results with classical IGA, while the

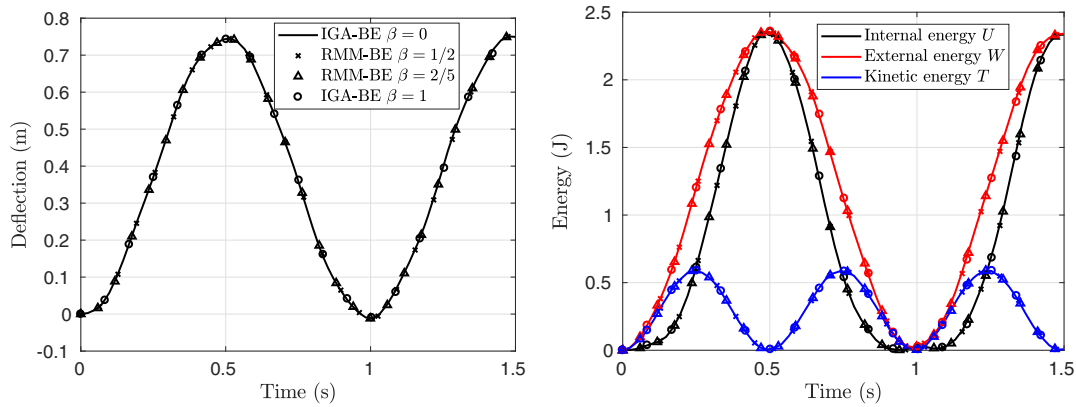


FIGURE 21 Results of the tip loaded cantilever beam discretized by the Bézier elements. Comparison of tip deflections $|u_z|$ obtained with the exact consistent and lumped mass matrices (isogeometric analysis [IGA]) and the reciprocal mass matrix (RMM) with parameters $\beta = 1/2$ and $\beta = 2/5$ (left). Evolution of the internal, external and kinetic energies in the beam (right)

RMM with $\Delta t \leq \Delta t_{\text{crit}}^{\text{RMM}}$ is able to obtain a stable and very accurate solution. In all the cases, initial conditions of the beam are assumed to be zero displacements and velocities, applying the full gravity load at the initial time step.

The results are shown in Figures 19 and 20 for NURBS and Figure 21 for Bézier elements. We have selected for comparison the RMM computed with different values of the parameter $\beta = \{0, 2/5, 1/2, 1\}$, representing the evolution of the tip deflection of the beam with both approximation methods in Figures 19 (right) and 21 (left). We also compare the time evolution of total internal U , external W , and kinetic T energies.

Finally, in Figure 20 (right), it is represented the relative error $(u - u_{\text{exact}})/|u_{\text{exact}}|$ of the tip displacement u , computed with the proposed RMM ($\beta = 2/5$). It is observed that the error remains under 0.12% during the 1.5 seconds of simulation, indicating a very good agreement with the reference solution.

9 | CONCLUSIONS

In structural dynamics, classical explicit time-integration methods equipped with a direct solver require an initial factorization of the mass matrix and repeat subsequent forward and backward substitution operations every time step. If we choose Cholesky factorization, for example, the total cost of this process is around $\mathcal{O}(n^3/3)$ flops plus $\mathcal{O}(2n^2)$ operations per time step for each forward-backward substitution. With a direct approximation of the inverse mass matrix, factorization cost is eliminated and operation count per time step is reduced to a sparse matrix-vector multiplication $\mathcal{O}(mn)$ flops, where m is the average number of nonzero entries per row.

This work presents a variational framework for the direct generation of inverse mass matrices that can be used for the IGA of elastodynamic problems. The method requires the definition of an appropriated dual basis for the momentum field and the influence of the selected reciprocal basis in the efficiency and accuracy of the results has been analyzed for the case of B-splines and Bézier elements. In particular, three types of dual bases have been studied: one LD and two GC based, respectively, on the inverse *Gram* matrix and a *weight-adjustment* of the primal basis through the Jacobian of the transformation.

It is observed that, in terms of computational efficiency and accuracy, LD dual basis combined with mass matrix parameterization produces an RMM that can be a better alternative than the LMM for all frequencies and IGA approximation orders. However, elementwise construction of LD dual basis functions for B-splines with the CMM ($\beta = 0$), produces divergent results. That is not the case for other approximations with C^0 continuity, like Bézier and high-order isoparametric finite elements for example, that produce RMMs that retain the p -convergence property for $\beta = 0$. In general, the combination of mass averaging ($\beta > 0$) with LD bases forbids p -convergence for B-spline and Bézier elements of order $p \geq 2$. On the contrary, the GC *Gram* basis is able to achieve high accuracy for any approximation order. Nevertheless, global dual bases produce fully populated inverses and entail higher computational costs. The inverse *Gram* basis requires the inversion of a block-diagonal symmetric matrix and *weight-adjusted* dual basis computational efficiency

greatly depends on the regularity of the mesh defined on the parametric space. Moreover, the final inverse mass matrix becomes a fully populated symmetric matrix.

In the present method, inter-patch compatibility and Dirichlet boundary conditions are handled by the method of LLMs. This process is completely general, avoids the need for dual basis function modifications near the boundary conditions, and is found to be computationally efficient because it only requires the factorization of a small element-like matrix associated with the constrained DOFs.

In conclusion, the proposed variational framework for the computation of IGA inverse mass matrices is completely general but, in terms of accuracy and efficiency, its results are influenced by a proper selection of the dual basis. The investigation of analytical LC basis for high-dimensional NURBS and more efficient algorithms for the GC dual basis computation remain an open issue, which we will consider in future work.

ACKNOWLEDGEMENTS

The work of J. Kopačka and R. Kolman was supported by the Centre of Excellence for Nonlinear Dynamic Behaviour of Advanced Materials in Engineering under grant CZ.02.1.01/0.0/0.0/15 003/0000493 (Excellent Research Teams) in the framework of Operational Program Research, Development and Education and by the Czech Science Foundation under project 17-22615S, 17-12925S, and 16-03823S within institutional support RVO:61388998. In addition, S. S. Cho was partially supported by the Nuclear Safety Research Program through the Korea Foundation of Nuclear Safety (KOFONS), granted financial resource from the Nuclear Safety and Security Commission (NSSC), Republic of Korea (No. 1503003).

ORCID

José A. González  <https://orcid.org/0000-0003-3282-0049>

R. Kolman  <https://orcid.org/0000-0002-8167-3535>

S. S. Cho  <https://orcid.org/0000-0003-0306-4694>

K. C. Park  <https://orcid.org/0000-0002-6303-1010>

REFERENCES

- Hughes TJR. *The Finite Element Method: Linear Static and Dynamic Finite Element Analysis*. Mineola, NY: Dover Publications; 2000.
- Zienkiewicz OC, Taylor RL, Zhu JZ. *The Finite Element Method: Its Basis and Fundamentals*. 6th ed. Burlington, MA: Elsevier Butterworth-Heinemann; 2005.
- Wu SR, Gu L. *Introduction to the Explicit Finite Element Method for Nonlinear Transient Dynamics*. Hoboken, NJ: John Wiley & Sons Inc; 2012.
- Belytschko T, Liu WK, Moran B, Elkhodary KI. *Nonlinear Finite Elements for Continua and Structures*. 2nd ed. Hoboken, NJ: John Wiley & Sons Ltd.; 2014.
- Garoni C, Speleers H, Ekström S-E, Reali A, Serra-Capizzano S, Hughes TJR. Symbol-based analysis of finite element and isogeometric B-spline discretizations of eigenvalue problems: exposition and review. *Arch Comput Methods Eng*. 2018. In press.
- Tkachuk A, Wohlmuth BI, Bischoff M. Hybrid-mixed discretization of elasto-dynamic contact problems using consistent singular mass matrices. *Int J Numer Methods Eng*. 2013;94(5):473-493.
- Tkachuk A, Bischoff M. Local and global strategies for optimal selective mass scaling. *Comput Mech*. 2014;53(6):1197-1207.
- Tkachuk A, Bischoff M. Direct and sparse construction of consistent inverse mass matrices: general variational formulation and application to selective mass scaling. *Int J Numer Methods Eng*. 2015;101(6):435-469.
- González JA, Kolman R, Cho SS, Felippa CA, Park KC. Inverse mass matrix via the method of localized Lagrange multipliers. *Int J Numer Methods Eng*. 2017;113(2):277-295.
- Park KC, Felippa CA. A variational framework for solution method developments in structural mechanics. *J Appl Mech*. 1998;65(1):242-249.
- Park KC, Felippa CA. A variational principle for the formulation of partitioned structural systems. *Int J Numer Methods Eng*. 2000;47:395-418.
- Park KC, Felippa CA, Gumaste UA. A localized version of the method of Lagrange multipliers and its applications. *Comput Mech*. 2000;24(6):476-490.
- González JA, Park KC, Felippa CA, Abascal R. A formulation based on localized Lagrange multipliers for BEM-FEM coupling in contact problems. *Comput Methods Appl Mech Eng*. 2008;197(6-8):623-640.
- Auricchio F, Beirão da Veiga L, Hughes TJR, Reali A, Sangalli G. Isogeometric collocation methods. *Math Models Methods Appl Sci*. 2010;20(11):2075-2107.

15. Auricchio F, Beirão da Veiga L, Hughes TJR, Reali A, Sangalli G. Isogeometric collocation for elastostatics and explicit dynamics. *Comput Methods Appl Mech Eng*. 2012;249-252:2-14.
16. Gao L, Calo VM. Fast isogeometric solvers for explicit dynamics. *Comput Methods Appl Mech Eng*. 2014;274:19-41.
17. Sangalli G, Tani M. Isogeometric preconditioners based on fast solvers for the Sylvester equation. *SIAM J Sci Comput*. 2016;6(38):A3644-A3671.
18. Hofreither C, Takacs S. Robust multigrid for isogeometric analysis based on stable splittings of spline spaces. *SIAM J Numer Anal*. 2017;55(4):2004-2024.
19. Donatelli M, Garoni C, Manni C, Serra-Capizzano S, Speleers H. Symbol-based multigrid methods for Galerkin B-spline isogeometric analysis. *SIAM J Numer Anal*. 2017;55(1):31-62.
20. Chan J, Evans JA. Multi-patch discontinuous Galerkin isogeometric analysis for wave propagation: explicit time-stepping and efficient mass matrix inversion. *Comput Meth Appl Mech Eng*. 2018;333:22-54.
21. Schaeuble A-K, Tkachuk A, Bischoff M. Variationally consistent inertia templates for B-spline- and NURBS-based FEM: inertia scaling and customization. *Comput Meth Appl Mech Eng*. 2017;326:596-621.
22. Cottrell JA, Reali A, Bazilevs Y, Hughes TJR. Isogeometric analysis of structural vibrations. *Comput Meth Appl Mech Eng*. 2006;195(41-43):5257-5296.
23. Hughes TJR, Evans JA, Reali A. Finite element and NURBS approximations of eigenvalue, boundary-value, and initial-value problems. *Comput Meth Appl Mech Eng*. 2014;272:290-320.
24. Hughes TJR, Reali A, Sangalli G. Duality and unified analysis of discrete approximations in structural dynamics and wave propagation: comparison of p -method finite elements with k -method NURBS. *Comput Meth Appl Mech Eng*. 2008;197(49-50):4104-4124.
25. Reali A. An isogeometric analysis approach for the study of structural vibrations. *J Earthq Eng*. 2006;10:1-30.
26. Bazilevs Y, Beirão da Veiga L, Cottrell JA, Hughes TJR, Sangalli G. Isogeometric analysis: approximation, stability and error estimates for h -refined meshes. *Math Models Methods Appl Sci*. 2006;16(7):1031-1090.
27. Cottrell JA, Hughes TJR, Bazilevs Y. *Isogeometric Analysis: Toward Integration of CAD and FEA*. Chichester, UK: John Wiley & Sons; 2009.
28. Piegel L, Tiller W. *The NURBS Book*. 2nd ed. Berlin, Germany: Springer-Verlag Berlin Heidelberg; 1997. *Monographs in Visual Communication*.
29. Borden MJ, Scott MA, Evans JA, Hughes TJR. Isogeometric finite element data structures based on Bézier extraction of NURBS. *Int J Numer Methods Eng*. 2011;87(1-5):15-47. <http://doi.org/10.1002/nme.2968>
30. Brivadis E, Buffa A, Wohlmuth B, Wunderlich L. Isogeometric mortar methods. *Comput Methods Appl Mech Eng*. 2015;284:292-319.
31. Seitz A, Farah P, Kremheller J, Wohlmuth BI, Wall WA, Popp A. Isogeometric dual mortar methods for computational contact mechanics. *Comput Methods Appl Mech Eng*. 2016;301:259-280.
32. Dornisch W, Stöckler J, Müller R. Dual and approximate dual basis functions for B-splines and NURBS – comparison and application for an efficient coupling of patches with the isogeometric mortar method. *Comput Methods Appl Mech Eng*. 2017;316:449-496.
33. Scherer K, Schumaker LL. A dual basis for L -splines and applications. *J Approx Theory*. 1980;29(2):151-169.
34. Schumaker LL. *Spline Functions: Basic Theory*. 3rd ed. Cambridge, UK: Cambridge University Press; 2007.
35. Lamichhane BP, Wohlmuth BI. Biorthogonal bases with local support and approximation properties. *Math Comp*. 2007;76(257):233-249.
36. Woźny P. Construction of dual bases. *J Comput Appl Math*. 2013;245:75-85.
37. Zou Z, Scott MA, Borden MJ, Thomas DC, Dornisch W, Brivadis E. Isogeometric Bézier dual mortaring: refineable higher-order spline dual bases and weakly continuous geometry. *Comput Methods Appl Mech Eng*. 2018;333:497-534.
38. Tkachuk A, Bischoff M. Variational methods for selective mass scaling. *Comput Mech*. 2013;52(3):563-570.
39. Felippa CA, Guo Q, Park KC. Mass matrix templates: general description and 1D examples. *Arch Comput Methods Eng*. 2014;22(1):1-65.
40. Kolman R, Plešek J, Červ J, Okrouhlík M, Pařík P. Temporal-spatial dispersion and stability analysis of finite element method in explicit elastodynamics. *Int J Numer Methods Eng*. 2015;106(2):113-128.
41. Graff KF. *Wave Motion in Elastic Solids*. Oxford, UK: Oxford University Press; 1975.
42. Wang D, Liu W, Zhang H. Novel higher order mass matrices for isogeometric structural vibration analysis. *Comput Methods Appl Mech Eng*. 2013;260:92-108.
43. Wang D, Liu W, Zhang H. Superconvergent isogeometric free vibration analysis of Euler-Bernoulli beams and Kirchhoff plates with new higher order mass matrices. *Comput Methods Appl Mech Eng*. 2015;286:230-267. <http://www.sciencedirect.com/science/article/pii/S0045782514005052>
44. Wang D, Liang Q, Wu J. A quadrature-based superconvergent isogeometric frequency analysis with macro-integration cells and quadratic splines. *Comput Methods Appl Mech Eng*. 2017;320:712-744. <http://www.sciencedirect.com/science/article/pii/S0045782517301366>
45. Park KC. Practical aspects of numerical time integration. *Comput Struct*. 1977;7(3):343-353.
46. Hulbert GM, Chung J. Explicit time integration algorithms for structural dynamics with optimal numerical dissipation. *Comput Methods Appl Mech Eng*. 1996;137(2):175-188.
47. Chang S-Y. An explicit method with improved stability property. *Int J Numer Methods Eng*. 2008;77(8):1100-1120.
48. Kolman R, Okrouhlík M, Berezovski A, Gabriel D, Kopačka J, Plešek J. B-spline based finite element method in one-dimensional discontinuous elastic wave propagation. *Appl Math Model*. 2017;46:382-395. <http://www.sciencedirect.com/science/article/pii/S0307904X17300835>
49. Kolman R, Plešek J, Okrouhlík M. Complex wavenumber Fourier analysis of the B-spline based finite element method. *Wave Motion*. 2014;51(2):348-359. <http://www.sciencedirect.com/science/article/pii/S0165212513001479>

50. National Agency for Finite Element Methods & Standards. *The Standard NAFEMS Benchmarks*. Glasgow, UK: NAFEMS; 1990.
51. Anděl P, Bastl B, Slabá K. Parameterizations of generalized NURBS volumes of revolution. *Eng Mech*. 2012;19(4):293-306.

How to cite this article: González JA, Kopačka J, Kolman R, Cho SS, Park KC. Inverse mass matrix for isogeometric explicit transient analysis via the method of localized Lagrange multipliers. *Int J Numer Methods Eng*. 2019;117:939–966. <https://doi.org/10.1002/nme.5986>

RESEARCH ARTICLE

On stability and reflection-transmission analysis of the bipenalty method in contact-impact problems: A one-dimensional, homogeneous case study

Ján Kopačka¹  | Anton Tkachuk²  | Dušan Gabriel¹  | Radek Kolman¹  |
Manfred Bischoff²  | Jiří Plešek¹

¹Institute of Thermomechanics of the Czech Academy of Sciences, Dolejšková 5, 182 00 Prague, Czech Republic

²Institute for Structural Mechanics, University of Stuttgart, Pfaffenwaldring 7, 70550 Stuttgart, Germany

Correspondence

Ján Kopačka, Institute of Thermomechanics, The Czech Academy of Sciences, Dolejšková 5, 182 00 Prague, Czech Republic.
Email: kopačka@it.cas.cz

Funding information

Centre of Excellence for Nonlinear Dynamic Behaviour of Advanced Materials in Engineering, Grant/Award Number: CZ.02.1.01/0.0/0.0/15_003/0000493; Czech Science Foundation (CSF), Grant/Award Number: 17-22615S and 16-03823S; CSF, Grant/Award Number: 17-12925S; DAAD-16-12/Projekt-ID 57219898

Summary

The stability and reflection-transmission properties of the bipenalty method are studied in application to explicit finite element analysis of one-dimensional contact-impact problems. It is known that the standard penalty method, where an additional stiffness term corresponding to contact boundary conditions is applied, attacks the stability limit of finite element model. Generally, the critical time step size rapidly decreases with increasing penalty stiffness. Recent comprehensive studies have shown that the so-called bipenalty technique, using mass penalty together with standard stiffness penalty, preserves the critical time step size associated to contact-free bodies. In this paper, the influence of the penalty ratio (ratio of stiffness and mass penalty parameters) on stability and reflection-transmission properties in one-dimensional contact-impact problems using the same material and mesh size for both domains is studied. The paper closes with numerical examples, which demonstrate the stability and reflection-transmission behavior of the bipenalty method in one-dimensional contact-impact and wave propagation problems of homogeneous materials.

KEYWORDS

bipenalty method, explicit time integration, finite element method, penalty method, reflection-transmission analysis, stability analysis

1 | INTRODUCTION

In contact-impact problems, the contact constraints are often enforced either by the Lagrange multiplier method or by the stiffness penalty method. In practice, the latter approach has gained substantial popularity in explicit dynamics, because its implementation is straightforward and does not require assembly and solution of a linear system of equations in each time step as in the Lagrange multiplier method, see details in Carpenter et al and Zhong.^{1,2} Moreover, the finite interface stiffness can be physically motivated. On the other hand, the choice of the penalty parameter influences the accuracy of the approximate solution. In addition, in contact-impact applications, the stiffness penalty method tends to decrease the critical time step size in conditionally stable time integration schemes like the central difference method (CDM).³ This is due to the fact that the stiffness-type penalty method can greatly increase the maximum eigenfrequency of a system. Note that this effect is not observed in enforcing of contact constraints by the Lagrange multiplier method. Modification of the penalty method with ephemeral penalty functions for contact-impact dynamics has been presented in de la Fuente

and Felippa,⁴ error analysis of penalty function techniques for constraint definition in linear algebraic systems has been published in Felippa,⁵ and iterative procedures for improving penalty function solutions of algebraic systems have been studied in Felippa.⁶

Generally, in the penalty method, an additional stiffness term corresponding to contact boundary conditions is applied to prevent penetration of the contacting bodies. In this sense, the penalty method can be viewed as a relaxation of the impenetrability condition. This is a new boundary condition with respect to the actual situation of penetration of bodies, and the penalty parameter can be interpreted as a spring stiffness corresponding to a contact boundary condition.

The penalty approach can be applied not only to the stiffness term but also to the inertia of the contact boundary condition. This technique is known as the mass penalty or the inertia penalty method. When both additional terms are involved, the method is called the *bipenalty* method. In the bipenalty method, one adds an extra mass term into the mass distribution corresponding to a contact domain of interest with a stiffness term at the same time. By means of adding the bipenalty terms (additional mass and stiffness terms concurrently) into the equations of motion corresponding to the contact pairs, we obtain a modified local dynamic system. In principle, we attune a frequency character of the equations of motion corresponding to the nodes for which contact conditions apply. In a special case, one can find a particular choice for the ratio of additional stiffness and mass parameters such that the frequency character of the boundary with the bipenalty term is not affected by the additional stiffness term, as it is the case in the standard penalty method. Moreover, in the bipenalty method, this frequency character is the same as the one of contact-free bodies. For this reason, we can determine a stability limit in explicit contact-impact finite element analysis neglecting contact constraints. This means we determine a stability limit for contact-free discretized bodies respecting only Dirichlet boundary conditions. This is the main motivation for using the bipenalty method in contact-impact problems solved by explicit finite element analysis.

The bipenalty method initially gained popularity for frequency domain problems, see Ilanko⁷ and Ilanko and Monterrubio.⁸ In contrast to the stiffness penalty approach, it significantly reduces one or more eigenfrequencies. In Askes et al.,⁹ the *bipenalty technique* was introduced for time domain problems, where both penalty formulations are used simultaneously. The goal of this method is to find the optimum of the so-called *critical penalty ratio* (CPR), defined as the ratio of stiffness and mass penalty parameters, so that the maximum eigenfrequency and the critical time step size of a contact-free discretized body are preserved. The calculation of CPR requires an analysis of the full bipenalized problem. Owing to mathematical difficulty, it limits the classes of elements that can be taken into account. To overcome this problem, a simple relationship between the CPR of an element and its maximum unpenalized eigenfrequency was derived in Hetherington et al.¹⁰ Thus, the multiple constraints and more complex element formulations can be directly accounted for Hetherington et al.¹¹ The effect of the penalty stiffness on the accuracy in contact problems has been studied in Huněk¹² and in Hetherington et al.,¹¹ where also the effect of damping penalty parameters has been analyzed.

The original ideas of the bipenalty method were independently developed for stabilizing numerical solutions for differential-algebraic equation systems (eg, in constrained multibody dynamics), like the Baumgarte method.¹³ In this method, the system of constraint equations $\Phi = \mathbf{0}$ is modified, and the equation system $\ddot{\Phi} + 2\alpha\dot{\Phi} + \beta^2\Phi = \mathbf{0}$, α and β being positive parameters, is solved instead of the equation system $\Phi = \mathbf{0}$ during the numerical solution of the index one differential-algebraic equation systems. In principle, the constraint forces are computed as sum of stiffness, damping, and inertia penalty terms for a general holonomic constraint. For an application of the Baumgarte method for multibody dynamic problems, see Lin and Huang.^{14,15} The stability of the Baumgarte method has been studied in Chiou et al.¹⁶ and the optimal choice of numerical parameters has been analyzed in Lin and Huang.¹⁷ However, the motivation of this development was the reduction of the differential index of the system and more robust *implicit* integration of the differential-algebraic equation system. The effect of the penalty and damping parameters for multibody systems is analyzed in detail in previous studies.^{14,16-18} The staggered penalty method in multibody problems has been used in Park and Chiou.¹⁹

In this paper, the bipenalty approach is studied for one-dimensional contact-impact problems in explicit finite element analysis. We study contact-impact problems of homogeneous bars with the same material parameters and cross-section. The attention is focused on the stability and accuracy properties including numerical artifacts of this algorithm, mainly on the reflection-transmission properties of waves running through discretized finite element domains connected by a bipenalized term. The paper is organized as follows: In Section 2.1, the formulation of the contact initial boundary value problem is presented, followed by the variational formulation in Section 2.2. The idea of the bipenalty approach for imposing contact constraints is described in Section 2.3. Finite element discretization is outlined in Section 2.4. Numerical stability of the explicit time integration scheme is discussed in Section 2.5. Next, the reflection-transmission error (RTE) analysis is briefly introduced in Section 4, and results of such an analysis are presented for the homogeneous case.

In addition, the spurious reflection for dimensionless penalty factors below 1 is discussed. Section 5 presents a stability test of the algorithm for the dynamic Signorini problem and the Huněk test as well as a numerical study of RTEs, followed by concluding remarks in Section 6.

2 | PROBLEM DESCRIPTION AND GOVERNING EQUATIONS

In this section, an overview of the fundamental equations of elastodynamic problems in solids, the variational formulation of the contact problem and the finite element method with the bipenalty method in contact problems are described alongside the basic description of the CDM as the most common explicit integrator with a stability limit. This description follows a previous work.²⁰ Both the 2 bodies contact problem and the Signorini contact problem, ie, the contact of a single body on a rigid obstacle, are considered.

2.1 | Contact initial/boundary value problem

A one-dimensional contact-impact problem of linear isotropic homogeneous bars is governed by the balance of linear momentum

$$Eu'' + b = \rho\ddot{u} \quad \text{in } \mathbf{I} \times \mathbf{T}, \quad (1)$$

where $\mathbf{I} = \bigcup_i \mathbf{I}_i = (x_i^l, x_i^r)$, $i = 1, 2$ is the union of intervals of spatial points $x_i \in \mathbf{I}_i$ defining the contacting bodies (see Figure 1), and $\mathbf{T} = (0, t_{\text{end}})$ is the time interval. Indeed, for the Signorini problem, depicted in Figure 1B, only one body is considered $\mathbf{I} = \mathbf{I}_1$. In Equation 1, $u(x, t) : \mathbf{I} \times \mathbf{T} \mapsto \mathbb{R}$ is the unknown displacement function, $b(x, t) : \bar{\mathbf{I}} \times \bar{\mathbf{T}} \mapsto \mathbb{R}$ is the prescribed volume intensity of body forces, where $(\bar{\bullet})$ denotes closure of a set. Further, $E \in \mathbb{R}$ is Young's elasticity modulus, and $\rho(x) : \bar{\mathbf{I}} \mapsto \mathbb{R}$ is the density.

For the sake of simplicity, the second partial derivative with respect to x is denoted by double prime, $(\bullet)''$, and the second partial derivative with respect to t by superimposed dots, $(\bullet)''$.

The governing Equation 1 is complemented by the initial and boundary conditions. The initial conditions are

$$u(x, 0) = u_0(x) \quad \text{in } \bar{\mathbf{I}}, \quad (2)$$

$$\dot{u}(x, 0) = v_0(x) \quad \text{in } \bar{\mathbf{I}}, \quad (3)$$

where $u_0(x) : \bar{\mathbf{I}} \mapsto \mathbb{R}$ is the initial displacement function and $v_0(x) : \bar{\mathbf{I}} \mapsto \mathbb{R}$ is the initial velocity function, both prescribed at time $t = 0$. The boundary conditions of Dirichlet and Neumann type are

$$u(x, t) = \bar{u}(x) \quad \text{in } \Gamma_u, \quad (4)$$

$$Eu'(x, t) = \bar{\sigma}(x) \quad \text{in } \Gamma_\sigma, \quad (5)$$

where $\bar{u}(x) : \Gamma_u \mapsto \mathbb{R}$ is the displacement function and $\bar{\sigma}(x) : \Gamma_\sigma \mapsto \mathbb{R}$ is the traction function, both constant in time. Γ_u and Γ_σ are sets of boundary points where displacements and stresses are prescribed. Further, the set $\Gamma_c = \{x_2^r, x_1^l\}$ of points on the contact interface is introduced for the formulation of 2 bodies contact problem, cf Figure 1A. Note that here, we have assumed that the first body is on the right, and therefore, its contact interface forms the left boundary point, x_1^l .

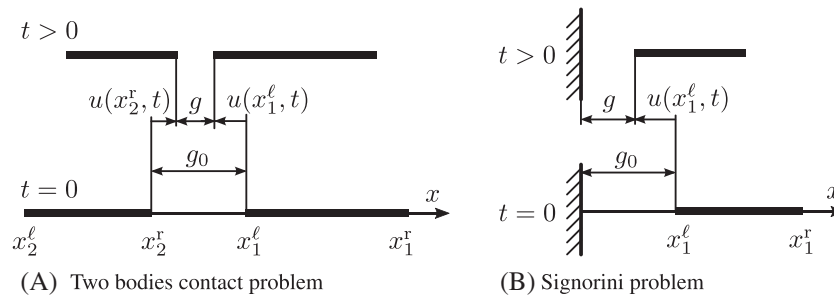


FIGURE 1 Definition of domains of interest, their boundaries, and the gap function

Analogously for the second body, for the Signorini problem, Γ_c reduces to single-element set $\Gamma_c = \{x_1^r\}$, cf Figure 1B. All 3 sets Γ_u, Γ_σ , and Γ_c disjointly cover the boundaries of intervals I_i , ie,

$$\Gamma_u \cup \Gamma_\sigma \cup \Gamma_c = \partial I, \quad (6)$$

$$\Gamma_u \cap \Gamma_\sigma \cap \Gamma_c = \emptyset. \quad (7)$$

Let us define the so-called gap function $g(t) : \bar{T} \mapsto \mathbb{R}$, which measures the distance between contacting points. For the 2 bodies contact problem, it is

$$\begin{aligned} g(t) &= - \{ [x_1^l + u(x_1^l, t)] - [x_2^r + u(x_2^r, t)] \} \\ &= - [u(x_1^l, t) - u(x_2^r, t) + x_1^l - x_2^r] \\ &= - [u(x_1^l, t) - u(x_2^r, t) + g_0], \end{aligned} \quad (8)$$

where g_0 denotes the initial gap. For the Signorini problem, the gap function can be considered as the special case of (8), assuming $x_2^r = 0$ and $u(x_2^r, t) = 0$

$$g(t) = - [u(x_1^l, t) + g_0]. \quad (9)$$

With the aid of the gap function, the contact constraints are prescribed by the Signorini-Hertz-Moreau conditions

$$g(t) \leq 0 \quad p_c(x, t) \geq 0 \quad g(t)p_c = 0 \quad t \in T, x \in \Gamma_c \quad (10)$$

also known as the Karush-Kuhn-Tucker (KKT) conditions. Here, assuming Hook's law, $p_c(x, t) = -Eu'$ is the contact pressure.

Note that the gap function has the positive sign in the case of penetration. Therefore, the inequality (10)₁ is called the impenetrability condition.

The second condition (10)₂ asserts a positive contact pressure. And finally, the equality (10)₃ is called the complementarity condition ensuring the complementarity between the gap function and the contact pressure.

2.2 | Variational formulation

For the finite element discretization, it is necessary to reformulate the strong form of the contact initial boundary value problem presented in the preceding section in a weak sense. The Hamilton's principle is a powerful tool that can be utilized to derive a discretized dynamic system of equations. It states that out of all admissible time histories of the displacement field, the solution is the one that minimizes the action functional

$$u = \arg \min \left(\int_T \mathcal{L}(u, \dot{u}) dt \right) \quad \text{subject to } g \leq 0, \quad (11)$$

where the Lagrangian function, $\mathcal{L}(u, \dot{u})$, is defined as

$$\mathcal{L}(u, \dot{u}) = \mathcal{T}(\dot{u}) - (\mathcal{U}(u) - \mathcal{W}(u)) \quad (12)$$

and where

$$\mathcal{T}(\dot{u}) = \int_I \frac{1}{2} \rho A \dot{u}^2 dx \quad (13)$$

$$\mathcal{U}(u) = \int_I \frac{1}{2} E A u^2 dx \quad (14)$$

$$\mathcal{W}(u) = \int_I u b A dx + \sum_{x \in \Gamma_\sigma} u A \bar{\sigma} \quad (15)$$

are the kinetic energy, the strain energy, and the work done by the external forces, respectively. Note that the cross-section area function $A(x) : \bar{T} \mapsto \mathbb{R}$ has been introduced.

2.3 | Bipenalty method

In dynamics, the simultaneous use of stiffness penalties and inertia (mass) penalties, called the bipenalty method, was originally proposed in Askes et al.⁹ Therein, the penalty ratio is defined as

$$R = \frac{\epsilon_s}{\epsilon_m} [\text{s}^{-2}], \quad (16)$$

where ϵ_s [$\text{kg}\cdot\text{m}^{-2}\cdot\text{s}^{-2}$] and ϵ_m [kg m^{-2}] are the stiffness and mass penalty parameter, respectively. Moreover, optimum values of the penalty ratios—the so-called CPRs—have been derived for a number of finite elements such that the critical time step size of the penalized system remains unaffected. A new method of calculating the CPR associated with a finite element formulation was developed in Hetherington et al.¹⁰ Recently, this research was extended to include systems with an arbitrary set of multipoint constraints¹¹ and to cohesive zone (surface) elements.²¹

The standard stiffness penalty method adds an extra term to the strain energy (14) to enforce the zero gap on the contact boundary

$$\mathcal{U}_p(u) = \int_I \frac{1}{2} EAu'^2 dx + \frac{1}{2} \epsilon_s A \langle g \rangle^2, \quad (17)$$

where the operator $\langle \bullet \rangle$ are the so-called Macaulay's brackets defined as

$$\langle \bullet \rangle = \frac{|\bullet| + \bullet}{2}. \quad (18)$$

Thus, in the particular case of Equation 17, this operator returns zero for a negative value of the gap function (ie, separation), and it returns the value of the gap function itself in the case of penetration.

Further, the inertia penalty term can also be added to the kinetic energy (13) to enforce a zero gap rate on the contact interface

$$\mathcal{T}_p(\dot{u}) = \int_I \frac{1}{2} \rho A \dot{u}^2 dx + \frac{1}{2} \epsilon_m A \dot{g}^2 H(g), \quad (19)$$

where $H(g)$ is the Heaviside step function, which ensures that the penalization term is active only in the case of penetration. Note the identity $\langle g \rangle = gH(g)$. Now, the penalized Lagrangian functional can be defined as

$$\mathcal{L}_p(u, \dot{u}) = \mathcal{T}_p(\dot{u}) - [\mathcal{U}_p(u) - \mathcal{W}(u)]. \quad (20)$$

The unknown displacement function $u(x, t)$ is sought through minimizing the action functional taking the form

$$\delta \int_T \mathcal{L}_p(u, \dot{u}) dt = 0, \quad (21)$$

where δ denotes the first variation.

Using the standard procedures, one arrives at the principle of virtual displacements

$$\int_I \delta u \rho \ddot{u} dx + \int_I \delta u' EAu' dx + \delta g AH(g) [\epsilon_m \dot{g} + \epsilon_s g] = \int_I \delta u Ab dx + \sum_{x \in \Gamma_\sigma} \delta u A \bar{\sigma}, \quad (22)$$

which provides the base for the finite element discretization. The terms in Equation 22 represent the virtual work of the inertia forces, internal forces, contact forces, body forces, and traction forces, respectively. It is worth noting that the term of the virtual contact work is expressed with the aid of the inertia and the stiffness penalty.

2.4 | Finite element method

In the following, the continuous Galerkin approximation method with linear shape functions is exploited. The interval I is subdivided into smaller intervals, which serve as the parent domains for finite elements

$$I = \bigcup_{e=1}^{n_{el}} I_e, \quad (23)$$

where $\mathbf{I}_e = [x_e^\ell, x_e^r]$ and the length of each element is $h_e = x_e^r - x_e^\ell$. On each of the finite elements, the linear shape functions are defined as

$$N_1(x) = \frac{x_e^r - x}{h_e} \quad N_2(x) = \frac{x - x_e^\ell}{h_e} \quad x \in \mathbf{I}_e. \quad (24)$$

With the aid of these shape functions, the unknown displacement function and its variation and derivative are discretized as

$$u(x, t) \approx u^h(x, t) = \sum_{a=1}^2 N_a(x) u_a^e(t) = \mathbf{H}^T \mathbf{u}_e \quad x \in \mathbf{I}_e, t \in \mathbf{T}, \quad (25)$$

$$\delta u(x) \approx \delta u^h(x) = \sum_{a=1}^2 N_a(x) \delta u_a^e = \mathbf{H}^T \delta \mathbf{u}_e \quad x \in \mathbf{I}_e, \quad (26)$$

$$u'(x, t) \approx (u^h)'(x, t) = \sum_{a=1}^2 N'_a(x) u_a^e(t) = \mathbf{B}^T \mathbf{u}_e \quad x \in \mathbf{I}_e, t \in \mathbf{T}, \quad (27)$$

where the newly introduced matrices have the form

$$\mathbf{H} = \begin{bmatrix} N_1 \\ N_2 \end{bmatrix} \quad \mathbf{B} = \begin{bmatrix} N'_1 \\ N'_2 \end{bmatrix} \quad \mathbf{u}_e = \begin{bmatrix} u_1^e \\ u_2^e \end{bmatrix} \quad \delta \mathbf{u}_e = \begin{bmatrix} \delta u_1^e \\ \delta u_2^e \end{bmatrix}. \quad (28)$$

Similarly, the gap function and its variation are discretized as

$$g(t) \approx g^h(t) = -\mathbf{N}^T \hat{\mathbf{u}}(t) - g_0 \quad t \in \mathbf{T}, \quad (29)$$

$$\delta g \approx \delta g^h = -\mathbf{N}^T \delta \hat{\mathbf{u}}, \quad (30)$$

where 3 new matrices have been defined. For the gap function (8) of the 2 bodies contact problem, they are defined as

$$\mathbf{N} = \begin{bmatrix} 1 \\ -1 \end{bmatrix} \quad \hat{\mathbf{u}} = \begin{bmatrix} u^h(x_1^r, t) \\ u^h(x_2^\ell, t) \end{bmatrix} \quad \delta \hat{\mathbf{u}} = \begin{bmatrix} \delta u^h(x_1^r) \\ \delta u^h(x_2^\ell) \end{bmatrix}, \quad (31)$$

and for the gap function (9) of the Signorini problem, they simplify to

$$\mathbf{N} = [1] \quad \hat{\mathbf{u}} = [u^h(x_1^r, t)] \quad \delta \hat{\mathbf{u}} = [\delta u^h(x_1^r)]. \quad (32)$$

Using the just introduced discretized functions together with standard finite element procedures to the variational formulation (22) yields the following system of nonlinear ordinary differential equations

$$\mathbf{M} \ddot{\mathbf{u}} + \mathbf{K} \mathbf{u} + \mathbf{R}_c(\mathbf{u}, \ddot{\mathbf{u}}) = \mathbf{R}, \quad (33)$$

where \mathbf{u} , $\dot{\mathbf{u}}$, $\ddot{\mathbf{u}}$ mark the global vectors of nodal displacements, velocities, and accelerations, respectively. \mathbf{M} is the global mass matrix, \mathbf{K} is the global stiffness matrix, and \mathbf{R}_c is the global contact residual vector, which is the source of the nonlinearity. Further, \mathbf{R} is the time-dependent global load vector. The global vectors and matrices are assembled in the usual fashion from the local (elemental) contributions. The element mass and stiffness matrices are given by

$$\mathbf{M}_e = \int_{\mathbf{I}_e} \rho A \mathbf{H} \mathbf{H}^T dx \quad \mathbf{K}_e = \int_{\mathbf{I}_e} E A \mathbf{B} \mathbf{B}^T dx. \quad (34)$$

The fully integrated elemental stiffness and consistent mass matrices are given as

$$\mathbf{K}_e = \frac{EA}{h_e} \begin{bmatrix} 1 & -1 \\ -1 & 1 \end{bmatrix} \quad (35)$$

and

$$\mathbf{M}_e = \frac{\rho h_e A}{6} \begin{bmatrix} 2 & 1 \\ 1 & 2 \end{bmatrix}, \quad (36)$$

where it was assumed that cross-section area A , Young's modulus E , and density ρ are constant. In the following, we will exclusively use the row-sum lumped mass matrix

$$\mathbf{M}_e = \frac{\rho h_e A}{2} \begin{bmatrix} 1 & 0 \\ 0 & 1 \end{bmatrix}, \quad (37)$$

which is preferred in explicit finite element analysis.

The global contact residual vector \mathbf{R}_c is assembled from the local counterpart $\hat{\mathbf{R}}_c$, which can be written as

$$\hat{\mathbf{R}}_c(\hat{\mathbf{u}}, \ddot{\hat{\mathbf{u}}}) = \hat{\mathbf{M}}_p \ddot{\hat{\mathbf{u}}} + \hat{\mathbf{K}}_p \hat{\mathbf{u}} + \hat{\mathbf{f}}_p \quad (38)$$

where

$$\hat{\mathbf{M}}_p = \epsilon_m AH(g) \mathbf{N} \mathbf{N}^T \quad \hat{\mathbf{K}}_p = \epsilon_s AH(g) \mathbf{N} \mathbf{N}^T \quad \hat{\mathbf{f}}_p = \epsilon_s AH(g) \mathbf{N} g_0. \quad (39)$$

Here, $\hat{\mathbf{M}}_p$ is the additional elemental mass matrix due to inertia penalty, $\hat{\mathbf{K}}_p$ is the additional elemental stiffness matrix due to stiffness penalty, and $\hat{\mathbf{f}}_p$ is the part of the elemental contact force due to the initial gap g_0 . An extension of the bipenalty method to a penalty formulations and to the large sliding case, ie, given in Belytschko and Neal²² and Gabriel et al,²³ is also possible.

Again, provided that the global vectors and matrices, \mathbf{M}_p , \mathbf{K}_p , \mathbf{f}_p , and \mathbf{u} are assembled in the usual fashion from the elemental contributions $\hat{\mathbf{M}}_p$, $\hat{\mathbf{K}}_p$, $\hat{\mathbf{f}}_p$, and $\hat{\mathbf{u}}$, the final form of the equations of motion for the bipenalty method in contact-impact problems is

$$(\mathbf{M} + \mathbf{M}_p) \ddot{\mathbf{u}} + (\mathbf{K} + \mathbf{K}_p) \mathbf{u} + \mathbf{f}_p - \mathbf{R} = \mathbf{0}, \quad (40)$$

which is solved numerically with respect to boundary and initial conditions, see Section 2.5.

Let us define dimensionless stiffness and mass penalty parameters for the one-dimensional case, β_m and β_s , as follows

$$\beta_s = \frac{h_e}{E} \epsilon_s, \quad \beta_m = \frac{2}{\rho h_e} \epsilon_m, \quad (41)$$

where h_e is the length of the element whose node is on the contact interface. For the 2 bodies contact problem, this results in the following additional stiffness and mass matrices

$$\hat{\mathbf{K}}_p = \frac{EAH(g)\beta_s}{h_e} \begin{bmatrix} 1 & -1 \\ -1 & 1 \end{bmatrix}, \quad (42)$$

$$\hat{\mathbf{M}}_p = \frac{\rho h_e AH(g)\beta_m}{2} \begin{bmatrix} 1 & -1 \\ -1 & 1 \end{bmatrix}. \quad (43)$$

As already mentioned, the diagonalized (lumped) mass matrix is preferred in explicit time integration. The corresponding diagonalized version of the additional mass matrix (43) obtained from row-sum lumping of absolute values of terms is

$$\hat{\mathbf{M}}_p = \rho h_e AH(g) \beta_m \begin{bmatrix} 1 & 0 \\ 0 & 1 \end{bmatrix}. \quad (44)$$

Note that for the Signorini problem, they simplify to one-by-one matrices

$$\hat{\mathbf{K}}_p = \frac{EAH(g)\beta_s}{h_e} [1], \quad (45)$$

$$\hat{\mathbf{M}}_p = \frac{\rho h_e AH(g)\beta_m}{2} [1]. \quad (46)$$

In the following, we will study the effect of the numerical parameters β_m and β_s on stability of the bipenalty method. The effect of the diagonalized mass matrix \mathbf{M}_p on stability of the bipenalty method in one-dimensional contact-impact problems is investigated in Section 3.

2.5 | Explicit time integration and numerical stability

We now consider the time integration of the semidiscretized system (33) by the CDM²⁴

$$(\mathbf{M}^t + \mathbf{M}_p^t) \frac{\mathbf{u}^{t+\Delta t} - 2\mathbf{u}^t + \mathbf{u}^{t-\Delta t}}{\Delta t^2} + (\mathbf{K}^t + \mathbf{K}_p^t) \mathbf{u}^t + \mathbf{f}_p^t - \mathbf{R}^t = \mathbf{0}. \quad (47)$$

Assuming that displacements are known at time $t - \Delta t$ and t , one can resolve unknown displacements at time $t + \Delta t$, where Δt marks the time step size. Note that the matrices \mathbf{M}_p^t and \mathbf{K}_p^t are time-dependent because they are associated with active contact constraints. This fact causes the system to be nonlinear.

In this paper, we use the following form of the central difference scheme for solving elastodynamic problems with contact constrains:

- Given $\mathbf{u}^t, \dot{\mathbf{u}}^{t-\Delta t/2}, \mathbf{R}^t$
- For given \mathbf{u}^t analyze contact, compute gap g , and contact forces $\mathbf{f}_p^t = -\mathbf{K}_p^t \mathbf{u}^t + \mathbf{f}_p^0$
- Compute accelerations $\ddot{\mathbf{u}}^t = (\mathbf{M}^t + \mathbf{M}_p^t)^{-1} (\mathbf{R}^t - \mathbf{K}^t \mathbf{u}^t + \mathbf{f}_p^t)$
- Midpoint velocities $\dot{\mathbf{u}}^{t+\Delta t/2} = \dot{\mathbf{u}}^{t-\Delta t/2} + \Delta t \ddot{\mathbf{u}}^t$
- New displacements $\mathbf{u}^{t+\Delta t} = \mathbf{u}^t + \Delta t \dot{\mathbf{u}}^{t+\Delta t/2}$
- $t \rightarrow t + \Delta t$

It is well known that the CDM for a linear system is conditionally stable. The linear stability theory establishes the upper bound of the time step size as

$$\Delta t \leq \frac{2}{\omega_{\max}}, \quad (48)$$

where ω_{\max} is the maximum eigenfrequency of the finite element mesh. Indeed, the computation of even a single eigenvalue of a large systems may be expensive. Therefore, it would be advantageous to have an estimate of the maximum eigenvalue that is easy to compute. Such an estimate is provided by the element eigenvalue inequality²²

$$\omega_{\max} < \max_e \omega_{\max}^e. \quad (49)$$

Note that the element eigenvalue inequality (49) is not limited to element level submatrices. The submatrices may be also an assembly of elements.

3 | STABILITY ANALYSIS OF BIPENALIZED ONE-DIMENSIONAL SYSTEMS

In this section, the stability limit for several one-dimensional bipenalized discretized finite element systems was computed, namely, the Signorini problem, the symmetric contact problem, and the double-sided contact problem. Special attention was paid to the effect of the bipenalty ratio on the stability behavior. In this paper, we find the optimum of the so-called CPR defined as the ratio of stiffness and mass penalty parameters so that the maximum eigenfrequency and the critical time step size are preserved.

3.1 | A Signorini problem—a truss finite element in one-side contact

Unfortunately, there are no stability theorems for contact-impact problems.²⁴ In this case, the stability theory for linear problems can be applied carefully. In practice, for example, the stability may be preserved by checking the energy balance during a nonlinear computation. In Belytschko and Neal,²² an upper bound for the stiffness penalty was derived. Moreover, it was shown that the stiffness penalty always decreases the stable time step size. In this work, we adopt this estimate for the bipenalty method following the Belytschko approach²² and previous work.²⁰

Let us consider a simple dynamic system, depicted in Figure 2, with 2 degrees of freedom. The system consists of one 1D constant strain truss element with lumped mass matrix. The active contact constraint is set at node 1 and initial gap

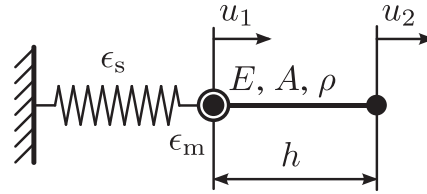


FIGURE 2 A scheme of the bipenalized Signorini problem

g_0 is considered to be equal to zero. The aim is to determine the maximum eigenfrequency of this system to estimate the stable time step size in the form (48). To this end, the eigenvalue problem can be formulated as

$$\frac{EA}{h} \begin{bmatrix} 1 + H(g)\beta_s & -1 \\ -1 & 1 \end{bmatrix} \mathbf{u} = \omega^2 \frac{\rho Ah}{2} \begin{bmatrix} 1 + H(g)\beta_m & 0 \\ 0 & 1 \end{bmatrix} \mathbf{u}, \quad (50)$$

where the displacement vector has the form $\mathbf{u} = [u_1, u_2]^T$. The additional stiffness matrix, (45), and mass matrix, (46), have been utilized during assembling of the global matrices of the bipenalized 2-degrees-of-freedom system. In what follows, the constant value of the Heaviside function $H(g) = 1$ is considered, so it is assumed that the contact interface will not open and, consequently, linear theory of stability can be applied. Let us define the maximum angular velocity of a separate linear finite element with the lumped mass matrix as $\omega_{max}^0 = 2c_0/h$, where c_0 marks the wave speed in a bar given by $c_0 = \sqrt{E/\rho}$. Then the corresponding critical time step size is given as $\Delta t_c^0 = 2/\omega_{max}^0 = h/c_0$.

The maximum eigenfrequency of the problem (50) is given by the relationship

$$\omega_{max} = \frac{c_0}{h} \sqrt{1 + \frac{(1 + \beta_s)}{(1 + \beta_m)} + \sqrt{1 + \frac{(1 + \beta_s)^2}{(1 + \beta_m)^2} + \frac{2(1 - \beta_s)}{(1 + \beta_m)}}}. \quad (51)$$

Now, it is useful to introduce a new dimensionless penalty ratio r as

$$r = \frac{1}{2} \frac{\beta_s}{\beta_m} = \frac{h^2}{4c_0^2} R \quad (52)$$

and the Courant dimensionless number C is defined as

$$C = \frac{c_0 \Delta t}{h}. \quad (53)$$

It should be mentioned that the well-known CFL (Courant-Friedrichs-Levy) condition for the linear finite element method with lumped mass matrices in the one-dimensional case reaches the value $C_r^0 = c_0 \Delta t_c^0 / h = 1$.

Substituting (51) into (48) using (53), the critical Courant number C_r for the model depicted in Figure 2 for the bipenalty method is obtained as

$$C_r = \frac{c_0 \Delta t_c}{h} = \frac{2}{\sqrt{1 + \frac{(1 + \beta_s)}{(1 + \beta_m)} + \sqrt{1 + \frac{2(1 - \beta_s)}{(1 + \beta_m)} + \frac{(1 + \beta_s)^2}{(1 + \beta_m)^2}}}} \quad (54)$$

with the property that the critical Courant number for the bipenalty ratio $r = 1$ reaches the value $C_r = 1$, and it is independent on the chosen stiffness penalty β_s . It should be pointed out that this is the main advantage of the bipenalty method.

The dependence of the critical Courant number C_r on the dimensionless stiffness penalty β_s is plotted in Figure 3, where the dimensionless penalty ratio r is used as the parameter. The curve for $r \rightarrow \infty$ (ie, $\beta_m \rightarrow 0$) corresponds to the standard stiffness penalty method. It illustrates the main disadvantages of the standard stiffness penalty method: The critical Courant number C_r rapidly decreases with increasing dimensionless stiffness penalty β_s . On the other hand, the curve

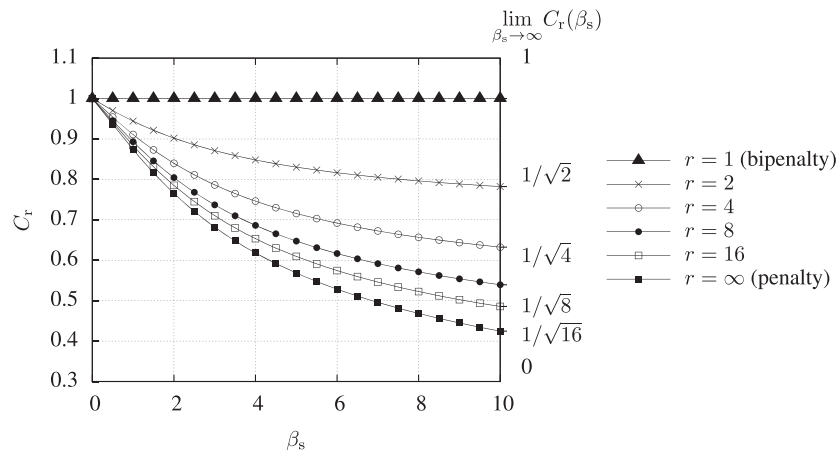


FIGURE 3 Bipenalized Signorini problem: dependence of the critical Courant number C_r on the dimensionless stiffness penalty β_s for selected dimensionless penalty ratios r

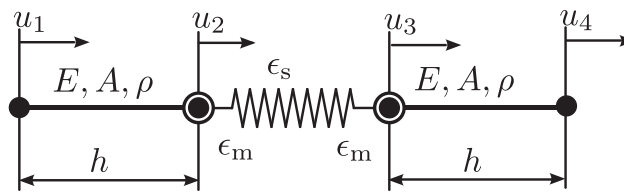


FIGURE 4 A scheme of the bipenalized symmetric one-dimensional contact problem

for $r = 1$ confirms the existence of the CPR, for which the stable time step size remains unchanged for an arbitrary value of the dimensionless stiffness penalty β_s . In addition, there are more curves in Figure 3 for dimensionless penalty ratios $r = 1, 2, 4, 8, 16$, and ∞ . For each of them, there are limits of the Courant number C_r for $\beta_s \rightarrow \infty$ on the right edge of the picture. Taking dimensionless ratios $r < 1$ does not decrease the critical time step size below the level of the unconstrained system. However, as it will be shown in the following section, this leads to a spurious reflection of the wave on the selected frequencies. It is clear that the bipenalty method with the penalty ratio equal to the CPR is superior over the standard stiffness penalty method.

3.2 | Symmetric contact problem

The next example of practical importance of a one-dimensional contact-impact problem is the symmetric contact model illustrated in Figure 4, where the bipenalty term joins 2 identical linear finite elements with lumped mass distribution. The lengths h are the same for both finite elements, as well as the geometrical and material quantities A, E , and ρ .

The corresponding eigenvalue problem for the bipenalty method in symmetric contact problem yields

$$\frac{EA}{h} \begin{bmatrix} 1 & -1 & 0 & 0 \\ -1 & 1 + \beta_s & -\beta_s & 0 \\ 0 & -\beta_s & 1 + \beta_s & -1 \\ 0 & 0 & -1 & 1 \end{bmatrix} \mathbf{u} = \omega^2 \frac{\rho Ah}{2} \begin{bmatrix} 1 & 0 & 0 & 0 \\ 0 & 1 + \beta_m & -\beta_m & 0 \\ 0 & -\beta_m & 1 + \beta_m & 0 \\ 0 & 0 & 0 & 1 \end{bmatrix} \mathbf{u} \tag{55}$$

and the corresponding eigenvalue problem with respect to the diagonalized version of the mass bipenalty term \mathbf{M}_p takes the form

$$\frac{EA}{h} \begin{bmatrix} 1 & -1 & 0 & 0 \\ -1 & 1 + \beta_s & -\beta_s & 0 \\ 0 & -\beta_s & 1 + \beta_s & -1 \\ 0 & 0 & -1 & 1 \end{bmatrix} \mathbf{u} = \omega^2 \frac{\rho Ah}{2} \begin{bmatrix} 1 & 0 & 0 & 0 \\ 0 & 1 + 2\beta_m & 0 & 0 \\ 0 & 0 & 1 + 2\beta_m & 0 \\ 0 & 0 & 0 & 1 \end{bmatrix} \mathbf{u}, \tag{56}$$

where the displacement vector is in the form $\mathbf{u} = [u_1, u_2, u_3, u_4]^T$, see Figure 4.

It was observed that the same stability results for this contact problem were obtained when using the consistent bipenalty mass matrix $\mathbf{M}_p(43)$ instead of the diagonalized one. Therefore, the diagonalized matrix \mathbf{M}_p given by (44) is preferred since the inversion of $(\mathbf{M} + \mathbf{M}_p)$ is trivial in the case of diagonal \mathbf{M} . Notes that by using diagonalized version of \mathbf{M}_p given by (44), we artificially increase the total mass of the bipenalty mass term, and the kinetical energy is affected, but the stability behavior does not change.

For that case, the maximum eigenvalue and corresponding critical time step size are not easy to compute analytically, and therefore, the values have been obtained numerically. The dependence of the critical Courant number C_r is plotted in Figure 5 for selected dimensionless penalty ratios $r = 1, 2, 4, 8, 16,$ and ∞ . The thin dashed lines in Figure 5 correspond to the Signorini problem. It should be noted that graphs both for the Signorini problem and the symmetric contact problem have similar character. However, the symmetric contact problem shows smaller values of the critical Courant number. On the other hand, the line corresponding to the penalty ratio $r = 1$ reaches an ideal case, ie, $C_r = 1$. It means that the bipenalty method with the penalty ratio $r = 1$ does not change the stability limit of the contact-free problem.

3.3 | Double-sided contact problem

Finally, the behavior of a double-sided contact problem is studied with the application of the bipenalty method. The scheme of the bipenalized double-sided contact problem is illustrated in Figure 6.

The eigenvalue problem for the double-sided bipenalized contact problem can be formulated as

$$\frac{EA}{h} \begin{bmatrix} 1 + \beta_s & -1 \\ -1 & 1 + \beta_s \end{bmatrix} \mathbf{u} = \omega^2 \frac{\rho Ah}{2} \begin{bmatrix} 1 + \beta_m & 0 \\ 0 & 1 + \beta_m \end{bmatrix} \mathbf{u}, \tag{57}$$

where the displacement vector has the form $\mathbf{u} = [u_1, u_2]^T$.

The dependence of the critical Courant number C_r is plotted in Figure 7 for selected dimensionless penalty ratios $r = 1, 2, 4, 8, 16,$ and ∞ . The thin dashed lines in Figure 7 correspond to the Signorini problem. In principle, graphs both for the Signorini problem and the double-sided contact problem have similar character. For that reason, it can be concluded

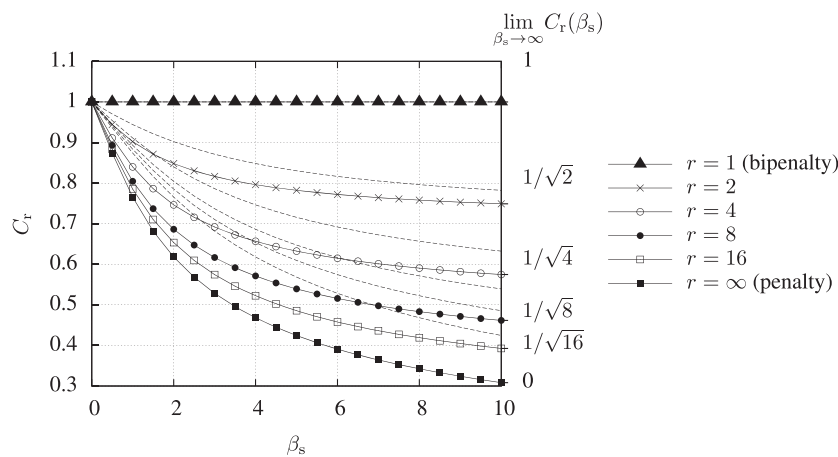


FIGURE 5 Bipenalized symmetric contact problem: dependence of the critical Courant number C_r on the dimensionless stiffness penalty β_s for selected dimensionless penalty ratios r . The thin dashed lines correspond to the Signorini problem

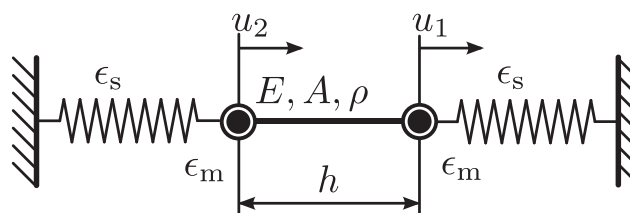


FIGURE 6 A scheme of the bipenalized double-sided one-dimensional contact problem

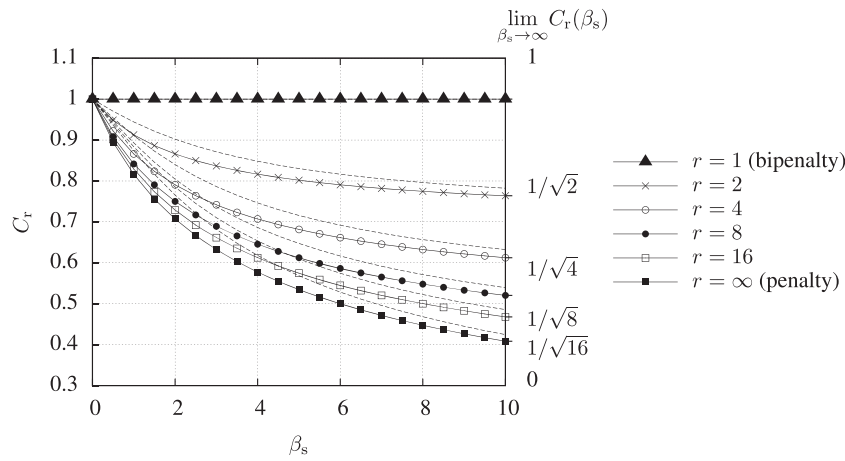


FIGURE 7 Bipenalized double-sided contact problem: dependence of the critical Courant number C_r on the dimensionless stiffness penalty β_s for selected dimensionless penalty ratios r . The thin dashed lines correspond to the Signorini problem

that the analytical estimates of the stability limit for the Signorini problem can be directly applied to the double-sided contact problem.

4 | REFLECTION-TRANSMISSION ERROR ANALYSIS

The contact interface introduces a discontinuity in the numerical model. Numerical treatment of this discontinuity has major effect on the accuracy. This effect is measured here by the error of transmission and reflection of a monochromatic plane wave assuming the persistent contact. In this analysis, we follow the textbook,²⁵ but the effect of bipenalty method is carefully investigated.

4.1 | Basic setup in 1D

Consider 2 elastic semi-infinite bars with a uniform cross-section persistently connected at the interface surface $x = 0$, see Figure 8. The bars are made of materials with Young's moduli E_1 and E_2 , mass densities ρ_1 and ρ_2 , respectively.

A monochromatic plane wave of frequency ω with a unit amplitude propagates in material 1 and falls on the interface. At the interface, the wave is partially transmitted and reflected. Thus, the solution in materials 1 and 2 can be written as

$$u_1(x, t) = 1 \cdot e^{i(\omega t - k_1 x)} + R \cdot e^{i(\omega t + k_1 x)} \quad u_2(x, t) = T \cdot e^{i(\omega t - k_2 x)}, \quad (58)$$

where R and T are the reflected and transmitted amplitudes, k_1 and k_2 are the wavenumbers in the corresponding material, and i is the imaginary unit. For the continuum 1D bar, the linear dispersion relation $k_i = \omega/c_{0i}$ is valid with wave speed $c_{0i} = \sqrt{E_i/\rho_i}$, $i = 1, 2$. The solution above satisfies equilibrium inside each material. The unknown amplitudes R and T must only satisfy continuity and equilibrium at the interface

$$u_1(0, t) = u_2(0, t) \quad \sigma_1(0, t) = \sigma_2(0, t), \quad (59)$$

which yields the system of 2 equations

$$\begin{cases} 1 \cdot e^{i(\omega t - k_1 \cdot 0)} + R \cdot e^{i(\omega t + k_1 \cdot 0)} = T \cdot e^{i(\omega t - k_2 \cdot 0)} \\ k_1 E_1 (1 \cdot e^{i(\omega t - k_1 \cdot 0)} - R \cdot e^{i(\omega t + k_1 \cdot 0)}) = k_2 E_2 T \cdot e^{i(\omega t - k_2 \cdot 0)}. \end{cases} \quad (60)$$

The latter system yields a well-known relation

$$T = \frac{2Z_1}{Z_1 + Z_2} \quad R = \frac{Z_1 - Z_2}{Z_1 + Z_2} \quad (61)$$

with $Z_i = \sqrt{E_i \rho_i}$ being the acoustic impedance for each material. In case of the spatially semidiscretized equation, the dispersion relation is not linear, and the discrete counterpart of the interface conditions (59) is to be considered. This results in discrete coefficients R^h and T^h , which are different from the exact ones (61).

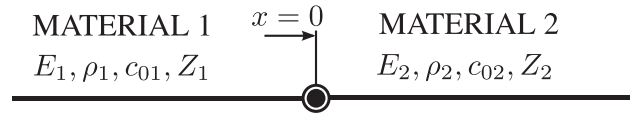


FIGURE 8 Scheme of semi-infinite bars with a uniform cross-section connected at an interface surface

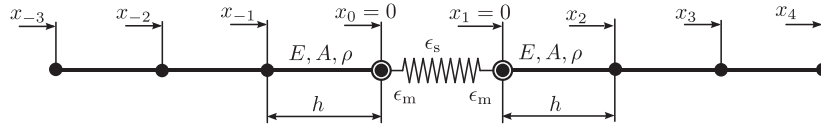


FIGURE 9 Scheme of semi-infinite discretized bars coupled by a bipenalty term

4.2 | Reflection-transmission analysis between 2 bars with the same material

Consider the 2 semi-infinite bars with element size h and the same material coupled with the bipenalty method, see Figure 9.

The solution in each domain is assumed to be

$$\begin{cases} U_j = 1 \cdot e^{i(\omega t - k_1^h \cdot h j)} + R^h \cdot e^{i(\omega t + k_1^h \cdot h j)} & j \leq 0 \\ U_j = T^h \cdot e^{i(\omega t - k_1^h \cdot h (j-1))} & j \geq 1 \end{cases} \quad (62)$$

with U_j being the displacement in the j th node and $k_1^h h = 2 \arcsin(\frac{\omega h}{2c_{01}})$ being the nonlinear dispersion relation for the 2-node bar with the lumped mass matrix.²⁵ The nodes with indices $j = 0$ and $j = 1$ are coupled using the bipenalty method. The equilibrium of nodes 0 and 1 reads

$$\begin{cases} (\cos(k_1^h h) - 1)(1 + R^h + \beta_m(1 + R^h - T^h)) + 1 - e^{ik_1^h h} + R^h(1 - e^{-ik_1^h h}) + \beta_s(1 + R^h - T^h) = 0 \\ (\cos(k_1^h h) - 1)(T^h - \beta_m(1 + R^h - T^h)) + T^h(1 - e^{-ik_1^h h}) - \beta_s(1 + R^h - T^h) = 0 \end{cases} \quad (63)$$

Solving the latter for the numerical reflection and transmission amplitudes yields

$$\begin{cases} R^h = \frac{\cos^2(k_1^h h) - 1}{D} \\ T^h = \frac{-2i(\beta_s + \beta_m(\cos(k_1^h h) - 1)) \sin(k_1^h h)}{D} \end{cases} \quad (64)$$

with

$$\begin{aligned} D = & 2\beta_m \left(\cos^2(k_1^h h) - \cos(k_1^h h) e^{-ik_1^h h} - \cos(k_1^h h) + e^{-ik_1^h h} \right) \\ & + 2\beta_s \left(\cos(k_1^h h) - e^{-ik_1^h h} \right) + \cos^2(k_1^h h) - 2 \cos(k_1^h h) e^{-ik_1^h h} + e^{-2ik_1^h h}. \end{aligned} \quad (65)$$

Note that the result in Equation 64 reduces to penalty formulation in case $\beta_m = 0$. The Taylor series expansions of T^h and R^h for small $k_1^h h$ (long wave approximation) yields

$$T^h = 1 - \frac{i}{2\beta_s} k_1^h h - \frac{1}{4\beta_s^2} (k_1^h h)^2 + \frac{i(2\beta_s^2 - 6\beta_m\beta_s + 3)}{24\beta_s^3} (k_1^h h)^3 + O((k_1^h h)^4), \quad (66)$$

$$R^h = \frac{i}{2\beta_s} k_1^h h + \frac{1}{4\beta_s^2} (k_1^h h)^2 - \frac{i(2\beta_s^2 - 6\beta_m\beta_s + 3)}{2} 4\beta_s^3 (k_1^h h)^3 + O((k_1^h h)^4). \quad (67)$$

Note that exact the value of the transmission T and reflection R amplitudes for $Z_1 = Z_2$ are one and zero, respectively. Analysis of the Taylor expansion allows the following conclusions on the basis of the leading term of error $T^h - T = -i/(2\beta_s)k_1^h h$

- The error is of first order in the element size h .
- The error constant decays quickly with increasing *stiffness* penalty parameter.
- The error is purely imaginary with negative sign, ie, phase shift (delay) of the front of the transmitted wave is expected.
- The mass penalty parameter β_m does not influence the leading term.

Further analysis is done with respect to energy density and amplitude of the transmitted wave. The energy density of the incident wave (unit amplitude) is $W = \rho A \omega^2 \cdot 1^2$ while energy density and amplitude of the transmitted wave read

$$W^h = \rho A \omega^2 |T^h|^2 = W \left(1 - \frac{1}{4\beta_s^2} (k_1^h h)^2 + \frac{4\beta_s^2 - 12\beta_m \beta_s + 3}{48\beta_s^4} (k_1^h h)^4 + O(k_1^h h)^6 \right), \quad (68)$$

$$|T^h| = 1 - \frac{1}{8\beta_s^2} (k_1^h h)^2 + O(k_1^h h)^4. \quad (69)$$

Equations 66 to 69 provide a fast estimate of the error for long wave approximations. Below, the error is examined for whole range of wavenumbers $0 < k_1^h h < \pi$.

Exact dependencies of the transmitted and reflected amplitude on the wavenumber and penalty ratios are given in Figure 10. Only a marginal error in transmission is observed for $r > 1$ (Figure 10B). For $r < 1$, transmission is close to one for all wavenumbers except a narrow frequency band (Figure 10A). At this narrow band, a spurious total reflection is observed. It is a special numerical artifact of the bipenalty method, and it can be easily quantified for this case. The numerator of the transmitted amplitude in (64) can be zero if and only if the multiplier $(\beta_s + \beta_m(\cos(k_1^h h) - 1))$ is zero. This can be satisfied only if

$$k_1^h h = \arccos\left(\frac{\beta_m - \beta_s}{\beta_m}\right) = \arccos(1 - 2r) \equiv 2 \arcsin(\sqrt{r}) \quad (70)$$

and allows to obtain the frequency of the total spurious reflection

$$\omega_{tsr} = \frac{c_{01}}{h} \sqrt{r}. \quad (71)$$

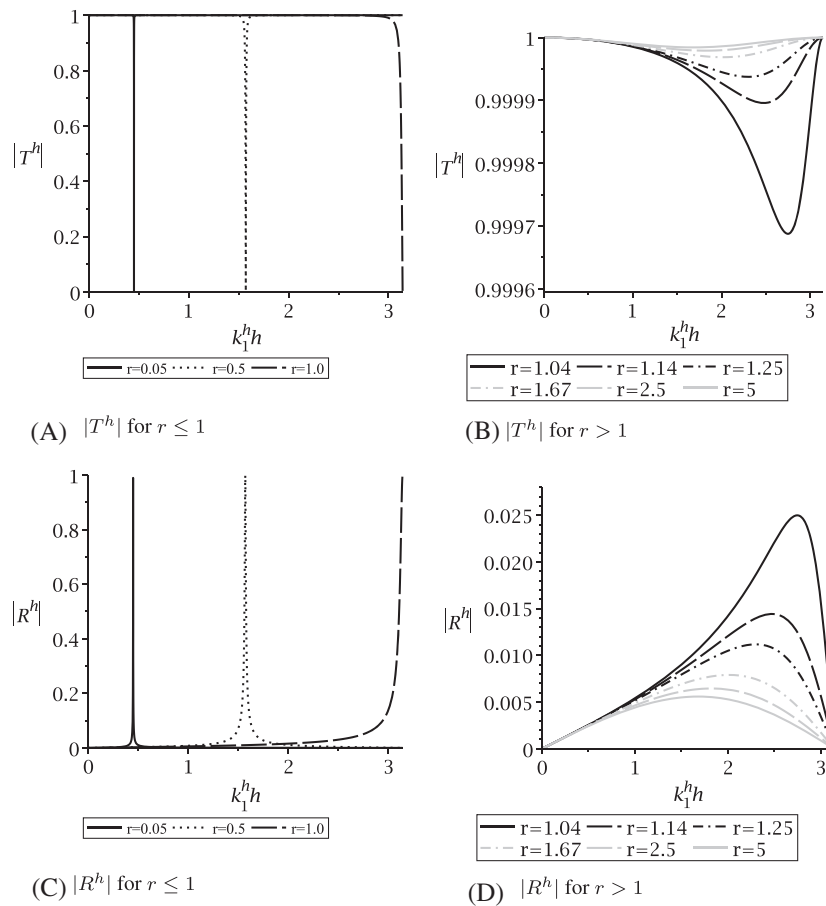


FIGURE 10 Amplitudes of the transmitted and reflected waves in dependency of dimensionless wavenumber $k_1^h h$ for the stiffness penalty $\beta_s = 100$ and for selected dimensionless penalty ratios r

At this frequency, the falling wave resonates with the bipenalty mass-stiffness subsystem and the bipenalty subsystem works as a free-end in a steady-state regime.⁷ A confirmation for this phenomenon is given in the numerical example in Section 5.3. The dependence of $k_{1,ISR}^h$ on r for $r < 1$ and the absence of the total spurious reflection for $r > 1$ can be observed in Figure 10C and 10D, respectively. The total spurious reflection for r equal to 0.05, 0.5, and 1.0 is observed at the dimensionless wavenumber 0.45103, $\pi/2$, and π , respectively, which is predicted by Equation 70.

It seems purely artificial to use $r < 1$ because increasing the mass penalty beyond $r = 1$ does not influence the critical time step size any more. But it may be relevant in case of contact of soft tissues. The stiffness penalty factor is driven by the bulk modulus. The mass penalty factor is then adjusted to that high value. At the same time, this magnitude of mass penalty is excessive for shear waves, where stiffness is driven by the shear modulus. This issue will be studied in the future work.

5 | NUMERICAL EXAMPLES

In this chapter, the properties of the bipenalty method in one-dimensional contact problems—the dynamic Signorini problem and the Huněk test—are numerically tested. Furthermore, a numerical study of RTEs on a numerical test is performed.

5.1 | Dynamic Signorini problem

In this section, the stability of explicit contact-impact algorithm using bipenalty technique was studied on the dynamic Signorini problem, which is represented by the motion of a bar that comes into contact with a rigid obstacle, see Figure 11. The bar of length $L = 1$ [m] with the initial velocity $v_0 = 1$ [$m \cdot s^{-1}$] is situated at a distance of $g_0 = 0$ [m] in front of the obstacle. The area of the bar section A [m^2], Young's modulus E [MPa] and density ρ [$kg \cdot m^{-3}$] are chosen to be unity. The setup of the example follows a previous work.²⁰

The bar is discretized by a regular finite element mesh containing one hundred 1D constant strain truss elements. The row-sum lumped mass matrices are used in combination with the CDM method for the time integration. The maximum eigenvalue of the mesh is $\lambda_{\max} = 4e4$ [s^{-2}] and the corresponding eigenfrequency is $\omega_{\max} = 200$ [s^{-1}].

Let us introduce the following dimensionless quantities

$$t^* = \frac{c_0 t}{L} \quad x^* = \frac{x}{L} \quad u^* = \frac{u(0, t)}{L} \quad F_c^* = \frac{c_0 F_c}{v_0 EA} \quad \sigma^* = \frac{\sigma A}{F_c}, \quad (72)$$

where t^* , x^* , u^* , F_c^* , σ^* are the dimensionless time, coordinate, contact displacement, contact force, and stress, respectively. F_c marks the contact force at the contact boundary. In the following figures, the results for the standard penalty method (left) and the bipenalty method (right) are plotted.

The dimensionless stiffness penalty β_s is chosen to 1.5. To verify the derived formula for the stability (54) defined by the critical Courant number C_r , the Courant number is set to $C = 0.82$, which is slightly higher than the critical value $C_r = 0.81649658$ for the penalty method. The results are shown in Figure 12A, where time distributions of the kinetic energy, the potential energy, the total energy, and the work done by contact forces are plotted. It is confirmed that the stability of the CDM is lost for the penalty method, whereas the solution obtained by the bipenalty method still perfectly conserved the total energy. When the Courant number C is set to 0.5, both methods are stable (see Figure 13).

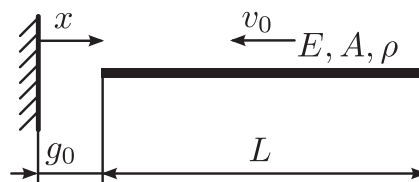


FIGURE 11 1D dynamic Signorini problem

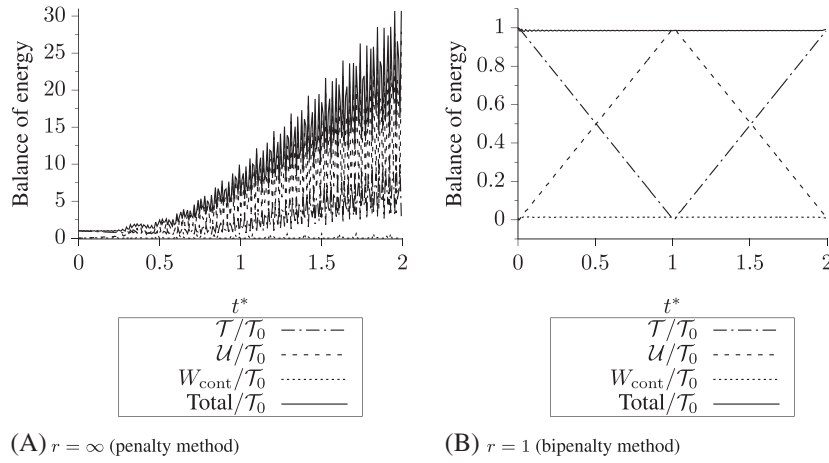


FIGURE 12 Time distribution of the balance of energy for $\beta_s = 1.5$ and $C = 0.82$. \mathcal{T} marks the kinetic energy, \mathcal{U} the strain energy, W_{cont} the work of the contact force, Total is the total energy, \mathcal{T}_0 is the kinetic energy at the initial time $t_0 = 0$

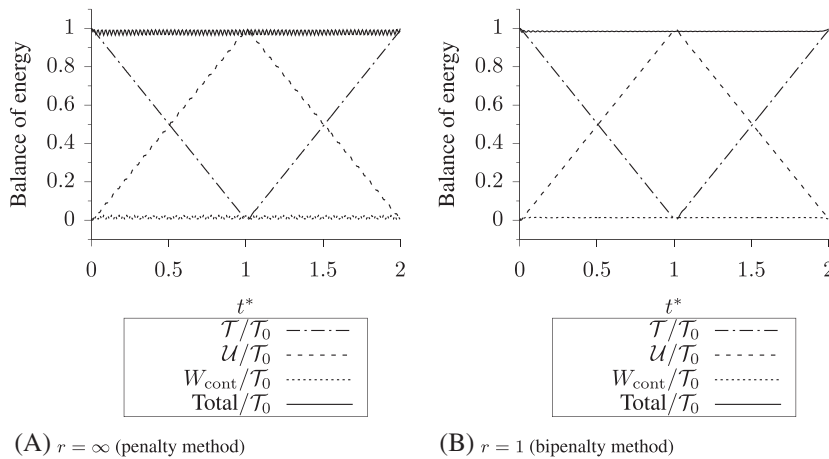


FIGURE 13 Time distribution of the balance of energy for $\beta_s = 1.5$ and $C = 0.5$

Note that the work of the contact force W_{cont} is almost zero. In fact, it should be exactly zero because the displacement is restricted to zero by the rigid obstacle. However, in the penalty-like methods, contact forces perform a spurious work on penetrations. This work converges to zero as β_s tends to infinity. Nevertheless, a finite value of the stiffness penalty parameter always results in a nonzero work of the contact force. One can also notice the presence of oscillations in the distributions of the potential energy and the work of contact forces, which result in oscillations in the distributions of the total energy. This phenomenon is primarily caused by the oscillations in the gap function, which will be discussed further.

Figure 14 shows the time distribution of the dimensionless contact displacement u^* (ie, the displacement of the node subject to a contact condition) for $\beta_s = 1.5$ and $C = 0.5$. The gap should be equal to zero during the impact, which is indicated by the exact solution in Figure 14. It is well known that penalty-like methods allow certain penetration of contact interfaces. As a result, the oscillations of kinematic and stress quantities can occur in impact problems. Figure 14B displays an attenuation of the oscillations for the bipenalty approach in comparison with the penalty method. However, from a certain value of the dimensionless stiffness penalty β_s , it is observed that the amplitude of oscillations are even higher for the bipenalty method than for the penalty method. An example is shown in Figure 15, where $\beta_s = 3.5$ is considered. The reason is probably that the oscillation of the contact displacement overshoot zero value. Thus, the contact constraint was deactivated, and the contact force disappears. In subsequent time steps, the contact constraint is again activated. Therefore, the system switches between 2 states, which generates the oscillations.

This phenomenon can also be observed in Figure 16, where the time distribution of the dimensionless contact force is plotted. Both distributions are bounded by zero. On the other hand, for the previously chosen value of the dimensionless

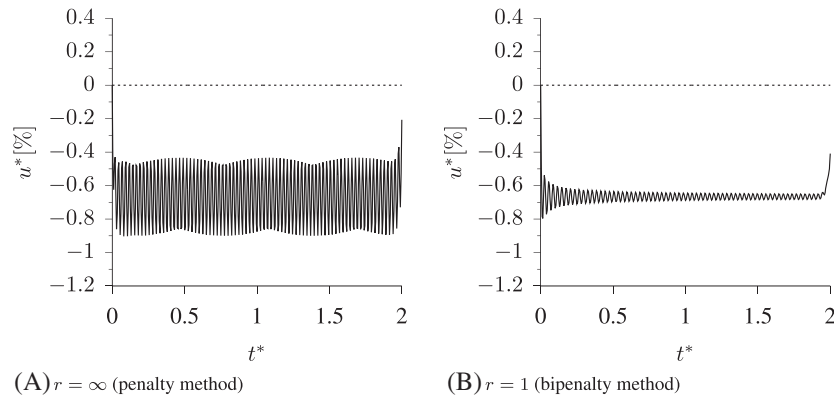


FIGURE 14 Time distribution of the dimensionless contact displacement for $\beta_s = 1.5$ and $C = 0.5$

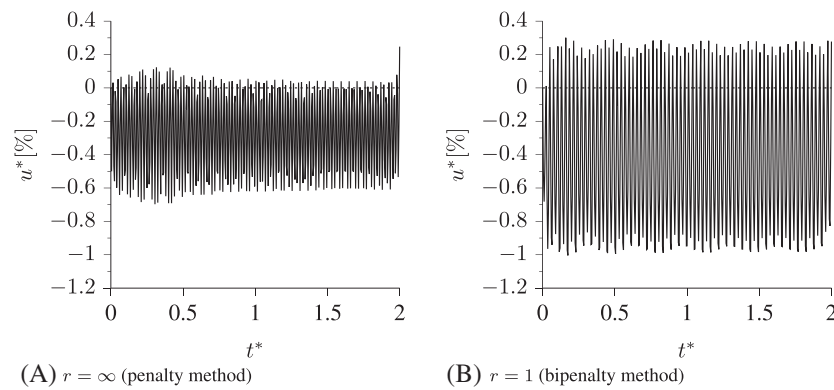


FIGURE 15 Time distribution of the dimensionless contact displacement for $\beta_s = 3.5$ and $C = 0.5$

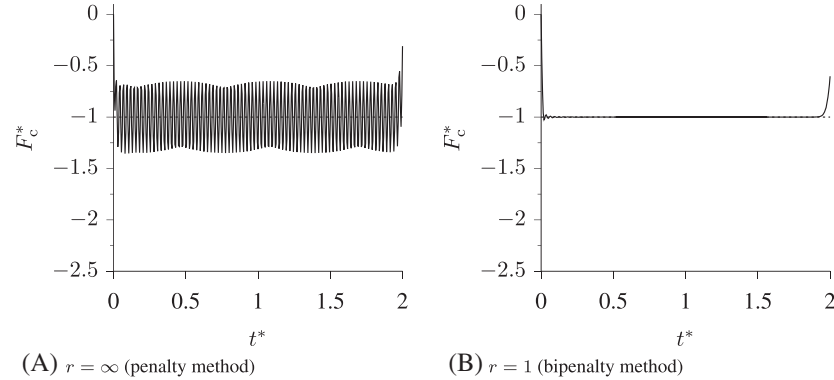


FIGURE 16 Time distribution of the dimensionless contact force for $\beta_s = 3.5$ and $C = 0.5$

stiffness penalty $\beta_s = 1.5$ time dependence of the dimensionless contact force oscillate around the exact solution as indicated in Figure 17. Similar to the distribution of the contact displacement in Figure 14B, the bipenalty method damps oscillations in the distribution of the contact force depicted in Figure 17B.

5.2 | One-dimensional impact of 2 bars with different lengths—the Huněk test

In this example, we follow the work by Huněk,¹² where the contact-impact problem of 2 bars of identical materials and with different lengths is studied. A scheme of this test is depicted in Figure 18. The left bar is moving to the right with a constant velocity v_{01} . The right bar with fixed right-hand side is at the rest. The geometrical, material, and numerical parameters were adopted from Huněk¹² as follows: the lengths $L_1 = 10$ [m] and $L_2 = 20$ [m], the Young's modulus

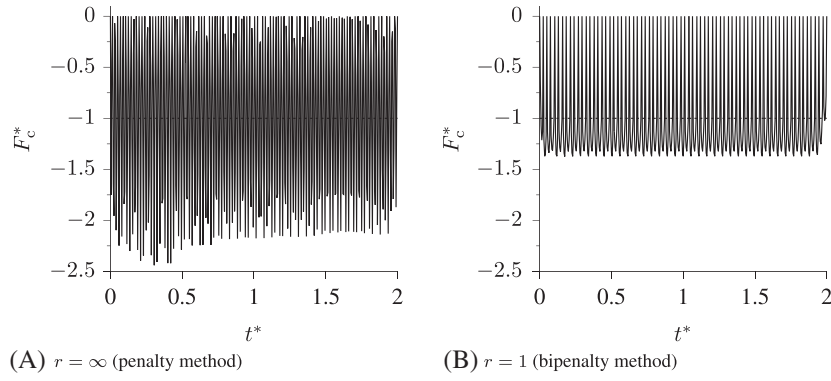


FIGURE 17 Time distribution of the dimensionless contact force for $\beta_s = 1.5$ and $C = 0.5$

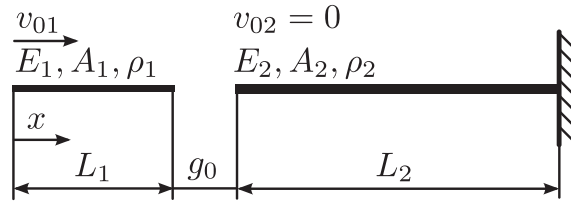


FIGURE 18 A scheme of the Huněk test

$E_1 = E_2 = 100$ [Pa], the mass density $\rho_1 = \rho_2 = 0.01$ [$kg \cdot m^{-3}$], the cross-sectional area $A_1 = A_2 = 1$ [m^2], the initial impact velocities $v_{01} = 0.1$ [m/s] and $v_{02} = 0$ [m/s], and the number of elements $n_1 = 50$, $n_2 = 100$, thus, the finite element lengths are set up as $h_1 = h_2 = 0.2$ [m], the initial contact gap $g_0 = 0$ [m], the duration time $T = 0.7$ [s]. The value of the contact force from the analytical prediction is $F = 0.05$ [N] for $t = 0 \dots 0.2$ [s] and $t = 0.4 \dots 0.6$ [s] and zero otherwise.

The both consistent and diagonalized additional mass matrices of the bipenalty term have been tested in this test. We can conclude that the results are identical, but in the case of diagonalized \mathbf{M}_p , the total mass of bipenalty mass term increases and the kinetical energy of the bipenalty system is disrupted.

Figures 19 and 20 show the time distributions of the contact force on the contacting node of the left bar for the Courant numbers $C = 0.2$ and $C = 0.999$, respectively. The influence of the stiffness penalty parameters $\beta_s = 0.125, 0.25$ and 1 together with the corresponding mass penalty parameters $r = \infty$ (for the penalty method) and $r = 1$ (for the bipenalty method with CPR) is investigated. The results for $C = 0.2$ (see Figure 19) given by both methods exhibit a stable character, which could be expected from the results obtained for the double-sided contact problem shown in Figure 5. Both the penalty and the bipenalty method suffer from oscillations for values of the stiffness parameter $\beta_s \geq 1$. On the other hand, the results show a delay effect in the contact force distribution for smaller values of the stiffness parameters (see the results for $\beta_s = 0.125$ and $\beta_s = 0.25$). This effect could be theoretically explained based on the reflection-transmission analysis discussed in Section 4. The results for the penalty method ($r = \infty$) with $C = 0.999$ (see Figure 20) show an unstable character. Here, the bipenalty method with CPR exhibits a stable behavior regardless of the choice of stiffness parameters β_s . However, the time distributions of contact forces for the bipenalty method with higher values of stiffness parameters β_s indicate oscillations. This effect will be analyzed in the future.

5.3 | Numerical study of reflection-transmission errors

Consider a uniform bar artificially split into 2 equal parts in the middle and coupled with the bipenalty method, see Figure 21. The right end of the bar is free while the left end is subjected to a harmonic force, which generates a monochromatic wave propagating toward the interface. The quantities of interest are stress evolution at points A and B that lie before and behind the interface, respectively.

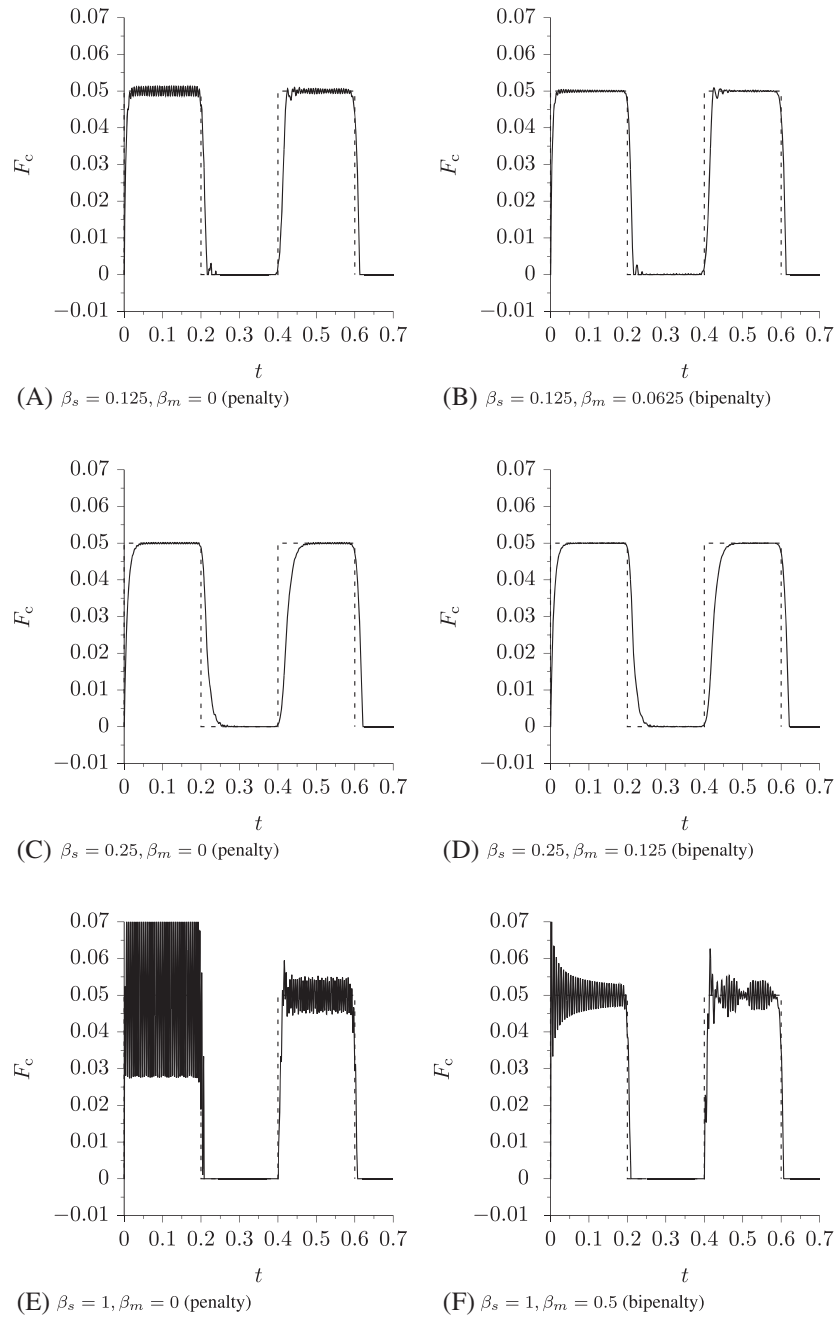


FIGURE 19 Results of the Huněk test: time history of contact forces for the penalty ($r = \infty$) and bipenalty ($r = 1$) methods for several stiffness parameters β_m and time step size corresponding to Courant number $C = 0.2$

We adopted geometrical, material, and numerical parameters of the test as follows: the length $L = 20$ [m], the Young's modulus $E = 1$ [Pa], the mass density $\rho = 1$ [$\text{kg} \cdot \text{m}^{-3}$], the cross-sectional area $A = 1$ [m^2], the amplitude of the external force $F_0 = 1$ [N], the number of elements in both halves of the bar $n_1 = 800, n_2 = 800$ ($h_1 = h_2 = 0.0125$ [m]), and bipenalty parameters $\beta_s = 2$ and $\beta_m = 200$. Three values of excitation frequencies are considered: 6.7882 [rad/s], 11.3137 [rad/s], and 15.8392 [rad/s]. They correspond to 60%, 100%, and 140% of the total spurious reflection given in Equation 71. Rayleigh damping and bulk viscosity is excluded from the simulation. Termination time t_{end} is chosen to be $1.375 L/c_0$. This choice prevents reflected signals at the points of interest: excitation at the left end—transmitted at the interface—reflected at the right end—arrive at point B (path length $1.375 L$), excitation at the left end—reflected at the interface—reflected at the left end—arrive at point A (path length $1.375 L$). The expressions from the analytical solution for the stress at points A and B read $\sigma_A = H(t - t_A) \sin(\omega(t - t_A))$ [Pa] and $\sigma_B = H(t - t_B) \sin(\omega(t - t_B))$ [Pa] with $t_A = 0.4375 L/c_0$ and $t_B = 0.5625 L/c_0$ being arrival times for the wave and $H(t)$ being the Heaviside function.

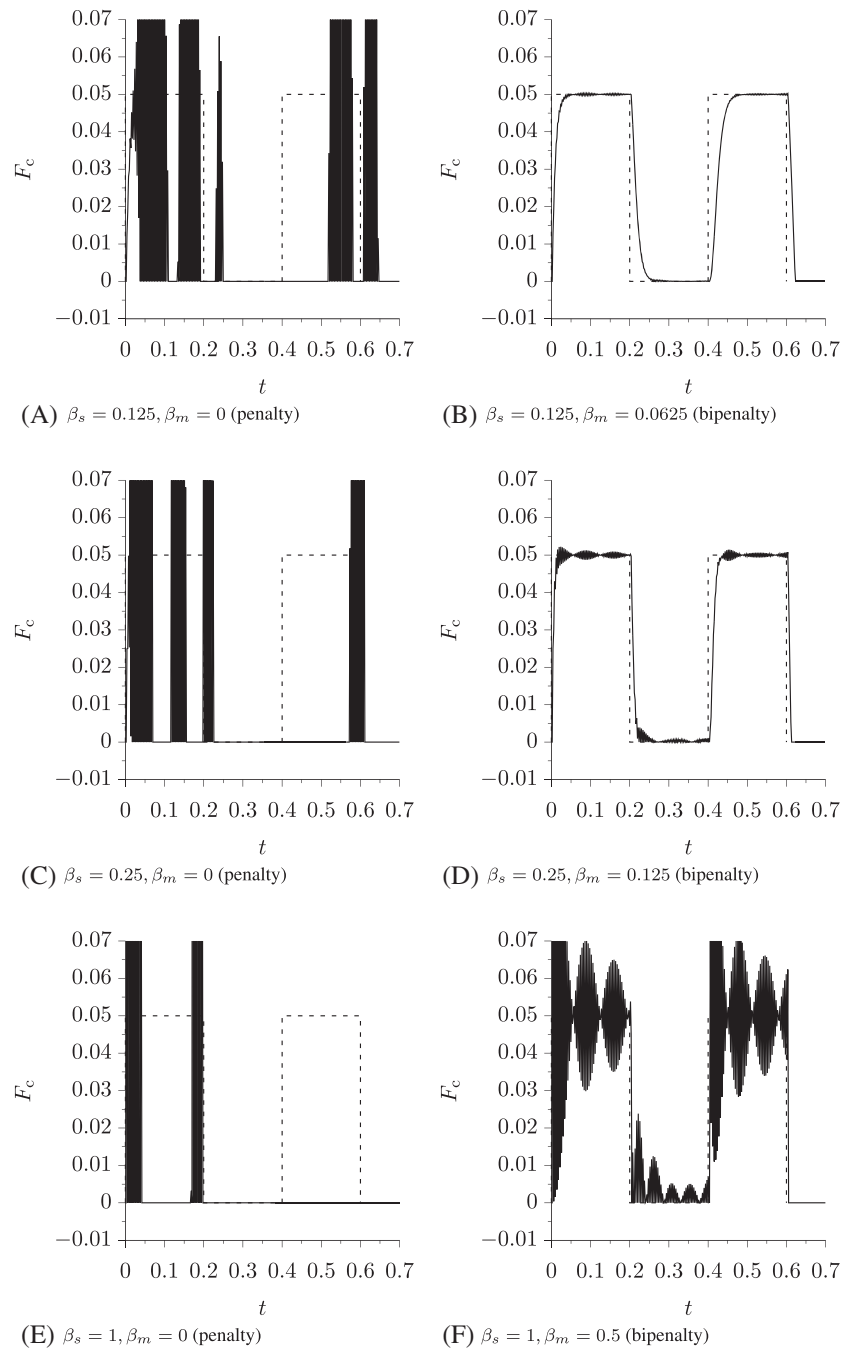


FIGURE 20 Results of the Huněk test: time history of contact forces for the penalty ($r = \infty$) and bipenalty ($r = 1$) methods for several stiffness parameters β_m and time step size corresponding to Courant number $C = 0.999$

Results for reflection-transmission of the stress wave are presented in Figure 22. Correct arrival times are observed at points A and B for all frequencies of the external force. If the frequency of the wave does not match the frequency of the total spurious reflection, then the wave is transmitted with the correct amplitude at point B and no superposition with the reflected wave at point A is observed. If the frequency exactly matches ω_{tsr} then the amplitude of the transmitted wave exponentially decays to zero with increasing time. In addition, clear superposition of the spuriously reflected wave with primary signal is observed at point A starting from the theoretically predicted time $0.5625 L/c_0$. By the end time, the stress amplitude at point A reaches twice the correct one.

This example confirms the existence of the artifact of total spurious reflection and verifies correctness of the formula (71) for the frequency of the total spurious reflection. Moreover, it illustrates that the steady solution is reached after 20 periods of the falling wave.

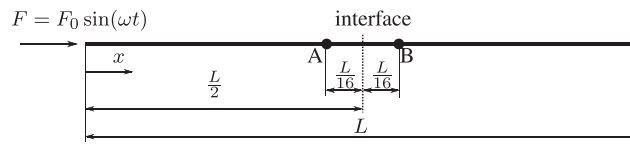


FIGURE 21 Setup of reflection-transmission error example

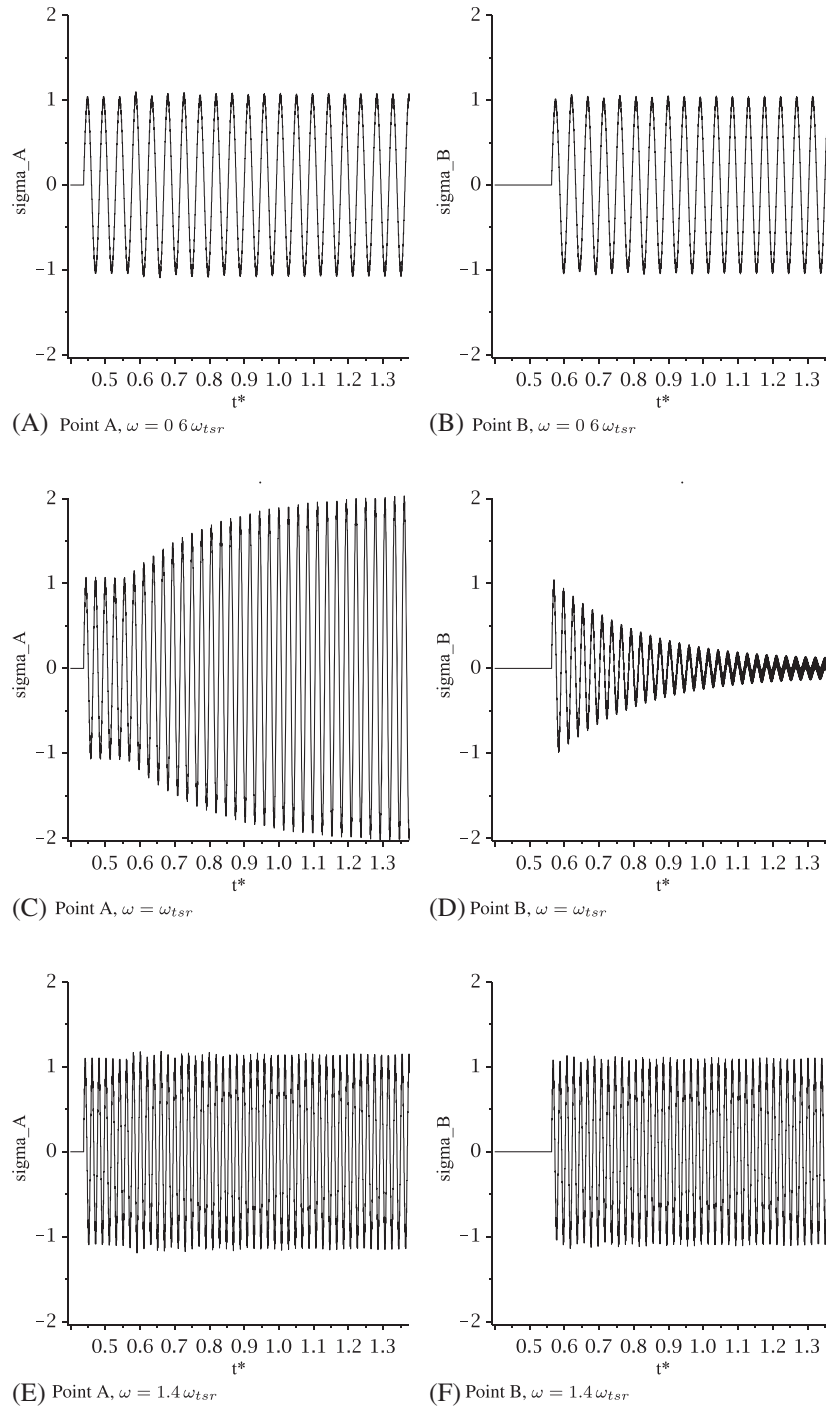


FIGURE 22 Stress histories at points A and B for different frequencies of excitation. Bipenalty parameters $\beta_s = 2, \beta_m = 200$. The Courant number is chosen as $C = 0.999$

6 | CONCLUSIONS

In this paper, the stability of an explicit contact-impact algorithm using the existing bipenalty approach in finite element analysis has been studied and analyzed for one-dimensional problems. The main attention has been paid on an upper bound estimation of the stable Courant number for the bipenalty method with respect to stiffness penalty and mass penalty parameters. This analysis is performed for several basic contact cases in one-dimensional problems. It is shown that the critical Courant number tends toward zero for the stiffness penalty parameter approaching infinity, whereas the mass penalty parameter is considered to be zero, ie, when only a pure penalty formulation is considered. On the other hand, setting the penalty ratio between mass and stiffness penalty parameters to *the critical penalty ratio* introduced by Askes in Askes et al⁹ preserves the stable Courant number at the level of the unpenalized system for an arbitrary value of the stiffness penalty parameter. The original method for computation of the critical penalty ratio is based on the highest frequency of a one-element subproblem with one active constraint with a rigid body. It considers cases for 2-node bar, Euler-Bernoulli beam and two-dimensional solid elements with lumped and consistent mass matrix approximations. In this paper, this method is extended to *double-sided* contact with 2 rigid bodies and to contact of 2 *homogeneous* deformable bodies in one dimension with lumped mass matrices.

The theoretical derivations in the first part of the paper are verified via numerical examples. The stability estimates give correct critical Courant numbers for a simple 1D dynamic Signorini problem and the Huněk test. Predicted dependencies of the critical time step size are confirmed: Pure penalty method decreases the critical time step size and the bipenalty method with critical penalty ratio preserves the critical time step size. It is an excellent property of the bipenalty method, which can be used in real numerical solutions of contact-impact problems. The two numerical contact-impact examples also revealed that both (penalty and bipenalty) methods caused spurious oscillations in the distributions of displacement and the contact force. This effect was especially obvious for higher values of stiffness penalty parameters, where contact damping is often used.²⁴ Solutions with bipenalty method tend to have less spurious oscillations.

Further, RTE analysis is performed in case of persistent contact for a monochromatic wave excitation. Analytical expressions for amplitudes of the transmitted and reflected waves are obtained and their dependency on stiffness and mass penalty are presented. First, this allows to compute the leading term of the transmission error. It is of the first order in element size and proportional to the inverse of *the penalty stiffness*. Moreover, this term is purely imaginary, ie, the main effect of the bipenalty coupling for long waves is a delay in the arrival time. This finding is relevant to explanation of the smearing of the contact force step in examples with low-penalty stiffness. Second, a spurious total reflection was found for dimensionless penalty ratios r less than one, which was also demonstrated with a transient example.

The estimation of the penalty parameter ensuring nonoscillating behavior of both methods will be investigated in further work together with implementation and testing the bipenalty method in multidimensional contact-impact problems. For example, it can be based on an existing symmetry preserving formulation for penalty contact given in Gabriel et al,²³ which is implemented in an in-house general purpose finite element code *PMD*.²⁶ Furthermore, the analysis of the bipenalty method in contact-impact problems for one-dimensional and multidimensional heterogeneous bodies will be investigated in detail. A preliminary study shows that the phenomenon of the total spurious reflection is also expected in these cases, and the local estimators are capable of accurate estimation of the critical penalty ratio. Finally, the bipenalty method will be adopted for a constraint stabilization technique for multibody dynamics with holonomic and nonholonomic constraints and compared with Baumgarte¹³ and Park and Chiou.¹⁹ Also our focus will be paid on correct diagonalization of bipenalty mass term without disruption of kinetical energy of the bipenalty system.

ACKNOWLEDGEMENTS

The work of D. Gabriel was supported by the European Regional Development Fund under Grant No. CZ.02.1.01/0.0/0.0/15_003/0000493 (Centre of Excellence for Nonlinear Dynamic Behaviour of Advanced Materials in Engineering). The work of R. Kolman was supported by the grant projects with 17-22615S of the Czech Science Foundation (CSF), the work of J. Plešek was supported by the grant projects with 17-12925S of CSF, and the work of J. Kopačka was supported by the grant projects with 16-03823S of CSF within institutional support RVO:61388998. The work was also supported by the bilateral mobility project DAAD-16-12 and Projekt-ID 57219898 funded via DAAD from Federal Ministry of Education and Research.

ORCID

Ján Kopačka  <http://orcid.org/0000-0002-2975-8347>

Anton Tkachuk  <https://orcid.org/0000-0001-8572-8532>

Dušan Gabriel  <https://orcid.org/0000-0002-7691-2191>

Radek Kolman  <http://orcid.org/0000-0002-8167-3535>

Manfred Bischoff  <http://orcid.org/0000-0003-1538-4281>

REFERENCES

1. Carpenter NJ, Taylor RL, Katona MG. Lagrange constraints for transient finite element surface contact. *Int J Numer Methods Eng*. 1991;32(1):103-128.
2. Zhong Z. *Finite Element Procedures for Contact-Impact Problems*, Oxford science publications. Oxford, England: Oxford University Press; 1993.
3. Dokainish MA, Subbaraj K. A survey of direct time-integration methods in computational structural dynamics. explicit methods. *Comput Struct*. 1989;32(6):1371-1386.
4. de la Fuente HM, Felippa CA. Ephemeral penalty functions for contact-impact dynamics. *Finite Elem Anal Des*. 1991;9(3):177-191.
5. Felippa CA. Error analysis of penalty function techniques for constraint definition in linear algebraic systems. *Int J Numer Methods Eng*. 1977;11(4):709-728.
6. Felippa CA. Iterative procedures for improving penalty function solutions of algebraic systems. *Int J Numer Methods Eng*. 1978;12(5):821-836.
7. Ilanko S. Introducing the use of positive and negative inertial functions in asymptotic modelling. Proceedings of the Royal Society of London A: Mathematical, Physical and Engineering Sciences. The Royal Society. 2005;461:2545-2562.
8. Ilanko S, Monterrubio LE. Bipenalty method from a frequency domain perspective. *Int J Numer Methods Eng*. 2012;90(10):1278-1291.
9. Askes H, Caramés-Saddler M, Rodríguez-Ferran A. Bipenalty method for time domain computational dynamics. *Proc Royal Soc A*. 2010;466:1389-1408.
10. Hetherington J, Rodríguez-Ferran A, Askes H. A new bipenalty formulation for ensuring time step stability in time domain computational dynamics. *Int J Numer Methods Eng*. 2012;90:269-286.
11. Hetherington J, Rodríguez-Ferran A, Askes H. The bipenalty method for arbitrary multipoint constraints. *Int J Numer Methods Eng*. 2013;93:465-482.
12. Huněk I. On a penalty formulation for contact-impact problems. *Comput Struct*. 1993;48(2):193-203.
13. Baumgarte J. Stabilization of constraints and integrals of motion in dynamical systems. *Comput Methods Appl Mech Eng*. 1972;1(1):1-16.
14. Lin ST, Huang JN. Numerical integration of multibody mechanical systems using Baumgarte's constraint stabilization method. *J Chin Inst Eng*. 2002;25(2):243-252.
15. Lin ST, Huang JN. Numerical integration of multibody mechanical systems using Baumgarte's constraint stabilization method. *J Chin Inst Eng*. 2002;25(2):243-252.
16. Chiou JC, Yang J, Wu SD. Stability analysis of Baumgarte constraint stabilization technique in multibody dynamic systems. *J Guid Control Dyn*. 1999;22(1):160-162.
17. Lin ST, Huang JN. Parameters selection for Baumgarte's constraint stabilization method using the predictor-corrector approach. *J Guid Control Dyn*. 2000;23(3):566-570.
18. Ascher UM, Petzold LR. Stability of computational methods for constrained dynamics systems. *SIAM J Sci Comput*. 1993;14(1):95-120.
19. Park KC, Chiou JC. Stabilization of computational procedures for constrained dynamical systems. *J Guid Control Dyn*. 1988;11(4):365-370.
20. Kopačka J, Gabriel D, Kolman R, Plešek J, Ulbin M. Studies in numerical stability of explicit contact-impact algorithm to the finite element solution of wave propagation problems. In: Computational Methods in Structural Dynamics and Earthquake Engineering (COMPdyn 2013) Papadrakakis M, Papadopoulos V, Plevris V, eds.; 2013; Kos, Greece:1-14. CD-ROM.
21. Hetherington J, Askes H. A mass matrix formulation for cohesive surface elements. *Theor Appl Fract Mec*. 2014;69:110-117.
22. Belytschko T, Neal MO. Contact-impact by the pinball algorithm with penalty and lagrangian methods. *Int J Numer Meth Eng*. 1991;31:547-572.
23. Gabriel D, Plešek J, Ulbin M. Symmetry preserving algorithm for large displacement frictionless contact by the pre-discretization penalty method. *Int J Numer Meth Eng*. 2004;61(15):2615-2638.
24. Belytschko T, Liu WK, Moran B. *Nonlinear Finite Element for Continua and Structures*. Chichester, West Sussex, England: John Wiley & Sons, Ltd; 2000.
25. Cohen Gary. *Higher-Order Numerical Methods for Transient Wave Equations*. Berlin, Heidelberg, New York: Springer Science & Business Media; 2013.
26. Plešek J, Gabriel D. PMD example manual, Institute of Thermomechanics, Academy of Sciences of the Czech Republic; 2000.

How to cite this article: Kopačka J, Tkachuk A, Gabriel D, Kolman R, Bischoff M, Plešek J. On stability and reflection-transmission analysis of the bipenalty method in contact-impact problems: A one-dimensional, homogeneous case study. *Int J Numer Meth Engng*. 2018;113:1607–1629. <https://doi.org/10.1002/nme.5712>

Partitioned formulation of contact-impact problems with stabilized contact constraints and reciprocal mass matrices

José A. González¹  | Ján Kopačka²  | Radek Kolman²  | Kwang-Chun Park³ 

¹Escuela Técnica Superior de Ingeniería, Universidad de Sevilla, Seville, Spain

²Institute of Thermomechanics, Academy of Sciences of the Czech Republic, Prague, Czech Republic

³Ann and H. J. Smead Aerospace Engineering Sciences, University of Colorado, Boulder, Colorado, USA

Correspondence

José A. González, Camino de los Descubrimientos s/n, Seville E-41092, Spain.
Email: japerez@us.es

Funding information

European Structural and Investment Funds, Operational Programme Research, Development and Education of the European Union, Grant/Award Number: CZ.02.1.01/0.0/0.0/15_003/0000493; Grantová Agentura České Republiky, Grant/Award Number: GA19-14237S

Abstract

This work presents an efficient and accuracy-improved time explicit solution methodology for the simulation of contact-impact problems with finite elements. The proposed solution process combines four different existent techniques. First, the contact constraints are modeled by a bipenalty contact-impact formulation that incorporates stiffness and mass penalties preserving the stability limit of contact-free problems for efficient explicit time integration. Second, a method of localized Lagrange multipliers is employed, which facilitates the partitioned governing equations for each substructure along with the completely localized contact penalty forces pertaining to each *free* substructure. Third, a method for the direct construction of sparse inverse mass matrices of the free bodies in contact is combined with the localized Lagrange multipliers approach. Finally, an element-by-element mass matrix scaling technique that allows the extension of the time integration step is adopted to improve the overall performance of the algorithm. A judicious synthesis of the four numerical techniques has resulted in an increased stable explicit step-size that boosts the performance of the bipenalty method for contact problems. Classical contact-impact numerical examples are used to demonstrate the effectiveness of the proposed methodology.

KEYWORDS

bipenalty contact, explicit time integration, inverse mass matrix, localized Lagrange multipliers, partitioned analysis

1 | INTRODUCTION

The task of simulating dynamic impact problems with penalty methods in a robust and efficient way, remains as one of the most elusive problems in computational contact mechanics. Among the different solution techniques available for the explicit solution of dynamic contact problems, the stiffness-penalty method is very popular mainly due to its efficiency and implementation simplicity. The principle of the penalty method implies that the contact impenetrability condition is satisfied only approximately, achieving a more precise fulfillment using stiffer penalty parameters. This makes penalty methods generally not consistent¹ within the variational formulation of the problem and the final matrix form is ill-conditioned.

Moreover, it is well known that the results of contact problems obtained via penalty-like methods are very sensitive to the magnitude of the penalty parameter. A direct consequence of an inexact fulfillment of the contact constraints

is nonzero penetration, which causes the contact stresses to produce nonphysical energy associated to the contact interfaces. Different rules of thumb, strongly based on experience, are then used in penalty methods to decide stable values for the stiffness penalty accompanied, at the same time, with acceptable violation of the contact constraints and affordable time integration steps. But these rules are problem dependent and it does not exist a general and theoretically sound solution to avoid all these effects, clearly limiting the applicability of penalty methods in contact applications.

Particularly in contact-impact problems, explicit time integration methods are normally preferred over implicit methods. In this article, we focus only on explicit time integration. A list of time integration strategies for contact-impact/dynamic contact problems in finite element modeling is mentioned in Reference 1. The explicit time schemes for the contact-impact problems have been employed in References 2-7. The explicit predictor–corrector algorithm has been designed for dynamic contact with smooth and nonsmooth surface geometries in Reference 8.

The reason for this is merely the efficiency gained by employing diagonal mass matrices to evaluate nodal accelerations, although explicit methods are conditionally stable and present a maximum time-step size limitation defined by the Courant restriction.⁹ However, sudden contact-impact events normally produce stress waves with high frequency content and a small time-step is required to accurately track the propagation of these waves in the solids. Also the use of diagonal mass matrices produces dispersion error and slower wave velocities, especially for the higher frequencies, representing its use a sacrifice of accuracy in the benefit of efficiency.

In general, the two most important concerns regarding the solution of contact-impact problems with explicit penalty methods are *robustness* and *efficiency*. In this context, *robustness* is mainly defined by the stability of the solution and the control of possible contact stress oscillations that are triggered by the impact, while *efficiency* refers to the group of techniques devised to reduce the total computational effort required per time step.

Starting with the stability issue, the main problem of the explicit penalty method in elastodynamics is that the stability limit of the time integration scheme can be seriously affected when large values of the stiffness penalty are used to enforce the fulfillment of the kinematic contact constraints.⁴ In fact, the critical time step for a stable solution is inversely proportional to the maximum system frequency and this frequency increases with higher values of the penalty stiffness parameter. To deal with this difficulty, in this work we adopt a mass–stiffness two-penalty approach or bipenalty method (BPM). In BPM, an extra term penalizing the kinetic energy associated to the violation of the contact velocity constraints is added to the variational form of the classical penalty method. Using the extra mass penalty, it is possible to control the high frequency spectrum and the maximum system frequency that defines the stability limit of the explicit time integration process. Furthermore, by selecting an optimal ratio for the mass and stiffness penalty parameters, it is demonstrated that the same stability limit can be preserved as the original problem without contact constraints. The stabilization of constraints through combined penalization of internal and kinetic energy terms was first proposed by Baumgarte¹⁰ in the context of multibody dynamics. The idea was later extended to contact-impact problems by Asano¹¹ and Armero.¹² In numerical analysis, BPM is known as the consistent penalty method^{13,14} and has been used for imposition of dynamic boundary conditions. Hetherington et al.¹⁵⁻¹⁷ extended the BPM for dynamical problems with constraints, contact problems and also applied the method to improve the stability limit of explicit time integration schemes. The BPM formulation proposed here, follows the work of Kopačka et al.^{18,19} for one-dimensional contact problems and extends it to the multidimensional case within the partitioned formulation.

Another important aspect affecting the robustness of contact-impact dynamic solution algorithms is the emergence of spurious oscillations in the contact stresses, characterized by a zig-zag effect consisting of a consecutive activation/deactivation of the contact constraints at consecutive time steps. These oscillations can propagate to the interior of the bodies leading to significant errors and a wrong prediction of the complete system response. This undesirable effect is attributed to the nonsmooth character of the normal contact law, generating an instantaneous change of velocities at the contact zone, associated to infinite accelerations and cause of oscillations in the contact stresses. Several numerical techniques and strategies have been proposed in the literature to control these spurious oscillations. Examples are the work of Doyen,²⁰ the stabilized implicit Newmark method for nonsmooth dynamics and contact problems,^{21,22} interface mass redistribution techniques,^{23,24} singular mass techniques,²⁵ and more recently, the regularization of the penalty constraint with a smooth contact stress transition.^{26,27} Another solution to the oscillation of contact stresses is the application of time explicit schemes based on a judicious combination of predictor and corrector phases for evaluating the kinematical quantities and states, like the stabilized explicit scheme with stiffness penalties proposed by Wu²⁸ for contact problems with large deformations. A modified predictor–corrector algorithm of this kind is proposed in this work for BPM.

On the other hand, we have all the factors affecting the overall *efficiency* of the numerical algorithm. In this category we group the reduction of the numerical cost per iteration and the extension critical time-step.

The most time consuming part of an explicit time integration method, sometimes after the evaluation of the vector of internal forces, comes with the solution of the linear system of equations. Theoretically, a multiplication of the inverse mass matrix by the vector of total forces is needed to compute the nodal accelerations at every time step. The inverse of a populated matrix is computationally expensive and the final inverse mass matrix is full while the original mass matrix is sparse. For this reason, even though the variationally consistent mass matrix (CMM) leads to optimal error estimates, a lumped mass matrix (LMM) obtained by row sum of the CMM or other diagonalized mass matrices are generally preferred.²⁹ Unfortunately, many impact problems normally include wave propagation with broad frequency content and even though the accuracy of LMM is acceptable for capturing the low-frequency response, it is unable to track high-frequency components. This makes contact-impact a typical application where the higher dispersion accuracy of CMM over LMM can be desirable.

A good solution to this dilemma is to employ a reciprocal mass matrix (RMM), that is, an approximation of the mass matrix inverse that is directly assembled without expensive operations. By using this inverse, only a cheap sparse matrix-vector multiplication is required to explicitly compute accelerations and advance the integration in time. The key idea of a RMM was introduced by Tkachuk and Bischoff^{30,31} and it is basically to exploit Hamilton's principle, discretizing both displacement and momentum fields with biorthogonal shape functions, to produce a RMM in the form of a second-order tensor product where only a diagonal projection operator needs to be inverted. This basic procedure also requires some cumbersome modifications of the RMM for the application of boundary conditions, a difficulty that can be circumvented by using localized Lagrange multipliers.³² Therefore, for explicit time integration of contact problems, the combination of RMM with BPM reveals as a perfect marriage for accuracy and stability. However, incorporating the mass penalties into the RMM is not direct and presents a new difficulty due to the fact that mass-inverse is not an additive property. Also note that if the global mass matrix is modified with mass-penalties, the inverse mass matrix needs to be recalculated every time there is a change in the contact conditions. In this work, these problems are solved in a consistent way by employing localized Lagrange multipliers.

The method of localized Lagrange multipliers (LLM) is a general variational framework used to solve partitioned systems in structural mechanics, also applicable to contact problems,³³⁻³⁵ that introduces between the solids in contact an intermediate surface endowed with independent degrees of freedom and treated with a FEM discretization to approximate the interface variables. Finally, this auxiliary contact surface is connected to the solids using classical Lagrange multipliers defined on the interface nodes, obtaining a formulation that naturally allows to uncouple the body equations of motion from the contact conditions. Adopting this approach, the RMM appearing in the solid equations and the mass penalty terms associated with the contact conditions can be consistently combined. The benefit of using LLM is then twofold. First, it alleviates the special treatments needed for the construction of an RMM. Second, it allows to separate the interface contact problem from the solid body equations. This way, the constructed inverse mass matrix appears unaltered in the equilibrium equations of the contacting bodies and it is not affected by the mass penalties, that remain exclusively in the partitioned equations of motion obtained for the contact interface.

Finally, an additional method is proposed to improve the efficiency of explicit time integration methods based on the extension of the critical time-step size. For this task and in order to alleviate the step-size limitations imposed by the mesh frequencies, whose response components contribute very little when low modes dominate the transient response, various mass matrix scaling techniques have been proposed. The basic idea behind a selective mass scaling (SMS)³⁶⁻⁴² is to alter the element mass matrix artificially in order to reduce the high frequencies of the dynamical system without affecting the low-mid frequencies. Most of these methods require either replacing existing elements by tailored elements and/or adopt element component-dependent time stepping procedures, leading to either elemental and/or global approaches, depending on how the modification of the mass matrix is made. Other techniques, like variationally selective mass scaling (VSMS)⁴³⁻⁴⁵ are based on templated variational forms of the elastodynamic problem with free parameters that are tuned for optimal mass scaling. For our particular application, SMS should be made compatible with the construction of the RMM, hence an element-by-element mass scaling is adopted to reduce/filter out the high frequencies of the dynamical system without affecting the low-mid frequencies.^{32,46}

In summary, the present study addresses in multiple fronts the explicit solution process of contact-impact problems with the objective of improving its applicability to real-life applications by integrating the following four algorithmic components:

1. The contact constraints are modeled by a bipenalty contact-impact formulation¹⁸ that incorporates stiffness and mass penalties preserving the stability limit of contact-free problems for efficient explicit time integration;
2. A method of localized Lagrange multipliers⁴⁷ is employed, which facilitates the partitioned governing equations for each substructure along with the completely localized contact penalty forces pertaining to each free substructure;
3. A method for the direct construction of sparse inverse mass matrices of the free bodies in contact³² is combined with the localized Lagrange multipliers approach;
4. An element-by-element mass matrix scaling technique⁴⁸ that allows the extension of the time integration step is adopted to improve the overall performance of the algorithm.

It will be shown that a judicious integration of these four algorithmic components produces an extremely efficient explicit contact-impact formulation that maintains stability and produces accurate results even near the critical time-step, under conditions totally forbidden for the standard stiffness penalty method heretofore.

The article is organized as follows. Section 2 formulates the contact problem and Section 3 formalizes the combination of the BPM with RMM through localized Lagrange multipliers. The RMM construction using dual basis functions is described in Section 4, while the final partitioned formulation of the contact problem with BPM is obtained in Section 5. Section 6 is dedicated to the derivation of an optimal mass-penalty ratio for BPM. Time integration using an explicit predictor–corrector algorithm to avoid oscillations is described in Section 7. The performance enhancement by extension of the critical time-step with SMS is discussed in Section 8. Finally, in Section 9, we present several numerical examples, where we test the accuracy of the proposed techniques, and Section 10 closes with the conclusions.

2 | FORMULATION OF THE CONTACT-IMPACT PROBLEM

At this point, the initial-boundary value problem of linear elastodynamics with consideration of frictionless contact is formulated in a strong sense. Without loss of generality, suppose two deformable bodies that can potentially be in contact at any time $t \in [0, T]$, see Figure 1. The position of the material particles of these bodies is described by means of position vectors $\mathbf{x}^{(i)}$, $i = 1, 2$ from the domain $\Omega = \Omega^{(1)} \cup \Omega^{(2)}$. The outer surface of this domain is disjointly covered by the boundaries Γ_D , Γ_N , and Γ_c , where boundary conditions of Dirichlet, Neumann, and contact type, respectively, are prescribed. The physical requirement of impenetrability of bodies is formulated using the basic contact kinematic quantity, the so-called gap function:

$$g_N = - \left[(\mathbf{x}^{(2)} + \mathbf{u}^{(2)}) - (\mathbf{x}^{(1)}(\bar{\xi}) + \mathbf{u}^{(1)}(\bar{\xi})) \right] \cdot \mathbf{n}^{(1)}(\bar{\xi}) = - (\mathbf{u}^{(2)} - \mathbf{u}^{(1)}(\bar{\xi})) \cdot \mathbf{n}^{(1)}(\bar{\xi}) - g_N^0, \quad (1)$$

which for given slave point $\mathbf{x}^{(2)} \in \Gamma_c^{(2)}$ gives the signed distance to its closes point projection, $\mathbf{x}^{(1)}(\bar{\xi}) \in \Gamma_c^{(1)}$, where $\bar{\xi}$ is the convective coordinate that parameterizes $\Gamma_c^{(1)}$ and the bar denotes the closest point projection coordinate, $\mathbf{n}^{(1)}$ is the

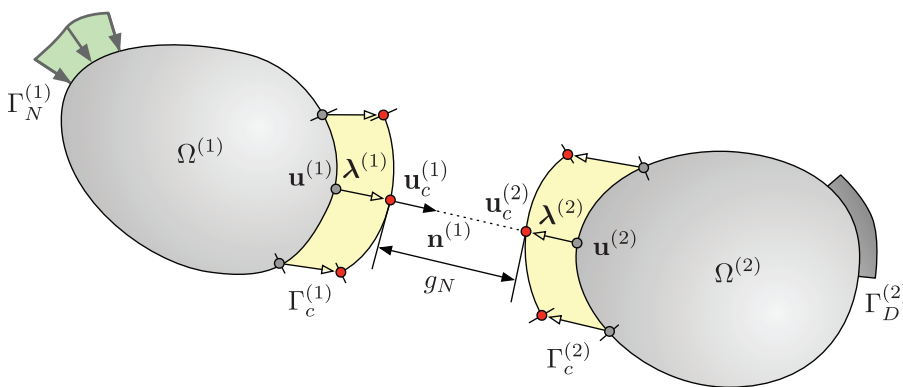


FIGURE 1 Representation of two bodies with domain $\Omega^{(i)}$ ($i = 1, 2$) in potential contact and definition of the normal gap function g_N . Localized Lagrange multipliers $\lambda^{(i)}$ are introduced on both sides $\Gamma_c^{(i)}$ of the contact interface to separate the solid equilibrium equations from the interface contact problem. Contact zones and body surfaces are represented separately for better visualization

outer normal vector at the current master point $\mathbf{x}^{(1)} + \mathbf{u}^{(1)}(\bar{\xi})$. Note that by the above definition, the gap is open for a negative value of the gap function. The problem of linear elastodynamics is governed by the balance of linear momentum supplemented by boundary and initial conditions:

$$\nabla \cdot \boldsymbol{\sigma} + \mathbf{f} = \frac{\partial \mathbf{p}}{\partial t} \quad (\mathbf{x}, t) \in \Omega \times [0, T], \quad (2)$$

$$\mathbf{u}(\mathbf{x}, t) = \hat{\mathbf{u}}(\mathbf{x}, t) \quad (\mathbf{x}, t) \in \Gamma_D \times [0, T], \quad (3)$$

$$\mathbf{t}(\mathbf{x}, t) = \hat{\mathbf{t}}(\mathbf{x}, t) \quad (\mathbf{x}, t) \in \Gamma_N \times [0, T], \quad (4)$$

$$\mathbf{u}(\mathbf{x}, t)|_{t=0} = \mathbf{u}^0(\mathbf{x}) \quad \mathbf{x} \in \Omega, \quad (5)$$

$$\dot{\mathbf{u}}(\mathbf{x}, t)|_{t=0} = \mathbf{v}^0(\mathbf{x}) \quad \mathbf{x} \in \Omega \quad (6)$$

with the displacement field $\mathbf{u}(\mathbf{x}, t)$ as a primary unknown, that is tied to the Cauchy stress tensor, $\boldsymbol{\sigma}$, through the symmetric part of the gradient of deformation, $\boldsymbol{\varepsilon} = \text{symm}(\nabla \mathbf{u})$, using Hooke's law $\boldsymbol{\sigma} = \mathbb{C} : \boldsymbol{\varepsilon}$, where \mathbb{C} is the fourth-order tensor of elastic constants. Further, \mathbf{f} is the vector of body forces per unit volume and $\mathbf{p} = \rho \dot{\mathbf{u}}$ is the momentum vector. The boundary condition of Dirichlet type (3) prescribes displacement field on Γ_D at all times $t \in [0, T]$. Similarly, the Neumann boundary condition (4) prescribes the value of the spatial derivative of the displacement field by means of a traction vector $\mathbf{t} = \boldsymbol{\sigma} \cdot \mathbf{n}$, where \mathbf{n} is the outer normal vector to Γ_N . Initial conditions (5) and (6) prescribe displacement and velocity fields at time $t = 0$ on the domain Ω .

On the other hand, we have the interface contact constraints expressed by the so-called Hertz–Signorini–Moreau conditions:

$$p_c(\mathbf{x}, t) \geq 0 \quad (\mathbf{x}, t) \in \Gamma_c \times [0, T], \quad (7)$$

$$g_N(\mathbf{x}, t) \leq 0 \quad (\mathbf{x}, t) \in \Gamma_c \times [0, T], \quad (8)$$

$$p_c(\mathbf{x}, t)g_N(\mathbf{x}, t) = 0 \quad (\mathbf{x}, t) \in \Gamma_c \times [0, T] \quad (9)$$

which can be understood at a more general level of constrained optimization as the KKT (Karush–Kuhn–Tucker) conditions. Condition (9), known as the *complementarity* condition, imposes that nonzero contact pressure, $p_c = -\mathbf{t} \cdot \mathbf{n}$, can only exist during contact and that separation is always accompanied by zero contact stresses. A final condition needs to be satisfied by the time integration strategy in order to achieve energy conservation:

$$p_c(\mathbf{x}, t)\dot{g}_N(\mathbf{x}, t) = 0 \quad (\mathbf{x}, t) \in \Gamma_c \times [0, T] \quad (10)$$

enforcing that pressure may only be generated during persistent contact, and therefore this equation is called the *persistence* condition.⁴⁹

Note that in addition to the displacement field, $\mathbf{u}(\mathbf{x}, t)$, the scalar field of contact pressure, $p_c(\mathbf{x}, t) \in \Gamma_c \times [0, T]$, is also unknown in the given formulation. To get rid of this dependence, the penalty method is used to regularize the contact conditions. This regularization consists in replacing the contact pressure with the expression:

$$p_c(\mathbf{x}, t) = \epsilon_s \langle g_N(\mathbf{x}, t) \rangle, \quad (11)$$

where ϵ_s is the stiffness penalty parameter and the operator $\langle \bullet \rangle$ denotes the so-called Macaulay's brackets defined as $\langle \bullet \rangle = \frac{|\bullet| + \bullet}{2}$. If persistence condition (10) is also regularized, it leads to the bpenalty method, as will be explained in the following section.

3 | BIPENALTY METHOD WITH RECIPROCAL MASS MATRIX AND LOCALIZED LAGRANGE MULTIPLIERS

To formulate the contact problem and for the reasons that will be explained later, instead of considering a direct interaction across the external surfaces of the two bodies, we duplicate the potential contact areas $\Gamma_c \subset \Gamma$ and tie them to the original solid surfaces using Lagrange multipliers. The contact problem is then reformulated in terms of an interaction between these auxiliary surfaces. To this end, we invoke Hamilton's principle for partitioned constrained

elastodynamics³² including penalized contact constraints.¹⁸ The variational form of the Hamiltonian can then be written using the following four-field expression:

$$\delta H(\mathbf{u}, \mathbf{p}, \mathbf{u}_c, \boldsymbol{\ell}) = \int_{t_1}^{t_2} \delta \{ T(\dot{\mathbf{u}}, \mathbf{p}) - U(\mathbf{u}) + W(\mathbf{u}) + W_c(\mathbf{u}, \mathbf{u}_c, \boldsymbol{\ell}) \} dt = 0, \quad (12)$$

where the vector fields $\mathbf{u}(\mathbf{x}, t)$, $\mathbf{p}(\mathbf{x}, t)$, $\mathbf{u}_c(\mathbf{x}_c, t)$, and $\boldsymbol{\ell}(\mathbf{x}_c, t)$ respectively represent the continuum displacement, momentum, contact interface displacements, and Lagrange multipliers, functions of the particle position $\mathbf{x} \in \Omega$, contact surface location $\mathbf{x}_c \in \Gamma_c$ and time $t \in [0, T]$.

In the components of the Hamiltonian action integral, δT is the virtual kinetic energy, δU the virtual potential energy, δW the virtual work done by the external loads and δW_c the virtual work due to contact constraints; magnitudes that can be respectively expressed:

$$\delta T(\dot{\mathbf{u}}, \mathbf{p}) = \int_{\Omega} \delta \left(\frac{1}{2} \mathbf{p} \cdot \dot{\mathbf{u}} \right) d\Omega, \quad \delta U(\mathbf{u}) = \int_{\Omega} \delta \boldsymbol{\varepsilon} : \boldsymbol{\sigma} d\Omega, \quad \delta W(\mathbf{u}) = \int_{\Omega} \delta \mathbf{u} \cdot \mathbf{f} d\Omega + \int_{\Gamma_N} \delta \mathbf{u} \cdot \hat{\mathbf{t}} d\Gamma \quad (13)$$

$$\delta W_c(\mathbf{u}, \mathbf{u}_c, \boldsymbol{\ell}) = - \int_{\Gamma_c} \delta \left(\frac{1}{2} \epsilon_s \langle g_N \rangle^2 \right) d\Gamma + \int_{\Gamma_c} \delta \left(\frac{1}{2} \epsilon_m \langle \dot{g}_N \rangle^2 \right) d\Gamma - \int_{\Gamma_c} \delta \{ \boldsymbol{\ell} \cdot (\mathbf{u} - \mathbf{u}_c) \} d\Gamma \quad (14)$$

with contact interface displacements \mathbf{u}_c defined only at the contact zone Γ_c and compatibilized with the body surface displacements \mathbf{u} by using a field of localized Lagrange multipliers $\boldsymbol{\ell}$. As external loads, we consider body forces per unit volume \mathbf{f} acting on the domain Ω with density ρ . Contact penalty terms enforce regularized contact conditions (7)–(10) by penalizing both the nonzero gap and the gap rate by introducing two quadratic penalty potentials into the variational formulation. This way, two different stiffness and mass penalty parameters are introduced and defined respectively as ϵ_s (kg/m²/s²) and ϵ_m (kg/m²).

Then, some manipulation is needed to eliminate the virtual velocity from the virtual kinetic energy term in (13). By making use of the momentum-velocity relation ($\mathbf{p} = \rho \dot{\mathbf{u}}$) in the following identity:

$$\frac{1}{2} \mathbf{p} \cdot \dot{\mathbf{u}} = \mathbf{p} \cdot \dot{\mathbf{u}} - \frac{1}{2\rho} \mathbf{p} \cdot \mathbf{p} \quad (15)$$

we can obtain an equivalent expression for the virtual kinetic energy per unit volume:

$$\delta \left(\frac{1}{2} \mathbf{p} \cdot \dot{\mathbf{u}} \right) = \delta \dot{\mathbf{u}} \cdot \mathbf{p} + \delta \mathbf{p} \cdot \left(\dot{\mathbf{u}} - \frac{1}{\rho} \mathbf{p} \right) \quad (16)$$

and finally performing an integration by parts of the second term of the last equation yields:

$$\int_{t_1}^{t_2} \delta \dot{\mathbf{u}} \cdot \mathbf{p} dt = - \int_{t_1}^{t_2} \delta \mathbf{u} \cdot \dot{\mathbf{p}} dt \quad (17)$$

relation that can be used to eliminate the virtual velocity field from the formulation.

Introducing previous identities, (16) and (17), into the principle of stationary action (12), we obtain the final four-field variational form of the Hamilton's principle for constrained elastodynamics with contact penalties:

$$\delta H(\mathbf{u}, \mathbf{p}, \mathbf{u}_c, \boldsymbol{\ell}) = \int_{t_1}^{t_2} \left\{ \int_{\Omega} \delta \mathbf{p} \cdot \left(\dot{\mathbf{u}} - \frac{1}{\rho} \mathbf{p} \right) d\Omega - \int_{\Omega} (\delta \mathbf{u} \cdot \dot{\mathbf{p}} + \delta \boldsymbol{\varepsilon} : \boldsymbol{\sigma}) d\Omega + \int_{\Omega} \delta \mathbf{u} \cdot \mathbf{f} d\Omega + \int_{\Gamma_N} \delta \mathbf{u} \cdot \hat{\mathbf{t}} d\Gamma \right. \\ \left. - \int_{\Gamma_c} \delta \mathbf{u} \cdot \boldsymbol{\ell} d\Gamma - \int_{\Gamma_c} \delta \boldsymbol{\ell} \cdot (\mathbf{u} - \mathbf{u}_c) d\Gamma + \int_{\Gamma_c} \delta \mathbf{u}_c \cdot \boldsymbol{\ell} d\Gamma - \int_{\Gamma_c} \delta g_N H(g_N) (\epsilon_m \ddot{g}_N + \epsilon_s g_N) d\Gamma \right\} dt = 0 \quad (18)$$

expression that will be used to derive the equations of motion.

Discretization in space of this mixed variational form is performed by using independent shape functions for displacements, momenta, and Lagrangian multipliers. We carry out then a standard mixed FEM discretization with independent shape functions for the different fields:

$$\mathbf{u}(\xi) = \mathbf{N}_u(\xi)\mathbf{u}, \quad \mathbf{p}(\xi) = \mathbf{N}_p(\xi)\mathbf{p}, \quad \mathbf{u}_c(\xi) = \mathbf{N}_u(\xi)\mathbf{u}_c, \quad \ell(\xi) = \mathbf{N}_\lambda(\xi)\lambda \quad (19)$$

but adopting compatible displacement shape functions between the solid boundary and the contact surface. Note also, see Figure 1, that the penetration can be related to the normal projection of the boundary displacement and expressed:

$$g_N(\mathbf{u}_c) = \mathbf{H}\mathbf{u}_c - g_N^0 \leq 0, \quad (20)$$

where $\mathbf{H}\mathbf{u}_c = \mathbf{u}_c^{(1)}\mathbf{n}^{(1)} - \mathbf{u}_c^{(2)}\mathbf{n}^{(1)}$ and matrix \mathbf{H} represents a geometrical operator from the boundary displacement field to the gap function. The particular form of this operator follows from the assumed contact discretization. The second time derivative of the gap function \ddot{g}_N is then in general:

$$\ddot{g}_N(\mathbf{u}_c, \dot{\mathbf{u}}_c, \ddot{\mathbf{u}}_c, t) = \ddot{\mathbf{H}}(t)\mathbf{u}_c + 2\dot{\mathbf{H}}(t)\dot{\mathbf{u}}_c + \mathbf{H}(t)\ddot{\mathbf{u}}_c \quad (21)$$

and in the following, the nonlinear matrices $\ddot{\mathbf{H}}$ and $\dot{\mathbf{H}}$ are omitted so that:

$$\ddot{g}_N(\mathbf{u}_c) = \mathbf{H}\ddot{\mathbf{u}}_c \quad (22)$$

including only the linear term. This means that we are assuming at the contact zone a slow variation of the normal vector during contact. It is needed to mention that these high-order terms should not be neglected in the case of fast changing normal direction, because tangential spurious oscillations could occur at the contacting points.

Introducing all these approximations in (18) one obtains the following set of semidiscrete equations:

$$\mathbf{A}^\top \ddot{\mathbf{u}} - \mathbf{C}\mathbf{p} = \mathbf{0} \quad \text{Momentum equation,} \quad (23)$$

$$\mathbf{A}\mathbf{p} + \mathbf{B}\lambda = \mathbf{r}_u \quad \text{Equilibrium equation,} \quad (24)$$

$$\mathbf{B}^\top \mathbf{u} - \mathbf{L}_c \mathbf{u}_c = \mathbf{0} \quad \text{Boundary and interface constraints,} \quad (25)$$

$$\mathbf{L}_c^\top \lambda = \mathbf{r}_c \quad \text{Equilibrium on the contact boundaries,} \quad (26)$$

where vector $\mathbf{r}_u = \mathbf{f} - \mathbf{f}^{int}$ is the external-internal forces residual, internal forces for linear problems are simply given by $\mathbf{f}^{int} = \mathbf{K}\mathbf{u}$ with \mathbf{K} the stiffness matrix, while the elemental matrix components are expressed:

$$\mathbf{A}_e = \int_{\Omega_e} \mathbf{N}_u^\top \mathbf{N}_p d\Omega, \quad \mathbf{C}_e = \int_{\Omega_e} \rho^{-1} \mathbf{N}_p^\top \mathbf{N}_p d\Omega, \quad (27)$$

$$\mathbf{B}_e = \int_{\Gamma_e} \mathbf{N}_u^\top \mathbf{N}_\lambda d\Gamma, \quad \mathbf{L}_{c_e} = \int_{\Gamma_e} \mathbf{N}_\lambda^\top \mathbf{N}_u d\Gamma, \quad (28)$$

where \mathbf{A} is the global projection matrix, \mathbf{C} is the global reciprocal mass matrix, \mathbf{B} is the boundary assembly operator, and \mathbf{L}_c is the localized multipliers assembly matrix.

The contact residual vector present in (26) can be written:

$$\mathbf{r}_c(\ddot{\mathbf{u}}_c, \mathbf{u}_c) = \mathbf{M}_p \ddot{\mathbf{u}}_c + \mathbf{r}_p(\mathbf{u}_c), \quad (29)$$

where $\mathbf{r}_p(\mathbf{u}_c) = \mathbf{K}_p \mathbf{u}_c - \mathbf{f}_p$ in the case of geometrically linear kinematics, with:

$$\mathbf{M}_p = \int_{\Gamma_c} \epsilon_m H(g_N) \mathbf{H}^\top \mathbf{H} d\Gamma, \quad \mathbf{K}_p = \int_{\Gamma_c} \epsilon_s H(g_N) \mathbf{H}^\top \mathbf{H} d\Gamma, \quad \mathbf{f}_p = \int_{\Gamma_c} \epsilon_s H(g_N) \mathbf{H} g_0 d\Gamma \quad (30)$$

being \mathbf{M}_p the additional mass matrix due to inertia penalty, \mathbf{K}_p the additional stiffness matrix due to stiffness penalty, vector \mathbf{f}_p the contribution to the contact force of to the initial gap g_0 , and $H(x)$ is the Heaviside function.

Finally, by eliminating symbolically the momentum variable (\mathbf{p}) from (23) and (24), one finds the classical equation of motion expressed in terms of displacements:

$$(\mathbf{A}\mathbf{C}^{-1}\mathbf{A}^T)\ddot{\mathbf{u}} + \mathbf{B}\lambda = \mathbf{r}_u \quad (31)$$

with the mass matrix approximated as:

$$\mathbf{M} = \mathbf{A}\mathbf{C}^{-1}\mathbf{A}^T \quad (32)$$

and observe that there must exist an inverse mass matrix, in the following denoted as \mathbf{M}^{-1} and expressed:

$$\mathbf{M}^{-1} = \mathbf{A}^{-T}\mathbf{C}\mathbf{A}^{-1} \quad (33)$$

assuming that the global projection matrix is invertible. Since our objective is to obtain inverse mass-matrices in efficient and accurate ways, we must find easily invertible *diagonal* or narrowly banded projection matrices. This can be accomplished by diagonalizing the projection matrix \mathbf{A} defined in (27) using $(\mathbf{N}_u, \mathbf{N}_p)$ biorthogonal shape functions.^{30,32}

Remark 1. Considering the structure of matrix \mathbf{H} defined in (20) that involves the same normal vector with opposite sign on each side of the contact areas, it is easy to deduce that the penalty matrix (30) contains identical pairs of rows and columns with opposite sign. Hence this matrix is singular by design, introducing opposite penalty forces on both sides of the contact interface.

4 | DUAL BASIS FUNCTIONS

Observing the expression obtained for the mass matrix inverse (33), we realize that a careful selection of the $(\mathbf{N}_u, \mathbf{N}_p)$ basis functions can simplify its calculation. In particular, by using displacement and momentum biorthogonal interpolation functions, we are able to construct a diagonal projection matrix in the form:

$$[\mathbf{A}_e]_{ij} = \int_{\Omega_e} [\mathbf{N}_u]_i [\mathbf{N}_p]_j d\Omega = \alpha_i \delta_{ij}, \quad \text{where } [\mathbf{A}_e]_{ij} = 0 \text{ for } i \neq j \quad (34)$$

with a trivial inverse that permits to compute the inverse mass matrix directly from the momentum matrix. Different dual interpolation functions of this kind, originally designed and tested for mortar methods, have been proposed in the literature. Specifically for the construction of reciprocal mass matrices, biorthogonal basis functions have been proposed under the framework of FEM^{30,32} and also IGA.⁴⁵

For the construction of our dual basis, the simplest alternative is the use of a local discontinuous biorthogonal dual basis^{50,51} obtained via an elementwise linear combination of the primal shape functions, providing discontinuous reciprocal basis functions that fulfill the partition of unity with the same support than their primal counterparts. A density-weighted dual basis $\mathbf{N}_p(\xi)$ of this type, orthogonal to the displacement interpolation functions $\mathbf{N}_u(\xi)$, can be written in matrix form as:

$$\mathbf{N}_p(\xi) = \rho(\xi)\mathbf{N}_u(\xi)\mathbf{M}_e^{-1}\mathbf{M}_e^L \quad (35)$$

valid for independent elements and where \mathbf{M}_e is an element-by-element constructed mass matrix:

$$\mathbf{M}_e = \int_{\Omega_e} \rho(\xi)\mathbf{N}_u^T(\xi)\mathbf{N}_u(\xi)d\Omega, \quad (36)$$

with \mathbf{M}_e^L defined as the lumped mass matrix obtained by row-sum of its components. The diagonal terms of \mathbf{M}_e^L correspond to values:

$$\mathbf{M}_e^L = \int_{\Omega_e} \rho(\xi)\mathbf{N}_u(\xi)d\Omega, \quad (37)$$

which are the ρ -weighted volumes under the shape functions. In this article, we focus on the linear shape functions, which produce these mass terms positive and \mathbf{M}_e^L is still positive-definitive mass matrix.

Linear finite element shape functions $N_u(\xi)$ and their associated dual basis functions $N_p(\xi)$ are represented in Figure 2. The orthogonality of these interpolation functions is easily demonstrated evaluating the projection matrix (34) at the element level:

$$\mathbf{A}_e = \int_{\Omega_e} \mathbf{N}_u^T(\xi) \mathbf{N}_p(\xi) d\Omega = \left\{ \int_{\Omega_e} \rho(\xi) \mathbf{N}_u^T(\xi) \mathbf{N}_u(\xi) d\Omega \right\} \mathbf{M}_e^{-1} \mathbf{M}_e^L = \mathbf{M}_e^L \quad (38)$$

obtaining by design a simple diagonal projection matrix \mathbf{A}_e that is equal to the lumped element mass matrix.

Finally, we can evaluate analytically the elemental momentum mass matrix from its definition (27), by substituting (35) and considering (38), with a very simple expression:

$$\mathbf{C}_e = \int_{\Omega_e} \rho(\xi)^{-1} \mathbf{N}_p^T(\xi) \mathbf{N}_p(\xi) d\Omega = \mathbf{M}_e^L \mathbf{M}_e^{-1} \left\{ \int_{\Omega_e} \rho(\xi) \mathbf{N}_u^T(\xi) \mathbf{N}_u(\xi) d\Omega \right\} \mathbf{M}_e^{-1} \mathbf{M}_e^L = \mathbf{M}_e^L \mathbf{M}_e^{-1} \mathbf{M}_e^L \quad (39)$$

confirming that it is possible to compute a RMM element-by-element without expensive operations.

The procedure followed for a direct assembly of the global inverse mass matrix \mathbf{M}^{-1} is described in Algorithm 1, where the consistent element mass matrix \mathbf{M}_e^C and the lumped element mass matrix \mathbf{M}_e^L are linearly combined as described in Section 8.1 and then scaled as explained in Section 8.2 to finally obtain the element RMM using relation (39).

Remark 2. The same projection matrix (38) but divided by the element's density, was proposed in a previous work³² for the construction of FEM reciprocal mass matrices under the assumption of constant density. For the general case of variable density, it was pointed out by Schaeuble et al.⁴⁵ that the construction of reciprocal matrices requires density to be included in the local support of the momentum field in order to satisfy mass conservation. This is now done in (35), producing a new expression for the elemental projection matrix \mathbf{A}_e .

It is finally noted that the production of RMMs requires the diagonal projection matrix \mathbf{A}_e to be positive definite. This means that the volume integrals of the shape functions over the finite element domain (37) should be positive. This condition is satisfied by linear FEM and IGA, but not by serendipity higher order elements, where a direct mass lumping procedure produces negative mass diagonal terms associated to the intermediate nodes.

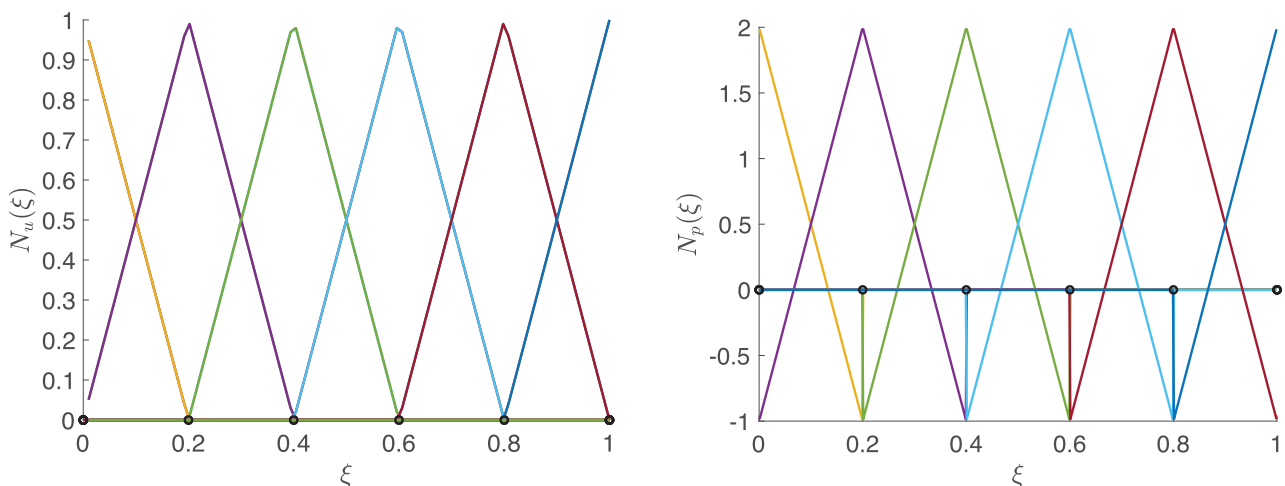


FIGURE 2 Representation in a normalized parameter space of linear shape functions $N_u(\xi)$ used for discretization of the displacement field (left) and their associated orthogonal basis functions $N_p(\xi)$ employed for approximation of momentum (right) for the particular case of constant density

Algorithm 1. Procedure for a direct assembly of the RMM

for $e = 1 \dots N_e$ do elements loop	
$\mathbf{M}_e = (1 - \beta)\mathbf{M}_e^C + \beta\mathbf{M}_e^L$	▷ Element by element assembly
$\mathbf{M}_e = \mathbf{M}_e + \mathbf{M}_e\Phi_h\mathbf{S}_h\Phi_h^T\mathbf{M}_e$	▷ Element mass matrix parametrization
	▷ Element mass matrix scaling
$\mathbf{A}_e = \hat{\mathbf{M}}_e^L \quad \rightarrow \quad \mathbf{A} = \mathbf{A}_{e=1}^{N_e} \mathbf{A}_e$	▷ Assemble diagonal projection matrix
$\mathbf{C}_e = \hat{\mathbf{M}}_e^L \hat{\mathbf{M}}_e^{-1} \hat{\mathbf{M}}_e^L \quad \rightarrow \quad \mathbf{C} = \mathbf{C}_{e=1}^{N_e} \mathbf{C}_e$	▷ Assemble reciprocal mass matrix
end for	
$\mathbf{M}^{-1} = \mathbf{A}^{-T} \mathbf{C} \mathbf{A}^{-1}$	▷ Compute global inverse mass matrix

5 | PARTITIONED FORMULATION OF THE CONTACT PROBLEM

A monolithic explicit BPM solution algorithm, without separating the contact conditions from the body equations, would require a reiterated inversion of the penalized global mass matrix ($\mathbf{M} + \mathbf{M}_p$), that is, the free-body mass matrix plus some inertia penalties changing in time due to different contact conditions. When the body mass matrix \mathbf{M} is not diagonal, this solution procedure involves solving linear systems of size equal to the total number of DOFs. This is extremely inefficient, hence we propose instead a partitioning strategy to uncouple the interface contact problem from the free-body equations. Moreover, in presence of contact conditions, a direct computation of the RMM through classical techniques would require complicated modifications of the biorthogonal shape functions.³⁰ We eliminate all these inconveniences by considering the structures as free-floating and applying the contact boundary conditions through localized Lagrangian multipliers.³⁵

The partitioning strategy works as follows. First, we reorganize the semidiscrete partitioned equations of motion (23)–(26) to obtain the following partitioned equation set:

$$\begin{bmatrix} \mathbf{M} & \mathbf{B} & \mathbf{0} \\ \mathbf{B}^T & \mathbf{0} & -\mathbf{L}_c \\ \mathbf{0} & -\mathbf{L}_c^T & \mathbf{M}_p \end{bmatrix} \begin{Bmatrix} \ddot{\mathbf{u}} \\ \lambda \\ \ddot{\mathbf{u}}_c \end{Bmatrix} = \begin{Bmatrix} \mathbf{r}_u \\ \mathbf{0} \\ -\mathbf{r}_p \end{Bmatrix}, \quad (40)$$

where the second equation is simply a twice time-differentiated version of (25). These are the partitioned equations of motion including mass penalization, where vector \mathbf{r}_p contains the classical stiffness penalty forces coming from the contact conditions. For the solution of these equations, it is important to remember that the mass penalty matrix \mathbf{M}_p is singular by design, for example, for total separation it is identically zero.

Now, with the intention of reducing the problem only to the contact boundary variables, let us isolate the partition accelerations from the first row of (40) to write the equation:

$$\ddot{\mathbf{u}} = \mathbf{M}^{-1} (\mathbf{r}_u - \mathbf{B}\lambda) \quad (41)$$

in which once again we emphasize that the computation of $\mathbf{M}^{-1} = \mathbf{A}^{-T} \mathbf{C} \mathbf{A}^{-1}$ does not require additional computational effort because the global projection matrix \mathbf{A} is diagonal. Then, the localized multipliers can be obtained from the second equation:

$$\lambda = \mathbf{M}_{bb} (\mathbf{B}^T \mathbf{M}^{-1} \mathbf{r}_u - \mathbf{L}_c \ddot{\mathbf{u}}_c) \quad (42)$$

with a reduced-to-the-boundary mass matrix $\mathbf{M}_{bb} = [\mathbf{B}^T \mathbf{M}^{-1} \mathbf{B}]^{-1}$ that is simply obtained by extracting the boundary components of the RMM and computing its inverse. Finally, substituting in the third row of (40) we find:

$$\ddot{\mathbf{u}}_c = \hat{\mathbf{M}}_p^{-1} (\mathbf{L}_c^T \mathbf{M}_{bb} \mathbf{B}^T \mathbf{M}^{-1} \mathbf{r}_u - \mathbf{r}_p) \quad (43)$$

with an effective penalty mass matrix:

$$\hat{\mathbf{M}}_p = \mathbf{M}_p + \mathbf{L}_c^T \mathbf{M}_{bb} \mathbf{L}_c \quad (44)$$

of a smaller dimension and pertaining only to the contact DOFs, therefore, its inversion or factorization is affordable. This is the equation we use to compute the contact zone accelerations directly from internal and penalty forces. Once the contact accelerations $\ddot{\mathbf{u}}_c$ are known, multipliers λ and global accelerations $\ddot{\mathbf{u}}$ can be subsequently calculated from (42) and (41).

Finally, note that to evaluate the normal gap $\mathbf{g}_N(\mathbf{u}_c)$ and define the contact conditions, we need first to compute the contact zone displacements \mathbf{u}_c . These displacements can be obtained from an explicit time integration of the global accelerations vector $\ddot{\mathbf{u}}_c$. However, this integration should be done carefully in order to avoid spurious oscillations in the contact states. A predictor–corrector time integration approach is adopted for this task that will be described later.

6 | OPTIMAL INERTIA PENALTY

We seek now an optimal setting for the penalty mass matrix with respect to a given stiffness penalty matrix, with the condition that the maximum frequency of the bipenalized contact problem and the contact-free problem are identical. If the maximum frequencies of these two problems are the same, the stability limit of the bipenalty problem will not be affected by the stiffness penalties activated at each contact constraint.

Proposition 1. *For one elastic solid with fixed normal contact conditions, the maximum frequencies of the bipenalized contact problem and the contact-free problem will be the same provided that the mass penalty matrix \mathbf{M}_p and the stiffness penalty matrix \mathbf{K}_p satisfy the relation:*

$$\mathbf{M}_p = \frac{1}{\omega_{max}^2} \mathbf{K}_p \quad \text{with} \quad \mathbf{K}\boldsymbol{\phi} = \omega_{max}^2 \mathbf{M}\boldsymbol{\phi},$$

where ω_{max} is the maximum frequency of the linearized contact-free problem and $\boldsymbol{\phi}$ its associated vibration mode.

Proof. Assuming zero external loads and zero initial contact forces, $\mathbf{f} = \mathbf{0}$ and $\mathbf{f}_p = \mathbf{0}$, we perform a linearization of the governing equation for the interface accelerations (43) obtaining:

$$(\mathbf{M}_p + \mathbf{L}_c^T \mathbf{M}_{bb} \mathbf{L}_c) \ddot{\mathbf{u}}_c = -\mathbf{L}_c^T \mathbf{M}_{bb} \mathbf{B}^T \mathbf{M}^{-1} \mathbf{K} \mathbf{u} - \mathbf{K}_p \mathbf{u}_c,$$

where we have substituted $\mathbf{r}_u = -\mathbf{K} \mathbf{u}$ and $\mathbf{r}_p = \mathbf{K}_p \mathbf{u}_c$ as the linearization terms of free-body and contact internal forces. Then, we imagine the system vibrating at the maximum frequency with global and contact interface modes $(\boldsymbol{\phi}, \boldsymbol{\phi}_c)$ and a boundary displacement compatibility equation (25) relating them in the form $\mathbf{B}^T \boldsymbol{\phi} = \mathbf{L}_c \boldsymbol{\phi}_c$. Because the free-body global vibration mode $\boldsymbol{\phi}$ corresponds to the maximum frequency ω_{max} , it is also fulfilled $\mathbf{B}^T \mathbf{M}^{-1} \mathbf{K} \boldsymbol{\phi} = \omega_{max}^2 \mathbf{L}_c \boldsymbol{\phi}_c$ and we can finally write:

$$-\omega_{max}^2 (\mathbf{M}_p + \mathbf{L}_c^T \mathbf{M}_{bb} \mathbf{L}_c) \boldsymbol{\phi}_c = -\omega_{max}^2 \mathbf{L}_c^T \mathbf{M}_{bb} \mathbf{L}_c \boldsymbol{\phi}_c - \mathbf{K}_p \boldsymbol{\phi}_c$$

from where it is derived the sought relation. ■

Additionally, it is also interesting to study what happens to the Lagrangian multipliers at this highest frequency with an optimal selection of the mass penalty matrix. For this, we first perform the linearization of (42):

$$\mathbf{M}_{bb}^{-1} \boldsymbol{\lambda} = \mathbf{B}^T \mathbf{M}^{-1} \mathbf{K} \mathbf{u} - \mathbf{L}_c \ddot{\mathbf{u}}_c \quad (45)$$

and substitute the vibration mode corresponding to the maximum frequency, to yield:

$$\mathbf{M}_{bb}^{-1} \boldsymbol{\lambda} = -\omega_{max}^2 \mathbf{B}^T \boldsymbol{\phi} + \omega_{max}^2 \mathbf{L}_c \boldsymbol{\phi}_c = \mathbf{0} \quad (46)$$

showing null contact forces corresponding to that particular mode shape.

In conclusion, the relationship $\mathbf{M}_p = \mathbf{K}_p / \omega_{max}^2$ for an optimal selection of the penalty mass matrix is valid for an arbitrary mass matrix, either exact inverse or reciprocal mass matrix. For its computation, it is only needed the maximum frequency of the linearized system. In this case, the maximum frequency of the bipenalized contact problem is not affected by the stiffness penalty term and the stability limit is the same than the contact-free problem. In real computations, one can use the setting of the mass penalty matrix $\mathbf{M}_p = \Delta t^2 \mathbf{K}_p$, where Δt is the time step size during the explicit time stepping.

7 | EXPLICIT PREDICTOR-CORRECTOR TIME INTEGRATION

Time integration of the semidiscrete equations of motion (40) is performed using a predictor–corrector scheme with splitting of body and contact accelerations,⁵² by following the process described in Algorithm 2. We adopt the central difference scheme, assuming that time integration has progressed until time t^n , with known displacements \mathbf{u}^n and velocities at time $t^{n-\frac{1}{2}} = t^n - \frac{\Delta t}{2}$ defined as $\dot{\mathbf{u}}^{n-\frac{1}{2}}$, to advance the solution one step further with time step size $\Delta t = t^{n+1} - t^n$ to obtain $\dot{\mathbf{u}}^{n+\frac{1}{2}}$ and \mathbf{u}^{n+1} .

In this process, to compute the contact boundary accelerations, we divide the computation of the current acceleration (43) into predicted and corrected terms in the form:

$$\ddot{\mathbf{u}}_c^n = \underbrace{\hat{\mathbf{M}}_p^{-1} \mathbf{L}_c^T \mathbf{M}_{bb} \mathbf{B}^T \mathbf{M}^{-1} \mathbf{r}_u^n}_{\text{prediction}} - \underbrace{\hat{\mathbf{M}}_p^{-1} \mathbf{r}_p^{n+1}}_{\text{correction}} = \ddot{\mathbf{u}}_{c,pred}^n - \ddot{\mathbf{u}}_{c,corr}^n. \quad (47)$$

In the proposed splitting scheme, bulk accelerations in the predictor phase $\ddot{\mathbf{u}}_{c,pred}^n$ and the correction accelerations $\ddot{\mathbf{u}}_{c,corr}^n$ are computed using a constant direct inverse mass matrix (33) without interference of the mass penalties in \mathbf{M}_p , that are included through the localized Lagrange multipliers in a small problem reduced to the contact unknowns.

Algorithm 2. Stabilized explicit predictor–corrector algorithm

$\mathbf{u}^0, \dot{\mathbf{u}}^0, \dot{\mathbf{u}}^{\frac{1}{2}} = \dot{\mathbf{u}}^0 + \frac{\Delta t}{2} \ddot{\mathbf{u}}^0$	▷ Initial conditions
$\mathbf{u}_c^0 = [\mathbf{L}_c^T \mathbf{L}_c]^{-1} \mathbf{L}_c^T \mathbf{B}^T \mathbf{u}^0, \dot{\mathbf{u}}_c^0 = [\mathbf{L}_c^T \mathbf{L}_c]^{-1} \mathbf{L}_c^T \mathbf{B}^T \dot{\mathbf{u}}^0$	▷ Initial conditions
for $n = 1 \dots n_{steps}$ do time loop	▷ Time integration loop
$\mathbf{u}^n = \mathbf{u}^{n-1} + \Delta t \dot{\mathbf{u}}^{n-\frac{1}{2}}, \quad \mathbf{u}_c^n = \mathbf{u}_c^{n-1} + \Delta t \dot{\mathbf{u}}_c^{n-\frac{1}{2}}$	▷ Explicit displacements
$\ddot{\mathbf{u}}_{c,pred}^n = \hat{\mathbf{M}}_p^{-1} \mathbf{L}_c^T \mathbf{M}_{bb} \mathbf{B}^T \mathbf{M}^{-1} \mathbf{r}_u^n$	▷ Predicted contact accelerations
$\dot{\mathbf{u}}_{c,pred}^{n+\frac{1}{2}} = \dot{\mathbf{u}}_c^{n-\frac{1}{2}} + \Delta t \ddot{\mathbf{u}}_{c,pred}^n$	▷ Predicted mid-point contact velocities
$\mathbf{u}_{c,pred}^{n+1} = \mathbf{u}_c^n + \Delta t \dot{\mathbf{u}}_{c,pred}^{n+\frac{1}{2}}$	▷ Predicted displacements
$\mathbf{r}_p^{n+1} = \mathbf{K}_p \mathbf{u}_{c,pred}^{n+1} - \mathbf{f}_p$	▷ Evaluate stiffness penalty forces
$\ddot{\mathbf{u}}_{c,corr}^n = \hat{\mathbf{M}}_p^{-1} \mathbf{r}_p^{n+1}$	▷ Contact correction of boundary accelerations
$\ddot{\mathbf{u}}_c^n = \ddot{\mathbf{u}}_{c,pred}^n - \ddot{\mathbf{u}}_{c,corr}^n$	▷ Corrected contact accelerations
$\lambda^n = \mathbf{M}_{bb} (\mathbf{B}^T \mathbf{M}^{-1} \mathbf{r}_u^n - \mathbf{L}_c \ddot{\mathbf{u}}_c^n)$	▷ Compute localized multipliers
$\ddot{\mathbf{u}}^n = \mathbf{M}^{-1} (\mathbf{r}_u^n - \mathbf{B} \lambda^n)$	▷ Obtain accelerations
$\dot{\mathbf{u}}^{n+\frac{1}{2}} = \dot{\mathbf{u}}^{n-\frac{1}{2}} + \Delta t \ddot{\mathbf{u}}^n, \quad \dot{\mathbf{u}}_c^{n+\frac{1}{2}} = \dot{\mathbf{u}}_c^{n-\frac{1}{2}} + \Delta t \ddot{\mathbf{u}}_c^n$	▷ Update mid-point velocities
end for	

8 | ACCURACY AND PERFORMANCE IMPROVEMENTS

In this section, two different techniques are applied at the element level and combined to enhance the accuracy and performance of the BPM. These techniques are *mass matrix parametrization* used to improve the accuracy at higher frequencies of the reciprocal mass matrix and SMS introduced to extend the critical time step by modification of the nonphysical mesh frequencies of the element.

8.1 | Mass matrix parametrization

Parametrization can be used to improve the accuracy of reciprocal mass matrices. For example,^{30,43,44} a family of reciprocal mass matrices can be constructed by incorporating parametrization into the variational form of the problem. By introducing free parameters, it is possible to create a family of mass inverses and later select the members of this family with best properties for different applications. Hence, the idea is to employ for the construction of matrices (38) and (39) a templated version of the element mass matrix. There exist several ways to parametrize mass matrices at the

element level, see Felippa et al.⁵³ for an exhaustive classification, being a consistent-lumped linear combination the simplest choice:

$$\mathbf{M}_e = (1 - \beta)\mathbf{M}_e^C + \beta\mathbf{M}_e^L \quad \beta \in [0, 1] \tag{48}$$

in which a parameter $\beta \in [0, 1]$ is used to balance between the element consistent mass matrix \mathbf{M}_e^C and lumped mass matrix \mathbf{M}_e^L . For example, using $\beta = \{0, \frac{1}{2}, 1\}$ the element mass matrix is then easily reduced respectively to the consistent mass matrix (CMM), averaged mass matrix (AMM), and lumped mass matrix (LMM).

In particular, for the construction of our RMM, the case $\beta = 1$ is not interesting because it reduces the reciprocal matrix to the common diagonal LMM with a trivial inverse. We mentioned that LMM computed by the row-sum technique is very popular in explicit dynamics.⁵⁴ Unfortunately, see Figure 3, the lumped mass matrix does not maintain the accuracy of the consistent mass matrix for high frequencies and finding better options would suppose an important advantage for explicit dynamics. It is well known that the frequencies of CMM converge from above, whereas the frequencies of LMM converge from below. Then, it remains the task of selecting an appropriated parameter β with the objective of beating the LMM accuracy with equivalent computational costs. Figure 3 shows that the RMM constructed with $\beta = \frac{1}{2}$ outperforms the accuracy of LMM and CMM. The dispersion-corrected RMM with $\beta = \frac{1}{2}$ reproduces the same behavior observed by Krenk⁵⁵ for the AMM in the one-dimensional wave equation modeled with linear finite elements.

8.2 | Element-by-element SMS

We describe here a simple method to reduce the highest frequencies of the system that can be combined with the proposed RMM for better efficiency. The mass scaling process is applied element by element although it could also be applied in a partitioned manner.⁴⁸ We start examining the original mode shapes of an element with n DOFs. These modes are obtained by solving the generalized eigenvalue problem:

$$\mathbf{K}_e \Phi_e = \mathbf{M}_e \Phi_e \Lambda_e \tag{49}$$

with the well-known eigendecomposition properties,

$$\begin{cases} \Phi_e^T \mathbf{K}_e \Phi_e = \Lambda_e \\ \Phi_e^T \mathbf{M}_e \Phi_e = \mathbf{I}_n \end{cases} \tag{50}$$

where n is the number of element DOFs, $\Phi_e \in \mathbb{R}^{n \times n}$ is a square matrix with the orthogonal mode shapes of the element, \mathbf{I}_n is the identity matrix of size n , and the diagonal matrix $\Lambda_e \in \mathbb{R}^{n \times n}$ contains the original element eigenfrequencies, that is, $\Lambda_e = \mathbf{diag}(\omega_1^2, \omega_2^2 \dots \omega_n^2)$.

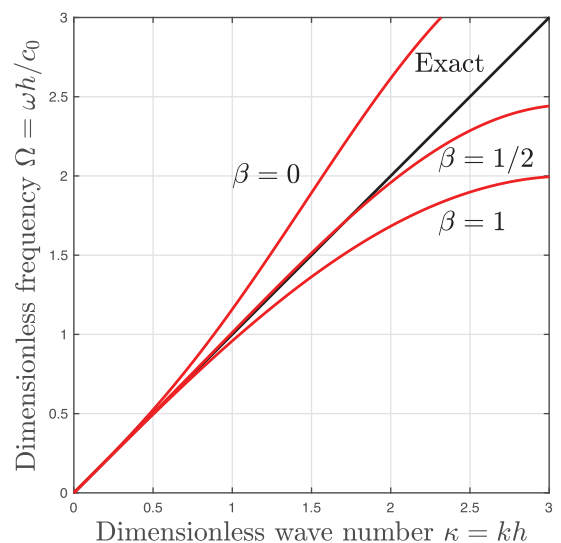


FIGURE 3 Analytical dispersion diagram of the proposed reciprocal mass matrix for an infinite bar modeled with linear elements and using different mass scaling parameters. Three values of $\beta = \{0, \frac{1}{2}, 1\}$ are considered, corresponding to CMM, AMM, and LMM, respectively. A lower dispersion error is observed in the high frequency range for $\beta = \frac{1}{2}$. Note that a dimensionless wave number $\kappa = \pi$ corresponds to a resolution of two elements per wave length

Then, after ordering the element frequencies in Λ_e , the n orthogonal mode shapes can be separated into r and $m = n - r$ low and high frequency mode shapes, respectively, in the form:

$$\Phi_e = [\Phi_l \quad \Phi_h], \quad (51)$$

where $\Phi_l \in \mathbb{R}^{n \times r}$ groups low-frequency modes whose responses are to be retained and $\Phi_h \in \mathbb{R}^{n \times m}$ collects high-frequency modes whose responses are to be filtered out. These orthogonal modes now fulfill,

$$\Lambda_e = \begin{bmatrix} \Phi_l^\top \mathbf{K}_e \Phi_l & \mathbf{0} \\ \mathbf{0} & \Phi_h^\top \mathbf{K}_e \Phi_h \end{bmatrix} = \begin{bmatrix} \Lambda_l & \mathbf{0} \\ \mathbf{0} & \Lambda_h \end{bmatrix}, \quad (52)$$

where $\Lambda_l \in \mathbb{R}^{r \times r}$ and $\Lambda_h \in \mathbb{R}^{m \times m}$ are diagonal matrices grouping with the corresponding low and high element frequencies.

The n orthogonal mode shapes of the element can be separated into high and low frequency modes in the form:

$$\Phi_e = [\Phi_l \quad \Phi_h], \quad (53)$$

where we have r retained low-frequency modes Φ_l and $s = n - r$ scaled high frequency modes Φ_h .

In order to scale only the high frequency modes of the element, without affecting the low frequency modes at the same time, we modify the element mass matrix in the form:

$$\hat{\mathbf{M}}_e = \mathbf{M}_e + \mathbf{M}_e \Phi_h \mathbf{S}_h \Phi_h^\top \mathbf{M}_e, \quad (54)$$

using the diagonal scaling matrix,

$$\mathbf{S}_h = \mathbf{diag}(s_1, s_2 \dots s_m), \quad (55)$$

where $\Phi_h \in \mathbb{R}^{n \times m}$ is now a retained set of higher mode shapes whose frequencies are deemed to be mesh frequencies and therefore to be filtered out; $\mathbf{S}_h \in \mathbb{R}^{m \times m}$ is a diagonal matrix to be discussed subsequently and m is the number of the higher mode shapes utilized.

Proposition 2. *The modified element mass matrix $\hat{\mathbf{M}}_e$ scales the high frequencies of the element by a factor $(\mathbf{I}_m + \mathbf{S}_h)^{-1}$, maintaining the element low frequencies unaffected, that is, the new element eigenvalues are given by the diagonal matrix:*

$$\hat{\Lambda}_e = \begin{bmatrix} \mathbf{I}_r & \mathbf{0} \\ \mathbf{0} & (\mathbf{I}_m + \mathbf{S}_h)^{-1} \end{bmatrix} \Lambda_e$$

with the same mode shapes \mathbf{X}_e than the original element.

Proof. It is very simple to demonstrate that the new tailored-mass eigenvalue problem:

$$\mathbf{K}_e \Phi_e = \hat{\mathbf{M}}_e \Phi_e \hat{\Lambda}_e$$

has exactly the same eigenvectors than the original one, with the same r low frequencies and s reduced high frequencies. This is demonstrated premultiplying by Φ_e^\top the previous expression, thanks to properties (50), revealing the new eigenvalues:

$$\Lambda_e = \Phi_e^\top \left(\mathbf{M}_e + \mathbf{M}_e [\Phi_l \quad \Phi_h] \begin{bmatrix} \mathbf{0} & \mathbf{0} \\ \mathbf{0} & \mathbf{S}_h \end{bmatrix} [\Phi_l \quad \Phi_h]^\top \mathbf{M}_e \right) \Phi_e \hat{\Lambda}_e = \left(\mathbf{I}_n + \begin{bmatrix} \mathbf{0} & \mathbf{0} \\ \mathbf{0} & \mathbf{S}_h \end{bmatrix} \right) \hat{\Lambda}_e$$

from where we can obtain $\hat{\Lambda}_h$ inverting a simple diagonal matrix. ■

It remains only the selection of the scaling parameters $\{s_1, s_2 \dots s_m\}$ and the number of modes to scale m . It is also important to mention that, although different mass-scaling methods have been proposed by other authors,^{43,44,56} the proposed mass-scaling technique is defined as selective in the sense that we can choose the number of modes to scale and this scaling is performed at the element level.

8.3 | Design of the scaling matrix

Finally, we seek an expression for the scaling matrix (55). Of several possible choices to construct \mathbf{S}_h , we propose the following formula:

$$\mathbf{S}_h = \omega_{cut}^{-2} \mathbf{\Lambda}_h - \mathbf{I}_m, \quad (56)$$

where ω_{cut} is a user-specified cut-off frequency beyond which all the higher frequencies will be filtered out. Substituting (56) in the result of Proposition 2, we observe that the modified frequencies take the form:

$$\hat{\mathbf{\Lambda}}_e = \begin{bmatrix} \mathbf{\Lambda}_l & \mathbf{0} \\ \mathbf{0} & \omega_{cut}^2 \mathbf{I}_m \end{bmatrix}. \quad (57)$$

It is observed from the preceding result that, while the lower modes and their mode shapes are preserved, the higher modes which are expected to consist of mesh frequencies are effectively filtered out and replaced by the cut-off frequency, ω_{cut} .

9 | NUMERICAL EXAMPLES

In this section, we present three classical contact-impact examples that are used to demonstrate how the proposed formulation can be used in practice. Our goal is twofold. First, we want to confirm that a combined mass–stiffness penalty approximation is able to reduce instabilities and increase the quality of the solution. That is, we want to demonstrate how spurious oscillations of the contact stresses can be effectively controlled by introducing optimal mass penalties combined with the predictor–corrector time integration scheme. Second, we wish to demonstrate how the RMM and SMS techniques presented here can be used to increase computational efficiency, without severely affecting the accuracy.

9.1 | Impact of two bars

In our first example, we study a benchmark contact-impact problem proposed by Huněk⁵⁷ consisting of two elastic one-dimensional bars of different lengths. A scheme of the test is shown in Figure 4, presenting a first bar moving to the right with constant velocity $v_{01} = 0.1$ m/s that impacts on the second bar, initially at rest and fixed on its right side. The bar lengths are $L_1 = 10$ m and $L_2 = 20$ m, with identical cross-sectional areas $A_1 = A_2 = 1$ m² and the same material properties: Young's modulus $E_1 = E_2 = 100$ Pa and density $\rho_1 = \rho_2 = 0.01$ kg/m³. Uniform linear finite element discretizations of constant element size $h_1 = h_2 = 0.2$ m are used for the bars, producing meshes of $n_1 = 50$ and $n_2 = 100$ finite elements. The bars are supposed to initiate contact at time $t = 0$ and therefore the initial gap g_N^0 is zero. The total simulation time is set to $T = 0.7$ s, the solution integrated with Courant number $C = 0.5$ and we focus on the contact forces occurring at the interface. There exists analytical solution for the contact forces of this particular example, consult Graff's book,⁵⁸ corresponding to a constant contact force of value $F_0 = 0.05$ N maintained for $t = 0 \dots 0.2$ s and $t = 0.4 \dots 0.6$ s, and zero otherwise.

To apply the bipenalty method, the stiffness penalty parameter ϵ_s is first normalized by the relation $\epsilon_s^* = \epsilon_s h_e / (\rho c_0^2 A)$, where $c_0 = \sqrt{E/\rho}$ is the wave velocity, to consider four different values of the dimensionless stiffness penalty corresponding to $\log_{10} \epsilon_s^* = \{1, 4, 8, 12\}$. The construction of a constant RMM is then made via Algorithm 1, starting from the average element mass matrix computed with $\beta = 0.5$. After this, an optimal mass penalty matrix \mathbf{M}_p is calculated as described in Section 6. In this case, it is observed that the stability limit of BPM is not affected by the stiffness penalty ϵ_s^* .

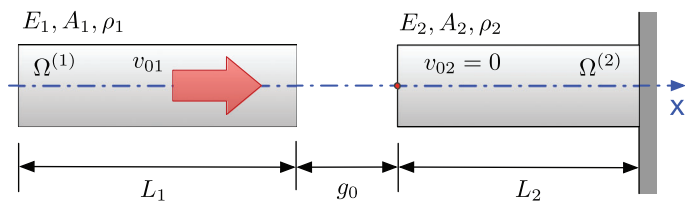


FIGURE 4 Scheme of the one-dimensional impact of two elastic bars with different length and material properties

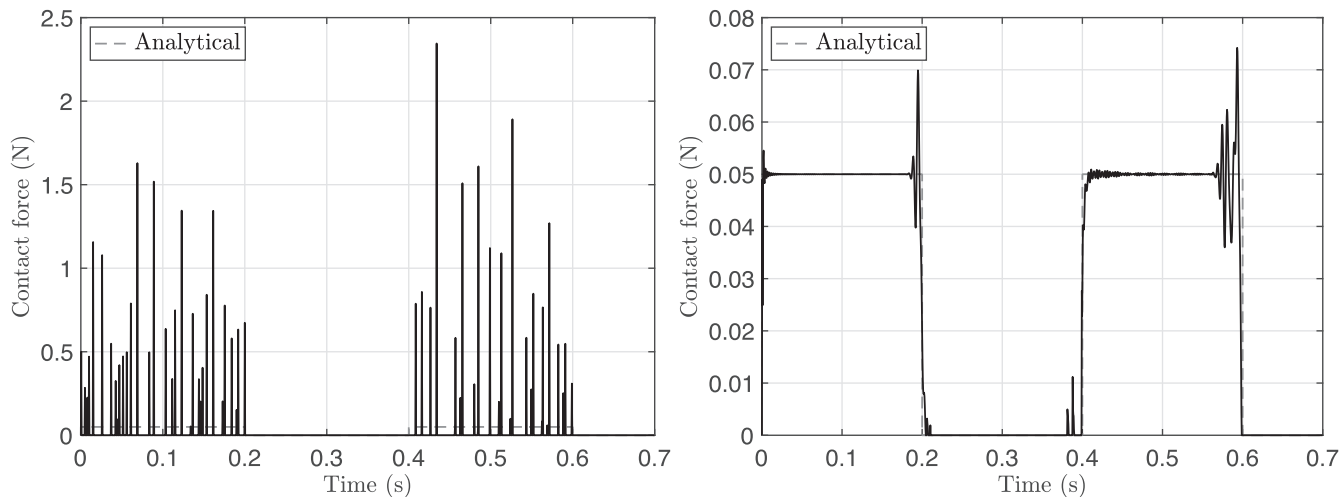


FIGURE 5 Time history of contact forces after the impact of two elastic bars, comparison of the solutions obtained for $\epsilon_s^* = 10$ with classical stiffness penalty method (left) and BPM with very large stiffness penalty $\epsilon_s^* = 1 \times 10^{12}$ and optimal mass penalty (right). BPM is able to improve the stability of the solution even for high values of the stiffness penalty. At the same time, the predictor–corrector time integration algorithm controls the swinging of contact forces

A cut-off frequency ω_{cut} for mass scaling is finally introduced so that the critical time step size is extended by factor 1.68 with respect to the nonscaled case.

After several numerical tests with different values of ϵ_s^* with different combination of mass matrices, we conclude that the results in the form of the time history of the contact forces do not depend on the particular value of ϵ_s^* and the stability limit of the contact-free problem is always preserved. In Figure 5, it is compared a time history of contact forces obtained with the traditional stiffness penalty method (left) and BPM (right). It is clear that more stable results are obtained with BPM, although the solution still presents some small oscillations at the contact force discontinuities attributed to the mesh resolution and Gibbs phenomenon. It is possible to reduce these nonspurious force oscillations equipping the time integration algorithm with a discontinuity capturing procedure, for example, Park scheme.⁵⁹

As a demonstration of the effect of combining RMM and SMS, we present in Figure 6 the contact forces obtained after reducing the maximum element frequency to ω_{cut} . We can see some improvement on the contact forces with mass scaling, the oscillations are not removed completely but have reduced their frequency. These stress spurious oscillations are a product of the temporal–spatial dispersion behavior of the finite element within the explicit time integration.⁶⁰

Finally, the energy balance during the contact process is shown in Figure 6. For its computation, the work associated to the contact constraint through the bipenalty term is evaluated as:

$$W_c = H(g_N) \left(\frac{1}{2} \dot{\mathbf{u}}_c^T \mathbf{M}_p \dot{\mathbf{u}}_c + \frac{1}{2} \mathbf{u}_c^T \mathbf{K}_p \mathbf{u}_c \right), \quad (58)$$

where $H(g_N)$ is a Heaviside function with unit value when the contact constraint is activated. In contact-impact problems, it is important to verify that the work associated to the contact constraints W_c remains numerically very small, ideally it should be zero, thus no energy is dissipated by the penalty terms during the enforcement of the contact constraints. We have checked on several numerical experiments that this condition is perfectly satisfied, after

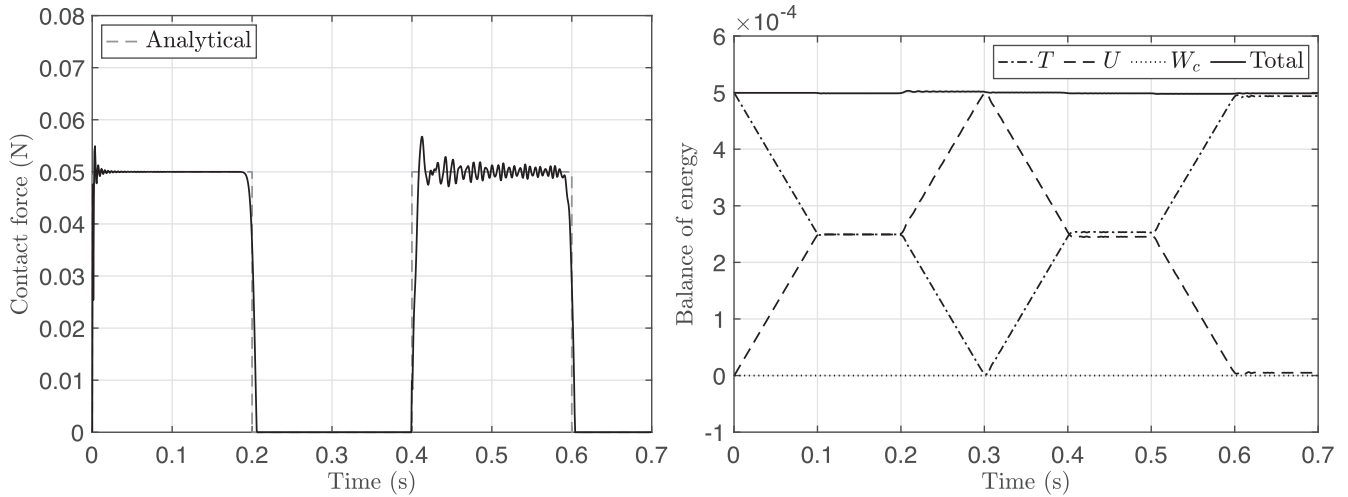
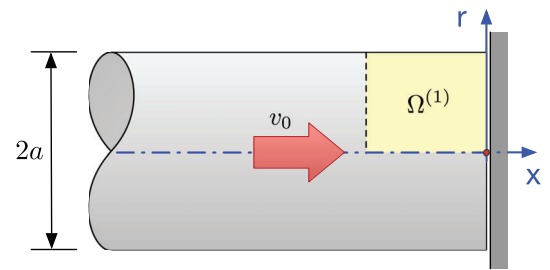


FIGURE 6 Effect of mass scaling in the time history of contact forces due to the impact of two elastic bars (left). Energy balance obtained using the scaled reciprocal mass matrix (right) expressed in terms of kinetic energy T , potential energy U , work of contact forces W_c , and total energy $T + U + W_c$

FIGURE 7 Scheme of the Taylor test of an elastic cylinder of radius a and uniform velocity v_0 impacting on a rigid wall. Only a domain $\Omega^{(1)}$ of size $1.2a \times a$ is modeled and discretized using a regular mesh of 100×50 axisymmetric quadrilateral elements



combining an optimal selection of the penalized bipenalty mass matrix \mathbf{M}_p with the predictor–corrector explicit time integration described in Algorithm 2. Kinetic and potential energies are simply computed by integration on the FEM domains.

9.2 | Taylor test of a perfectly elastic cylinder

As a second benchmark problem we adopt the *Taylor test* of a perfectly elastic cylinder, a classical problem with semi-analytical solution.⁶¹ In particular, we consider the case of a cylinder with radius $a = 1\text{m}$ and initial velocity $v_0 = 1\text{m/s}$ impacting on a rigid wall, as schematically represented in Figure 7. The problem is treated as axisymmetric, meshing only a rectangular domain $\Omega^{(1)}$ near the contact zone of length $L = 1.2a$ using a regular mesh of 100×50 fully integrated quadrilateral finite elements.

The material is considered purely elastic steel, with Young modulus $E = 210\text{GPa}$, Poisson coefficient $\nu = 0.3$ and mass density $\rho = 7850\text{kg/m}^3$. The velocity of primary and secondary waves in the cylinder can be respectively expressed by the elastic constants of the propagating medium as $c_L = \sqrt{(\lambda + 2G)/\rho}$ for the *longitudinal* and $c_T = \sqrt{G/\rho}$ for the *transverse* wave speed, where λ is the first Lamé parameter of the material and G the shear modulus.

9.2.1 | Time integration stability limit

It is well known from classical penalty contact methods, that an increase of the dimensionless penalty stiffness $\epsilon_s^* = \epsilon_s h_e / (\rho c_L^2)$ without mass penalties $\epsilon_m = 0$ affects very significantly the stability limit of the time integration

algorithm used.¹⁸ In general, the critical Courant number $C_{cr} = \Delta t_{cr}^p / \Delta t_{cr}$, defined as the ratio between the critical time step after penalization Δt_{cr}^p and the critical time step without penalization Δt_{cr} , is lower than one and decreases rapidly with the penalty stiffness parameter ϵ_s^* . This effect is observed in Figure 8 for $r = \infty$, where this stability limit has been computed.

In the bipenalty case, the ratio between stiffness and mass penalty is controlled by the nondimensional parameter:

$$r = \frac{\epsilon_s}{2\epsilon_m} \left(\frac{h_e}{2c_L} \right)^2, \quad (59)$$

where c_L is the speed of elastic longitudinal waves and h_e is the finite element size. This definition produces bipenalty with similar mass and stiffness penalty coefficients for $r \rightarrow 1$. The value $2c_L/h_e$ corresponds to maximum angular frequency ω_{max} for infinite two-dimensional mesh of bilinear finite elements with the lumped mass matrix, see work.⁶⁰ As it is known from Reference 16, the optimal ratio is given as $r=1$ and it is related to ω_{max} of finite elements in contact.

In Figure 8, it is represented the reduction of the critical Courant number C_{cr}^p/C_{cr} for different values of the stiffness penalties ratio obtained for our benchmark problem. Note that, for a fixed stiffness penalty ϵ_s^* , it is possible to find the exact mass–stiffness penalty ratio r needed to achieve a critical Courant number necessary for stability. This value of the ratio r defines our required mass penalty ϵ_m for stability.

9.2.2 | Classical stiffness penalty contact analysis

First, as a reference, we solve the impact problem by imposing a zero horizontal displacement boundary condition to the nodes located at the contact zone. The results are presented in Figure 9 (top) in the form of dimensionless normal contact pressure $\sigma_z^* = \sigma_x c_L / (\lambda v_0)$ obtained at equispaced radial locations $r^* = r/a$ for different nondimensional values of time $t^* = t c_L / a$. Eigenvalue analysis of the constrained mesh, reveals a maximum frequency with critical time step $\Delta t_{cr}^* = 0.0033$ and the solution is computed with a stable Courant number $C = 0.9$ using a time-step size $\Delta t^* = 0.003$.

We verify in Figure 9 (top-left) that the computed numerical solution is very close to the semianalytical solution obtained by Červ et al.⁶¹ for three representative values of time $t^* = \{0.25, 1, 2\}$. On the right, it is represented the evolution of contact pressure in the contact zone. The wave propagation, after an instant contact occurring at $t^* = 0$, is defined by a plane pressure dilatational wave or primary P-wave that starts to propagate with velocity c_L along the cylinder, leaving behind the same state of stress caused by the impact of a half-space. At the same time, the size of this constant stress region is successively decreased by an unloading pressure wave generated at the contact edge of the rod $r^* = 1$ that arrives to the center of the cylinder at $t^* = 1$. This unloading dilatational wave is then followed by slower shear waves propagating from the same point at the velocity of transverse waves c_T .

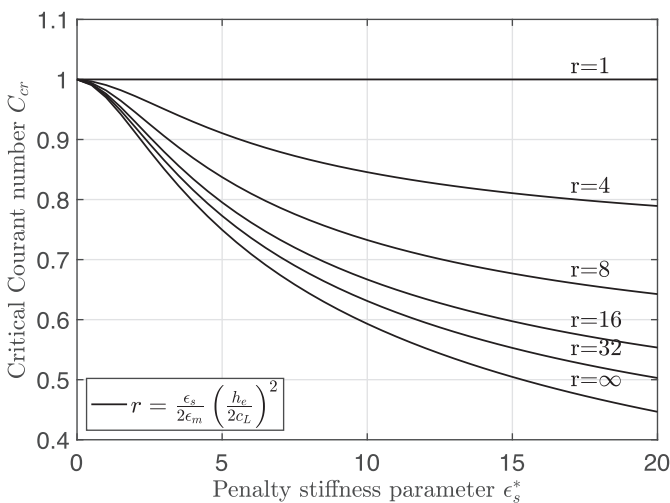


FIGURE 8 Stability limit of the Taylor impact problem represented as a function of the dimensionless stiffness penalty ϵ_s^* and the mass–stiffness penalty ratio r . The curve for $r = \infty$ corresponds to the classical penalty method $\epsilon_m = 0$ and $r = 1$ represents the optimal bipenalty selection

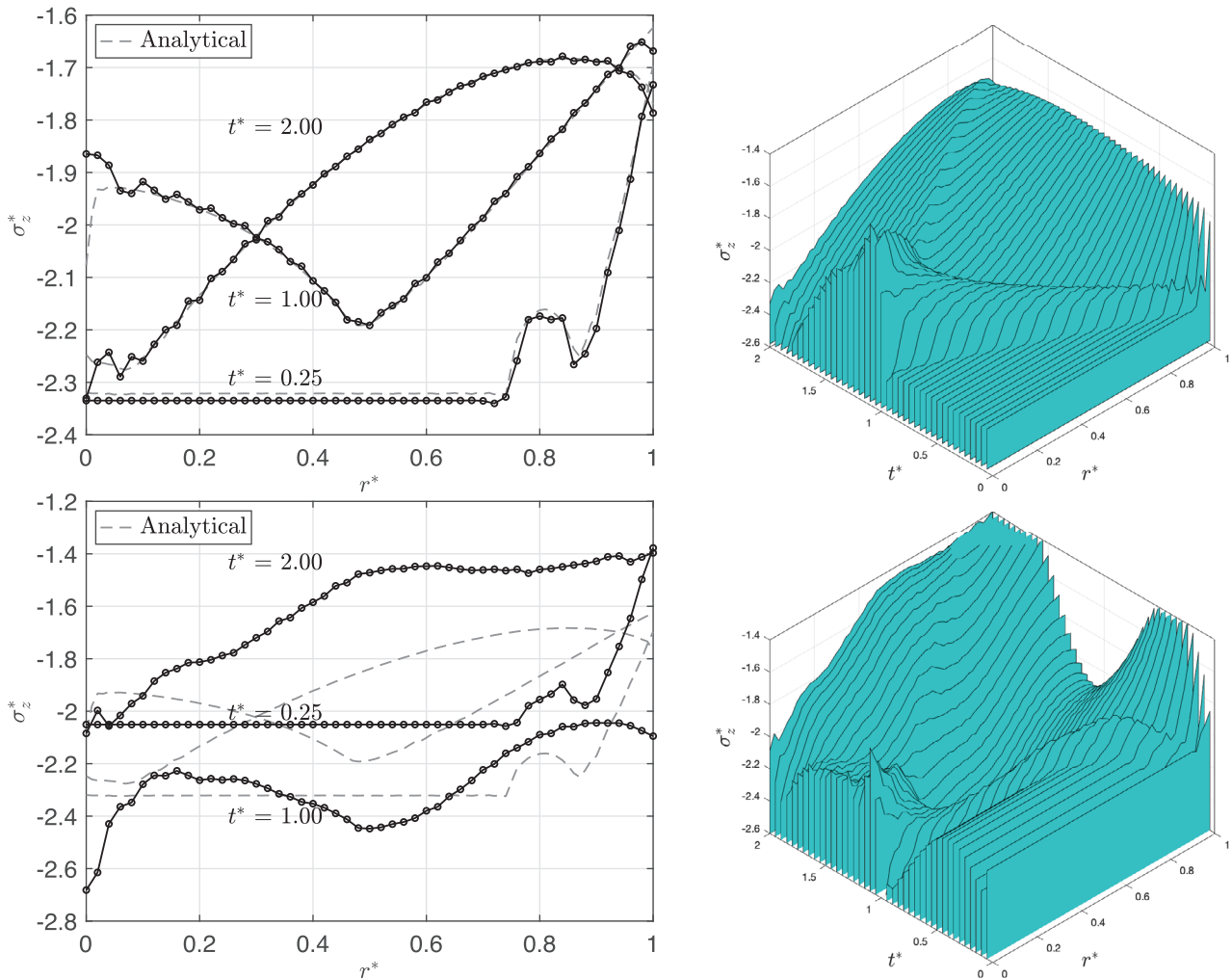


FIGURE 9 Taylor impact problem. Comparison with semianalytical solution of the contact pressures σ_z^* at three particular instants $t^* = \{0.25, 1, 2\}$ (left) and evolution of the contact pressure (right), computed by imposing a zero horizontal displacement boundary condition (top) and with the classical penalty contact algorithm approach $r = \infty$ (bottom). The standard stiffness penalty method (bottom) produces oscillations in the contact stresses that propagate inside the cylinder spoiling the temporal accuracy

Now, we try to solve the same situation with the classical stiffness penalty approach by using a dimensionless stiffness penalty $e_s^* = 50$ with factor $r \rightarrow \infty$, eliminating this way the mass penalty. In this new case and compared with the perfectly rigid contact case, some flexibilization of the contact constraint is introduced reducing the maximum frequency of the system and extending the critical time-step to $\Delta t_{cr}^* = 0.0095$. Then, the time integration step is selected from an admissible value $C = 0.87$ of the Courant number and the solution integrated with $\Delta t^* = 0.0083$. The new results, obtained exclusively with stiffness penalization, are presented in Figure 9 (bottom) where the initiation of contact pressure oscillations is clearly observed. This type of contact dynamic instabilities are immediately propagated to the interior of the domain degrading the solution.

9.2.3 | Contact analysis with BPM

We revisit the problem maintaining the same dimensionless stiffness penalty $e_s^* = 50$ but this time introducing bipenalty stabilization, with an optimal mass–stiffness penalty ratio $r = 1$, as described in Algorithm 2. The addition of mass penalties to the contact conditions slightly increases the critical time step to $\Delta t_{cr}^* = 0.0098$, therefore we are able to solve the problem with the same time step $\Delta t^* = 0.0083$ used previously for the $r \rightarrow \infty$ case. The results are presented in Figure 10 (top), where we observe that mass stabilization is able to recover accuracy and suppress the spurious oscillations. The

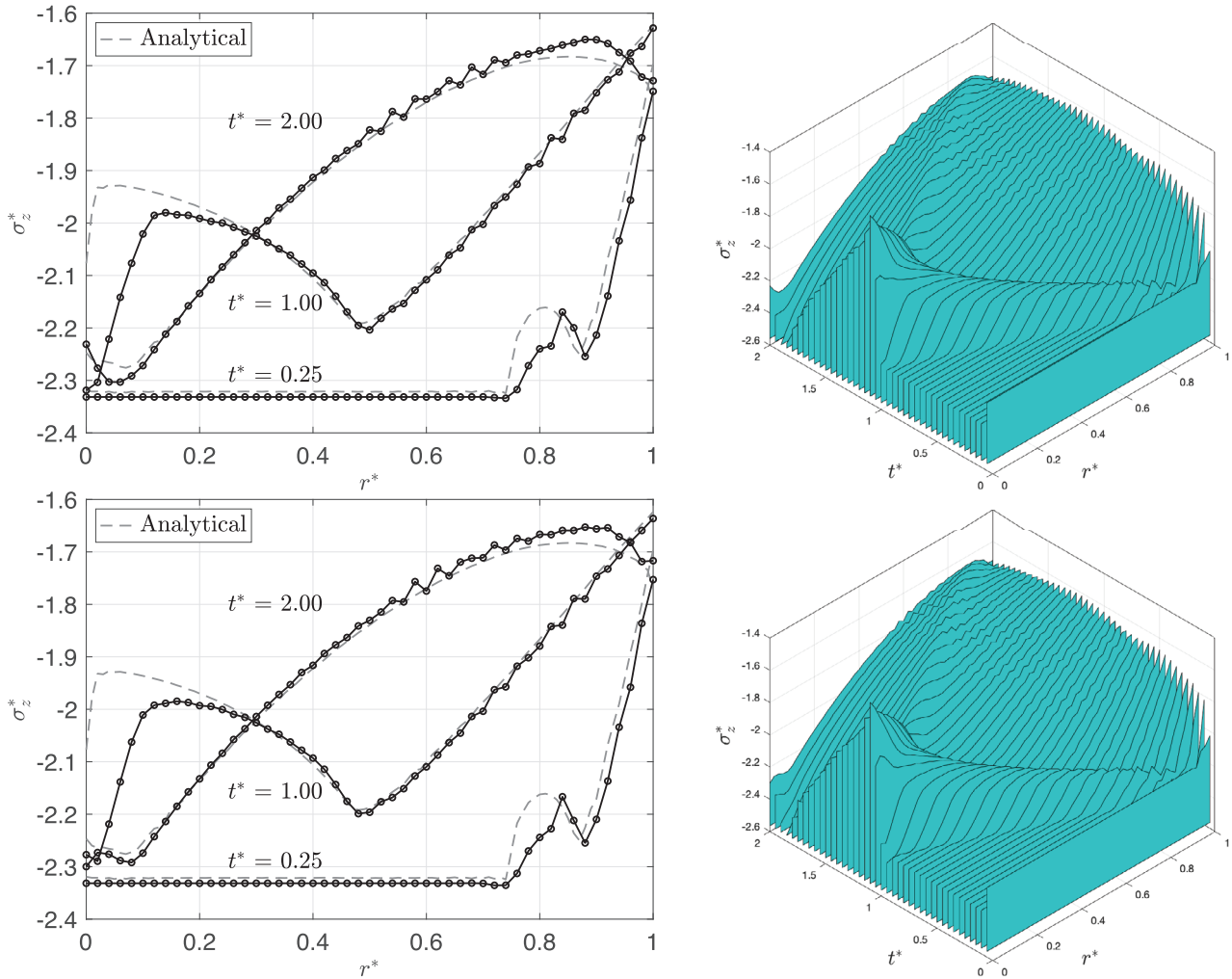


FIGURE 10 Taylor test solutions computed with optimal mass–stiffness BPM stabilization ($r = 1$). Results for different time instants obtained with exact AMM inverse (top) and the proposed RMM (bottom). Undesired oscillations on the contact stresses can be effectively reduced with BPM stabilization

combination of stiffness and mass penalties has the benefit of stabilizing the oscillation of stresses occurring at the contact zone. It is also noticed that the artificial contact flexibility introduced by the stiffness penalty is responsible for a short delay in the contact initiation, making the unloading pressure wave originated at the contact edge to arrive a little bit later to the center axis of the cylinder.

The small penetrations made by the contact surface of the cylinder into the rigid wall are finally evaluated by computing the evolution of the dimensionless normal gap $g_N^* = g_N/r$ in the contact area, see Figure 11. The normal gaps obtained with the exact AMM inverse (left) and the proposed RMM (right) are very similar, demonstrating for this problem that the introduction of the RMM does not affect the penetration values.

9.2.4 | RMM and SMS

Next, we turn our attention to the issue of computational performance. Note that the previous results required to compute an expensive factorization of the average mass matrix for the free cylinder. We repeat the experiment but using the proposed RMM, an efficient sparse approximation of the inverse mass matrix, directly computed as described in Algorithm 1. This new method of approximation of \mathbf{M}^{-1} , that is needed to obtain the body final accelerations, reduces drastically the number of operations to perform per time step. The new solutions are presented in Figure 10 (bottom), where we can barely appreciate differences with the results obtained using the exact AMM inverse, same figure (top).

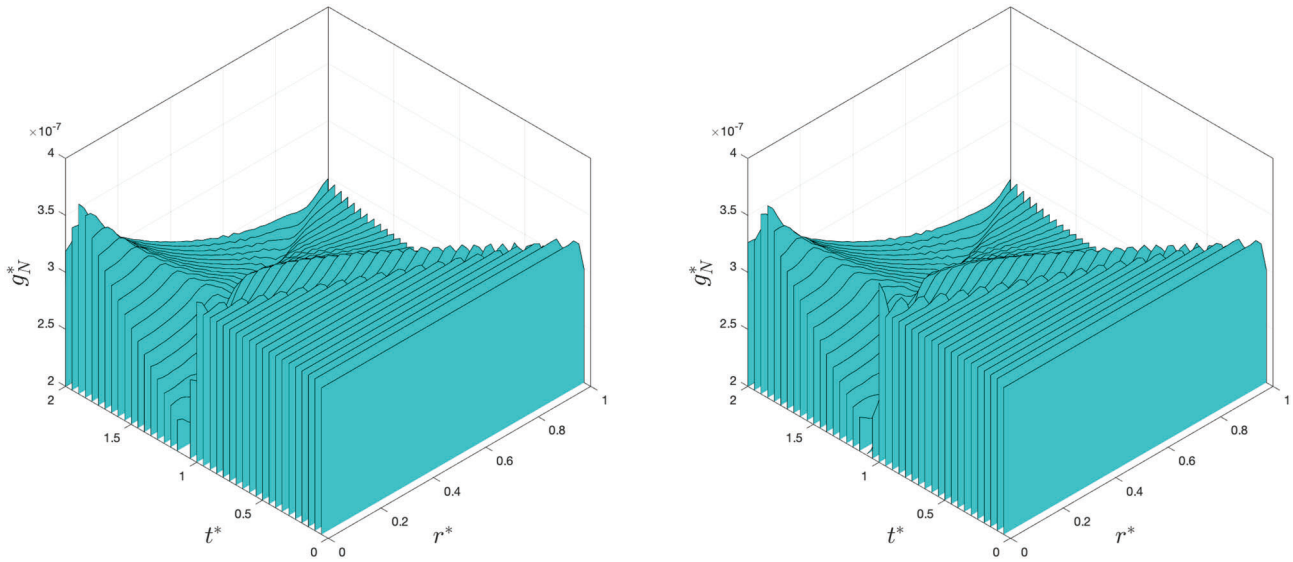


FIGURE 11 Evolution in the contact zone of the normal gap g_N^* for the Taylor test solved with BPM. The exact AMM inverse (left) and the proposed RMM (right) produce almost identical results in terms of violation of the normal gap condition (8)

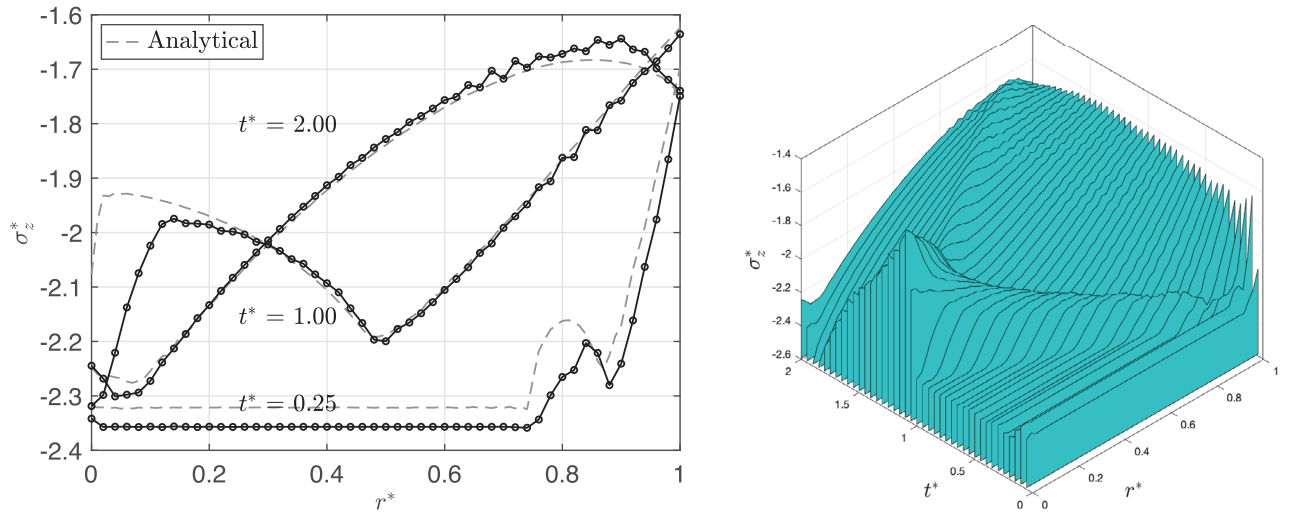


FIGURE 12 Taylor test computed with bipenalty stabilization, scaled element mass matrix, and reciprocal mass matrix. The three highest element frequencies have been reduced to 55% of the initial maximum element frequency and this reduction allows to double the time integration step. We observe that this reduction does not seriously affect accuracy (left) and maintains stability in the contact stresses (right)

An extra performance enhancement can be achieved with an extension of the critical time through element SMS. For this purpose, we apply the technique described in Section 8 and start by performing an eigenvalue analysis of the basic quadrilateral finite element used in the discretization. This computation reveals a dimensionless maximum element frequency $\omega_e^* = 0.6785$, with $\omega_e^* = \omega_e h_e / (2\pi c_L)$ where ω_e is the dimensional element frequency and h_e the element size.

Starting from a parametrized element mass matrix \mathbf{M}_e with $\beta = \frac{1}{2}$, a scaled element mass matrix $\hat{\mathbf{M}}_e$ is constructed using Algorithm 1. The scaled element eigenvalues are defined through (56), by adopting a cut-off frequency $\omega_{cut}^* = 0.3713$ and scaling only the three highest element modes. With this modification, the complete system eigenvalue analysis reveals a higher critical time step $\Delta t_{cr}^* = 0.0171$ and finally the problem is solved using $\Delta t^* = 0.0167$, a time integration step two times larger than the previous one. The results obtained by combining these three different techniques at the same time: BPM stabilization, RMM and SMS, are presented in Figure 12. We observe that the reduction of the maximum element frequencies does not seriously affect accuracy and maintains stable the contact stresses.

In conclusion, the results obtained for the Taylor problem exclusively with stiffness penalization $r = \infty$, contained in Figure 9 (bottom), demonstrate that the standard stiffness penalty contact method is not always able to produce stable results, even integrating in time with a Courant number $C < 1$. On the other hand, Figure 10 reveals that BPM with optimal ratio $r = 1$ yields completely stable solutions. Furthermore, the performance of BPM can be greatly improved by constructing free-body reciprocal mass matrices from scaled element mass matrices, with very similar results as shown in Figure 12.

9.3 | 2D Hertz problem

Finally, we test the performance of the solution algorithm with nonconformal contact and nonmatching meshes. For this task, we choose the 2D dynamic Hertz problem between elastic cylinders. In our case, see Figure 13 (left), both cylinders have the same geometry and material parameters but different discretizations. The radius of cylinders is $R = 4$ m and a linear elastic material with Young's modulus $E = 1000$ Pa, Poisson's ratio $\nu = 0.2$, and density $\rho = 1$ kg/m³ is considered. The initial velocity of the approaching cylinders is given by uniform velocity fields $\mathbf{v}_0^{(1)} = \{0, -v_0\}^T$ and $\mathbf{v}_0^{(2)} = \{0, v_0\}^T$ with $v_0 = 2$ m/s. The problem is modeled as a two-dimensional solid under plane strain condition.

The same problem has been studied by Miyazaki and Park³⁴ and Otto et al.,²⁷ where an analytical approximate solution based on Hertz hypotheses is derived for the distance between the center of the two cylinders and the total contact force as a function of time. This analytical solution is used to assess the quality of the proposed procedure. For this case, the total contact force and energy histories are the monitored quantities.

Nonconformal meshes with different mesh sizes of bilinear four-node and fully integrated quadrilateral elements are used to discretize the cylinders, with a size ratio of master-slave contact elements of 0.75, as represented in Figure 13 (right). The Gauss-point-to-segment (GPTS) contact algorithm described by Otto et al.²⁷ is used, with twenty quadrature points per contact segment, considering the upper cylinder with coarser mesh as the master surface and the lower one with finer mesh the slave.

This problem differs from the previous numerical examples in that the contact boundary is not known a priori and the size of the contact zone changes with time. It is, therefore, a full-fledged contact process that introduces certain difficulties. Mainly, the evolving contact boundary that activates different contact quadrature points/contact nodes in successive time steps. In this case, it has been observed that a larger time step increases the error of contact boundary estimation in the predictor part of the predictor–corrector algorithm. As a result, although the time step is selected close

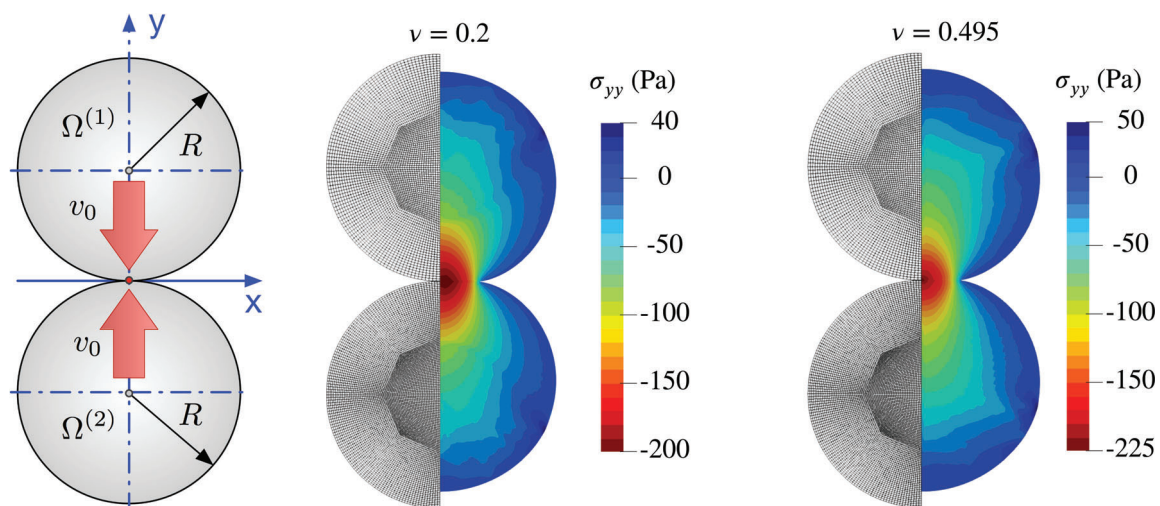


FIGURE 13 Scheme of the dynamic Hertz problem of two elastic cylinders of the same radius R impacting each other with initial velocity v_0 (left). The domains $\Omega^{(1)}$ and $\Omega^{(2)}$ are considered as the master and slave body, respectively. Nonconforming meshes are used, with a size ratio of master/slave contact elements of 0.75. Detail of the nonmatching cylinder meshes and contour of vertical stresses at time $t = 0.379$ s for Poisson's ratio $\nu = 0.2$ (middle), and the quasi-incompressible case $\nu = 0.495$ (right)

to the critical time step with respect to the stability limit, the solution may include oscillations caused by inaccurate prediction of the contact boundary. It has been observed that these oscillations disappear for lower values of the time step.

9.3.1 | Classical stiffness penalty and BPM

Like in the previous example, the problem is solved first using the classical stiffness penalty approach. The dimensionless penalty parameter is chosen to be $\epsilon_s^* = 4.7$ which, according to the graph of Figure 8, corresponds to a critical Courant number $C_{cr} = 0.75$ for the classical stiffness penalty method, that is, with factor $r \rightarrow \infty$. Eigenvalue analysis of the unconstrained mesh reveals a maximum frequency with critical time step $\Delta t_{cr} = 1.12$ ms. To ensure the stability of the time integration, a stable value of the Courant number $C = 0.707$ was chosen and the solution is computed using the time-step size $\Delta t = 0.79$ ms. At the same time, the problem is solved with identical dimensionless penalty parameter, $\epsilon_s^* = 4.7$, and the time step size, $\Delta t_{cr} = 0.79$ ms, using a monolithic BPM contact algorithm without decoupling the contact zone from the body equations and with factor $r = 1$.

The results of both approaches are compared in Figure 14. On the left, we see the time course of the contact force and on the right the energy balance. The evolution of the contact force for the classical stiffness penalty method in Figure 14 (upper left) shows considerable oscillations. From the course of the energy balance in Figure 14 (upper right), we can see that the loss of stability of the time integration occurred only at the end during the unloading of the cylinders just before the end of the impact. It can, therefore, be assumed that this behavior is due to the geometric instability caused by the changing contact boundary.

In contrast, the time course of the contact force for the monolithic BPM contact analysis shown in Figure 14 (bottom left) shows no oscillations and closely matches the numerical result obtained by Otto et al.²⁷ using a nonlinear penalty regularization. From the course of the energy balance in Figure 14 (bottom right), we see that the total energy is conserved

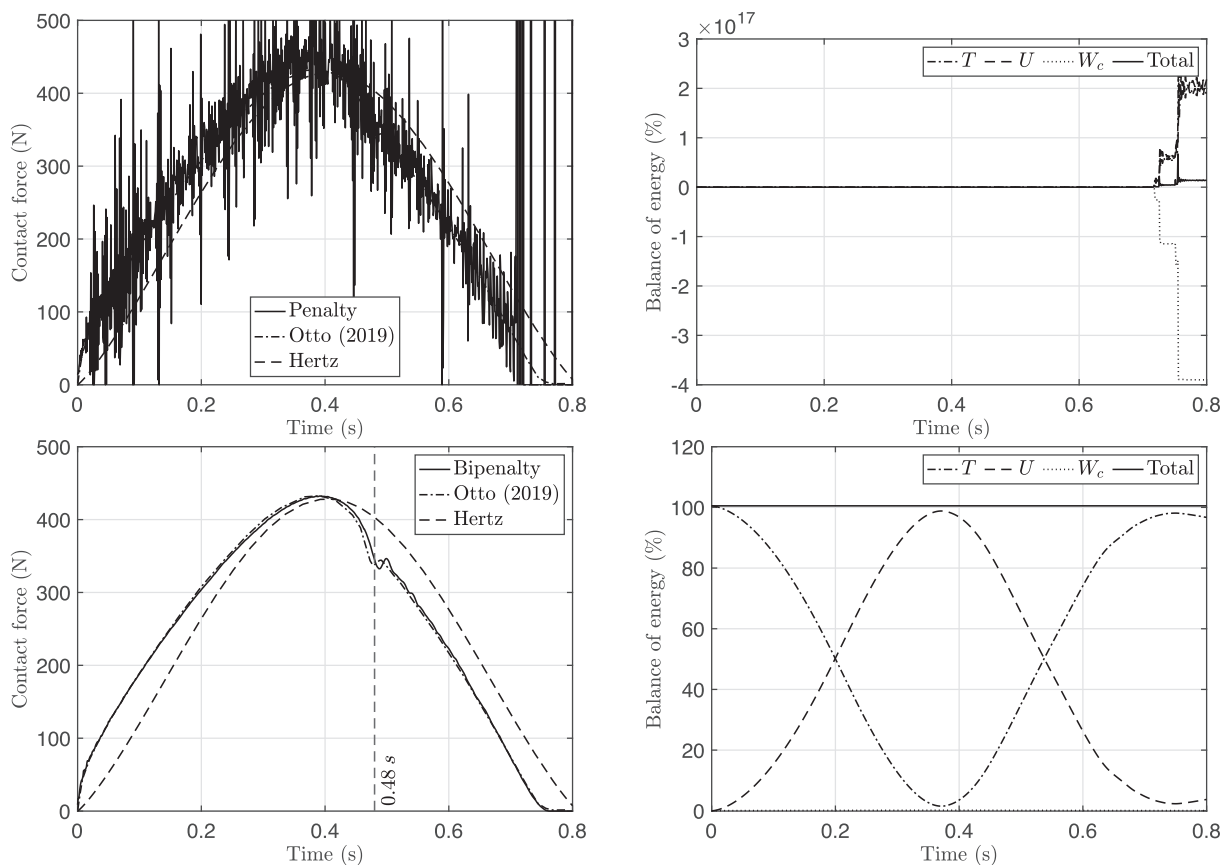


FIGURE 14 Dynamic Hertz problem solved with Courant number $C = 0.707$ and exact CMM. Results obtained using the classical stiffness penalty method (top) and BPM with $r = 1$ (bottom)

throughout the time integration. Note that the work done by the contact forces is very small, which indicates that the contact restrictions are satisfied with almost zero penetration.

The Hertz analytical solution assumes that the contact surfaces are small and that the inertial forces are equally distributed in the cylinders. As a result, the propagation of elastic waves in the cylinders is not considered. This analytical solution thus underestimates the contact forces at the beginning of the impact, when the inertia of the body near the contact interface increases the contact forces and, during the unloading of the impact, overestimates the contact forces, when the velocity of the cylinder centers decreases. The omission of the effect of elastic wave propagation is clearly visible at time $t = 4R/c_L = 0.48$ s, 14 (bottom left), when the oscillation caused by the reflection of the longitudinal elastic wave occurs and that is only captured by the numerical solution. Logically, Hertz's solution is not able to reproduce this small oscillation in the contact force and in general any phenomena associated to wave propagation.

9.3.2 | RMM and SMS

Although the results obtained with the monolithic BPM analysis and exact CMM are qualitatively satisfactory, it is noted that a repeated inversion of the penalized global mass matrix is required every time the contact conditions change. This process is inadequate from the point of view of numerical performance and the proposed RMM approach is much more efficient. Specifically, to increase the accuracy, AMM is employed and the RMM calculated using Algorithm 1. The inversion of the penalized global mass matrix is then avoided by adopting the partitioned formulation described in Algorithm 2. Eigenvalue analysis of the unconstrained mesh with averaged mass matrix reveals a critical time step $\Delta t_{cr} = 0.9$ ms which is about twenty percent smaller than that the time-step needed for a LMM. Considering the same stable value of the Courant number, $C = 0.7$, the solution is computed using the time-step size $\Delta t = 0.64$ ms. The results for the input parameters defined in this way are shown in Figure 15 (top).

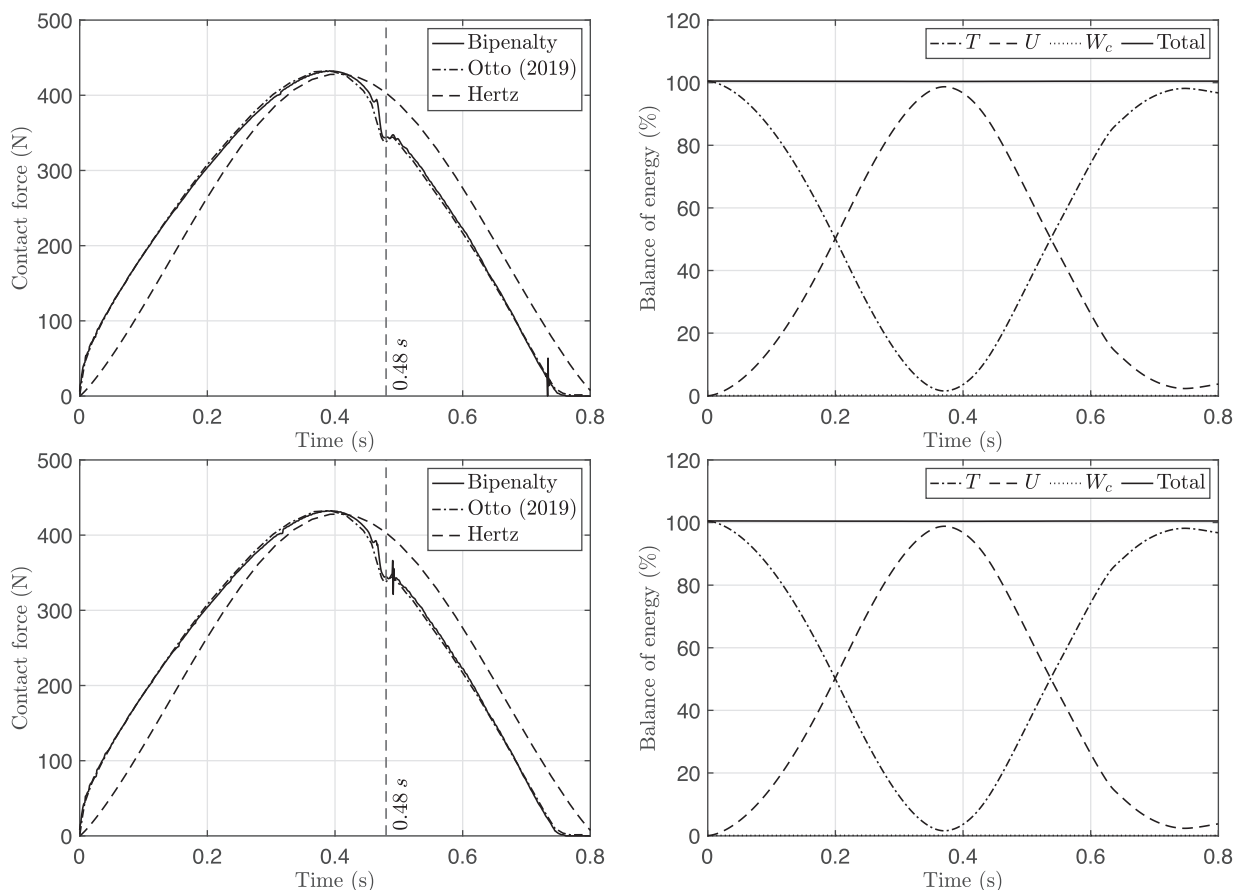


FIGURE 15 Dynamic Hertz problem solved with Courant number $C = 0.707$ and the averaged reciprocal mass matrix. Results obtained using bipenalty with the complete RMM (top) and RMM scaled with a cut-off frequency $\omega_{cut} = 1600$ rad/s (bottom)

In addition, if the SMS technique introduced in this article is employed, the time step can be further increased. In Figure 15 (bottom) the results for the cut-off angular frequency $\omega_{\text{cut}} = 1600$ rad/s are presented. This value of cut-off frequency leads to a time-step size $\Delta t = 0.81$ ms which is slightly larger than the case with a diagonal LMM. Except for a single oscillation of the contact force, the results in Figure 15 agree well with the solution obtained using the monolithic BPM without partitioning. This leads us to the conclusion that the proposed approach greatly improves the numerical performance of the stabilized BPM for contact analysis.

Finally, the same problem is analyzed with Poisson's ratio $\nu = 0.495$ to model a quasi-incompressible elastic material. Due to the new incompressibility constraint, the velocity of the longitudinal waves is multiplied by a factor $c_{L2}/c_{L1} = 5.5137$ while the transverse wave speed is slightly reduced to $c_{T2}/c_{T1} = 0.8959$. Hertz theory also predicts a 12.7% increment of the maximum contact pressure. The cylinders are discretized using the same nonmatching meshes as in the previous case and the mean dilation method is applied to alleviate the volumetric locking effects. Figure 13 (right) contains the results for a RMM constructed with $\beta = \frac{1}{2}$ and applying SMS with $\omega_{\text{cut}} = 1600$ rad/s. Specifically, the contours of vertical stresses produced at the instant of maximum contact force $t = 0.378$ s are shown in this figure.

10 | CONCLUSIONS

A combination of four related techniques for the solution of contact-impact problems has been proposed, which consists of mass–stiffness bipenalty method (BPM) for stabilization of the contact constraints, reciprocal mass matrices (RMM) to improve computational efficiency, localized Lagrange multipliers (LMM) for a simpler combination of the two previous methods, prediction–correction-based time integration for the control of oscillations and selective mass scaling (SMS) to extend the critical time-step. The resulting methodology is completely element-independent and can be easily adapted to different contact formulation approaches.

In view of the results obtained from the solutions of benchmark problems, we can conclude the following:

- In BPM, for an arbitrary value of the stiffness penalty parameter, by setting the mass–stiffness penalty ratio to the critical value $r = 1$ it is possible to preserve a stable Courant number at the level of the unpenalized system. Contrary to what occurs with the classical penalty method, the BPM variants permit to increase the stiffness penalty and maintain stability without reducing the critical time-step.
- BPM and RMM can be effectively combined by using a partitioned approach based on LLM. This way, mass matrix factorizations are not needed and the operation count per time-step of explicit integration methods is reduced to a sparse-matrix vector multiplication with nm flops, where n is the number of DOFs and m is the average number of nonzero entries per row. This allows to use nondiagonal global mass matrices in an efficient way, increasing accuracy for contact-impact problems.
- For high values of the stiffness penalty, BPM cures the stability problems while a predictor–corrector contact algorithm can be an effective tool to control oscillations in the contact stresses associated to the nonsmooth character of the normal contact law. However, this condition is not fulfilled by other time integration schemes. For example, BPM combined with classical central differences would preserve stability but not eliminate the contact oscillations.
- The proposed element-by-element SMS allows to multiply the critical time step by a factor of two without severe degradation of the solution. Although this seems a modest improvement, note that combined with BPM we are doubling the critical time-step corresponding to the case without penalization. This gain may be further increased by adopting partition-by-partition SMS strategies.⁴⁸
- With BPM and scaling the RMM it is possible to make computations with larger time-steps than the critical time-step for a diagonal lumped mass matrix with better accuracy. Also the computational effort per time-step would be comparable to the use of diagonal mass matrices.

In conclusion, the proposed methodology is nonintrusive and simple to implement, hence it can be easily adapted to existent explicit codes with the objective of improving their performance and accuracy in the simulation of penalty contact-impact problems. As future work, we plan to extend the formulation for contact-impact problems under nonlinear mechanical behaviors (e.g., large plasticity problems) including dynamic instability problems and friction.

ACKNOWLEDGMENTS

The work of J. Kopačka has been supported by the grant projects with No. GA19-14237S of the Czech Science Foundation (CSF) within institutional support RVO:61388998. The work of R. Kolman has been funded by the project No. CZ.02.1.01/0.0/0.0/15_003/0000493, Centre of Excellence for Nonlinear Dynamic Behaviour of Advanced Materials in Engineering (CeNDYNMAT) from the European Structural and Investment Funds, Operational Programme Research, Development and Education of the European Union.

DATA AVAILABILITY STATEMENT


The data that support the findings of this study are available from the corresponding author upon reasonable request.

ORCID

José A. González  <https://orcid.org/0000-0003-3282-0049>

Ján Kopačka  <https://orcid.org/0000-0002-2975-8347>

Radek Kolman  <https://orcid.org/0000-0002-8167-3535>

Kwang-Chun Park  <https://orcid.org/0000-0002-6303-1010>

REFERENCES

1. Wriggers P. *Computational Contact Mechanics*. 2nd ed. New York, NY: Springer; 2006.
2. Hallquist JO, Goudreau GL, Benson DJ. Sliding interfaces with contact-impact in large-scale Lagrangian computations. *Comput Methods Appl Mech Eng*. 1985;51(1–3):107-137. [https://doi.org/10.1016/0045-7825\(85\)90030-1](https://doi.org/10.1016/0045-7825(85)90030-1).
3. Benson DJ, Hallquist JO. A single surface contact algorithm for the post-buckling analysis of shell structures. *Comput Methods Appl Mech Eng*. 1990;78(2):141-163. [https://doi.org/10.1016/0045-7825\(90\)90098-7](https://doi.org/10.1016/0045-7825(90)90098-7).
4. Belytschko T, Neal MO. Contact-impact by the pinball algorithm with penalty and Lagrangian methods. *Int J Numer Methods Eng*. 1991;31:547-572. <https://doi.org/10.1002/nme.1620310309>.
5. Carpenter NJ, Taylor RL, Katona MG. Lagrange constraints for transient finite element surface contact. *Int J Numer Methods Eng*. 1991;32(1):103-128. <https://doi.org/10.1002/nme.1620320107>.
6. Benson DJ. Computational methods in Lagrangian and Eulerian hydrocodes. *Comput Methods Appl Mech Eng*. 1992;99(2):235-394. [https://doi.org/10.1016/0045-7825\(92\)90042-I](https://doi.org/10.1016/0045-7825(92)90042-I).
7. Heinstein MW, Mello FJ, Attaway SW, Laursen TA. Contact-impact modeling in explicit transient dynamics. *Comput Methods Appl Mech Eng*. 2000;187(3–4):621-640. [https://doi.org/10.1016/S0045-7825\(99\)00342-4](https://doi.org/10.1016/S0045-7825(99)00342-4).
8. Cirak F, West M. Decomposition contact response (DCR) for explicit finite element dynamics. *Int J Numer Methods Eng*. 2005;64(8):1078-1110. <https://doi.org/10.1002/nme.1400>.
9. Courant R, Friedrichs K, Lewy H. On the partial difference equations of mathematical physics. *IBM J Res Dev*. 1967;11(2):215-234.
10. Baumgarte J. Stabilization of constraints and integrals of motion in dynamical systems. *Comput Methods Appl Mech Eng*. 1972;1(1):1-16. [https://doi.org/10.1016/0045-7825\(72\)90018-7](https://doi.org/10.1016/0045-7825(72)90018-7).
11. Asano N. A virtual work principle using penalty function method for impact contact problems of two bodies. *Bull JSME*. 1986;29(249):731-736. <https://doi.org/10.1299/jsme1958.29.731>.
12. Armero F, Petöcz E. Formulation and analysis of conserving algorithms for frictionless dynamic contact/impact problems. *Comput Methods Appl Mech Eng*. 1998;158(3–4):269-300. [https://doi.org/10.1016/S0045-7825\(97\)00256-9](https://doi.org/10.1016/S0045-7825(97)00256-9).
13. Paraskevopoulos EA, Panagiotopoulos CG, Manolis GD. Imposition of time-dependent boundary conditions in FEM formulations for elastodynamics: critical assessment of penalty-type methods. *Comput Mech*. 2009;45(2):157. <https://doi.org/10.1007/s00466-009-0428-x>.
14. Panagiotopoulos CG, Paraskevopoulos EA, Manolis GD. Critical assessment of penalty-type methods for imposition of time-dependent boundary conditions in FEM formulations for elastodynamics. *Computational Methods in Earthquake Engineering*. Dordrecht, Netherlands: Springer; 2011:357-375.
15. Hetherington J, Askes H. Penalty methods for time domain computational dynamics based on positive and negative inertia. *Comput Struct*. 2009;87(23–24):1474-1482. <https://doi.org/10.1016/j.compstruc.2009.05.011>.
16. Hetherington J, Rodríguez-Ferran A, Askes H. A new bipenalty formulation for ensuring time step stability in time domain computational dynamics. *Int J Numer Methods Eng*. 2012;90:269-286. <https://doi.org/10.1002/nme.3314>.
17. Hetherington J, Rodríguez-Ferran A, Askes H. The bipenalty method for arbitrary multipoint constraints. *Int J Numer Methods Eng*. 2013;93:465-482. <https://doi.org/10.1002/nme.4389>.
18. Kopačka J, Tkachuk A, Gabriel D, Kolman R, Bischoff M, Plešek J. On stability and reflection-transmission analysis of the bipenalty method in contact-impact problems: a one-dimensional, homogeneous case study. *Int J Numer Methods Eng*. 2018;113(10):1607-1629. <https://doi.org/10.1002/nme.5712>.
19. Kolman R, Kopačka J, González JA, Cho SS, Park KC. Bi-penalty stabilized technique with predictor-corrector time scheme for contact-impact problems of elastic bars. *Math Comput Simul*. 2021. <https://doi.org/10.1016/j.matcom.2021.03.023>.
20. Doyen D, Ern A, Piperno S. Time-integration schemes for the finite element dynamic Signorini problem. *SIAM J Sci Comput*. 2011;33(1):223-249. <https://doi.org/10.1137/100791440>.

21. Kane C, Reppetto EA, Ortiz M, Marsden JE. Finite element analysis of nonsmooth contact. *Comput Methods Appl Mech Eng*. 1999;180:1-26. [https://doi.org/10.1016/S0045-7825\(99\)00034-1](https://doi.org/10.1016/S0045-7825(99)00034-1).
22. Deuffhard P, Krause R, Ertel S. A contact-stabilized Newmark method for dynamical contact problems. *Int J Numer Methods Eng*. 2008;73(9):1274-1290. <https://doi.org/10.1002/nme.2119>.
23. Khenous HB, Laborde P, Renard Y. Mass redistribution method for finite element contact problems in elastodynamics. *Eur J Mech A/Solids*. 2008;27:918-932. <https://doi.org/10.1016/j.euromechsol.2008.01.001>.
24. Tkachuk A, Wohlmuth BI, Bischoff M. Hybrid-mixed discretization of elasto-dynamic contact problems using consistent singular mass matrices. *Int J Numer Methods Eng*. 2013;94(5):473-493. <https://doi.org/10.1002/nme.4457>.
25. Renard Y. The singular dynamic method for constrained second order hyperbolic equations: application to dynamic contact problems. *J Comput Appl Math*. 2010;234(3):906-923. <https://doi.org/10.1016/j.cam.2010.01.058>.
26. Otto P, De Lorenzis L, Unger JF. A regularized model for impact in explicit dynamics applied to the split Hopkinson pressure bar. *Comput Mech*. 2016;58(4):681-695. <https://doi.org/10.1007/s00466-016-1311-1>.
27. Otto P, De Lorenzis L, Unger JF. Explicit dynamics in impact simulation using a NURBS contact interface. *Int J Numer Methods Eng*. 2020;121(6):1248-1267. <https://doi.org/10.1002/nme.6264>.
28. Wu SR. A variational principle for dynamic contact with large deformation. *Comput Methods Appl Mech Eng*. 2009;198:2009-2015. <https://doi.org/10.1016/j.cma.2008.12.013>.
29. Duczek S, Gravenkamp H. Critical assessment of different mass lumping schemes for higher order serendipity finite elements. *Comput Methods Appl Mech Eng*. 2019;350:836-897. <https://doi.org/10.1016/j.cma.2017.08.035>.
30. Tkachuk A, Bischoff M. Direct and sparse construction of consistent inverse mass matrices: general variational formulation and application to selective mass scaling. *Int J Numer Methods Eng*. 2015;101(6):435-469. <https://doi.org/10.1002/nme.4805>.
31. Tkachuk A. Reciprocal mass matrices and a feasible time step estimator for finite elements with Allman's rotations. *Int J Numer Methods Eng*. 2020;122(5):1401-1422. <https://doi.org/10.1002/nme.6583>.
32. González JA, Kolman R, Cho SS, Felippa CA, Park KC. Inverse mass matrix via the method of localized lagrange multipliers. *Int J Numer Methods Eng*. 2017;113(2):277-295. <https://doi.org/10.1002/nme.5613>.
33. Rebel G, Park KC, Felippa CA. A contact formulation based on localized Lagrange multipliers: formulation and application to two-dimensional problems. *Int J Numer Methods Eng*. 2002;54:263-297. <https://doi.org/10.1002/nme.426>.
34. Miyazaki Y, Park KC. A formulation of conserving impact system based on localized Lagrange multipliers. *Int J Numer Methods Eng*. 2006;68:98-124. <https://doi.org/10.1002/nme.1703>.
35. González JA, Park KC, Felippa C, Abascal R. A formulation based on localized Lagrange multipliers for BEM-FEM coupling in contact problems. *Comput Methods Appl Mech Eng*. 2008;197:623-640. <https://doi.org/10.1016/j.cma.2007.08.020>.
36. Macek RW, Aubert BH. A mass penalty technique to control the critical time increment in explicit dynamic finite element analyses. *Earthq Eng Struct Dyn*. 1995;24(10):1315-1331. <https://doi.org/10.1002/eqe.4290241003>.
37. Olovsson L, Unosson M, Simonsson K. Selective mass scaling for thin walled structures modeled with tri-linear solid elements. *Comput Mech*. 2004;34(2):134-136. <https://doi.org/10.1007/s00466-004-0560-6>.
38. Olovsson L, Simonsson K. Selective mass scaling for explicit finite element analyses. *Int J Numer Methods Eng*. 2005;63(10):1436-1445. <https://doi.org/10.1002/nme.1293>.
39. Askes H, Nguyen D, Tyas A. Increasing the critical time step: micro-inertia, inertia penalties and mass scaling. *Comput Mech*. 2011;47(6):657-667. <https://doi.org/10.1007/s00466-010-0568-z>.
40. Cocchetti G, Pagani M, Perego U. Selective mass scaling and critical time-step estimate for explicit dynamics analyses with solid-shell elements. *Comput Struct*. 2013;127:39-52. <https://doi.org/10.1016/j.compstruc.2012.10.021>.
41. Lombardo M, Askes H. Lumped mass finite element implementation of continuum theories with micro-inertia. *Int J Numer Methods Eng*. 2013;96(7):448-466. <https://doi.org/10.1002/nme.4570>.
42. Ye W, Bel-Brunon A, Catheline S, Rochette M, Combescure A. A selective mass scaling method for shear wave propagation analyses in nearly incompressible materials. *Int J Numer Methods Eng*. 2017;109(2):155-173. <https://doi.org/10.1002/nme.5276>.
43. Tkachuk A, Bischoff M. Variational methods for selective mass scaling. *Comput Mech*. 2013;52:563-570. <https://doi.org/10.1007/s00466-013-0832-0>.
44. Tkachuk A, Bischoff M. Local and global strategies for optimal selective mass scaling. *Comput Mech*. 2014;53:1197-1207. <https://doi.org/10.1007/s00466-013-0961-5>.
45. Schaeuble AK, Tkachuk A, Bischoff M. Variationally consistent inertia templates for B-spline- and NURBS-based FEM: inertia scaling and customization. *Comput Methods Appl Mech Eng*. 2017;326:596-621. <https://doi.org/10.1016/j.cma.2017.08.035>.
46. González JA, Kopačka J, Kolman R, Cho SS, Park KC. Inverse mass matrix for isogeometric explicit transient analysis via the method of localized Lagrange multipliers. *Int J Numer Methods Eng*. 2019;117:939-966. <https://doi.org/10.1002/nme.5986>.
47. Park KC, Felippa CA. A variational principle for the formulation of partitioned structural systems. *Int J Numer Methods Eng*. 2000;47:395-418. [https://doi.org/10.1002/\(SICI\)1097-0207\(200011/30\)47:1/3<395::AID-NME777>3.0.CO;2-9](https://doi.org/10.1002/(SICI)1097-0207(200011/30)47:1/3<395::AID-NME777>3.0.CO;2-9).
48. González J, Park KC. Large-step explicit time integration via mass matrix tailoring. *Int J Numer Methods Eng*. 2020;121(8):1647-1664. <https://doi.org/10.1002/nme.6282>.
49. Hauret P, Le Tallec P. Energy-controlling time integration methods for nonlinear elastodynamics and low-velocity impact. *Comput Methods Appl Mech Eng*. 2006;195(37):4890-4916. <https://doi.org/10.1016/j.cma.2005.11.005>.
50. Lamichhane BP, Wohlmuth BI. Biorthogonal bases with local support and approximation properties. *Math Comput*. 2007;76(257):233-249. <https://doi.org/10.1090/S0025-5718-06-01907-7>.

51. Seitz A, Farah P, Kremheller J, Wohlmuth BI, Wall WA, Popp A. Isogeometric dual mortar methods for computational contact mechanics. *Comput Methods Appl Mech Eng*. 2016;301:259-280. <https://doi.org/10.1016/j.cma.2015.12.018>.
52. Wu SR. A priori error estimates for explicit finite element for linear elasto-dynamics by Galerkin method and central difference method. *Comput Methods Appl Mech Eng*. 2003;192(81):5329-5323. <https://doi.org/10.1016/j.cma.2003.08.002>.
53. Felippa CA, Guo Q, Park KC. Mass matrix templates: general description and 1D examples. *Arch Comput Methods Eng*. 2015;22(1):1-65. <https://doi.org/10.1007/s11831-014-9108-x>.
54. Auricchio F, Beirão da Veiga L, Hughes TJR, Reali A, Sangalli G. Isogeometric collocation for elastostatics and explicit dynamics. *Comput Methods Appl Mech Eng*. 2012;249-252:2-14. <https://doi.org/10.1016/j.cma.2012.03.026>.
55. Krenk S. Dispersion-corrected explicit integration of the wave equation. *Comput Methods Appl Mech Eng*. 2001;191(8-10):975-987. [https://doi.org/10.1016/S0045-7825\(01\)00297-3](https://doi.org/10.1016/S0045-7825(01)00297-3).
56. Frias G, Aquino W, Pierson K, Heinstein M, Spencer B. A multiscale mass scaling approach for explicit time integration using proper orthogonal decomposition. *Int J Numer Methods Eng*. 2014;97:799-818. <https://doi.org/10.1002/nme.4608>.
57. Huněk I. On a penalty formulation for contact-impact problems. *Comput Struct*. 1993;48(2):193-203. [https://doi.org/10.1016/0045-7949\(93\)90412-7](https://doi.org/10.1016/0045-7949(93)90412-7).
58. Graff KF. *Wave Motion in Elastic Solids*. New York: Dover Publications; 1975.
59. Park KC, Lim SJ, Huh H. A method for computation of discontinuous wave propagation in heterogeneous solids: basic algorithm description and application to one-dimensional problems. *Int J Numer Methods Eng*. 2012;91:622-643. <https://doi.org/10.1002/nme.4285>.
60. Kolman R, Plešek J, Červ J, Okrouhlík M, Pařík P. Temporal-spatial dispersion and stability analysis of finite element method in explicit elastodynamics. *Int J Numer Methods Eng*. 2015;106(2):113-128. <https://doi.org/10.1002/nme.5010>.
61. Červ J, Adamek V, Valeš F, Gabriel D, Plešek J. Wave motion in a thick cylindrical rod undergoing longitudinal impact. *Wave Motion*. 2016;66:88-105. <https://doi.org/10.1016/j.wavemoti.2016.05.007>.

How to cite this article: González JA, Kopačka J, Kolman R, Park K. Partitioned formulation of contact-impact problems with stabilized contact constraints and reciprocal mass matrices. *Int J Numer Methods Eng*. 2021;122:4609-4636. <https://doi.org/10.1002/nme.6739>

